CERN–2009–01
CARE–Conf–08–029–HHH
19 January 2009

ORGANISATION EUROPÉENNE POUR LA RECHERCHE NUCLÉAIRE
CERN EUROPEAN ORGANIZATION FOR NUCLEAR RESEARCH

WAMSDO Workshop

Accelerator magnet superconductors, design and optimization

CERN, Geneva, Switzerland, 19–23 May 2008

Proceedings

Editor: E. Todesco

GENEVA
2009

CERN–300 copies printed–January 2009

Abstract

This report contains the proceedings of the CARE-HHH-AMT Workshop on Accelerator Magnet Superconductors, Design and Optimization (WAMSDO) held at CERN from 19 to 23 May 2008. The needs in terms of superconducting magnets for the accelerator projects were discussed, mainly for the LHC interaction regions and injector upgrades, and for the GSI FAIR complex. The first part of the workshop focused on the development of superconductor and cables, i.e., low-loss Nb-Ti cables, Nb_3Sn and high-temperature superconductors. An industry session summarized the actual plans and status of the activities in the main European industries. Then, a worldwide status of the high field magnets programme was presented. A special session was devoted to fast cycled magnets, including FAIR facilities and LHC injector upgrades. A final session focused on the optimization methods and numerical tools for magnet design.

Preface

The science (or, as many would say, the art) of superconducting magnets for accelerators relies on knowledge of several different fields, such as electromagnetism, mechanics and material science. This is the third and last of the workshops on magnet design organized in the framework of the European Programme FP6 by the CARE-HHH network. The first workshop, WAMS, was more focused on superconductors, and the second one, WAMDO, rather on magnet design and optimization. In this third workshop we include aspects concerning both magnet design and superconductor development, to describe the present status and to draw perspectives for future R&D activities.

Magnet requirements

The opening session of the workshop was devoted to the magnet requirements coming from current or future projects. The possibilities for a LHC luminosity upgrade have been studied for several years, requiring the difficult task of identifying the LHC luminosity bottlenecks before having the first collisions. The unanimous opinion is that the present 70 mm aperture of the interaction region quadrupoles is too small, and that larger-aperture quadrupoles are needed. The upgrade has recently been split into two phases: the first one, scheduled for 2013, requires 120 mm aperture 10-m-long quadrupoles in Nb-Ti (see the contribution of R. Ostojic, p. 1). This first phase aims at an increase of a factor 2.5 with respect to nominal luminosity, i.e., 2.5×10^{34} cm^{-2}s^{-1}. Half of this increase would come from the stronger focusing (β^* = 0.25 m instead of 0.55 m) allowed by the larger-aperture quadrupoles, and the other half from an increase of the bunch intensity. A second phase would push the focusing to the limit given by the Nb_3Sn technology, i.e., $\beta^* = 0.15$ m, through quadrupoles with an even larger aperture of 130–150 mm. This quadrupole aperture is somewhat larger than the original proposal made by the U.S. LHC Accelerator Research Program (LARP), which considered 90 mm aperture magnets. Today several 90 mm aperture models are being built, successfully validating the technology, and a 120 mm aperture quadrupole, which could be used as a spare for Phase I, is in the design phase.

The upgrade of the chain of the LHC injectors has also been the object of a long series of studies: today, LINAC4 has just started the civil engineering works and a conceptual design for the PS upgrade (PS2) is being finalized. Even though the present baseline for the PS2 considers normal conducting magnets, a superferric option is still on the table. This option could also be interesting for a future upgrade of the SPS. This requirement of relatively low field (2–4 T), fast cycling magnets also comes from the construction of SIS 100 and SIS 300 in GSI, Darmstadt. Both a superferric option and a standard cosθ design with low losses are being considered. These magnets could offer a reliable and more environmentally friendly alternative to the normal conducting technology.

In order to test cables used for superconducting magnets, one needs a background magnetic field which is usually generated by solenoids and/or dipoles. These magnets used in test facilities need a large aperture to house the samples. At CERN, a replacement of the FRESCA facility with a 100 mm aperture dipole in the range of 13–15 T, making use of the NED cable, is under study.

For a linear collider such as the ILC or CLIC, a large set of superconducting magnets is foreseen (see the slides of M. Tartaglia available on the conference web site `http://indico.cern.ch/conferenceDisplay.py?confId=28832`): for example, the foreseen ILC hardware zoo includes quadrupoles, steering dipoles, wigglers and undulators; in most cases the chosen option is the superferric one. Future projects such as muon colliders or neutrino factories present the challenging feature of having a large radiation load in the beam mid-plane: this could require innovative solutions for the magnet design such as the open mid-plane option, strongly supported by R. Gupta in recent years. The Farthest Energy Frontier (FEF) which is conceivable today with present technology, infrastructure and costs limitations is the LHC doubler (see the slides of L. Evans available

on the conference web site `http://indico.cern.ch/conferenceDisplay.py?confId=28832`). This new machine, making use of most of the LHC infrastructure, would require 15 T dipoles in Nb_3Sn with an aperture of about 40 mm. The LBNL model HD2, recently tested, has parameters which fall in this range.

The first results from LHC physics will be an extremely important piece of information to help understand where to go.

Materials, strands and cables

The research on superconductors is focused on several issues. For the Nb-Ti, which has been the workhorse for accelerator magnets for 30 years, the main research line aims at low-loss cables for fast cycling magnets. The topic of losses in superconducting fast cycling magnets is still far from being closed, both theoretically and from a manufacturing point of view. The main challenge is to find a strand layout that can minimize losses, achieve the necessary J_c, and that can be manufactured. Getting a strand with thinner and thinner filament size is not the only issue: considerations about the transverse resistivity, the geometry of the cable, and the design of the whole magnet are also relevant (see the contributions by M. N. Wilson, G. Volpini, U. Gambardella, and V. Pantsyrny, pp. 8–23). An extension of the work on low-loss cables to Nb_3Sn was presented by T. Collings, p. 42.

Nb_3Sn has for a long time been considered as the natural successor of Nb-Ti, allowing to roughly double the field from 8–10 T to 15–20 T, in the same range of temperatures (1.9–4.2 K). The progress in the development of Nb_3Sn cables towards larger critical currents has been impressive: in the past ten years the current density in the non-copper part has doubled (see the A. Godeke and T. Boutboul contributions, pp. 24–29). At the same time, recent analyses show that very large critical current densities can produce self-field instabilities limiting the performances (see the contribution by B. Bordini, p. 51); this analysis accounts for the reduced performance of LARP quadrupoles at 1.9 K. This could be the sign that the quest for larger and larger current densities at 12–15 T has reached its natural limit, or that, if one wants to still pursue this direction, new parameters have to be taken into account in the cable design.

One of the main issues of Nb_3Sn is its sensitivity to strain. Several techniques can be used to study this complex issue and many other characteristics, related both to the strand layout and to the magnet design and optimization. Metallographic techniques, calorimetric analysis, synchrotron radiation, and measurements of critical current under strain have been used for Nb_3Sn strands for the ITER and for the NED projects (see contributions by M. Jewell, C. Scheuerlein, and B. Seeber pp. 30–41).

A special cable layout used for fusion projects such as ITER is the so-called cable-in-conduit, aiming at higher current and having a more efficient cooling with respect to the Rutherford cable used for accelerator magnets. A full review of the performance of both Nb-Ti and Nb_3Sn cable-in-conduit used in ITER is given in the contribution of R. Wesche, p. 68.

For accelerator magnets, and even more for fusion magnets, the issue of radiation resistance is critical. A complete overview of the radiation resistance of Nb-Ti and Nb_3Sn, focused on a particle spectrum relative to the debris of the collision in the LHC upgrade, can be found in the contribution by R. Flükiger, p. 55. With the present knowledge of radiation loads, both Nb-Ti and Nb_3Sn should not suffer from a degradation of performance over the expected lifetime of the magnets. The limitation to the magnet lifetime would rather come from other materials such as the plastic used for end spacers or the epoxy used for Nb_3Sn impregnation.

New superconductors are discovered every year, and some materials have shown impressive progress. This is the case of MgB_2, a material which was discovered in 2001, whose field range is 2–4 T at 20 K and 5–10 T at 4.2 K. The current industrial developments aiming at having long cables with large current densities are described in the contributions of G. Grasso and G. Giunchi, pp. 78–88. High-temperature superconductors have been used for power lines and current leads in the LHC. The current state-of-the-art of HTS materials, mainly Bi-2212 and YBaCuO, and their applications, is given in the contributions of P. Tixador and of M. Noe, pp. 89–97.

High-field magnets

The results on high-field magnets constitute the core of these proceedings. The present design for the Nb-Ti upgrade of the LHC interaction quadrupoles is presented by P. Fessia, p. 101. Three different projects aiming at constructing accelerator-quality Nb_3Sn magnets are under way in the U.S. The LARP collaboration is building large-aperture quadrupoles for the LHC interaction region upgrade, including several short models to test two mechanical structures, and a 3.4-m-long model, see the contributions of P. Ferracin, P. Wanderer, S. Caspi, and H. Felice, pp. 105–122. FNAL is developing high-field long dipoles, and LBNL has built and tested a short dipole based on a block coil and a bladder and keys structure, reaching a bore field of 13.5 T, see the contribution of P. Ferracin, p. 105.

Europe, mainly busy during the past ten years with LHC construction, started the NED programme in 2004 to develop a Nb_3Sn conductor within European industry. The programme is now successfully ending: a new initiative has been financed by the EU to build a large-aperture dipole of 13 T with a large aperture to upgrade the cable test station at CERN, see the contribution of G. De Rijk, p. 128. In CEA-Saclay, the Nb_3Sn programme aiming at building an LHC-like quadrupole with Nb_3Sn coils is slowly but steadily progressing: the final magnet test should be carried out in 2008 (see the contribution of J. M. Rifflet, p. 131). Japan is exploring the possibility of building accelerator magnets with Nb_3Al, a conductor whose critical surface is not far from Nb_3Sn but which has a negligible degradation due to strain (see the contribution of K. Sasaki, p. 132).

Other magnet projects

To break the barrier of 20 T one needs to go to high-temperature superconductors. Today, these materials have been used to construct high-field solenoids; the present state-of-the-art is given in the contribution by D. Larbalestier, p. 136.

A recent project which is in the final stage, and will be commissioned in the next months, is the JPARC facility for neutrino physics. It makes use of combined-function superconducting magnets, which are a first in terms of magnet design. This option is of great interest for all machines where compactness is a relevant issue.

Fast cycled magnets

In the past, low-energy machines have always made use of normal conducting magnets. Indeed, during the past years the GSI laboratory has chosen a superconductive technology for a low-energy machine, and superferric or superconductive options are being considered for several machines, including the LHC injectors. The possibility of having beam transfer lines made with superferric magnets is explored in the contribution of H. Piekarz, p. 142, including both the LTS and the HTS options. The superferric magnets that will be used for the SIS100 are presented by E. Fischer, p. 147. The Discorap project, aiming at building a low-loss $\cos\theta$ curved dipole in the 4 T range for the SIS300 facility is presented in the contributions by P. Fabbricatore and M. Sorbi, pp. 157–162.

Magnet design optimization and test

Magnet design relies on the use of several codes for computing and optimizing the electromagnetic layout, mechanical structure, losses, and protection. The Roxie code, which has taken an important place in the community of accelerator magnet designers, has recently included quench analysis. An outline of the new features and of the future developments is given by B. Auchmann, p. 163. On the other hand, in the phase of conceptual design it can be useful to have also analytical or semi-analytical approaches for a fast exploration of the parameter space. A summary of semi-analytical estimates for the short sample limit, Lorentz stresses, and magnetic energy as a function of the main coil parameters is given by E. Todesco, p. 168. The state-of-the-art of the magnetic measurements at CERN is given by M. Buzio, p. 172. The two final papers by Schnizer are devoted to the measurements of SIS100 and SIS300 magnets, and to their optimization.

Further information on the workshop can be accessed from its home web site,
`http://indico.cern.ch/conferenceDisplay.py?confId=28832`.

Conference organizing committee: L. Bottura, G. De Rijk, J. Kerby, L. Rossi, E. Todesco

These proceedings have been published in paper and electronic form. The paper copy is in black and white; the electronic version contains colour pictures. Electronic copies can be retrieved through:
`http://care-hhh.web.cern.ch/CARE-HHH/LUMI-06/Proceedings/proceedings_lumi06.htm`

The compilation of these proceedings would not have been possible without the help of the conveners and speakers. The organizational support by the workshop secretary Claudine Bosteels is also gratefully acknowledged. In particular, we would like to thank all the participants for their stimulating contributions and lively discussions.

The WAMSDO workshop was sponsored and supported by the European Community-Research Infrastructure Activity under the FP6 "Structuring the European Research Area" programme (CARE, contract number RII3-CT-2003-506395).

Geneva, 15 December 2008

E. Todesco

Contents

[1] A paper was not submitted to the proceedings. However, the slides presented are available in electronic form at `http://indico.cern.ch/conferenceDisplay.py?confId=28832`.

[2] Paper published as A. Nijhuis, Y. Ilyin, W. Abbas, 'Axial and transverse stress-strain characterisation of the EU dipole high current density Nb_3Sn strand', *Supercond. Sci. Technol.* **21** (2008) 065001.

High-temperature superconductors
(conveners: A. Ballarino and A. Siemko)

Industry session
(convener: H. Ten Kate)

High-field magnets
(conveners: E. Todesco and G. L. Sabbi)

Other magnet projects
(convener: J. Kerby)

[1] A paper was not submitted to the proceedings. However, the slides presented are available in electronic form at `http://indico.cern.ch/conferenceDisplay.py?confId=28832`.

Fast cycled magnets
(convener: G. De Rijk)

Magnet design, optimization and test
(convener: S. Farinon)

[1] A paper was not submitted to the proceedings. However, the slides presented are available in electronic form at `http://indico.cern.ch/conferenceDisplay.py?confId=28832`.

LHC INTERACTION REGION UPGRADE – PHASE-I

R. Ostojic, CERN, Geneva, Switzerland

Abstract

The LHC is starting operation with beam in 2008. The primary goal of CERN and the LHC community is to ensure that the collider is operated efficiently, maximizing its physics reach, and to achieve the nominal performance in the shortest term. Since several years the community has been discussing the directions for upgrading the experiments, in particular ATLAS and CMS, the LHC machine and the CERN proton injector complex. A well substantiated and coherent scenario for the first phase of the upgrade, which is foreseen in 2013, is now approved by CERN Council. In this paper, we present the goals and the proposed conceptual solution for the Phase-I upgrade of the LHC interaction regions. This phase relies on the mature Nb-Ti superconducting magnet technology, with the target of increasing the luminosity by a factor of 2-3 with respect to the nominal luminosity of 10^{34} $cm^{-2}s^{-1}$, while maximising the use of the existing infrastructure.

GOALS AND MILESTONES OF THE PHASE-I UPGRADE

The LHC, the largest and most complex endeavour in the history of high-energy physics, is ready for beam. By mid-2008, all of the machine sectors have been cooled down and the commissioning activities have almost been completed. The LHC construction effort has been considerable and has required important international participation. In parallel with its construction, the HEP and accelerator communities have been discussing possible routes towards increasing the reach of this unique scientific facility. The approach, given in the strategy document of CERN Council [1], is clear: to maximize the physics reach, any upgrade of the LHC in the first several years of running must comply with the operations schedule and the existing infrastructure. On the other hand, LHC relies on the injector chain and its reliability. These accelerators, in particular the venerable PS, must have priority in maintenance and upgrade. These boundary conditions have lead to a phased approach to the upgrade of the LHC accelerator complex [2], which includes as the first phase the construction of a 160 MeV H^- proton linac (Linac4) and the upgrade of the LHC low-β triplets.

The goal of the Phase-I upgrade of the LHC interaction regions is to enable focusing of the beams to a β* of 0.25 m and to improve the reliability of operation at a luminosity of 2-3 10^{34} $cm^{-2}s^{-1}$. The upgrade concerns in the first place the low-β triplets in the two high-luminosity experiments, ATLAS and CMS, assuming the same interfaces with the experiments as at present (located at 19 m on either side of the IP). The low-β quadrupoles will feature a wider aperture than the present ones and will use the technology of Nb-Ti Rutherford-type cables cooled at 1.9 K developed for the LHC dipoles. The D1 separation dipoles, as well as a number of other element in the beam line will also be modified so as to comply with a larger beam envelope associated with β* of 0.25 m. However, the present cooling capacity of the cryogenic system and the other main infrastructure will remain unchanged, and will eventually limit the luminosity reach of the upgrade.

The LHC interaction region upgrade – Phase-I has been approved by CERN Council in Dec 2007. The elements of the upgrade have been discussed in a series of meetings and a conceptual design has been presented in July 2008. It is foreseen that the full technical design report will be completed by mid-2009. Later the same year, results from model magnet tests should be available. The production of the quadrupoles and other magnets is planned for 2010-2012. An important milestone is a string test in 2012 that should resolve any outstanding issue and minimize the commissioning time of the new magnets in the tunnel environment. The installation of the new triplets and other equipment is foreseen in a six-month shutdown in 2013, which coincides with the final stages of Linac4 commissioning and the first phase of ATLAS and CMS upgrades.

UPGRADE CONSTRAINTS

The low-β triplets presently installed in the LHC, shown in Fig. 1, were built by a collaboration of CERN, Fermilab, KEK and LBNL [3]. The quadrupoles have a coil aperture of 70 mm and use Nb-Ti superconductor cables that allow an operating gradient of 205 T/m. The 1.9 K cooling, electrical powering and all protection and control signals are fed to the triplet by an in-line feedbox, shown in the foreground of Fig. 1. The triplets are positioned at L*=23 m from the IP, and allow a β* of 55 cm which corresponds to nominal LHC luminosity of 10^{34} $cm^{-2}s^{-1}$.

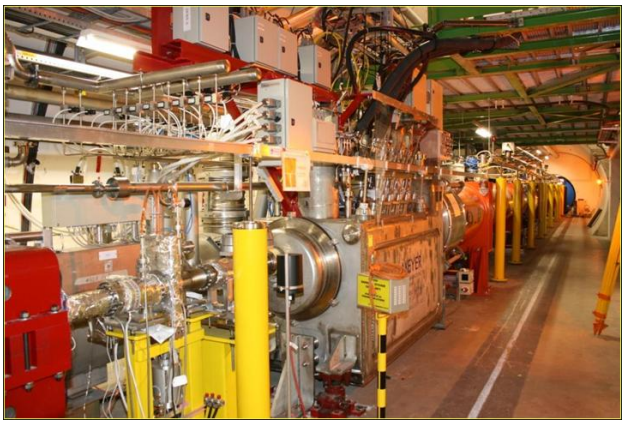

Figure 1: The low-β triplet in the ATLAS insertion.

The most effective way of reducing β* is to reduce the distance of the triplet to the interaction point (IP). The idea is not new and several attempts have been made already for the nominal LHC to arrange the different beam, vacuum and alignment equipment sitting in between the experimental area (19 m) and the triplet so as to reduce L*. Unfortunately, this equipment is extremely densely packed and is located inside heavy shielding with limited access. In spite of detailed studies, no possibility has been found to bring the triplets forward while maintaining the agreed upon interfaces between the experiments and the LHC machine.

The cryogenic power is brought to the triplets in ATLAS and CMS insertions by the compound cryo-line (QRL) from the cryogenic islands located in the LHC even points [4]. Since they are at the extremity of QRL, the total cooling power available for the triplets will depend on the as-built heat loads in the adjacent arcs, which will be known better only after the first runs of the LHC with beam. In any case, the total power available for the triplets cannot exceed 500 W at 1.9 K, which is the maximum power the sub-cooler installed in the QRL can provide for the triplets. It should be noted that at present the cooling capacity available for the triplet in Sector 4-5 (left side of CMS) is smaller than for the others as the RF cavities in IR4 use about 4 kW of the total capacity of 23 kW at 4.5-20 K of the cryo-plant servicing this sector. It should also be noted that the sectorization of the QRL does not allow to warm-up the insertion magnets separately from the arcs. Hence, four LHC sectors have to be warmed-up to exchange the triplets in ATLAS and CMS insertions.

It is clear that any increase of cooling requirements, in particular those related to the increase of luminosity above 2-3 10^{34} $cm^{-2}s^{-1}$ will need dedicated cryogenic plants serving the inner triplets around ATLAS and CMS. Their installation will most likely require a certain level of civil engineering in the underground areas. These changes are best done at the time of the Phase-II upgrade when the two experiments will also perform their own extensive modifications.

As shown in Fig. 1, all major equipment of the triplets is located in the LHC tunnel, with the exception of the power converters which are housed in alcoves adjacent to the machine tunnel (in ATLAS), or parallel to the experimental cavern (in CMS). The alcoves are separated from the tunnel by shielding walls, through which water-cooled cables run linking the power converters to the triplet feedboxes. Access for maintenance of the equipment in the tunnel, in particular of the current leads, is difficult and may have consequences on the LHC operation. In view of the even higher radiation levels after the upgrade, it is necessary to remove all delicate equipment from the tunnel, including the feedboxes, and place it in low radiation areas. Such areas are very scarce around the ATLAS and CMS triplets, and it may be necessary to further shield the alcoves.

The access and transport of magnets to and from ATLAS and CMS implies long hauls over several kilometres alongside the chain of cold magnets. Although care had been taken during LHC design to enable transport of magnets at any time, the LHC tunnel is tight and transport of equipment is a delicate operation. Preparing the triplets for transport therefore has to be carefully planned. In any case it is clear that all new equipment has to comply to the allowed transport envelope, which coincides with the length, mass and cross-section of the LHC main cryo-dipole.

It is well known from the optics and beam studies made during the LHC design that a reduction of β* has a number of consequences on the performance of the machine. The chromatic aberrations, linear and of higher order, are particularly serious and must be carefully controlled and compensated. Of particular concern is the off-momentum beta-beating, $\Delta\beta(\delta)/\beta(0)$, which must be compensated in the triplets and in the betatron and momentum cleaning insertions (IR7 and IR3). It should be noted that a $\Delta\beta(\delta)/\beta(0)$ larger than about 10% leads to mixing in the 6-D phase space that may corrupt the collimation system [5]. As chromatic aberrations concern the LHC as a whole, new optics solutions are required for the Phase-I upgrade goal of $\beta^*=0.25$ m while using the existing corrector circuits to their maximum potential.

THE PROPOSED CONCEPTUAL DESIGN

LHC optics

As mentioned in the last section, the Phase-I upgrade requires a new optics solution for the LHC which minimizes chromatic aberrations. Such solutions, based on imposing a $\pi/2$ betatron phase advance between IP1 and IP5, have been studied in the past for the nominal LHC, but without a fully satisfactory result. A new approach has been devised recently [6], which is based on using the sextupole families in the two sectors adjacent to each triplet to excite a $\Delta\beta(\delta)$ wave that interferes in phase and cancels the wave generated by the triplet. The solution requires that the cell phase advance is very close to $\pi/2$ and that a well defined phase relation exists between the IP and the arc. Under these circumstances it has been shown that the long-standing problem of $\Delta\beta(\delta)/\beta(0)$ compensation can be resolved. Using the maximal current of the sextupole families, the off-momentum beta-beating can be reduced below 10% everywhere in the LHC for $\beta^* \geq 0.25$ m. Furthermore, these phase conditions also enable compensation of the spurious dispersion in the ring, generated by the large crossing angle, proportional to $1/\sqrt{\beta^*}$. However, as these phase conditions have to be achieved in all the arcs and insertions, the integer tune of the LHC changes, and the tune split is reduced from 5 to 3. Further work is still necessary to fully validate the proposed solution at injection, possibly including machine studies in the LHC itself.

Besides the phase conditions imposed by the ring optics, the optics in the ATLAS and CMS insertions must be consistent with the parameters of the magnets in the

dispersion suppressors and matching sections (Q4-Q11) and of the other equipment, which will remain after the Phase-I upgrade. This concerns in particular the strength and aperture of the quadrupoles, and the aperture of the collimators and absorbers. Several possibilities were examined and it was found that as a general rule the shorter the focusing length of the new triplet the larger is the aperture margin in the matching sections, but the lower the flexibility of matching. On the other hand, by displacing Q4 and Q5 quadrupoles towards the arc by 10-15 m, the aperture and matching conditions for a given triplet can be improved. The longest Nb-Ti triplet that can be matched to the rest of the insertion is about 40 m long, and is given by the available strength and aperture of the dispersion suppressor quadrupoles.

On the basis of these studies it was concluded that the appropriate solution for the Phase-I triplet is a quadrupole with a coil aperture of 120 mm and an operating gradient of 120 T/m. It was also estimated that displacing the matching section to a new position has a considerable impact on a number of infrastructural elements (e.g. the QRL cryo-line and the DSL superconducting link), and that it would need to be done during the same shutdown as the replacement of the inner triplets. It was hence concluded that Phase-I upgrade should assume that the magnets of the matching sections remain as they stand.

Triplet layout

The present LHC low-β triplet, shown in Fig. 2, is of the symmetric type with the two outboard magnets, Q1 and Q3 with a magnetic length of 6.6 m, while the two inner magnets, Q2A and Q2B (housed in the same cryostat), have a length of 5.7 m. The interconnect lengths between Q1-Q2 and Q2-Q3 are slightly different. The orbit and other correctors are distributed in all three quadrupoles. The separation dipole D1 is composed of six modules of normal conducting magnets.

The triplet for the Phase-I upgrade will necessarily be longer than the present one, as the operating gradient is about 40% lower (coil aperture is 70% larger). Nevertheless, the intention is to follow the symmetric layout as much as possible, as it offers a number of important advantages. A preliminary layout is also shown in Fig. 2, and features four identical magnets, each about 10 m long, and identical interconnects. There are clear advantages of having identical magnets for the timely and cost-effective production. For similar reasons, it is proposed to group the corrector magnets in a separate unit placed on the upstream side of the triplet. Finally, a superconducting D1 dipole replaces the present normal conducting magnets, such that the full length of the new triplet string is almost identical to the present one.

A number of issues still need to be resolved for the new triplet. For example, the preliminary studies have shown that for realistic alignment of the quadrupoles the orbit correction with a reduced set of orbit dipoles results in a comparable residual orbit error and favourable strength requirements. However, the control of the beam position at the IP requires further studies. The number and position of the BPMs also has to be defined, as well as the space necessary for linking the triplet to the cryo-line and the current buses. Also, a precise evaluation is needed of the gain obtained in case the two central quadrupoles Q2A and Q2B were to have a slightly different length, as in the present triplet. All these and other open questions will be resolved in the coming months as the technical design proceeds to completion (mid- 2009).

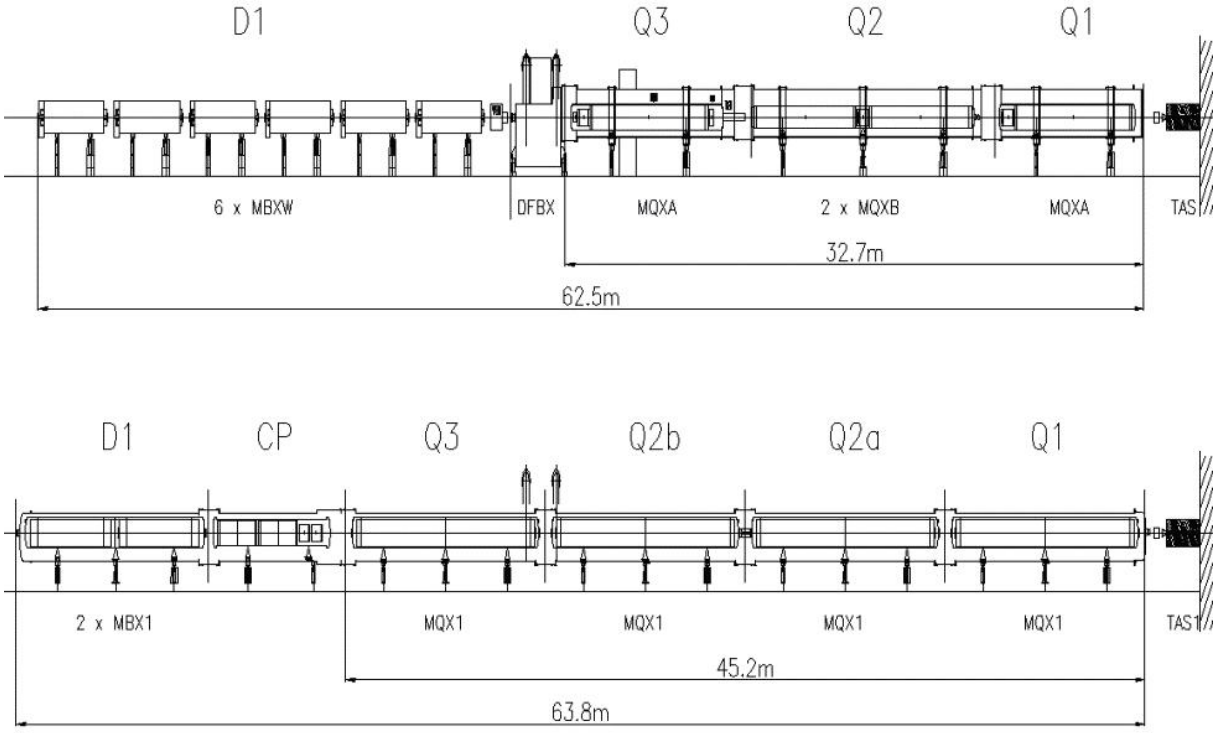

Figure 2: Layout of the present LHC triplet (top) and proposed layout of the Phase-I triplet (bottom).

Powering and magnet protection

The considerably larger stored energy in the new low-β quadrupoles requires that the magnet protection be revisited. In the present design, the triplet magnets are protected by built-in quench heaters. When a quench signal is issued, the quench heaters in all magnets are activated irrespective of the source of the quench signal. As the powering circuit does not contain energy extraction resistors the full magnetic energy is dissipated in the cryogenic system. The temperature of the magnets and helium pressure after quench are therefore high, and the time to cool the triplet back to the nominal operating temperatures is comparatively long. Nevertheless, the system has proven to be fully operational and reliable.

The new low-β quadrupoles will also be equipped with quench heaters. However, to improve the magnet protection, and at the same time reduce the cryogenic recovery time, the powering circuits for the Phase-I triplets will also include energy extraction. The presently preferred scheme, shown in Fig. 3, consists of two identical circuits, each covering two magnets (Q1-Q2A, Q3-Q2B). In addition to the main 12 kA power converter, a 2 kA trim is foreseen to allow for full optics flexibility. Quench detectors will be of the bridge type, similar to the present ones. Several possibilities were considered for the switches, extraction resistors and bypass protection. The final choice remains to be made, but the primary criteria will be the radiation hardness and volume of the equipment.

The quench protection units, power converters and the feedboxes will be housed in shielded areas away from the machine tunnel. The feedboxes will be connected to the magnets with a cold link. Several types of superconducting links, carrying currents up to 6 kA and cooled with supercritical helium, already exist in the LHC. The new ones must carry 12 kA for the main quadrupole circuits, as well as lower currents for the correctors. They should preferably be based on He-gas cooling to avoid additional cryogenic distribution. New developments using MgB_2 wires are actively investigated.

Protection from particle debris

With ever higher luminosities the protection of magnets and other equipment from particles generated in the collisions is of crucial importance. The starting point is to ensure that the magnets can sustain steady-state heat loads generated by the particle debris with adequate margin with respect to the quench limit. This issue has been studied in considerable detail for the present triplets and the coil protection was steadily improved until a factor of three safety margin with respect to estimated quench limits was achieved [7].

As the power density from the debris scales with luminosity, it is clear that protection efficiency for a luminosity three times the nominal one must be higher

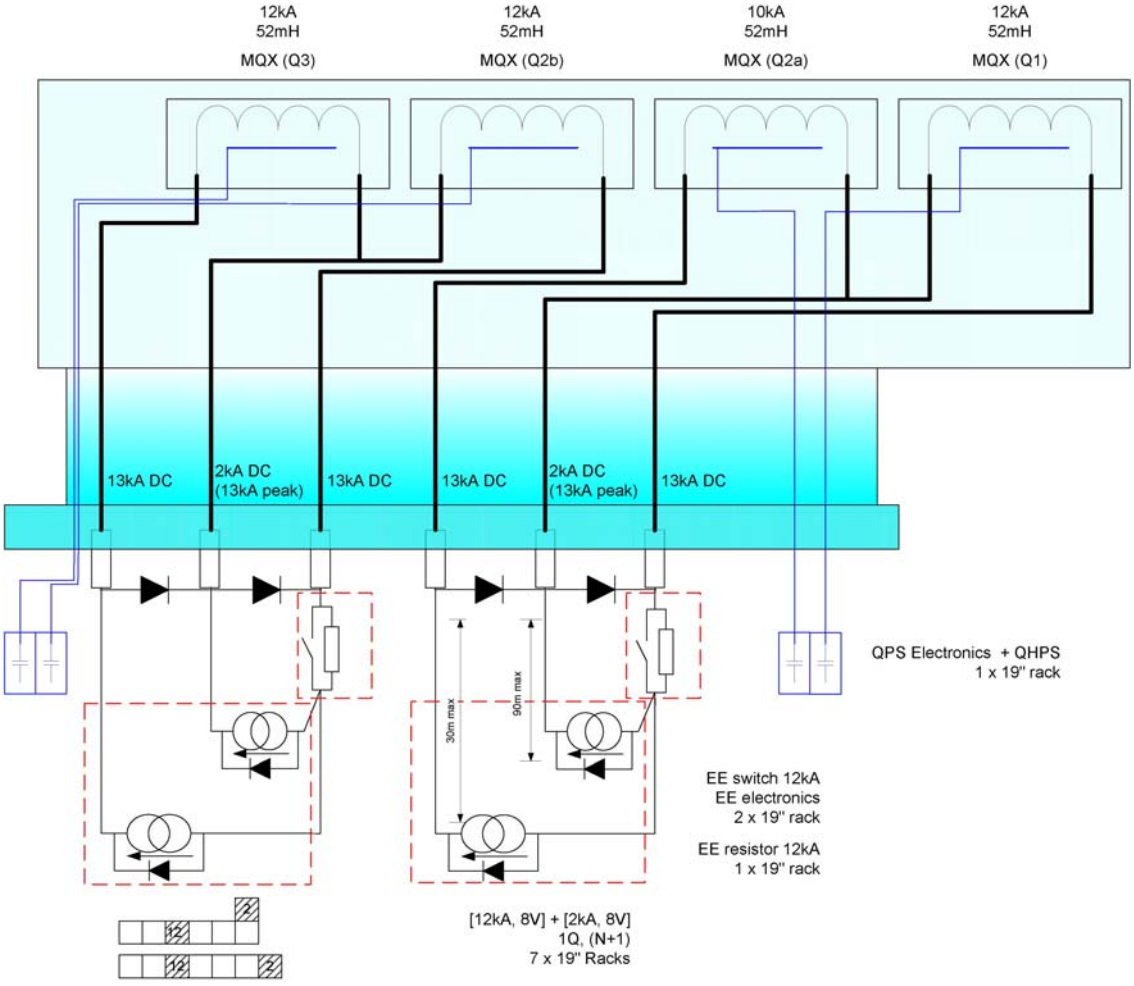

Figure 3: Proposed split-powering scheme for the Phase-I triplet.

than in the present triplet. It is assumed for the purposes of the conceptual design that the heat transfer properties of the new low-β quadrupoles will be the same as in the present magnets, although work has started on improvements. The design limit for power density (4.3 mW/cm^3) is therefore assumed identical. Studies performed recently for several candidate layouts have shown that the increased aperture of the quadrupoles has a beneficial effect on the protection efficiency [8]. In fact, for a luminosity 2.5 times the nominal, it was shown that the peak power density is within the design limits for most of the magnets. It is only between Q1 and Q2 that the peak exceeds the limit. Fortunately, due to a reduced aperture requirement for Q1, additional shielding can be included as part of the beam screen assembly, effectively eliminating the peak. The additional heat load is evacuated by the beam screen (5-20 K), which needs to be taken into account for its design. Similar local solutions may also be needed in the interconnects between the magnets. Furthermore, all cases studied show that the estimated total heat load in the triplet magnets is about 400 W at 1.9 K, which is still compatible with the existing maximum cooling capacity.

Very important elements for magnet protection are the two absorbers, TAS and TAN, which already exist in the LHC. The function of these elements remains identical. However, due to the modified magnet apertures and increased luminosity changes are necessary in their design. The main function of the TAS, located between the experiment border (19 m) and the Q1 quadrupole, is to shield the triplet and reduce backscatter to the experiments. Its vacuum chamber is designed such to be as close as possible to the beam envelope. Since the beam size and excursion will increase due to lower β*, the vacuum chamber of all four TAS in ATLAS and CMS must be replaced. The most effective way, in terms of access, handling and costs, is to build new TAS bodies and vacuum chambers. This is also an opportunity to introduce a cooling system, as the total heat load in the TAS body will be about 400 W.

The TAN is located 140 m from the IP. Its role is to protect all downstream equipment from the neutral particles at the point where the two beams transit from a common to separate vacuum chambers. The present TAN is perfectly adequate for the luminosity of 10^{34} cm^{-2}s^{-1} and β* of 0.55m. However, for a luminosity 2.5 times higher the TAN will receive about 600 W. Furthermore, for a β* approaching 0.25 m, the aperture of the present TAN may become the limiting element in the insertions. It is therefore quite probable that the TAN will have to be replaced.

The debris power in the magnets is also a generator of considerable radiation dose. In the present triplets, a peak dose of 3.5 MGy is expected in the coil for a standard annual run during which 75 fb^{-1} of luminosity are accumulated. In the new triplets the dose in the coil inner layer is estimated at about 1 MGy/100 fb^{-1}, but has a strong radial dependence and may be up to three times higher in the innermost strands of the cable. With these estimates in mind we have assumed that the magnets and all other equipment for the Phase-I upgrade must comply with a lifetime of at least 500 fb^{-1}. This integrated luminosity is compatible with the lifetime of the ATLAS and CMS experiments before their full upgrade (Phase-II), planned for later in the next decade.

A compulsory requirement for the design of the new triplets is strict application of ALARA principles. This is in particular the case for the interconnects, which have to be designed such that their servicing and disconnection can be done with tooling adapted for work in radiation environment. The materials used for magnet construction, in particular the steels, have to be checked for traces of cobalt to limit activation.

A further consequence of high luminosities is the expected level of hadron fluence in the tunnel and in surrounding areas where electronics equipment will be housed. Following the CNGS run in 2007, which has revealed that high energy charged hadrons (>20 MeV) may provoke electronics failure due to single event upsets with higher probability than previously assumed, a campaign has began at CERN to estimate the hadron fluence in LHC underground areas. The information available at present indicates that the alcoves close to ATLAS and CMS may be exposed to high fluence. Appropriate solutions are being looked at.

Tunnel integration

As mentioned beforehand, the power converters and quench protection equipment for the present triplets are housed in the alcoves, while the feedboxes and cryogenic instrumentation are in-line with the triplet or below the cryostats. Unfortunately, the equipment layout around ATLAS and CMS is not identical. In fact, the equipment alcoves on the two sides of CMS are quite different, while they are symmetric in ATLAS. As one could expect with civil engineering, the beam tunnels are different too! This has all led to a situation where the feedboxes and the layout of the equipment are different for all triplets in the LHC. The design goal for the Phase-I upgrade is to at least have identical feedboxes for all four triplets, since it is unlikely that the layout of other equipment can be standardized.

The available space in the alcoves is shared with other machine equipment and is almost fully occupied. Nevertheless, in reviewing the situation it has been possible to identify appropriate locations for the new power converters, feedboxes and protection equipment. For ATLAS, the space reserved includes the UJ caverns (ground and first floors), the UL passageway, as well as the US cavern, which is mostly used for the ATLAS electrical equipment. The situation in CMS is more difficult, and at present the most promising solution is to place all the equipment in the UL by-pass, which serves for magnet transport and is presently empty. In both cases, additional studies are necessary to find the appropriate solutions to reduce the length of the cold links while keeping most of the equipment in low radiation areas. Minimal civil engineering may still be necessary.

Matching sections

The present matching sections comprise three stand-alone superconducting magnets separated by warm sections, which contain the collimators, beam instrumentation and vacuum equipment, as well as elements of the energy extraction system for the main dipole circuits in the adjacent arcs. The area is also used for forward physics experiments that need direct access to the beam-line. An example of the complexity and congestion is show in Fig. 4 for the section between the TAN and D2 dipole. Most of this equipment will remain in service after the Phase-I upgrade.

The magnets in the matching section are cooled in a saturated helium batch at 4.5 K and are powered through a superconducting link which is about 120 m long. Studies made during the LHC design have determined that a change of their operating temperature to 1.9 K is technically very difficult due to the limited size of the QRL "jumpers" and increased number of connections to the headers that would be required in this case. In the arcs, these connections are distributed over several cells. The increase of the strength or of the temperature margin of the magnets is therefore not feasible without considerable complications. For all these reasons it has been decided that the design of the insertions for the Phase-I upgrade should proceed assuming that the magnets and their operating margins remain unchanged.

Figure 4: Beam instrumentation, collimators and other equipment presently installed in between the TAN (red object on the left) and the D2 separation dipole (blue cryostat on the right) in the ATLAS matching section.

Reduction of β* inevitably leads to tighter aperture in the matching section magnets and nearby equipment. Protection against the beam halo, which is at present assured by a pair of tertiary collimators designed to protect the triplets, will most likely need to be extended to other magnets as well. In addition, as already remarked, the TAN may very well become the limiting aperture in the insertions and will require extensive modifications. The new protection equipment and other interventions in the matching sections (e.g. realignment of the critical warm elements) will be done during normal shutdown periods for the LHC, foreseen at the beginning of every calendar year. The design of the new equipment must take into account the implications on the background in the experiments, which is expected to be an important issue for high-luminosity runs of the LHC.

MAGNETS FOR THE PHASE-I UPGRADE

The magnets for the Phase-I upgrade will extensively use the technological developments made for the LHC. Nevertheless, the design of the new magnets is not without concerns due to higher stored energy, forces and stresses, and increased heat loads and radiation dose.

Quadrupoles

The low-β quadrupoles will use the existing LHC dipole cables arranged in a 120 mm aperture coil providing a field gradient of 120 T/m, with an operating margin of around 80%. The magnet design will also include as much as possible other materials available from the LHC production, in particular the high-strength steel for the collars and magnetic iron for the laminations. The outer diameter of the magnet will be 570 mm, equal to the outer diameter of the LHC dipole.

The quadrupoles will be cooled in static pressurized helium bath at 1.9 K with a single heat exchanger of the bayonet-type, as is presently the case for magnets in the LHC arcs. The heat exchanger will have a diameter of 95 mm, dimensioned for the ultimate cooling capacity of 500 W. The laminations will be designed to improve the heat transfer from the coil via the stand-alone collars.

With all these factors in mind, the conceptual design of the magnet is fairly well defined. Optimization studies are now on-going in view of improving the cable insulation scheme for better heat transfer. The cross-section of the coil will also be refined for robustness of the field multipoles with respect to the component tolerances. The end-spacers and quench heaters, both of which are known to be delicate components, will also be optimised and their compatibility with respect to the required radiation hardness will be ensured.

Correctors

The proposed triplet layout includes a smaller number of orbit correctors than the present triplet, with proportionally increased strength. These magnets will also serve for generating a crossing angle for the beams and their separation at the IP before collision. Hence, they are equally important as any other dipole and should be constructed with the same level of reliability and robustness in mind. The nested dipole correctors based on epoxy-impregnated coil are not considered appropriate for the Phase-I performance goals and other solutions using Rutherford-type cables are being investigated. Besides helium transparency, this type of coils should also profit from larger temperature margin offered by the 1.9 K cooling. However, their design requires careful optimization and must include the full powering circuit, in

particular the power converter which will necessarily need to provide higher currents than the present 600 A.

Higher order multipole correctors are also foreseen for the Phase-I upgrade. Their specification will be based on the field quality estimates for the low-β quadrupoles and D1 dipole, presently in discussion. The skew quadrupole and sextupole correctors are expected to have similar strengths as the present ones, and hence their design will follow the established techniques. Care will be taken to provide better protection and improved radiation hardness.

D1 dipoles

The present D1 separation dipole comprises six normal conducting magnets with a pole gap of 63 mm. Clearly, the magnet gap must be increased to match the aperture of the triplet. Recent cost estimates have determined that the most effective solution for the D1 dipole is a superconducting magnet with a field in the 4 T range.

The preferred solution for D1 dipoles is to use the well established DX magnet, which has been serving well in RHIC since many years. This magnet has a coil aperture of 180 mm with a warm bore of 140 mm [9], which is more than enough for the Phase-I purposes. The DX operating field is 4.4 T and its magnetic length 3.7 m. Two such magnets are necessary for the D1, which will be about 10 m long, as shown in Fig. 2. The magnet will be cooled at 4.5 K and could be either a semi- or a fully stand-alone unit. The parameters of the magnet are such that it could remain in the insertions for the Phase-II upgrade. Discussions are presently ongoing with BNL and US-DOE to determine the possibilities of constructing the D1 cryo-dipoles as part of the US contribution to the LHC upgrade.

PROJECT ORGANIZATION AND COLLABORATIONS

The LHC IR upgrade Phase-I is organized as a CERN project since the beginning of 2008. In this framework, the work-packages have been defined with clear technical goals and milestones. Project engineers have been assigned and preliminary estimates of the necessary resources and costs have been made. This structure will be updated following the conceptual design review (July 2008). Communication within the project is assured by regular plenary meetings chaired by the project leader. The quality assurance of the technical specifications and change control will use the EDMS and EVM systems developed for the LHC.

The project plan foresees that the production of the low-β quadrupoles, their cryostating and cold testing is performed in CERN workshops and testing facilities. Nonetheless, to profit from the engineering expertise in other institutions, CERN has invited European and US laboratories to contribute significantly to the Phase-I upgrade. As a result, as part of the "SLHC-Preparatory Phase" project (CNI, 7th EU Framework Programme), other European laboratories (CEA and CNRS-France, CIEMAT-Spain, STFC-UK) will participate in the design of the quadrupoles, correctors and associated production tooling. Furthermore, within the special French contribution to the implementation of the European strategy for particle physics (CERN "White paper"), a considerable participation of CEA and CNRS is foreseen in providing the components for magnets and cryostats and manufacture of the correctors. These two collaborations are well under way, with formal agreements already signed and in effect. It is also expected that the US laboratories, which have contributed decisively to the construction of the present LHC triplets, will participate in the LHC upgrade, both Phase-I and Phase-II. Discussions with the American partners are ongoing and it is expected that for Phase-I they will provide the D1 magnets and a significant part of the cold powering system.

CONCLUSIONS

In the first few years of operation it is expected that the LHC luminosity will gradually increase and that the collider will reach its nominal performance. In order to facilitate continued improvement, several upgrade projects have been launched both for the injector chain and the LHC itself. The Phase-I upgrade of the ATLAS and CMS interaction regions is focused on removing the known bottlenecks in the low-β triplets and enabling reliable operation of the machine at the luminosity of 2-3 10^{34} $cm^{-2}s^{-1}$, limited by the existing cryogenic capacity. The implementation of the upgrade is foreseen in 2013, when Linac4, the first section of the new injection chain will also come into operation. It is also expected that ATLAS and CMS will perform substantial modifications at this time to prepare for higher even rates. The shortest route for providing the new low-β quadrupoles in this time frame is to use the available LHC dipole cable and the existing technology of 1.9 K cooling. The Phase-I upgrade project is now in place to achieve this ambitious goals.

REFERENCES

[1] The European strategy for particle physics, CERN/2685.
[2] R. Garoby, Proc. EPAC'08, Genoa, Italy (2008), p.3734.
[3] R. Ostojic et al, Proc. PAC'05, Knoxville, TN (2005), p.2798.
[4] LHC Design Report, CERN-2004-003.
[5] R. Assmann, private communication.
[6] S. Fartoukh, to be published.
[7[N. Mokhov et al, LHC Project Report 633, Apr 2003.
[8] E. Wildner et al, Proc. EPAC08, Genoa, Italy (2008), p. 2584, and p.2590.
[9] M. Anarella et al., NIM A499(2003)280-315.

ADVANCES IN LOW LOSS NBTI STRAND AND CABLE

Martin N. Wilson: Consultant, Brook House, 33 Lower Radley, Abingdon, OX14 3AY, UK.

Abstract

The new fast ramping accelerators will require NbTi conductors with lower ac losses than hitherto. Finer filaments will be needed, which will demand significant improvements in the double stack production process. Eddy current coupling between filaments within the wire must be reduced by increasing the transverse resistivity across the matrix, but this increase must be achieved without increasing the longitudinal resistivity too much. Coupling within cables must be reduced without impeding current sharing between strands. Cored cables offer the best way of achieving this compromise.

INTRODUCTION

Early work on superconducting particle accelerators was directed towards a fast ramping fixed target machine, where ac loss in the superconductor is a major design problem. Wires containing many fine filaments separated by resistive barriers and cables with a substantial resistance between the strands were all developed at this time. Subsequently however the emphasis in accelerators shifted to storage rings, where much slower ramp times were acceptable. Fine filaments were still needed to achieve the required field quality, but the other features needed for low ac loss were no longer required and the pace of development slowed somewhat.

With the arrival of the Facility for Antiproton and Ion Research FAIR at GSI [1] and the possibility of a new fast cycling injector for the LHC at CERN, interest in fast ramping NbTi conductors has resurfaced. It is time to dust off the old work and push it further.

Much of subject matter of this paper, presented as a talk at WAMSDO, is about to be published as part of a broader review [2], so this paper will not repeat every detail of the talk, but will concentrate on the main points and recommendations for future work.

For ramped accelerator magnets, achieving an economic refrigeration load and reaching the desired maximum field without performance loss due to overheating depends on keeping the ac losses within bounds. There are three main sources of loss in the superconductor when a magnet is ramped up to field:

(i) hysteresis losses within the filaments of NbTi.
(ii) eddy current coupling losses between filaments in the wire.
(iii) eddy current coupling losses between wires in the cable.

The following sections will treat each of these loss components in turn.

HYSTERESIS LOSS

The hysteresis loss power in a single filament of superconductor exposed to a changing field is

$$P = \dot{B}\frac{2}{3\pi}J_c(B)d_f \qquad (1)$$

where d_f is the filament diameter. Clearly, low loss demands fine filaments, which implies many filaments in the wire. Present generation accelerator magnets use wires with ~ 7 μm diameter filaments, but finer sizes of 2-3 μm are needed for the new fast ramping machines.

Wire Manufacture

Multifilamentary wires are made by cladding rods of NbTi in copper, drawing them to a hexagonal cross section and stacking them in an extrusion container. The best quality wires are made using a single stack process as illustrated in Fig 1.

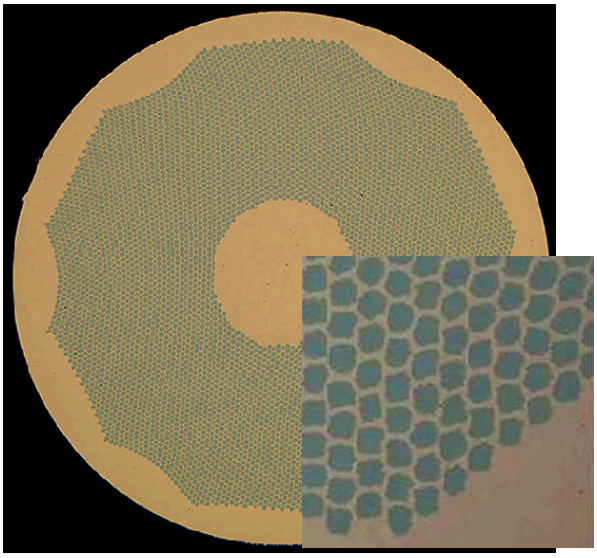

Fig 1: A single stack wire with 6264 filaments (photo courtesy of European Advanced Superconductors)

Practical considerations limit the number of rods which can be stacked to about 15,000, although a single stack of 38,000 filaments has been made using a technique in which the rods are grouped into clusters surrounded by a thin shell [3]. In general however, more filaments require a double stack process in which bundles of filaments are drawn hexagonal and then re-stacked for a second extrusion to produce wires like the one shown in Fig 2.

During the pre-heating needed for extrusion, there is a danger that the titanium will react with the copper to form hard particles of an intermetallic compound. These particles do no reduce in size as the wire is drawn down and are likely to cause breakage when the filaments reach a similar size. To guard against this problem, the NbTi rods are wrapped in a thin niobium diffusion barrier.

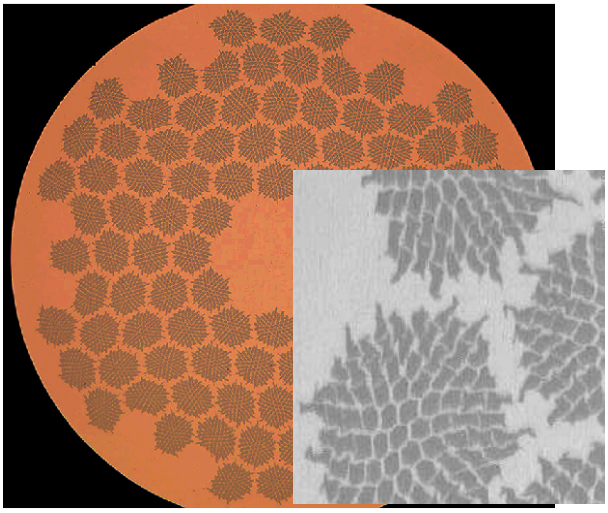

Fig 2: A double stack wire with 102 × 85 filaments (photo courtesy of European Advanced Superconductors)

Filament Uniformity.

As wires are drawn down to finer filament diameters, J_c as measured from the transport current decreases, but the inherent J_c, as measured from magnetization, remains the same. On closer examination, it turns out that n reduces with filament size, where n is the exponent in the following empirical expression for the growth of resistivity with increasing current.

$$\rho(J) = \rho_o \left\{ \frac{J}{J_o} \right\}^n \qquad (2)$$

Part of this resistive transition is ascribed to flux flow resistance in the NbTi, but the major part is thought to be caused by non uniformities in the longitudinal direction or 'sausaging' of the filaments. This is a fabrication problem and more work is needed here if 2-3μm filaments are to be produced with a good current density.

As may be seen in Fig 2, filaments also become distorted in cross section and this has negative consequences for the losses because the d_f in (1) refers to the largest dimension perpendicular to the field. Table 1 presents some measurements made for FAIR of the ratio between J_c measured by magnetization and by transport current. For the best magnet performance, we clearly want to minimize this ratio, ie get minimum loss for maximum transport current.

Table 1: J_c from magnetization and transport current

stack	single	double Cu	double CuMn	double sector
J_{cmag}/J_{ctrans}	0.94	1.40	1.23	1.10

It may be seen that the single stack wire is much better in this respect. The double stack is worse – not surprisingly in view of the obvious distortion of the filaments shown in Fig 2. The third wire is of similar construction, but with CuMn alloy next to the filament. This alloy is somewhat harder than pure Cu and therefore closer to the filaments in mechanical properties, so it presumably gives them better support during wire drawing. Finally, the innovative 'sector' geometry shown in Fig 3 groups the filaments into bundles that fit together more naturally at the second stage extrusion and therefore produces less distortion of filaments at the edge of the bundles. It gives the best result so far for double stacked wires.

Fig 3: Double stack wire with innovative sector geometry (photo courtesy of European Advanced Superconductors)

LHC conductors have ~8000 filaments of ~7 μm size in a wire of ~1 mm diameter. Future fast ramping machines might require filaments as small as 2μm, which would demand ~90,000 filaments in a 1mm diameter wire – clearly beyond the possibility of single stacking. So these future machines are going to demand some improvements in the process techniques of double stacking.

Proximity Coupling

Eq (1) predicts a linear decrease in loss with reducing filament size but in practice we find that, below a size of ~3μm, the loss starts to increase again [4]. The problem is caused by proximity coupling, an effect whereby the copper between the filaments becomes weakly superconducting when its thickness falls below ~ ½ μm. Collings [5] has shown that the effect can be suppressed by adding ~ ½ wt% of manganese to the copper. As noted above, this may also reduce filament distortion by hardening the copper.

Sumption [6] finds that the niobium barrier, which is put around fine filaments to suppress intermetallic formation, may be responsible for launching the Cooper pairs across the copper. So an alternative way of avoiding proximity coupling might be to miss out the barrier and avoid the intermetallic by extrusion at low temperature or by adding silicon to the copper [7].

COUPLING BETWEEN THE FILAMENTS

In changing fields the filaments of a multifilamentary wire are coupled together by eddy currents which cross the matrix. These eddy currents increase the loss by:

$$P_e = \frac{\dot{B}_i^2}{\mu_o} 2\tau = \frac{\dot{B}_i^2}{\rho_{et}} \left(\frac{p}{2\pi} \right)^2 \qquad (3)$$

where τ is the decay time of the eddy currents, ρ_{et} is the effective transverse resistivity across the matrix and p is the twist pitch. Fig 4 shows some experimental values of ρ_{et} for two wires, obtained by measuring magnetization as a function of ramp rate. Also shown are values of ρ_{et} calculated using the methods of [8]. Note the effect of magnetoresistance in the copper.

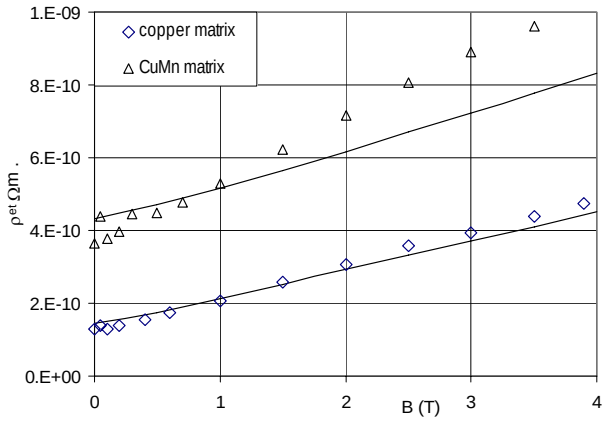

Fig 4: Measured and calculated values of effective transverse resistivity for two wires.

The lower curve of Fig 4 is for a wire with pure copper matrix, as used in all superconducting accelerators built so far. This level of ρ_{et} has been quite adequate to control the losses in storage rings with ramp times of 100 to 1000 sec, but the faster ramps of the new accelerators need more resistance. The upper curve of Fig 4 is for a wire in which the matrix immediately surrounding the filaments is CuMn, with the rest of the wire pure Cu. As already noted, in addition to its higher resistivity, CuMn brings the benefits of suppressed proximity coupling and improved processing. However, ρ_{et} for this wire is increased by only a factor 3, although the CuMn alloy has ~100× the resistivity of pure copper at 4K. The reason for this is that ρ_{et} comprises many parallel paths and it necessary to block all of them if the resulting resistivity is to be increased. The simplest way would be to make the whole matrix from resistive alloy, but this would bring problems of stability and quench protection.

On stability, it was a matter of early experience that even the smallest coils made from wires with a resistive matrix suffered severe training problems. The effect may be quantified roughly in terms of minimum quench energy MQE, defined as the smallest pulse of heat (on a short length of wire for a short time) needed to trigger a quench. Fig 5 plots the MQE computed for a typical accelerator magnet wire as a function of matrix resistivity in the longitudinal direction. It may be seen that there is almost a linear dependency and that the energy needed to trigger a quench with CuMn is ~100 times less than with pure Cu. The result will inevitably be less reliable magnet performance and more training.

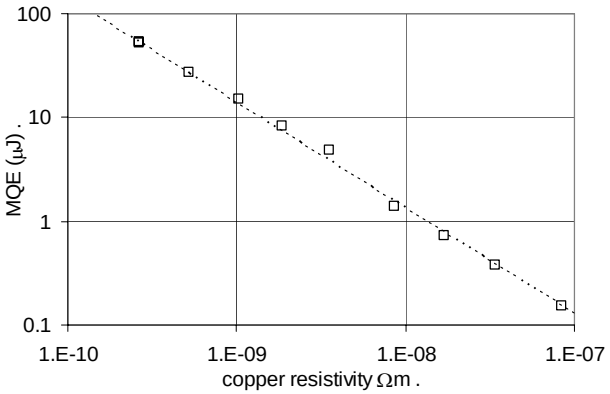

Fig 5: Computed MQE versus matrix resistivity for a typical accelerator wire (0.85mm dia, 50% of I_c at 4.5T)

The challenge therefore is to design a matrix with anisotropic resistivity: large in the transverse direction to control losses and small in the longitudinal direction for large MQE and therefore good stability. Fig 6 shows an early attempt to reach this goal; it had a strongly anisotropic resistivity, but was very difficult to manufacture. There is scope for future innovation in this direction.

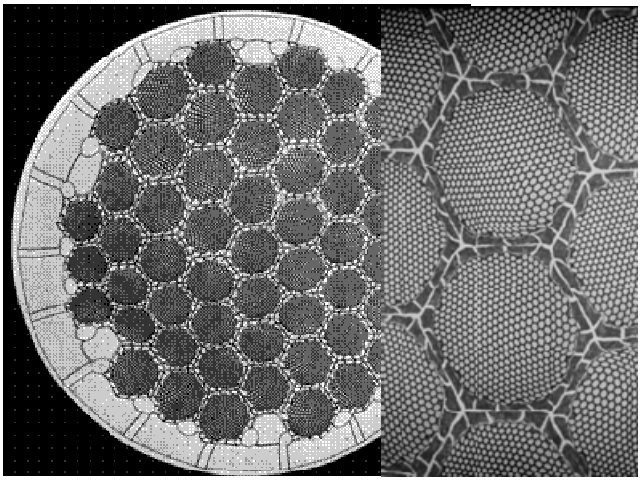

Fig 6: Composite wire with CuNi barriers to produce highly anisotropic resistivity [9]

CABLES

All accelerator magnets to date have been made from Rutherford cable. For reasons of stability and current sharing, the strands are never insulated from each other. Electrical contact between the strands enables eddy currents to flow in changing field, which produces more ac loss. Not surprisingly, these losses are greatest when the field is perpendicular to the broad face of the cable, but there are also different loss mechanisms depending on how the currents flow [2]. As sketched in Fig 7, the contact resistance between strands is of two types: crossover resistance R_c and adjacent resistance R_a. Losses from crossover resistance $Q`_{tc}$ are much greater than adjacent losses $Q`_{ta}$,

$$\frac{\dot{Q}_{tc}}{\dot{Q}_{ta}} = \frac{R_a}{R_c}\frac{N(N-1)}{20} \qquad (4)$$

where N is the number of strands in the cable, usually ~30-40. Because the rolling process produces greater contact areas for R_c, it has been found that $R_c \sim R_a / 7$. The crossover loss is thus ~ 400× the adjacent loss.

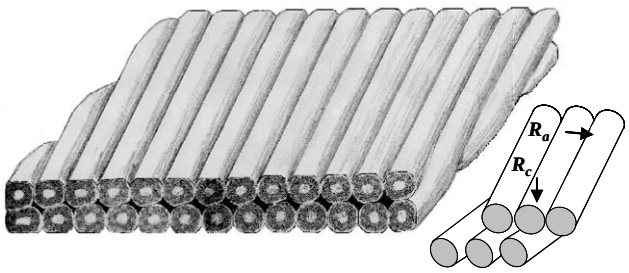

Fig 7: Rutherford cable showing the two types of inter-strand contact resistance.

To control losses in a fast ramped magnet, it is necessary to increase the contact resistance, but this makes it more difficult for the currents to share evenly – so the resistance should not be increased any more than necessary. From (4) it is clear that the best way of reducing loss without impairing the current sharing too much is to increase R_c while keeping R_a low. The traditional method of increasing contact resistance by oxidizing the wire surface won't work because it increases R_c and R_a by about the same factor. A better way is to make a 'cored cable' with a thin resistive foil on its mid plane, which can produce a factor of up to 1000 in anisotropy between R_c and R_a [10].

Inter–strand resistance can also affect the stability of the cable against external disturbances. Fig. 8 shows some measurements of MQE made by applying heat pulses to one strand of a cored cable [11]. It may be seen that smaller values of R_a move the MQE from the lower branch corresponding to the MQE of a single wire, to the upper branch where the whole cable is involved. It is worth remembering that 100 μJ is the energy released by dropping a pin just 100 mm. Clearly the upper branch and lower R_a is preferred!

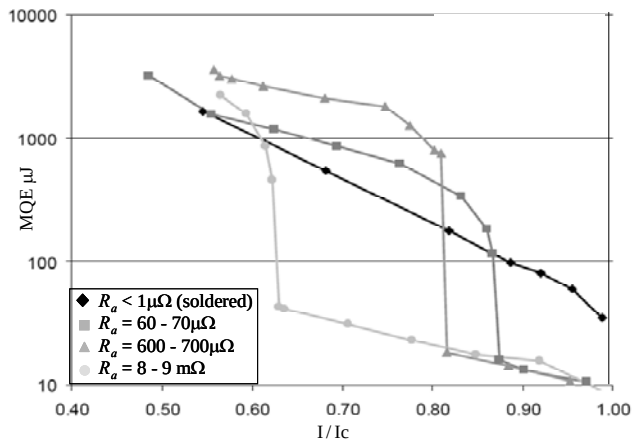

Fig 8: MQE measured for cored cables with different R_a

CONCLUSIONS & RECOMMENDATIONS

Although it cannot match the critical field or temperature of the newer superconductors, NbTi is still the best for pulsed applications because it offers the finest filaments in precise geometries and the ability to produce anisotropic resistivity in the matrix by the use of resistive barriers. To produce the 2-3 μm diameter filaments needed for the next generation of fast ramping accelerators, double stacking will be needed. Further development is needed here to keep all the filament cross sections round so that losses will not be increased by shape effects. Possible strategies are the use of novel geometries and/or CuMn next to the filaments, which will also suppress proximity coupling.

For coupling losses, both between filaments in the wire and between wires in the cable, there is a trade-off between loss and stability. The essence of good design is to control the losses without compromising stability too much. Minimum quench energy MQE is a simple unique number for a given conductor under given conditions and gives a fair measure of stability. It is strongly recommended as a criterion for deciding on whether a chosen configuration of resistive barriers will reduce the wire performance significantly. It may also be a help in those difficult judgements about matrix: superconductor ratio, temperature margin etc for a new magnet if there is available a body of experience on the MQE and performance of existing magnets.

Coupling losses within the wires must be controlled by using resistive barriers. There is scope for innovation in designing new geometries which increase ρ_{et} without increasing the MQE too much and which can be fabricated in long lengths. For cables it seems that cores offer the best prospects for reducing loss while retaining a reasonable inter-strand contact for stability and current sharing.

Although NbTi has been around for as long time, there is still lots of work to do.

REFERENCES

[1] G. Moritz, 'Superconducting magnets for the international accelerator facility for beams of heavy ions and antiprotons at GSI, IEEE Trans Appl Sup 13 p1329-1334 (2003).

[2] M.N. Wilson, 'NbTi Conductors with very low loss: A review', Cryogenics 48 p381-395 (2008).

[3] H. Kanithi et al, "A Novel Approach to Make Fine Filament Superconductors ", Supercollider 4, pp. 341-47 (1992).

[4] Ghosh AK, Sampson WB, Gregory E, Kreilick TS: IEEE Trans MAG 23 No 2 p 1724, (1987).

[5] Collings EW: Adv Cryo Eng Vol 34 p 867 (1988)

[6] Sumption MD, Collings EW: Adv. Cryo. Eng. (Materials) 42 p1175 (1997)

[7] Tachikawa K et al IEEE Trans Appl. Sup. Vol 3 No 1 p1374 (1993)

[8] Duchateau JL, Turck B, Ciazynski D: chapter B 4.3 in 'Handbook of Applied Superconductivity' ed B Seeber, pub Institute of Physics, London (1998)

[9] Popley RA, Sambrook DJ, Walters CR, Wilson MN: Proc. 1972 Applied Superconductivity Conference, Annapolis, IEEE pub 72CH0682-5-TABSC, p 516.

[10] Soika R et al: IEEE Trans Appl. Sup. Vol 13 No 2 p 2380 (2003)

[11] Willering GP et al: IEEE Trans Appl. Sup. Vol 18 No 2, p1253 (2008).

LOW LOSS WIRE DESIGN FOR THE DISCORAP DIPOLE*

G. Volpini#, F. Alessandria, G. Bellomo, M. Sorbi, INFN Milano, LASA Laboratory, Italy
P. Fabbricatore, S. Farinon, R. Musenich, INFN Genova, Italy
U. Gambardella, INFN LNF, Italy
J. Kaugerts, G. Moritz, M. N. Wilson, GSI, Darmstadt, Germany

Abstract

The SIS-300 synchrotron of the new FAIR facility at GSI (Germany) will use fast-cycled superconducting magnets. Its dipoles will be pulsed at 1 T/s; for comparison, LHC is ramped at 0.007 T/s and RHIC at 0.042 T/s. Within the frame of a collaboration between INFN and GSI, INFN has funded the project DISCORAP (*DIpoli SuperCOnduttori RApidamente Pulsati,* or Fast Pulsed Superconducting Dipoles) whose goal is to design, construct and test a half-length (4 m), curved, model of one lattice dipole. This paper focuses on the low loss superconducting wire design, and in particular to the transverse resistivity calculations and the dynamic stability verification.

WIRE CHARACTERISTICS

INFN has awarded a contract to for the manufacture of five unit lengths of superconducting Rutherford cable for the DISCORAP dipole model magnet [1]; two units will have a larger filament diameter, and three a smaller one (see Table 1); these will referred to as 1st and 2nd generation, respectively. Only two units are strictly required for the magnet manufacture and this redundancy should allow the comparison of different wire design solutions and to face manufacture problems.

The main characteristics of the superconducting wire are described in Table 1.

A cross section of the wire is shown in Fig. 1. The coloured zones represent the inter-bundle barriers, the hexagons represent the filamentary zones, with NbTi filaments embedded in a CuMn matrix both in the 1st and in the 2nd generation. The rest of the wire is in high-purity copper.

Besides having filaments with different diameters, the two generations have different bundle barrier material: the 1st generation in Cu and the 2nd generation in CuMn.

Table 1: Wire Main Characteristics

Diameter after coating	0.825 ± 0.003		mm
Filament twist pitch	5 +0.5 -0		mm
Effective Filament Diameter	1st generation	3.5	μm
	2nd generation	2.5	μm
Interfilament matrix material	Cu-0.5 wt% Mn		
Ic @ 5 T, 4.22 K	> 541		A
ρ_t at 4.22 K	0.4 + 0.09 *B* [T]		nΩ·m
Cu+CuMn:NbTi ratio (α)	>1.5 ± 0.1		

*Work supported by INFN and partly by GSI
Email: giovanni.volpini@mi.infn.it

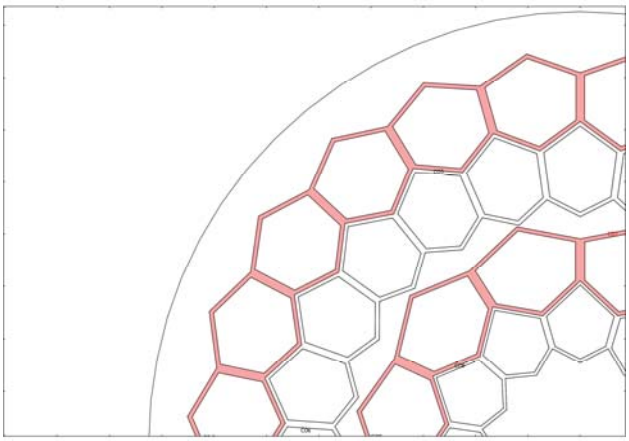

Figure 1: A detail of the wire cross section.

LOSSES EDDY & TRANSVERSE CURRENTS

Problem Statement

The largest loss contribution comes from the hysteretic losses within superconducting filaments. These losses are proportional to the filament diameter, and this motivates the quest for smaller filaments.

A second contribution is represented by the losses generated by Joule dissipation in the resistive matrix due to the currents induced by a changing external magnetic field, normal to the wire axis. These currents flow:

i) In loops composed by different superconducting filaments and closed through the matrix, in a plane normal to the wire axis. These are the interfilamentary currents;

ii) In circuits lying in planes parallel to the wire axis, entirely in the resistive matrix. These are the eddy-currents.

The contribution from i) + ii) to the power loss per unit volume is given by (in W/m^3):

$$q = j^2/\sigma = \sigma\,[\dot{B}^2 x^2 + (\partial_x \varphi)^2 + (\partial_y \varphi)^2] \quad (1)$$

($\dot{B}$ is the external magnetic field ramp rate, σ is the resistive matrix conductivity and x the direction normal to the magnetic field and to the wire axis), where the first term between square parentheses accounts for the eddy currents, and the gradient terms describe the interfilamentary currents.

The potential can be computed from the Laplace's equation,

$$\nabla^2 \varphi(x, y) = 0 \qquad (2)$$

with proper boundary conditions:

$$\partial_n \varphi(R_0, \vartheta) = 0$$

which describe the confinement of the currents inside the wire (R_0 is its radius), and

$$\varphi_{BC}(R, \vartheta) = \frac{\dot{B}\, L\, R}{2\,\pi} \cos(\vartheta)$$

(L is the filament twist pitch) valid on the filamentary zone boundaries, which takes into account the current entering/exiting into/from the filaments.

Once the total power dissipation Q found integrating Eq. 1 over the wire cross section has been computed, we express it in terms of transverse resistivity by means of

$$\rho_t = \frac{\dot{B}^2}{Q}\left(\frac{L}{2\pi}\right)^2$$

We therefore emphasize that we use the term "transverse resistivity" in a broader meaning, to describe both the sources i) and ii) of dissipation described above.

Solving the Problem: Analytical Approach

Duchateau *et al.* [2] have developed a model, based on a simplified geometry, with cylindrical symmetry. In this model, equations (1) and (2) may be solved analytically.

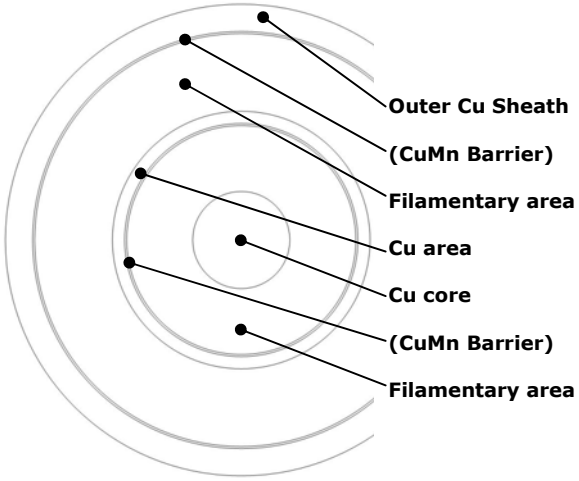

Figure 2: Annular region geometry model for the wire.

We have improved their approach, to better suit our geometry, increasing the number of annular regions from 4 to 7 (see Fig. 2). The Laplace equation has then been solved, and the power term integrated explicitly.

Solving the Problem: FEM Solution

Equations (1) and (2) were solved also by means of a FEM simulation, performed with COMSOL 3.4. This allows a more realistic description of the wire geometry. In Fig. 3 we show the potential φ (colour map), and the current density due to the interfilament coupling, for a second generation wire, where both the barriers (shown in Fig. 1) are in CuMn. The total power dissipation Q is found by numerical integration of (1). From Q we compute the effective transverse resistivity.

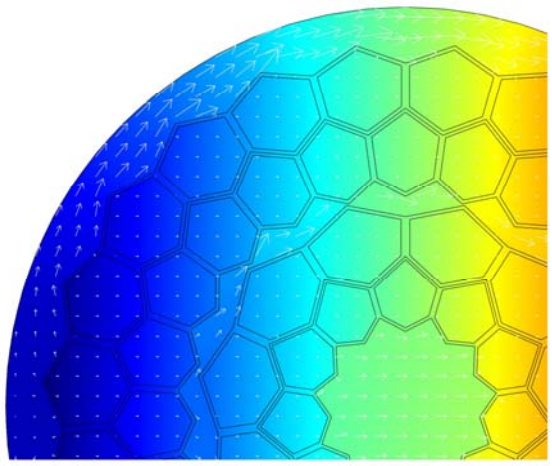

Figure 3: Coupling currents (white arrows) and coupling potential colour map for a 2nd generation wire.

Comparison of the Analytical and FEM Results

Fig. 4 shows a comparison of the transverse resistivity values obtained with the analytical and FEM methods: we notice that have a good agreement, 15% or better, between the two approaches, the FEM results being always lower than those obtained from the analytical methods. This is a very good results, since the geometry approximation done in the analytical model is rather crude, as it can be appreciated comparing Fig. 1 and Fig. 2.

The computations have been done under two extreme hypotheses regarding the contact resistance between the NbTi filaments and the CuMn, referred to as "good coupling" and "poor coupling" in Fig. 4; in the former this resistance is zero and therefore the NbTi acts as a "shortcut" for the transverse current, while in the latter the contact resistance is very high, and the NbTi does not contribute at all to the transverse current flow. The uncertainty on the precise value of filament/matrix contact resistance introduces a discrepancy from 8% to 28% on the transverse resistivity.

From Fig. 4 we see that the 2nd generation is expected to have a transverse resistivity about 50% higher than the first one, at all fields.

In all the cases the results comply with the specification value reported in Table 1, represented here by the black line.

The contribution from eddy-currents to the total losses for $\dot{B}$ = 1 T/s, ranges from 10% to 15%, depending on the hypotheses.

We have also considered a further possibility, with only the outer barrier in CuMn and the inner one in Cu. The computed values of transverse resistivity are also shown in Fig. 4, for B = 5 T, marked with a dot. We will not pursue this solution, since its performances appear too close to the 1st generation.

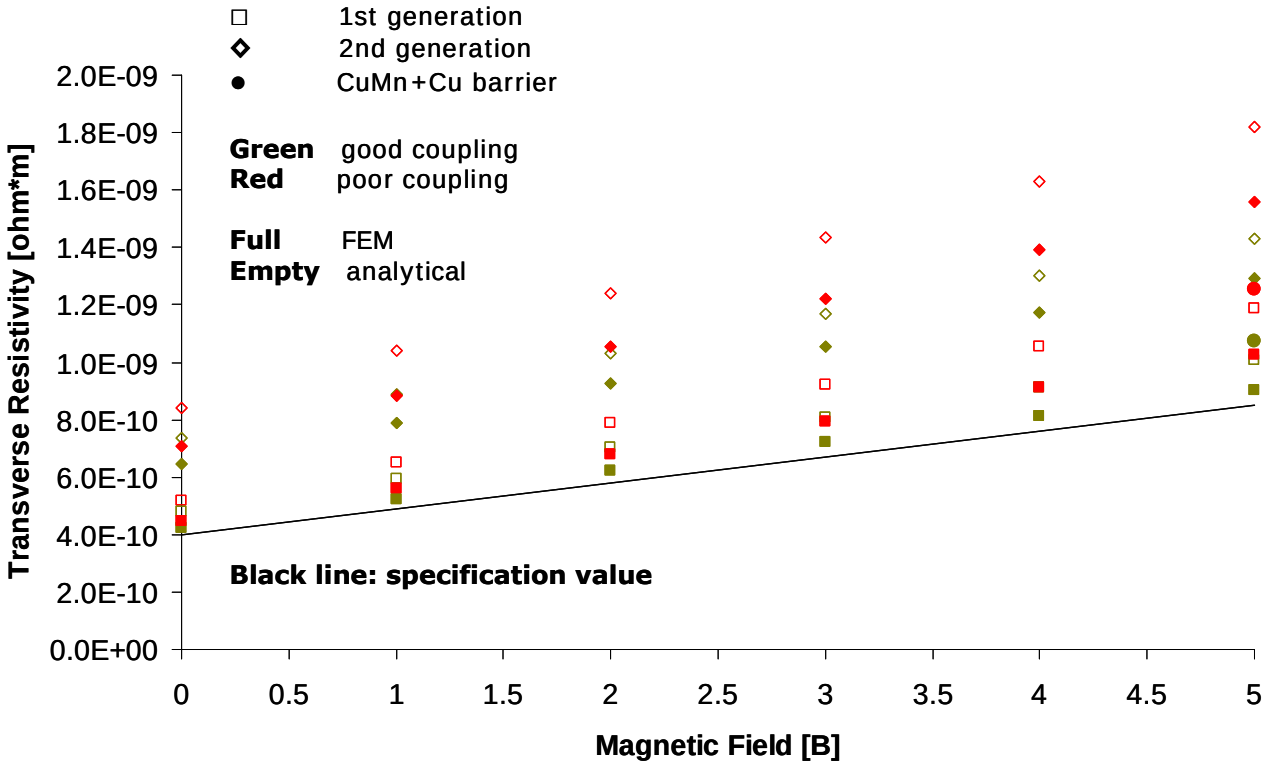

Figure 4: Comparison of transverse resistivity from analytical and FEM methods.

WIRE DYNAMIC STABILITY

We investigate the thermal stability following the approach described in [3], [4]. In this context the critical element is represented by a single filamentary bundle, whose width must satisfy:

$$D_{bundle} < D_{\max} = 4\sqrt{2}\sqrt{\frac{k_{th}\Delta\theta\,(1-\lambda)}{\lambda J_c^2 \rho_{el}}}$$

where: k_{th} is the filamentary bundle thermal conductivity, estimated assuming a weighed average beteween NbTi and CuMn yielding 1.9 W/mK; $\Delta\theta$ is the temperature margin; λ is the NbTi fill factor in the filamentary bundle, 0.588; J_c is the critical current @ 4.2 K, 5 T, 2700 A/mm^2; ρ_{el} is the matrix copper resistivity @ 4.2 K, 5 T, 3.5 10^{-10} Ω·m.

With these numbers D_{max} = 137 µm; the bundle area width is 60−70 µm, which is reasonably smaller than D_{max}; the margin for stability seems comparable to that of the layouts envisaged by [3].

CONCLUSIONS

Low-loss, fine filaments NbTi Rutherford cable is now manufactured by Luvata Fornaci di Barga (Italy) for the pulsed dipole long model, under contract from INFN.

Two generations of wire are foreseen, the first with 3.5 µm filaments and the second with 2.5 µm filaments. Transverse resistivity has been computed by means of two different methods, one analytical and a FEM, and their results are in good agreement.

Larger uncertainties arise from unknown features, like the precise value of the contact resistance between the CuMn matrix and the NbTi filaments.

All the results comply with the transverse resistivity specified by DISCORAP.

REFERENCES

[1] G. Volpini *et al.,* "Low-Loss NbTi Rutherford Cable for Application to the SIS-300 Dipole Magnet Prototype"; IEEE Trans. Appl. Supercond., 18, Issue 2, June 2008 pp 997-1000

[2] J. L. Duchateau, B. Turck and D. Ciazynski, "Coupling current losses in composites and cables: analytical calculations", Ch. B4.3 in "Handbook of Applied Superconductivity", IoP 1998.

[3] M. N. Wilson, GSI Fast-Pulsed Synchrotron Project Report no. 29-2, Apr. 26, 2007.

[4] M. N. Wilson, Superconducting Magnets, p 156, Clarendon Press, Oxford 1983.

Magnetization measurements and analyses on thin filament NbTi wires for SIS300 synchrotron superconducting dipoles*

U. Gambardella†, INFN Frascati, Italy
G. De Marzi, ENEA Frascati, Italy
P. Fabbricatore, S. Farinon, R. Musenich, INFN Genova, Italy
F. Alessandria, G. Bellomo, M. Sorbi, G. Volpini, INFN Milano, Italy
J. Kaugerts, G. Moritz, GSI Darmstadt, Germany

Abstract

In order to minimise the heat generation in the fast cycled superconducting dipoles foreseen for the synchrotron SIS300 at FAIR, thin filaments NbTi wires must be developed (see presentation of G. Volpini). Following the previous efforts carried out many years ago in SSC developments, we have analyzed some thin filament NbTi wires obtained either from laboratories or industry. These wires give us the opportunity to set up suitable metodology for studying the wire needed to the manufacturing of SIS300 dipoles. We use a magnetic characterization, by means of vibrating sample magnetometer, to get important informations in the wire performances. Rather than the usual critical current density computation, this presentation will deal with typical aspects of thin filaments NbTi wires which can be experimentally derived: the transverse resistivity, the presence of magnetic materials, and the proximity effect.

INTRODUCTION

The requirement of low dissipation superconducting wires for fast ramped dipoles, such us the one under development within the INFN project NTA-DISCORAP, supports measuring techniques able to provide fast and reliable data from wires under investigation. In order to reduce hysteretic losses of the superconducting material it is customary to reduce the superconducting filament size in the wire but this increases the filament number and consequently reduces the filament spacing[1][2]. In fact in a superconducting cylinder the hysteretic losses Q_h in one cycle may be computed from its radius a and the critical current density J_c with eq.1:

$$Q_h = \frac{8}{3\pi} J_c a B_m \qquad (1)$$

where B_m is the maximum value of the ramping magnetic field. These parameters may have noticeable drawbacks both in the wire manufacturing process, and in the wire superconducting features. In this paper we summarize the experience we made using two Vibrating Sample Magnetometer (VSM), MagLab 2000 by Oxford Instruments, to analyze the superconducting features in thin filaments NbTi wires formerly developed in previous projects.

* Work supported by INFN NTA-DISCORAP project
† P.O.Box 13, 00044 Frascati, Italy - *e*-mail gamba@sa.infn.it

EXPERIMENTAL ANALYSIS

We shall divide the experimental analysis in three ranges of the applied magnetic field: a) low field region; b) high field region; c) cycles to compute losses.

Low magnetic field

It is a good practice to have a detailed behavior of the $M(H)$ curve from the zero field cooling (ZFC) state of a wire. Although the measure is time consuming we consider that this curve reflects the first full diamagnetic response of a wire, thus it is a signature of the superconducting volume, effective or apparent, we are dealing with. In this curve is reflected the size of filaments and eventually the weak coupling among them.

The experimental curves of the magnetization M

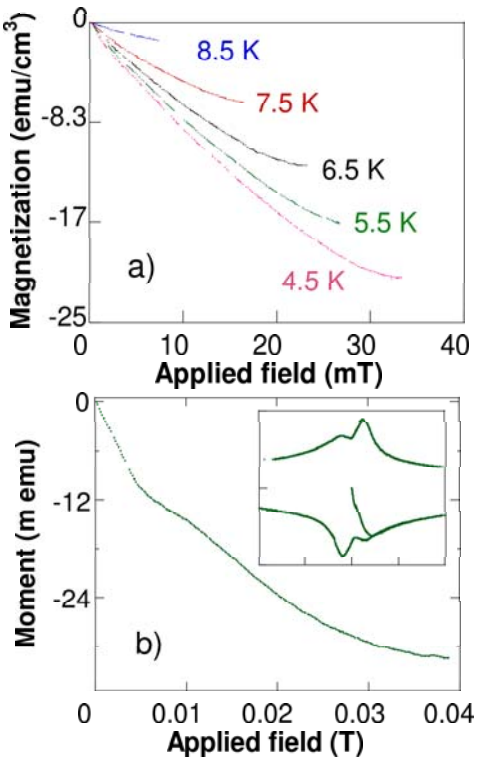

Figure 1: a) low field virgin magnetization for IGC944; b) low field virgin magnetization for SC357, in the inset is shown the $M(H)$ cycle $\pm$0.2T.

recorded in sample IGC 944b (a 2.6 μm filaments wire) are shown in Fig. 1a) as a function of the applied magnetic field $\mu_0 H$ at different temperatures. The linear slopes of the curves are related to the superconducting volumes by

$$V = -\frac{1}{\chi_0}\frac{dm}{dH} \tag{2}$$

where m is the magnetic moment and χ_0 the susceptibility.

This analysis is widely applied to wires, taking into account of the proper demagnetization factor, but in the case of thin filaments wires the results is quite far from the nominal volume expected from geometry (typically lower). In addition the temperature behavhior does not follow the penetration depth temperature behavior $(1-t^4)^{-1/2}$, being t the reduced temperature. The problem arises when the filament radius r becames comparable to the magnetic penetration depth λ: in this occurence the χ deviates from its bulk value. This dependence of χ with the ratio r/λ has been computed for simple geometry[3] and can be used to correct the χ value to be used in eq.2.

In thin filament wires the number of filaments increases thus reducing spacing among them. At a certain point, due to proximity effect (PE) superconducting coupling among filaments occurs[4]. This weak superconductivity has a clear signature: usually low field strength is enough to break the coupling. However weak couplings induce an excess of irreversible magnetization at low field values. Its occurence is revealed by a changing slope of the $M(H)$ curve at low field, starting from a ZFC condition, as shown in Fig. 1b) for SC357 (a 5 μm filaments wire with pure Cu matrix). In the inset of the same figure it is shown how this phenomena may also affect the $M(H)$ cycle which appears similar to a flux jump phenomena.

High magnetic field

There are no large differences between standard NbTi wires and thin filaments wire from the point of view of VSM critical current measurements. One peculiarity of thin filament wires is that, to avoid weak coupling phenomena, magnetic impurities, like Mn, are diluted in the Cu matrix. The presence of magnetic impurities in the wire is observed in the $M(H)$ curve, being more and more evident as the magnetic field increases. In Fig. 2 it is reported the $M(H)$ curve for the sample SC356 (a 5 μm filaments wire with CuMn matrix), where the presence of Mn is detectable at 15K (in the normal state) from the linear slope of $M(H)$ curve, which adds to the regular magnetization shape in the superconducting state (at 4.5K) of the wire. Though this contribution does not affects the ΔM value, used for the critical current computation, there are difficulties in computing the reversible and irreversible parts of the curve as the $M(T)$ behavior of the CuMn matrix cannot be measured independently and canceled. This hinder some specific feature, like the Ginzburg-Landau parameter κ which could be derived from the reversible magnetization near the upper critical field[5].

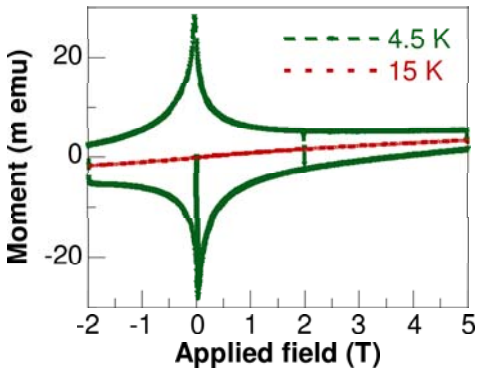

Figure 2: $M(H)$ cycle for SC356: normal (15K) and superconducting (4.5K) states.

Finally it is worth noting that the excess of reversible magnetization due to the magnetic impurities could also affect field quality, if not considered, when designing magnets with wires made of CuMn matrix.

Magnetic cycles and losses

The low loss wires have strategic applications in fast ramped magnets, where, in addition to the irreversible magnetization losses, the coupling losses among filaments became relevant. The lucky fact is that the magnetic impurities increase the local Cu resistivity, reducing the coupling currents between adjacent filaments, which arise under changing transverse magnetic fields.

This resistivity is called transverse resistivity $\rho_\perp$, and is intimately connected to the current distribution in the complicated geometry of a twisted multifilamentary wire. To be more precise $\rho_\perp$ is not only a material property but it includes the current flow path determined by the local shielding currents. One of the way to determine this parameter is to measure $M(H)$ cycle under controlled field ramp rate. In the approximation of wire time constant $\tau \ll T_m$, being T_m the time required to ramp the field to the highest value B_m the specific loss per unit cycle is[6]:

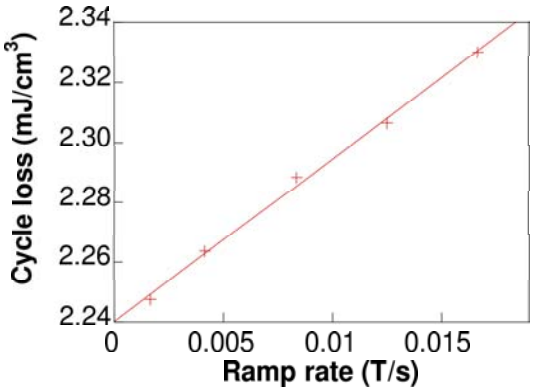

Figure 3: Loss computed at different ramp rates for SC356.

$$Q_{tot} = Q_h + \frac{B_m^2}{2\mu_0}\frac{8\tau}{T_m} \quad (3)$$

As the hysteretic losses are independent of the ramp rate the relationship between ramp rate and losses is related to τ. Though the VSM has maximum ramp rate of 1 T/min, thus it is not designed to investigate dynamical losses, the above mentioned relationship is still detectable. In Fig.3 the loss value computed in one cycle ($4 \pm 0.5T$) as a function of the ramp rate is shown for the sample SC356 at 4.5 K. A linear fit can be easily found, giving a value for $\tau \sim 2ms$. The time constant can then be used to estimate the transverse resistivity, once the geometrical conditions are known. In our case the sample length is much lower than the filament twist pitch thus the relationship between τ and $\rho_\perp$ is[7]:

$$\tau = \frac{1}{2\pi^2}\mu_0\frac{l^2}{\rho_\perp} \quad (4)$$

Being the sample length $l \sim 4mm$ from eq.4 we obtain the value $\rho_\perp \sim 3.5 \times 10^{-10}\Omega \cdot m$. Such value is not far from values obtained by using ac analysis in different NbTi wire also made of CuMn matrix[8].

CONCLUSION

Magnetic measurements performed by using a VSM equipments can be a fast and reliable method for studying superconducting features of low losses NbTi wires. Among others, the analysis of key features of low loss wires, such as the transverse resistivity, can be approached. To finalize our work in this field, we are extending the ramp rate capabilities of our VSM to extend investigations up to 3 T/min. In this way we shall have more dynamic range to analyze for a better estimation of $\rho_\perp$.

ACKNOWLEDGEMENTS

Authors are indebted to A. Ferrentino, University of Salerno, for his technical support.

REFERENCES

[1] E.W. Collings, proc. ECOMAG Workshop, Frascati, Oct 26-28, 2005, `http://ecomag-05.web.cern.ch/ecomag-05/`

[2] M. N. Wilson, proc. ECOMAG Workshop, Frascati, Oct 26-28, 2005, `http://ecomag-05.web.cern.ch/ecomag-05/`

[3] F. Gomory, Supercond. Sci. Technol. 10 (1997), p. 523-542.

[4] M.D. Sumption, S. Takacs, E.W. Collings, Adv. Cryogenic Eng. (Materials) 44, edited by Balachandran *etal.*, Plenum Pless, New York 1998, p. 1085-1092.

[5] M. Tinkham, "Introduction To Superconductivity", Second Edition, McGraw-Hill 1996, p. 160.

[6] M. N. Wilson, " Superconducting Magnets", Clarendon Press 1983, §8.3

[7] G. Witz, X. D. Su, K Kwasnitza, R. Flukiger, Physica C 384 (2003) 334

[8] P. Fabbricatore, private communication

ADVANCES IN ITER RELEVANT Nb-Ti AND Nb_3Sn STRANDS AND LOW-LOSS NbTi STRANDS IN RF

A. Shikov, V. Pantsyrny, A. Vorobieva, L. Potanina, V. Drobyshev, N. Kozlenkova, E. Dergunova, I. Gubkin, S. Sudyev, Bochvar Research Institute of Inorganic Materials (VNIINM), Rogova St. 5, 123060 Moscow, Russia

Abstract

The review of the main results of R&D directed on the enhancement of ITER relevant NbTi and Nb_3Sn strands performance recently carried out in Russia (the Bochvar Institute) are presented.

For ITER PF type (NbTi) strands with Cu/non Cu ratio of 1.6 the attainment of ITER specified critical current density (J_c) ≥ 2900 A/mm^2 (5 T, 4.2 K) has been shown. For Toroidal Field (TF) strands (Nb_3Sn) the influence of doping and layout peculiarities of the wires produced by bronze method on their current-carrying ability has been investigated. It was shown that with non-doped matrix and doped filaments J_c exceeds 800 A/mm^2 (12 T, 4.2 K) while with the application of the doped bronze and non-doped filaments it exceeds 900 A/mm^2.

Internal-tin Nb_3Sn strand meeting the ITER TF specification requirements was also developed and fabricated. The results of testing of CICC samples in a SULTAN facility have shown that performance parameters are higher than ITER qualification requirements

Low loss model fine filament NbTi strands, intended for operating in fields with a ramp rate from 1 up to 4 T/s, has been developed and manufactured. The use of commercial MN-5 alloy (Cu-5wt.%Ni) and the Cu-0.5wt.%Mn alloy for matrix of strands are discussed. The critical current density higher than 2700 A/mm^2 (5 T, 4.2 K was shown to be attainable.

NB-TI STRANDS

In the Russia the development of Nb-Ti strands for ITER Project was based on the rich experience accumulated during almost 40 years of the development of the technical NbTi strands for different applications. Several typical examples of such strands that were produced commercially at the Ust-Kamenogorsk plant (established in 1970-s in the USSR) are presented in the Fig.1.

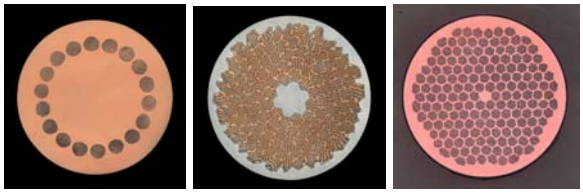

Figure 1: The Nb-Ti strands for different applications: a) for MRI tomographs, b) for AC electro technical devices, c) Strand for accelerator UNK (CKHT-8910-042).

The strand CKHT-8910-042 presented in the Fig.1c was designed for the accelerator UNK and produced commercially in amount of more than 100 tons. The strand of 0.85 mm in dia with the filaments diameter of 6 μm had the critical current density Jc (5T, 4.2K) - 2500 A/mm^2.

In the framework of ITER Project the RF Party has manufactured the Nb-Ti Cable (~0.5 ton), and shipped it to EFDA for further fabrication of the model Poloidal Field Coil Insert (PFCI). The testing of PFCI planned to be carried out in Japan (JAERI) in CSMC in June 2008. The cross section of this strand is presented in Fig. 2.

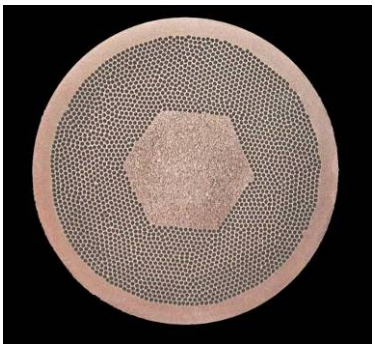

Figure 2: The Nb-Ti strand for ITER model coil PFCI. Strand diameter: 0.73 mm, number of filaments: 2346, filament diameter: 9.8 μm, Cu/non Cu ratio: 1.4, J_c > 2700 A/mm^2 (5T, 4.2K) (measured values: 2800-2900 A/mm^2).

In the frame of ITER Project the RF has to produce 40 t of Nb-Ti strands for PF 1&6 conductors and fabricate PF1 coil. The first model strands produced industrially from the billets 250 mm in diameter is presented in Fig. 3.

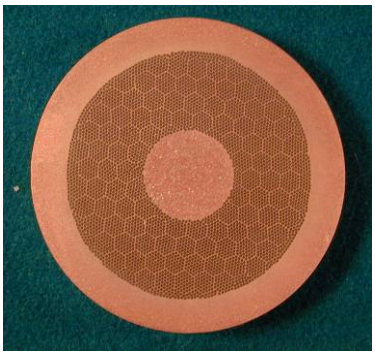

Figure 3: The Nb-Ti strand for ITER PF1&6 coils. Strand diameter: 0.73 mm, Cu/nonCu ratio: 1.6, filament diameter: 6.8 μm.

It was shown that the designed strands with Cu/non Cu ratio 1.6 met the requirements of ITER Specification for 4.2 K, 5T (J_c = 2900 A/mm^2), but at the high temperature (6.5 K) and in the high magnetic field of 6 T J_c was dropped to less than 100 A/mm^2.

For low loss Nb-Ti strands supposed to be used in the relatively high ramp rate magnetic field the specific specifications have to be met. Strands should be with small diameter filaments embedded in a resistive matrix and contain the resistive barriers. Minimum specification for J_c at 4.2 K and 5 T is 2500 A/mm^2; filament diameter reduction has to be attained with negligible coupling. Maximum effective filament diameter D_{eff} is 3 μm, with a target D_{eff} of 2 μm. An effective filament diameter of 3 μm corresponds to a hysteresis loss Q_h of 65 mJ/cm^3 of Nb-Ti for a bipolar field cycle +/- 3 T. An effective filament diameter of 2 μm corresponds to a Q_h of 48 mJ/cm^3 of Nb-Ti for a bipolar field cycle +/- 3 T.

Two types of resistive alloys were used as a matrix material – commercial available Cu-Ni alloys with Ni content from 5 to 10 wt%, and Cu-0.5%Mn alloy produced by induction vacuum melting. This alloy has RT resistivity of 3.41-3.42 μΩ·cm and resistivity in liquid helium – 1.70 μΩ·cm.

Fine filament (3.5 μm in diameter) NbTi strand for operating in fields with sweep rate up to 4 T/s was developed in Bochvar Institute (BI). The strand was fabricated by a single stacking method. Each of 10644 filaments was surrounded by a matrix of commercial MN-5 alloy (Cu-5wt.%Ni). The spacing was 0.5 μm. The central Cu core, tubes and the external sheath are fabricated from Cu with (R_{273}/R_{10}) > 250. RRR of the final strand is ~ 200. The cross section of this wire is shown in Fig. 4.

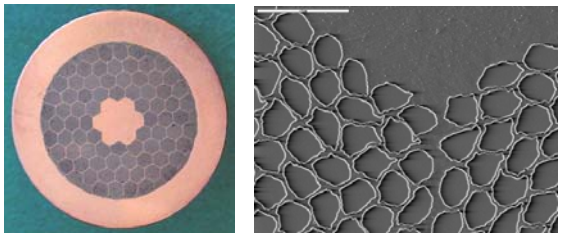

Figure 4: Low loss Nb-Ti strand 0.65 mm in diameter. Number of filaments: 10644; Cu/non Cu ratio: 1.8; combined matrix – Cu/ Cu-5wt.%Ni.

The properties of the wire were as follow: $J_c \geq 2900$ A/mm^2 (5 T, 4.2 K). The hysteresis losses = 51 kJ/m^3 per wire and 144 kJ/m^3 per superconducting volume.

Nb-Ti strands in resistive matrix for nuclotron type cable were designed for application in fast rate changing (up to 4T/s) magnetic field [1]. The design and cross section of trapezoidal cross section NbTi/Nb/Cu-5%Ni/Cu strand with 10374 filaments (6μm) fabricated by single stacking from billet 150 mm in diameter are presented in Fig. 5. Cu/non Cu ratio= 1.8. Nb-Ti, Nb, CuNi and Cu occupy 33.3%, 2.7%, 18.5% and 45.5% of the strands cross-section area respectively [2].

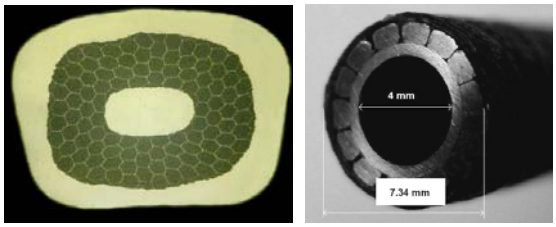

Fig.5. Low loss Nb-Ti strand designed for nuclotron magnets working at fast rate changing (up to 4T/s) magnetic field. Left: cross section of the strand. Right: cable for nuclotron magnet.

The AC losses were measured by calorimetric method at field amplitudes 1.05 T and 0.54 T. At nominal for SIS 100 dipole field rate of 4 T/s and field amplitude B=1.05 T the losses value normalized to overall strand volume are less than 30 mJ/cm^3 and 80 mJ/cm^3 for NbTi (see Fig. 6) [3].

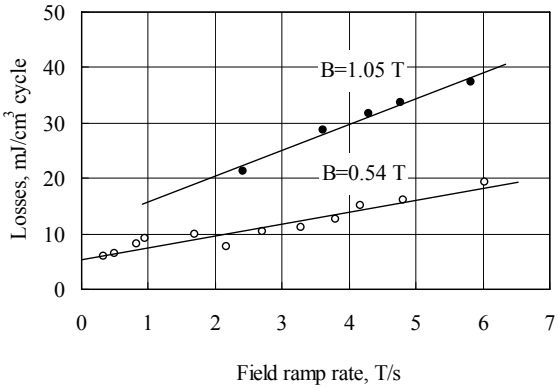

Figure 6: Hysteresis losses of the Nb-Ti trapezoidal cross section strand in different field ramp rates.

ITER-TYPE NB_3SN STRANDS

Starting from the middle of 1970-s both main types of Nb_3Sn multifilamentary strands (bronze and internal tin) were under the development. The typical cross sections of these early designed strands are shown in Fig. 7.

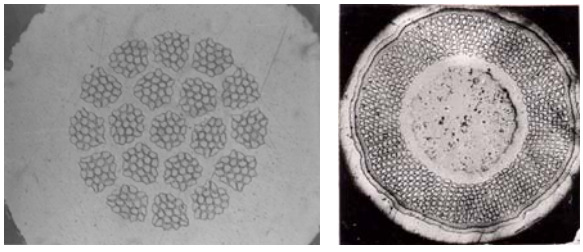

Figure 7: Cross sections of the Nb_3Sn strands; non stabilized bronze processed strand, 361 filaments (left); Cu stabilized Internal tin strand, 650 filaments (right).

For large magnet systems of fusion reactors the bronze processed strands were chosen to be used primarily because of simpler reaction heat treatment needed which assumed only solid state diffusion process for Nb_3Sn phase formation. Non-stabilized Nb_3Sn strand for Tokamak T-15 is presented in Fig. 8 altogether with the Rutherford type conductor, which was produced from these strands by applying the stabilizing copper after reaction heat treatment through the electrolysis process.

Figure 8: Left: Cross section of the Non stabilized bronze processed strand 1.5 mm in diameter; number of filaments: 14641; filaments diameter: 5 μm; J_c @ 8 T: 510 A/mm^2; average I_c: 900 A. Right: cross section of conductor for T-15; critical current @ 8 T is ~ 11.5 kA, i.e., ~ 110% of single strands current ability (11×900 A).

Approximately 90 tons of conductors were produced in an industrial way, which assumed production of more than 25 tons of strands.

In the frame of ITER Project the stabilized Nb_3Sn bronze processed strand (see Fig. 9, left) was developed and produced in amount of 1 ton. This strand was used for the fabrication of ITER TF Conductor (see Fig. 9, right) by cabling and jacketing in the Ti seamless tube.

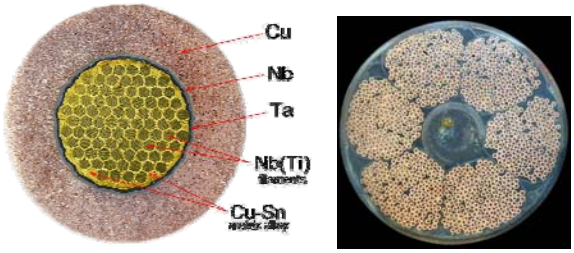

Figure 9: Left: cross section of stabilized bronze processed strand for ITER TFCI; diameter=0.81 mm, J_c @ 12T > 550 A/mm^2, hysteresis losses (+/-3T) < 200 mJ/cm^3, RRR > 100, Cu/(non Cu) = 1.5. Right: cross section of the cable in conduit conductor for TFCI.

The effect of degradation under mechanical loading was identified as an important issue for large magnet systems wound with CICC on the stage of ITER large model coils program. The strands with enhanced mechanical strength were developed (see Fig. 10). Mechanical strength was significantly (in a factor of 1.3-1.5) increased by replacing of certain part of stabilizing Cu on the nanostructured Cu-Nb layer. J_c of reinforced strands maintains at the same level.

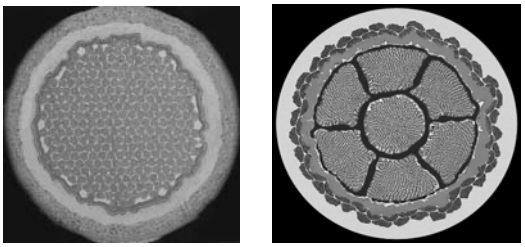

Figure 10: Strengthened by nanostructured CuNb alloy Nb_3Sn strands. Left: bronze processed strand with Cu-Nb layer replacing outer part of stabilizing Cu. Right: internal tin strand with Cu-Nb rods replacing the inner part of stabilizing Cu.

Due to overcome the consequences of the possible degradation of superconducting properties the new enhanced specification on the critical current density of TF strands (J_c >750 A/mm^2) was introduced by ITER. Development and fabrication of Nb_3Sn IT strand, meeting enhanced ITER TF specification for TF conductor's SULTAN sample testing has been performed (see Fig. 11 and Table 1). Fabricated strand total amount is ~110 kg (22.5 km).

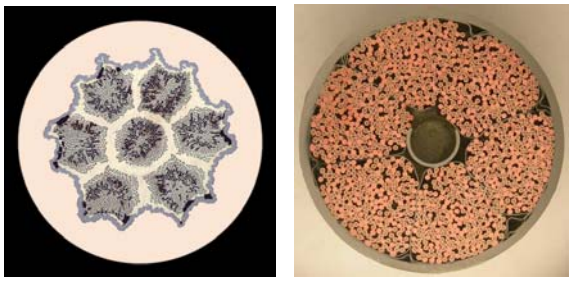

Figure 11: Cross sections of the internal tin Nb_3Sn strand, with J_c=830-950 A/mm^2, Non-Cu hysteresis losses (±3T; 4.2 K)=850-980 kJ/m^3 (left) and TF Conductor SULTAN sample, which met new ITER Specification Option 1 (right).

It is well known that in internal tin strand much higher J_c could be attained (up to 3000 A/mm^2 at 12 T, 4.2 K) due to the practical absence of limitation on the tin amount available for the Nb_3Sn phase formation. The comparison of the design features and properties of ITER type and so called high J_c internal tin strands is given in the Table 1. The quality of Nb_3Sn phase after heat treatment with last stage at 575° C 150 h + 650° C 200 h is essentially close to a quality observed in bronze processed strands (uniaxed grains and average grain size - approximately 90 nm).

The analysis of microstructure enables to suggest that large increase of J_c (not proportional to the increase of volume fraction of Nb_3Sn phase) is probably caused by the bridging of filaments. At the same time too strong bridging is negative for a stability of the strands.

Table 1. Properties of the ITER type and high J_c type internal tin Nb_3Sn strands

	ITER	High J_c
J(non Cu), [A/mm^2] (12 T, 4.2 K, 0.1 μV/cm, no external strain)	745	2070
Calculated volume fraction of Nb3Sn inside diffusion barrier, %	38.9	45.8
Qh, Hysteresis Loss [mJ/cm^3 non-Cu], @± 3T	~300	>1000
Calculated J_c(Nb_3Sn) [A/ mm^2] @12 T, 4.2 K	**2180**	**4850**

The practically attainable volume fraction of Nb_3Sn phase in bronze process strand is ~ 35% in the area inside the diffusion barrier. Therefore the requirement of J_{nc}= 800 A/mm^2 (12 T, 4.2 K) assumes the attaining of critical current density in Nb_3Sn phase equal to ~ 2700 A/mm^2. Three main possible ways of J_c increase could be considered:

- increase of quantity of Nb_3Sn phase (increase of Sn in bronze matrix);
- increase of quality of Nb_3Sn phase (increase of pinning by modification of microstructure);
- controlled bridging (optimization of the strand's design).

In the Cu-Sn matrix alloys the Sn content gradually increased from 10wt.% up to the limit of 16wt.%. The artificial doping of the Nb filaments by Ti has been designed and proved to be effective for both types of Nb_3Sn strands (bronze processed and internal tin) improving the quality of the Nb_3Sn microstructure by diminishing of the average grain size and almost eliminating the nonuniformity in microstructure of the Nb_3Sn layer. The bronze processed Nb_3Sn strands with controlled bridging of filaments were designed (see Figs. 12-13).

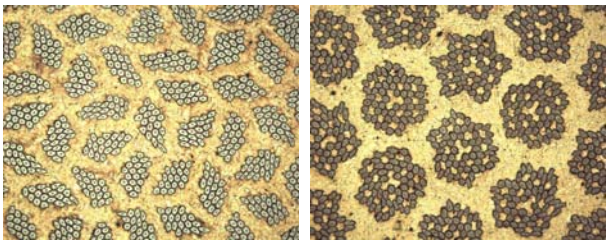

Figure 12: Bronze processed Nb_3Sn strands with controlled bridging of filaments.

As it was expected the J_c of the strands increased significantly to the values higher than 750 A/mm^2 (12 T, 4.2 K) in conditions of the same content of tin in bronze matrix. Also as expected the level of hysteresis losses increased proportionally to the diameter of the groups of filaments and attained the levels of 546 kJ/m^3 (for strand in Fig. 12, left) and 786 kJ/m^3 (for strand in Fig. 12, right) for standard ± 3T testing. The strands with controlled bridging and lower level of hysteresis losses (Q_h<350 kJ/m^3) were also designed (see Fig. 13, right).

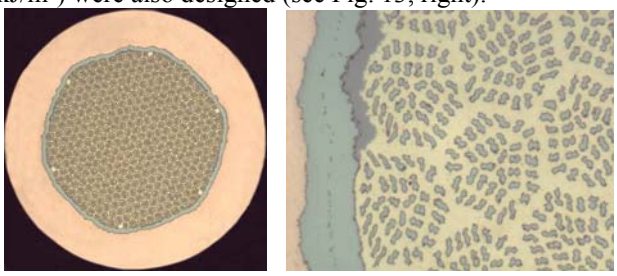

Figure 13: Bronze processed Nb_3Sn strands with controlled bridging of filaments and low hysteresis losses.

The critical current properties for the fields in the range of 8 T to 12 T are presented in Fig. 14. It was shown that for the diameter of the strand 0.82 mm (ITER specification) the values of J_c exceeded 900 A/mm^2.

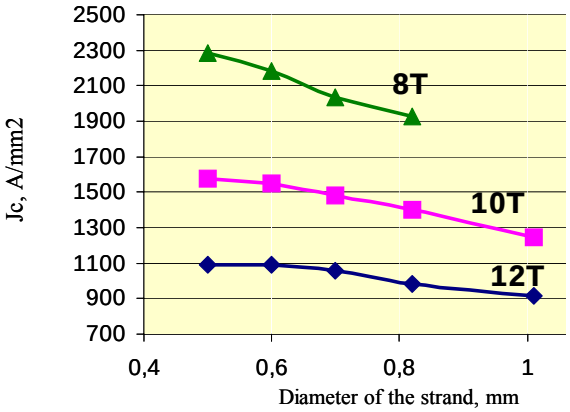

Figure 14: Dependence of J_c vs. strand diameter for the bronze processed strand with controlled bridging and low hysteresis losses.

CONCLUSIONS

Nb-Ti strands with Cu/non Cu ratio 1.4-1.6 designed for the use in ITER PF 1&6 coils have $J_c \geq$ 2900 A/mm^2 (5 T, 4.2 K) and meet the ITER specification.

Nb-Ti strands with low-loss for application in Fast Cycled Superconducting Magnets made a good progress recently (strands with 3-4 μm filaments in resistive matrixes have been produced), and the work is ongoing. Still some R&D work has to be done to attain target value.

Bronze processed ITER type Nb_3Sn strands made a good progress in critical current density, attaining 800 A/mm^2 (non-Cu, 12 T, 4.2 K) in commercially produced wires. In laboratory scaled wires 900 A/mm^2 (non-Cu, 12 T, 4.2 K) has been attained. The internal tin technology has been successfully proved by testing a full scale TF conductor sample in SULTAN facility.

REFERENCES

[1] Baldin A. M.et al., "Superconducting fast cycling magnets of the Nuclotron", in *IEEE Transaction on Applied Superconductivity* **5**, pp. 875-877 (1995).

[2] Khodzhibagiyan H.G. et al., “Design of new hollow superconducting NbTi cables for fast cycling synchrotron magnets,” in *IEEE Transaction on Applied Superconductivity* **13**, pp. 3370-3373 (2003).
[3] Vedernikov G.P., Shikov A.K., Potanina L.V. et al., "Multifilament superconducting wire based on NbTi alloy in a combined copper/copper-nickel matrix", in *Advances in Cryogenic Engineering* 50B**,** edited by U.B. Balachandran, Melville, New York. 2004, pp. 330-337.

ADVANCES IN Nb_3Sn PERFORMANCE

A. Godeke*, Ernest Orlando Lawrence Berkeley National Laboratory, Berkeley, CA 94720, USA

Abstract

Nb_3Sn wires with non-Cu critical current densities (J_c) that surpass 3 $kAmm^{-2}$ at 12 T and 4.2 K are commercially available in piece lengths longer than 10 km. Accelerator-type magnets that utilize these conductors have achieved record magnetic fields. This article summarizes key developments in the last decade that have led to these significant improvements in the performance of Nb_3Sn wires.

INTRODUCTION

The non-Cu J_c of Internal-Tin wires has approximately doubled from 1993 to 2003 [1]. Dipole magnets, constructed using Internal-Tin wires, have achieved consistently increasing magnetic fields, up to a present record of 16 T [2]. The article starts with a summary of the main properties of Nb_3Sn, discusses how optimizations of these properties have lead to the high J_c values, and provides an overview of existing and promising new wire manufacturing techniques.

MAIN PROPERTIES OF Nb_3Sn

Composition and superconducting properties

Nb_3Sn was discovered in 1954 by Matthias *et al.* [3]. Nb_3Sn is not a line compound, but is stable from about 18 to 25 at.% Sn [4]. In this composition range, it occurs in the A15 structure and this phase is generally referred to as A15. Two Sn rich line compounds, Nb_6Sn_5 and $NbSn_2$ are also stable below 930°C. The A15 phase undergoes a slight cubic to tetragonal distortion at temperatures below 43 K for compositions above about 24.5 at.% Sn, which has detrimental effects on the upper critical magnetic field (H_{c2}). The tetragonal phase therefore has to be prevented. The net effect of Sn deficiency is a suppression of the achievable field-temperature phase boundary [5]. The H_{c2} and critical temperature (T_c) are maximized at an optimal composition of about 24.5 at.% Sn. Alloying with Ti and Ta has limited effect on T_c. It does, however, prevent the tetragonal distortion from occurring and increases the resistivity, both of which result in an increase of H_{c2} [6]. An optimal H_{c2} is obtained with 1.5 at.% Ti addition and with 4 at.% Ta addition. The difference in effectiveness of Ti and Ta can be explained by assuming that Ta appears at the Nb sites, leading to $(Nb_{1-x}Ta_x)_3Sn$, and that Ti appears at the Sn sites, leading to $Nb_3(Sn_{1-x}Ti_x)$ [7].

* Electronic mail: agodeke@lbl.gov

Pinning capacity

A summary on literature results indicates a consistent, logarithmic dependence of the maximum pinning force on reciprocal grain size [4]. This dependence indicates that the grain boundaries are the main pinning centers in Nb_3Sn. The grain size in Nb_3Sn wires is only slightly dependent on the reaction time, but depends very strongly on the reaction temperature [8]. Optimal pinning of flux-lines occurs when the average grain boundary density approaches the flux-line spacing. The flux-line spacing for optimal alignment of the flux-line lattice with grain boundaries, a_0, can be calculated through $a_0 = (3/4)^{\frac{1}{4}}(\phi_0/\mu_0 H)^{\frac{1}{2}}$ [9], in which ϕ_0 is the magnetic field quantum and H is the magnetic field. This leads to $a_0 = 12$ nm, for a typical medium operating magnetic field of 12 T. The average grain size in wires ranges from 100 to 200 nm and is therefore one order too large for optimal pinning. The larger flux-line density compared to the grain boundary density leads to collective pinning and causes the field dependence of the pinning force to peak at only 20% of H_{c2}, i.e. typically around 5 T, resulting in a strongly reduced pinning force at operational magnetic fields in the 10 to 15 T range [8]. A reaction at an as low as possible temperature is therefore desirable, but this conflicts with the goal to obtain Sn-rich A15 volumes in wires. The heat treatment is therefore always a compromise in present wires.

Strain dependence

Strain has a detrimental effect on the superconducting properties. Present understanding suggests that strain modifies the phonon frequency spectrum and density of states [10, 11], and thus changes the electron-phonon interaction strength. The net effect of this on the superconducting properties is a reduction of the available field-temperature phase boundary ($H_{c2}(T)$) [12, 13, 14, 15]. The dominant strain component that causes this reduction of $H_{c2}(T)$ is the distortional second, or deviatoric, strain invariant [16, 17]. H_{c2} and T_c have, in first approximation for practical deviatoric strain values, a linear dependence on deviatoric strain [16, 18], which translates to a parabolic-like dependence of the critical current in wires under axial strain [14]. Several models have been developed over the years to describe the strain dependence of Nb_3Sn. These range from empirical one dimensional axial strain models [19, 20], and empirical three dimensional strain models [15, 18], to more fundamental oriented approaches [10, 11] that provide insight on the relative effects of the various strain invariants [21]. An excellent review of these developments was recently provided by Markiewicz [22]. There are ongoing efforts to generate

a deeper level of understanding of the exact physics that determines the non-hydrostatic strain dependence in practical superconductors. An notable example of this is the work of Salvetti and collaborators at the Massachusetts Institute of Technology, who attempt to calculate the strain sensitivity of Nb_3Sn using ab-initio calculations [23]. In conclusion it can be stated that a deeper understanding of strain sensitivity is under development, but at present it is unclear whether it will be possible to address and improve the strain sensitivity of practical conductors.

STATUS OF COMMERCIAL Nb_3Sn WIRES

Bronze processed wires

The Bronze process can be considered to be the 'classic' Nb_3Sn wire manufacturing process. It is a proven technology and Bronze wires are being produced by a large number of manufacturers in long lengths with very fine (about 5 μm) filaments. The achievable non-Cu J_c[1] is, however, limited to substantially below 1 kAmm^{-2} as a result of the limited solubility of 16% Sn in Cu. This results in a rapidly depleting Sn source, which causes a Sn gradient of around -4 at.% Sn μm^{-1} in the A15 [24], and therefore a low A15 fraction that is rich in Sn.

Powder-in-Tube wires

European Advanced Superconductors Powder-in-Tube (PIT) wires were first made by the Dutch Energy Research Foundation (ECN) in the Netherlands and have been commercialized by Shape Metal Innovation, Enschede, the Netherlands (SMI), which is now part of European Advanced Superconductors, Hanau, Germany (EAS). The history and development of PIT wires is extensively reviewed elsewhere [8]. The PIT process combines an abundant Sn source with a relatively large current density (over 2500 Amm^{-2}) and fine filaments (around 35 μm). The abundant Sn source results in relatively high Sn content in the A15, with a typical Sn gradient of around -0.3 at.% Sn μm^{-1}. This means that PIT wires contain a relatively large A15 fraction that is rich in Sn. Wires can presently be manufactured at SMI/EAS in about 45 kg net production units. The maximum non-Cu J_c has recently surpassed 2600 Amm^{-2} in 1.25 mm wires, comprising 288 filaments at 35 μm. These wires were developed for the Next European Dipole (NED) program.

Supercon Inc. PIT wires are also produced at Supercon, Shrewsbury MA, USA, as is extensively described elsewhere [8]. Supercon abandoned the use of $NbSn_2$ powder, in favor of alternative powders, renaming the process to Internal-Tin-Tube process. Their most recent process involves pure Sn in Nb tubes that contain Nb-47wt.%Ti tubes that forms Nb-1.5at.%Ti alloy (and thus optimized ternary Nb_3Sn) during the reaction. The Nb(-alloy) tubes are surrounded by a thin Ta layer that allows for a full reaction of the tubes without the risk of poisoning the stabilizing Cu with Sn. Non-Cu J_c values of 1800 Amm^{-2} have been achieved in this layout.

SupraMagnetics SupraMagnetics, Plantsville, CT, is producing PIT wires with jet milled Cu_5Sn_4 powder as described elsewhere [2]. This powder is more cost effective and provides more Sn for the reaction compared to the $NbSn_2$ powder that is originally used in PIT wires. A key modification in SupraMagentic's wire design is the use of octagonal, as opposed to hexagonal, filaments, which enables the implementation of Monel and Glid Cop Al-15 as internal strengthening inside the wires. 52 filament wires with 17.2% Monel between the filaments have been drawn down to 0.25 mm diameter, resulting in 20 μm filaments. Recent versions incorporating Glid Cop and 52 filaments have been drawn down to 0.5 mm diameter. Non-Cu J_c values of 2000 Amm^{-2} have been achieved in earlier Monel reinforced wires.

Supergenics I LLC Supergenics, Jefferson, MA, in collaboration with HyperTech Research, Columbus, OH, are developing promising PIT-like wires employing pure Sn and Sn-alloy cores as a Sn source. Proof-of-principle single sub-element wires of this type at 0.25 mm diameter, have achieved non-Cu J_c values of 2572 and 2733 Amm^{-2} in versions without, and with a Ta diffusion barrier, respectively. Wires with 246+25 filaments at 18 μm carry a non-Cu J_c of 2050 Amm^{-2}, whereas versions with 35 μm filaments have achieved 2250 Amm^{-2}. A billet of 37 mm diameter and 1 m long was successfully used to manufacture 2 km of wire at 0.7 mm diameter. The companies are presently scaling up to a 37 mm diameter billet with 5 m length.

Internal-Tin wires

The development of Internal-Tin (IT) wires, mostly focussing on IT wires from Oxford Instruments Superconducting Technology (OST), was recently reviewed by Dietderich [2]. OST has switched from Modified Jelly Roll and Hot Extruded Rod processes, to the Rod Restack Process (RRP®) as the standard manufacturing process. OST produces low loss, medium current wires, that utilize Nb 47wt.%Ti rods in the subelements to provide the alloying Ti. A single Ta diffusion barrier surrounds the entire subelement stack. J_c values between 800 and 1200 Amm^{-2} are typically obtained in these wires, and the filaments inside the subelements are designed to remain separated after reaction. OST also produces high current versions of the RRP® wires, in which the filaments inside the subelements are designed to grow together, through removal of the inter-filamentary Cu, to form a single A15 volume. Each subelement is surrounded by a Nb-Ta diffusion barrier, which is designed to partially react and con-

[1] All values are at 12 T, 4.2 K without self-field corrections, unless stated otherwise.

tribute to the J_c. 54/61 filament versions of the high current RRP® design are manufactured in lengths over 10 km, with filaments around 80 μm and J_c values that surpass 3000 Amm^{-2}. Compositional analysis on the high current wires indicates the the Sn content is relatively flat at about 24 ± 1 at.% Sn in the A15 volume [25]. High current RRP® wires therefore have a large A15 fraction that is close to optimal composition. This high Sn-rich A15 fraction, and an optimization of the A15 fraction in the non-Cu, are the main reasons these wires carry record current densities. The production of the high current wires is presently measured in tons per year with consistent J_c values of 2960 ± 110 Amm^{-2} and residual resistive ratio's (RRR) around 200. A relatively large effective filament diameter, in combination with a very high J_c, and RRR values that can be reduced as a result of barrier deformations during the cabling process, however, results in low and medium field instability issues in the high current wires. OST initially attempted to counteract these by applying Ta rods inside the subelements to sub-divide the A15 ring, but this proved difficult to scale up to large production units. OST is therefore presently addressing the relatively large subelement size by restacking to reduce the sub-element size. The most successful present version is a 114/127 restack that yields sub-elements around 40 μm in diameter and further restacks are under development.

SUMMARY

The recognition of a high Sn content in the A15 being a prime parameter to produce very high current density Nb_3Sn wires has resulted in the development of 3000 Amm^{-2} class Internal-Tin wires that are now commercially manufactured in long lengths. Wires manufactured with the Powder-in-Tube process are achieving J_c values that are now approaching similar current densities. The manufacture of very high current density wires with effective filaments below 50 μm is a common target for both processes. Bronze processed wires are, as a result of the limited solubility of Sn in Cu, presently not achieving record current densities, but their very small filament diameter of around 5 μm renders Bronze processed wires still desirable for applications that require very low losses. Alternative wire manufacturing processes are under development. These alternative approaches show very promising potential, but none is yet being produced commercially.

ACKNOWLEDGMENTS

This work was supported by the Director, Office of Science, High Energy Physics, US Department of Energy under contract No. DE-AC02-05CH11231. The author would like to acknowledge valuable input from colleagues at:

- Lawrence Berkeley National Laboratory, Berkeley, CA, USA
- University of Twente, Enschede, the Netherlands
- Applied Superconductivity Center and the National High Magnetic Field Laboratory, Florida State University, Tallahassee, FL, USA
- Plasma Science and Fusion Center, Massachusetts Institute of Technology, Cambridge, MA, USA
- University of Geneva, Geneva, Switzerland

and from the following companies for their valuable input and approval to include their latest results:

- Shape Metal Innovation, Enschede, the Netherlands
- European Advanced Superconductors, Hanau, Germany
- Supercon, Shrewsbury MA, USA
- SupraMagentics, Plantsville, CT, USA
- Supergenics I LLC, Jefferson, MA, USA
- Oxford Instruments Superconducting Technology, Carteret, NJ, USA

REFERENCES

[1] J. A. Parrell, M. B. Field, Y. Zhang, and S. Hong, Adv. Cryo. Eng. (Materials) **50B**, 369 (2004).

[2] D. R. Dietderich and A. Godeke, Cryogenics **48**, 331 (2008).

[3] B. T. Matthias, T. H. Geballe, S. Geller, and E. Corenzwit, Phys. Rev. **95**, 1435 (1954).

[4] A. Godeke, Supercond. Sci. and Techn. **19**, R68 (2006).

[5] M. C. Jewell, A. Godeke, P. J. Lee, and D. C. Larbalestier, Adv. Cryo. Eng. (Materials) **50B**, 474 (2004).

[6] M. Suenaga, D. O. Welch, R. L. Sabatini, O. F. Kammerer, and S. Okuda, J. Appl. Phys. **59**, 840 (1986).

[7] R. Flükiger et al., Supercond. Sci. and Techn. **21**, 054015 (2008).

[8] A. Godeke, A. den Ouden, A. Nijhuis, and H. H. J. ten Kate, Cryogenics **48**, 308 (2008).

[9] A. Godeke and D. R. Dietderich, Improved pinning in Nb_3Sn through grain refinement and alloying, To be published, 2008.

[10] W. D. Markiewicz, Cryogenics **44**, 767 (2004).

[11] W. D. Markiewicz, Cryogenics **44**, 895 (2004).

[12] A. Godeke, B. ten Haken, and H. H. J. ten Kate, IEEE Trans. Appl. Supercond. **12**, 1029 (2002).

[13] A. Godeke, *Performance Boundaries in Nb_3Sn Superconductors*, PhD thesis, Univ. of Twente, Enschede, The Netherlands, 2005.

[14] A. Godeke, B. ten Haken, H. H. J. ten Kate, and D. C. Larbalestier, Supercond. Sci. and Techn. **19**, R100 (2006).

[15] B. ten Haken, A. Godeke, and H. H. J. ten Kate, J. Appl. Phys. **85**, 3247 (1999).

[16] B. ten Haken, *Strain effects on the critical properties of high-field superconductors*, PhD thesis, Univ. of Twente, Enschede, The Netherlands, 1994.

[17] B. Ten Haken, A. Godeke, and H. H. J. Ten Kate, IEEE Trans. Appl. Supercond. **5**, 1909 (1995).

[18] A. Godeke, B. Ten Haken, and H. H. J. Ten Kate, Physica C **372−376**, 1295 (2002).

[19] J. W. Ekin, Cryogenics **20**, 611 (1980).

[20] D. M. J. Taylor and D. P. Hampshire, Supercond. Sci. and Techn. **18**, S241 (2005).

[21] W. D. Markiewicz, IEEE Trans. Appl. Supercond. **15**, 3368 (2005).

[22] W. D. Markiewicz, Supercond. Sci. and Techn. **21**, 054004 (2008).

[23] M. Salvetti, T_c strain sensitivity of Al, Nb, Nb_3Sn and Nb_3Al using ab-initio computations, Private communication, 2008.

[24] V. Abächerli et al., IEEE Trans. Appl. Supercond. **15**, 3482 (2005).

[25] P. J. Lee and D. C. Larbalestier, IEEE Trans. Appl. Supercond. **15**, 3474 (2005).

OPTIMIZATION OF THE HEAT TREATMENT SCHEDULE FOR NEXT EUROPEAN DIPOLE (NED) POWDER IN TUBE NB_3SN STRAND*

T. Boutboul, L. Oberli, CERN, Geneva, Switzerland
A. den Ouden, University of Twente, the Netherlands, D. Pedrini, G.. Volpini, INFN, Milan, Italy.

Abstract

A Nb_3Sn strand was successfully developed by the company SMI for Next European Dipole (NED) activity and on the basis of Powder-In-Tube (PIT) method. This strand, after the standard reaction recommended by the firm (84 h @ 675 °C), presents attractive performances as a critical current density in the non-copper part of ~ 2500 A/mm^2 for 4.2 K and 12 T applied field, an effective filament diameter of ~ 50 µm and limited flux jumps at low magnetic fields. Heat treatment optimization studies are currently performed at CERN to try to optimize the strand electric abilities. For this purpose, various heat treatment schedules were already investigated with a plateau temperature as low as 625 °C. The preliminary results of these studies are summarized here.

INTRODUCTION

The Next European Dipole (NED) project is a Joint Research activity of the Coordinated Accelerator Research in Europe (CARE) program [1]. Initially, the main goal of NED was to design, to develop and to build a large aperture and high-field (~ 15 T) dipole magnet. However, due to financial constraints, NED was mainly limited to the development and the fabrication of a high-performance Nb_3Sn conductor. The strand specifications for NED, summarized in [2], are very demanding. Indeed, in addition to very high critical currents targeted, corresponding to 3000 A/mm^2 in the non-copper part at 4.2 K and 12 T applied field, an effective filament diameter of ~ 50 µm is requested for a strand diameter of 1.25 mm. To achieve this goal it is then necessary to stack between 250 and 300 sub-elements within the final wire, which is obviously not a trivial task. In 2004, two orders were placed at Alstom-MSA (Internal Tin method) and SMI (Powder In Tube route).

During the R&D phase, SMI developed successfully [2] a strand, B215, including 288 filaments (~ 50 µm in diameter). This strand was produced in a lone length of 950 m and the maximal critical current ever measured for the heat treatment (HT) schedule recommended by the firm (84 h @ 675 °C) is 1397 A, corresponding to ~ 2500 A/mm^2 in the non-copper part at 4.2 K and 12 T. This strand presents fair RRR values (in the 70-80 range) and magnetization measurements showed only few flux jumps [2-3].

Following the reaction HT, the Nb_3Sn phase of a PIT strand is composed of a coarse grain region (1-2 µm in diameter, ~ 30 % of the A15 phase) and fine grain area (~ 200 nm). These coarse grains have a negligible contribution to the critical current. In addition, smaller fine grains, in principle obtained with lower temperature heat treatments, are more favourable from critical current point of view. Therefore, in this work, the idea was to optimize the critical current of the B215 PIT wire by decreasing the reaction temperature in order to, tentatively, further reduce fine Nb_3Sn grain size and to lower coarse grain ratio in overall A15 phase. The main results of this study are presented here.

*This work was supported in part by the European Community-Research Infrastructure Activity under the FP6 "Structuring the European Research Area" program (CARE, contract number RII3-CT-2003-506395

MAIN RESULTS

Due to limited amount of available B215 strand, a systematic optimization study with a broad scanning of both reaction temperature and duration was not feasible. Instead, a specific HT schedule was selected, the critical current and the RRR were measured and the cross-section of the reacted strand was examined by means of a microscope to evaluate the extent of the reacted area. At last, according to these results, the next HT schedule was chosen. Treatments were performed with a plateau temperature between 625 °C and 675 °C and a duration in the 84-320 hours range.

120 h @ 650 °C

- I_c data was found to be ~ 1 % larger than for standard HT (84 h @ 675 °C), in non-copper part J_c ~ 2520 A/mm^2.
- Cabling degradation appeared to be fairly reasonable: 4-8 % as compared to 10-12 % degradation observed for standard HT.
- RRR > 100 for virgin strand, i.e. better than standard HT (70-80). For extracted strands, no observed degradation (RRR ~ 100), contrary to standard HT (RRR ~ 30-60).

320 h @ 625 °C

- I_c ~ 1500 A @ 12 T and 4.2 K, + 7 % as compared to standard HT, in non-copper part J_c ~ 2670 A/mm^2!! New world record for a PIT strand!
- High RRR data for virgin strands: RRR ~ 220

SEM examinations

- Such examinations showed that, despite the 7 % increase in I_c, 320 h @ 625 °C sample presents slightly less reacted Nb_3Sn than standard HT sample.

- 320 h @ 625 °C sample has indeed higher quality Nb_3Sn with a higher Sn content (24.7 at. % Sn versus 24.2 at. %) and a lower mean fine grain size (~ 160 nm versus ~ 180 nm).
- However, reducing reaction temperature did not reduce coarse grain area which remains ~ 30 % of the total reacted Nb_3Sn region.

PERSPECTIVES

Measurements are currently underway at Nijmegen University to confirm the excellent critical current results for 320 h @ 625 °C and to assess the cabling degradation on both I_c and RRR. An additional heat treatment will be shortly launched at 625 °C but with duration longer than 320 hours in order to assess the critical current limits of the B215 PIT strand.

ACKNOWLEGMENTS

Many thanks to: E. Barisone, A. Bonasia, Z. Charifoulline, S. Geminian, P. Jacquot, G. Jesse, D. Leroy, S. Mathot, D. Richter, J.-L. Servais (CERN), B. Seeber (Geneva University), S. Wessel (Twente University).

REFERENCES

[1] A. Devred et al., Supercond. Sci. Technol. 19 (2006) S67-83.

[2] T. Boutboul et al., "Nb_3Sn conductor development and characterization for NED", J. Phys.: Conf. Ser. 97 (2008) 012211.

[3] A. Devred, T. Boutboul and L. Oberli, "Status of NED conductor development", IEEE/CSC & ESAS European Superconductivity News Forum (2007), ST5

METALLOGRAPHIC INVESTIGATION OF FRACTURE BEHAVIOR IN ITER-STYLE NB_3SN SUPERCONDUCTING STRANDS

M.C. Jewell[#], P.J. Lee, D.C. Larbalestier, National High Magnetic Field Lab, Tallahassee, FL, USA
A. Nijhuis, University of Twente, Enschede, The Netherlands

Abstract

In this work we specify the extent to which fracture in two ITER-style Nb_3Sn composite strands occurs in a collective or individual manner, under mechanical tension and bending from the TARSIS apparatus at the University of Twente. A bronze-route strand from European Advanced Superconductors (EAS), which has very uniform, well-spaced filaments, has a widely distributed (200 μm) fracture field and exhibits a composite of individual and collective cracks. An internal tin strand from Oxford Instruments – Superconducting Technology (OST) demonstrates much more localized, collective fracture behavior. The filaments in this strand are about four times larger (in area) than the filaments in the EAS strand, and also agglomerate significantly during heat treatment upon conversion of the Nb to Nb_3Sn. These results demonstrate that the architecture of the strand can play a significant role in determining the mechanical toughness of the composite, and that strand design should incorporate mechanical considerations in addition to electromagnetic and fabricability considerations.

INTRODUCTION

Fracture of Nb_3Sn filaments is a primary cause of irreversible critical current degradation in cable-in-conduit magnet systems utilizing Nb_3Sn composite wire. Under large Lorentz forces, the accumulated magnetic pressure can cause individual filaments or collections of filaments to fracture, preventing them from carrying electrical current. In general, the brittle Nb_3Sn phase fractures intergranularly and leaves the ductile interfilamentary Cu and any unrected Nb intact.

However, there exists relatively little data in the extant literature to describe the mechanisms and microstructural features that lead to crack formation and propagation. In fact, direct observation of the number, size, and distribution of fracture events in Nb_3Sn composite wire has received surprisingly little attention by the superconducting community. Zhang, Ochiai, and Osamura [1] evaluated fracture using metallography in bronze-processed wires in 1989. Their uniaxial strain test (conducted at room temperature) concluded that lower Nb_3Sn fractions in the composite actually increased fracture due to the matrix more effectively transferring load to the filaments. Van Oort [2] also examined fracture behavior after cabling by metallography and noticed that fracture incidents seemed to be correlated with microstructural features such as Kirkendall voids. Lee [3] has detected fracture events in Nb_3Sn tape conductor using an acoustic emission (AE) technique. While AE is attractive because it is non-destructive, the spatial resolution of the technique is not sufficient to image cracks in the 3 – 5 μm filaments of modern Nb_3Sn strand.

There is also not a great deal of relevant literature available from the wider metal-matrix composite (MMC) community. In the vast majority of MMC systems, the filamentary component is designed to improve the mechanical properties (strength, stiffness, or toughness) of the composite. Most experimental characterization and modeling efforts focus on how the filamentary structure affects the fracture or fatigue properties of the matrix. There are few applications for which the continuous mechanical integrity of the filaments is important for its own sake. Nevertheless, there are a few tantalizing clues in the literature to suggest that filament architecture can play an important role in determining the fracture behavior of the composite. For example, the results of Brockenbrough [4] suggest that the filament stacking pattern (square, hexagonal, etc.) has a very significant effect on the constitutive response of aluminum-boron MMC material as measured in transverse tension and transverse shear.

In this study, we will compare the fracture morphology (as revealed by metallography) of two commercially useful Nb_3Sn ITER-style conductors that have been subjected to electromechanical testing in the TARSIS apparatus at the University of Twente.

EXPERIMENTAL PROCEDURE

The TARSIS strain rig is a unique device invented at the University of Twente (Netherlands) that allows for the simultaneous mechanical deformation and critical current testing of Nb_3Sn superconducting strands. A more complete description of the technique and some representative results may be found here [5]. TARSIS can be equipped a periodic bending probe that uses a series of protruding bulges, arranged in a periodic fashion around the circumference of a barrel, to apply a combination of tension and periodic bending to the superconducting sample. In the sample set investigated here, the bending probe had a wavelength of 5 mm.

Each sample was extracted from the probe after full electromagnetic characterization, and metallographically mounted in the plane perpendicular to the loading direction. This allows for purely tensile (at the full wavelength position) and purely compressive (at the half wavelength position) regions to be imaged for damage characterization. Metallographic polishing was performed using SiC paper for rough grinding and flattening, followed by fixed diamond abrasives at 15 μm and 8 μm and diamond paste on napless cloth at 3 μm and

1 µm. Final polishing was performed on a napless chemo-textile cloth using 0.05 µm colloidal silica.

Imaging was performed on a Zeiss 1540 XB Field Emission Scanning Electron Microscope (FESEM) using both secondary (SE) and backscatter electron (BSE) detectors.

RESULTS AND DISCUSSION

Figures 1 and 2 show longitudinal cross section of EAS and Oxford ITER strands, respectively, near the peak bending position where fracture occurs. The inset in each image shows a transverse cross section of the strand being imaged, and also specifies the maximum peak bending strain on the sample, along with the fraction of initial critical current (I_c) remaining after testing.

The EAS strand is a bronze-process strand comprised of 8305 filaments segregated into 151 sub-bundles. The filaments are in general well-separated one from another, both before and after heat treatment. The filaments have an average post-heat treatment area of 9.0 µm^2, which corresponds to an effective circular diameter of 3.4 µm.

The Oxford strand is an internal tin strand comprised of 3097 filaments segregated into 19 sub-bundles. The filaments in this strand, while well-separated before heat treatment, tend to agglomerate after conversion from Nb to Nb_3Sn. These filaments are also much larger than the EAS filaments, with an area of 31.1 µm^2, which corresponds to an effective circular diameter of 6.3 µm.

The fracture morphology resultant from the TARSIS test is shown for EAS and Oxford strands in figures 1 and 2, respectively. The thick, horizontal layer on the top and bottom of each image is the Ta diffusion barrier of the wire. The EAS strand demonstrates a combination of individual and collective cracking events. The cracking is distributed over approximately 200 µm of wire length, and although some sub-bundles do fracture in a collective manner, there is no single dominant fracture event, despite this strand being deformed to 1.7% peak bending strain. At that strain value, the strand still retained 15% of its original I_c value.

The Oxford strand, by contrast, exhibits a completely collective cracking event. The entire damage region consists of a single crack that propagates through the peak bend strain position. The spatial extent of the fracture field is very narrow (less than 10 µm). Interestingly, the sub-bundle cores (the locations of the Sn reservoir prior to reaction in this internal Sn strand), which are now primarily filled with Cu, do not, in general, fracture. The interpretation here is that the soft, ductile Cu arrests crack growth, but since the brittle filaments form a partially agglomerated annulus around the core, the cracks can propagate circumferentially. Note that this relatively simple damage layer degrades I_c to just 3% of its original value, compared to 15% remaining for the EAS strand with the much wider fracture field.

There are at least two clear implications from this work. First, that the architecture of the stand – the size, spacing, and agglomeration of the filaments – can have a significant impact on the fracture properties of the material.

Figure 1. EAS 5 mm bend fracture field after TARSIS testing. The spatial extent of the fracture field is ~200 µm, with a balanced mixture of correlated and non-correlated fracture events.

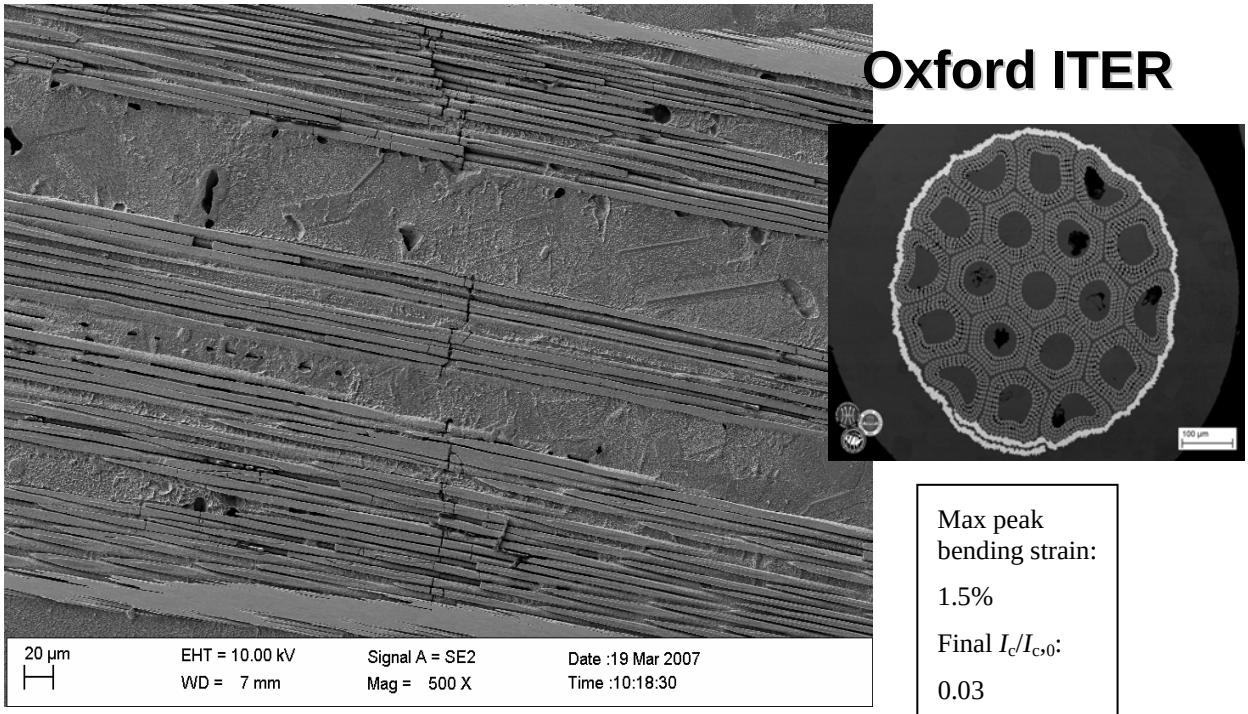

Figure 2. Oxford ITER 5mm bend fracture field after TARSIS testing. Here, the fracture is clearly centered around a central crack, with almost no ancillary damage whatsoever.

In particular the larger, more highly agglomerated Oxford filaments provide a much more conducive environment for the propagation of cracks than the smaller, well-distributed filaments of the EAS design. In the EAS strand, the interfilamentary Cu arrests crack growth more effectively since the cracks can not find a mechanically connected path to jump from filament to filament.

The second implication of this work is that the extent to which fracture is individual or collective plays a key role in determining the I_c degradation experienced by the strand. The EAS strand has, numerically, over an order of magnitude more cracks than the Oxford strand, yet resists I_c degradation much better since the cracks are more individual and less collective in nature.

CONCLUSIONS

Two ITER candidate strands were evaluated metallographically for fracture propensity after electromechanical testing in the TARSIS apparatus at the University of Twente. The bronze-process EAS strand has small (3.4 µm diameter), well-separated filaments, and the resulting fracture field is distributed over 200 µm, with a mixture of individual and collective fracture events. The internal tin Oxford strand, by contrast, has larger (6.3 µm dimater) filaments that are partially agglomerated. Here, the fracture pattern is highly collective.

The more collective cracking clearly has a more significant impact on the I_c, with the Oxford strand falling to just 3% of its original value, compared with 15% in the EAS strand. Thus, there is a clear role for strand manufacturers to help provide mechanical toughness to Nb_3Sn strands through the design process.

REFERENCES

[1] W. Zhang *et al.*, *Mater. T. JIM*, **30**, p. 932 (1989)
[2] J.M. van Oort, "Critical Current Degradation in Nb_3Sn Superconductors in Accelerator Magnets," Ph.D. thesis, University of Twente, Netherlands (2000)
[3] M.-R. Lee *et al.*, *Compos. Sci. Technol.*, **61**, p. 2017 (2001)
[4] J.R. Brochenbrough *et al.*, *Acta. Metall. Mater.*, **39**, p. 735 (1991)
[5] W.A.J. Wessel *et al.*, *Adv. Cryo. Eng. (Materials)*, **50**, p. 466 (2004)

SYNCHROTRON RADIATION TECHNIQUES FOR THE CHARACTERIZATION OF NB_3SN SUPERCONDUCTORS

C. Scheuerlein[1], M. Di Michiel[2], F. Buta[3], H. Reichert[4], L. Thilly[5]

[1] European Organization for Nuclear Research (CERN), CH-1211 Geneva 23, Switzerland

[2] European Synchrotron Radiation Facility (ESRF), 6 rue Jules Horowitz, F-38000 Grenoble, France

[3] University of Geneva, Group of Applied Physics (GAP), CH-1211 Geneva 4, Switzerland

[4] Max Planck Institut für Metallforschung, Heisenbergstraße 3, D-70569 Stuttgart, Germany

[5] University of Poitiers, Laboratoire de Métallurgie Physique, F-86962 Futuroscope, France.

Abstract

The high flux of high energy x-rays that can be provided through state-of-the-art high energy synchrotron beam lines has enabled a variety of new experiments with the highly absorbing Nb_3Sn superconductors. We report different experiments with Nb_3Sn strands that have been conducted at the ID15 High Energy Scattering beam line of the European Synchrotron Radiation Facility (ESRF). Synchrotron x-ray diffraction has been used in order to monitor phase transformations during *in-situ* reaction heat treatments prior to Nb_3Sn formation, and to monitor Nb_3Sn growth. Fast synchrotron micro-tomography was applied to study void growth during the reaction heat treatment of Internal Tin strands. The elastic strain in the different phases of fully reacted Nb_3Sn composite conductors can be measured by high resolution x-ray diffraction during *in-situ* tensile tests.

INTRODUCTION

Non-destructive methods like high energy diffraction or micro-tomography can complement the destructive microscopic techniques that are commonly used for the materials characterisation of Nb_3Sn superconductors.

Due to the low x-ray energy of laboratory x-ray sources, diffraction measurements with such sources are done in reflection geometry and are limited to a penetration depth of some tens of μm. Therefore, such experiments can not be used for non-destructive studies of Nb_3Sn strands. In contrast, neutrons or high energy x-rays from synchrotron sources allow *in-situ* diffraction measurements in transmission geometry with the highly absorbing Nb_3Sn strands. The x-ray transmission as a function of x-ray energy that has been calculated for a Ta alloyed Internal Tin (IT) strand with different diameters is shown in Figure 1. For the 1.25 mm-diameter strand, x-ray energies above 70 keV are needed for measurements under optimum conditions.

Here we describe three synchrotron experiments for the materials characterisation of Nb_3Sn strands, notably powder diffraction for phase analysis during *in-situ* reaction heat treatment (HT), fast synchrotron micro-tomography with μm spatial resolution for monitoring void growth during *in-situ* HT, and high resolution diffraction for measuring the 3-D strain state in the different phases of the composite superconductors under *in-situ* tensile loading.

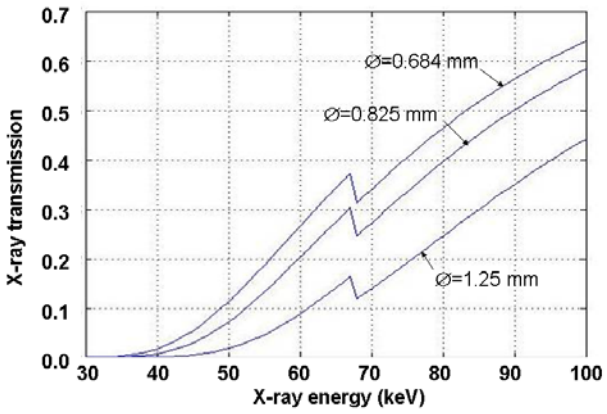

Figure 1: X-ray transmission as a function of x-ray energy for an Internal Tin Nb_3Sn strand with different diameter as a function of x-ray energy. The x-ray transmission for obtaining optimum signal-to-noise ratio in tomography is about 20 %.

SYNCHROTRON X-RAY DIFFRACTION FOR PHASE ANALYSIS DURING IN-SITU REACTION HT

The phase transformations that occur during the reaction HT of Nb_3Sn superconductors prior to the superconducting A15 phase formation can degrade the microstructural and microchemical Nb_3Sn homogeneity and, thus, have a detrimental influence on the critical properties of the fully reacted superconductor. The phases that are formed strongly depend on the strand design.

Powder diffraction measurements in transmission geometry can be used for *in-situ* phase analysis in Nb_3Sn strands. A high flux of high energy x-rays is needed in order to acquire diffractograms with sufficient signal-to-noise-ratio that allows to monitor the growth of weakly diffracting phases formed during the reaction HT, as for instance the orthorhombic $NbSn_2$ and Nb_6Sn_5 [1].

Synchrotron x-ray diffraction measurements were carried out at the ID15B high energy beamline of the ESRF in transmission geometry, using a 87.000 keV monochromatic x-ray beam. Debye Scherrer diffraction pattern were acquired in transmission geometry using a 2-

D detector. A diffraction pattern acquired for a Nb_3Sn PIT strand with a MAR345 image plate detector is shown in Figure 2 before and after radial integration.

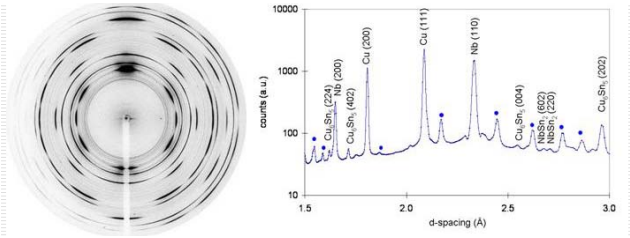

Figure 2: Debye Scherrer diffraction pattern acquired with a MAR345 image plate detector. In the right plot the same pattern is shown after radial integration. The diffractogram of the PIT strand has been acquired at RT subsequent to 490 °C HT. The diffraction peaks of a Cu-Nb-Sn phase are indicated by full dots.

For *in-situ* heating a dedicated furnace built at ID15 that enables an accurate sample temperature control during the diffraction experiments has been added to the experiment. In Figure 3(a) we show a sequence of 85 diffractograms that has been obtained with a PIT strand during *in-situ* reaction HT with a ramp rate of 60 °C h^{-1} and subsequent 4 hours isothermal heating at 675 °C. A semi-quantitative description of the phase transformations is shown in Figure 3(b).

NB_3SN PHASE GROWTH MONITORED BY SYNCHROTRON X-RAY DIFFRACTION

The Nb_3Sn growth kinetics during isothermal HT can be monitored by measuring prominent Nb_3Sn diffraction peak areas acquired during *in-situ* reaction HT. In Figure 4 the Nb_3Sn growth in the PIT B215 strand during 660 °C HT is shown. During the first 20 h diffractograms have been acquired *in-situ* (empty symbols). Longer heat treatments have been realised *ex-situ* (full symbols).

SYNCHROTRON MICRO-TOMOGRAPHY FOR MONITORING THE FORMATION OF VOIDS DURING IN-SITU REACTION HEAT TREATMENT

Void formation in Nb_3Sn strands degrades the microstructural strand homogeneity and causes localized stress concentrations and therefore can degrade the electromechanical properties of the superconductor. A quantitative description of void volume, shape and distribution within Nb_3Sn strands can be obtained using synchrotron micro-tomography. Sample preparation artefacts can be excluded by non-destructive tomography measurements.

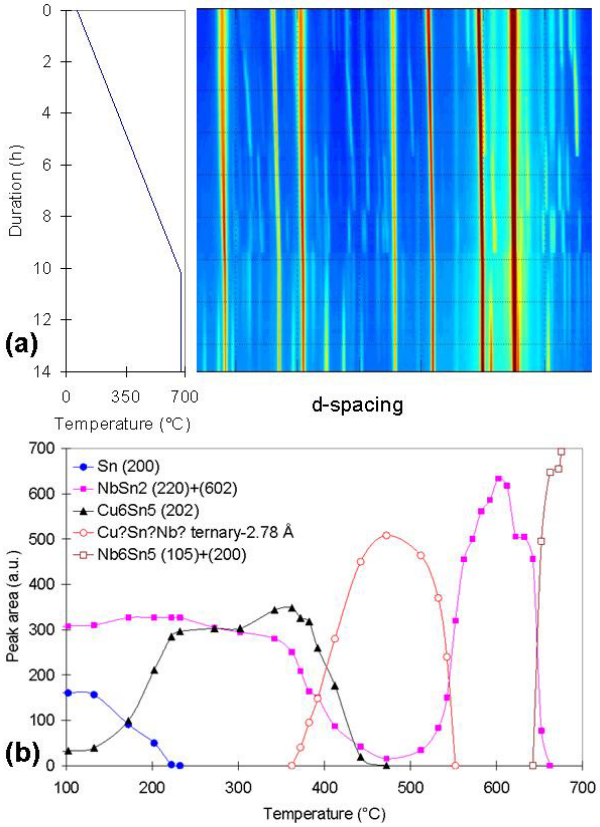

Figure 3: Variation of the diffraction patterns of a Nb_3Sn PIT strand during *in-situ* HT with a ramp rate of 60 °C h^{-1} and 4 hours isothermal 675 °C HT (a). The evolution of the diffraction peak areas of all Sn containing phases, apart from α-bronze, is shown in (b).

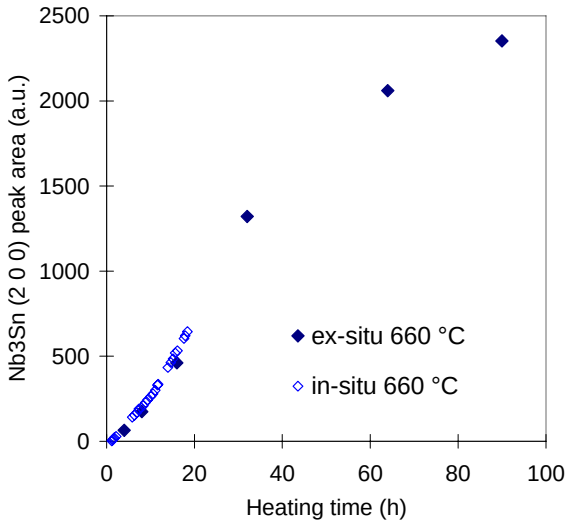

Figure 4: Nb_3Sn growth during isothermal 660 °C HT of PIT B215 monitored by Nb_3Sn (200) diffraction peak area measurements.

The distribution of the voids that are formed during the reaction HT of an IT strand can be seen in the transverse and longitudinal strand cross sections shown in Figure 5.

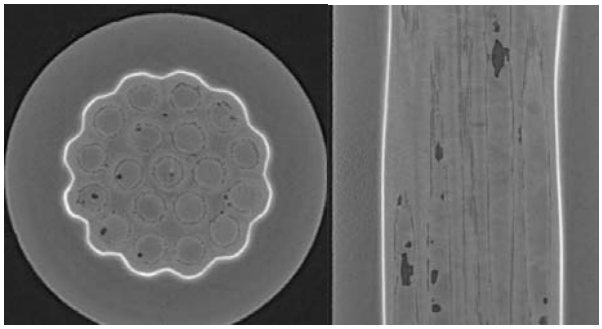

Figure 5: Transverse (left) and longitudinal strand cross section of an IT Nb_3Sn strand after *ex-situ* 580 °C HT.

The resolution of synchrotron micro-tomography measurements at ID15A is sufficient for the detection of the interfilament voids in IT strands that are formed as a consequence of differences in diffusion coefficients of Sn and Cu and Cu in Sn. The size of these voids shown in Figure 6 is about 1 µm.

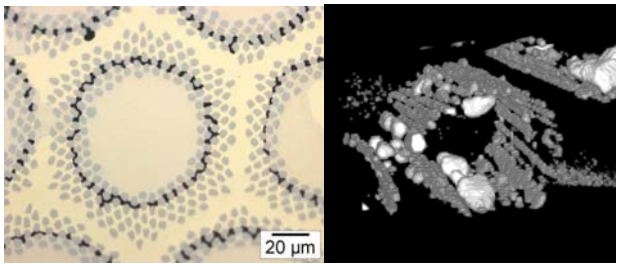

Figure 6: Optical micrograph of a strand cross section (left) and 3-D tomogram of the interfilament voids in one diffusion center of an IT Nb_3Sn strand after *ex-situ* 580 °C HT.

Due to the short acquisition time of less than one minute per tomogram, tomography experiments during *in-situ* HT are possible at the ID15A beamline of ESRF [2].

A sequence of 114 tomograms has been acquired during an *in-situ* HT of the IT strand shown in Figures 5 and 6. In Figure 7 a 3-D view of the voids formed in the Sn source regions of the IT strand at different temperatures is shown. The tomograms have been acquired during *in-situ* HT with a ramp rate of 60 °C h^{-1} with three additional isothermal holding steps for 2 h at 200 °C, 5 h at 340 °C and 2 h at 540 °C.

After the acquisition of each tomogram the strand sample has been moved in a monochromatic 88.005 keV x-ray beam for a diffraction measurement. The combination of micro-tomography and diffraction in one experiment allows to distinguish between different void growth mechanisms. The comparison of the void volume and Cu_3Sn volume as a function of the HT temperature (see Figure 8) shows that part of the voids in IT strands are formed because of density changes upon the formation of intermetallic phases [3].

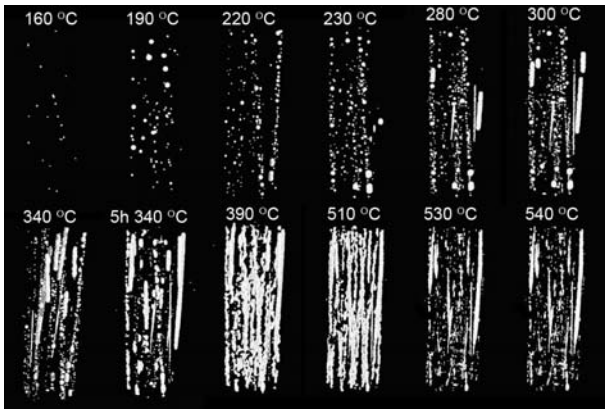

Figure 7: Voids inside an IT Nb_3Sn strand at different temperatures during *in-situ* reaction HT [3].

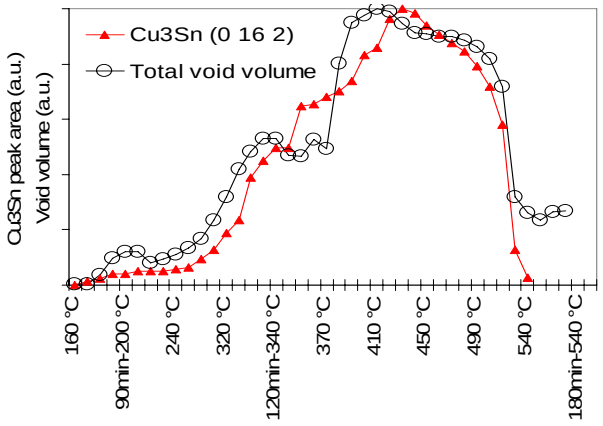

Figure 8: Comparison between the void volume and the Cu_3Sn volume formed during the reaction HT of an IT Nb_3Sn strand.

HIGH RESOLUTION SYNCHROTRON DIFFRACTION FOR MEASURING THE 3-D STRAIN STATE WITHIN NB_3SN COMPOSITE CONDUCTORS DURING IN-SITU TENSILE LOADING

High resolution diffraction measurements are a widely used tool for measuring the residual stress in a variety of different materials. In the case of Nb_3Sn composite wires, high resolution diffraction measurements can be applied for instance to measure the internal stresses caused by the mismatch of thermal expansion coefficients during the cool down from the processing temperature to the operating temperature and to measure the strain state in the different strand phases as a function of an externally applied wire stress, e.g. during a tensile test. As an example, the stress distribution in bronze route design Nb_3Sn strands at room temperature and at 4.2 K has been measured by neutron diffraction [4]. Because of the relatively low neutron flux it was necessary to use bundles of parallel aligned strands in order to increase the sample volume in order to acquire diffractograms with sufficient signal-to-noise-ratio within reasonable durations.

When the elastic strain of the different wire phases needs to be measured under a well defined uniaxial tensile stress, diffraction measurements must be carried out with a single strand configuration. At the POLDI strain scanning experiment at the SINQ neutron source of the Paul Scherrer Institut (PSI) it has become possible to study single multifilament composite wires under well defined macroscopic stress [5] [6]. However, acquisition times for acquiring Nb_3Sn neutron diffractograms with sufficient statistics are still in the order of hours and only the strongest Nb_3Sn reflection could be measured.

Due the high x-ray flux that can be provided at ID15, which exceeds the neutron flux of the most powerful neutron sources by many orders of magnitude, synchrotron experiments can be much faster and only a small sample volume is needed. At ID15B using a Trixell Pixium 4700 detector diffractograms with excellent signal-to-noise-ratio can be acquired in 10 seconds. This allows to perform diffraction measurements during *in-situ* tensile tests with standardised strain rates.

The relatively small scattering angles of the high energy x-rays used make it possible to add a dedicated tensile rig for stress-strain measurements of superconducting strands within a glass LHe cryostat (provided by University of Geneva) to the ID15B beamline and still record diffractograms with a large d-spacing interval [7].

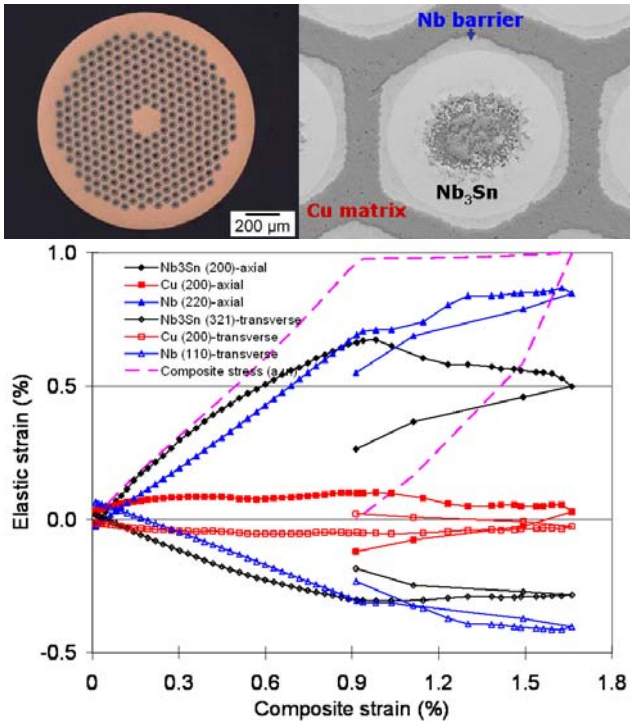

Figure 9: Elastic strain determined from selected reflections of the different phases of a fully reacted PIT strand, as a function of the composite strain, measured at 4.2 K with an extensometer. The nearly stress free lattice parameter used for the calculation of the elastic strain is an estimate.

Figure 9 shows preliminary results of the elastic strain in the different phases of a fully reacted PIT strand as a function of the composite strain measured with an extensometer. The resolution of the diffraction measurements that can be achieved is better than 0.01 %.

CONCLUSION

The continuously increasing x-ray flux provided through high energy synchrotron beam lines has enabled several new experiments with Nb_3Sn composite conductors. The main advantage of high energy synchrotron radiation experiments as compared to destructive microscopic techniques is that measurements can be performed *in-situ*. A better understanding of the superconductor processing could be obtained through the combination of different synchrotron techniques in one experiment, i.e. diffraction and micro-tomography during *in-situ* HT. High resolution synchrotron diffraction measurements can provide new information about the strain state within composite conductors under mechanical loading.

REFERENCES

[1] M. Di Michiel, C. Scheuerlein, "*Phase transformations during the reaction heat treatment of powder-in-tube Nb_3Sn superconductors"*, Supercond. Sci. Technol. 20, (2007) L55-L58.

[2] M. Di Michiel, J.M. Merino, D. Fernandez-Carreiras, T. Buslaps, V. Honkimäki, P. Falus, T. Martins, O. Svensson, "*Fast microtomography using high energy synchrotron tomography*", Rev. Sci. Instrum. 76, 043702, (2005)

[3] C. Scheuerlein, M. Di Michiel, A. Haibel, "*On the formation of voids in Nb3Sn superconductors*", Appl. Phys. Lett., 90, 132510, (2007)

[4] W. Goldacker, R. Flükiger, IEEE Transactions on Magnetics 21(2), 807-810 (1985)

[5] L. Thilly, P.O. Renault, V. Vidal, F. Lecouturier, S. Van Petegem, U. Stuhr, H. Van Swygenhoven, "*Plasticity of multiscale nanofilamentary Cu/Nb composite wires during in situ neutron diffraction: Codeformation and size effect*", Appl. Phys. Lett. 88, 91906, (2006)

[6] C. Scheuerlein, U. Stuhr, L. Thilly, "*In-situ neutron diffraction under tensile loading of powder-in-tube Cu/Nb3Sn composite wires: effect of reaction heat treatment on texture, internal stress state and load transfer*", Appl. Phys. Lett. 91(4), 042503, (2007)

[7] F. Buta, C. Scheuerlein, M. Di Michiel, B. Seeber, R. Flükiger, "*High resolution X-ray diffraction experiments to investigate the electromechanical behavior of Nb_3Sn superconducting wires*", poster presentation at the SPS Annual Meeting, Geneva, 2008

ELECTROMECHANICAL BEHAVIOUR OF PIT Nb_3Sn WIRES FOR NED*

B. Seeber, C. Senatore, F. Buta and R. Flükiger, University of Geneva-GAP, Geneva, Switzerland
T. Boutboul, C. Scheuerlein, L. Oberli and L. Rossi, CERN, Geneva, Switzerland

Abstract

The critical current vs. axial tensile strain and transverse compressive force for two PIT Nb_3Sn conductors, manufactured by SMI (now EAS), has been investigated. In addition, the distribution of the critical temperature has been determined by specific heat measurements. After identical reaction heat treatments wire #B207 has a slightly broader T_c distribution than wire #B215 and less volume fraction of Nb_3Sn. The behaviour under axial tensile strain is as expected, although the strain for maximum current, ε_m, is relativly low. However the studied wires are rather sensitive to transverse compressive forces. For instance at 10 kN and 15 T the critical current is reduced to 48% of its initial value and recovers only partially after unloading.

INTRODUCTION

For the construction of superconducting magnets the knowledge of the strand characteristics is important. In the case of Nb_3Sn, which is particularly sensitive to mechanical loads, detailed data on the critical current vs. axial tensile/compressive strain as well as under transverse compressive stress are requested. This information is especially needed where the limits of the superconductor are approached, e.g. for high field dipole magnets like NED (Next European Dipole).

The studied Nb_3Sn PIT conductors, produced by SMI (now EAS), are candidates for NED. They are designed for an optimum critical current at the required field but no measures have been taken so far for mechanical reinforcement. In the first part of this paper the critical current as a function of axial tensile strain at different fields is presented. In the second part the critical current vs. transverse compressive force at various fields is reported. Finally the response to mechanical loads on these PIT wires is compared to that of a Nb_3Sn bronze route wire.

SAMPLE CHARACTERISTICS

The investigated PIT wires have been manufactured by SMI (now EAS). Both samples, #B207 and #B215, have an almost identical layout with a nominal OD of 1.25 mm, 288 Nb/Nb_3Sn filaments with a diameter of about 50 μm and a twist pitch length of 20 mm. The Cu/non-Cu area is slightly different and the quality of the powder is lower for wire #B207 (for unknown reasons). A micrograph of #B207 can be seen in Fig. 1 while the most important characteristics are summarized in Table I. After the reaction heat treatment at 675°C for 84 hours, the values of the residual resistivity ratio, *RRR*, measured according to IEC 61788-11, were relatively high (Table I). They present an average over two and six measurements for wire #B207 and #B215, respectively.

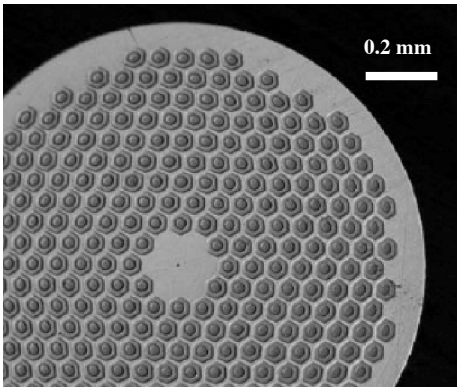

Figure 1. Micrograph of the investigated PIT wires #B207 with 288 hexagonal filaments of about 50 μm in size.

TABLE I. CHARACTERISTICS OF THE STUDIED Nb_3Sn WIRES

Strand ID	PIT #B207	PIT #B215
Size (mm)	Ø 1.25	Ø 1.25
Number of filaments	288	288
Filament size (μm)	~ 50	~ 50
Filament twist pitch (mm)	20	20
Cu / non-Cu area	0.96	1.22
Reaction heat treatment (vacuum)	675°C/84h	675°C/84h
Residual resistance ratio – RRR	195	211

RESULTS

Calorimetric T_c distribution

In order to investigate the superconducting properties over the whole wire volume, we have developed a method of analysis based on specific heat measurements. In fact, any gradient in the Sn content causes a distribution of T_c in the wire. Since this distribution cannot be determined by conventional techniques, due to percolation and/or magnetic shielding effects, a particular deconvolution method of the specific heat data was developed, allowing the determination of the precise distribution of T_c in multifilamentary Nb_3Sn wires [1]. A further advantage of this technique is the possibility of performing the

*This work was supported in part by the Swiss National Science Foundation through the National Centre of Competence in Research, "Materials with Novel Electronic Properties, MANEP" and by CERN.

measurements in the presence of the matrix, i.e. under thermal pre compression.

The specific heat for wire #B207 and #B215 was measured from 2 to 25 K at zero field and at 14 T, applying a long relaxation technique [2]. A CERNOX chip was used both as sample holder and as thermometer/heater.

In order to separate the superconducting transition of the filaments from the background of phonons and normal electrons, the specific heat of the normal state has been subtracted for each sample from the curve measured at zero field. The specific heat of the normal state in the temperature range 2-20 K has been determined from the data above the superconducting transition measured at high field. In particular the data above 13 K have been fitted according to the law $c_{fit}(T) = \gamma T + \beta_3 T^3 + \beta_5 T^5$ by imposing the conservation of the entropy, i.e.

$$\int_0^{20\,\mathrm{K}} \frac{c_{fit}(T)}{T} dT = \int_0^{20\,\mathrm{K}} \frac{c(T, B=0)}{T} dT \qquad (1)$$

The superconducting transitions detected by specific heat for the two wires are illustrated in Fig. 2. The transition corresponding to the unreacted Nb is also present.

The height of the specific heat anomaly at the superconducting transition is directly related to the gap energy of the superconductor. Since the specific heat curves in Fig. 2 have been normalized to the total mass of the wires (Cu + filaments), the height of the anomaly provides an estimation of the relative A15 amount in the different samples. In particular wires #B207 and #B215 exhibit the same onset T_c but the superconducting jump is higher for wire #B215, indicating a higher amount of A15 phase (~ 5%). The Sn composition gradient inside the filaments determines the broadening of the superconducting transition. Note that at zero field, the onset of the superconducting transition of the A15 filaments is well above 18 K, due to the addition of Ta in the Nb tubes. An increase of T_c with respect to the value for pure Nb_3Sn was already reported by Suenaga et al. [3].

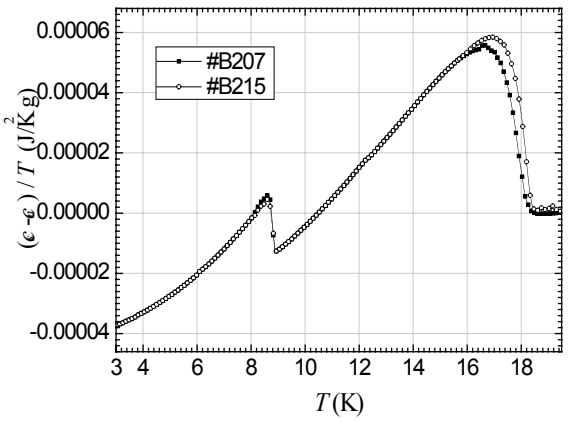

Figure 2. Specific heat for the superconducting volume of wire #B207 (solid squares) and #B215 (open circles); around 9 K the superconducting transition of the unreacted Nb it is clearly visible.

The T_c distributions obtained from the model in Ref. [1] are reported in Fig. 3. The temperature corresponding to the maximum of the distribution is higher in the case of wire #B215, thus indicating a smaller Sn gradient and a slightly higher Sn content in the A15 layer of wire #B215 with respect to wire #B207.

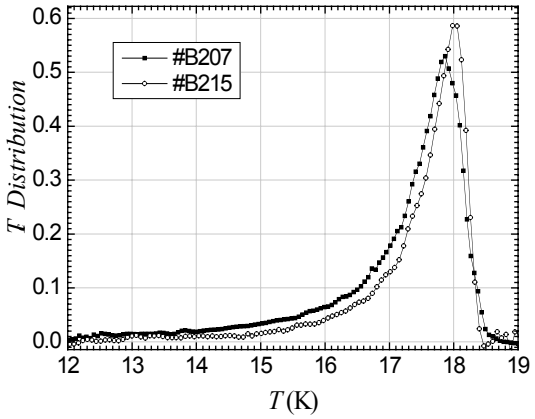

Figure 3. T_c distribution in wires #B207 (solid squares), #B215 (open circles), obtained by the deconvolution of

Critical current vs. axial tensile strain

The dependence of the critical current under axial tensile strain was investigated with our Walters spring probe [4]. For this purpose the superconducting wire is mounted on the Walters spring in a precisely machined groove. An intentional axial backlash allows the wire to be cooled down in the strain free state. Then the critical current for zero strain is measured at the highest available field (reduced Lorentz force) by rotating the spring in the tensile direction until an increase of I_c is detected. After warming up to room temperature, the superconducting wire is soldered over its total length. Finally the probe is cooled to 4.2 K a second time and the critical current for zero applied strain can be found by rotating the Walters spring in the appropriate direction. This process requires a reversible I_c behaviour in the considered strain window, which is normally the case.

Fig. 4 summarizes the measurements at different magnetic fields up to 21 T, the maximum available field in our laboratory. Data below 15 T are not available due to the limitation of the sample current power supply of 1000 A. Due to quench problems at the current terminals of wire #B215 at 15 T, data points near the maximum of the critical current could not be obtained. However, two points could be measured at higher strain allowing a fit to the data. In general, the I_c values for wire #B207 are considerably lower in comparison to those of #B215. There is also a shift of the strain position for maximum I_c, ε_m, from 0.14% to 0.18%, indicating a higher thermal prestrain for wire #B215.

The reversibility of I_c upon unloading has also been studied for wire #B215 at 19 T (Fig. 4c). The critical current, as well as the n value recover completely until a tensile strain of 0.31%. Further loading to 0.36% revealed a partial damage of the wire so the irreversibility limit, ε_{irr}, is situated in the range between 0.31% and 0.36% strain. A Kramer extrapolation at zero tensile strain yields a B_{c2}(4.2 K) of 24.8 T and 25.0 T for wire #B207 and #B215, respectively. These values increase at ε_m to 25.0 T and 25.8 T, respectively.

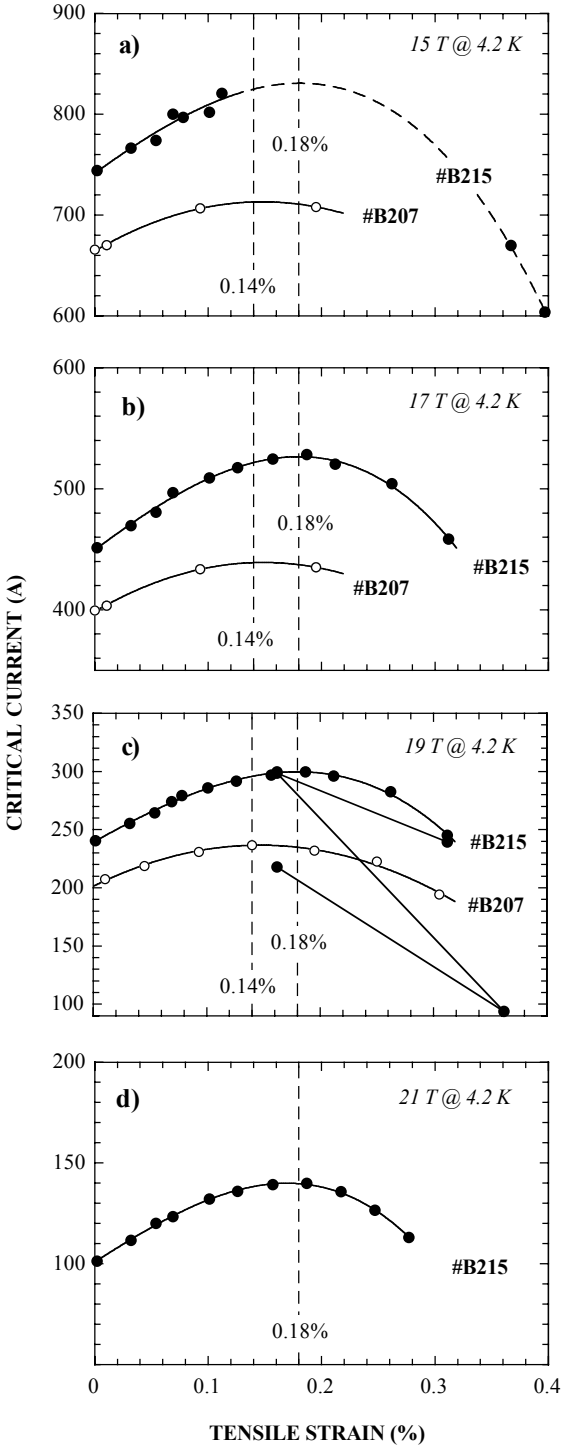

Figure 4. Critical current (0.1 μV/cm) as a function of axial tensile strain at different magnetic fields.

Critical current vs. transverse compressive force

Superconducting wires (strands) within a cable are subject to bending and pinching (transverse compressive stress) [5], [6]. The degradation of I_c depends on the cable pattern and of the sensitivity of the Nb_3Sn wires submitted to mechanical loads. Stress sensitivity, an inherent property of Nb_3Sn, can substantially be influenced by the layout of the wire, which is different for the known manufacturing processes (bronze route, internal tin route or powder in tube/PIT). The behaviour under bending conditions can in principle be estimated from I_c vs. axial tensile strain/stress measurements [7], while the determination of pinching effects requires a specially designed experimental setup.

We have developed a new probe allowing the study of the critical current as a function of transverse compressive forces up to 40 kN in magnetic fields up to 21 T [8]. The gauge length over which the transverse force is applied is 120 mm thus allowing the application of very low voltage criteria as well as the study of the influence of the twist pitch length. In Fig. 5 the critical current vs. transverse compressive force at various fields for wire #B215 is shown. The behaviour is very similar to that of wire #B207 [9]. The field dependence can be seen more clearly in Fig. 6 where the normalized critical current I_c/I_{c0} is plotted against the transverse compressive force. Note that the main difference appears at forces below 2 to 3 kN. This range of forces is linked to a strong reduction of the Kramer B_{c2}(4.2K).

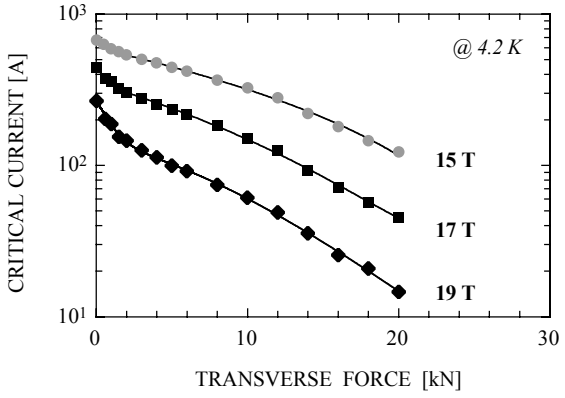

Figure 5. Critical current (0.1 μV/cm) vs. transverse compressive force at different magnetic fields for wire #B215.

The reversible/irreversible behaviour of I_c after unloading has been studied too. Because irreversibility

does not depend of the applied magnetic field, measurements have been carried out at 19 T. The result is summarized in Fig. 7. The data for unloading have been obtained as follows: after application of the indicated transverse compressive force (abscissa) the force was removed and the critical current was measured. Note that the critical current already shows an irreversible

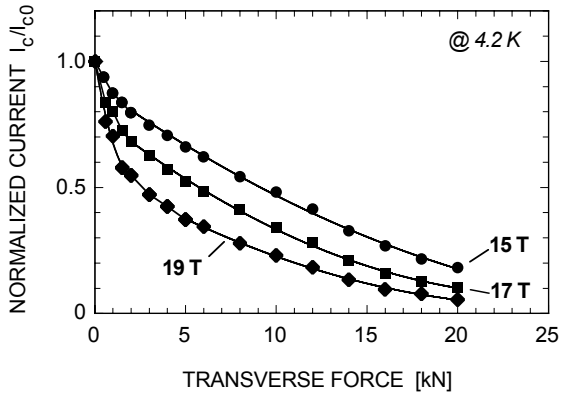

Figure 6. Normalized critical current I_c/I_{c0} as a function of transverse compressive force at different magnetic fields for wire #B215.

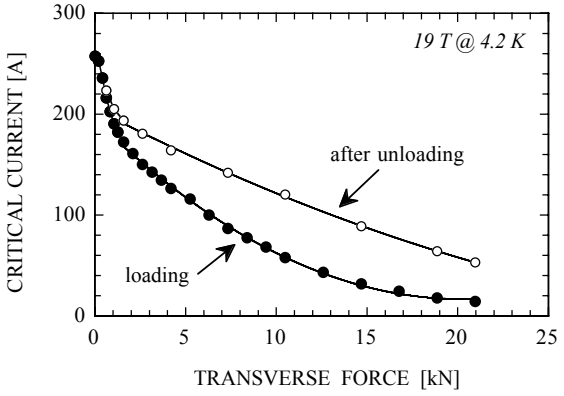

Figure 7. Critical current (0.1 μV/cm) vs. transverse compressive force of wire #B215 for loading and unloading. The values for unloading are measured after removing the force (x-axis) thus indicating partial recovery.

behaviour for forces as small as 1 kN and recovers only partially for higher forces.

DISCUSSION

It is interesting to note that the relatively small difference in the distribution of T_c between #B207 and #B215 has a rather important consequence for the critical current. First, it has been seen by specific heat that the volume fraction of Nb_3Sn in wire #B215 is about 5% higher. Second, the T_c distribution of #B215 is smaller and the position of the peak at higher temperature. It is expected that a smaller distribution of T_c gives a smaller distribution of B_{c2}, although the situation is complicated by the observation of T. Orlando et al. that the highest T_c material does not have the highest B_{c2} [10]. In any case an average B_{c2} enters in the temperature scaling law of Nb_3Sn.

$$J_c B = C B_{c2}^{2.5} b^{0.5} (1-b)^2 \qquad (2)$$

where J_c is the current density, B is the applied magnetic field, C is a constant and b is the reduced field B/B_{c2}. So a slightly higher B_{c2}, as it has been observed for #B215, contributes to a higher I_c.

The different ε_m values may come from the various Cu/non-Cu fractions. Wire #B215 has a measured Cu/non-Cu area of 1.22 (0.96 for #B207). In addition, the amount of unreacted Nb surrounding the Nb_3Sn filaments may also play a role. In fact the specific heat measurements reveal a higher volume fraction of unreacted Nb in wire #B207. Because the thermal contraction of Nb at 4.2 K is relatively small in comparison to that of Nb_3Sn, a higher volume fraction of Nb decreases the thermal prestrain exerted by the copper matrix.

Inspecting Fig. 6 the rate of degradation of the normalized critical current depends strongly of the magnetic field but only for transverse forces < 2 kN. The higher the field the more sensitive is I_c against a transverse force. At higher forces the rate is almost independent of field. It is speculated that the observed behaviour is related to the Kramer B_{c2} of undamaged filaments. Actually there is a particularly strong reduction of B_{c2}(4.2 K) between zero and 2 – 3 kN transverse force which flattens at higher forces. A similar situation has been observed in wire #B207 [9].

Finally Fig. 7 indicates that permanent damage of filaments already occurs at transverse forces as low as 1 kN, while for higher forces a partial recovery is observed. Farinon et al. have shown that at room temperature in a round wire there are two conical zones, parallel to the transverse force, where filaments are deformed [11]. With increasing deformation cracks appear parallel to the force. Assuming a similar situation at 4.2 K and taking into account the twist pitch length of 20 mm, every filament of the strand is exposed several times to deformation and breakage over the gauge length of 120 mm where the transverse compressive force is applied.

Comparing the obtained results for the PIT Nb_3Sn wire with a bronze route wire reveals that the degradation of I_c is much less pronounced in the bronze route conductor [12]. At 19 T a force of 10 kN reduces the critical current to 23% of I_{c0} for the #B215 wire, compared to 60% of I_{c0} for the bronze wire. At the relevant field for NED, 15 T, these values are 48% and 80% of I_{c0}, respectively.

CONCLUSION

In this work it has been shown that the quality of the powder (T_c distribution) plays an important role for the critical current performance of PIT wires. This was observed not only near zero axial tensile strain but also at higher strain values, in particular at ε_m. With respect to bronze route and internal tin Nb_3Sn conductors the measured ε_m is relatively low, indicating a reduced thermal prestrain.

The present layout of PIT Nb_3Sn conductors was found to be extremely sensitive to transverse compressive forces. This sensitivity is enhanced with increasing magnetic fields. There is some recovery of I_c upon unloading but most of the conductor filaments are damaged. This is presumably due to the rather big size of the filaments and to the presence of voids (porosity).

ACKNOWLEDGMENT

The authors thank Ph. Lebrun and D. Leroy from CERN for their initiative and continuous encouragement of this work. In particular we thank A. Ferreira, R. Modoux, R. Pellet and D. Zurmühle for their excellent technical assistance.

REFERENCES

[1] C. Senatore, D. Uglietti, V. Abächerli, A. Junod, R. Flükiger, "Specific heat, a method to determine the T_c distribution in industrial Nb_3Sn wires prepared by various techniques", IEEE Trans. Appl. Supercond., 17 (2007), 2611.

[2] D. Sanchez, A. Junod, J.-Y. Genoud, T. Graf, and J. Muller, "Low-temperature specific heat of the 123, 124 and 247 phases of Y-Ba-Cu-O in magnetic fields up to 14 Tesla", *Physica C*, 200 (1992), 1.

[3] M. Suenaga, D. O. Welch, R. L. Sabatini, O. F. Kammerer, and S. Okuda, "Superconducting critical-temperatures, critical magnetic-fields, lattice-parameters, and chemical-compositions of bulk pure and alloyed Nb_3Sn produced by the bronze process", J. Appl. Phys., 59 (1986), 840.

[4] B. Seeber, D. Uglietti, V. Abächerli, P.-A. Bovier, D. Eckert, G. Kübler, P. Lezza, A. Pollini and R. Flükiger, "Critical current versus strain measurement up to 21 T and 1000 A of long length superconducting wires and tapes", Rev. Sci. Instrum., 76 (2005), 093901.

[5] N. Mitchell, "Comparison between predictions and measurements of the superconducting performance of Nb_3Sn cable in conduit conductors with transverse load degradation", Supercond. Sci. Technol. 21 (2008), 054005.

[6] A. Nijhuis, Y. Ilyin and W. A. J. Wessel, " Spatial periodic contact stress and critical current of a Nb_3Sn strand measured in TARSIS", Supercond. Sci. Technol. 19 (2006), 1089.

[7] J. W. Ekin, "Mechanical properties and strain effects in superconductors", in *Superconductor Material Science: Metallurgy, Fabrication and Applications* (S. Foner and B. B. Schwartz, eds.), New York, Plenum (1981), 455.

[8] B. Seeber, A. Ferreira, V. Abächerli, T. Boutboul, L. Oberli and R. Flükiger, "Transport properties up to 1000 A of Nb_3Sn wires under transverse compressive stress", IEEE Trans. Appl. Supercond., 17 (2007), 2643.

[9] B. Seeber, A. Ferreira, F. Buta, C. Senatore, T. Boutboul, L. Oberli and R. Flükiger, "Transport properties of a PIT Nb_3Sn strand under transverse compressive and axial tensile stress", IEEE Trans. Appl. Supercond., 18 (2008), 976.

[10] T. P. Orlando, J. A. Alexander, S. J. Bending, J. Kwo, S. J. Poon, R. H. Hammond, M. R. Beasley, E. J. McNiff and S. Foner, "The role of disorder in maximizing the upper critical field in the Nb-Sn system", IEEE Trans. MAG-17 (1981), 368.

[11] S. Farinon, T. Boutboul, A. Devred, P. Fabbricatore, D. Leroy and L. Oberli, "FE model to study the deformation of Nb_3Sn wires for the Next European Dipole (NED)," *IEEE Trans. Appl. Supercond*., 17 (2007), 1136.

[12] B. Seeber, A. Ferreira, V. Abächerli and R. Flükiger, "Critical current of a Nb_3Sn bronze route conductor under uniaxial tensile and transverse compressive stress," *Supercond. Sci. Technol.*, 20, (2007), S184

INTERSTRAND COUPLING AND MAGNETIZATION IN NB_3SN RUTHERFORD CABLES

E. W. Collings and M. D. Sumption,

Laboratories for Applied Superconductivity and Magnetism (LASM), Dept. of Materials Science and Engineering, The Ohio State University, Columbus, OH 43210, U.S.A

Abstract

It is well known by now that interstrand coupling in NbTi Rutherford cables can be suppressed by separating the strand layers with an "insulating" foil or core, typically of stainless steel (SS). Based on the results of an extensive series of studies of NbTi cables with coated strands and cores, the LASM group and its collaborators went on to measure the coupling losses and associated magnetizations of Nb_3Sn-wound cables incorporating various kinds of cores and several core widths. In Nb_3Sn cables the relatively large product of critical current density and effective strand diameter ($J_c.d_{eff}$) dictates a relatively large low-field persistent current magnetization. The relationship of this to the coupling magnetization at low- and high fields is discussed.

BACKGROUND STUDIES: NB-TI CABLES

Since the pioneering work of Wilson and his colleagues at the then Rutherford Laboratory [1][2] the results of AC conductor research and development have provided a vast literature on eddy-current and coupling loss and its suppression in terms of strand- and conductor design. Cable-level coupling currents have been a recurrent problem in the design of NbTi accelerator magnet cables both as-wound and fully impregnated with resistive solder [3]. Reduced eddy current losses were obtained when a Cu-10Ni barrier was installed around the filamentary bundle within the strand. Lowest coupling losses occur when the strands are individually insulated, the advantage of which is offset by conductor instability. At both Fermilab (FNAL) and at the former SSC Laboratory strand coatings were favored as way of reducing coupling loss. The influence of coatings on the ramp-rate dependence of loss in Tevatron magnets was discussed by Wake et al. [4]. From just the standpoint of loss full ebonol coating was superior to so-called "zebra coating" (alternate windings of ebonol and stabrite) which in turn was superior to full stabrite coating. Subsequent work addressed the questions of pressure and curing temperature on cable loss. Coupling loss was found to be enhanced if the cables were exposed simultaneously to pressure and heat treatment before measurement [5][6][7]. Taking a cue from these early studies the present authors, now at the Laboratory for Applied Superconductivity and Magnetism (LASM) began a series of investigations into the effect of strand coatings and subsequently cable cores on coupling loss in subsize and full-size Rutherford cables. Initially such variants in cable design were compared and quantified just in terms of "loss per cycle" of an applied AC field. Later the losses were converted to crossover and side-by-side "interstrand contact resistances" (ICR), $R_\perp$ and $R_{//}$, respectively, using the following standard network-derived expressions [8] in which $Q_\perp$ represents the "face-on, FO" loss when the applied field is perpendicular to the broad face of the cable and $Q_{//}$ represents the "edge-on, EO" loss

$$Q_\perp = \left(\frac{4}{3}\right)\left(\frac{w}{t}\right)L_p B_m\left[\frac{N^2}{20R_\perp}+\frac{1}{NR_\parallel}\right].\left(\frac{dB}{dt}\right) \quad .$$

$$= \left(\frac{2\pi^2}{3}\right)\left(\frac{w}{t}\right)L_p B_m^2\left[\frac{N^2}{20R_\perp}+\frac{1}{NR_\parallel}\right].f \qquad 1(a)$$

$$Q_{//} = \left(\frac{t}{w}\right)L_p B_m\left[\frac{1}{NR_\parallel}\right].\left(\frac{dB}{dt}\right)$$

where w is the cable width, t the cable thickness, L_p the twist pitch, N the number of strands, and B_m the field sweep amplitude. Moreover one has

$$dQ_\perp / df = \left(\frac{\pi^2}{30}\right)\left(\frac{w}{t}\right)L_p B_m^2 N^2\left[\frac{1}{R_{\perp,eff.}}\right] \qquad 1(b)$$

LASM's research on coupling loss in cables was stimulated initially by the problems encountered by the SSC's high energy booster (HEB) magnets. Subsequently LASM's interest became coupled to the interests of the large hadron collider (LHC) and high energy particle accelerators in general. During low energy particle injection and beam accumulation the dipolar field, B, is necessarily small (B_{inj} for the LHC is 0.54 T); then between injection and operation at 8.4 T the dipoles must be ramped at rates, dB/dt, of 7 mT/s. During field ramping the Rutherford cable is the seat of interstrand coupling currents (ISCCs) that loop around a half-pitch of the cable and through the crossover and side-by-side ICRs, $R_\perp$ and $R_{//}$, respectively. Field ramping also generates "supercurrents" [9] or boundary-induced coupling currents (BICCs) [10] that flow over the whole cable length and induce field errors that conform to the period of the twist pitch. BICCs are caused by a dB/dt or by an ICR that varies sharply with distance along the cable, hence the term "boundary". In order to achieve tight control of the particle beam during injection, acceleration, and storage it is necessary to minimize field distortions caused by ISCCs and BICCs [11]. Both of these are suppressed by increasing ICR. But since too high a value reduces cable stability [12] a compromise is

sought. Thus for a standard LHC-type cable $R_{\perp}$ should be about 15±5 μΩ [11] and $R_{//}$ not less than 0.2 μΩ [10].

We first studied the influence of full strand coating on coupling loss/ICR using a boil-off calorimeter installed at the University of Twente (UoT) [13][14]. The 11-strand test cables had been wound at the Lawrence Berkeley National Laboratory (LBNL) from "SSC-type" strands plated with Ni, Ni+Cr, Cr (2 μm and 5 μm), black Cu oxide, red Cu oxide, electroless Ni-P, and electroless Ni-Fe. Interstrand contact resistances were obtained from the initial slopes of the Q vs. f curves and also more-or-less directly in the LASM's vibrating-sample magnetometer (VSM) using a "diamond-current-simulator" attachment [13]. Using both 11-strand sub-size-cables and LHC-type cables the influences of strand surface condition and coatings, heat treatment (time/temperature) and measurement pressure on ICR was also the subject of detailed study [15]. LASM's initial measurements of LHC-class Rutherford cables with various strand coatings (bare-Cu, Ni, stabrite) and thin ribbon-like cores of various materials (kapton, stainless steel (SS), and Ti) were made magnetically at the Japan National Laboratory for High Energy Physics (KEK) [16] and calorimetrically at UoT. As a result of these experiments the strong supression of coupling loss by the presence of the "insulating" core was clearly demonstrated, $R_{\perp}$ showing increases of typically two orders of magnitude [14]. By varying the thickness of the core it was possible to study the influence of "internal compaction" on the coupling loss [17][18]. Furthermore the equipment at KEK provided an opportunity to study the influence of "external compaction" i.e. in-cryostat uniaxial pressure (0, 35, and 78 MPa) on the coupling loss [16]. A result of particular interest and importance had to do with the response of stabrite-coated cables to external compaction at 4.2 K. In terms of total loss per cycle (0T-1T-0T) the stabrite cable cured at 170°C responded strongly to pressure. The loss of the uncored cable increased from 3.7 to 20 (10^4J/m^3) in response to an increase in pressure of from 0 to 78 MPa, whereas that of the SS-cored cable remained flat (4.1 to 4.1 x 10^4J/m^3) over that range, see for example Figure 1.

At this stage is it necessary to draw attention to the quantity $R_{\perp,eff}$ defined above in Equations (1). In the standard uncored cable the "face-on, FO," loss, $Q_{\perp}$, is dominated by coupling currents circulating through the cross-over interstrand contacts of resistance $R_{\perp}$ whereas in the cored cable measured in an FO field the controlling ICR is the side-by-side value $R_{//}$.

Thus we have chosen to use $R_{\perp,eff}$ (a so-called "effective ICR") as an *index of interstrand coupling strength* when comparing the losses of uncored, partially cored, and fully cored cables.

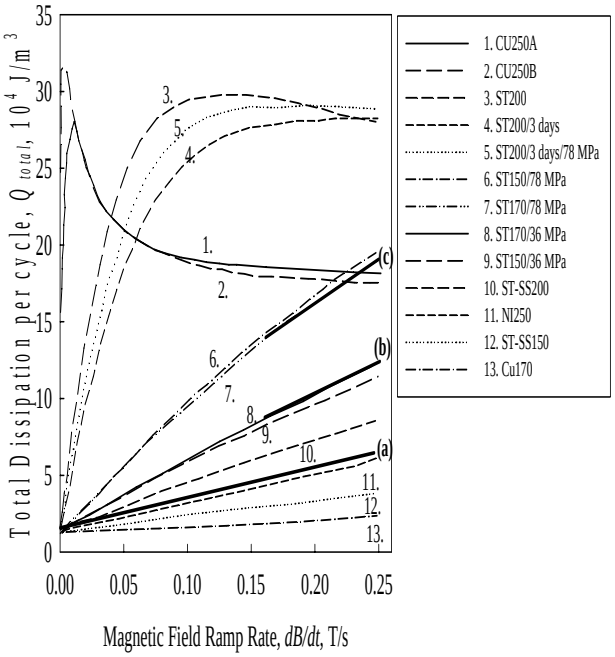

Figure 1: Total loss vs frequency for several cables with coatings and cores. Code "CU" represents bare Cu, "ST" represents stabrite coating, "NI" represents Ni plating, "ST-SS" represents cored stabrite. Line-(a) represents uncored stabrite at 0 Mpa and cored stabrite at all pressures. Lines (b) and (c) represent uncored stabrite at 36 and 78 MPa, respectively [16].

The presence of a stainless steel core strongly suppresses the coupling losses of Rutherford cables wound with *bare-Cu* strand [19][20]. The effective ICR, $R_{\perp,eff}$, of a set of "research-design" cables measured under "pressure release" increased from 5 to 2500 μΩ upon the insertion of a 12.5 μm thick SS core. This impressive result is illustrated in Figure 2 and again in Figure 3 which goes on to show how the ICR of the cored cable decreases with increase in core thickness (12-25-50 μm) as the "internal compaction" increases the strands' side-by-side contact.

In a subsequent series of studies particular attention was given to the properties of standard and cored *stabrite*-coated LHC-type cables. Of particular interest were the effects of

- internal compaction produced by increasing the core thickness at fixed cable thickness [18][21], see Figure 4;
- external compaction by rolling the able to reduced thickness [18][21], see Figure 5;
- varying the width of the stainless steel core [18][21][22].

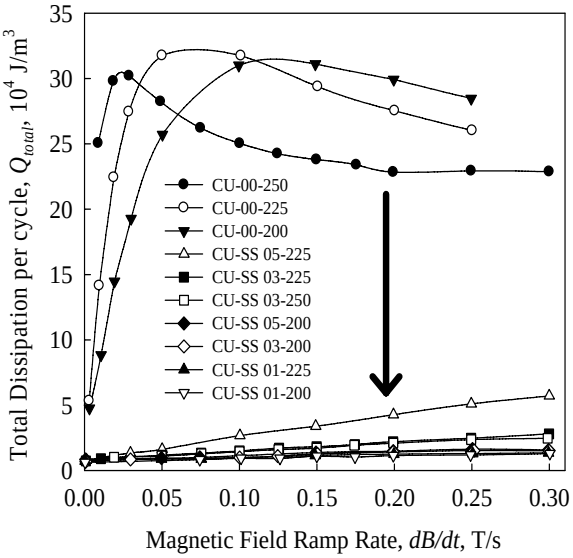

Figure 2: AC losses of bare-Cu cables without a core (upper curves) and after insertion of SS cores of various thicknesses [19].

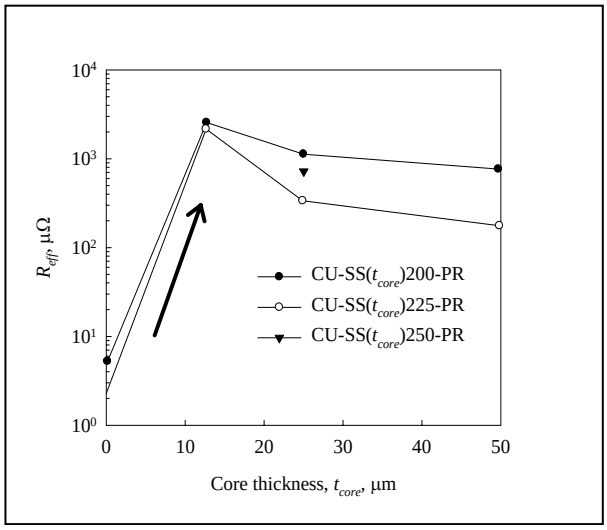

Figure 3: $R_{\perp,eff}$ in response to insertion of cores of thickness 0.5 mil (12.5 μm), 1 mil. (25μm), and 2 mil (50 μm) [20].

Figure 4 illustrates the increase in $R_{\perp,eff}$ that accompanies the insertion of the core (t_{core}, $0 \rightarrow 25$ μm) followed by a small decrease as increasing core thickness improves the side-by-side contact (cf. Figure 3).

In Figure 5 we start of with a cored cable and apply gradually increasing levels of external compaction. The 170°C-cured cable experiences a rapid decrease in $R_{\perp,eff}$ again due to improving side-by-side contact; not so for the cable cured at 200°C whose strands are well sintered.

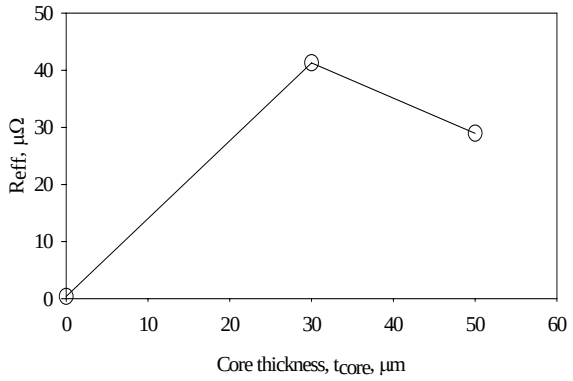

Figure 4: $R_{\perp,eff}$ vs. core thickness, t_{core}, for stabrite-coated cables cured at 200°C [18].

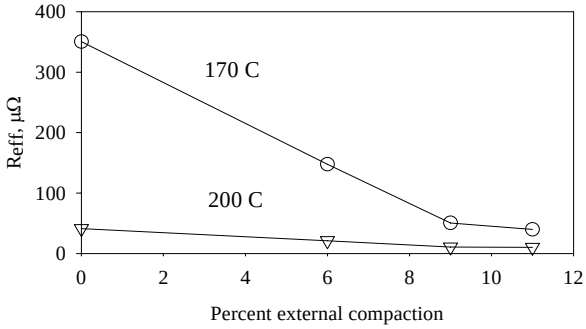

Figure 5: $R_{\perp,eff}$ vs. percent external compaction for stabrite-coated cables cured at 170°C and 200°C [18].

The effect on per-cycle loss, Q_{total} of varying the core width is illustrated in Figure 6 for 28-strand stabrite cables 15 mm wide wound with cores of width w_{core} = 0, 3.2, 6.4, 9.5. and 12.7 mm, corresponding to about 0%, 20%, 50%, 75% and 100% of the available cable width. Figure 7 presents the cable-loss data in terms of $R_{\perp,eff}$. The figure shows that the goal of 15 μΩ would be achieved at a core width of 8.5 mm or 67% of $w_{core,max}$. Shown for comparison in the figure (at position "CN") is the measured $R_{\perp,eff}$ of an uncored stabrite cable that had received the CERN-recommended heat treatment of 8h/200°C in air. At 26.7 μΩ its $R_{\perp,eff}$ is equivalent to that of a cable with a core of width ~68% of w_{max} .

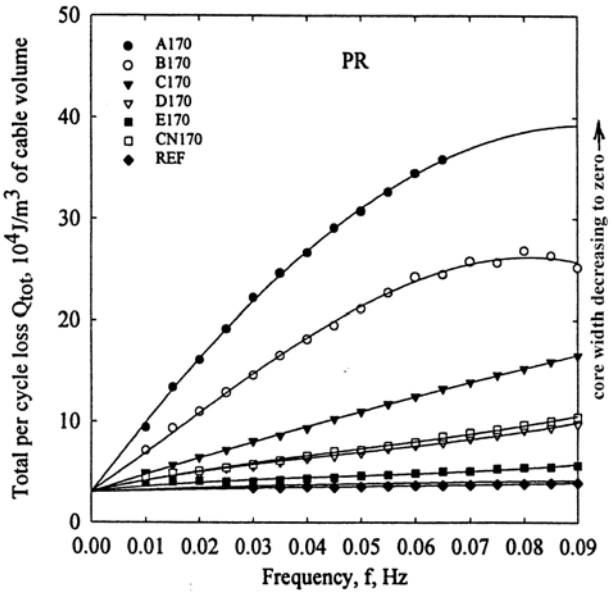

Figure 6: Loss vs. frequency for a series of cored stabrite cables with cores of widths 0, 3.2, 6.4, 9.5, and 12.7 mm (full) cured at 170°C. Included is a result for an uncored "CERN-processed" stabrite cable, CN170, cured at 200°C, see [18],[21] and [22].

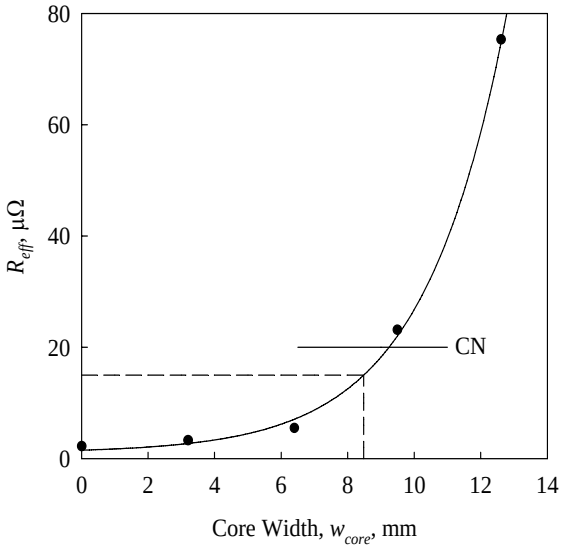

Figure 7: $R_{\perp,eff}$ vs.core width for the cables of Figure 6

These NbTi-cable-based studies of strand coatings, preparation heat-treatment conditions, the effects of internal and external compaction, coupling loss suppression by the introduction of cores, and the effects of varying the core width, provided the background for extensive research into the properties of standard- and specially prepared Nb_3Sn cables.

COUPLING LOSS, ICR AND MAGNETIZATION IN NB_3SN CABLES

Coupling loss and ICR

Some AC loss results for a set of Nb_3Sn cables in the face-on (FO) and edge-on (EO) orientations are depicted in Figure 8. In many cases the coupling loss is so high that $R_{\perp,eff}$ can no longer be derived from a linear Q vs f slope, Equation (1b), as was generally the case for NbTi cables. Instead, the so-called "critical-frequency" approach must be used.

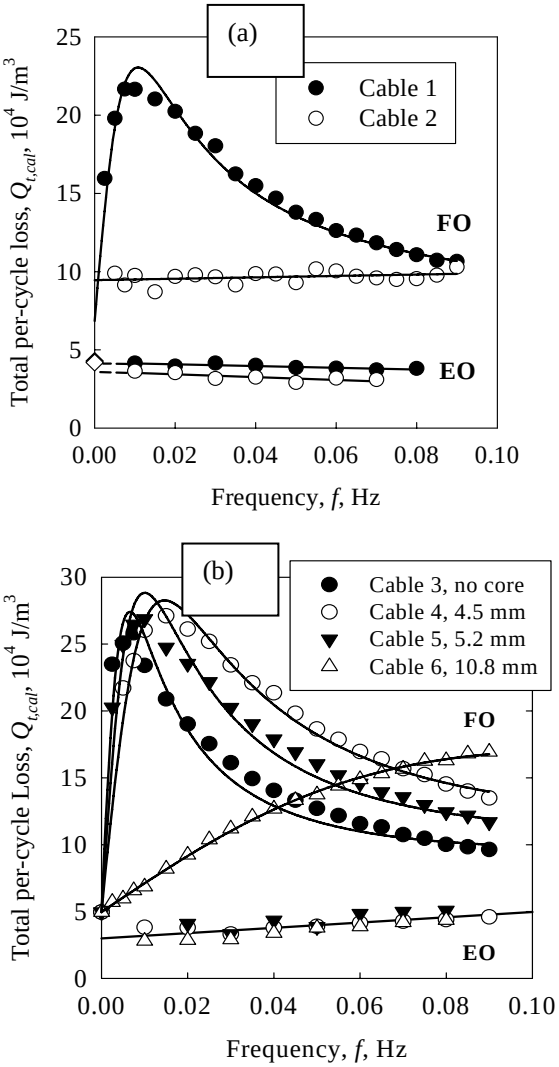

Figure 8: (a) AC losses for an un-cored Nb_3Sn cable (filled circle) compared with those for a full-cored cable [33]. (b) AC losses for un-cored (filled circle) and variously cored Nb_3Sn cables. Even the 10.0 mm core is in this case only partially effective, cf. (a) [32].

The simultaneous generation and decay of coupling currents gives rise to a maximum in Q (f) at a critical

frequency $f_C = 1/2\pi\tau_C$ (where τ_C is the corresponding relaxation time) following the general relationship:

$$Q(f) = Q_0 \frac{f / f_c}{1 + (f / f_c)^2} \qquad (2)$$

This applies to strand eddy currents as well as cable- and cable-stack coupling currents with relaxation times of τ_{cab} and τ_{stack}, respectively. Relationships between the individual-cable relaxation time τ_{cab} and the relaxation time of the stack τ_{stack} lead to f_c– based ICR values designated $R_{\perp,fc}$. According to Verweij [10]:

$$R_{\perp,fc} = 2\pi(DE) f_c \qquad (3)$$

which is obtained by combining $\tau_{cab} R_\perp = D$ (where D is a function of the individual-cable properties, N and L_p, see Equation (1)) with $\tau_{stack} / \tau_{cab} = 1/(2\pi f_C \tau_{cab}) = E$ (where E is a function of w/t and N_C, the number of cables in the stack). Typical Q vs f curves following the Equation (2) prescription are depicted in Figures 9 and 10.

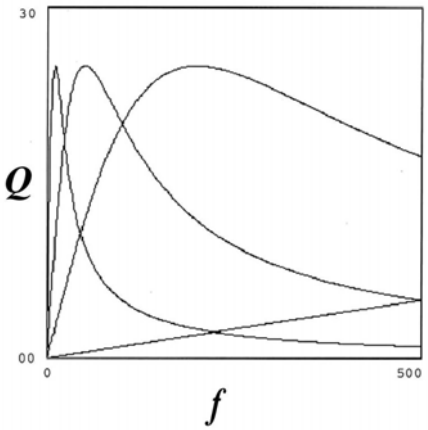

Figure 9: Loss vs. frequency. Each cable has a single homogeneous ICR, each given by its initial slope *dQ/df* and/or its critical frequency, f_C – cf. Figure 2.

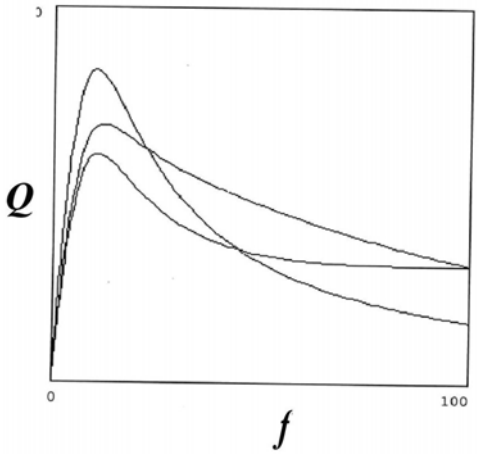

Figure 10: Loss vs. frequency. Each cable exhibits a blend of two ICRs, one common to all cables and the other different for each cable. Thus each curve possesses a second f_C that elevates its tail, see [30].

In collaboration with LBNL and the Fermi National Accelerator Laboratory (FNAL) an extensive series of specially wound and treated Nb_3Sn cables were prepared for AC-loss measurement at UoT. Particular attention was paid to the following issues:

- ICR in response to the introduction of a core and to variation of core design;
- Cable designs for improved stability;
- ICR in response to variation of cable pre-heat-treatment (surface) condition and to variation of final heat-treatment conditions;
- ICR in response to variation of core width;
- the cables' so-called "hysteretic loss" or persistent current magnetization based on the properties of the component strands.

Introduction of the core and variation of core design

Over a period of several decades numerous groups have modified the ICR of NbTi cables by applying metallic or insulating coatings to the strands either before or after cabling. Strands have been coated with Cr, Ni, NiCr, SnNi, Zn, ZnNi, CuO, NiP, or dip-coated SnAg (stabrite). In comparison to NbTi/Cu the severity of Nb_3Sn's RHT (Reaction Heat Treatment) leaves only a few options open for pre-RHT surface treatment. In fact only two surface treatments have received practical consideration: Cr plating and carbon deposition from a synthetic oil coating decomposed during RHT. Our group believes that the most effective and reproducible way of controlling the ICR of a Nb_3Sn Rutherford cable is through the introduction of an SS core. As demonstrated in [23] the presence of a full width thin SS core can result in a substantial increase in $R_{\perp,eff}$ e.g from 1.8 to 70 μΩ. The latter value is arguably too high to ensure stability, for which reason reduced-width cores were recommended, see below. The ICR of a Nb_3Sn cable can also be altered through changes in the actual strand architecture which moderates the current flow across the contacts between crossing strands [24]. An interesting core arrangement implemented by LBNL consisted of a double core: two strips of bimetallic Cu/SS sandwiched together with the SS surfaces (with their attached native oxide layer) facing each other [25]. The idea was to inhibit cross-over contact in the usual way while at the same time improving side-by-side contact (hence current sharing and stability) by allowing the Cu surfaces to sinter to the strands.

Cable designs for improved stability

Additional Cu included in the internal structure of the cable was intended to contribute stability. Of course the Cu can also be attached to the outside of the cable either as a pair of strips placed on the outside surfaces, or as a continuous strip helically wound along the outside of the cable. The purpose of the added Cu, which is intended to diffusion bond to the strands during RHT, is to improve stability and provide passive quench protection.

Although we were not set up to measure those quantities, AC loss experiments were performed on cored cables to explore whether the Cu was added at the expense of coupling loss. It turned out that the added Cu was beneficial; in the test sample studied $R_{\perp,eff}$ was lowered from an immeasurable high value (not unexpected for a resistive-core cable) into the range of 30-60 μΩ.

ICR dependence on heat treatment

As stated above, many different surface coating have been applied to NbTi strand in order to control the properties of the cable wound from them. But the severity of Nb_3Sn's RHT leaves only a few options open for pre-RHT surface treatment, e.g. Cr plating and the application or retention of lubricating oil which subsequently decomposes to C during RHT. Since the effects of applied surface coatings had been well researched it was decided, in a collaboration with LBNL, to examine the influences of various pre-RHT cable-cleaning procedures (acetone rinsing, HCl rinsing) on the ICR of uncored cables. Although the ICRs were mostly in the range of 0.2 – 1.6 μΩ , one of the clean uncored cables produced an ICR of 13±2 μΩ. The results are evidently so unpredictable that one or other of the above contact-controlling techniques is recommended.

In a companion series of studies, this time in collaboration with FNAL, we explored the influence of preparation conditions (insulation, RHT, and impregnation schedules) on the ICRs of uncored cables as determined at UoT using both calorimetric and magnetic techniques. All cables measured exhibited a principal $R_{\perp,eff}$ of 0.4 μΩ although one of the cables exhibited a secondary $R_{\perp,eff}$ of 4 μΩ. It turned out that these experiments provided the first quantitative evidence for $R_{\perp,eff}$ variability in Nb_3Sn cables, one that could be resolved into two distinct $R_{\perp,eff}$s. Such $R_{\perp,eff}$ anisotropy or inhomogeneity would be favored by the severe turks-heading which, applied to the cable during its final stage of formation, results in a pronounced flattening of the strands along its edges, thereby setting the stage for the development of uneven interstrand contact during further compaction and heat treatment. Further aspects of cable inhomogeneity are discussed in [30]

ICR dependence on core width

Calorimetric and magnetic measurements were made at UoT on a series of 14-mm-wide Rutherford cables wound at FNAL with cores of widths 4.5, 5.2, and 10.8 mm. The resulting FO-measured $R_{\perp,eff}$s were compared with that of the uncored cable whose uncored $R_{\perp,eff}$ of 0.19 μΩ conformed well to the results of several previous measurements e.g. 0.16-0.4 μΩ. On the other hand, the cored results were much lower than expectation; and unlike those of the earlier measurements these $R_{\perp,eff.}$s did not increase monotonically with core width, cf. Figure 7.

Furthermore the intended full-width core yielded an $R_{\perp,eff.}$ of only 8 μΩ, i.e., very much lower than the expected 50-100 μΩ for a full-width core. The explanation has to do with the locations and effective widths of the cores both of which were studied using scanning electron microscopy (SEM). Undulation of the core's cross-section as it follows the curves of the nested strands causes it to shrink below its nominal width such that the widest core was not only less than full width (covering only 77% of the 12.2 mm (I.D.) available cable width) but also off-center. We estimate based on Figure 7 and reference [21] that a coverage increase of from 75% to 100% could result in a four-fold increase in $R_{\perp,eff.}$ which in this case could raise $R_{\perp,eff}$ to about 32 μΩ. An even greater increase would accompany the shift of the core to the center of the cable and bring its $R_{\perp,eff.}$ more into line with previously measured values [24][25].

ICR of cored and un-cored Nb_3Sn Rutherford cables

We conclude this discussion of core effects with a tabulation of the collected results of our ICR measurements on cored and uncored Nb_3Sn Rutherford cables. Due to interstrand sintering the uncored ICRs are generally very small – mostly around 0.3 μΩ according to Table 1. A full width core may raise the ICR into the 25-50 μΩ range although some very high values (200 μΩ and immeasurably large, **"∞"**) have been obtained. Narrow and/or misplaced cores are not very effective in reducing coupling loss.

Table 1: Nb_3Sn Cables -- Collected Effective- ICR Results, $R_{\perp,eff}$, μΩ

NO CORE	**Full-width core**	**Ref.**
<0.1 (0T), 2.7 (1T)	33 (0T), 78 (1T)	[24]
0.24	23	[25]
	24	"
	53	"
	"∞"	"
0.15 (0T), 0.4 (1T)		[28][29]
13.0 (0T), 11.5 (1T)		"
1.47 (0T), 3.09 (1T)		"
0.33 (0T), 1.27 (1T)		"
0.30 (0T)		"
0.4, 4		[30]
0.19, 0.21	8	[31][32]
0.31	209	[33]

HYSTERETIC OR PERSISTENT CURRENT MAGNETIZATION OF NB3SN CABLES

Magnetization near injection

Underlying both field quality and flux-jump stability, strand- and hence cable magnetization may be considered to be a "critical defining parameter" in precision dipole applications [34]. As deduced in [34] the persistent current shielding-magnetization of a NbTi LHC-type cable at injection, $M_{sh.inj.cable}$(1.9K,0.54T) is estimated to be about 4.9 kA/m. We show this to be commensurate with the cable's coupling-current magnetization during the injection ramp, $M_{coup(ramp)}$. Starting with Equation (1a) and recognizing that in general $Q_{\perp} = 4M_{coup}B_m$ we find:

$$M_{coup} = \left(\frac{1}{3}\right)\left(\frac{w}{t}\right)L_p\left(\frac{dB}{dt}\right)\left[\frac{N^2}{20R_{\perp,eff}}\right] \qquad (4)$$

We next insert a set of typical cable parameters, such as a width w of 15 mm, a thickness t of 1.78 mm (giving a ratio w/t=7.99), L_p=55.1 mm, N=28 strands and a dB/dT of 7 mT/s, we obtain

$$M_{coup(ramp)} = \frac{4.03x10^4}{R_{\perp,eff}\,(\mu\Omega)} \text{ A/m } (\text{J/m}^3\text{T}) \qquad (5)$$

After inserting the LHC-recommended value $R_{\perp,eff}$ = 15 μΩ we find $M_{coup(ramp)}$ = 2.69 kA/m. Both this and $M_{sh.inj.cable}$ are easily corrected electromagnetically. Not so for Nb_3Sn Rutherford cables whose hysteretic magnetizations, based on VSM measurements on strands to ±400 mT [33] have been shown to be about 3x10^5 J/m^{3}T (300 kA/m) two orders of magnitude higher, Figure 11.

In simple un-cored cables the quantity $R_{\perp,eff}$ defined in Equations (1a) and (1b) is a true interstrand contact resistance. But in association with Equation (4), and Equation (5) as a special case, it becomes an index of coupling magnetization. Furthermore, magnetization in general can be usefully parameterized in terms of $R_{\perp,eff}$.

With this in mind we repeat, in principle, the low-field cable-magnetization calculation, previously based on NbTi J_c data [34], this time for a Nb_3Sn cable at 4.2 K assuming (i) a Kramer-extrapolated $J_{c,non\text{-}Cu,0.5T}$ = 16.8 x $J_{c,non\text{-}Cu,12T}$, (ii) a strand fill-factor of 0.5, (iii) a cable packing factor of 0.9, such that $J_{c,cab,0.5T}$ = 0.5 x 0.9 x 16.8 x $J_{c,non\text{-}Cu,12T}$ = 7.56 $J_{c,non\text{-}Cu,12T}$. It follows that:

$$M_{cab,0.5T}(A/m) = \left(\frac{2}{3\pi}\right)J_{c,cab,0.5T}(A/m^2)\times d_{eff}(m)$$

$$= 1.60\times J_{c,non-Cu,12T}(A/mm^2)\times d_{eff}(\mu m) \qquad (6)$$

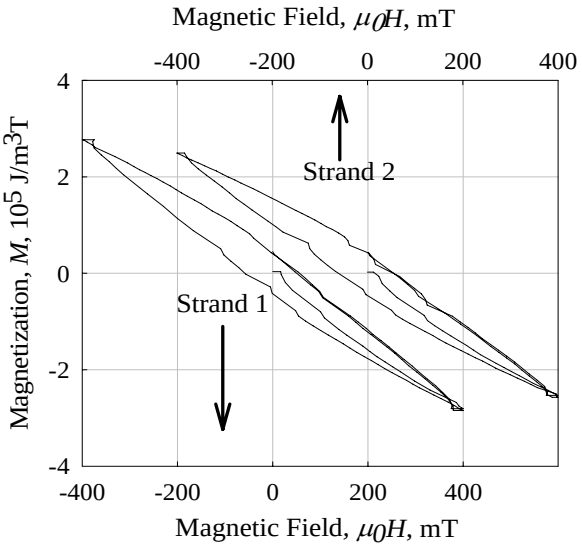

Figure 11: VSM-measured hysteresis loops for a pair of Nb_3Sn extracted strands for "un-penetrated" field-sweep amplitudes of ±400 mT [33].

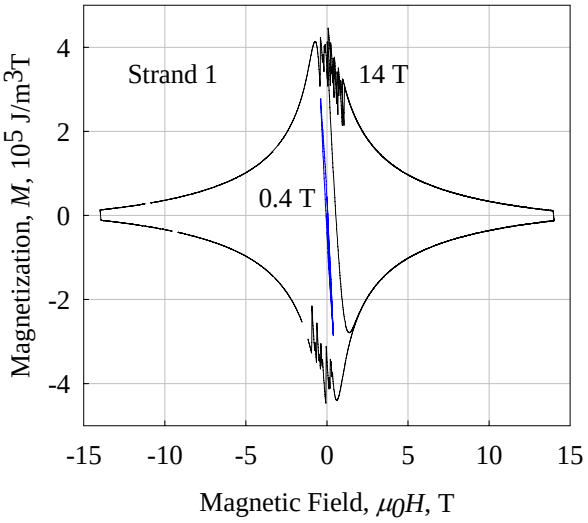

Figure 12: VSM-measured hysteresis loops for a Nb_3Sn extracted strand at field-sweep amplitudes of ±400 mT and ±14 T [33].

with $J_{c,non\text{-}Cu,12T}$ = 3000 A/mm^2 as for a good quality HEP strand, and a typically measured d_{eff} of ~80 μm $M_{cab,0.5T}$ = 3.84x10^5 A/m and the corresponding individual-strand magnetization would be 4.27x10^5 A/m. This is in good agreement with the fully penetrated magnetization data of Figure 12, and again two orders of magnitude greater than the NbTi values.

We next couple together Equations (5) and (6) in order to obtain an explicit expression for $R_{\perp,eff}$ in the injection region, demonstrating its use as a "magnetization parameter". The result is:

$$R_{\perp,eff}(\mu\Omega) = \frac{2.5\times10^4}{J_{c,non-Cu,12T}\times d_{eff}} \quad (7)$$

with J_c in A/mm^2 and d_{eff} in μm

Equation (7) plotted in Figure 13 shows that the use of Nb_3Sn strand leads to $R_{\perp,eff}$s that are mostly below 0.3 μΩ, which from a magnetization standpoint seems to negate the purpose of introducing a core.

Cable magnetization at higher fields

The above analyses emphasize the unsuitability of Nb_3Sn cable for low field precision-field operation. Its high persistent current magnetization degrades quality, Equation (5), and produces flux jumping, Figure 12. The situation improves rapidly as the magnet's operating point moves towards higher fields for two reasons: (1) In moving from 0.5 T to 12 T, for example, the strand's $J_c(H)$ decreases by a factor 16.8 (based on the above mentioned Kramer factor) or 18.3 according to Figure 12. (2) The transport current needed to generate the field reduces the strand's magnetization by a factor (1-i^2), e.g. [35]. Assuming a high-field *i* of 0.8 the combined magnetization-reduction factor would be 1/49. This would raise the $R_{\perp,eff}$ of, for example, a d_{eff} = 30 μm 2.5 kA/mm^2 strand from 0.32 μΩ (point **x** in Figure 13) to an acceptable 15 μΩ.

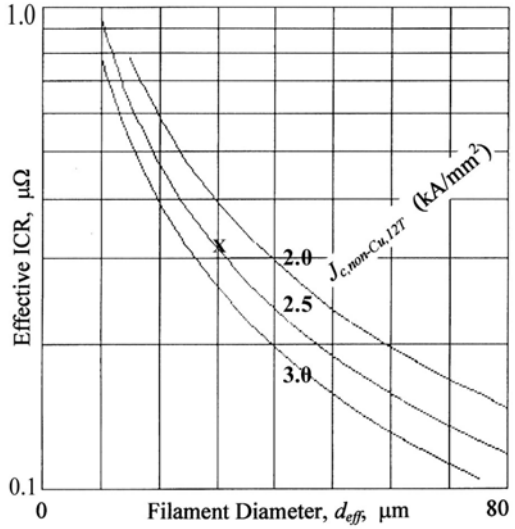

Figure 13: "Effective ICR", regarded as a magnetization parameter, plotted as function of d_{eff} for three values of $J_{c,non-Cu,12T}$ (kA/mm^2)

CONCLUSIONS

- NbTi-cable studies pointed the way by showing how:
  - The introduction of a full-width SS core strongly suppresses coupling loss and the crossover ICR , $R_\perp$ (and its "effective" value, $R_{\perp,eff}$).
  - The core-suppressed $R_{\perp,eff}$ could be tuned by vary the width of the core.
- The above ideas were transferred into the Nb_3Sn cable program wherein it was again shown that strong loss suppression and increased ICR would accompany the introduction of SS cores and composite cores of SS and Cu.
- In experiments on a set of Nb_3Sn cables with cores of various widths it was found that:
  - ICR varied rapidly with core width;
  - Narrow cores produced little loss suppression;
  - The level of suppression was sensitive to the position of the core indicating that care is needed to ensure that the core is well centered.
- The EO loss tended to be frequency independent and hence attributable to the "hysteretic" persistent-current magnetization of the strands.
- Under LHC injection conditions, B_{inj} = 540 mT and $(dB/dt)_{inj}$ = 7 mT/s, strand magnetization also dominates the FO magnetization of the Nb_3Sn cable. As a result of excessive magnetization and the associated flux jumping the Nb_3Sn Rutherford cable is unsuitable for low-field operation.
- Away from injection, and in operating fields of 12 T or more, the cable magnetization drops by a factor of at least 49 into an acceptable range of values.

ACKNOWLEDGEMENTS

We welcome the opportunity to acknowledge the following institutions for providing the facilities that enabled this research: the Lawrence Berkeley National Laboratory (LBNL), Berkeley, CA, USA; the Fermi National Accelerator Laboratory (Fermilab, FNAL), Batavia, IL, USA; the Ohio State University (OSU), Columbus, OH, USA; the Japan National Laboratory for High Energy Physics (KEK), Tsukuba-shi, Ibaraki, Japan; the Applied Superconductivity Center, University of Twente (UoT), Enschede, Netherlands. We also acknowledge our many collaborators who during their participation were located at the institutions mentioned: D.R. Dietderich, R.M. Scanlan (LBNL), G. Ambrosio , E. Barzi, D. Turrioni, R. Yamada, A.V. Zlobin (FNAL), S.W. Kim, T. Shintomi, M. Wake (KEK), Yu.A. Ilyin, A. Nijhuis, H.H.J. ten Kate, A.P. Verweij (UoT). We are also thankful for the skilled technical assistance and advice provided in the areas of : *cable winding*, H.C. Higley (LBNL), R. Rusy (FNAL); *cable pack pressurization and heat treatment*, L.A. Barnhart (OSU), R. Hannaford, E. Palmerston, A. McInturff (LBNL), B. Bianchi (FNAL); *resin impregnation under vacuum*: R. Hannaford, M. Morrison, J. Smithwick (LBNL), F. Buta (Global Research and Development, Inc), J Yue (HyperTech Research Ltd); *extracted-strand magnetization measurement*: M.A. Susner (OSU).

REFERENCES

[1] M.N. Wilson, C.R. Walters, J.D. Levin, et al., *J. Phys. D: Appl. Phys.* **3** 1517-1583 (1970)

[2] G.H. Morgan, *J. Appl. Phys.* **44** 3319-3322 (1973)

[3] J.A. Eikelboom and J.A. Roeterdink, *IEEE Trans. Magn.* **24** 1463-1466 (1988)

[4] W. Wake, D. Gross, R. Yamada, et al., *IEEE Trans. Magn.* **15** 141-142 (1979)

[5] Y.Z. Lei, T. Shintomi, A. Terashima, et al., *IEEE Trans. Appl. Supercond.* **3** 747-750 (1993)

[6] A. Kimura, N. Kimura, Y. Makida, et al., *IEEE Trans. Magn.* **30** 2515-2518 (1994)

[7] G.T. Mallick, Jr., D. Natelson, W. J. Carr, Jr., et al., *IEEE Trans. Appl. Supercond.* **3** 744-746 (1993)

[8] V.E. Sytnikov, G.G. Svalov, S.G. Akopov, et al., *Cryogenics* **29** 929-930 (1989); see also V.E. Sytnikov, and I.B. Peshkov, *Adv. Cryo. Eng. (Materials)* **40** 537-542 (1994)

[9] L. Krempasky and C. Schmidt, *Physica C* **310** 327-334 (1998)

[10] A.P Verweij, *Ph.D. Thesis*, University of Twente Press, 1995

[11] Z. Ang, I. Bejar, D. Richter, et al., *IEEE Trans. Appl. Supercond.* **9** 735-741 (1999)

[12] A.K. Ghosh, W.B. Sampson, S.W. Kim, et al., *Physica C* **310** 335-339 (1998)

[13] M.D. Sumption, H.H.J. Ten Kate, R.M. Scanlan, et al., *IEEE Trans. Appl. Supercond.* **5** 692-696 (1995)

[14] M.D. Sumption, R.M. Scanlan, A. Nijhuis, et al., *Adv. Cryo. Eng. (Materials)* **42** 1303-1311 (1997)

[15] M.D. Sumption, E.W. Collings, R.M. Scanlan, et al., *Cryogenics* **39** 197-208 (1999)

[16] E.W. Collings, M.D. Sumption, R.M. Scanlan, et al., *Adv. Cryo. Eng. (Materials)* **42** 1225-1232 (1997)

[17] E.W. Collings, M.D. Sumption, S.W. Kim, et al., *IEEE Trans. Appl. Supercond.* **7** 962-966 (1997)

[18] M.D. Sumption, R.M. Scanlan, and E.W. Collings, *IEEE Trans. Appl. Supercond.* **11** 2571-2574 (2001)

[19] E.W. Collings, M.D. Sumption, S.W. Kim, et al., *Proc. 16th ICEC/ICMC Conference*, ed. By T. Haruyama, T. Mitsui, K. Yamafuji (1996)

[20] M.D. Sumption, E.W. Collings, R.M. Scanlan, et al., *Supercond. Sci. Tech.* **14** 888-897 (2001)

[21] M.D. Sumption, E.W. Collings, R.M. Scanlan, et al., *Cryogenics* **41** 733-744 (2001)

[22] M.D. Sumption, E.W. Collings, A. Nijhuis, et al., *Adv. Cryo. Eng. (Materials)* **46** 1043-1049 (2000)

[23] M.D. Sumption, E.W. Collings, R.M. Scanlan, et al., *Adv. Cryo. Eng. (Materials)* **44** 1077-1084 (1998)

[24] M.D. Sumption, E.W. Collings, R.M. Scanlan, et al., *Cryogenics* **39** 1-12 (1999)

[25] M.D. Sumption, R.M. Scanlan, Yu.A. Ilyin, et al., *Adv. Cryo. Eng. (Materials)* **50** 781-788 (2004)

[26] E.W. Collings, M.D. Sumption, R.M. Scanlan, et al., *Adv. Cryo. Eng. (Materials)* **48** 1153-1160 (2002)

[27] M.D. Sumption, E.W. Collings, R.M. Scanlan, et al., *IEEE Trans. Appl. Supercond.* **13** 2376-2379 (2003)

[28] E.W. Collings, M.D. Sumption, D.R. Dietderich, et al., *Adv. Cryo. Eng. (Materials)* **52** 851-858 (2006)

[29] E.W. Collings, M.D. Sumption, D.R. Dietderich, et al., *IEEE Trans. Appl. Supercond.* **16** 1200-1203 (2006)

[30] E.W. Collings, M.D. Sumption, G. Ambosio, et al., *IEEE Trans. Appl. Supercond.* **17** 2494-2495 (2007)

[31] E.W. Collings, M.D. Sumption, E. Barzi, et al., *Adv. Cryo. Eng. (Materials)* **54** 285-292 (2008)

[32] E.W. Collings, M.D. Sumption, E. Barzi, et al., *IEEE Trans. Appl. Supercond.* **18** 1370-1373 (2008)

[33] E.W. Collings, M.D. Sumption, M.A. Susner, et al., *IEEE Trans. Appl. Supercond.* **18** 1301-1304 (2008)

[34] E.W. Collings, M.D. Sumption, and E. Lee, *IEEE Trans. Appl. Supercond.* **11** 2567-2570 (2001)

[35] M.A.R. LeBlanc, *Phys. Rev. Lett.* **11** 149-152 (1963)

SELF-FIELD INSTABILITIES IN HIGH-J_C Nb_3Sn STRANDS: THE EFFECT OF COPPER *RRR*

B. Bordini, CERN, Geneva, Switzerland

Abstract

High critical current density (J_c) Nb_3Sn conductor is the best candidate for next generation high field (> 10 T) accelerator magnets. Although very promising, state of the art high-J_c Nb_3Sn strands suffer of magneto-thermal instabilities that can severely limit the strand performance. Recently it has been shown that at 1.9 K the self field instability is the dominating mechanism that limits the performance of strands with a low (<10) Residual Resistivity Ratio (*RRR*) of the stabilizing copper. At CERN several state of the art high–J_c Nb_3Sn wires have been tested at 4.2 K and 1.9 K to study the effects on strand self-field instability of: *RRR* and strand impregnation with stycast. To study the effect of the *RRR* value on magneto-thermal instabilities, a new 2-D finite element model was also developed at CERN. This model simulates the whole development of the flux jump in the strand cross section also taking into account the heat and current diffusion in the stabilizing copper. In this paper the main conclusions drown from this study are reported.

INTRODUCTION

High critical current density (J_c) Nb_3Sn conductor is the best candidate for next generation high field (> 10 T) accelerator magnets. Although very promising, state of the art high-J_c Nb_3Sn strands suffer of magneto-thermal instabilities [1]-[6] that can severely limit the strand performance [6]-[9]. There are two types of magneto-thermal instabilities: 'Magnetization' instability due to the magnetization of the superconducting filaments [1][2] and mainly depending on J_c, on the effective filament size (D_{eff}) and on the Residual Resistivity Ratio (*RRR*) of the stabilizing copper; 'Self-field' instability due to the uneven distribution of the transport current within the strand [3][4] and mainly depending on J_c and the strand diameter. The effect of *RRR* on the self-field instability has not been much studied in high-J_c Nb_3Sn conductor and is one of the topics of this paper.

Magnetization instability has been the primary cause of the limited quench performance (40-70 % of the short sample limit) at 4.4 K of some Nb_3Sn high field magnets built at FNAL [10] and LBNL [9] [11] in the early 2000s. In these magnets the stability current (I_s) of the conductor (i.e., the minimum current at which the conductor can have a premature quench due to magneto-thermal instability) occurred at very low magnetic fields (~0-3 T) and it was significantly lower than the magnet intrinsic critical current (I_c); hence, since in the magnet there are always regions where the magnetic field is low, the magnet quenched when the current reached the stability current value. The low value of the stability current was due to the large D_{eff} (70 - 100 μm) of the conductor, to the high J_c (1700-1900 A/mm^2 at 4.2 K and 12 T) and to the low Residual Resistivity Ratio (*RRR*<10) of the stabilizing copper. At present, the problem of magnetization instability at 4.4 K is contained through optimized heat treatments and cabling processes that guarantee a high *RRR* (>150). Using such approach, the U.S. LHC Accelerator Research Program (LARP) collaboration (which consists of four US laboratories, BNL, FNAL, LBNL, and SLAC, who collaborate with CERN on the Large Hadron Collider) was able to build and test a 1-m-long quadrupole (TQS01) based on a Nb_3Sn Modified Jelly Roll strand produced by Oxford Superconducting Technology (OST) (J_c ~1900 A/mm^2; D_{eff} ~70 μm) that reached more than 80 % of the short sample limit both at 4.4 K and 1.9 K, and did not show evidences of magneto-thermal instabilities [12]. Recently, the LARP collaboration built two 1-m-long quadrupoles and a 4-m-long racetrack based on the more performing Rod Re-Stack Process (RRP®) strand produced by OST (J_c >2400 A/mm^2; D_{eff} ~70 μm): at 4.4 K, these magnets reached more than 85 % of the short sample limit [12][13][14].

In a previous paper [6] it has been shown that at 1.9 K the self-field instability is the dominating mechanism that limits the performance of high-J_c Nb_3Sn strands with a low *RRR* (<10). It was also shown [6] that for RRP® strand with low *RRR*: 1) the minimum quench current due to the self-field instability, that is the self-field stability current ($I_{s\text{-}SF}$), is lower at 1.9 K than at 4.2 K and; 2) at 1.9 K the $I_{s\text{-}SF}$ can be considerably lower than the critical current at 12 T. The self-field instability might be the cause of the limited quench performance at 1.9 K of the latest magnets based on the RRP® conductor built by the LARP collaboration [12][13]. At 1.9 K the quench current of these magnets did not practically change with respect to the 4.4 K case, and this behavior cannot be attributed neither to critical current degradation (the magnets were retested at 4.4 K reaching the previous current values) nor to mechanical instability (often the quench current values at 1.9 K were lower than those obtained at 4.4 K).

At CERN several state of the art high–J_c Nb_3Sn wires have been tested at 4.2 K and 1.9 K to see if the conclusions drawn for samples with low *RRR* can be extended to samples with higher *RRR* values and to study the effects on strand stability of *RRR* and strand impregnation with stycast. The strand samples were heat treated and tested on grooved cylindrical Ti-Alloy barrels (ITER barrel). The wires tested included RRP® strands produced by OST and Powder In Tube (PIT) strands

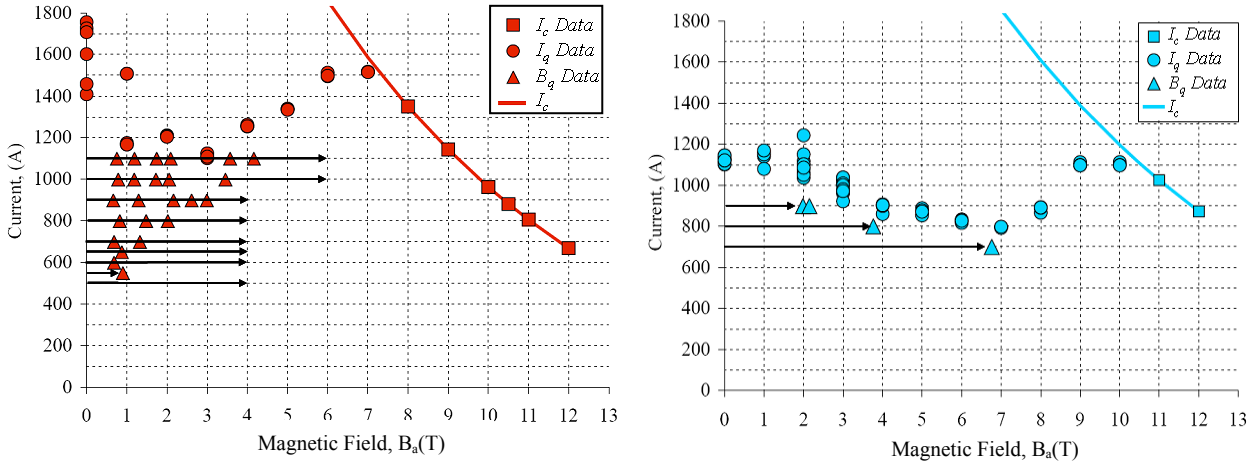

Figure 1: V-I (I_c and I_q data) and V-H (B_q data) measurement results at 4.2 K (plot *a*) and 1.9 K (plot *b*) for a 0.8 mm RRP® strand with copper *RRR*=8 [6].

produced by ShapeMetal Innovation - European Advanced Superconductors (SMI-EAS).

To study the effect of the *RRR* value on magneto-thermal instabilities, a new 2-D finite element model was also developed at CERN. This model simulates the whole development of the flux jump in the strand cross section also taking into account the heat and current diffusion in the stabilizing copper. In this paper the main conclusions drawn from this study are reported; a more detailed presentations of the experimental results and of the model can be found elsewhere [15].

SELF FIELD INSTABILITY IN HIGH-J_C Nb_3Sn STRANDS WITH LOW *RRR*

In a previous study it was found that at 1.9 K magnetization instability does not play a significant role on the quench performance of high-J_c Nb_3Sn wire with low *RRR* (<10), indeed during V-H measurements the local minimum of the quench current at low fields (0-3 T), confirmed at 4.2 K (see B_q data in Fig. 1*a*), disappeared at 1.9 K (see B_q data in Fig. 1*b*) [6]. At 1.9 K, the self-field instability is the dominating instability mechanism. A semi-analytical model, supported by experimental measurements, demonstrated that for these strands the self-field instability is characterized by 3 stability regions: an 'high field' stable region where the conductor can reach its intrinsic critical current; an 'intermediate field' region where the premature quench current depends on the severity of the perturbation that initiates the magneto-thermal instability and is higher than a certain minimum, $I_{qMin\text{-}SF}$ *(B)*; a 'low field' region where the premature quench current value does not depend on the amount of the perturbation and a quench can occur as soon as the current is higher than $I_{qMin\text{-}SF}$ *(B)*. Furthermore, the self field stability current $I_{s\text{-}SF}$ occurs in the 'intermediate field' region (~ 3-8 T at 4.2 K and ~ 7-11 T at 1.9 K for the 0.8 mm RRP® strand) and it is lower at 1.9 K than at 4.2 K (see Fig. 2). This conductor behavior could be a serious problem for accelerator magnets based on high-J_c Nb_3Sn conductor that have to work at 1.9 K. At CERN the effect of *RRR* on the strand self-field stability was investigated to see if a high *RRR* value can solve this stability problem at 1.9 K; the main results are reported in the next section.

MAIN RESULTS

Testing at CERN seven 0.8 mm 54/61 RRP® strand samples with a similar J_c (>2500 A/mm^2 at 4.2 K and 12 T), it was found that:

1. At 4.2 K in the 'low field' region (0-3 T) the *RRR* value has not a large effect on the self field stability (the premature quench current during V-I measurements [6] increases only few percentages passing from *RRR*=8 to

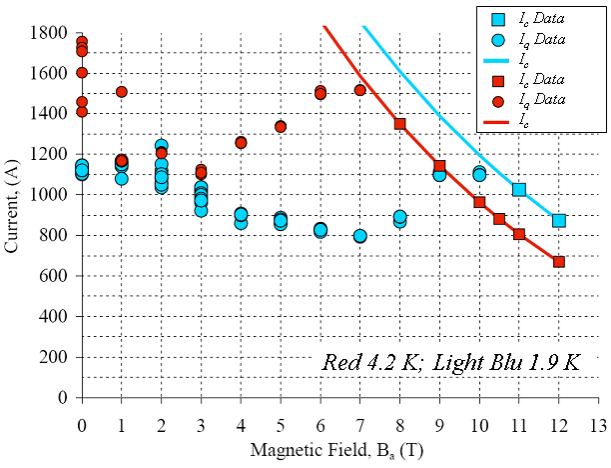

Figure 2: V-I measurements of a 0.8 mm RRP® strand with copper *RRR*=8 [6]: comparison between the results obtained at 4.2 K and at 1.9 K.

RRR=120 or from *RRR*=140 to *RRR*=290);

2. At 1.9 K in the 'low field' region (0-7 T) the self-field stability significantly improves passing from *RRR*=8 to *RRR*=120 (during V-I measurements the premature quench current gets more than 50 % larger), further increasing the *RRR* does not produce significant effects;
3. In the 'intermediate field' region (3-8 T at 4.2 K and 7-11 T at 1.9 K) it was not possible to find experimental evidence, both at 4.2 K and 1.9 K, of the quench performance improvement by increasing the *RRR* value;
4. In the 'intermediate' field region the self-field instability is much more sensitive, with respect to the 'low field' region, to the amount of energy released by the perturbation that initiates the magneto-thermal instability; the larger is the perturbation, the lower is the quench current due to the self-field instability;
5. This strong sensitivity in the 'intermediate field' region and the difficulty of exposing all the samples to exactly the same perturbation spectrum is most likely the cause of what was observed in point 3;
6. Independently of the *RRR* value, the minimum quench current due to the self-field instability, that is the self-field stability current ($I_{s\text{-}SF}$), occurs in the 'intermediate field' region and is lower at 1.9 K than at 4.2 K;
7. If the energy released by the perturbation that triggers the magneto-thermal instability is sufficiently high, at 1.9 K the self-field stability current ($I_{s\text{-}SF}$) can be significantly lower than the strand critical current (I_c) at 12 T and 4.2 K even for strands with an high *RRR* value and with $I_{s\text{-}SF}$(4.2 K)> I_c(12 T, 4.2 K);
8. V-H measurements performed at 1.9 K confirmed that magnetization instability does not play a significant role at 1.9 K even in strand with high *RRR* values;
9. Covering a strand (*RRR* ~120) with a 1 mm thick layer of stycast did not significantly change the premature quench current values at 4.2 K while it systematically decreased the minimum quench current due to the self field instability of about 10% at 1.9 K in the 'low field' region (0-7 T).

The test of a 0.8 mm PIT strand with a J_c equal to 2224 A/mm^2 (at 4.2 K and 12 T) and a *RRR*=27 showed that this strand is much more self field stable than the previous RRP® strands; at 1.9 K, the self field stability current $I_{s\text{-}SF}$ is almost twice larger than the critical current at 12 T. This improved stability with respect to the RRP® strands is due to the lower critical current density and to the different strand layout. Indeed, the PIT wire had a larger amount of copper in between the superconducting sub-elements, a larger copper to non-copper ratio and a smaller sub-element size with respect to the RRP® strand; all these solutions allow improving the dynamic stabilization of the strand. More details regarding these measurements can be found in [15].

The test at CERN of two round 0.7 mm RRP® strand samples showed that a small local damage of the copper stabilizer can completely jeopardize the dynamic stabilization of a high-J_c Nb_3Sn strand with a high global *RRR*. The strand for preparing these two samples is the same used by the LARP collaboration for building magnet models [12][13][14] and it was send to CERN by Arup Ghosh (BNL) in the framework of a collaboration between LARP and CERN. The two samples were heat treated together (at the University of Geneva) following the procedure used for reacting LARP magnets; straight samples for *RRR* measurements were also inserted in the oven. After the heat treatment one sample presented a small copper burst (see Fig. 3). A comparison of the critical and stability current measurements of the two samples at 4.2 K an 1.9 K shows that although this small damage did not degrade the critical current of the sample, it drastically reduced its magneto-thermal stability (the stability current at 4.2 K and 1.9 K gets reduced of a factor of two and it was even lower than the strand critical current at 12 T and 4.2 K). The damage consisted in the local reduction of the *RRR* and of the amount of stabilizing copper. The huge difference in the stability performance of the two samples is also due to the high global *RRR* value (a *RRR* larger than 250 was measured on the straight samples).

A new numerical model for simulating magneto-thermal instabilities was developed at CERN. This model, based on the finite element method, simulates the whole development of the flux jump in the strand cross section also taking into account the heat and current diffusion in the stabilizing copper and the strongly non linear transition of the superconductor to the normal state [15]. The model shows that the self-field instability is significantly dependent on the level of energy of the initial perturbation (the higher the perturbation the lower the quench current). This is true until the current reaches a certain minimum value of the premature quench current, $I_{qMin\text{-}SF}$ *(B)*, below which it seems not to decrease independently from the strength of the perturbation. Furthermore, the lower is the magnetic field, the lower is the value of the perturbation energy beyond which the quench current is equal to $I_{qMin\text{-}SF}$*(B)*. From this

Figure 3: Picture of a round 0.7 mm RRP® strand that had a copper burst during the heat treatment. The wire is mounted on a Ti-Alloy barrels (ITER barrel).

calculation one can conclude that for a certain perturbation energy, there are three stability regions: a 'low field' region ($0<B<B_{LF}$) where the quench current is practically equal to $I_{qMin\text{-}SF}(B)$; an 'high field' stable region ($B>B_S$) where the conductor reaches its intrinsic critical current and; an 'intermediate field' region ($B_{LF}<B<B_S$) where premature quenches occur but the quench current is higher than $I_{qMin\text{-}SF}(B)$. These stability regions were already predicted by our previous semi-analytical model [6], the novelty being that the values of B_{LF} and B_S depends on the level of energy of the initial perturbation. From the model, one can also conclude that increasing the *RRR* above 120 has not a significant stabilization effect while passing from *RRR* less than 10 to 120 may have a significant stabilizing effect at high fields (at low fields the effect of *RRR* is rather limited). Nevertheless the stabilizing effect of *RRR* at high fields is drastically reduced when the energy released by the initial perturbation is sufficiently high. More details on the model and its results can be found in [15].

CONCLUSIONS

Strand measurements show that at 1.9 K the self-field instability is the dominating mechanism that limits the performance of high–J_c Nb_3Sn wires and the magnetization instability does not play a significant role. For these strands, the minimum quench current due to the self-field instability, that is the self field stability current ($I_{s\text{-}SF}$), is lower at 1.9 K than at 4.2 K; at 1.9 K, even if the *RRR* of the stabilizing copper is high, the $I_{s\text{-}SF}$ can be lower than the critical current (I_c) at 12 T and 1.9 K and, in case of strong perturbations the $I_{s\text{-}SF}$ can be even lower than the I_c at 12 T and 4.2 K. This behaviour could explain the performance of the latest Nb_3Sn LARP magnets based on the RRP® conductor that, at 1.9 K, had equal or even lower quench currents with respect to the 4.4 K case. At 1.9 K, increasing the *RRR* from 8 to 120 is beneficial for the strand self-field stability, while further increasing the *RRR* value does not produce significant effects. Strand measurements also showed that covering the strand with a 1 mm thick layer of stycast reduced the quench current at 1.9 K of less than 10 %.

A new numerical model for simulating magneto-thermal instabilities was developed. This model, based on the finite element method, simulates the whole development of the flux jump in the strand cross section also taking in to account the heat and current diffusion in the stabilizing copper and the strongly non linear transition of the superconductor to the normal state. Preliminary results show that the new model is in good agreement with the experimental data. The model also shows that the self-field instability is characterized by three stability region and in the 'intermediate field' region is strongly sensitive to the perturbation energy that initiates the magneto-thermal instability. Consistently with the experimental data the model predicted that the self-field stability current ($I_{s\text{-}SF}$) occurs in the 'intermediate' field region and if the perturbation energy is sufficiently high (but still much lower than the minimum quench energy) $I_{s\text{-}SF}$ can be lower than the intrinsic critical current at 12 T even with high *RRR* values of stabilizing copper.

REFERENCES

[1] R. Hancox, "Stability against flux jumping in sintered Nb_3Sn", Phys. Lett.,vol. 16, pp. 208, 1965

[2] P. S. Swartz and C. P. Bean, "A Model for Magnetic Instabilities in Hard Superconductors: The Adiabatic Critical State", J. Appl. Phys., vol. 19, pp. 4991, 1968

[3] M. N. Wilson, "Superconducting Magnets", Clarendon Press, pp. 139-141, Oxford, 1983

[4] R. G. Mints, A. L. Rakhmanov, "Critical current of a superconductor", Sov. Tech. Phys. Lett., vol 2, no. 6, Jun. 1976

[5] V.V. Kashikhin, A.V. Zlobin, "Magnetic instabilities in Nb_3Sn strands and cables", IEEE Trans. Appl. Supercond., vol. 15, no. 2,pp. 1621–1624, Jun. 2005

[6] B. Bordini, E. Barzi, S. Feher, L.Rossi, A.V. Zlobin, "Self-Field Effects in Magneto-Thermal Instabilities for Nb-Sn Strands", IEEE Trans. Appl. Supercond., vol. 18, no. 2, pp. 1309 - 1312, Jun. 2008

[7] B. Barzi, et al., "Instability in Transport Current Measurement", IEEE Trans. Appl. Superconduct., vol 15, no.2, pp. 3364-3367, Jun. 2005.

[8] A. K. Ghosh, L. D. Cooley, A. R. Moodenbaugh, "Investigation of instability in high J_c Nb_3Sn strands", IEEE Trans. on Appl. Supercond., vol. 15, no. 2, pp. 3360–3363, Jun. 2005

[9] D. R. Dieterich et al , "Correlation between strand stability and magnet performance", IEEE Trans. Appl. Supercond., vol. 15, no. 2,pp. 1524–1528, Jun. 2005

[10] A. V. Zlobin et al , "R&D of Nb_3Sn Accelerator Magnets at Fermilab", IEEE Trans. Appl. Supercond., vol. 15, no. 2,pp. 1113–1118, Jun. 2005

[11] D. R. Dieterich, A. Godeke , "Nb_3Sn Performance and Potential in the USA – Wires and Cables", Cryogenics , vol. 48, Issues 7-8, pp. 331-340, July-August 2008

[12] S. Caspi et al , "Test and Analysis of Technology Quadrupole Shell (TQS) Magnet Models for LARP", IEEE Trans. Appl. Supercond., vol. 18, no. 2, pp. 179-183, June 2008

[13] R. C. Bossert et al , 'Development and Test of LARP Technological Quadrupole Models of TQC Series', IEEE Trans. Appl. Supercond , vol. 18, no. 2, pp. 175-178 June 2008

[14] P. Wanderer et al. 'Larp Long Racetrack Coil Program', IEEE Trans. Appl. Supercond., vol. 17, NO. 2, pp. 1140-143 June 2007

[15] B. Bordini, L.Rossi, "Self Field Instability in High-J_c Nb_3Sn Strands with High Copper Residual Resistivity Ratio", 4LX04 to be presented at ASC 08

IRRADIATION EFFECTS IN LOW T_C SUPERCONDUCTORS

René Flükiger

Department of Condensed Matter Physics (DPMC) & Applied PhysicsGroup (GAP)
University of Geneva, 1211 Geneva 4, Switzerland

Abstract

The effects of neutron irradiation on the superconducting parameters T_c, B_{c2} and J_c of Nb_3Sn are reviewed in view of the determination of the radiation limit in the LHC upgrade magnets. The variation of J_c in binary as well as in Ti and Ta alloyed Nb_3Sn wires is presented. The coexisting defect mechanisms in irradiated Nb_3Sn type compounds are briefly presented and a model is discussed explaining the site exchange mechanism which leads to a decrease of atomic ordering after irradiation.

Based on calculations of F. Cerutti and coworkers (CERN), the neutron fluence at the inner winding of the quadrupole Q2a is estimated to values below 10^{18} neutrons /cm^2 for a life time of 10 years, which is within the safety margin with respect to the critical current density and B_{c2}.

INTRODUCTION

The construction of future colliders with higher energies implies the use of superconducting dipoles and quadrupoles with increasing magnetic fields. As an example, the envisaged magnetic field in the LHC upgrade project will be as high as 15 T. At the present state of knowledge, such dipoles have to be wound on the basis of round wires, which limits the possible choice of industrially available superconducting materials to Nb_3Sn, Nb_3Al (both crystallizing in the A15 type structure) and Bi-2212. However, Bi-2212 wires still exhibit weak mechanical properties, while Nb_3Al can be produced in kilometer lengths, but is not yet available in large quantities. The present paper will thus only consider the effect of high energy irradiation on the low T_c superconductor Nb_3Sn.

The question arises whether the intense radiation produced by the collisions in the high LHC upgrade energy collider has an influence on the magnetic fields produced by the superconducting dipoles and quadrupoles. Of particular interest for the present paper are the Phase I and Phase II upgrades, with a luminosity of 2.5×10^{34} cm^{-2}s^{-1} and 10^{35} cm^{-2}s^{-1}, i.e. 2.5 and 10 times larger than nominal LHC, respectively. This question is treated based on recent calculations of the maximum neutron fluence (also called radiation dose in a number of other publications) acting on a well localized magnet location (the quadrupole). These calculations have been recently performed by F. Cerutti et al. [1] at CERN.

The present paper is a review about the known neutron irradiation data on Nb_3Sn wires, based on neutron irradiation experiments performed before 1986. After this date, irradiation works have been performed on HTS superconductors and more recently, on MgB_2 [2]. The mechanism of irradiation effects in A15 type compounds will be discussed, and a model explaining the observed changes of the superconducting properties is presented. The variation of T_c, B_{c2} and the electrical resistivity ρ_o of Nb_3Sn wires with radiation will be discussed, as well as the effects on the critical current density, J_c, with and without additives.

These data show that the effect of neutron radiation fluence on the critical current density of Nb_3Sn wires during 10 years, the estimated lifetime of the LHC upgrades, will not affect the critical current density of the Nb_3Sn wires. This is also valid for the quadrupole magnets Q2a, where the highest radiation fluence is expected [1] (see also Fig. 1).

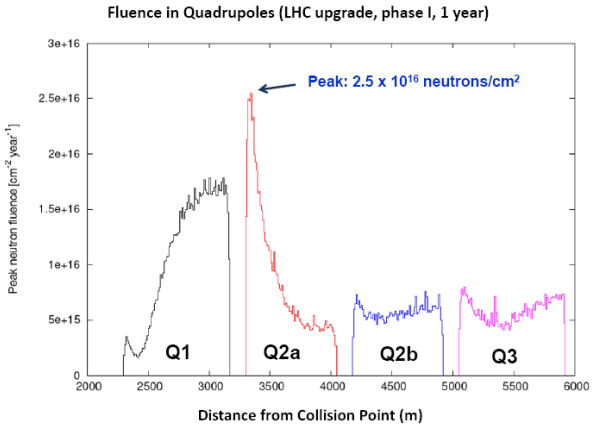

Figure 1: Calculated peak neutron fluence in phase I of LHC upgrade as a function of distance from the collision point, indicating a maximum for the inner winding of the quadrupole Q2a, as calculated by Cerutti et al. [1]).

THE NEUTRON RADIATION FLUENCE AT THE INNER WINDING OF LHC QUADRUPOLES

The collisions in a high energy collider produce a very

*This work was supported in part by the Swiss National Science Foundation through the National Centre of Competence in Research, "Materials with Novel Electronic Properties, MANEP".

intense radiation, its intensity increasing with energy. Neutron radiation has a strong influence on all the components of the collider, i.e. the superconductor, the stabilizer and the insulator. It is well-known that the superconducting properties of most superconductors depend on the radiation fluence, and the question arises whether significant radiation-induced effects (e.g. decreased values of T_c and of the critical field, increased resistivity, etc.) will lead to a reduced magnet performance within the time of operation, which may reach several years.

When calculating these effects, it is important to know the spectrum of the various radiations interacting with the magnets. At the collision site, a very strong radiation environment will be created. Estimates for the produced radiation at the collision site yield particle energies up to 10 GeV, the radiation being composed by charged pions, protons, neutrons, photons, electrons,…. [3]. It follows that adequate shielding is vital in order to reduce these radiations to an acceptable level. Taking into account the planned shielding conditions as well as the distance between the collision site and the magnets, the maximum radiation load acting on the magnets has been recently calculated by Cerutti et al. [1]. It was found that after interaction with the shielding material, the radiation spectrum reaching the closest magnets (the quadrupoles) will be composed by:

Photons	87 %
Neutrons	6 %
Electrons	3.5 %
Positrons	2.5 %
Pions (+/-)	0.4 %
Protons	0.15 %.

It has been shown that neutron radiation has a strong effect on the superconducting properties of Nb_3Sn, while the effect of photons, electrons and photons is negligible. Since the total amount of pions ad protons does not exceed 10% of the calculated intensity for neutrons, the present estimation will be done under the assumption that neutrons are the main source of damage to the superconductors. All other radiation sources will be neglected when considering the effect on the superconductor. Their effect on the insulator materials has to be analyzed separately and will not be treated in the present paper.

The calculations of Cerutti et al. [1] show that the neutron energy has a pronounced peak around 1 MeV. The neutron energies used in the previous works studying the effects of radiation damage on the superconducting properties of superconductors vary between 1 and 14 MeV (Sweedler et al. [4]) and 14 MeV (Weber et al. [5], Guinan et al. [6] and Weiss et al. [7]). A comparison between the various known data shows that within this energy range, one does not expect a strong difference between the effects of neutron radiation on the superconducting properties. As shown in Fig. 1, the highest fluence will be reached at the inner winding of the quadrupole Q2a, at a distance of 33 m from the collision point. The expected maximum radiation fluence was calculated to 2×10^{16} n/cm^2 per year, assuming an operation of 200 days a year. For a total operation time of 10 years, the maximum fluences at the inner winding of the quadrupole Q2a after the upgrades of Phase I and Phase II will thus be 2.5×10^{17} n/cm^2 and 10^{18} n/cm^2, respectively. In Section VI, the effect of these fluences on T_c and J_c will be analyzed for both, binary and alloyed Nb_3Sn wires. An explanation for the higher sensitivity to radiation damage for alloyed Nb_3Sn wires with respect to binary wires will be discussed.

THE EFFECTS OF NEUTRON IRRADIATION ON SUPERCONDUCTORS

Effect on T_c of various superconducting compounds

As mentioned above, the main damage at the magnet site in LHC upgrade phase I is expected to be caused by neutron irradiation. The overwhelming amount of neutron irradiation data of Low T_c (or LTS) superconductors has been performed prior to 1987, after which most work was performed on High T_c (or HTS) compounds. In Fig. 2, the variation of T_c vs. ϕt is shown for the most known Low T_c superconductors: Laves phases (HfV_2) [9], Chevrel phases ($PbMo_6S_8$) [10], MgB_2 [2]. T_c for NbTi [8] is not shown here, but is even less radiation sensitive than V_2Hf.

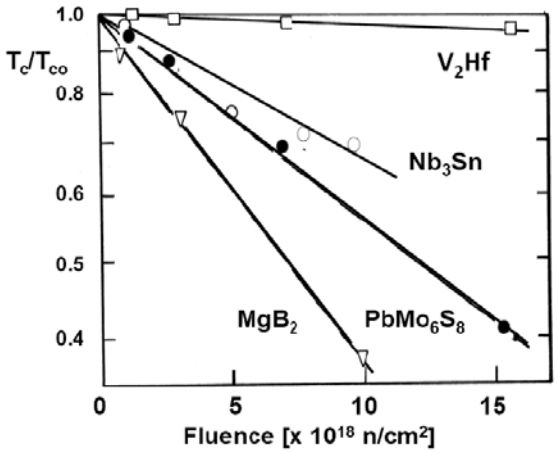

Figure 2: Variation of T_c vs. neutron fluence, ϕt, for various known low T_c superconductors. Laves phases (HfV_2) [9], Chevrel phases ($PbMo_6S_8$) [10], Nb_3Sn [4], MgB_2 [2].

Although NbTi and HfV_2 are little affected by neutron radiation, these materials must be excluded due to their too low H_{c2} values. Chevrel phases exhibit very high H_{c2}, but never reached the industrial level. In addition, they exhibit a relatively low T_c value (14 K in wires) and

astronger radiation sensitivity with respect to Nb_3Sn. MgB_2 has also a stronger sensitivity to neutron irradiation than Nb_3Sn, but the value of B_{irr} is not high enough for magnets producing 15 T.

The data for the HTS compounds Bi-2212, Bi-2223 and Y-123 are not shown here, but it must be noted that even if they show a relatively strong decrease of T_c with neutron fluence, this would be of little importance for operation at 4.2 K. Indeed, T_c, J_c and B_{c2} would still be sufficiently high for this temperature. As mentioned above, mechanical stability for Bi-2212 and the tape geometry for Bi-2223 and Y-123 are at present important obstacles excluding their use in collider magnets.

Radiation effects on T_c of several A15 type compounds

It appears from Fig. 2 that Nb_3Sn is well suited for being used in LHC upgrade, no significant decrease of T_c being observed up to radiation fluences up to 10^{18} n/cm^2. The decrease of T_c in various A15 type compounds as a function of the irradiation fluence, ϕt, for neutrons with $E \leq 1$ MeV at irradiation temperatures $T_{irr} \leq 150$°C is represented in Fig. 3. The data on V_3Si, Nb_3Ge, Nb_3Al, Nb_3Pt, Nb_3Ga and Mo_3Os are extracted from Sweedler et al. [4,14], while V_3Ga was analyzed by Francavilla et al. [15] and $Mo_{.40}Tc_{.60}$ by Giorgi et al. [16]. It is remarkable that the variation of T_c with ϕt is very similar for V_3Si, Nb_3Ge, Nb_3Al, Nb_3Pt, Nb_3Ga and V_3Ga, in contrast to Mo_3Os and $Mo_{.40}Tc_{.60}$, where the decrease of T_c is considerably smaller.

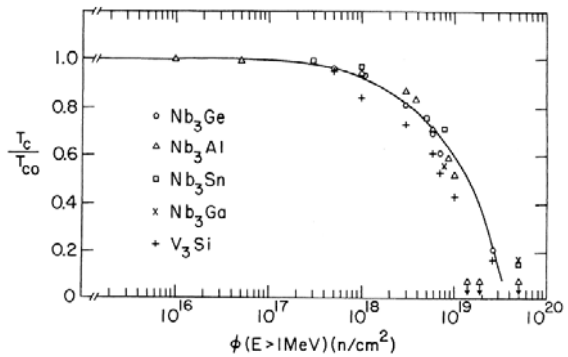

Figure 3: T_c as a function of neutron fluence ($E \leq 1$ MeV, $T_{irr} \leq 150$°C) for various A15 type compounds (all data from Sweedler et al. [4]).

From X ray diffractometry, Sweedler et al. [4,14] concluded that the decrease of T_c at doses up to 10^{19} n/cm^2 (where $T_c/T_{co} \sim 0.5$) is mainly caused by a decrease of the long-range atomic order parameter, S.

From X ray diffractometry, Sweedler et al. [4,14] established that the decrease of T_c at doses up to 10^{19} n/cm^2 (where $T_c/T_{co} \sim 0.5$) is mainly caused by a decrease of the long-range atomic order parameter. S. Pande [17] proposed another explanation for the observed correlation between radiation dose and T_c, based on TEM observations, revealing the presence of depleted zones in irradiated samples. As previously shown in an unpublished Internal Report (Flükiger [18]), calorimetric measurements constitute a definitive proof for the validity of the "disordering" model proposed by Sweedler et al. [4,14]. This will be discussed in detail in the following.

Irradiation temperature

At 1.8 K, the operation temperature of LHC and LHC upgrades, vacancies show any mobility, and site exchanges can only occur by the energy of transmitted by the multiple collisions. An increase of the irradiation temperature, T_{irr}, will lead to self-annealing effects. There is no complete series of measurements on irradiations at T < 10 K and T > 300K, and a comparison can only be made using the data of different authors, who worked at with neutrons of different energies, between 0.1 and 14 MeV. The conversion from 0.1 to 14 MeV is problematic, and several approaches to find appropriate conversion factors have given unsatisfactory results. For this reason, the nominal fluences will be used for the present comparison, well knowing that a certain error is introduced.

Söll et al. [19] performed neutron irradiations (E > 0.1 MeV) of Nb_3Sn diffusion wires at 4.6 K and moved the samples from the irradiation position to the test cryostat without warmup. The irradiation was performed up to a fluence of 3.9×10^{18} n/cm^2, after which a T_c reduction of 0.8 K was observed. After irradiation at >150 °C (in reality, the temperature before irradiation was 300 K) to 10^{18}/cm^2 (E>1 MeV), Sweedler et al. [4] reported a similar decrease in T_c, which indicates that changes in superconducting properties of Nb_3Sn after irradiation at > 150°C may be similar to effects of 4.6 K irradiation. This was later roughly confirmed by J_c measurements by Hahn et al. [20]. Söll et al. [21] extended their cryogenic irradiations to a fast neutron fluence of 10^{19} n/cm^2 (E>0.1 MeV) at $T_{irr} \sim 10$ K. A slight extrapolation of their results reveals that a fluence of ~ 1.2×10^{19} n/cm^2 would be required to reduce T_c to 13.5 K, the value obtained by Sweedler et al. [4] at >150 °C after a higher fluence of 5×10^{18} n/cm^2 (E>1 MeV). Again, this confirms that there is a small, but not negligible difference between the decrease of T_c after irradiation at ~ 10 K and at > 150 °C. It follows that there is only a weak recovery from 4.2 K to room temperature.

Meier-Hirmer and Küpfer [22] irradiated V_3Si single crystals with fast neutrons at 240 °C. As shown in Fig. 4, the decrease of T_c with increasing fluence ϕt is substantially reduced for T_{irr} = 240 °C [22] when compared with data taken at $T_{irr} \leq 150$°C by Sweedler et al. [23]. The observed lower decrease of T_c after heavy irradiation fluences with higher T_{irr} values has its origin in thermal recombination effects during irradiation. The data in Fig. 4 show that the activation of vacancies at between

$T_{irr} \leq 150$ and 240 °C has the effect of an annealing which increases the long-range order parameter of the crystal.

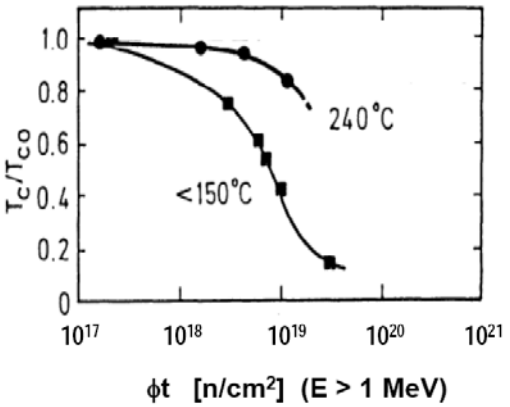

Figure 4: T_c of V_3Si as a function of fast neutron irradiation fluence ϕt for various irradiation temperatures. $T_{irr} \leq 150$°C (Sweedler et al. [23], T_{irr} = 240°C (Küpfer et al. [22]).

COEXISTING DEFECT MECHANISMS IN IRRADIATED A15 TYPE COMPOUNDS

From the wealth of published data, it follows that the decrease of T_c in irradiated A15 type compounds has been attributed to three competing defect mechanisms. These mechanisms are analyzed in the following.

Homogeneous Defects (decrease of long-range atomic ordering)

The "defects" are here lattice sites occupied by the wrong atoms (in analogy to the quenched state), also called "antisite defects". A decrease of the long-range order parameter S (defined by van Reuth et al. [24] in irradiated A15 compounds was first observed by Sweedler and Cox [23] in Nb_3Al. It was later confirmed by Moehlecke et al. [25] for Nb_3Pt and by Cox and Tarvin [26] for V_3Si, while Schneider et al. [27] reported a decrease of S in Nb_3Al after irradiation with 700 keV N^{2+} ions. It is important to note that the attribution of the observed effects on the superconducting properties of A15 type compounds after irradiation to a change of atomic ordering implies the assumption of *homogeneous* disordering over the sample volume. The decrease of T_c is explained by changes of the electronic density of states at the Fermi level.

Inhomogeneous defects (disordered microregions or "depleted zones")

The defects are represented by the depleted zones of 4 nm diameter, generally observed by means of TEM microscopy in solids after high energy irradiation [17]. The depleted zones can be either highly disordered or amorphous, and were also called "disordered microregions" by Pande [17, 24]. The presence of inhomogeneities was also observed by Nikulin et al. [29], by means of small angle neutron scattering. The inhomogeneous defect mechanism [17] assumes that the matrix enclosing the depleted zones is essentially unaffected by the radiation, in contrast to the antisite defect mechanism (disordering) [14,18], which is based on a homogeneous decrease of the atomic order parameter over the whole sample volume.

As pointed out by Pande [17], the weakening of A15 superstructure lines after irradiation, (which is interpreted as a decrease of S [14,18], could also arise from an increasing volume fraction of disordered microregions (also called depleted zones), concentrated in regions of ~ 5 nm diameter. The inhomogeneous defect mechanism explains an overall degradation of the super-conducting properties by the proximity effect [17] between the ordered, high T_c matrix and the disordered low T_c micro-regions of a size comparable to the coherence length, ξ_o ~ 4 nm.

Static Displacement of the Atoms from their Equilibrium Positions

This kind of defect was first observed by Meyer [30] and Testardi et al. [31] after heavy irradiation of V_3Si single crystals by means of the channeling technique. The existence of all three defect types α, β and γ is based on sound experimental data. It is also ascertained that all three types of defects occur simultaneously during irradiation. In the past, each of these defects has been independently made responsible for the decrease in T_c. Depending on the total radiation fluence, each one of these defect types will be dominant over the concurrents. As will be shown in the following, antisite defects (or decreasing atomic ordering) are mainly responsible for the observed decrease of T_c for radiation doses up to ~ 10^{19} n/cm^2, while inhomogeneous defects and static displacement are dominant for higher doses, where the value of T_c is too low for being of interest for the present considerations. The effects of high energy radiation on A15 type compounds are complex and are schematically represented in Fig. 5.

Volume change after irradiation

The number of vacancies in unirradiated A15 type compounds at 300K is generally below 2 x 10^{-3}, the experimental error limit. This is in agreement with other dense structures, for which vacancy concentrations of the same order of magnitude have been reported. The only case where a measurable amount of vacancies could be produced in A15 crystals was reported by Cox and Tarvin [26], who found that the density of a V_3Si single crystal after a fast neutron irradiation dose of 22.2×10^{18} n/cm^2 decreased by -0.3%. This observation allows the estimation whether a lattice expansion of Nb_3Sn filaments

after irradiation has to be taken into account for LHC upgrade II.

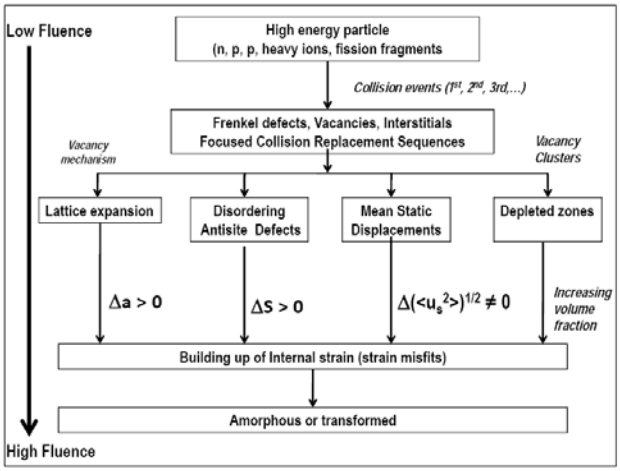

Figure 5: Schematic representation of the radiation induced effects in A15 type compounds, with increasing fluence (R. Flükiger [18]).

Assuming a total fluence of 10^{18} n/cm^2, on the quadrupole Q2a after 10 years of operation, the decrease of density inside the Nb_3Sn filaments is estimated to - 0.03%. This would correspond to a volume expansion of + 0.03%, and thus of a linear expansion of ~ 0.01%, thus creating an additional stress acting on the filaments. A comparison with the effect of uniaxial stress or compressive transverse stress on J_c of Nb_3Sn wires shows that an increase of stress by 0.01 % as a consequence of irradiation would cause a small, but non negligible effect on J_c. Additional precise irradiation measurements should be performed on multifilamentary Nb_3Sn wires samples, not only as single wires but in the same configuration as in the cable, comprising all reinforcing and insulating elements. This rough estimation shows that that the additional stress effect due to radiation damage on J_c after 10 years of operation of LHC upgrade phase II may be below 5%.

CORRELATION BETWEEN ANTISITE DEFECTS AND T_C AFTER NEUTRON IRRADIATION

Several arguments can be invoked for proving the validity of antisite disorder as the dominant mechanism influencing the variation of T_c vs. ϕt for radiation doses up to ~ 10^{19} n/cm^2:

- Homogeneous distribution of the antisite defects over the whole sample after irradiation, detected by specific heat measurements;
- Comparison between the variation of T_c vs. the order parameter S for A15 type compounds after irradiation and after fast quenching from high temperatures (in both cases, S is measured by diffraction methods);
- Irradiation with high energy electrons and neutrons.

Homogeneous distribution

The question about a *homogeneous* distribution of the damage can be answered on the basis of the known low temperature specific heat measurements before and after irradiation for the A15 type compounds Nb_3Sn [32], Nb_3Al [33] and V_3Si[34].

The measurements of Cort et al. [33] for Nb_3Al are represented in Fig. 6, showing the specific heat jump at T_c after irradiation at 150°C at a fluence of 13×10^{18} n/cm^2. The transition width was found to increase from 0.8 to 1.3 K, for a significant decrease of T_c from 18 to 10K. The compound V_3Si was studied by calorimetry by Viswanathan et al. [34] after neutron irradiation at 200°C at a fluence of 22.2×10^{18} n/cm^2. A decrease of T_c from 17 to 7.5 K was found, the width ΔT_c increasing slightly from 0.5 to 1.2 K. The specific heat measurements of Karkin et al. [32] on Nb_3Sn before and after neutron irradiation are shown in Fig. 7. These authors studied the effect of neutron irradiation at 80°C in Nb_3Sn. At a dose of 10^{19}n/cm^2 they found a T_c value of 12.5 K, while the transition width ΔT_c measured by specific heat increased from 0.8 to 2.5 K.

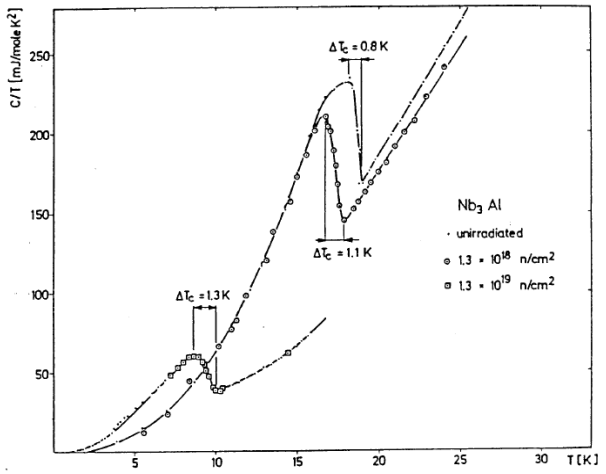

Figure 6: Specific heat of Nb_3Al before irradiation and after neutron doses of 1.3×10^{18} and 1.3×10^{19} n/cm^2, respectively. The linear representation C/T vs. T has been chosen in order to visualize the moderate increase in ΔT_c with dose (after Cort et al. [33]).

Table 1. Specific heat data of the compounds Nb_3Sn, V_3Si and Nb_3Al after neutron irradiation. Indicated are the T_c values before and after irradiation as well as the transition width ΔT_c.

Compound	Mass (g)	T_{co} (K)	T_{irr}(°C)	Fluence	T_c (K)	T_c/T_{co}	ΔT_c	
Nb_3Sn	11.0	17.9	80	10 x 10^{19}	12.5	0.69	2.5	[28]
Nb_3Al	0.2	18.7	150	13 x 10^{19}	9.6	0.51	0.5	[29]
V_3Si	1.5	17.1	200	22 x 10^{19}	7.5	0.44	0.7	[30]

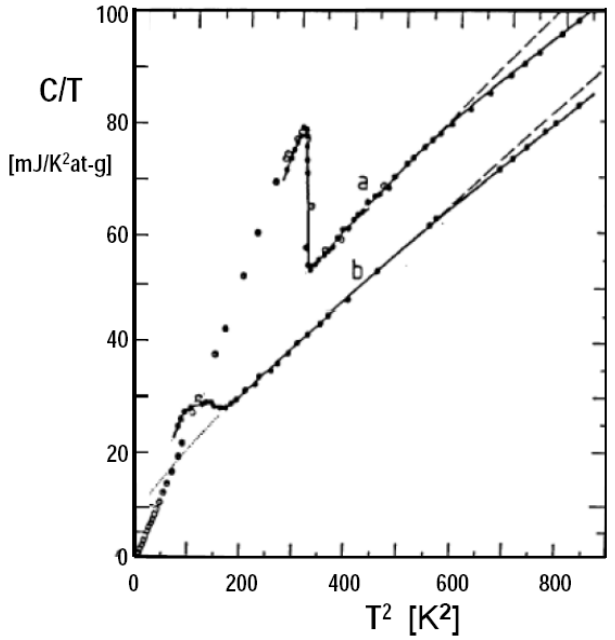

Figure 7: Specific heat of Nb_3Sn, a) in the unirradiated state and b) after a dose of 10^{19} n/cm^2 according to Karkin et al. [32]. For unirradiated Nb_3Sn at lower temperatures, data of Junod et al. [35] have been superposed.

When comparing the transition width of superconducting compounds after irradiation, one has to take into account the nuclear heat recovery, which depends on the size of the sample. Viswanathan et al. [34] pointed out that V_3Si single crystals with masses of ≥ 1 g exhibited additional heating during irradiation, leading in one case even to a visible darkening of the surface, i.e. to estimated temperatures T_{irr} of 300°C and above. This is due to increasing difficulties in transferring the nuclear heat to the sample environment (Argon gas) with increasing volume to surface The masses of V_3Si and Nb_3Al were 1.5 and ~1 g, respectively, in contrast to Nb_3Sn, which had 11 g [32]. The latter had a T_c value of 12.5 K, which is markedly higher than 9.9 K, the value estimated from the behavior of T_c vs. ϕt for small samples in Fig. 3.

The corresponding values for Nb_3Al and V_3Si are 9.6 and 7.6 K, which is in good agreement with the values reported in Table 1. It can thus be estimated that the increase of T_c due to nuclear heat recovery at ϕt=10^{19} n/cm^2 for this "heavy" Nb_3Sn samples is ~ 1.5 K. It follows that for the 3 systems Nb_3Sn, Nb_3Al and V_3Si, heavy neutron irradiations up to fluences of 2×10^{19}n/cm^2 only causes a very small enhancement of the transition width, ΔT_c. It is interesting that for a neutron fluence reducing T_c to about 50% of the initial value, the transition width ΔT_c is only enhanced by ≤ 1K.

In the specific heat curves, there is no trace of the original superconducting transition temperature, T_{co}, in any of the 3 systems Nb_3Sn, Nb_3Al and V_3Si after irradiation. This implies that the amount of depleted zones (with considerably lower T_c) is very small and cannot account for the observed decrease of the superstructure lines. After having shown that the damage is homogeneous, this is a strong argument in favour of the antisite defect mechanism as the dominant one up to 10^{19} n/cm^2.

Comparison between irradiated and quenched A15 type compounds

Quench induced disordering constitutes a particularly simple case, where the only possible defects are the antisite defects (up to a few %) and quenched-in vacancies (≤ 0.02% at 300K). No direct comparison between neutron irradiation and quenching has been performed on Nb_3Sn and the data reported here concern the system Nb_3Pt, another A15 type compound.

Fig. 8 shows the variation of T_c for Nb_3Pt vs. the long-range order parameter, S, after fast quenching from temperatures up to 1900 °C by Flükiger et al. [36] and after from neutron irradiation (E>1 MeV) by Moehlecke et al. [37].

It follows from Fig. 8 that the variation of T_c vs. S is the same, regardless whether the compound was fast quenched or irradiated. This constitutes an additional argument in favour of variations of the degree of atomic for the observed decrease of T_c after irradiation up to fluences of 10^{19} n/cm^2.

Irradiation with High Energy Electrons and Neutrons

According to Seeger [38], the complex situation in an irradiated crystal can be described as follows. The high energy particle transfers a kinetic energy, E_T, to an atom of the target, the primary knock-on atom. At sufficiently high values of E_T, this atom will be removed from its equilibrium lattice site: a Frenkel defect is formed. Due to inelastic collisions with electrons, the energy of the primary knock-on atom towards the end of its path falls to values of the order of E, the displacement energy (~ 25 eV), and almost every collided atom is displaced [39].

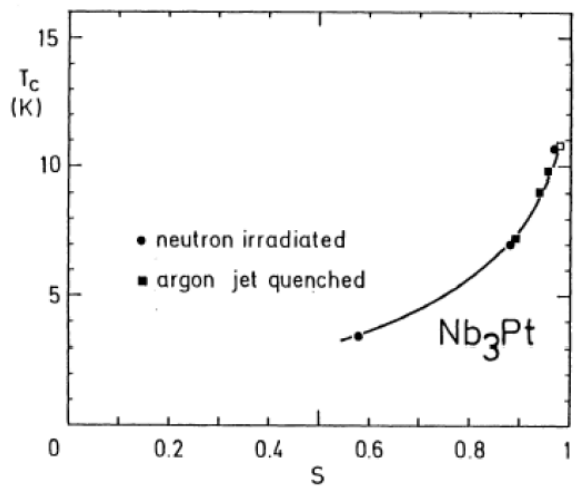

Figure 8; T_c vs. long-range order parameter S (determined by X ray diffraction) for Nb_3Pt after fast quenching from different temperatures [36] and after neutron irradiation [37].

As a result of this displacement cascade, regions with high concentrations of vacancies are formed, called "depleted zones" by Seeger [38], which are surrounded by a zone enriched with interstitial atoms. In A15 type compounds, the existence of depleted zones has first been reported by Pande [17,24], who called them "disordered microregions". In reality, the structure of this region can be either amorphous, of the A15 type (but strongly disordered), or of another structure type, as for example bcc (A2 type) in Nb_3Al [40] or in $Nb_{\sim 3}Si$ [41]. The term "disordered zone" seems thus to be more appropriated and will be adopted in the present work.

A further strong argument in favour of ordering effects was given by Ghosh et al. [42] and Rullier-Albenque et al. [43]. These authors used the fact that electrons with energies of the order of 1 MeV do not produce the displacement cascade (or disordered zones) described above, in contrast to irradiation with fast neutrons or high energy ions. Due to their low mass, electrons of 1 MeV create only isolated Frenkel defects (Schulson [44]). Rullier-Albenque et al. [43] have irradiated Nb_3Ge films (with T_{co} = 19.5 K) with 1 MeV neutrons and with 2.5 MeV electrons, respectively, while Ghosh et al. [42] performed an analogous experiments on Nb_3Sn films, which were irradiated with 2 MeV He ions and with 2 MeV electrons. Both investigators came to the same conclusion, i.e. a strong decrease of T_c is observed, regardless of the nature of the projectile. In particular, it was found that the ratio $\Delta T_c/\Delta\rho_{irr}$ (where ρ_{irr} is the increase of residual resistivity after irradiation) for Nb_3Ge does not differ between fast neutron and high energy electron irradiation. For $\Delta\rho_{irr}$ values between 0.1 and 10 μΩ·cm, the ratio $\Delta T_c/\Delta\rho_{irr}$ remained almost unchanged, close to 0.1 K [43]. Although these experiments do not give a direct evidence that the order parameter is the same in both cases, they lead to an important conclusion: the presence of "disordered zones" is not necessary to cause a decrease of T_c. This result is analogous to that of fast quenching experiments, and furnishes an additional proof for atomic ordering effects as the dominant effect causing the decrease of T_c after neutron irradiation.

THE SITE EXCHANGE MECHANISM IN IRRADIATED A15 TYPE COMPOUNDS

Vacancy diffusion: the "virtual" lattice site (or split vacancy)

In the tightly packed A15 structure, each atom is closely surrounded by its neighbors. The atoms would need to be considerably compressed before any two could squeeze past one another and interchange positions as required for ordering changes. Among different possible diffusion mechanisms, vacancy diffusion is the most probable one. It is based on the fact that at thermal equilibrium each solid at a temperature above zero contains a certain number of vacant lattice sites. An atom will now jump into a neighbouring vacancy, thus creating a new vacant site. Atoms and vacancies undergo a series of position exchanges, in order that a very small number of vacant lattice sites is sufficient to induce a substantial diffusion. Most studies dealing with diffusion have been undertaken on bcc or fcc structures. In the A15 structure, however, the situation is more complex, the *6c* and *2a* sites being not equivalent from the point of view of electronic bonding. Indeed, interactions beween atoms on the *6c* and on the *2a* sites are characterized by metallic bonding, white the intrachain bonding between two A nearest neighbors is of the covalent type, as was shown by Staudenmann [45], who established electron density maps of V_3Si. This covalent bond is correlated with the very short AA distances on the chains of A15 type compounds, which are noticeably shorter than the sum of the atomic radii of the A element. This configuration leads to highly nonspherical shapes for the A atoms. The region of covalent bonding between two A atoms on *6c* sites will be called "overlapping region" in the following. This region corresponds to a high electron density in V-Si [45].

The question arises whether this overlapping (or covalent bonding) between two A neighbors on the chain sites still resides if one of them is next to a *6c* vacancy. Welch et al. [46,47] have shown by means of pair potential calculation that such an individual vacancy of an A atom on a 6c site is unstable. They found that the state of lower energy corresponds to a configuration where one of the two A atoms adjacent to the single *6c* vacancy is shifted towards a new site which is equidistant from the next two A neighbors (see Fig. 9). This particular type of "split vacancy" [46,47], located in the overlapping region

corresponds to a nonequilibrium state and will thus in the following be called "virtual" lattice site [48].

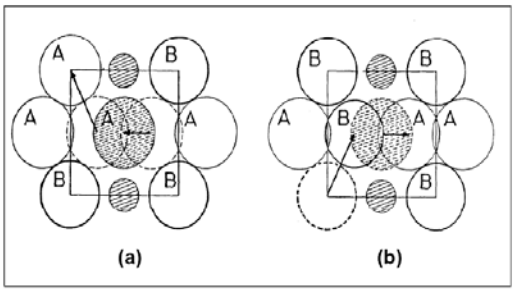

Figure 9: A ←→B exchanges by vacancy diffusion in A15 type compounds A_3B. a) Jump of an A atom into a B vacancy, followed by the occupation of the "virtual" site by the neighbour A atom, b) Jump of a B atom into an equilibrium A site (two-step processes). Small circles: overlapping region between two A atoms or region of covalent bonding (Flükiger [18,48]).

It thus appears that the vacancy diffusion mechanism in the A15 type structure comprises two steps, in contrast to the one-step mechanism acting in simple bcc or fee structures. Since the calculations of Welch et al. [46,47] show that the mobility of *6c* vacancies is quite high, the author has used the "virtual site " concept as a basis for a mechanism of homogeneous disordering in irradiated A15 tape compounds [18,48].

Disordering by Focused Replacement Collision Sequences

In spite of the fact that the observations in Section V strongly support a homogeneous decrease of the long-range order parameter over the whole sample volume in irradiated A15 type compounds, a question arises: How is it possible that a homogeneous decrease of S implying site exchanges over several lattice spacings can occur during irradiations at temperatures $T \leq 100°C$, where little thermal diffusion takes place?

Under these conditions, disordering in irradiated A15 type compounds can be caused either by a) local cascade replacements or b) focused replacement collision sequences, a superposition of both being even more probable.

Local Cascade Replacements

Interaction between high energy incident particles and the lattice atoms produces a cascade, i.e. the atoms are displaced to produce Frenkel defects in a three-dimensional zone, the disordered (or depleted) zone [38,39]. Simultaneously, an even larger number of atoms change their mutual positions (i.e. they are replaced), thus producing locally a decrease of the degree of ordering. In principle, it could be argued that the atomic replacements produced in the cascade would be sufficient to produce disorder in the whole A15 lattice.

However, this argument cannot be generalized, since electron irradiation of A15 type compounds causes the same effect on the superconducting transition temperature, T_c, and the electrical resistivity [43] but produces only isolated Frenkel defects rather than depleted zones (or cascades). Thus, an additional mechanism must be effective in causing a homogeneous decrease of the order parameter. Such a mechanism, requiring atomic transport over several interatomic distances (the condition for a collective phenomenon) is constituted by the focused replacement collision sequences.

Focused Replacement Collision Sequences.

The so-called focusing replacement collision sequences, introduced by Seeger [38,39] represent the transport of matter and energy in irradiated crystals along dense crystallographic directions. Regardless of the crystal structure, an interstitial atom produced by irradiation processes is transported several interatomic distances away from its associated Frenkel vacancy, along these "focalizing" crystallographic directions. Focused replacement collision sequences can occur at the external boundaries or depleted zones with sizes of 4 to 5 nm for neutron irradiation [17,24] and up to 15 nm for irradiation with ^{32}S ions [50]. At these boundaries, highly disordered regions are adjacent to the matrix, and a sufficient but still small number of virtual sites is thus occupied, a necessary condition for the occurrence of focused replacement collision sequences (it may be recalled that this number is still very small, < 0.1 %). As irradiation further proceeds, the number of occupied virtual sites will increase, thus leading to an increase of site exchange processes. At the same time, thermal reordering will occur, as follows from the recombination theory of Liou and Wilkes [51].

It can be immediately seen that in the unirradiated state the replacement collision sequences in A15 type compounds occurring in the <100> and <111> directions, i.e. along the chains and the diagonal of the cube, are not effective in producing A ←→ B site exchanges. The only focusing direction where collision sequences could in principle produce A ←→ B site exchanges is the <102> direction. However, the atomic sequence in the <102> direction is oABAoABAo, the space between two ABA sequences coinciding with the region of overlap of two A atoms on the chain being perpendicular to the {100} plane. It can be easily shown that this configuration excludes extended site exchanges. Indeed, the potential encountered by A or B atoms on their way along the <102> direction, calculated using a Born-Mayer interatomic potential [52]shows that $V_{A\rightarrow B}$ and $V_{B\rightarrow A}$ are of the same order of magnitude, ~ 10 eV, while $V_{A\rightarrow A}$ reaches 52 eV.

The situation in irradiated crystals is, however, quite different from that encountered prior to irradiation. With

the occupation of the virtual sites (a very small number of occupied non-equi1ibrium sites represented in Fig. 9 is sufficient), the potential $V_{A\rightarrow A}$ is considerably lowered. The new sequence of atoms in the focalizing <102> direction around the occupied virtual site is now oABAAABAoABAo or oABABABA0ABAo, depending on the occupation of the virtual site by an A or a B atom, respectively (see Fig. 10).

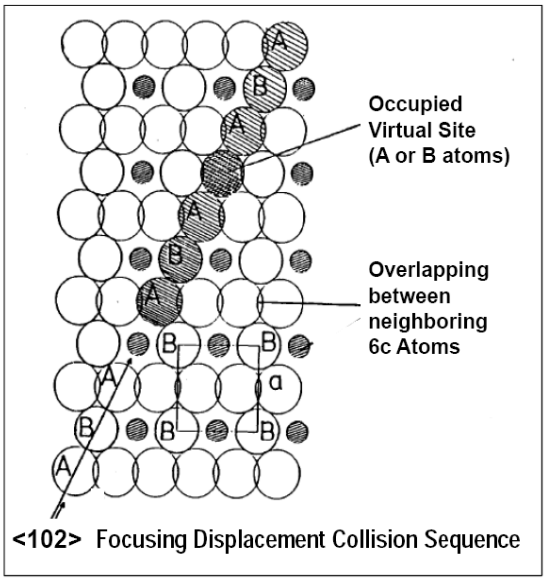

Figure 10: Focusing replacement collision sequences in A15 type compounds. Representation of the {100} plane of the A15 lattice (the radii are scaled for Nb_3Al). The small circles correspond to the overlapping region between two A atoms belonging to the chains perpendicular to the {100} plane. The occupation of the virtual site by an A or a B atom leads to the sequences oABAAABAo or oABABABAo, respectively instead of oABAoABAo as in the unirradiated case, thus enabling A←→B site exchanges in the <102> direction, a is the lattice parameter (Flükiger [18,48]).

As mentioned above, a very small amount of vacancies (or occupied virtual sites) is sufficient for the occurrence of the present mechanism. It should be recalled that for example, density measurements have revealed ~ 0.3 % of lattice vacancies in neutron irradiated V_3Si after a fluence of 22.2×10^{18} n/cm^2, corresponding to a decrease of T_c to a value less than one half of the initial T_c value. Due to the very large number of replacement collisions over the whole crystal volume during the whole irradiation time, the virtual sites will be many times occupied and abandoned again, alternatively by A or B atoms, respectively. The latter constitute a "bridge" between neighbouring ABA sequences, thus allowing A ←→ B exchanges over several interatomic distances. This is a necessary condition for a homogeneous decrease of the degree of ordering over the whole crystal after irradiation at low temperatures.

A very important conclusion can be drawn from a consideration of the close neighborhood of an occupied "virtual" lattice site. Its nearest neighbors, 6 A and 2 B atoms, are in close contact with the interstitial, which is either an A or a B atom. In the {100} plane, this leads to a hexagonal arrangement, as shown in Ref. 18. If the interstitial atom is of the A type, the occupation of the virtual site leads to 4 additional AA contacts, with AA distances of 5/16a = 0.559 a, thus 6% more than the AA distances in the chains, a/2. In addition, there are 2 AB contacts with interatomic distances of a/2 compared to 9/16a in the unirradiated A15 lattice, .i.e. 6% shorter.

This situation can be compared to that in quench disordered A15 type compounds, where the AB distances are the same, i.e. a/2. The case of a B element occupying the virtual site with 4 AB and 2 BB close contacts is more interesting. The AB distances are now 5/16a, i.e. they are still the same as in the unirradiated A15 structure, but the BB distances are now 36% shorter (a/2 with respect to 3a/2). This would mean that in each case, BB distances shorter than the sum of two B radii would be encountered. Such an "overlapping" between B elements is only possible in the nonequilibrium situation caused by low temperature irradiations or in a dynamic situation during site exchanges at high temperature. It is particularly interesting to consider the case of nontransition B elements, where such close BB contacts are expected to cause strong electrostatic repulsive forces. The occurrence of such BBB sequences furnishes the key for understanding the causes of the lattice expansion and the static displacements observed in irradiated A15 type compounds (see Fig. 7).

From these remarks, it can be recognized that the diffusion in the A15 type structure is not a single vacancy diffusion as suggested by Sweedler et al. [23] nor it corresponds to a so-called interstitialcy diffusion mechanism, where the atom diffuses from a normal site to an interstitial site. In the case of the A15 structure, the situation is complicated by the fact that a jump into the virtual site (which is an interstitial site) requires simultaneously a rearrangement of the other atoms.

NEUTRON IRRADIATION AND ITS EFFECTS ON J_C AND B_{C2} OF MULTI-FILAMENTARY NB_3SN WIRES

There are only two investigations on alloyed Nb_3Sn wires, by Weber et al. [5] (E>0.1 MeV) and by Weiss et al. [7] (E=14 MeV). The latter compared the behavior of binary and alloyed Nb_3Sn wires at T_{irr} = 300K and performed J_c vs. B measurements at higher fields (between 14 and 20 T).

Variation of T_c

As shown in Fig. 11, the variation of T_c vs. ϕt at low fluences is very similar for binary and alloyed wires: at 10^{18} n/cm^2 the T_c reduction is close to 4% for fluences up to ~ 20% at 2×10^{18} n/cm^2 [7]. At the highest fluences in Ref. 7, i.e. 4×10^{18} n/cm^2, ΔT varies between – 2.3 and – 2.6 K for the binary wires. The variation ΔT for alloyed wires is slightly higher: - 2.9 K for Ti additions and – 3.3 K for Ta additions. The slightly larger decrease for Ta additions may be caused by the considerably larger amount of Ta (3.5 at.%) in the filaments with respect to Ti (~ 1 at.%). As recently shown, the fact that Ta and Ti occupy different lattice sites prior to irradiation (Ta on Nb sites, Ti on Sn sites) may give an explanation for the observed difference [53]. As will be shown in the following, a considerably larger difference is observed when comparing the variation of J_c with fluence.

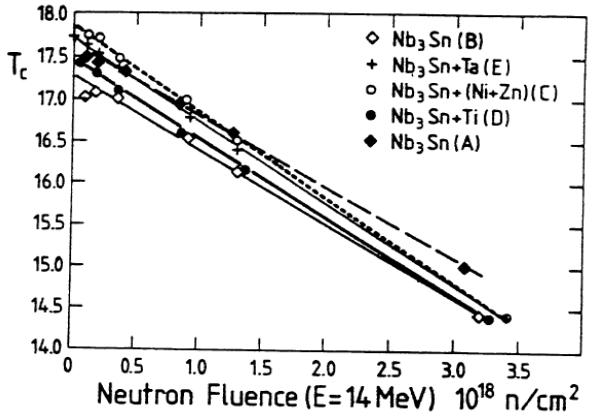

Figure 11: T_c vs. fluence ϕt for binary and alloyed Nb_3Sn multifilamentary wires after irradiation with 14.8 MeV neutrons at 300 K. Wire A: binary, 10'000 filaments, wires B, C, D and E: 19 filaments (Weiss et al. [7]).

Binary multifilamentary Nb_3Sn wires

In view of the use of multifilamentary alloyed Nb_3Sn wires in the LHC upgrade collider, it is interesting to know the effects of the expected neutron radiation on J_c at 15 T at fluences up to 10^{19}n/cm^2. As mentioned in Section V, fast neutron irradiation of Nb_3Sn causes a decrease of the long-range order parameter, S, which causes the decrease of T_c.

A second consequence of the decrease of S is the enhancement of the electrical resistivity ρ_o, which is correlated to the enhancement of the upper critical field, B_{c2}. At low fluences, this leads to a situation where T_c decreases, but B_{c2} increases. This means that at a given magnetic field, the initial values of J_c also increase: all known investigations report a maximum of J_c. At higher fluences, the decrease of T_c becomes the dominant effect, and B_{c2} decreases again.

An example for the binary multifilamentary wire [7] is shown in Fig. 12. The maximum of J_c/J_{co} and B_{c2} is reached at 0.8×10^{18} n/cm^2. The increase of the ratio J_c/J_{co} at the maximum fluence is strongest for the highest fields and reaches ~ 2.1 at 15 T and ~ 3.5 at 20 T.

As mentioned before, a certain difference is observed between the fluence values given in different papers. This is illustrated by a comparison with a publication of Weber et al. [5], where the same maximum of J_c/J_{co} ~ 2 was reached after neutron irradiation at 300 K for a fluence of 1.1×10^{19} n/cm^2 (E>0.1 MeV). It follows that the conversion factor between 14 MeV and > 0.1 MeV is close to 1.4. The maximum of B_{c2}* was reached at the same ratio J_c/J_{co}, the initial value of 21.4 T being enhanced to ~ 22.5 T [7].

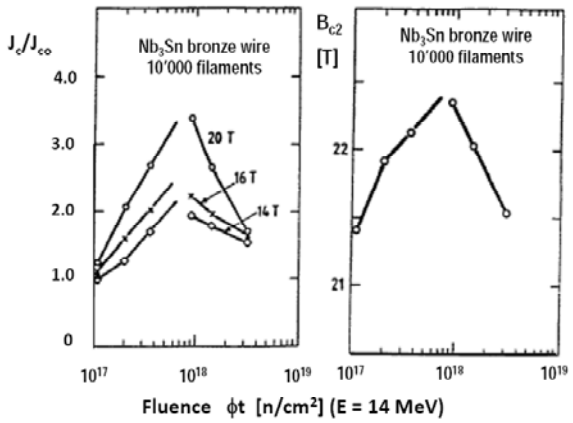

Figure 12: J_c/J_{co} and B_{c2}* of a 10000 filament binary Bronze Route Nb_3Sn wire after neutron irradiation at 300K (E=14 MeV). B_{c2}* is the critical field at 4.2 K determined by the Kramer extrapolation (Weiss et al. [7]).

Alloyed multifilamentary Nb_3Sn wires

The trend towards a stronger degradation for neutron irradiated wires observed for T_c vs. ϕt (see Fig. 13) is even accentuated when comparing the behavior of the normalized critical current density, J_c/J_{co}, and the upper critical field, B_{c2}, with fluence. The results for the Ti alloyed wire with the composition (Nb-1.6wt.%Ti)$_3$Sn are represented in Fig. 13. The most evident differences between the irradiated binary wires in Fig. 12 and the Ti and Ta alloyed wires are [7]:

a) The fluence ϕt_m at which T_c and B_{c2}* reach their maximum is 0.18×10^{18} n/cm^2 for the Ti alloyed wire (Fig. 11), i.e. it is four times smaller than for binary Nb_3Sn wires, where ϕt_m is 0.8×10^{18} n/cm^2. For the Ta alloyed wire, ϕt_m is very close to that of the Ti added wire: it is slightly below 0.2×10^{18} n/cm^2, as shown in Fig. 12. In their paper, Weiss et al. [7] also mention another additive, Ni+ Zn, which leads to a smaller enhancement of J_c, the amount of substituted elements in the filaments being smaller. For this rather unusual additive, the value of ϕt_m

lies at ~ 0.25×10^{18} n/cm^2, i.e. close to the values for Ti and Ta alloyed wires. It can be concluded that irradiation of alloyed Nb_3Sn wires with 14 MeV neutrons at 300 K has a very similar effect on the maximum value of J_c/J_{co}.

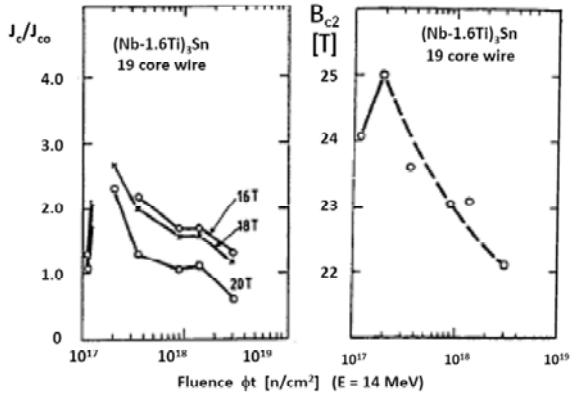

Figure 13: J_c/J_{co} and B_{c2}* of a 19 core (Nb-1.6wt.%Ti)$_3$Sn produced by the Bronze Route after neutron irradiation at 300 K (Weiss et al. [7]).

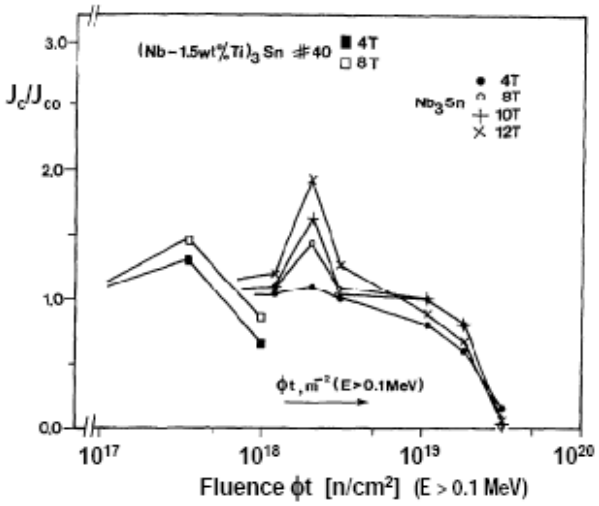

Figure 14: J_c/J_{co} and B_{c2}* of a 19 core (Nb-1.6wt.%Ti)$_3$Sn produced by the Bronze Route after neutron irradiation at 300 K (Weber et al. [5]).

b) The enhancement of J_c/J_{co} at ϕt_m for the same value of $h^*=H/H_{c2}$* is smaller for alloyed than for binary wires. At h^*=0.7, J_c/J_{co} for the Ti and Ta alloyed wires is ~3 and 1.2, respectively, which is considerably smaller than for binary Nb_3Sn (~ 4.5 for the binary 19 core wire and 2.2 for the binary 10'000 filament wire) (see Figs. 12).

c) In view of the application in LHC upgrade, it is interesting to know at what fluence J_c/J_{co} starts to be lower than 1 under an applied field of 15 T. It is remarkable that for both binary wires, this is the case for fluences close to 1 x 10^{19} n/cm^2, which is considerably higher than for alloyed wires. For the additives Ti and Ni+Zn, the corresponding fluences are estimated to 5 and 4 x 10^{18} n/cm^2. A much stronger effect was observed for the Ta alloyed wire, where J_c/J_{co} = 1 is already reached at 0.3 x 10^{18} n/cm^2! This tendency is confirmed by neutron

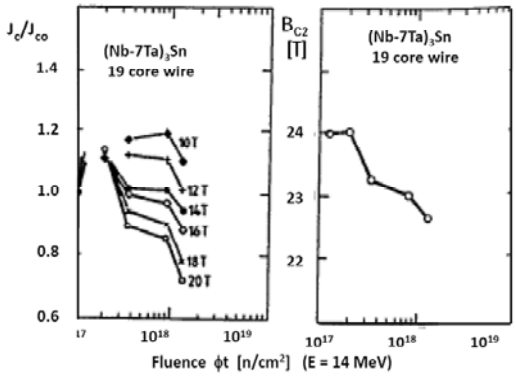

Figure 15: J_c/J_{co} and B_{c2}* of a 19 core (Nb-7wt.%Ta)$_3$Sn produced by the Bronze Route after neutron irradiation at 300 K (Weiss et al. [7]).

irradiation measurements of Weber et al. [5], who reported measurements up to 12 T and found J_c/J_{co} = 1 at 7×10^{18} n/cm^2 for binary Nb_3Sn wires, but 0.8×10^{18} n/cm^2 for (Nb-1.5wt%Ti)$_3$Sn wires.

It follows that alloyed wires are much more sensitive to radiation than binary wires. This can be explained by the disordering effect of the various additives. Indeed, it was found in unirradiated samples that the maximum of J_c is reached when the initial residual resistivity ρ_o of the ordered binary Nb_3Sn system is enhanced to values of 30-35 μΩ·cm by the substitution of the additives into the A15 lattice [53]. In binary wires, the necessary fluence to reach this optimum value of ρ_o (and thus B_{c2}) is considerably higher than in alloyed wires. Before irradiation, the ρ_o value of alloyed wires is already close to the optimum value of 30-35 μΩ·cm. Irradiation will thus only lead to a small enhancement of B_{c2}, followed by a decrease with higher fluences.

CONDITIONS FOR NB_3SN WIRES IN THELHC UPGRADE

Radiation damage on the superconducting properties

As shown in Fig. 1 [1], the highest fluence in LHC upgrade will occur at the Quadrupoles Q2a, the second highest fluence being expected for the quadrupole Q1. For a total operation time of 10 years, calculating 200 operation days a year, the total fluence at the inner winding of the quadrupole Q2a after the upgrades of Phase I and Phase II will be 0.25×10^{18} n/cm^2 and 10^{18}

n/cm^2, respectively. For the quadrupole Q2 (external winding), the corresponding fluences are 0.17×10^{18} n/cm^2 and 0.68×10^{18} n/cm^2, the total fluence for the quadrupoles Q2b and Q3 being considerably smaller. No problem is expected for the dipoles. Since the highest radiation damage will be expected on the inner winding of the quadrupole Q2a, the present estimation will be limited to this location.

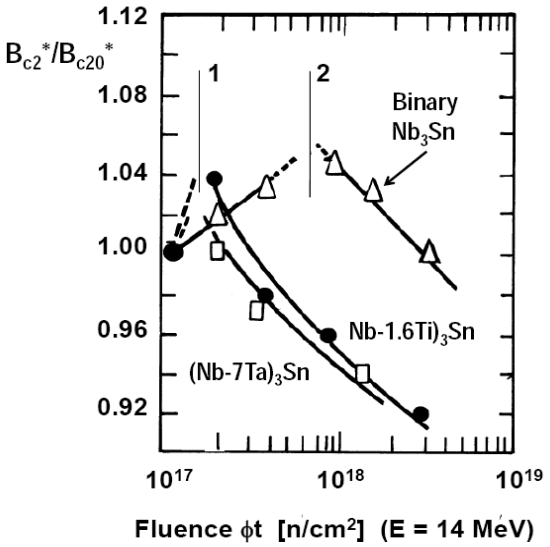

Figure 16: Variation of the upper critical field of binary and alloyed Nb_3Sn wires (additives: Ti and Ta), after Weiss et al. [7].

Radiation induced change of Cu resistivity and thermal stability

A point to be discussed when analyzing the properties of Nb_3Sn wires in view of operation in a LHC upgrade collider at ≥ 15 T is the effect of neutron radiation on the thermal stability. Little is known about the change of the electrical resistivity of pure Cu submitted to neutron irradiation. Fabritsiev et al. [54] studied the effects of neutron irradiation on the electrical resistivity of precipitation hardened (PH) and dispersion strengthened (DS) copper alloys in the fast neutron reactor BOR-60 with doses of $8\text{-}16\times10^{21}$ n/cm^2 and in the mixed spectrum neutron reactor SM-2 with doses of $3.7\text{-}5.5\times10^{21}$ n/cm^2. The experimental data on the change $\Delta\rho$ in electrical resistivity of DS-type copper alloys irradiated in the BOR-60 reactor show that irradiation to 7-10 dpa at T=340-450 ^{o}C causes a drop in electrical conductivity by not more than 20%. The obtained results show that in mixed-spectrum reactors the rate of $\Delta\rho$ normalized to the dpa is about 20 times as high as in fast neutron reactors. The conclusion is made that the calculations performed for ITER must take into account the presence of appreciable fluxes of thermal neutrons in certain components of the reactor. The latter will play a decisive role in the drop in thermal conductivity of copper alloys in these components. This problematics may be of smaller importance in LHC upgrade, the neutron spectrum being narrower. Nevertheless, this question must be studied in detail if the thermal stability of the magnets has to be guaranteed for the whole lifetime of approximately 10 years.

CONCLUSIONS

An overlook of the effects of neutron irradiation on the superconducting parameters T_c, B_{c2} and J_c of Nb_3Sn wires as reported in the literature has been given in view of the determination of the radiation limit in the LHC upgrade magnets. The coexisting defect mechanisms in irradiated Nb_3Sn type compounds are briefly presented and a model is discussed explaining the site exchange mechanism which leads to a decrease of atomic ordering after irradiation.

The variation of J_c in binary as well as in Ti and Ta alloyed Nb_3Sn wires is presented, showing a higher sensitivity to neutron radiation for the latter. Based on calculations of F. Cerutti and coworkers (CERN), the neutron fluence at the inner winding of the quadrupole Q2a is estimated to values below 10^{18} neutrons /cm^2 for a life time of 10 years, which is within the safety margin with respect to the critical current density and B_{c2}.

ACKNOWLEDGMENTS

The author would like to thank Dr. F. Cerutti and his team from CERN for their calculations on the neutron fluence at the quadrupole LHC upgrade, which constitutes the basis of the present estimations.

REFERENCES

[1] F. Cerutti, A. Mereghetti, M. Mauri, E. Widmer, CERN, to be published.

[2] M. Putti, R. Vaglio, J.M. Rowell, Supercond. Sci. Technol. 21 (2008) 043001

[3] Huhtinen, CERN, 42nd Workshop, "Innovative Detectors for Supercolliders", Erice, Sicily, Italy, 28 Sep - 4 Oct 2003.

[4] A.R. Sweedler, D.G. Schweizer, G.W. Webb, Phys. Rev. Lett. 33 (1974) 168.

[5] H.W. Weber, Adv. Cryo. Eng. 32 (1986) 853.

[6] M.W. Guinan, R.A. van Konynenburg, J.B. Mitchell, Internal Report UCID-20048, Lawrence Livermore Lab. Livermore, California, 1984.

[7] F. Weiss, R. Flükiger, W. Maurer, P.A. Hahn, M.W. Guinan, IEEE Trans. Magn., MAG-23 (1987) 976.

[8] B.S. Brown, H.C., Freyhardt, T.H. Blewitt, J. Appl. Phys. 45 (1974) 2724.

[9] B.S. Brown, J.W. Hafstrom, T.E. Klippert, J. Appl. Phys. 48 (1977) 1759.

[10] A.R. Sweedler, G.W. Webb, T.H. Geballe, B.T. Matthias, E. Corenzwit, Natl. Techn. Info Service, U.S. Dept. of Commerce, Springfield, Va. (USA), Vol. II, 1975), p. 422.
[11] K. Ogiknbo, T. Terai, K. Yamaguchi, M. Yamawaki, Proc. M^2S-HTSC-VI Materials, Houston, Texas, USA, 2000, 341.
[12] G. W. Schulz, C. Klein, H. W. Weber, S. Moss, R. Zeng S., R. Sawh, Y. Ren, R. Weinstein Appl. Phys. Lett. 73 (1998) 3935.
[13] R. Fuger, M. Eisterer, F. Hengstberger, H.W. Weber, Physica C 468 (2008)1647.
[14] A.R. Sweedler, D.E. Cox, L. Newkirk, J. Electronic Materials 4 (1975) 883.
[15] T.L. Francavilla, B.N. Das, D.V. Gubser, R.A. Meussner, S.T. Sekula, J. Nucl. Mater. 72 (1978) 203.
[16] A.L. Giorgi, G.R. Stewart, E.G. Szklarz, C.L. Snead, Jr., Sol. State Comm. 40 (1981) 233.
[17] C.S. Pande, Sol. State Comm. 24 (1977) 241.
[18] R. Flükiger, Internal Report # KfK-4204, Kern-forschungszentrum Karlsruhe,Germany, 1987.
[19] M. Söll, H. Bauer, K. Boening, R. Bett, Physics Letters 51A (1975) 83.
[20] P.A. Hahn, M.W. Guinan, L.T. Summers, T. Okada, D.B. Smathers, J. Nuclear Mater. 179-181 (1991) 1127.
[21] M. Söll, K. Boning, H. Bauer, J. Low Temp. Phys., 24 (1976) 631.
[22] R. Meier-Hirmer and H. Küpfer, J. Nucl. Mater., 109 (1982) 593.
[23] A.R. Sweedler, D.E. Cox, S. Moehlecke, J. Nucl. Mater., 72 (1978) 50.
[24] E.C. van Reuth and R.M. Waterstrat, Acta Cryst., B 24 (1968) 186.
[25] S. Moehlecke, A.R. Sweedler, D.E. Cox, Phys. Rev. B 21 (1980) 2712.
[26] D.E. Cox and J.A. Tarvin, Phys. Rev. B18 (1978) 22.
[27] U. Schneider, G. Linker, O. Meyer, J. Low Temp. Phys., 47 (1982) 439.
[28] C.S. Pande, Phys. Status Solidi (a) 52 (1979) 687; C.S. Pande, J. Nucl. Mater. 72 (1978) 83.
[29] Y.M. Nikulin, V.Y. Arkhipov, B.N. Goshchitskii, Fiz. Metal. Metalloved. 41 (1976) 202.
[30] O. Meyer and B. Seeber, Sol. State Comm. 22 (77) 603.
[31] L.R. Testardi, J.M. Poate, H.J. Levinstein, Phys. Rev. B 15 (1977)2570.
[32] A.E. Karkin, A.V. Mirmelshtein, V.E. Arkhipov, B.N. Goshchtskii, phys. stat. sol. (a) 61 (1980) K117.
[33] B. Cort, G.R. Stewart, C.L. Snead, Jr., A.R. Sweedler, S. Moehlecke, Phys. Rev. B 24 (1981) 3794.
[34] R. Viswanathan and R. Caton, Phys. Rev. B 18 (1978) 15.
[35] A. Junod, J. Muller, H. Rietschel, E. Schneider, J. Phys. Chem. Solids 39 (1978) 317.
[36] R. Flükiger, S. Foner, E.J. McNiff, Jr., in "Superconductivity of *d* and *f* Band Metals", Eds. H. Suhl and M.B. Maple, Academic Press Inc., 1980, p.265.
[37] S. Moehlecke, D.E. Cox, A.R. Sweedler, J. Less-Common Metals, 62(1978)111; Sol. State Comm. 23 (1977) 703.
[38] A. Seeger, in Proc. 2nd UN Intl. Conf. Peaceful Uses of Atomic Energy (Geneva), Vol. 6, (1958) 250.
[39] A. Seeger, in "Radiation Damage in Solids, IAEA (Vienna), Vol. 1, 1962, 101.
[40] U. Schneider, G. Linker, O. Meyer, J. Low Temp. Phys., 47 (1982) 439.
[41] J. Ruzicka, E.L. Haase, O. Meyer, in "Superconductivity in d- and f- band metals", Eds. W. Buckel and W. Weber, Kernforschungszentrum Karlsruhe, 1982, p.107
[42] A.K. Ghosh, H. Wiesmann, M. Gurvitch, H. Lutz, O.F. Kammerer, C.L: Snead, A. Goland, M. Strongin, J. Nucl. Mater. 72 (1978) 70.
[43] F. Rullier-Albenque, S. Paidassi, Y. Quéré, J. Physique 41 (1980) 515.
[44] E.M. Schulson, J. Nucl. Mater. 83 (1980) 230.
[45] J.L. Staudenmann, Helv. Phys. Acta, 47 (1974) 39; J.L. Staudenmann, Solid State Comm., 23 (1977) 121.
[46] D.O. Welch, G.J. Dienes, O.W. Lazareth, Jr., R.D. Hatcher, IEEE Trans. Magn., MAG-19 (1983) 889.
[47] D.O. Welch, G.J. Dienes, O.W. Lazareth, Jr., R.D. Hatcher, J. Phys. Chem. Sol., 45(1984) 1225
[48] R. Flükiger, Proc. LT 17, Karlsruhe, Eds. A. Schmid, W. Weber, H. Wühl, North-Holland, 1984, p. 609.
[49] R. Flükiger, Adv. Cryo. Engrg., Vol. 32(1986)873
[50] E. Schneider, P. Schweiss, W. Reichardt, in Proc. Conf. Neutron Scattering, Gatlinburg, Tenn. (USA), 1976, Vol. 1, p.223.
[51] K.Y. Liou, P. Wilkes, J. Nucl. Mater. 87 (1979) 317.
[52] F. Rullier-Albenque, PhD Thesis, 1984, University of Paris/Orsay (F)
[53] R. Flükiger, D. Uglietti, C. Senatore, F. Buta, Cryogenics 48 (2008) 293.
[54] S.A. Fabritsiev, E.A. Azizov, A.B. Mineev, V.A. Korotkov, Plasma Devices and Operations, 13 (2005) 223.

RESULTS OF CONDUCOR TESTING IN SULTAN: A REVIEW*

R. Wesche#, M. Bagnasco, P. Bruzzone, M. Calvi, F. Cau, R. Herzog, C. Marinucci, B. Stepanov,
Ecole Polytechnique Fédérale de Lausanne, Centre de Recherches en Physique des Plasmas,
Association EURATOM-Confédération Suisse, 5232 Villigen PSI, Switzerland

Abstract

In the last few years, the DC performance of a large number of sub- and full-size NbTi as well as Nb_3Sn cable-in-conduit (CIC) conductors was tested in the SULTAN facility of CRPP. The "potential" DC performance of various CIC conductors was estimated from the measured strand data. In the present work, the DC performance of CIC conductors, measured in SULTAN, is compared with this "potential" DC performance. The DC performance of NbTi sub- and full size CIC conductors has been found to be in good agreement with the "potential" conductor performance. For Nb_3Sn CIC conductors, the situation is more complex because of the strain sensitivity of the critical current. Evidence for strand damage, caused by the large Lorentz forces, has been found in Nb_3Sn sub-size conductors. Finally, a summary of the results of the tests of the ITER-TF Nb_3Sn conductors is provided. Again the measured DC performance is compared to the "potential" performance.

INTRODUCTION

The unique SULTAN test facility [1] provides the possibility to measure the critical current of large cable-in-conduit (CIC) conductors of approximately 3.5 m length in background fields of up to 11 T. In a comparison of the measured CIC conductor critical current with the strand performance, the variation of the magnetic field within the conductor cross-section due to the self-field contribution needs to be taken into account. Moreover, a current imbalance originating from the resistance distribution in the joints may reduce the critical current. In the case of Nb_3Sn-based CIC conductors the strain state of the strands in the cable is not exactly known. Furthermore, Nb_3Sn is a brittle material, which is sensitive to micro-crack formation leading to an irreversible degradation of the current carrying capacity of the strands. For a single Nb_3Sn CIC conductor, it is therefore difficult to identify the reasons of unexpectedly low performance.

In order to get deeper insight in the relations between strand and conductor performances, the statistics of the results of the measurement of the critical current or the current sharing temperature in various NbTi and Nb_3Sn CIC sub- as well as full-size conductors is considered in the present work. The basis for this statistical approach is the comparison of the measured conductor critical current or current sharing temperature with the "potential" performance estimated from the strand data.

*This work, supported by the European Communities under the contracts of association between EURATOM and CRPP, was carried out within the framework of the European Fusion Development Agreement. The views and opinions expressed herein do not necessarily reflect those of the European Commission. The technical support of the Paul Scherrer Institute PSI is greatly acknowledged.
#rainer.wesche@psi.ch

CONDUCTOR PROPERTIES

NbTi Cable-in-Conduit Conductors

The main properties of the considered sub- and full-size conductors, used for the comparison of NbTi strand and CIC conductor performances, are listed in Table 1. A more detailed description of the conductors can be found in [2] and [3]. In the full-size conductors, the two conductor legs are connected by a bottom joint close to the high field region. A single SULTAN full-size sample, consisting of two different conductor legs, allows us to test two different conductors of similar performance in a single measurement campaign. In the sub-size conductors, the bottom joint is replaced by a U-bend leading to a hairpin sample.

Table 1: Main Properties of the NbTi CIC Conductors

CICC	Strand/Coating	Cabling Pattern	N_{NbTi}
NbTi #1	A/Ni	(1 sc + 7 Cu)×3×4×4	48
NbTi #2	B/SnAg	(1 Cu + 6 sc)×3×4×4	288
NbTi #3	B/Ni	(1 Cu + 6 sc)×3×4×4	288
NbTi #4	B/Ni & wraps	(1 Cu + 6 sc)×3×4×4	288
NbTi #5	C/Ni	(1 Cu + 6 sc)×3×4×4	288
PFIS L	D/Ni & wraps	(3×4×4×5)×6	1440
PFIS R	D/Ni	(3×4×4×5)×6	1440
LCJ	D/Ni	(1 Cu + 9 sc)×4×4×6	864

Nb_3Sn Sub-Size Cable-in-Conduit Conductors

For seven Nb_3Sn sub-size conductors, the strand and CIC conductor performances have been compared. The strand type and the conductor dimensions are listed in Table 2. Further conductor properties are gathered in Table 3. The hairpin conductors VAC-T and VAC-B were both fabricated of VAC Nb_3Sn strands left over from the fabrication of the Central Solenoid Model Coil (CSMC). The two conductors are distinguished by the cabling pattern. VAC-T is a triplet-based conductor, whereas VAC-B is a braided conductor. A more detailed description of the conductors can be found in [4]. The dipole pre-prototype conductor (DIPP) was manufactured of OST strands with non-copper critical current densities of 1100 A/mm^2 at 12 T and 4.2 K (electric field criterion of 0.1 μV/cm) [5].

Table 2: Dimensions of Nb_3Sn Sub-Size CIC Conductors

CICC	Strand	Dimensions (mm)
VAC-T	VAC CSMC	14.5 Jacket / 12.5 Cable
VAC-B	VAC CSMC	14.52 Jacket / 12.52 Cable
DIPP	OST1	18.4 × 7.7 Jacket 16.4 × 5.7 Cable
PITSAM 1	OST dipole	21.1 × 9.5 Jacket 17.9 × 6.3 Cable
PITSAM 2	OST dipole	12.6 × 12.6 Jacket 9.1 × 9.1 Cable
PITSAM 3	OST dipole	15.4 × 10.5 Jacket 11.9 × 7.0 Cable
PITSAM 5	OST dipole	12.57 × 12.57 Jacket 9.1 × 9.1 Cable

A special feature of the PITSAM 5 conductor is the change of the pitches in the region of the U-bend. This means that the pitches are short in the left leg, while they are long in the right leg.

Table 3: Cable Pattern and Twist Pitches of the Nb_3Sn Sub-Size CIC Conductors

CICC	Cable Pattern	N_{sc}	Twist Pitch (mm)
VAC-T	3×3×4×4	144	51/76/136/167
VAC-B	29 (braid) × 5	145	167
DIPP	3×3×3×4 (24 Cu)	84	58/95/139/213
PITSAM 1	3×3×4×4	144	58/95/139/213
PITSAM 2	3×3×3×4 (60 Cu)	48	58/95/139/213
PITSAM 3	3×3×3×4 (60 Cu)	48	58/95/139/213
PITSAM 5	3×3×3×4 (60 Cu)	48	34/95/139/213 83/140/192/213

Nb_3Sn Full-Size Cable-in-Conduit Conductors

In the case of 14 Nb_3Sn full-size conductors a complete characterisation of the strands is available. The main properties of the seven full-size SULTAN samples are gathered in Table 4. The SULTAN samples TFAS 1 and TFAS 2 are of Toroidal Field Model Coil (TFMC) type [6], [7]. The cable pattern of these conductors is 3×3×5×4×6. In the conductors TFAS 1 EAS and TFAS 2 OCSI all 1080 strands are superconducting, whereas in TFAS 1 OST2 and TFAS 2 OKSC each first stage triplet consists of 2 Nb_3Sn strands and one copper wire, i.e. 720 Nb_3Sn strands and 360 Cu wires. All other full-size Nb_3Sn CIC conductors are of ITER type (see also [8]). The cabling pattern of the ITER conductors is {(2 Nb_3Sn + 1 Cu) × 3 × 5 × (5 + core)} × 6, where the cores consist of 3 × 4 copper wires. Thus, the number of Nb_3Sn strands is 900, while the number of copper wires is 522. In the TFPRO 2 OST2 conductor, the pitches of the first stages were significantly enlarged.

Table 4: Main Properties of Nb_3Sn SULTAN Full-Size Samples (L Left Leg, R Right Leg)

CICC Strand L/R	Dimensions (Jacket) (mm)	Twist Pitch (mm)
TFAS 1 EAS/OST2	40.4/37.2	45/87/126/166/415
TFAS 2 OCSI/OKSC	40.4/37.2	45/87/126/166/415
TFPRO 1 EAS/EAS	L 43.45/40.25 R 42.05/38.85	45/87/126/245/460
TFPRO 2 OST2/OST1	L 41.45/38.25 R 42.05/38.85	116/182/245/415/440 45/87/126/245/460
JATF 1 Mitsubishi/Hitachi	43.9/40.6	45/85/130/250/450
JATF 2 Hitachi/Mitsubishi	42.7/39.3	45/85/130/250/450
KOTF KAT/KAT	L 43.7/40.5 R 43.7/39.9	42/80/125/240/450

STRAND PROPERTIES

NbTi Strands

The temperature and field dependencies of the non-Cu critical current density of all NbTi strands have been described by the following scaling law [9]

$$J_c(B,T) = \left(\frac{C_0}{B}\right)\left(1-t^{1.7}\right)^{\gamma} b^{p}\left(1-b\right)^{q} \qquad (1)$$

where $t = T/T_c$, $b = B/B_{c2}(T)$, T_c the critical temperature and B_{c2} the upper critical field.

$$B_{c2}(T) = B_{c20}\left(1-t^{1.7}\right) \qquad (2)$$

The properties of the NbTi strands and the corresponding scaling parameters are gathered in Table 5.

Table 5: NbTi Strand Scaling Parameters

Strand	A	B	C	D
d (mm)	0.87	0.70	0.70	0.73
Cu:non-Cu	1.12	1.05	7.5	1.41
p	1.55	1.65	1.4	1.92
q	1.85	1.80	1.55	2.03
γ	1.79	1.88	1.90	2.22
C_0 (kA T/mm^2)	286	271	181	477
T_c (K)	8.79	8.74	8.95	9.02
B_{c20} (T)	16.00	15.89	15.48	14.90

Nb_3Sn Strands

There exist several scaling relations to describe the field, temperature and strain dependencies of the critical current density of Nb_3Sn strands. In the present work, for all Nb_3Sn strands except the Korean KAT strand the Twente [10], [11] and the Durham scaling relations [12] have been used.

In order to define the strand scaling parameters, the Twente and the Durham scaling relations are briefly described. The Twente scaling relations can be written as

$$I_c(B,T,\varepsilon)=\frac{C_1}{B}\cdot s(\varepsilon)\cdot\left(1-t^{1.52}\right)\cdot \left(1-t^2\right)\cdot b^{0.5}\cdot(1-b)^2 \tag{3}$$

with

$$t=\frac{T}{T_c^{\,*}(\varepsilon)} \qquad b=\frac{B}{B_{c2}^{\,*}(T,\varepsilon)} \tag{4}$$

$$B_{c2}^{\,*}(T,\varepsilon)\cong B_{c2m}^{\,*}(0)\cdot s(\varepsilon)\cdot\left(1-t^{1.52}\right) \tag{5}$$

$$T_c^{\,*}(\varepsilon)=T_{cm}^{\,*}(0)\cdot s(\varepsilon)^{1/3} \tag{6}$$

$$s(\varepsilon)=1+\frac{C_{a1}\left(\sqrt{\varepsilon_s^{\,2}+\varepsilon_{0,a}^{\,2}}-\sqrt{(\varepsilon-\varepsilon_s)^2+\varepsilon_{0,a}^{\,2}}\right)-C_{a2}\cdot\varepsilon}{1-C_{a1}\cdot\varepsilon_{0a}} \tag{7}$$

$$\varepsilon_s=\frac{C_{a2}\cdot\varepsilon_{0,a}}{\sqrt{C_{a1}^{\,2}-C_{a2}^{\,2}}} \tag{8}$$

$$\varepsilon=\varepsilon_a+\varepsilon_m \tag{9}$$

where B is the magnetic field, B_{c2}* the inhomogeneity averaged, effective upper critical field, B_{c2m}* the inhomogeneity averaged maximum upper critical field at $\varepsilon = 0$, T the temperature, T_c* the inhomogeneity averaged maximum critical temperature at $B = 0$, ε the strain, ε_a the applied axial strain, ε_m the thermal pre-compression strain, ε_s the axial difference between a three dimensional deviatoric strain minimum and the position of the maximum in axial strain sensitivity results and $\varepsilon_{0,a}$ the remaining strain component. Three superconducting parameters (C_1, B_{c2m}*(0), T_{cm}*) and four deformation related parameters (C_{a1}, C_{a2}, $\varepsilon_{0,a}$, ε_m) need to be determined by a least squares fit to the measured strand data. The scaling parameters for the EAS, OST2 and OST dipole strands are gathered in Table 6. The scaling parameters are based on measurements performed at the University of Twente.

Table 6: Nb_3Sn Strand Twente Scaling Parameters

Strand	**EAS**	**OST2**	**OST dip.**
C_{a1}	71.39	81.69	114.14
C_{a2}	28.28	35.25	82.75
$\varepsilon_{0,a}$ [%]	0.25	0.15	0.237
ε_m [%]	-0.12	-0.06	-0.11
B_{c2m}*(0) [T]	35.75	34.02	29.05
T_{cm}*(0) [K]	16.52	16.21	15.91
C_1 [A·T][a)]	12171 TFAS 12407 TFPRO	17790 TFAS 17624 TFPRO	49405

[a)] Adjusted to the results of the witness strand measurements.

The Durham scaling relations can be written as

$$J_e(B,T,\varepsilon)=A(\varepsilon)\cdot\left[T_c^{\,*}(\varepsilon)\cdot\left(1-t^2\right)\right]^2 \left[B_{c2}^{\,*}(T,\varepsilon)\right]^{n^*-3}b^{p-1}(1-b)^q \tag{10}$$

with

$$B_{c2}^{\,*}(T,\varepsilon)=B_{c2}^{\,*}(0,\varepsilon)\cdot\left(1-t^{\nu}\right) \tag{11}$$

$$\left(\frac{A(\varepsilon)}{A(0)}\right)^{w/u}=\left(\frac{T_c^{\,*}(\varepsilon)}{T_c^{\,*}(0)}\right)^{w}=\frac{B_{c2}^{\,*}(0,\varepsilon)}{B_{c2}^{\,*}(0,0)}=1+c_2\cdot\varepsilon^2+c_3\cdot\varepsilon^3+c_4\cdot\varepsilon^4 \tag{12}$$

where J_e is the engineering critical current density, $b = B/B_{c2}$*(T,ε) and $t = T/T_c$*(ε). The scaling parameters for the VAC CSMC [13], OST1, OCSI, OKSC, Mitsubishi and Hitachi strands are gathered in Table 7.

Table 7: Nb_3Sn Strand Durham Scaling Parameters

Strand	**VAC**	**OST1**	**OCSI**
p	0.4625	0.9631	0.8869
q	1.452	2.229	2.174
n*	2.457	2.532	2.500
ν	1.225	1.518	1.500
w	2.216	2.423	2.200
u	0.051	0.1155	0
$A(0)$ [$Am^{-2}T^{3-n^*}K^{-2}$] [a)]	1.004×10^7	4.32×10^7	2.87×10^7
T_c*(0) [K]	17.58	16.71	17.50
B_{c2}*(0,0) [T]	29.59	29.72	28.47
c_2	-0.6602	-0.7816	-0.7392
c_3	-0.4656	-0.6318	-0.5071
c_4	-0.1075	-0.1732	-0.0838

Table 7: Nb_3Sn Strand Durham Scaling Parameters (continued)

Strand	OKSC	Hitachi	Mitsubishi
p	0.4556	0.6231	0.4422
q	1.723	1.9221	2.064
n^*	2.642	2.5203	2.7756
ν	1.318	1.52	1.52
w	2.43	1.8195	1.6132
u	-0.811	-0.6282	-0.9198
$A(0)$ [$Am^{-2}T^{3-n^*}K^{-2}$]	1.26×10^{7} a)	4.30×10^{7}	2.17×10^{7}
$T_c^*(0)$ [K]	17.22	17.26	17.10
$B_{c2}^*(0,0)$ [T]	29.41	29.46	28.21
c_2	-1.0768	-0.6462	-0.889
c_3	-1.1514	-0.4536	-0.9423
c_4	-0.4125	-0.09534	-0.3503

a) Adjusted to the results of the witness strand measurements.

The VAC CSMC, OST1, OCSI and OKSC strands were characterised at Durham University. The strand scaling parameters of the Mitsubishi and Hitachi strands were provided by the Japanese ITER team.

COMPARISON OF CABLE AND STRAND PROPERTIES

The variation of the magnetic field within a SULTAN sample of circular shape is to a first approximation

$$B(r) = B_b + \frac{\mu_0 I}{2\pi r_c}\left(\frac{r}{r_c} + \frac{r_c}{R-r}\right) \qquad (13)$$

where I is the operating current of the CIC conductor, μ_0 is the permeability of free space, r_c is the radius of the cable space, R is the distance of the two conductor legs and r is a coordinate perpendicular to the background field B_b generated by the SULTAN facility. For simplicity, it is assumed that the field contours remain parallel to the background field. In the case of rectangular conductors, the maximum and the minimum fields in the central plane of the conductor have been calculated numerically. It is supposed that the field varies linearly between these two values within the conductor cross-section. Due to the twist pitch, the strands cycle in and out of the high field region. The average electric field is calculated under the assumption that in a sufficiently long CIC conductor (i.e. longer than one cable pitch) each strand is found with the same probability at any position of the cable cross-section. In addition, a uniform current distribution among insulated strands is considered, i.e. no inter-strand current sharing is allowed. The resulting average electric field for a circular CIC conductor without central channel is

$$\frac{E_{av}}{E_c} = 2\int_{-r_c}^{+r_c} \frac{\left(r_c^{\,2} - r^2\right)^{1/2}}{\pi r_c^{\,2}} \left(\frac{J}{J_c(B,T,\varepsilon)}\right)^n dr \qquad (14)$$

where J is the non-copper operation current density and E_c = 0.1 μV cm^{-1}. In our calculations, the integral was replaced by a summation with a step width of 0.01 r_c. The conductor temperature within the cross-section is supposed to be constant. Furthermore, the difference between the conductor and helium temperature has been neglected in the comparison with the experimental data. By definition, the cable critical current density is reached when the calculated average electric field, E_{av}, equals E_c. In the case of full-size conductors with a central channel [14] or of rectangular conductors, it is necessary to adjust Eq. (14) to the geometry in question.

RESULTS

NbTi CIC Conductors

The measured and the calculated "potential" current sharing temperatures of NbTi sub-size cable-in-conduit conductors are compared in Fig. 1. The measured current sharing temperatures of all considered NbTi sub-size cable-in-conduit conductors are close to the "potential" values. The deviations from the "potential" values are typically of the order of 0.1 K. In the case of the conductors NbTi #2 and #3, the current sharing temperature was also measured after cyclic loading. The cyclic loading was performed by charging the conductor for 1400-times with a current of 40 kA in a background field of 5 T generated by the SULTAN facility. In both conductors, the current sharing temperatures, measured before and after cyclic loading, are not significantly different. This result reflects the fact that NbTi strands are not very sensitive to mechanical damage.

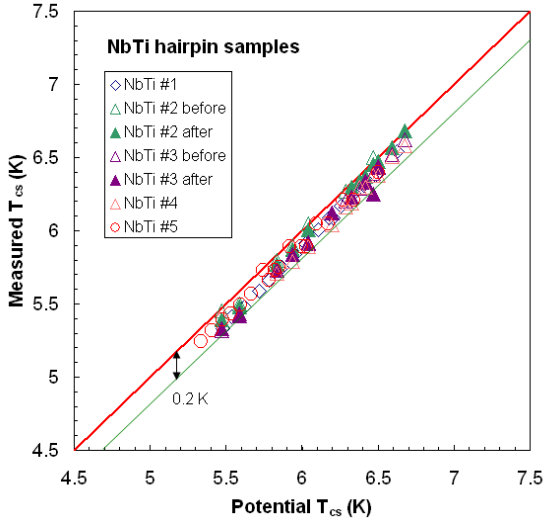

Figure 1: Measured versus "potential" current sharing temperature for NbTi hairpin (sub-size) CIC conductors.

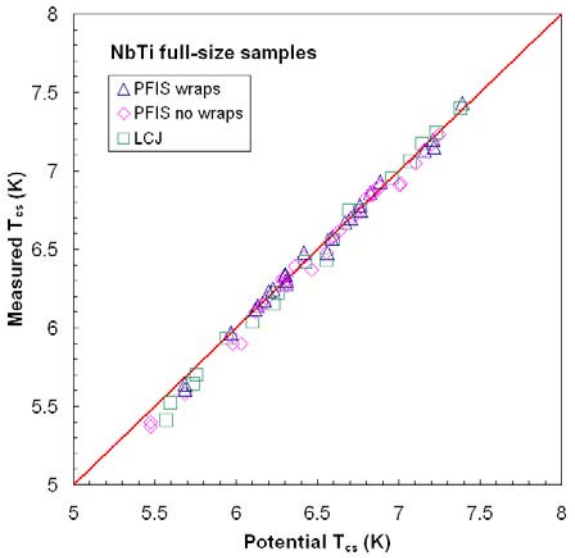

Figure 2: Measured versus "potential" current sharing temperature for NbTi full-size CIC conductors.

The ac losses, measured after cyclic loading, were considerably lower than those found before cyclic loading [2]. The observed change in the ac losses is the consequence of an increased transverse resistance between adjacent strands. The absence of a change of the critical current and the current sharing temperature of NbTi #2 and #3 after cyclic loading suggests that the current distribution among the strands is not significantly altered.

In Fig. 2, the measured current sharing temperatures of full-size NbTi conductors are shown as a function of the "potential" values. The agreement of measured and "potential" values is even better than in the case of the sub-size conductors. The deviations from the potential values are typically less than 0.1 K.

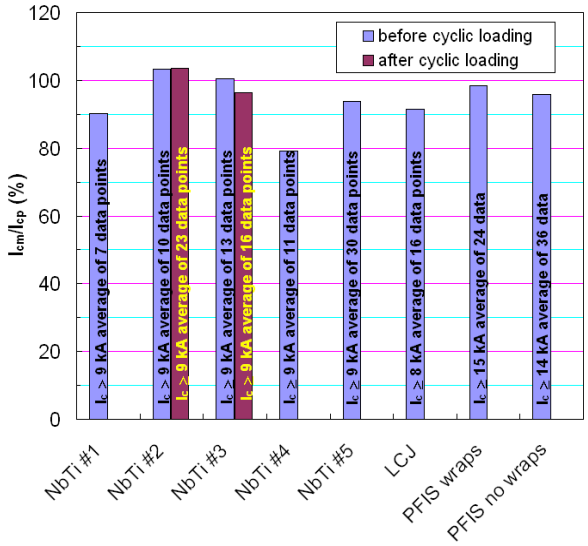

Figure 3: Ratio of measured to "potential" critical current for NbTi sub- and full-size CIC conductors.

In Fig. 3, the ratios of the measured to the "potential" critical current are shown for both the sub- and full-size NbTi CIC conductors. For seven out of eight conductors, this ratio exceeds 90%. Again the effects of cyclic loading on the performance of the two tested conductors NbTi #2 and #3 are negligible. In one of the sub-size conductors (NbTi #4), characterised by Ni coating of the strands and the presence of sub-cable wraps, the ratio of measured to "potential" critical current reaches only ≈80%.

The deviations of measured and "potential" values include the errors of the temperature measurements of the SULTAN sample, the uncertainties in the strand scaling relation and deviations from the assumed uniform current distribution. Before the mounting of the temperature sensors was improved at the end of the year 2006 the accuracy of the measurement of the conductor temperature was approximately ±0.05 K. In the case of NbTi #3, this accuracy of the temperature measurement leads to an uncertainty of ±10% in the cable critical current at a field of 6 T and a temperature of 6 K. In the measurement of the critical current of Strand B, the accuracy of the temperature measurement was about ±0.02 K, which is equivalent to an error bar of ±5% for the strand critical current at 6 T and 6 K. The scaling relation for the strand critical current tends to underestimate I_c below 6 T, whereas it overestimates I_c above 6 T in the case of Strand B. The errors related to strand scaling parameters are in the range of interest typically less than 8%. Moreover, the assumption that each strand is found with the same probability at any position of the cable cross-section is not exactly correct for the relatively short lengths of conductor in high field in a SULTAN test. Based on these considerations, we can conclude that cable critical currents, which exceed 90% of the "potential" values, suggest that in the conductor in question the current carrying capacity of the superconducting strands is fully used.

Nb_3Sn Sub-Size CIC Conductors

The comparison of cable and strand performances is more complex in the case of Nb_3Sn conductors. The upper critical field and the transition temperature of Nb_3Sn depend on the strain state of the superconductor. As a consequence, the critical current is a function of temperature, field and strain. In general, the strain state of the Nb_3Sn in a CIC conductor is different from that in a single strand measurement for example on a Ti6Al14V ITER barrel. As long as the strain does not exceed a critical value the critical current depends reversibly on this parameter. Application of a strain exceeding the critical value leads to micro-crack formation in the brittle Nb_3Sn filaments. The irreversible reduction of the critical current is reflected by the fact that the critical current, measured after unloading, is lower than the initial I_c value found before any loading. The estimation of a "potential" cable critical current suffers from the not exactly known strain state of the Nb_3Sn strands in a cable-in-conduit conductor.

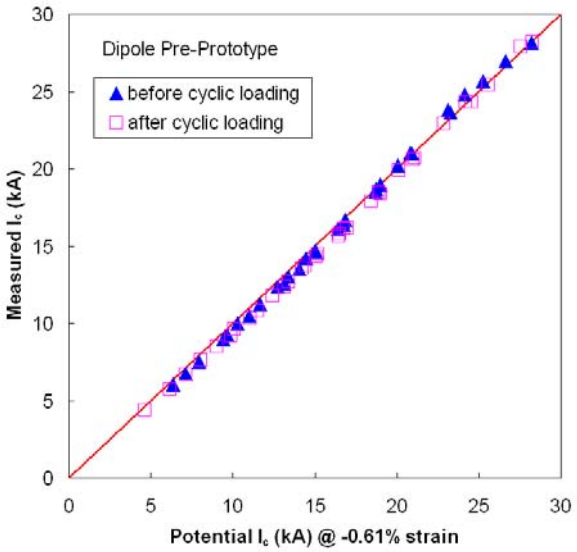

Figure 4: Measured critical current of the dipole pre-prototype (DIPP) conductor as a function of the "potential" values.

First, the results of two Nb_3Sn sub-size conductors of rectangular cross-section, which show a very good DC performance, are presented. In Fig. 4, the measured critical currents of the dipole pre-prototype (DIPP) conductor [5] are shown as a function of the "potential" critical currents. The calculation of the "potential" critical current is based on a strain of -0.61%. This value seems to be reasonable for a CIC conductor with stainless steel conduit. Due to the differences in the coefficients of thermal expansion of stainless steel and the Nb_3Sn strands the cool-down from the reaction temperature for the formation of Nb_3Sn (≈650°C) to 4.2 K leads to a compressive strain in the strands, while the jacket experiences a tensile strain.

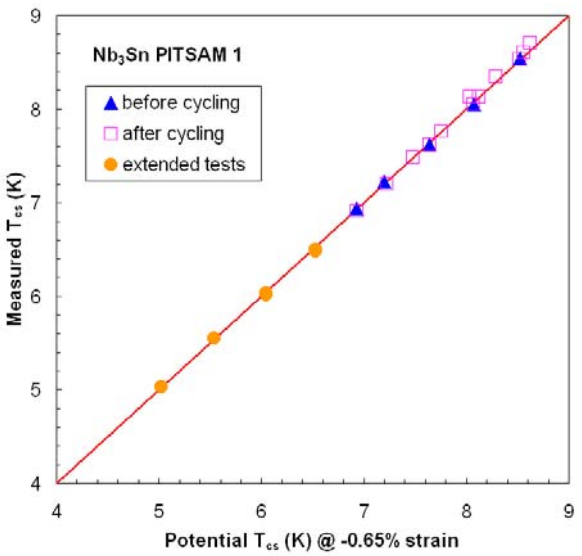

Figure 5: Measured T_{cs} values of the PITSAM 1 conductor as a function of the "potential" values.

The agreement of the measured and the "potential" critical current is excellent, as illustrated in Fig. 4. Moreover, 1000 load cycles at a current of 22 kA in a background field of 9 T were found to have a negligible effect on the critical current of the DIPP conductor. The DC performance of the DIPP conductor can be well described by not degraded strands and a single strain value of -0.61%. In contrast to the results for the CSMC model coil [15], [16], it is not necessary to introduce a load-dependent extra strain ($\varepsilon_{extra} \propto \mathbf{I}\times\mathbf{B}$) to describe the data.

In Fig. 5, the current sharing temperature (T_{cs}), measured in the PITSAM 1 conductor [17] is compared to the "potential" values. To obtain a good agreement of measured and "potential" values it was necessary to enhance the strain to -0.65%. The results of the PITSAM 1 conductor are consistent with not degraded strands and a strain of -0.65%. Again the whole data set can be described by a single value of strain, which is independent of the transverse load. Furthermore, the T_{cs} values measured after 1000 load cycles at 21 kA in a field of 11 T are not significantly different from those found before cyclic loading. The absence of cyclic load degradation is a further hint that the strands in this conductor are not degraded. In the further considerations, we will use a strain of -0.65% as a reference value for the calculation of the "potential" I_c and T_{cs} values.

Two other hairpin Nb_3Sn CIC conductors were fabricated of VAC strands left over from the fabrication of the CSMC. One of these conductors is braided, whereas the other is triplet-based [4]. In Fig. 6, the measured current sharing temperatures are compared with the "potential" values, which are based on a strain of -0.65%. The T_{cs} values of the braided conductor are closer to the

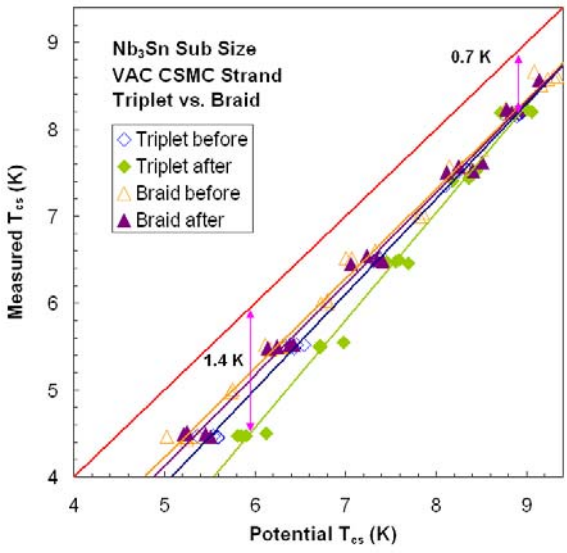

Figure 6: Measured versus "potential" T_{cs} values of the VAC-B and VAC-T conductors. The performance of the braided conductor (VAC-B) is closer to the "potential" values than that of the triplet-based conductor.

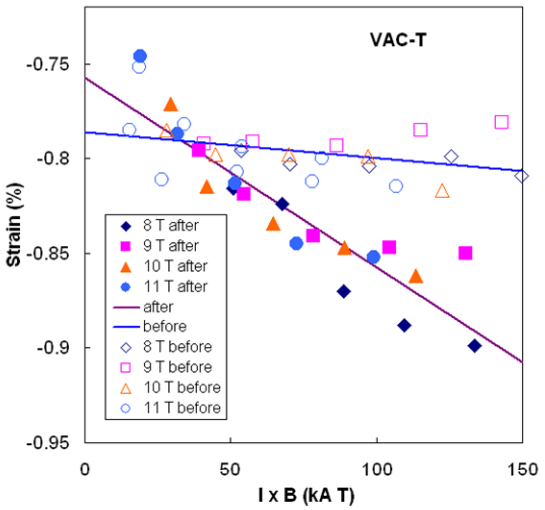

Figure 7: Strain values required to get a matching of cable and strand performances.

"potential" values than those of the triplet-based conductor. Moreover, the effect of cyclic loading on the T_{cs} of VAC-B is relatively small. The data, measured in the magnetic field range of 8 to 11 T, scatter around the trend lines. Especially for the triplet-based conductor VAC-T the difference of measured and "potential" T_{cs} increases with decreasing temperatures after cyclic loading, i.e. is larger at high I_c values. In principle, a matching of the cable T_{cs} values with the strand data can be always obtained by adjusting of the strain value for individual data points. The values of strain, obtained for the VAC-T conductor before and after cyclic loading are shown in Fig. 7. The results seem to indicate that the strain depends to a first approximation linearly on the transverse load. Nevertheless, the evolution of the performance of the conductor performance with cyclic loading suggests that the conductor is irreversibly degraded due to micro-crack formation in the Nb_3Sn filaments.

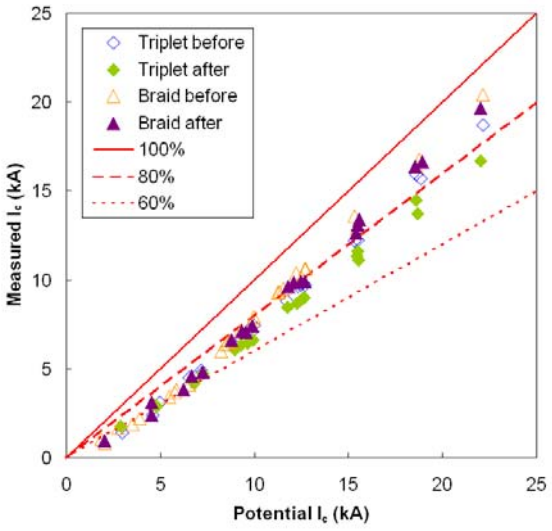

Figure 8: Measured versus "potential" I_c for the triplet- and braid-based conductors VAC-T and VAC-B.

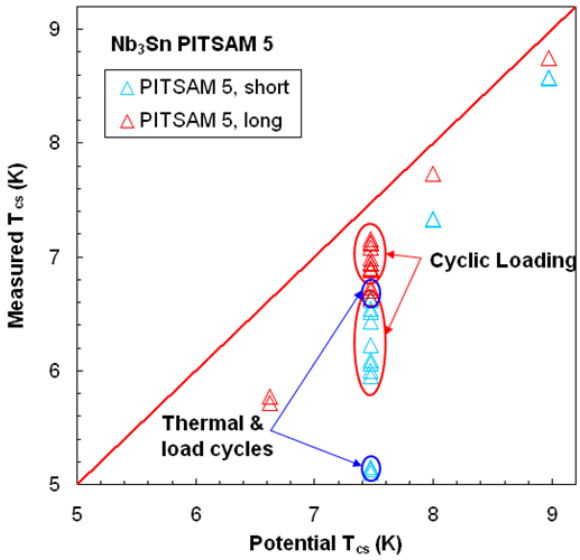

Figure 9: Comparison of the T_{cs} values, measured in the two legs of different pitch, with the "potential" T_{cs} values for a strain of -0.65%.

In Fig. 8, the measured critical current is shown as function of the "potential" values for a single strain value of -0.65%. Considering critical currents well above 10 kA, we find that the critical currents of the braided conductor, measured before and after cyclic loading, are close to 90% of the "potential" critical current. For VAC-T, the critical currents, measured before cyclic loading, reach approximately 85% of the "potential" values. After 1000 load cycles the critical current is reduced to ≈75% of the "potential" values.

In the case of the PITSAM 5 conductor, the pitch was changed in the region of the U-bend. Therefore, the twist pitch is short in the left conductor leg, whereas it is long in the right leg. In Fig. 9, the performances of the two conductor legs are compared to the "potential" T_{cs} values for a strain of -0.65%. The current sharing temperatures of the leg with longer pitches are higher than those of the leg with short pitches. In both conductors, T_{cs} decreases with cyclic loading (800 load cycles at 17 kA in a field of 8 T). However, the reduction is much more pronounced for the leg with the short pitches. After 800 load cycles the conductor is warmed up to room temperature and again cooled down to ≈4.5 K. After the thermal cycle and also after 100 additional load cycles the current sharing temperature was measured again at 17 kA in a field of 8 T. The "potential" T_{cs} is around 7.5 K. The reduction of T_{cs} due to the thermal cycle is much larger for the leg with short pitches. Thus, the measurement of T_{cs} at 9 T and 17 kA was only possible in the leg with long pitches (see data at "potential" T_{cs} of ≈6.6 K).

A summary of the performance of the considered Nb_3Sn sub-size CIC conductors after cyclic loading is presented in Fig. 10. The measured critical current is again compared with the "potential" values for a strain of -0.65%. The pre-prototype conductor (DIPP) and PITSAM 1 clearly reach the "potential" values.

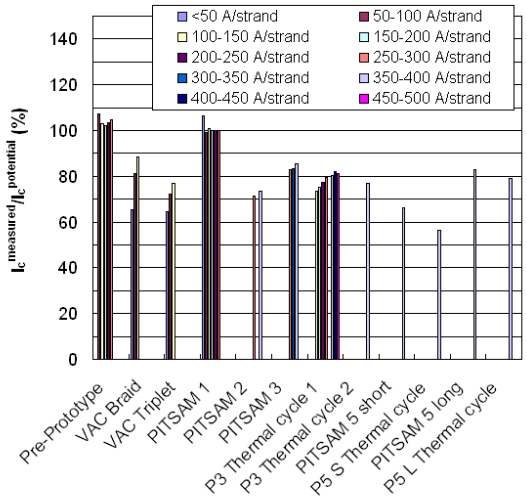

Figure 10: Comparison of the I_c values of various sub-size conductors, measured after cyclic loading, with the "potential" critical current. For some of the conductors, the effect of thermal cycles is also illustrated.

For VAC braid (VAC-B), PITSAM 3 and PITSAM 5 with long pitches, the critical current reaches ≈80% of the potential values. VAC-T, PITSAM 2 and PITSAM 5 with short pitches reach approximately 70% of the "potential" critical current after cyclic loading. A moderate effect of thermal cycles was observed for PITSAM 3 and PITSAM 5 with the long pitches. In PITSAM 5 with short pitches a pronounced reduction of the critical current was found after a single thermal cycle. Conductors of rectangular shape (DIPP, PITSAM 1 & 3) seem to be less sensitive to degradation than round (VAC-T) or square conductors (PITSAM 2 & 5). Longer pitches were also found to be advantageous (PITSAM 5 long).

Nb_3Sn Full-Size CIC Conductors

In a first campaign two European SULTAN samples TFAS 1 (EAS and OST legs) and TFAS 2 (OCSI and OKSC legs) were tested. The cabling pattern of these conductors is of TFMC-type. In the other full-size conductors the cabling pattern is that envisaged to be used for the ITER TF conductors.

In Fig. 11, the measured T_{cs} values of the four TFAS conductors are compared with the "potential" values for a strain of -0.65%. For the TFAS-OST conductor, the initial T_{cs} values are well above the "potential" values, suggesting that the strain in this conductor is considerably smaller than -0.65%. The trend lines for the TFAS-OST conductor indicate that the T_{cs} at 50 kA after cyclic loading is 1 K lower than the initial value. The TFAS-EAS and OKSC conductors show a less pronounced performance loss with cyclic loading. The TFAS-OCSI conductor was found to be relatively insensitive to cyclic load degradation in spite of the fact that the initial T_{cs} values are well below the "potential" current sharing temperatures.

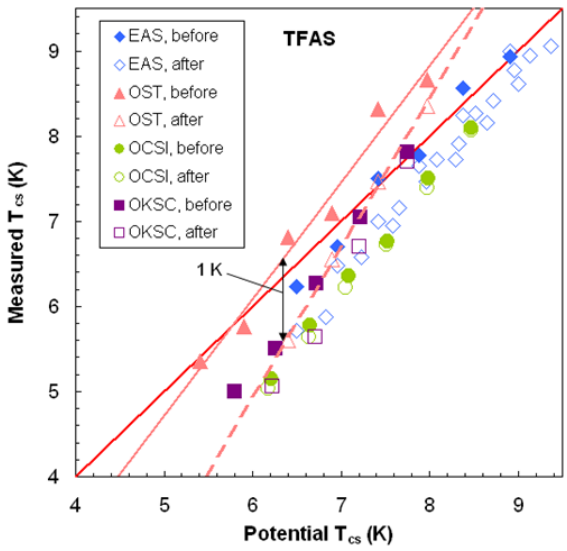

Figure 11: Comparison of the T_{cs} values of the four TFAS conductors, measured before and after cyclic loading, with the "potential" values for a strain of -0.65%.

In Fig. 12, the measured T_{cs} values of the two EAS legs of TFPRO 1 are plotted as a function of the potential values. The two legs are only distinguished by slightly different void fractions (EAS1: 33.8%, EAS2: 29.2%) [8]. Most of the measured data points of both conductors are slightly above the "potential" T_{cs} values suggesting that the strain in these two conductors is slightly lower than -0.65%. The data suggest that the performance of the EAS2 leg is slightly better than that of the EAS1 leg. Nevertheless, the strand current carrying capacity is practically fully used in both conductor legs. In addition, we found no evidence for cyclic load degradation.

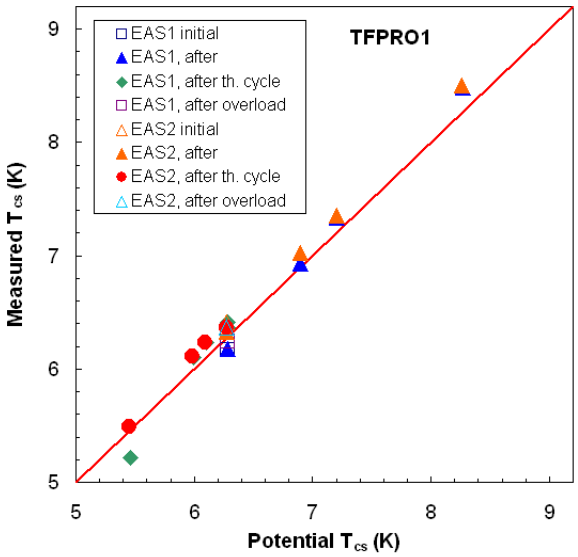

Figure 12: Measured T_{cs} values of TFPRO 1 EAS1 and EAS2 legs versus the "potential" values.

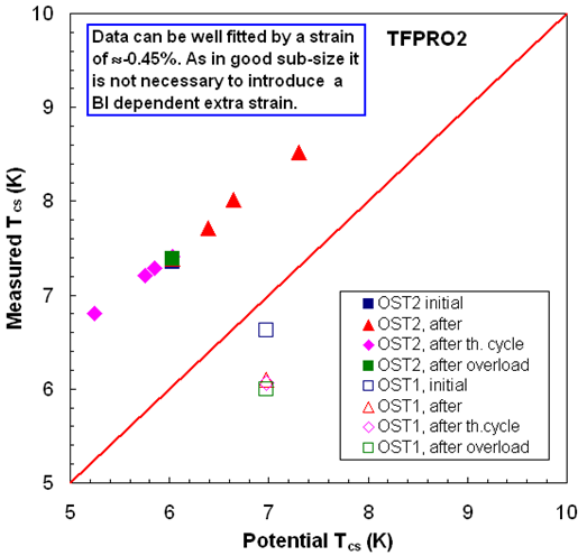

Figure 13: Measured T_{cs} values of TFPRO 2 OST1 and OST2 legs versus the "potential" values. The data for OST2 are consistent with not degraded strands and a strain around -0.45%.

The measured T_{cs} values of TFPRO 2 OST2 are well above the "potential" values for a strain of -0.65%, as illustrated in Fig. 13. The data are consistent with not degraded strands and a single strain value of ≈-0.45% independent of the transverse load. No performance evolution with cyclic loading was observed. On the other hand, the OST1 leg shows T_{cs} values below the "potential" values. Moreover, the T_{cs} after cyclic loading is significantly reduced.

For various full-size CIC conductors, the ratios of the measured to the "potential" critical current after cyclic loading are presented in Fig. 14. Especially for the TFAS conductors this ratio depends on current.

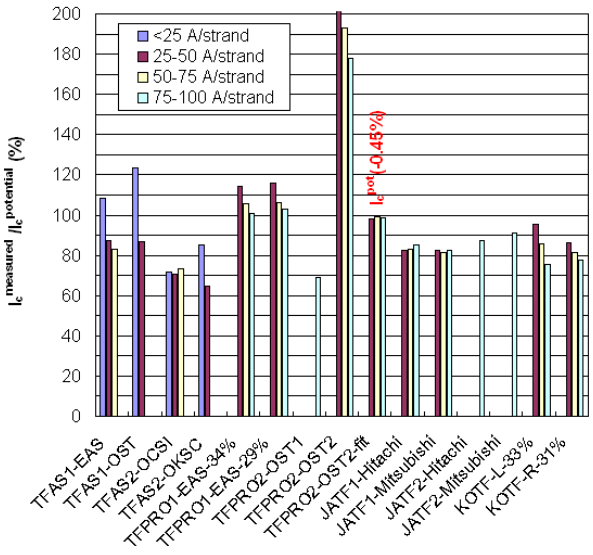

Figure 14: Performance summary of various full-size CIC conductors.

In the case of the TFAS conductors with strongly current-dependent ratios of measured to "potential" critical current the data can be well described by a combination of reduced strain values and a reduced effective superconductor cross-section [6]. The reduced cross-section seems to originate from micro-crack formation in the Nb_3Sn filaments. Considering currents of more than 75 A per strand the potential critical current has been achieved in the TFPRO2 OST2 and the TFPRO1 EAS1 & 2 conductors. The Japanese conductors JATF1 & 2, fabricated of Mitsubishi and Hitachi strands, reach 83 to 91% of the "potential" values. In the two legs of the Korean SULTAN sample KOTF 75 to 78% of the "potential" critical current has been achieved. The ratio of measured to "potential" I_c is below 70% for the TFPRO 2 OST1 conductor.

CONCLUSION

The measured critical current of NbTi full- and sub-size CIC conductors reaches typically more than 90% of the "potential" values. Only in the sub-size conductor NbTi #4 this ratio is ≈80%. The deviation of the measured current sharing temperatures from the potential values is typically less than 0.1 K. In addition, the two conductors NbTi #2 & #3, exposed to cyclic loading, did not show any degradation. These results suggest that a current non-uniformity originating from the resistance distribution in the joints does not severely degrade the performance of the SULTAN NbTi samples.

In the case of two sub-size Nb_3Sn conductors (DIPP, PITSAM 1), the measured T_{cs} values reach the "potential" values for strain values of -0.61% (DIPP) and -0.65% (PITSAM 1). Both conductors have been found to be insensitive to cyclic load degradation. A further aspect of importance is the fact that the complete data sets of these two conductors can be well described by a single value of strain independent of the transverse load, i.e. the value of **I**×**B**. In other conductors, the initial T_{cs} values were found to be well below the "potential" values for a strain of -0.65%. Typically these conductors show also a performance reduction with cyclic loading or after thermal cycles.

The current sharing temperatures of the TFAS full-size CIC conductors [6] were found to be significantly below the "potential" values. Moreover, pronounced cyclic load degradation was found in the TFAS 1 OST conductor. A first series of ITER-type conductors showed an improved performance. In the TFPRO 1 EAS conductors, the measured T_{cs} values were close to the "potential" values and cyclic load degradation is absent. The TFPRO 2 OST2 conductor showed excellent performance, however, the strain seems be much smaller than -0.65%. The data suggest that the real strain is as low as ≈-0.45% in this conductor. This single strain value provides a good description of the whole data set independent of actual transverse load. The extra strain needed to describe the behaviour of some conductors may therefore simply reflect that some damage is present in these conductors.

Especially the TFPRO 2 OST1 conductor showed a performance well below the "potential" values. Furthermore, the current sharing temperature declined with cyclic loading. Despite of performances that are much better in the ITER-type conductors than in the TFAS conductors, there remain doubts if in all ITER conductors the current carrying capacity of the strands is fully used.

REFERENCES

[1] P. Bruzzone, A. Anghel, A. Fuchs, G. Pasztor, B. Stepanov, M. Vogel, G. Vecsey, IEEE Trans. Appl. Supercond. 12 (2002) 520. doi: 10.1109/TASC.2002.1018457

[2] R. Wesche, A. Anghel, B. Stepanov, M. Vogel, P. Bruzzone, Cryogenics 45 (2005) 755. doi: 10.1016/j.cryogenics.2005.10.002

[3] R. Wesche, B. Stepanov, P. Bruzzone, IEEE Trans. Appl. Supercond. 16 (2006) 819. doi: 10.1109/TASC.2006.871274

[4] P. Bruzzone, B. Stepanov, R. Wesche, Advances in Cryogenic Engineering (Materials) 52 (2006) 558.

[5] P. Bruzzone, B. Stepanov, R. Wesche, A. Portone, E: Salpietro, A. Vostner, A. della Corte, IEEE Trans. Appl. Supercond. 16 (2006) 894. doi: 10.1109/TASC.2006.873320

[6] P. Bruzzone, M. Bagnasco, D. Ciacynski, A. della Corte, A. Di Zenobio, R. Herzog, Y. Ilyin, B. Lacroix, L. Muzzi, A. Nijhuis, B. Renard, E. Salpietro, L.S. Richard, B. Stepanov, S. Turtù, A. Vostner, R. Wesche, L. Zani, R. Zanino, IEEE Trans. Appl. Supercond. 17 (2007) 1370. doi: 10.1109/TASC.2007.898504

[7] D. Ciazynski, Fus. Eng. Des. 82 (2007) 488. doi: 10.1016/j.fusengdes.2007.01.024

[8] P. Bruzzone, B. Stepanov, R. Wesche, E. Salpietro, A. Vostner, K. Okuno, T. Isono, Y. Takahashi, H.C. Kim, K. Kim, A.K. Shikov, V.E. Sytnikov, IEEE Trans. Appl. Supercond. 18 (2008) 459. doi: 10.1109/TASC.2008.922266

[9] L Bottura, IEEE Trans. Appl. Supercond. 10 (2000) 1054. doi: 10.1109/77.828413

[10] A. Godeke 2005, Performance boundaries in Nb_3Sn superconductors, PhD thesis, University of Twente, ISBN 90-365-2224-2.

[11] A. Godeke, B. ten Haken, H.HJ. ten Kate, D.C. Larbalestier, Supercond. Sci. Technol. 19 (2006) R100. doi: 10.1088/0953-2048/19/10/R02

[12] D.M. Taylor, D.P. Hampshire, Supercond. Sci. Technol. 18 (2005) 2041. doi: 10.1088/0953-2048/18/12/005

[13] D.M.J. Taylor, D.P. Hampshire, *Test of advanced Nb_3Sn strands*, Durham University, Final report EFDA03-1126 2003.

[14] R. Wesche, R. Herzog, P. Bruzzone, Supercond. Sci. Technol. 21 (2008) 054001. doi: 10.1088/0953-2048/21/5/054001

[15] R. Zanino, N. Mitchell, L. Savoldi Richard, Cryogenics 43 (2003) 179. doi: 10.1016/S0011-2275(03)00035-3

[16] N. Mitchell, Fus. Eng. Des. 66-68 (2003) 971. doi: 10.1016/S0920-3796(03)00237-0

[17] A. Vostner, P. Bauer, R. Wesche, U. Besi Vetrella, B. Stepanov, A. della Corte, A. Portone, E. Salpietro, IEEE Trans. Appl. Supercond. 18 (2008) 544. doi: 10.1109/TASC.2008.921329

CURRENT MgB_2 WIRE PERFORMANCE AND THEIR INDUSTRIAL DEVELOPMENT

G. Grasso, S. Brisigotti, D. Pietranera, A. Tumino, S. Berta, R. Penco and E. Demencik,
Columbus Superconductors SpA, Genova, Italy
V. Braccini, A. Malagoli, M. Vignolo, M. Tropeano, C. Fanciulli, M. Putti, and C. Ferdeghini,
CNR-INFM, Genova, Italy

Abstract

Although just recently discovered as a superconductor, Magnesium Diboride has already demonstrated its clear potential for an effective use in a variety of applications. With its critical temperature of about 40 K, MgB_2 gives the opportunity to operate devices at cryogenic temperatures of the order of 20 K, allowing for the use of alternative, cost effective, and simpler technologies than liquid helium. Suitable processes for long lengths wire manufacturing have been demonstrated in the recent years. This work will focus on the preparation of MgB_2 based superconducting wires by the Powder-In-Tube method, using the so-called 'ex-situ' process. The main physical and structural characteristics of these wires will be finally reported and briefly discussed.

INTRODUCTION

Just a few months after the discovery of superconductivity in Magnesium Diboride MgB_2, it became clear that this material would have been competing in the near future with the existing superconductors in industrial applications, in particular in the field of superconducting magnets. To date, only seven years later, the impressive advancement of industrially manufactured wires and prototype magnets based on MgB_2 is a practical demonstration that those initial ideas were basically accurate.

A number of different routes have been developed to improve the wire processing and to achieve high critical current densities J_c in MgB_2. Several groups [1–4] have followed the so-called ex situ technique, while the majority [5–10] have preferred to use the in situ technique. Both ways are based on the powder in tube (PIT) method but while the first uses fully reacted MgB_2 powders, the latter starts from a mixture of unreacted Mg and B.

The work presented in this paper refers entirely to conductors manufactured by the ex situ PIT process. Indeed, while the in situ route presents several advantages as low cost, high fill factor, high speed process, low temperature reaction processes, and relatively easy MgB_2 nanoparticle doping, the ex situ technique currently appears to be more suitable for the development of long conductors and complex multifilamentary wire geometry, allowing for a better control of the powder granulometry and purity degree as well, and finally it leads to more robust conductors that can be readily employed to realize magnets by the Wind and React process.

Due to the aforementioned reasons, the $J_c(B)$ behaviour of the ex situ conductors has not been always as high as in the in situ case. Therefore, a deeper development of the starting MgB_2 powders in the ex situ process is needed in order to further enhance J_c, at least at magnetic fields of the order of 2–4 T at 20 K and 5–10 T at 4.2 K. In fact these are most likely the typical operating conditions for the conductors when we consider their most widespread use in superconducting magnets.

Nevertheless, especially from the point of view of industrial applications, improving the starting MgB_2 powders for the ex situ fabrication process seems to be a feasible way to make this material definitely competitive. The doping and the granulometry control are two straightforward ways to run along at the beginning of such optimisation process.

In this paper, an overview of the results reached in the recent past on MgB_2 conductors is briefly reported. First, we will present the technique developed for the fabrication of mono- and multifilamentary tapes in long lengths and an overview of their main properties. Secondly, we will show how the tape performances can be improved by modifying the properties of the starting MgB_2 powders: in this case, the transport J_c vs. B behaviour of monofilamentary tapes fabricated through the ex situ technique will be reported up to very high fields. We will focus on the addition of SiC nanoparticles to the B before the reaction with Mg, on the high energy ball milling of MgB_2 powders alone and with the addition of SiC or C.

PREPARATION OF EX-SITU MgB_2 WIRES

Through the ex situ technique, pre-reacted MgB_2 powders are filled inside metallic tubes in order to manufacture both mono- and multifilamentary conductors. The powders are currently prepared from a mixture of commercial amorphous B (95– 97% purity) and Mg (99% purity), heat treated at about 900 °C in Ar atmosphere, producing rather pure MgB_2 with some residual traces of MgO in a quantity well below 10 wt%. Pure Ni tubes are filled with such reacted powders with a packing density of about 1.3 g/cm^3, and are subjected to wire drawing down to a diameter of about 2 mm, followed by several steps of cold rolling and a final sintering stage at 900–1000 °C in Ar.

In the case of multifilamentary tapes, monocore wires prior to cold rolling are packed again inside a new Ni tube with a multifilamentary layout. The multifilamentary configuration has allowed to obtain wires and tapes that still show similar J_c values than the monocore ones, but capable of sustaining a larger bending strain together with a reasonably limited fluctuation of the superconducting cross-section along their entire length.

Practical applications considering the use of a superconducting material, however, require further precautions and protective measures in case of a quench. This scope is usually achieved by closely adding OFHC (oxygen-free high conductivity) Copper in parallel with the superconducting wire. Due to the chemical incompatibility of MgB_2 with most of the highly conductive metallic pure elements, however, the best solution we have found to date is the insertion of a diffusion barrier with the purpose of separating the superconducting filaments from the highly conductive metal.

We have concretize this approach by introducing a copper core in the centre of the conductor, properly coated by a thin barrier to limit its chemical diffusion towards MgB_2. The resulting composite is incorporated in the central part of a superconducting wire comprising a plurality of MgB_2 filaments arranged in a ring around the core. The barrier has to be made of a material capable of chemically, but not electrically insulate the copper core and it has to be compatible with MgB_2.

Mostly for economical reasons we are currently using pure iron for the barrier material in our standard materials. In Fig. 1, a typical transverse cross-section of this type of multifilamentary conductor is reported.

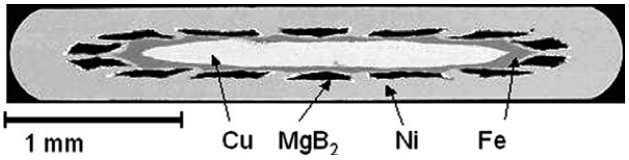

Fig. 1. Cross-section of a Cu-stabilized multifilamentary tape with 14 filaments.

The cross-section is 3.5 x 0.65 mm^2 (width x thickness) and the superconducting filling factor is just 8-9% of the entire cross section, i.e. about 0.2 mm^2. The first example of long length (1.53 km) of multifilamentary conductor was achieved in April 2005; at present, Columbus Superconductors is able to produce up to 1.78 km in a single piece by a reproducible process that has been already successfully completed more than 100 times. The picture of one of such unit lengths is shown in Fig. 2.

Fig. 2. 1.6 km standard stabilized multifilamentary MgB_2 tape in only one piece.

SUPERCONDUCTING PROPERTIES OF THE 'STANDARD' MULTIFILAMENTARY TAPES

The transport critical current I_c was measured using the standard four-probe method in varying magnetic field applied both perpendicular and parallel to the tape surface direction and at different temperatures. In Figs. 3 and 4 the I_c behaviour as a function of the temperature and of the magnetic field is reported as measured by Kitaguchi at NIMS in Tsukuba, Japan, on short multifilamentary conductors cut from a unit length exceeding 1.6 km.

The I_c value drops quickly as the magnetic field increases; nevertheless there is direct evidence of the reproducibility of the tape properties: the measurements performed on two different standard tapes cut at different places from the same batch of conductor give almost identical I_c values in magnetic field and at all temperatures (Fig. 4).

A number of practical applications would benefit from the possibility of employing an MgB_2 conductor to realize windings that can be operated in persistent mode. The potential for a superconducting material of sustaining relevant persistent currents for a long period of time is usually judged by analyzing the exponential n-factor of the *V–I* characteristics. A high *n*-factor (above 30) is generally considered as a proof for a highly homogeneous superconductor with rather strong pinning centres, and therefore low flux line relaxation should occur.

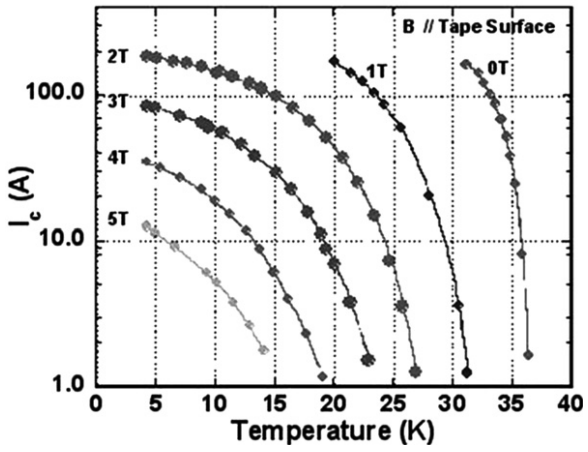

Fig. 3. I_c vs. T at different magnetic fields (parallel to the tape surface) for a standard multifilamentary MgB_2 tape.

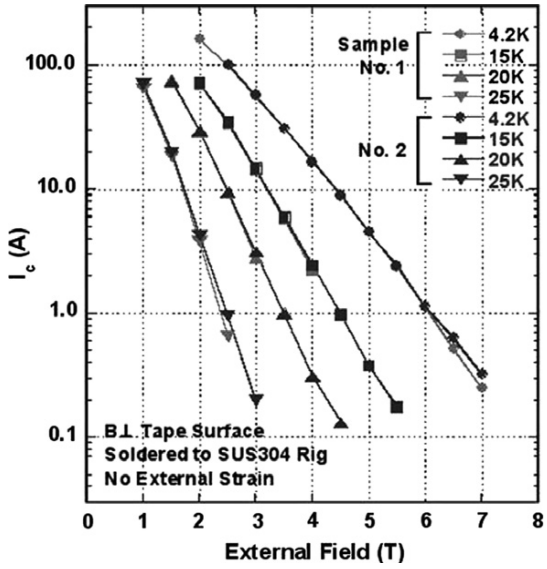

Fig. 4. Comparison between I_c vs. B at different temperatures for two samples cut from two different long conductors: different samples have reproducible performances.

So far, MgB_2 tapes present n-factor between 30 and 100 at fields below 5 T at 4.2 K, making it possible to conclude that the critical current density of MgB_2 tapes is not severely limited by microstructural defects and inhomogeneities along their length.

IMPROVEMENT OF THE PERFORMANCES OF THE CONDUCTOR

It is well known that in the production process of MgB_2 conductors, several parameters have a direct influence on J_c in the superconducting filaments, and that relevant transport properties can be achieved only after optimising the superconducting and/or microstructural properties of the initial powders and of the constituents composing the conductor itself.

The first example of long length (1.53 km) of multifilamentary MgB_2 conductor reached a transport critical current of about 110 A @ 20 K, 1.2 T (5 x 10^3 A/cm^2 of engineering J_c). Considering that the amount of superconducting material in this conductor was very low (filling factor of 10%), its J_c at 20 K, 1.2 T on the MgB_2 fraction was about 5 x 10^4 A/cm^2. To date, after about three years, the average results are in the order of 320 A @ 20 K, 1.2 T, i.e. almost a factor of three higher than at the beginning, translating into a J_c at 20 K, 1.2 T larger than 10^5 A/cm^2.

In parallel with the optimisation of the production parameters, an intense research activity on the powder production to achieve higher critical current densities by the ex situ process has been also carried out [11].

In particular, positive results were obtained (a) by the addition of SiC nanoparticles to B before the reaction with Mg, (b) by high-energy ball milling of MgB_2 powders alone and (c) together with the addition of SiC or C. As a test of the effective improvement of these modified powders, monofilamentary tapes were fabricated following the ex-situ route of the PIT method and their I_c values were measured.

The first attempt to improve the magnetic field performance of MgB_2 has been pursued through the SiC nanoparticles inclusion in the precursors during the MgB_2 powder synthesis. In Fig. 5 the transport I_c at 4.2 K in a magnetic field up to 13 T is reported with the field perpendicular and parallel to the tape surface for monofilamentary tapes prepared with undoped and SiC-doped powders.

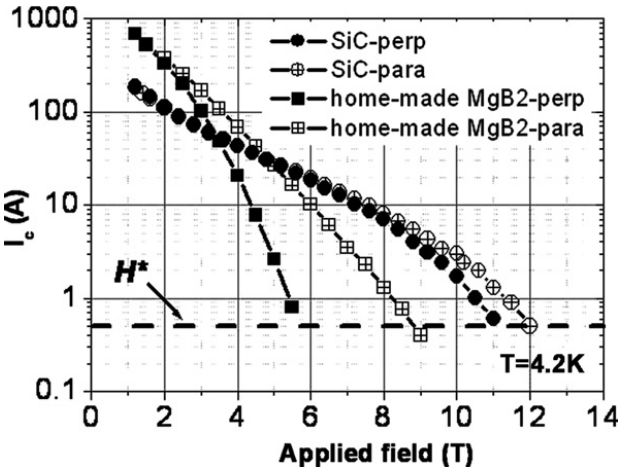

Fig. 5. Transport I_c vs. magnetic field at 4.2 K in both orientations for undoped MgB_2 and MgB_2 prepared from SiC-doped B.

We notice that even if I_c is clearly lower at low magnetic fields, the magnetic field dependence is significantly improved at high fields, while the anisotropy

of I_c, visible in our undoped tapes for magnetic field above 2–2.5 T, is significantly suppressed.

High-energy ball milling was performed on undoped MgB_2 powders in order to lower their particle size significantly and to improve the performances of the conductors in high magnetic fields by adding more effective grain boundary pinning. In Fig. 6, J_c as a function of the magnetic field is shown at 4.2 K (a) and 20 K (b) as extracted from the M–H loops with the applied field perpendicular to the tape surface, measured with a commercial 5.5 T MPMS Quantum Design Squid Magnetometer [12].

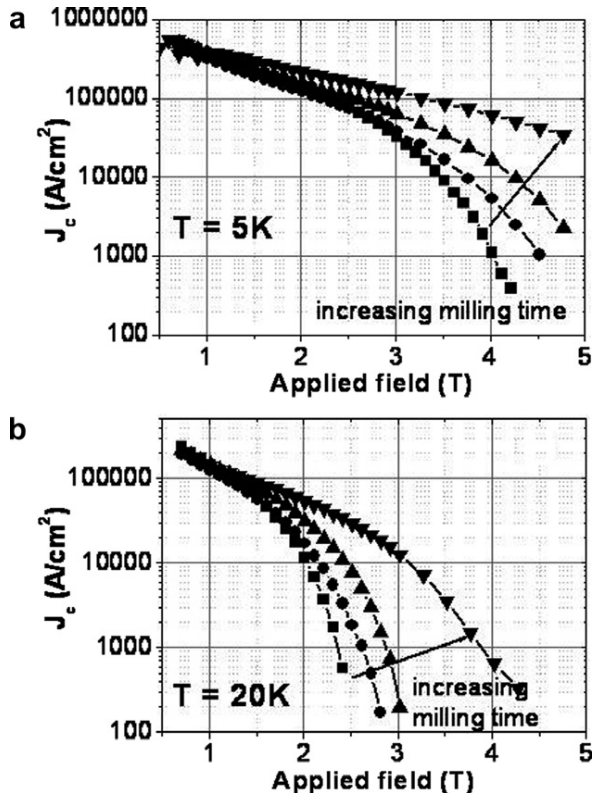

Fig. 6. Magnetic J_c vs. magnetic field at (a) 5 K and (b) 20 K in perpendicular orientation for undoped MgB_2 by increasing the milling time.

The magnetization measurements were performed at 5 K and 20 K on portions of conductors selected from the same wire batch used for the transport measurements. The magnetic field was applied both perpendicular and parallel to the tape surface. We notice that, while J_c is only slightly changing at low fields, a substantial improvement is obtained at higher fields by increasing the milling time, together with a significant decrease of the anisotropy.

This is better represented in Fig. 7, where the magnetic J_c is reported in both perpendicular and parallel orientation for the not milled MgB_2 and the sample prepared with the powders milled for the longest time, both at 5 K and 20 K.

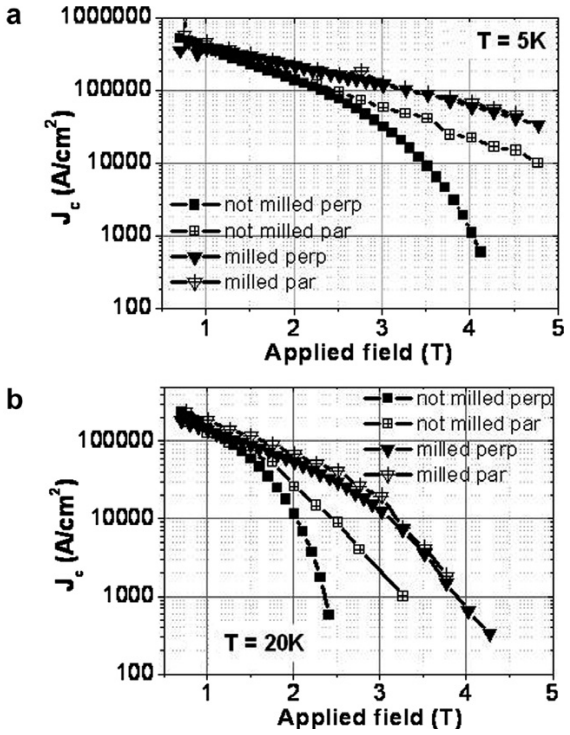

Fig. 7. J_c data extracted from the M–H loops in perpendicular and parallel orientation for the not milled and the highest-time milled samples at (a) 5 K and (b) 20 K.

There might be several explanations for this effect. First of all, the effect of the cold working procedure on the grain orientation is probably less relevant if the grains are much smaller. Furthermore, the current is determined by percolative paths that might be more relevant in the milled powders in which the grains are smaller, giving a stronger effect at higher field where the direct superconducting paths are suppressed.

Due to the strong improvement of the tape performances in magnetic field in samples prepared with ball milled powders, the procedure was also repeated with SiC nanoparticles and carbon additions.

In Fig. 8, the transport I_c is shown for a standard not milled sample and two tapes prepared with milled MgB_2 powders for the same duration but respectively with and without SiC addition, measured both in perpendicular and parallel orientation. We can see that the magnetic field behaviour is significantly improved in the doped powders with respect to the undoped case, and the anisotropy is strongly suppressed.

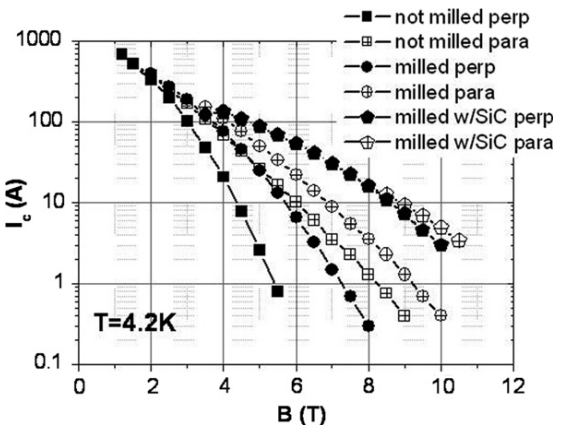

Fig. 8. Transport I_c in magnetic field at 4.2 K for tapes prepared with not milled powders compared with a tape prepared with milled MgB_2 powders and MgB_2 powders milled the same time with SiC nanoparticles.

The same procedure was followed with Carbon addition, that was ball-milled together with the MgB_2. In Fig. 9 the transport I_c is shown at 4.2 K in magnetic field for tapes made from the undoped powders, the milled powders, the MgB_2 milled for the same time and twice this time with addition of C. The effect of milling with C is even stronger concerning the behaviour at high magnetic fields.

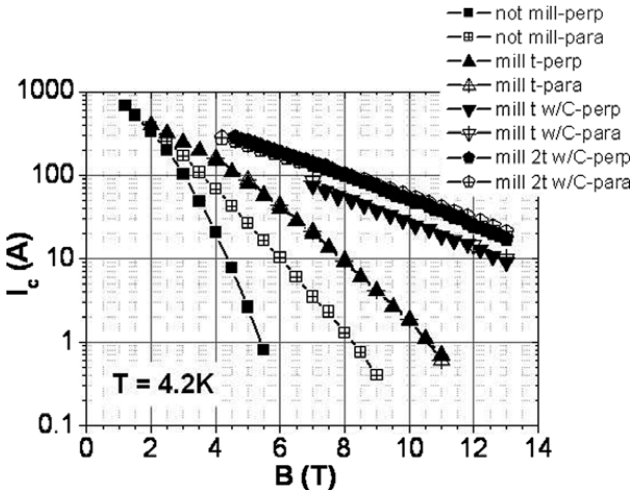

Fig. 9. Transport I_c in magnetic field at 4.2 K for tapes prepared with not milled powders compared with a tape prepared with milled MgB_2 powders, MgB_2 powders milled the same time and twice the time with carbon.

In the best sample, a critical current of 20 A – which corresponds to about 10^4 A/cm^2 – is reached at 13 T.

All these positive results – in particular, the use of milled powders with or without carbon – are being extended now to the production of large powder batches for the fabrication of long length multifilamentary conductors with improved properties.

The result of this R&D work confirms the possibility of a commercial use of MgB_2 in the high field region, considering in particular the very promising level of J_c of about 10^4 A/cm^2 reached at 13 T in liquid helium (Fig. 9).

REFERENCES

[1] W. Goldacker et al., Superconcond. Sci. Technol. 14 (2001) 787.

[2] G. Grasso, A. Malagoli, C. Ferdeghini, S. Roncallo, V. Braccini, A.S. Siri, Appl. Phys. Lett. 79 (2001) 230.

[3] H.L. Suo, C. Beneduce, X.D. Suo, R. Flu¨ kiger, Supercond. Sci. Technol. 15 (2002) 1058.

[4] R. Flukiger, P. Lezza, C. Beneduce, N. Musolino, H.L. Suo,Supercond. Sci. Technol. 16 (2003) 264.

[5] Y. Wang, T. Plackowski, A. Junod, Physica C 355 (2001) 179.

[6] S.X. Dou, S. Soltanian, J. Horvat, X.L. Wang, S.H. Zhou, M. Ionescu, H.K. Liu, P. Munroe, M. Tomsic, Appl. Phys. Lett. 81 (2002) 3419.

[7] S. Soltanian, X.L. Wang, I. Kusevic, E. Babic, A.H. Li, H.K. Liu, E.W. Collings, S.X. Dou, Physica C 361 (2001) 84.

[8] J. Wang, Y. Bugoslavsky, A. Berenov, L. Cowey, A.D. Caplin, L.F. Cohen, J.L. MacManus Driscoll, L.D. Cooley, X. Song, D.C. Larbalestier, Appl. Phys. Lett. 81 (2002) 2026.

[9] S. Jin, H. Mavoori, C. Bower, R.B. van Dover, Nature 411 (2001) 563.

[10] H. Kumakura, A. Matsumoto, H. Fujii, H. Kitaguchi, K. Togano, Physica C 382 (2002) 93.

[11] V. Braccini, A. Malagoli, A. Tumino, M. Vignolo, C. Bernini, C. Fanciulli, G. Romano, M. Tropeano, A.S. Siri, G. Grasso, IEEE Trans. Appl. Supercond., in press.

[12] V. Braccini, D. Nardelli, A. Malagoli, A. Tumino, C. Fanciulli, C. Bernini, A.S. Siri, G. Grasso, IEEE Trans. Appl. Supercond. 15 (2005) 3211.

THE REACTIVE Mg-LIQUID INFILTRATION TO OBTAIN LONG SUPERCONDUCTING MgB_2 CABLES

G.. Giunchi, EDISON SpA - R&D Division, Milano, Italy

Abstract

An alternative "in situ" process to the MgB_2 wire manufacturing is represented by the Reactive Mg-Liquid Infiltration (Mg-RLI) process [1], in which the precursor wire is constituted by a metallic sheath encasing a central Mg rod, surrounded by the B powders. We demonstrated that this peculiar "internal Mg" assembly is able to produce very dense superconducting material of high critical current density, with an acceptable fill factor, up to 0.28. Furthermore the Mg-RLI allows also to easily dope the MgB_2 material either by carbon or nanoSiC powders. In order to realize long cables with this technique, two different approaches may be applied. The first one relies on the assembly of thin wires, fine enough that the liquid Mg cannot freely percolate along the wire during the reaction, and the second one relies on the assembly of thick hollow wires, reacted with a continuous supply of Mg to avoid deficiency of Mg in some part of the precursor wire. Both techniques have been demonstrated feasible and the relative usefulness is discussed. As far as the large superconducting magnets are concerned, either for future physics applications or for fusion reactors, it will be evident the great advantage of the low weight of the MgB_2 wires, other than their good performances at intermediate high magnetic fields: typically of the order of 4T at temperatures of about 20K.

INTRODUCTION

The MgB_2 conductors are generally manufactured by a Powder in Tube process, performed either by "in situ" or by "ex situ" routes, so named in order to distinguish where the MgB_2 is formed. These two alternative processes gives rise to wires or tapes with different superconducting properties. Today the most performing MgB_2 wires have been obtained by the "in situ" route [2], but the realization of a long superconducting cable from the wire is a process which is not without difficulties. Furthermore, in order to build superconducting magnet prototypes one needs the more demanding "wind and react" technology. On the other hand, long superconducting tapes have been manufactured with the "ex situ" route. This route, even if less performing, has demonstrated its applicability in the manufacturing of large magnet prototypes through the more friendly "react and wind" technology [3]. Notwithstanding the strong competition in the field of the superconducting magnets, based on a field/temperature performance rather than on a cost/performance base, attempts to maximize the current density of the wires in higher magnetic fields or at higher temperatures have been done. For this reason the "in situ" route appears as the most appealing long term alternative to MgB_2 conductors, especially in view of the possibility, in a near future, to easily manufacture long superconducting cables. In the framework of the "in situ" processes, the Mg-RLI technology, applied to the MgB_2 superconducting wire manufacturing, presents important benefits, related to the high level of the superconducting properties of the resulting material, to the relatively easy processing scheme, that can be applied to several cabling options that will guarantee high mechanical strength, crucial for large magnets manufacturing.

THE Mg-RLI TECHNOLOGY FOR MgB_2 DENSE WIRES

In the conventional solid state reaction route, to obtain MgB_2, a mixture of B and Mg fine powders is usually reacted. Indeed, this procedure conducts to poorly sintered materials, when not used appropriate hot high pressure conditions. The presence of porosity has been well documented in the MgB_2 bulk and wires manufacturing, if the "in situ" case is applied in a conventional way, i.e. with powders mixing. This porosity is due to the poor sintering ability of the MgB_2 material together with the intrinsic volume reduction, of about 25% , during the reaction. The final product, at the best, will have a density of 75% of the theoretical value and this happens, no matter will be the size of the initial powders. To avoid this pitfall, we have introduced an innovative way to react the B and Mg: allowing the infiltration of liquid Mg inside a preform of B powders [4]. In such a way it is possible to obtain an almost full dense MgB_2 without external pressure. The possibility to realize the infiltration reaction inside the boron powder, even for high deepness, is based on unexpected chemical behaviour of the reactants. From our experience, two main driving forces favour this behaviour: a) the aforementioned volume contraction which induce more liquid to reach the reacting zone; b) the existence of a precursor phase of the reaction, when crystalline boron is used: a boron rich Mg boride, Mg_2B_{25}, that we have discovered and fully structurally characterized inside our MgB_2 material [5,6]. After reaction, the zone where the Mg was located remains practically void and the zone where the B powders ware stacked results fill of MgB_2. In the peculiar case of the wires manufacturing, it was possible to obtain, directly from the reaction, either hollow or Mg filled superconducting wires [7].

Wires features

The typical feature of a monofilament precursor wire, used in the Mg-RLI process, is displayed in Figure 1A. After reaction, two peculiar arrangements of the resulting monofilament superconducting wires are possible: a wire

with the hole filled by Mg metal, Figure 1B, and a wire with unfilled hole, Figure 1C. The fill factor, related to the MgB_2 superconducting material, is in both cases about 25%. Other features that may represent key variables in the wire processing and on the final wire properties, are:

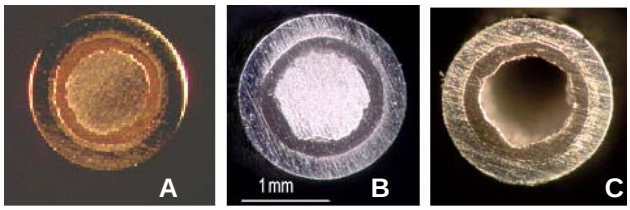

Figure 1: Optical microscope images of : A) precursor wire with internal Mg surrounded by B powder; B) superconductive MgB_2 wire with Mg-filled hole; C) superconductive MgB_2 wire with unfilled hole

- the material of the external metallic sheath, made by Fe or, preferably, by Monel;
- the presence or not of a thin interlayer of Nb, between the external sheath and the boron;
- the addition of appropriate doping elements to the B powders;
- the purity of the B powders.

The Mg filled wires have many interesting advantages: an higher thermal stability, an electrical shunt that can prevent damages during a quench, a more robust structure that protect the MgB_2 part from mechanical damaging .

MgB_2 microstructure

An example of the quality of the MgB_2 material resulting from the Mg-RLI process, applied to the wires, is illustrated in Figure 2, where the lack of porosity is highlighted. The pictures show the typical morphologies of the MgB_2 material deriving from two different boron powders. The wire A was obtained by using microcrystalline β-rhombohedral boron and the SEM image shows the presence of darker grains, few microns in size, embedded in the pure MgB_2 materials. These grains are constituted by a mixture of MgB_2 and of the impurity phase Mg_2B_{25}, being the superconducting phase the continuous matrix. With the aid of an aerial X-ray fluorescence microanalysis [6] we estimate a mean presence of the Mg_2B_{25} phase of about 7mol%, with a max percentage of 40% inside the darker grains. The wire B was obtained by using really amorphous boron: the corresponding SEM image shows very little amount of the boron-rich phase and also the aerial compositional analysis indicates a low percentage, about 0.3 mol%, of Mg_2B_{25} with respect to the MgB_2. In both wires there is no visible porosity in the MgB_2 part, at a SEM resolution, like in the cases when the material is prepared with high pressure apparatus.

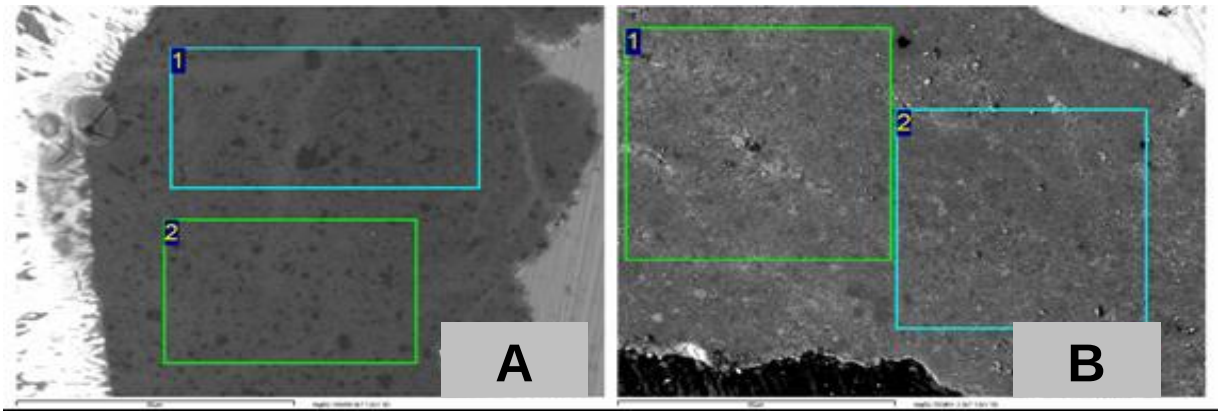

Figure 2: SEM images of the MgB_2 material : A) wire with Mg_2B_{25} impurity , B) wire without Mg_2B_{25} impurity

SUPERCONDUCTING PROPERTIES

The most important superconductive characteristic is represented by the critical current density as a function of magnetic field and of the temperature. Challenging conditions for the application of MgB_2 material may be a temperature of 20 K at a maximum magnetic field of 4T or a temperature of 4.2 K at a magnetic field of 10 T. The measurement of the offset of the R(T) curve, at different magnetic flux, gives a detailed information of the irreversibility field, B_{irr}, i.e. the upper limit of the practical magnetic flux that the material can sustain. The measured B_{irr}, for several wires obtained by Mg-RLI, shows a clear effect of the impurities on the improving of the irreversibility field, as expected by the increase of the pinning centres. For example, at 20 K, it has been evaluated the B_{irr} values of 4.8 , 6 and 6.1 T, respectively for the wires derived from amorphous B (no impurity), microcrystalline B (Mg_2B_{25} impurity) and amorphous B added by 6 at.% C [7].

As far as the critical current density is concerned, the actual performance of the Mg-RLI wires are on the edge of the best published results, even if a distinction must be done between short wires and commercial-like long wires or tapes. In Table 1 are collected some recent J_c values

measured for the best short wires or tapes produced by different research groups, taking as reference conditions (20 K @ 4 T) and (4.2 K @ 10 T). The large spread of values reflects many variables in the preparation: the use of B powders of different purity or grain size, different additives and different thermal treatments used by the various groups. In particular, among the Mg-RLI type wires, the very recent data of a Japanese team has substantially improved our old data by using 99.99% pure boron, a peculiar SiC additive and an optimized thermal treatment [8].
The best J_c values of the MgB_2 wires, at 4.2 K and 10 T, now compares favourably also with the best NbTi wires that amounts to about 200 A/mm^2 [9]

Table 1 - Best J_c values of MgB_2 short wires or tapes

MgB_2 short sample	Jc (20K@4T)	Jc (4.2K@10T)	Ref.
nanoSiC dop/PIT (Karlsruhe)	200	200	2
B4C+SiC dop/PIT (Geneve)	75	150	2
HE mill+nanoC/PIT(Dresden)	240	600	10
SiC dop/PIT (Ohio)	200*	200	11
HE mill/PIT (Genova)	8	40*	12
C dop/Mg-RLI (Milano)	60	80	15
SiC dop/Mg-RLI (Tsukuba)	-	400	8

Values in A/mm^2 * extrapolated value

As far as the km long wires or tapes are concerned, there are two products: i) a tape of Columbus Superconductors (I) and ii) a wire of Hypertech Research (US, Ohio). The tape is of the "ex situ" type and, at the moment, has been used to wind a magnet for MRI with the "react and wind" technique [12]. The wire is of the "in situ" type and has been used to wind some prototype magnets with the "wind and react" technique [13].
In Figure 3 the behaviour of $J_E(B)$ of these two conductors, at 4.2 K, is drawn, together with our Mg- RLI undoped monofilament wire of external diameter of 0.52 mm, measured on a meter long wire wound in an ITER barrel [14].

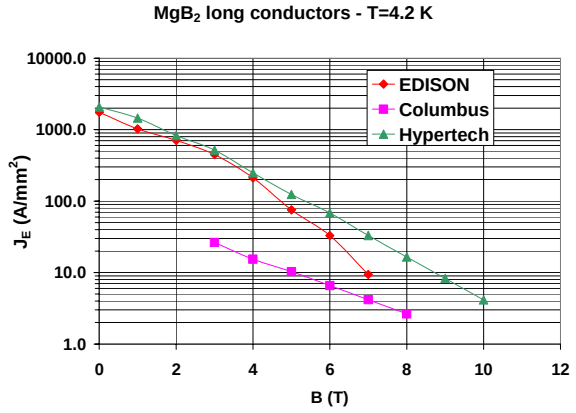

Figure 3: Engineering critical current density of a 0.53 mm diameter Mg-RLI monofilament wire , compared to the reported long commercial-like conductors

The rapid decrease of J_E at high field, for the reported Mg-RLI wire, is due to the absence in it of any additive to improve the pinning strength. Better results are expected with C or SiC addition, as already found in short samples [15].

Mg-RLI WIRES POTENTIALITY

Key characteristics of the practical superconducting wires, other than a high fill factor and a good mechanical strength, are a high thermal stability and low AC losses. One of the golden rules to implement both last characteristics is the reduction of the superconducting material thickness. In the conventional NbTi metallic superconductors this is achieved by a multi-filamentary assembly and by large reduction in the wire drawing operations. The brittle materials like A15 superconductors and High Temperature Superconductors, MgB_2 included, cannot be thinned in the superconducting state, so it is a common practice to make the precursor ductile wires thinner, and then to react them after drawing. This procedure exposes the resulting superconducting wires to mechanical failures, during the magnet winding or during its full in current operation, due to the magnetic forces. The thickness of the superconducting parts in such cases is limited and also the possibility to obtain stranded cables is confined to the thinner wires, excluding the tapes. We have verify the capability of the Mg-RLI wires to be thinned and stranded.

A Mg-RLI monofilament precursor wire, having the external sheath in Monel/Nb, has been successfully reduced to an external diameter of 0.250 mm, for a length of 6 m [14] maintaining the peculiar circular symmetry, as reported in Figure 4, of the original wire. In the corresponding reacted wire the MgB_2 has a thickness of about 20 micron and a SC area of about $8x10^{-3}$ mm^2, corresponding to a fill factor of about 16%.

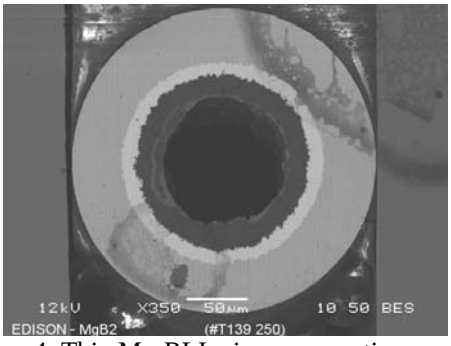

Figure 4: Thin Mg-RLI wire cross section

The drawability of the Mg-RLI precursor wire was quite unexpected, due to the well known brittleness of the metallic Mg. We have realized that the B powders acts as a lubricant for the Mg and prevent the crack initiation on its surface.

Concerning the stranded cables, we have tested a prototype cable made of 3 x 7 Mg-RLI monofilaments of 1 mm thickness each, with a twist pitch of about 50 mm, for a total cable length of 2 m. The precursor strand is shown in Figure 5. After reaction, the transport properties of the cable where measured by inductive method [16].

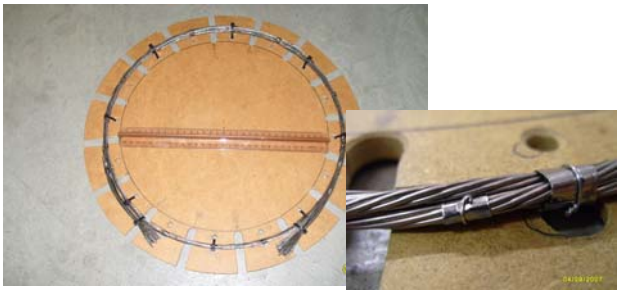

Figure 5: A 2m long stranded cable, made of 21 monofilament Mg-RLI wires

Typical values of the critical current are 17 kA and 5 kA at 14.6 K, and at 0 and 2 T field respectively. These values correspond to an engineering critical current density of the cable, at the respective conditions, of 400 A/mm^2 and 116 A/mm^2 [17].

CABLING OPTIONS

In order to build large superconductive magnets by MgB_2, useful for physics experiments or for fusion reactors, working at temperatures higher than 4.2 K, it will be crucial to design a superconducting cable that allows the "react and wind" techniques, but of substantially higher performances with respect to the actual one. In this respect the Mg-RLI technology offers, in principle, new options for cabling.

Hollow monofilament cable

This is the case in which the cable presents a hollow non superconducting core, eventually filled by stabilizing Mg. A cross section of such kind of cable is given in Figure 6. The external sheath can be Monel with a thin layer of Nb to avoid the MgB_2 contamination, during reaction. This design will be more useful in DC applications, due to the large thickness of the superconducting material.

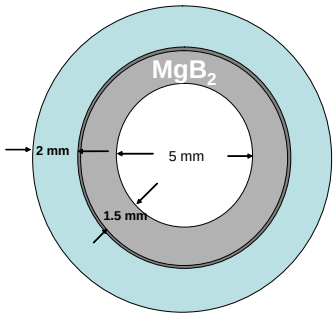

Figure 6: Cross section model of an hollow monofilament cable. The core can be filled by Mg for stabilizing purpose

The size of this cable may be tailored according to the needs. As an example if we consider the need to transport about 7 kA at 20K @ 4T, the estimation of the cable dimensions are OD= 12 mm, ID=5mm, assuming a fill factor of 30% and a critical current density optimal value of Jc = 200 A/mm^2. This cable should be manufactured starting from large composite billets, and then being reduced by drawing operations on long benches. Typically, in order to obtain a 900 m long cable one has to start from a 360 mm OD, 1 m long billet. The reaction of this cable can be done in a circular furnace of several meters in diameter, with Mg reservoir to supply Mg during reaction. The winding diameter of the cable in the furnace should be similar to the winding diameter of the final magnets, to avoid too large bending stress. .

Multifilament cable

This kind of cable is more similar to the usual multiwire cable, designed with the A15 materials. A typical cross section is modelled in Figure 7. The thin diameter of the component wires allows the use this cable also in AC conditions.

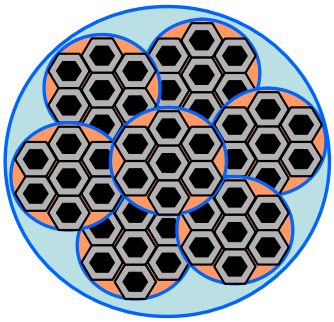

Figure 7: Model cross section of multiwire cable, made of 7x7 Mg-RLI wires

This kind of cable will have a max fill factor of 15%, due to the presence of multiple metallic sheaths. Therefore , returning to the previous example, if we assume the same OD of 12 mm and an assembly of 49 monofilaments, we can foresee the need of more performing MgB_2 wires, with J_c at least of about 400 A/mm^2 at 20 K and at 4 T, which is at the moment the limit of the MgB_2 best performances. Indeed this design will require also some stabilizing agent that could be copper braided between the MgB_2 filaments, which will introduce further penalty in the fill factor. The reaction of this kind of cable can be either similar to the previous one, with the entire cable inserted in a circular oven, or like a Cable in Conduit Conductor (CICC), where already reacted stranded wires are inserted in a tube. For this cabling design the drawing operations will not require long linear benches, but the manufacturing is expected to be more costly, due to the various assembling operations.

Massive cable

This cable design may be considered as an extension of the Mg-RLI technology that we apply to the MgB_2 bulk manufacturing. In peculiar cases, where high currents of the order of several tens of Amperes are available, and DC operation are used, one can design a magnet with a low number of spires. The cable, made of massive MgB_2, may have different types of cross section: rectangular, circular or of different shape, depending on the disposition of the reacting elements B and Mg inside the

metallic sheath. In Figure 8 two hypothetical model cross sections are shown.

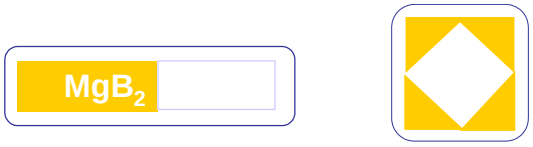

Figure 8: Model cable cross sections for massive MgB_2. The void part, inside the cable, can be alternatively filled with Mg.

With this cabling design a very high fill factor can be realized, of the order of 50%. The reaction, in such a case, will be strictly of the kind "wind and react". In order to compare the performances of this cabling with respect to the previous examples, assuming to realize the same magnetic field in the pancake, the needed Jc of the MgB_2 will be about 100 A/mm^2 at 20 K and at 4 T. The cross sectional area of the cable may be between 5-10 cm^2, transporting currents of 25-50 kA. The length of this kind of cable will be limited to about 100–200 meter.

DISCUSSION AND CONCLUSIONS

The use of the Mg-RLI technology in the manufacturing of the MgB_2 cables may open new possibilities in the design of the superconducting cables for large magnets. Here we sketched some possible designs, but many other options can be considered and analysed. Other than the cryogenic energy saving, a further key characteristics of the future MgB_2 magnets will be their low weight, with respect to the magnets made by the classical low temperature superconductors. It is possible to estimate the weight of the various MgB_2 pancake magnets obtainable by the different presented options of the Mg-RLI cables. It has been assumed as reference magnet a large pancake of 5 m of OD and with 20 x 10 cm^2 winding cross section. This kind of magnet may be the building block of an external poloidal magnet for fusion, where the operative conditions of 20 K and 4 T start to be acceptable. In Table 2 the weights of the superconducting MgB_2 magnets are compared with an equivalent copper type electromagnet.

Table 2 – Tentative superconductive pancakes of MgB_2 vs standard resistive solution (copper).

MgB_2 Cable	L (m)	Turn	I (kA)	Diam (mm)	Fill factor (%)	Jc (A/mm^2)	weight (kg)
multi	1809	120	7.2	12	15	420	1750
Mono	1809	120	7.2	12	30	210	1100
Mass.	150	10	87	90x 19	60	85	830
Copper	1809	120	7.2	12	100	60	2700

As it is evident the MgB_2 solutions are all largely lighter than the copper case. Between the MgB_2 options the massive cable is far the best in term of the needed critical current density and consequently in term of weight. Nevertheless the choice between the various MgB_2 designs will be mainly driven by the applications.
It will be of practical interest to initiate explorative programs to validate the various design options and, in the mean time, also the quality of the MgB_2 materials will be improved, especially referring to the behaviour in high magnetic fields.
Last but not least are the economic issues, that favours the MgB_2 not only due to the relatively low cost of the raw materials, but also for a relative friendly manufacturing. In this respect the Mg-RLI process appears to be one of the most affordable.

ACKNOWLEDGEMENTS

The author acknowledges the interest of Prof. Bruno Coppi in the development of the Mg-RLI technology, in view of the application of MgB_2 cables to some fusion poloidal magnets for the IGNITOR project.

Mike Sumption of the Ohio State University and Mike Tomsic of Hypertech Research are acknowledged for the fine wire manufacturing and characterization.

REFERENCES

[1] G. Giunchi, et al., "High performance new MgB_2 superconducting hollow wires" Supercond. Sci. Techn. 16 (2003) 285.
[2] M. Dhalle, "Highlight of the EU FP6 HIPERMAG strep", Enschede (2008).
[3] V. Braccini , D. Nardelli , R. Penco , G. Grasso, "Development of ex situ processed MgB_2 wires and their applications to magnets" Physica C 456 (2007) 209.
[4] G. Giunchi, "High density MgB_2 obtained by reactive liquid Mg infiltration" International Journal of Modern Physics B 17 (2003) 453.
[5] G. Giunchi, L. Malpezzi, N. Masciocchi "A new crystalline phase of the boron-rich metal-boride family: the Mg_2B_{25} species" Solid State Sciences 10 (2006) 1202.
[6] G. Giunchi, C. Orecchia, L. Malpezzi, N. Masciocchi "Analysis of the minority crystalline phases in bulk superconducting MgB_2 obtained by reactive liquid Mg infiltration" Physica C 433 (2006) 182.
[7] G. Giunchi, et al., "Superconducting characteristics of MgB_2 wires obtained by Reactive Liquid Mg Infiltration" Mater. Res. Soc. Symp. Proc. 946 (2006) 04-03.
[8] J. M. Hur, K. Togano, A. Matsumoto, H. Kumakura, H. Wada, K. Kimura "Fabrication of high performance MgB_2 wires by an internal Mg diffusion process" Cond-mat (2007) 0712-2273.
[9] 2004 Outokumpu Test Report for OK54 superconductor No.97307, spool 10660
[10] W. Häßler, M. Herrmann, C. Rodig, M. Schubert, K. Nenkov and B. Holzapfel "Further increase of the

critical current density of MgB_2 tapes with nanocarbon-doped mechanically alloyed precursor" Supercond. Sci. Techn. 21 (2008) 062001.
[11] M. D. Sumption, M. Bhatia, M. Rindfleisch, M. Tomsic and E. W. Collings, "Transport properties of multifilamentary, *in situ* route, Cu-stabilized MgB_2 strands: one metre segments and the $J_c(B, T)$ dependence of short samples" Supercond. Sci. Techn. 19 (2006) 155.
[12] A. Malagoli et al., Adv. Sci. Techn. 47 (2006) 238.
[13] M. Tomsic et al., Physica C 456 (2007) 203.
[14] M. Rindfleisch (Hypertech Research, OH) private communication (2008).
[15] G. Giunchi, G. Ripamonti, E. Perini, T. Cavallin, E. Bassani, "Advancements in the Reactive Liquid Mg Infiltration technique to produce long superconducting MgB_2 tubular wires" IEEE Trans. Appl. Supercond. 17 (2007) 2761.
[16] R. Musenich, M. Greco, M. Razeti and G. Tavilla "Electrical characterization of a multi-strand MgB_2 cable" Supercond. Sci. Techn. 20 (2007) 235.
[17] R. Musenich, private communication (2007)

ADVANCES IN HTS MATERIALS

P. Tixador, INP, G2Elab / Institut Néel, Grenoble, France.

Abstract

HTS (High Temperature Superconductor) offer great opportunities to reach higher magnetic flux densities when compared with LTS (Low Temperature Superconductor). The upper generally accepted limit of 23 T using Nb3Sn can be overstep with HTS.

HTS Bi-2212 round wires have shown critical current densities as higher than 1000 MA/m^2 under 45 T at 4.2 K. The road for very high fields is open. The round shape suits rather well for magnets, especially with high current specifications since the "classical" high current cables (Rutherford, CIC) require elementary round conductor. The absence of current anisotropy in round conductor is another advantage.

The YBaCuO coated conductors (HTS second generation conductors) show large opportunities for high fields. Their higher mechanical performances (IBAD process) compared to Bi conductor bring advantages for high field magnets.

The protection of HTS magnet is an identified issue since degradations have been observed in several magnets after a quench. A state of the art of HTS materials, especially in Europe, will be presented.

INTRODUCTION

The demand for very high field superconducting magnets increases in several fields such as high energy physics or NMR [1]. Fig. 1 shows the critical characteristics, the basic superconducting property for magnets. From this figure, it is clear that LTS have a limit at about 23 T whereas HTS show no limitation in terms of transport properties up to 45 T at least.

In order to design a superconducting (SC) magnet, one should take into account other parameters than the critical characteristic. Stability and protection are two other relevant parameters [2]. The MQZ (Minimum Propagation Zone) and the propagation velocity of the normal zone are two quantitative quantities for stability and protection respectively. The specific heat plays a predominant part but with opposite sense. A large specific heat improves the stability (higher MQZ) but makes the protection more difficult (lower propagation velocity). The specific heats of materials increase rapidly with temperature (Fig. 2). So the operation at higher temperatures enhances the stability but the protection will be delicate.

Mechanics is fundamental for high field magnets where the electromagnetic Lorentz forces are huge. The stress level is higher than about 150 MPa. The SC wires and conductors should withstand very high stresses/deformations without transport property degradation. HTS are brittle ceramics and the wire and conductor architectures must manage the force.

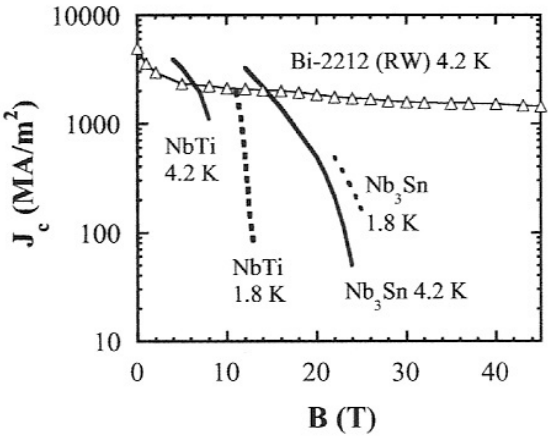

Figure 1: Critical characteristics for NbTi and Nb_3Sn (LTS) and Bi-2212 (HTS).

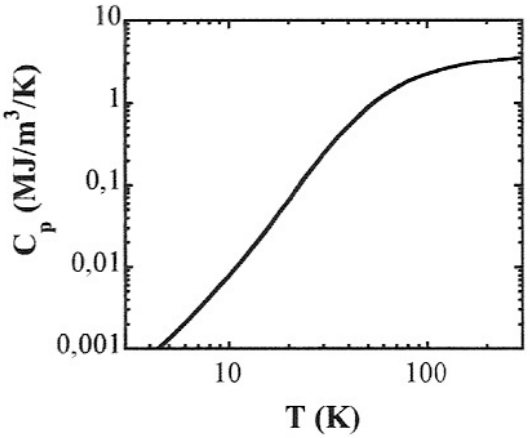

Figure 2: Specific heat per unit volume for copper versus temperature

HTS MATERIALS AND WIRES

After the early years devoted to new superconductor discovery, researches have focused mainly on the development of wires with the two compounds without noxious elements: BiSrCaCuO (BSCCO) and YBaCuO (YBCO). This task has been particularly difficult due to the complexity of these materials. Moreover, the wire should remain inexpensive to be used in other applications than niches.

Fig. 3 shows the irreversibility lines for BSCCO and YBCO. Above the irreversibility field (H*) the superconductor dissipates energy and shows then little interest for magnets. The irreversibility line of YBCO is better than the BSCCO one (Fig. 3) despite a lower critical temperature (92 K compared to 110 K (Bi-2223)). But the conditions for YBCO to carry a high transport are

much more severe than for BSCCO. That is why the first generation (1G) of high Tc wires uses BSCCO. 1G is produced in kilometer lengths since some years [3, 4]. YBCO wires are the 2nd generation (2G) and the first hectometre lengths are produced [5, 6, 7, 8].

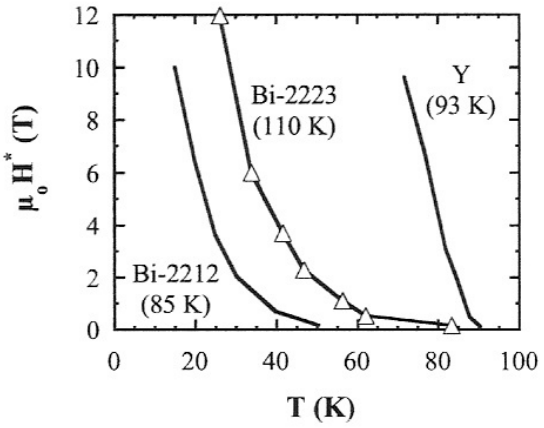

Figure 3: Irreversibility lines for Y, Bi-2212 and Bi-2223 (critical temperatures).

1G BI PIT WIRES

1G uses the BiSrCaCuO compound in the form of fine powder embeded in silver tubes (PIT (Powder In Tube) technique). The wire undergoes mechanical and heat treatments. The 1G process is basically a metallurgical one (drawing, rolling and annealing). The wire forms a classical multifilament composite (Fig. 4).

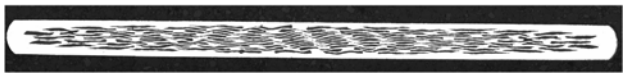

Figure 4: Cross section of a PIT Bi tape from Nexans (Nexans picture).

Two stœchiometries are industrially developed: Bi2Sr2CaCu2O (Bi-2212) and Bi2Sr2Ca2Cu3O (Bi-2223). The Bi-2212 shows better transport properties compared to Bi-2223 at temperatures lower than about 15 K even when the field is in the favourable direction for the tape (longitudinal direction, parallel to the ab plans). Fig. 5 shows some critical characteristics for 1G at 4.2 K.

Bi-2212 may be produced as tapes or round wires [9] (Fig. 6). Only Bi-2223 tapes (Fig. 4) can be elaborated. Tapes show anisotropy (Fig. 5) with a higher sensitivity to the transverse field, parallel to the c axis. Round wires are isotropic and better suit for magnet design. Bi-2212 round wires may be used in conventional high current conductor.

Fig. 7 shows a Rutherford cable with 30 Bi-2212 wires [10]. To date the maximum current-carrying capacity of another Bi-2212 Rutherford cable from Showa was 12 kA at 4.2 K in a back-up field of 0.6 T [11].

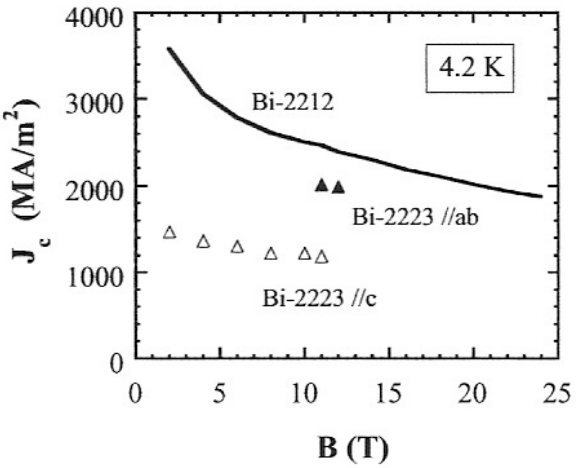

Figure 5: Critical characteristics for Bi-2212 and Bi2223 (longitudinal and transverse directions) at 4.2 K, from D. Larbalestier (Bi-2212: OST round wire, Bi-2223: Sumitomo tape).

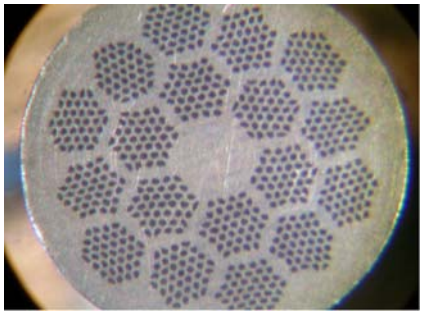

Figure 6: Cross section of a PIT Bi round wire from Nexans (CEA/IRFU picture).

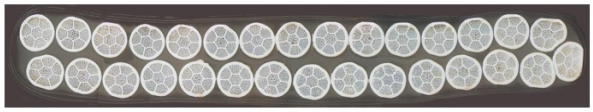

Figure 7: Cross section of a 30 Bi strand Rutherford cable from Nexans (Nexans picture).

Bi-2223 wires must be reacted before winding (R & W technique). For Bi-2212 the reaction may be before or after the winding (W & R or R & W techniques). In general the winding with unreacted wire is preferred since the fragility is then minimum. The bend diameter is also minimum with the W & R process. Dipoles or quadrupoles may experience very short bend diameters in the coil ends. W & R Bi-2212 coils show problems: some conductor leakage can occur. The reaction still has to be optimized.

To improve the mechanical properties of 1G wires an Ag alloy (AgMg) sheath is used but the critical tensile stress remains around 100 MPa. The critical stress is the stress at which the critical current degradation is 5 % and reversible. The tensile critical stress may be increased up

to 250 MPa by reinforcement by soldering stainless steel tapes to the 1G wire.

The degradation of Bi PIT magnets after a quench remains an issue [12]. The relevant parameter is not only the hot spot temperature but dT/dx and dT/dt also play important parts [13].

1G wires remain expensive due to the Ag matrix and they have to operate at low temperatures under magnetic fields (Fig. 3). 2G are more interesting from these two points of view and concentrate the main researches and developments about HTS wires.

2G Y COATED CONDUCTORS

The requirements to elaborate a flexible wire with YBCO are much more stringent than for 1G. To fulfil these severe conditions, YBCO is deposited under the form of a very thin epitaxial layer (µm) on a flexible metallic substrate (highly biaxially textured Ni alloy (RABiTS route (Rolling Assisted Bi-axially Textured Substrate)) or stainless steel with a highly biaxially textured layer (YSZ, MGO) (IBAD route (Ion-Beam-Assisted Deposition)) through buffer layers so their name: coated conductors (Fig. 8). A shunt layer (Ag, Au) ends the stack and the coated conductor generally is encapsuled by a normal metal (Cu or stainless steel). The architecture (number and nature of layers) may be complex (up to a dozen layers) and still is under researches and investigations.

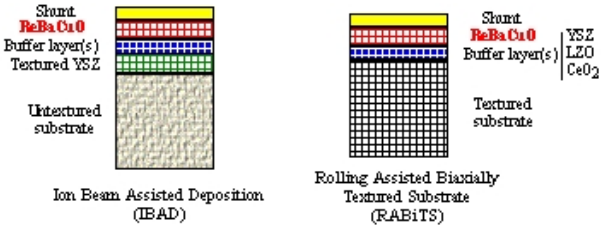

Figure 8: The two main routes of 2G Y coated conductors.

The 2G process associates metallurgical process for the substrate and thin film technology for all the layers deposited on the substrate.YBCO coated conductor are always reacted before winding.YBCO is only a very small fraction of the wire (1% or less), but due to the huge critical current densities (typically higher than 10 000 MA/m^2, 77 K, 0 T) the wire transport current remains high. It is usually expressed in Ampere per unit width of the wire (A/cm-w) to get rid of the superconducting fraction.

Company (Country)	Conductor architecture	Short sample		Long lengths		
		I_c (A/cm)	J_c (MA/m^2)	I_c (A/cm)	Length (m)	I_c*L (A/m)
SuperPower-inc (USA)	$YBCO_{MOCVD}/LMO_{PLD}/MgO_{PLD}/MgO_{IBAD}$	721	22 000	190	790	150 100
SuperPower-inc (USA)	$YBCO_{MOCVD}/LMO_{PLD}/MgO_{PLD}/MgO_{IBAD}$	721	22 000	362	103	37 284
Fujikura (Japan)	$GdBCO_{PLD}/CeO_{2PLD}/GZO_{IBAD}$	540	22 000	305	368	112 166
SRL-ISTEC (Japan)	$YBCO_{MOCVD}/CeO_{2PLD}/GZO_{IBAD}$	480	12 000	213	245	52 185
SRL-ISTEC (Japan)	$YBCO_{MOD}/CeO_{2PLD}/GZO_{IBAD}$	735	24 000	250	56	14 000
AMSC (USA)	$YBCO_{MOD}/CeO_{2PLD}/YSZ_{PLD}/Y_2O_{3\ PLD}/NiW_{RABiTS}$	560	40 000	400	94	32 900
EHTS (Germany)	$YBCO_{PLD}/CeO_{2PLD}/YSZ_{IBAD}$	574	36 000	253	100	25 300

Table 1: some best performances of coated conductors throughout the world (spring 2008).

Table 1 gives the state of the art of the coated conductor at the beginning of 2008. It specifies the deposition techniques.2G cost is potentially low with a possible operation under magnetic field at 50 – 60 K (Fig. 3). The researches are extremely active throughout the word about 2G whose prospective applications are much broader compared to 1G. Chemical deposition methods (MOD, i.e., Metal-Organic Deposition), (MOCVD, i.e., Metal-Organic Chemical Vapor Deposition) [14] are particularly suit for low cost processes when compared to physical deposition methods (PLD, i.e., Pulsed Laser Deposition), (TE, i.e., Thermal Evaporation), …, which are very effective but more expensive.

The mechanical behaviour of 2G is mainly defined by the substrate. The IBAD route with a stainless steel substrate shows higher performances compared to the

RABiTS route with a Ni alloy substrate. IBAD tapes show a critical tensile stress higher than 600 MPa but RABiTS tapes show already tensile values higher than 300 MPa.

For instance 2G are only produced under the form of an anisotropic tape. This geometry is not ideal for a SC magnet. Round or lightly aspected shape with no critical current anisotropy is preferred. High current conductors are not easy to design, even if Roebel bars have been realized [15, 16].

As in any superconductors, the vortex pinning determines the critical current density in coated conductors [17]. Due to the very low coherence length in YBaCuO nanoscale vortex pinning centers are required. BZO (BaZrO3) nanodots meet these requirements and improve a lot the transport current capacity under field. Enhancement of a factor 20 at 1 T and 77 K has been measured [18], increasing the irreversibility field up to 10.7 T at 77 K. These results show that the current capacities of coated conductors are still not reached and that substantial improvements are in progress.

CONCLUSIONS

HTS show excellent abilities for very high field magnets (higher than about 23 T) when LTS can no more be used. Bi2Sr2CaCu2O round wires have a critical current density larger than 1000 MA/m2 below 45 T at 4.2 K. The stability of HTS magnets operating at temperatures above 20 K is improved compared to LTS ones. But quench detecting and magnet protection pose some problems and are an issue today.

The Bi-2212 round wire is an excellent candidate for high field magnets. In addition to its excellent transport isotropic properties, its round form suits well for magnet design and high current conductors (Rutherford cable, CICC). Several Rutherford cables have been already realized. Indeed, Bi-2212 round wires are for a niche market and pose then a problem for industrial production.

YBaCuO coated conductors concentrate the main effort about HTS conductor researches and developments due to a potential lower cost compared to Bi and a more favourable irreversibility line. The huge challenges for these materials to carry currents have been overstepped and hectometer lengths are now available with high performances. The excellent mechanical properties especially for the IBAD route are an advantage for high field magnets. The present flat tape form of the coated conductors with anisotropic properties is not ideal for magnets.

HTS are always not well understood and large improvements are still possible. They are clearly already excellent candidates for high field magnets.

REFERENCES

[1] J. Schwartz, "The how & why of high field SC solenoids", MT 20 plenary talk, Philadelphia, Sept 2007.

J. Schwartz, T. Effio, X. Liu, Q. V. Le, A. L. Mbaruku, H. J. Schneider-Muntau, T. Shen, H. Song, U. P. Trociewitz, X. Wang, H. W. Weijers, "High Field Superconducting Solenoids Via High Temperature Superconductors", IEEE Transactions on Applied Superconductivity, vol. 18, 2008, pp. 70-81.

[2] M.N. Wilson, "Stabilization, protection and current density : some general observations and speculations", Cryogenics, vol. 31, 1991, pp. 449-503.

[3] B. Huang, X.Y. Cai, G.N. Riley, D. Larbalestier, D. Yu, M. Teplitsky, A. Otto, S. Fescher, R.D. Parrella, "Progress in BI-2223 tape performance", Advances in cryogenic engineering, vol. 48, 2002, pp. 717-723.

[4] N. Ayai, M. Kikuchi, K. Yamazaki, S. Kobayashi, S. Yamade, E. Ueno, J. Fujikami, T. Kato, K. Hayashi, K. Sato, R. Hata, J. Iihara, K. Yamaguchi, J. Shimoyama, "The Bi-2223 Superconducting Wires With 200A-Class Critical Current" IEEE Transactions on Applied Superconductivity, vol. 17, 2007, pp. 3075-3078.

[5] A. P Malozemoff, S Fleshler , M Rupich, C Thieme, X Li, W Zhang, A Otto, J Maguire, D Folts, J Yuan, H-P Kraemer, W Schmidt, M Wohlfart, H-W Neumueller, "Progress in high temperature superconductor coated conductors and their applications", Superconductor Science and Technology, vol. 21, 2008, 034005 (7 pp).

[6] Y. Shiohara, M. Yoshizumi, T. Izumi, Y. Yamada, "Present status and future prospect of coated conductor development and its application in Japan", Superconductor Science and Technology, vol. 21, 2008, 034002 (7pp).

[7] V. Selvamanickam, Y. Chen, X. Xiong, Y.Y. Xie, J.L. Reeves, X. Zhang, Y. Quiao, K.P. Lenseth, R M. Schmidt, A. Rar, D.W. Hazelton, K. Tekletsadik, "Recent progress in second generation HTS conductor scale-up at Superpower, IEEE Transactions on Applied Superconductivity, vol. 17, 2007, pp. 3231-3234.

[8] A. Usoskin, L. Kirshhoff, J. K,noke, B. Prause, A. Rutt, V. Selsjij, D.E. Farrell, "Processing of long length YBCO coated conductors based on stainless steel tapes", IEEE Transactions on Applied Superconductivity, vol. 17, 2007, pp. 3235-3238.

[9] H. Miao, K. R. Marke, M. Meinesz, B. Czabaj, S. Hong, "Round Multifilament Bi-2212/Ag wire development for high field magnet applications", Materials Science Forum, vol. 546-549, 2007, pp. 1927-1930.

[10] D. W. Ha, S. C. Kim, J. G. Oh, H. S. Ha, N. J. Lee, K. J. Song, T. H. Kim, R. K. Ko, H. S. Kim, S.K. Park, S. K. Lee, Y. M. Roh, S.S. Oh, "Influence of Filament Number on Workability and Critical Current Density of Bi-2212/Ag Superconducting wires", IEEE Transactions on Applied Superconductivity, vol. 17, 2007, pp. 3099-3102.

[11] T. Hasegawa, J. Nishioka, N. Ohtani, Y. Hikichi, R. Scanlan, R. Gupta, N. Hirano, S. Nagaya, "12 kA HTS Rutherford Cable," IEEE Transactions on Applied Superconductivity, vol. 14, 2004, pp. 1066-1069.

[12] S.R. Foltyn, L. Civale, J.L. Macmanus-Driscoll, Q.X. Jia, B. Maiorov, H. Wang, M. Maley, "Material science challenges for high temperature superconductor wire", Nature materials, vol. 6, 2007, pp. 367-373.

[13] J. Gutierrez, A. Llordés, J. Gazquez, M. Cibert, N. Roma, S. Ricart, A. Pomar, F. Sandiumenge, N. Mestres, T. Puig, X. Obradors, "Strong isotropic flux pinning in solution-derived YBaCuO nanocomposite superconductor films", Nature materials, vol. 6, 2007, pp. 631-642.

[14] X. Obradors, T. Puig, A. Pomar, F. Sandiumenge, N. Mestres, M. Coll, A. Cavallaro, N. Roma, J. Gazquez, J.C. Gonzalez, O. Castano, J. Gutierrez, A. Palau, K. Zalamova, S. Morlens, A. Hassini, M. Gibert., S. Ricart, J.M. Moreto, S. Pinol, D. Isfort, J. Bock, "Progress towards all-chemical superconducting YBaCuO coated conductors", Superconductor Science and Technology, vol. 19, 2006, pp. S13-S26

[15] W. Goldaker, R. Nast, G. Kotzyba, S.I. Schlachter, A. Frank, B. Ringsdorf, C. Schmidt and P. Komarek: Journal of Physics: Conference series 43, 2006, pp. 901-904.

[16] U.P. Trociewitz, B. Czabaj, S. Hong, Y. Huang, D.C. Knol, D.C. Larbalestier, W.D. Markiewicz, H.Miao, M. Meinesz, X. Wang, J. Schwartz, "Quench studies on a layer-wound Bi2Sr2CaCu2Ox /AgX coil at 4.2 K", Superconductor Science and Technology, vol. 21, 2008, 025015 (5 pp).

[17] N.J. Long, R. Badcock, P. Beck, M. Mulholland, N. Ross, M. Staines, H. Sun, J. Hamilton, R. G. Buckley, "Narrow Strand YBCO Roebel Cable for Lowered AC Loss", IEEE/CSC & ESAS European Superconductivity News, No. 3, January 2008.

[18] T. Effio, U.P. Trociewitz, X. Wangand, J. Schwartz, "Quench induced degradation in Bi2Sr2CaCu2O8+x tape conductors", Superconductor Science and Technology, vol. 21, 2008, 045010 (10 pp).

HTS APPLICATIONS

M. Noe, R. Heller, W.H. Fietz, W. Goldacker, Th. Schneider, Forschungszentrum Karlsruhe, Karlsruhe, Germany

Abstract

Superconductivity has found many attractive applications in medicine, science, power systems, engineering, transport and electronics. One of the most prominent applications of superconductivity are superconducting magnets e.g. MRI magnets, NMR magnets, accelerator magnets, and magnets for fusion; most applications still use low temperature superconductors.

Since the discovery of high temperature superconductivity (HTS) in 1986 there has been a tremendous progress in R&D of HTS material, wires and applications. Especially for power system applications, HTS offers considerable economic benefits. Many HTS demonstrator or prototype applications have been built and successfully tested, and some HTS applications like cables and superconducting fault current limiters seem very close to commercialisation. This paper gives an overview about the present and future HTS applications in power applications, high field magnets and current leads. In addition results of the Forschungszentrum Karlsruhe program to develop HTS technology for magnet applications are presented. A special focus is set on the development of HTS magnets for fusion application.

INTRODUCTION TO HTS APPLICATIONS

There are several families of HTS available. Hg- or Tl- compounds offer the highest T_c values of 134 K and 125 K, respectively, but for reason of environmental aspects BSCCO and YBCO superconductors with T_c values of approx. 110 K and 92 K, respectively, are in the focus of actual development. An overview about High-T_c superconducting materials with a focus on power application is given in [1].

The common feature of all HTS materials is the presence of CuO_2 layers that host the superconductivity. Perpendicular to these planes it is very difficult to achieve a good conductivity which causes a strong anisotropy. Thus the critical current is anisotropic as well as its dependence on the magnetic field. For the field anisotropy calculated from $H_{c2,//}$ over $H_{c2,\perp}$ (parallel and perpendicular to the superconducting CuO_2 planes) a factor of 5–7 for YBCO, and 50–200 for Bi-2223 has been found [2]. Therefore a strong texture in the HTS material is necessary to achieve good transport properties. Grain boundaries in the grown materials can cause additional problems for transport currents [1, 3]. Only when neighboring grains have almost the same orientation e.g. only small angle grain boundaries are present, a high critical current is achieved. These properties demand for an almost perfect texture of the HTS materials.

BSCCO HTS-tapes are commercially available nowadays and can be used in low and high field applications depending on the temperature. BSCCO is nowadays ready for technical applications but the operating temperature has to be adjusted to the applied magnetic field. At temperatures of 77 K, external fields are very detrimental to the critical current j_c, i.e., the maximum current that can be carried by the conductor. In the case of low magnetic fields, e.g. in self-field like in power transfer lines or current leads, such a conductor consisting of BSCCO-2223 in a stabilizing silver matrix is capable to carry a typical current of 80 A for a 4 mm wide and 0.2 mm thick tape. At temperatures of approx. 20 K and below these BSCCO tapes can be used even in much higher external fields (e.g. at 12 Tesla which is the field of the ITER TF coils).

For YBCO conductors the basic problems are solved for short samples and the transfer to long lengths in an industrial process is the challenge now. Due to the fast progress of coated conductor development in recent years and the promising cost perspectives, special interest is focused on this material which is a good candidate for present and future HTS applications.

POWER APPLICATIONS

The applications in which superconductivity has the potential to be effective in an electric power system can be separated into two general classes [4]. The first class includes cables, motors, generators, and transformers where superconductors replace resistive conductors. The second class includes technologies that will be enabled by superconductivity and that have little or at most limited capability if conventional materials are used. Examples are superconducting magnetic energy storage (SMES) and fault-current limiters (FCLs).

Many demonstrator and prototype tests showed the technical feasibility of HTS in power system applications; examples are rotating machines, cables, transformers, current limiters, SMES. Superconducting cables and superconducting fault current limiters seem very close to commercialisation. Power system applications may open a continuous demand for HTS and therefore accelerate the R&D for HTS material and tapes. At a cost level of less than 10 k€ per kA a broad application of HTS devices seems very likely. Compared to conventional solutions the HTS devices should be comparable in cost but the reliability and the problem-free integration has to be demonstrated.

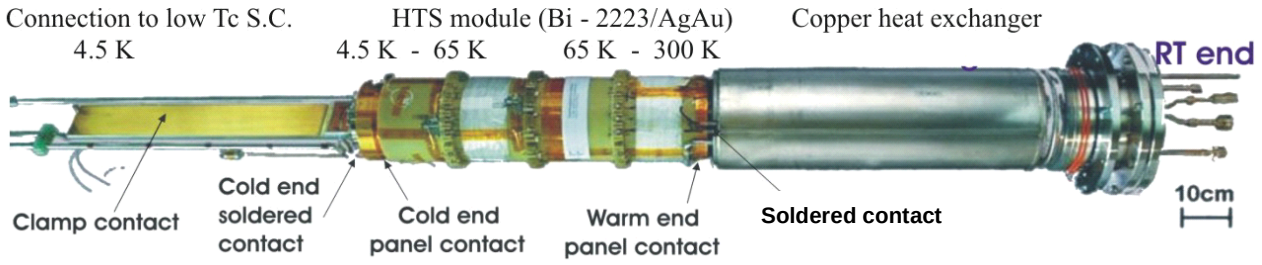

Figure 1: 68 kA HTS current lead developed at the Forschungszentrum Karlsruhe using Bi-2223/AgAu tape.

HTS FOR CURRENT LEADS

Current leads are the component of a sc magnet system where commercialized HTS material can be used because the external field is usually well below 0.5 T. A large scale application for an HTS current lead (up to 13 kA) was developed for LHC [9]. A second example is the ITER HTS current lead demonstrator (HTS-CL, 68 kA) which has been developed and built by the Forschungszentrum Karlsruhe in collaboration with the Centre Recherches en Physique des Plasmas, Switzerland in the frame of an EU Fusion Technology task. This HTS-CL consists of two main parts, the HTS module that uses BSCOO-2223/AgAu tapes embedded in stainless steel and the copper heat exchanger. The HTS module is cooled by heat conduction from the 4.5 K end and covers the temperature range between 4.5 K and 65 K. The conventional heat exchanger covers the temperature range from 65 K to room temperature and is actively cooled by 50 K He gas. At the 4.5 K end, a clamp contact provides the connection to the superconducting bus bar. A picture of the HTS-CL is shown in Fig. 1.

The maximum steady state current of the HTS-CL was 80 kA which exceeds the value of 68 kA needed for the ITER TF coils. In addition it was shown that even when the He-cooling has been blocked, a current of 68 kA could be carried for more then 6 minutes which shows the stability of this current lead. Last but not least it could be shown that the He-refrigerator power consumption was reduced by a factor of 5 compared to conventional current leads. Details of the development and test results can be found in [10-13]. This development has brought ITER to the decision to use HTS-CL for the ITER magnet system which can save about 22 kW refrigerator power. In the meantime, other fusion devices under operation or construction like EAST (China), W7-X (Germany) and JT60-SA (Japan) plan to use HTS current leads [14-16].

HTS FOR HIGH FIELD MAGNETS

One key application for HTS is high field magnets. Here the main emphasis is not the operation at higher temperature but to reach high magnetic field levels which are beyond the limit of low temperature superconductors. Possible areas are:

- high field magnet test facilities for scientific research;
- high field magnets for NMR;
- high field wide bore magnets for MRI;
- high field magnets for accelerators.

The Forschungszentrum Karlsruhe has a long term experience in the development of superconducting high field magnets. A series of high field solenoidal magnet systems up to 20 T (JUMBO, HOMER-I, HOMER-II) are available in the laboratory. Within successful long term collaboration with Bruker BioSpin high field NMR magnets (750 MHz, 800 MHz, 900 MHz) were developed and now the target is 1 GHz. Presently the main focus is on the development of HTS insert coils for the test facility HOMER-II.

Most magnet systems in operation so far consist of low temperature superconductors, the main effort worldwide is now focused on HTS insert coils. First test coils for magnetic field of 5 – 8 T in background fields up to 20 T have been achieved so far [5-8]. Although the test coils reached their expected field levels, they suffered from degradation and destruction, e.g. ballooning of the conductor during He-II operation [6, 7]. Obviously there is necessity for further R&D.

HTS FOR FUSION MAGNETS

The cooling power of a fusion power plant like ITER is determined by the 4.5 K cooling of the LTS magnet system, the cryo-pumps, the neutral beam pellet injection and by the 80 K cooling of the radiation shield. In total a room temperature electric power of about 33 MW is required [17]. Using HTS magnets, the cooling power can be reduced by about 20 - 30%, depending on the temperature level. For example for LN2 cooling the complex radiation shield can be avoided which allows a more compact and simpler machine with additional savings of investment and operation costs.

Principally both, BSCCO and YBCO coated conductor could be used for fusion coils [18]. In the case of BSCCO, tapes are available but the operation temperature is limited to approximately 20 K if high magnetic fields are required. This limits the attractiveness to use BSCCO drastically. However, as discussed above the YBCO coated conductor is underway to be available in long lengths and will allow

Figure 2: Nb_3Sn conductor of the TF model coil of ITER made of about 1000 superconducting and Cu strands embedded in a stainless steel conduit.

an operation temperature in the range of 65 K or even higher.

Both HTS materials are available in the form of small tapes with high aspect ratio only which makes an optimization of ac-loss properties difficult. On the other hand this optimization is essential because for fusion coils high ac-losses can not be tolerated because this would increase the needed cooling power. The effort that has been spent to optimize classical fusion conductors with respect to ac-losses can be illustrated by showing the conductor of the TF model coil (TFMC) of ITER (Fig. 2). This conductor contains about 1000 Nb_3Sn strands in a multiple twisted cable layout embedded in a stainless steel conduit [19]. The complexity of this cable illustrates the need for an optimization of a fusion cable with respect to ac-losses and cryogenic performance. A future HTS cable has to be compared with such a sophisticated "classical" fusion cable i.e. the gain due to a higher operating temperature with a HTS fusion cable can not be balanced by much higher ac-losses. On the other hand it should be clearly said that the development of the Nb_3Sn cable shown above took more than 15 years from the first idea to the final cable layout. For a HTS fusion conductor we are in the start position now and it will take an adequate time to find optimized solutions.

Following the requirements taken from various studies, the suitable HTS material and a suitable cable design has to be developed to achieve [20]:

- high engineering current 10 – 30 kA in the conductor at a specific temperature 50 – 70 K and magnetic field 10 – 15 T;
- sufficient mechanical strength (stress-strain characteristics) or option for reinforcement;
- tolerable hot spot and quench behaviour of the HTS conductor (stabilisation);
- optimized current distribution, i.e., feasibility of good joints and optimized interstrand resistance and inductance;
- possibilities to limit AC losses;
- good cooling possibilities, e.g., Nitrogen, Helium, Neon or Hydrogen;

Figure 3: View of the 16 strand ROEBEL assembled coated conductor (RACC).

- tolerable activation of materials due to neutron flux.

First ideas to use HTS tapes by forming a Roebel bar type conductor have been developed at the Forschungszentrum Karlsruhe [21]. Fig. 3 shows an example of a 16 strand ROEBEL assembled coated conductor (RACC) made from YBCO coated conductor (Superpower), which carried a current of 1 kA at 77 K and self field [22]. A 45 tape cable is under preparation. Adequate cabling and bundling techniques have to be developed first in the laboratory scale and must then be transferred to industry.

The development, construction and demonstration of a High Temperature Superconductor coil system for Fusion is a scientific and technologic long term challenge which has to be tackled already now for becoming ready in time. This work should be done in close collaboration of European associations and industry.

The Forschungszentrum has started a long term program HTS4Fusion to develop HTS conductors for fusion magnets:

1. Conductor development:
   a. HTS material development;
   b. development of cabling/bundling techniques for both wires and tapes;
   c. develop HTS cable concept for 20 kA class 12 T, >50 K;
   d. characterisation of HTS strands and sub-size cables in upgraded FBI (warm bore);
   e. conductor development.
2. Structural material in the cryogenic lab:
   a. prepare material database for structural materials beyond ITER;
   b. tests of advanced structural materials.
3. Demo-Solenoid:
   a. Demo-Solenoid design & construction;
   b. Demo-Solenoid test in TOSKA;
4. HTS TF-Demonstration Coil.

This program shall be linked to other associations coordinated by the European Fusion R&D program.

SUMMARY

The actual status of LTS/HTS application is summarized in Table 1. It is shown that high temperature superconductors have many attractive applications in medicine, science and power systems engineering. Until now, HTS have reached a

commercial stage in induction heater magnets and in current leads. Regarding magnets, R&D is underway in high field applications for research and NMR/MRI and has started in accelerator applications and fusion. Although it is challenging to reach with HTS applications the LTS level, large progress is expected within the next decade.

Table 1: Outlook HTS Applications

	LTS now	HTS now
MRI Magnets	☑	-
NMR Magnets	☑	-
Accelerator Magnets	☑	-
Fusion Magnets	☑	-
SMES Magnets	☑	-
Induction Heater Magnets	-	☑
Current Leads	-	☑

REFERENCES

[1] D. Larbalestier et al., “High-Tc superconducting materials for electric power applications”, Nature 414 (2001) 368-377.

[2] G. Blatter et al., "Vortices in high-temperature superconductors", Rev. Mod. Phys. 66 (1994) 1125-1388.

[3] D. Verebelyi et al., “Low angle grain boundary transport in YBa2Cu3O7-d coated conductors”, Appl. Phys. Lett. 76 (2000) 1755-1757.

[4] W.V. Hassenzahl et al., “Electric Power Applications of Superconductivity”, Proceedings of the IEEE, Vol. 92, No. 10, October 2004, 1655-1674

[5] H.W. Weijers et al., “The generation of 25.05 T using a 5.11 T Bi2Sr2CaCu2Ox superconducting insert magnet”, Supercond. Sci. Technol. 17 (2004) 636–644

[6] T. Kiyoshi et al., “Generation of high magnetic fields using superconducting magnets”, Fusion Engineering and Design 81 (2006) 2411 - 2415

[7] M. Beckenbach et al., “Manufacture and test of a 5 T Bi-2223 insert coil”, IEEE Trans. on Appl. Supercond. Vol. 15 No. 2 (2005) 1484 – 1487

[8] http://www.superpower-inc.com

[9] A. Ballarino et al., “13000-A HTS current leads for the LHC accelerator: From conceptual design to prototype validation”, in Proc. Of Eucas 2003, Sorrento, Italy, LHC Project Report 696

[10] R. Heller et al., “Development of High Temperature Superconductor Current Leads for 70 kA”, IEEE Trans. on Appl. Supercond. Vol 12 No. 1 (2002) 1285-1288.

[11] R. Heller et al., “Design and Fabrication of a 70 kA Current Lead using Ag/Au stabilized Bi-2223 Tapes as a Demonstrator for the ITER TF-Coil System”, IEEE Trans. on Appl. Supercond. Vol. 14, No. 2 (2004) 1774-1777

[12] R. Heller et al., “Experimental Results of a 70 kA High Temperature Superconductor Current Lead Demonstrator for the ITER Magnet System”, IEEE Trans. on Appl. Supercond. Vol. 15 No. 1 (2005) 1496-1499.

[13] R. Wesche et al., “Design of High Temperature Superconductor Current Leads for ITER”, Fusion Engineering and Design 82 (2007) 1385-1390

[14] S. Wu et al., “An overview of the EAST project”, Fusion Engineering and Design 82 (2007) 463-471

[15] R. Heller et al., “Electrical, Mechanical and Thermal Characterization of Bi-2223/AgAu Material for Use in HTS Current Leads for W7-X”, IEEE Trans. on Appl. Supercond. Vol. 18 No. 2 (2008) 1443-1446

[16] A. Pizzuto et al., “JT-60SA Toroidal Field Magnet System”, IEEE Trans. on Appl. Supercond. Vol. 18 No. 2 (2008) 505-508

[17] J.L. Duchateau et al., “Estimation of the recycled power associated with the cryogenic refrigeration power of a fusion reactor based on TORE SUPRA experiment and ITER design”, Nucl. Fusion 46 (2006) 94–99

[18] P. Komarek, “Potential and desire for HTS application in thermonuclear fusion”, Fusion Engineering and Design 81 (2006) 2287–2296

[19] A. Ulbricht et al., “The ITER toridal field model coil project”, Fusion Engineering and Design 73 (2005), 180-327

[20] G. Janeschitz et al., “High Temperature Superconductors for Future Fusion Magnet Systems – Status, Prospects and Challenges”, presented at 21st IAEA Fusion Eng. Conf., Chengdu, China, 16. – 21. 10.2006

[21] W. Goldacker et al., “High current DyBCO-ROEBEL Assembled Coated Conductor (RACC),” Journal of Physics, Conference Series 46 (2006) 901

[22] W. Goldacker et al., “ROEBEL Assembled Coated Conductors (RACC): Preparation, Properties and Progress”, IEEE Trans. on Appl. Supercond. Vol. 17 (2) (2006) 3398-3401

STATUS AND PERSPECTIVES AT BABCOCK NOELL

W. Walter, Babcock Noell GmbH, Würzburg, Germany

Abstract

Babock Noell GmbH (BNG) is a magnet manufacturer known in particular for its engagement in large scale projects such as LHC or Wendelstein 7-X. The series production of 416 LHC Dipoles was successfully completed in 2006 and the fabrication of the 50 non-planar coils was finished by the Wendelstein consortium in March this year. A number of large scale projects such as ITER and FAIR are in the short term horizon. Nevertheless BNG has proven broader capabilities, other than large scale production, which extend from feasibility studies, to prototyping and design optimization. Lately, for example, we are involved in prototyping dipoles for FAIR, manufacturing a high field Nb_3Sn dipole for EFDA and developing a superconducting undulator for FZK. The aim of this presentation is to show the current status, capabilities, projects and future goals at BNG .

INTRODUCTION TO BABCOCK NOELL

Babcock Noell is active in the product areas of nuclear service, nuclear technology, magnet technology and environmental technology throughout the world and, in doing so, successfully implements the experience gained over four decades. With approximately 250 employees who are predominantly employed in the engineering area, our performance spectrum extends from the development, planning, supply and commissioning right up to the operating of the plants and equipment we supply.

Already in the 70s Babcock Noell was providing components for large research facilities like, for example, the vacuum tank for the Petra accelerator ring in Hamburg. In the early 90s Babcock Noell entered in the field of magnet technology with the development of large superconducting magnet systems for high-energy physics and nuclear fusion. There then followed contracts for the series magnets for the fusion experiment “Wendelstein 7-X” and the Hadron collider “LHC” in the research centre CERN, Geneva. A unique coil production was developed and an assembly plant established for these purposes. Today we design and produce magnets, coils, undulators and spectrometers for various international research facilities. We also undertake individual development tasks for these purposes. We have particular experience in the use of superconductors in magnet systems.

LOOKING BACK AT LHC AND W7-X

Magnet Manufacturing at Babcock Noell (BNG) was dominated by two large contracts in the beginning of the millenium:

- 416 main dipole magnets for the Large Hadron Collider (LHC) at CERN
- 50 non-planar coils for the stellerator fusion experiment Wendelstein 7-X of the Max-Planck-Institute for Plasma Physics at Greifswald

Figure 1: LHC main dipole manufacturing at BNG

Figure 2: Welding of a coil casing for a Wendelstein 7-X non-planar coil

BNG produced in total 416 magnets about 30 tons each for the LHC, i.e. about 12,500 tons of superconducting magnets with a maximum production rate of about 3.5 magnets per week. Within the consortium Wendelstein, BNG produced 50 non-planar coils, which implied e.g.

200 tons of cast material, 6.4 million hand-made weld points and 23 km of bent cooling tubes.

In November 2005, BNG delivered the 416th LHC main dipole to CERN and in March 2008, the 50th non-planar coil for Wendeltstein 7-X was completed. The following chapters try to describe the BNG focus after the successful completion of the above mentioned projects.

FOCUS

The upcoming large scale projects such as FAIR, ITER and XFEL have just started and cannot provide a continuous work-load after the end of the above mentioned projects. BNG therefore enlarged its portfolio in order to generate additional business in the area of magnet technology. The variety of magnets was extended from Cu and NbTi Systems to Nb_3Sn and permanent magnet systems. However, magnets for large scale accelerators and fusion projects remain as cornerstone in Babcock Noell's portfolio

RECENT PROJECTS AT BABCOCK NOELL

Nb_3Sn High Field Dipole for EFDA (EDIPO)

As contractor of EFDA and on the basis of an EFDA magnet design, BNG is manufacturing a high field Nb_3Sn dipole. A cable in conduit conductor will be operated for this magnet at 20 kA to reach the nominal field of 12.5T.

Figure 3: Winding machine with test winding for the Nb_3Sn dipole.

Undulators

In 2006, the companies Accel, Danfysik and Babcock Noell were awarded contracts for the manufacturing of prototype undulators for the XFEL project at DESY, Hamburg. BNG built a 5m long device with a 316LN beam, whereas the other companies built 2m long devices with Aluminium beams. BNG delivered its device first, in the beginning of 2007.

Figure 4: Assembly of a 5m long undulator prototype for XFEL

Additional 11 undulators for the upgrade of the PETRA lightsource at DESY, are being build by BNG at the moment. The ambitious goal is to deliver 11 devices within 11 month time.

Apart from that, BNG also builds a superconducting undulator to be installed at the ANKA lightsource at the Karlsruhe research centre.

Functional Systems

In addition to the above mentioned projects, BNG offers also to design and build magnet systems from scratch. In order to include such functional systems in the BNG portfolio, additional engineers/physicists with a background in the relevant technologies were hired and additional software tools were acquired and programmed. At the moment BNG is building a solenoid system for a Neutron-Spin-Echo (NSE) spectrometer to be installed at the Spallation Neutron Source (SNS) in Oak Ridge, USA by the Jülich Research centre. A NSE spectrometer measures tiny velocity changes of the neutrons encoded by the neutrons spin clock at a sample while the Neutron spin precesses in large magnetic fields following Bloch's equation. This instrument will be the best of its class both with respect to resolution and dynamic range. In order to reach this ambitious goal, a large magnetic precision field integral before and after the sample is required which directly scales linearly with the resolution of the instrument. Therefore superconducting technology is used to allow for a higher magnetic field integral. The solenoids generate an integrated magnetic flux density of 1.8 Tm. In order to reduce the fringe field, active shielding is foreseen and modern pulse-tube cryocoolers

cool the NbTi windings below Tc while minimizing vibrations. A special feature of this magnet is a real time position measurement system for the cold mass with an accuracy in the order of micrometers during operations.

Figure 5: Factory test of a solenoid system for a NSE spectrometer

CONCLUSION

After the successful completion of the contracts for the LHC main dipoles and the Wendelstein 7-X non-planar coils, BNG restructured successfully. The portfolio at BNG has been considerably extended to include permanent-magnetic and Nb_3Sn magnet systems, functional systems and magnets for lightsources. However, magnets for large scale accelerators and fusion experiments remain to be a cornerstone of BNG's business also in the future.

REFERENCES

[1] F. Eyßelein et.al., "Series Production of Challenging Superconducting Magnets. The Experience of W7-X non-planar Coils and LHC Dipoles", IEEE Transactions on Applied Superconductivity, Volume 16 Number 2, p. 236 (2006).

[2] H. Scheller et.al., "The Productio of non-planar Coils for the Wendelstein 7-X experiment: a (self-) critical review", IEEE Transactions on Applied Superconductivity, Volume 18 Number 2, p. 451 (2008).

[3] E. Theisen et.al., "Status of the EDIPO Nb_3Sn Dipole Manufacture", SOFT'08, Rostock, September 2008.

[4] W. Walter et.al., "Design of a Pair of Superconducting Solenoids for a Neutron-Spin-Echo Spectrometer at the SNS", IEEE Transactions on Applied Superconductivity, Volume 17 Number 2, p. 1209 (2007).

MAGNETS FOR THE PHASE I LHC UPGRADE*

P. Fessia

Abstract

The scope of the LHC Upgrade Phase I is to make possible the focusing of the beams to a β*=0.25 m in IP1 and IP5, and provide reliable operation of the LHC at a luminosity of 2 10^{34} cm^{-2} s^{-1}. Presently the time-line of the project foresees the installation of the equipment in the tunnel during the LHC shut-down of 2012 in order to be operational for physics run 2013. This document tries to review the requirements of the project in term of magnets, the related choices and status and frame of the development.

INTRODUCTION

The LHC experiments are presently installed in points 1, 2, 5 and 8 around the circumference of the machine. On the left and on the right of each point the experimental insertions provide the final focussing of the beams before their collision. The two high luminosity experiments ATLAS and CMS are installed in point 1 and point 5 respectively. In the frame of the LHC Upgrade Phase I it is planned to change the magnetic elements of the 4 insertions around these 2 points; this is valid both for the low-β quadrupoles and for the correctors. The present configuration starting from the IP is the following:

1) Q1: it is the 1st low-β quadrupole. It is MQXA [1] type; it has been designed and produced by KEK (Japan). A dipole corrector is integrated in this unit (MCBX).
2) Q2: this unit is made of 2 MQXB type quadrupoles [2]. They have been designed and produced by Fermilab (U.S.A.); it also integrates a dipole corrector (MCBX).
3) Q3: this unit is equal to the Q1 for what concerns the low-β quadrupole. It integrates a MCBXA, a dipole corrector also equipped with sextupole and dodecapole correctors, a skew quadrupole corrector and a sextupole corrector.
4) DFBX: this is a dedicated cryogenic feed box. The unit feeds the elements from Q1 to Q3 with the required cryogenic supply and it integrates the current leads required to power the quadrupole and the corrector magnets.
5) D1: separation dipole.

The four quadrupole magnets are based on superconducting technology and their working temperature is 1.9 K. The aperture diameter is 70 mm and the gradient 215 T/m. The D1 is a normal conducting dipole.

BOUNDARY CONDITIONS

The following hypotheses have to be taken as basis of the new magnets design and of their integration:

1) The interfaces between the LHC and the experiments remain unchanged at ± 19 m respect to the interaction point
2) The cooling capacity of the cryogenic system and other main infrastructure elements shall remain unchanged.
3) The new quadrupole shall make use of the LHC dipole superconducting cable. See Table 1 [3].

Table 1: SC cable characteristics

	Inner layer	**Outer Layer**
Number of strands	28	36
Mid-thickness	1.9±0.006 mm	1.48±0.006 mm
Width	15.10 mm	15.10 mm
Critical current I_c 10 T, 1.9 K	>13750 A	
9 T, 1.9 K		>12960 A
dI_c/dB	>4800 [A/T]	>3650 [A/T]

4) The new magnets shall be compatible with the present tunnel geometry, no civil engineering work is foreseen
5) The technologies, materials and tooling to be employed shall be derived as much as possible from the recent development for the LHC in order to minimise the project budget and limit the development time and risk.

The use of known technologies and solutions brings also to profit from existing tooling. In particular a large workshop able to build and repair the 15 m long LHC Main Dipole is being installed at CERN providing a very valuable infrastructure that should used for the assembly of the new low-β quadrupoles. The design of this magnet should be, where possible, compatible with this existing assembly line. With the same logic the use of the existing reserve in low carbon steel for the iron yoke laminations and the use of the available low permeability austenitic steel strip for the collars would allow mitigating the financial exposure and reduce the supply time.

LAY-OUT

The new lay-out would foresee to have the 4 quadrupoles separated in 4 independent units each one cryostated separately. In addition the correctors would be installed in a separate cold mass equipped with its own cryostat. This solution has the advantage, respect to the present one, to detangle the production of the quadrupole units from the corrector availability; it provides more

*This project has received funding from the European Community's Seventh Framework Programme (FP7/2007-2013) under the Grant Agreement n° 212114

flexibility and it separates the 12 KA bus bars, necessary to feed the quadrupoles, from the 600 A bus bars necessary for the correctors. The 4 quadrupoles units are called Q1, Q2a, Q2b, Q3 and the corrector cold mass Corrector Package. The cryogenic feed box would be substitute by a technical module being the terminal for a superconducting link. This will provide the electrical feeding from a remote installed feed box equipped with the necessary current leads.

HEAT DEPOSITION

The experimental insertions, due their proximity to the interaction point, are submitted to an important heat deposition due to the collision debris. Extensive studies [4] on the subject are being carried out with the aim to insure safe operation of the magnets and to indentify, if necessary, corrective actions. The aim is to guarantee that

1) In the superconducting cable the quench limit of 4.3 mW/cm^3 is not exceeded
2) The installed cryogenic capacity of 400 W at 1.9 K is enough to guarantee the functioning of the magnets

The main results of the work show that

- The most exposed magnet would be the Q2a
- In this magnet the limit of 4.3 mW/cm^3 would be exceeded if no actions is taken
- Extra shielding is necessary and a 1st shielding of stainless steel in Q1 of 13 mm thickness is enough to bring the deposition on Q2a below the limit

Table 2 reports the repartition of the loads among the different components.

Table 2: Heat loads in the low-β quadrupoles

Item	Q1[W]	Q2a[W]	Q2b[W]	Q3[W]
Beam screen	14	5	10	14
Shielding	56	-	-	-
Cold Bore	7	6	12	16
SC cable on mid plane	17	11	23	25
Collars	21	10	18	25
Iron yoke	24	10	15	22

The average linear power densities in each magnet varies from 5.4 W/m in the Q2a till the 11.2 W/m in the Q3

MAGNETS

The low-β quadrupole

As previously stated these magnets will use the LHC Main Dipole superconducting cable for the conductor distribution; a two layers cosθ solution is at the moment the preferred option. These magnets would provide a gradient between 130 T/m and 110 T/m in the possible aperture range from 110 mm to 130 mm with a total quadrupole magnetic length for each insertion between 36 m and 38 m [5,6]. A possible conductor distribution for a 120 mm aperture is shown in Fig.1. This solution would provide an operational gradient of 152 T/m at short sample and 121.5 T/m at the operating current.

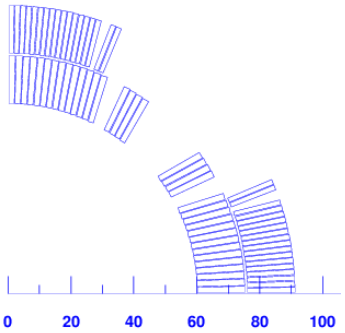

Figure 1: Tentative conductor distribution for a 120mm aperture.

In order to improve the heat transfer from the cable to the super fluid helium new possible insulation schemes are being studied. The aim is using the well known polyimide tapes in different topology to increase the channels between the helium bath and the cable core. A presently studied solution [7] foresees the application of a 3 layer system where the intermediate one has the function to create an open helium path between the cable edges and the rest of the conductor (see Fig.2).

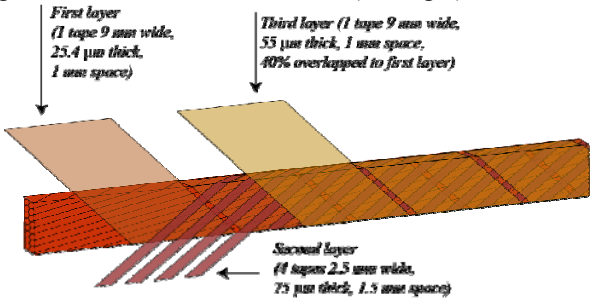

Figure 2: Proposed insulation system.

Concerning the mechanical structure the present favored solution uses self supporting austenitic steel collars. A structure with 2 keys per quadrant has been selected with an angle between mid-plane and the keys of 15°, this solution provides the best compromise between the repartition of the forces between the 2 keys (best solution 2 keys near the mid-plane) and the stiffening effect that the keys have on the structure when they are moved a part. Fixing as design parameter the maximum allowable radial movement of the coil on the mid-plane, it is possible to find the corresponding collar thickness. It has been decided to limit this movement to less than 60 μm; this brings to a collar thickness of 39 mm for 130 mm aperture magnet and to 36 mm for a 120 mm aperture. Fig. 3 shows the Von Misses distribution of the stresses in the collar for a 120 mm aperture case [8].

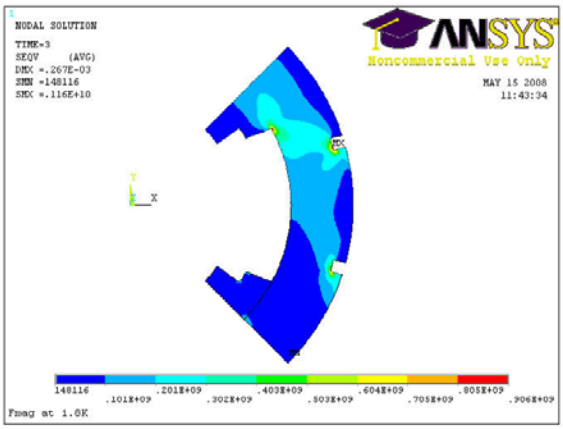

Figure 3: Von Misses stress distribution in a collar for a 120 mm aperture, at short sample condition.

Correctors

At the moment the following correctors are deemed necessary and are under development:

1) A dipole corrector with an integrated strength of 6 Tm and an estimated central field of about 3T. Two units would be necessary: one for the horizontal and one for the vertical plane
2) A skew quadruple with an integrated strength of 20 T and gradient of 40 T/m
3) A sextupole corrector with an integrated strength of 0.01 T at r=17 mm

The studies are at the moment addressing the possibility to upscale the design of the present correctors installed in the LHC.

COLLABORATIVE FRAME

The LHC Upgrade Phase I is not only a CERN approved construction project but it is at the centre of more general collaboration efforts. Various high value agreements have been or are being established that are instrumental for the final success of the project:

SLHC-PP

The Preparatory Phase of the Large Hadron Collider upgrade (SLHC-PP) is a project co-funded by the European Union in its 7th Framework Programme, CERN and 16 European research institutes and universities.

SLHC-PP comprises coordinating, support and technical activities. Among the other Work-Package N.6 groups 5 institutes with the aim to develop the prototypes necessary to proof the feasibility of the magnets necessary for the LHC upgrade phase I. These institutes are

- CERN: European Organization for Nuclear Research, Switzerland
- CEA-Saclay: Commissariat à l'Energie Atomique, France
- CIEMAT: Centro de Investigaciones Energéticas, Medioambientales y Tecnológicas, Spain
- CNRS-IN2P3: Centre National de Recherche Scientifique, France
- STFC: Science and Technology Facilities Council, United Kingdom

CERN and CEA will be involved in the design and fabrication of the low-β quadrupole model and prototype, STFC and CIEMAT will develop the models and prototypes of two types of correctors, CNRS-IN2P3 will be the main actor in the development of the prototype cryostat for the new quadrupole.

Special contributions

Two special contributions are being discussed and finalised:

- An exceptional contribution from of France to CERN: CEA and CNRS would take care of the supply of key components for the series production of the low-β quadrupoles and of the correctors
- A contribution from the US laboratories for the supply of the new D1 superconducting separation dipoles.

CONCLUSIONS

The LHC upgrade of phase I requires the design of at least 4 types of different magnets, among them a very demanding large aperture quadrupole. In total it is foreseen to build 20 quadrupoles including spares. Other 20 units are the needed correctors. The design studies have started and they have not put in evidence show stoppers for the project. It is a major construction work and the first step to guarantee that the LHC will remain a scientific instrument at the frontier satisfying the requirement of the community of the high energy physics. Several collaborations are being set to guarantee the successful completion of the project.

ACKNOWLEDGMENTS

The author wish to thank all the people member of the LIUWG (LHC Insertions Upgrade Working Group) and the collaborators from the participating institutes.

REFERENCES

[1] A. Yamamoto, et al., "Production and measurement of the MQXA series of LHC low- beta insertion quadrupoles" IEEE Trans. Appl. Supercond. 15 (2005) 1084.

[2] S. Feher, et al., "Test results of LHC interaction regions quadrupoles produced by Fermilab" IEEE Trans. Appl. Supercond. 15 (2005) 1090.

[3] O. Bruning, et al., "The LHC Design Report" CERN 2004-003 pp. 157.

[4] E. WIldner, F. Cerutti, et al., "LHC luminosity upgrade: protecting insertion region magnets from collision debris" EPAC 2008, 2584.

[5] J. P. Koutchouk, et al., "A Solution for Phase-one Upgrade of the LHC Low-beta Quadrupoles Based

on Nb-Ti" CERN-LHC-PROJECT-Report-1000 (2007).

[6] F. Borgnolutti and E. Todesco, "130 mm Aperture Quadrupoles for the LHC Luminosity Upgrade" PAC 07, 350

[7] D. Tommasini, "A new cable insulation scheme improving heat transfer to superfluid helium in Nb-Ti superconducting accelerator magnets" EPAC 2008, 2467.

[8] F. Regis, "Study of the quadrupole collar structure" presentation at LHC Interaction Upgrade Working Group on 15/05/2008, see http://www.cern.ch/liuwg

TEST RESULTS OF HD2, A HIGH FIELD Nb_3Sn DIPOLE WITH A 36 MM BORE *

P. Ferracin#, LBNL, Berkeley, CA 94720, U.S.A.

Abstract

The Superconducting Magnet Program at Lawrence Berkeley National Laboratory (LBNL) has developed the 1 m long Nb_3Sn dipole magnet HD2. With tilted (flared) ends to avoid obstructing a 36 mm clear bore, HD2 represents a step towards the use of block-type coils in high-field accelerator magnets. The coil design has been optimized to minimize geometric harmonics and reduce the conductor peak field in the end region, resulting in an expected short sample dipole field of 15 T. The support structure is composed by an external aluminum shell pre-tensioned with pressurized bladders and interference keys, and by two stainless steel end plates compressing the coil ends through four aluminum axial rods. We report on magnet design, assembly, and test results, including training performance, quench locations, and strain gauge measurements

INTRODUCTION

The Superconducting Magnet Program at Lawrence Berkeley National Laboratory (LBNL) is continuing the development of Nb_3Sn high field magnets for the next generation of HEP colliders. The superconducting dipole HD2, recently fabricated and tested at the LBNL test facility, represents the first application of block-type coils to accelerator-quality dipole magnets. The conceptual design of the magnet was described in [1], whereas the mechanical analysis of the structure and the magnet fabrication were respectively reported in [2] and [3]. In this paper, after a brief overview of the magnet design and parameters, we present the results of two magnet tests, including strain gauge measurements (recorded during assembly, cool-down and excitation), training curve and quench locations.

MAGNET DESIGN

The HD2 magnet design (Fig. 1, left) features two block-type coils wound around a titanium alloy (Ti 6Al-4V) pole. The pole includes a round cutout to provide room for a 3.65 mm thick stainless steel (Nitronic 40) bore tube with a clear aperture of 36 mm. The coils are supported by horizontal and vertical pads. Vertical pushers and horizontal rails transfer the load from the pads to the coils. Two yoke halves, made of 50 mm thick iron laminations, and a 41 mm thick aluminum shell provide the external coil pre-load through vertical and horizontal interference keys. The diameter of the cold mass is 705 mm. The structure is pre-loaded with water pressurized bladders.

*Work supported by the U.S. D0E (No. DE-AC02-05CH11231)
#pferracin@lbl.gov

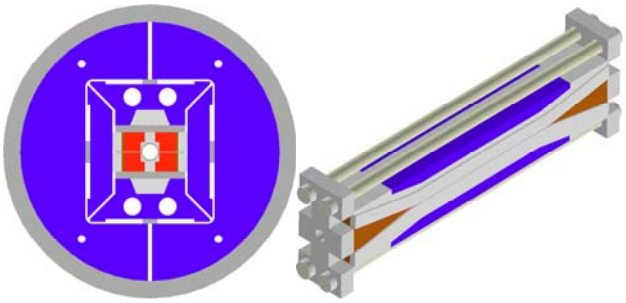

Figure 1: HD2 cross-section (left) and coil end support system (right)

The coil has a straight section of about 481 mm and it tilts up (flares) at a 10^o angle in both ends through hard-way bends. After the hard-way bends, the flared region features a short straight section. The tilted ends are supported vertically by aluminum-bronze wedges surrounding the bore tube and axially by two end-plates pushed against the coil by four aluminum rods (Fig. 1, right).

CONDUCTOR AND MAGNET PARAMETERS

The two coil modules of HD2 are composed of two layers wound from a continuous length of cable made of 51 RRP strands with a 0.8 mm diameter. The cable is 22.008 mm wide and 1.401 mm thick. Three coils were fabricated: assuming strand properties from coil 1 (Fig. 2), the magnet has a maximum bore field of 15.1 T (4.2 K), with a conductor peak field of 15.9 T at a current of 17.4 kA. Coil 2 and 3 feature a short sample peak field about 0.6 T higher than coil 1.

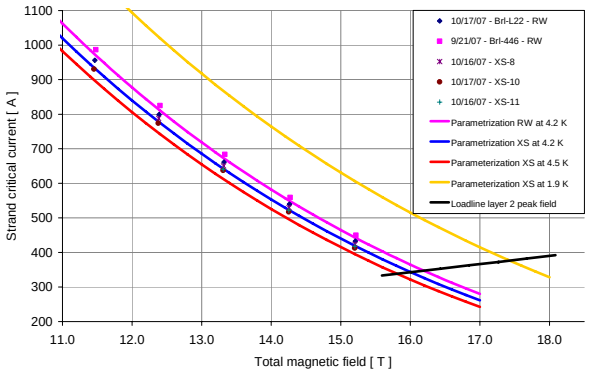

Figure 2: Critical current (A) vs. applied field (T) measurements and parameterization curves of virgin (round) and extracted strands used for coil 1.

MAGNETIC ANALYSIS

The conductor peak field of 15.9 T is located in the pole turn of layer 2 along the straight section (Fig. 3), where the pole turn of layer 1 has a margin of 0.6 T. In the end region (Fig. 4), the field decreases from 15.8 T at the beginning of the ramp to 14.8 T in the end pole turn.

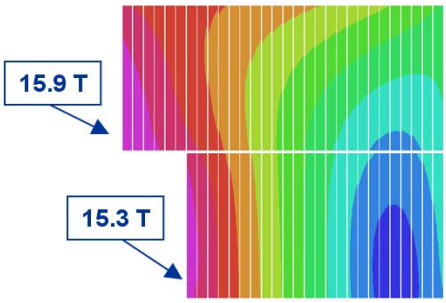

Figure 3: Maximum conductor field (T) in the straight section.

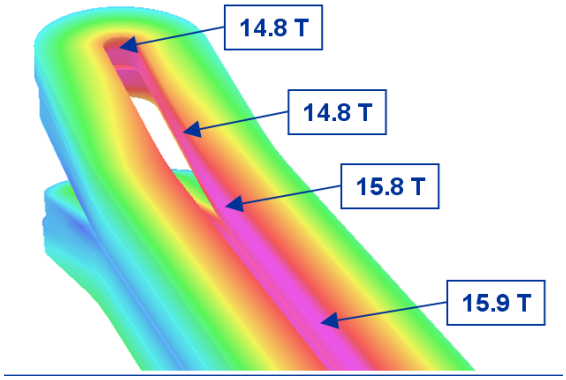

Figure 4: Maximum conductor field (T) in the end region.

MECHANICAL ANALYSIS

Straight section

The main component of electro-magnetic force in HD2 is horizontal and directed outwardly. In order to prevent the pole turn to separate from of the Ti pole, the coil is pre-compressed after cool-down to an average stress of 150 MPa (Fig. 5, right).

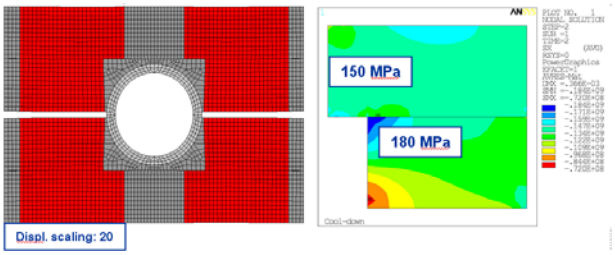

Figure 5: Coil stress conditions after cool-down: deformed shape of a 2D finite element model with displacements enhanced by a factor 20 (left) and horizontal stress (MPa) in the coil (right).

Because of the deformation of the bore tube, depicted in Fig. 5 (left), the coil area next to the square corners in layer 1 does deflect as much as the mid-plane area, generating a high stress point of 180 MPa in the coil.

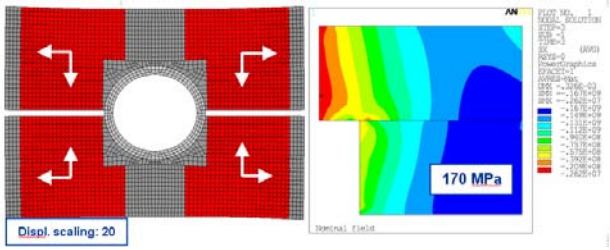

Figure 6: Coil stress conditions during excitation: deformed shape of a 2D finite element model with displacements enhanced by a factor 20 (left) and horizontal stress (MPa) in the coil (right).

During excitation, as the e.m. forces push the conductor horizontally towards the pads and vertically towards the mid-plane (Fig. 6, left), the stress in the coil region next to the pole decreases (Fig. 6, right) and the highest stress of 170 MPa is now located in the low-field area of the coil.

End region

The mechanical conditions of the coil end regions have been simulated by a 3D mechanical model (Fig. 7, left). The axial component of the e.m. force in the ends tends to separate the conductor from the pole.

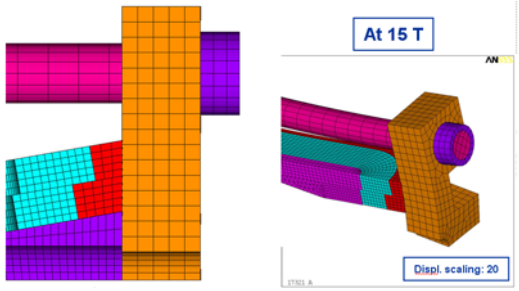

Figure 7: 3D model of the magnet end region (left), and deformed shape during excitation with displacements enhanced by a factor 20 (right).

Following the same principle adopted for the straight section, the end support system is designed to prevent such a separation and minimize conductor motion when the magnet is energized. The computed deformed shape of Fig. 7 (right) indicates that the compression of the end shoes obtained by the end-plate is expected to maintain the pole turn in contact with the pole.

TEST RESULTS

Two tests were carried out: HD2a and HD2b. In both tests coil 1 (limiting coil) and coil 2 were used. The shell was pre-tensioned at 293 K to 35 MPa and reached 140 MPa after cool-down (Fig. 8), corresponding to a maximum expected coil stress of 150 MPa. The average rod tension increased from 35 to 90 MPa during cool-down (Fig. 9).

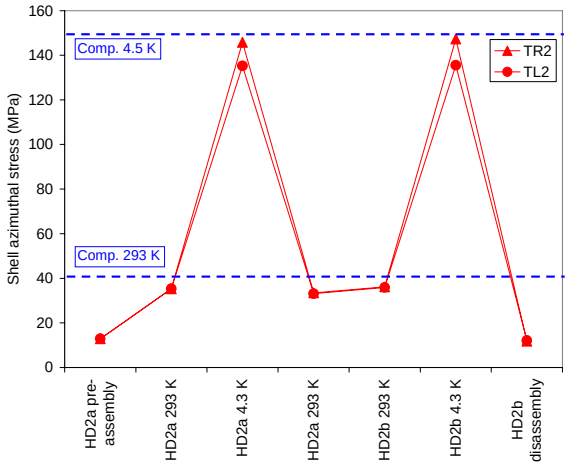

Figure 8: Shell azimuthal stress (MPa) during assembly, cool-down and tests.

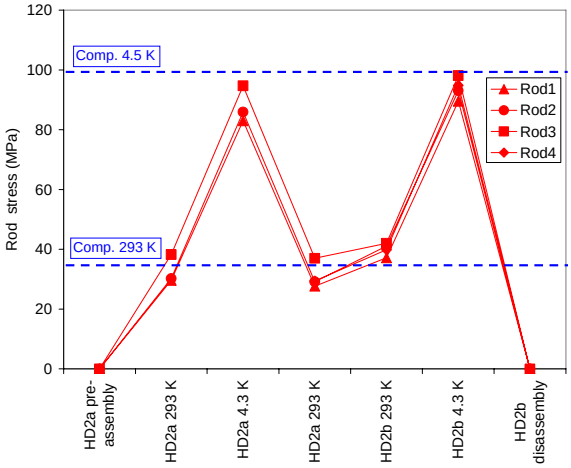

Figure 9: Rod axial stress (MPa) during assembly, cool-down and tests.

Training quenches and quench locations

During the HD2a test, the magnet had a first quench at 12.0 T of conductor peak field, corresponding to 73% of the expected magnet limits and to a bore field of 11.4 T (Fig. 10). The highest current was reached at quench #18, with a conductor peak field of 14.0 T, corresponding to 87% of the expected magnet limits and to a bore field of 13.3 T. During the HD2b test the magnet had a first quench at 11.5 T of conductor peak field, corresponding to 71% of the expected magnet limits and to a bore field of 11.0 T (Fig. 10). The highest current, identical to the one recorded during the previous test, was reached at quench #31. Because of a failure of the extraction system, a higher number of MIITS where released after quench #31. As a results, coil 1 exhibit an higher ramp-rate sensitivity. After reducing the ramp rate, the magnet reached the previous maximum current quench at #39.

Out of 14 training quenches of the HD2a test, almost all evenly distributed between the two coils, 12 were located in the layer 1 pole turn, towards the end of the straight section (Fig. 11). During the HD2b test (Fig. 12), before quench #31, 4 (6) quenches occurred in coil 1 (2). After quench #31 all quenches were located in coil 1.

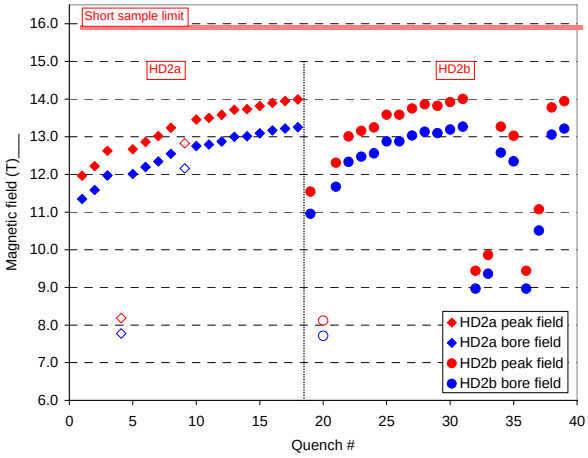

Figure 10: Training quenches of HD2a and HD2b.

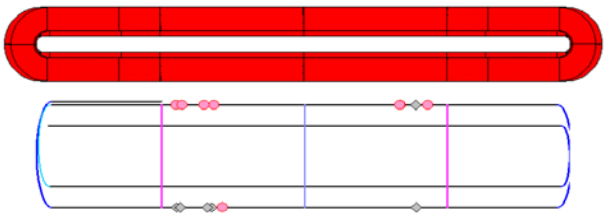

Figure 11: HD2a quench locations: coil 1 (gray markers) and coil 2 (pink markers).

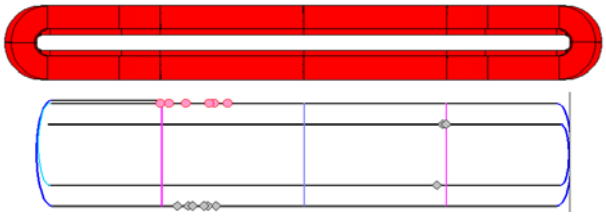

Figure 12: HD2b quench locations: coil 1 (gray markers) and coil 2 (pink markers).

REFERENCES

(1) G. Sabbi, et al., “Design of HD2: a 15 T Nb_3Sn dipole with a 35 mm bore”, IEEE Trans. Appl. Supercond. 15 (2005) 1128.

(2) P. Ferracin, et al., “Mechanical design of HD2, a 15 T Nb_3Sn dipole magnet with a 35 mm bore”, IEEE Trans. Appl. Supercond. 16 (2006) 378.

(3) P. Ferracin, et al., “Development of the 15 T Nb_3Sn Dipole HD2”, IEEE Trans. Appl. Supercond. 18 (2008) 277.

Nb_3Sn MAGNET DEVELOPMENT FOR LHC LUMINOSITY UPGRADE*

P. Wanderer#, Brookhaven National Lab, Upton, NY 11973, U.S.A.

Abstract

This paper presents the main points of magnet R&D for a LHC Luminosity Upgrade carried on through the LHC Accelerator Research Program (LARP) work on magnets at Berkeley, Fermilab, and BNL. Work on materials and on racetrack magnets is described in some detail. The others areas of LARP work are only outlined here and discussed in detail in other talks at this meeting.

INTRODUCTION

The main goals of LARP are to reach 200 T/m in a 90 mm, 3.6-m-long Nb_3Sn quadrupole by the end of 2009, to fully qualify Nb_3Sn magnets for use in the LHC, and to supply Nb_3Sn magnets for the LHC Phase 2 Luminosity Upgrade.

MATERIALS

The Nb_3Sn strand now in use for LARP magnets is the 54/61 RRP® internal tin strand made by Oxford Superconducting Technologies. The designation 54/61 refers to the number of subelements in use (54), compared to the number possible (61), as indicated in Fig. 1. The strand has a diameter of 0.7 mm, a J_c of at least 2400 A/mm^2 (12 T, 4.2 K), and a RRR greater than 100. The heat treatment of the strand was optimized to achieve a J_c consistent with 220 T/m and suppression of low-field instabilities.

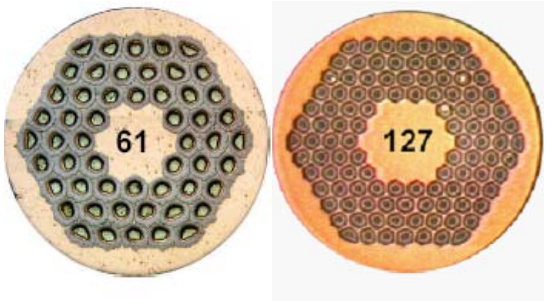

Figure 1. Photographs of the cross sections of 0.7 mm diameter Nb_3Sn strand, 54/61 (left) and 108/127 (right).

Magnets with larger aperture, likely needed for LHC, will require a larger-diameter strand. The materials group is now studying recently produced RRP 108/127 as a strand that can be used in the range 0.8 – 1.0 mm with acceptable instability (Fig. 1).

Thus far, LARP has received from OST 688 kg of 54/61 at 0.7 mm. Recently, 180 kg of 108/127 with a larger spacing between the subelements was delivered with most of the strand at a diameter of 0.8 -1.0 mm. An order for 85 kg of 54/61 with increased copper spacing between the subelements has been placed. The increased spacing mitigates the deformation of the subelements during cabling. The 54/61 standard material is of high quality, as indicated by the good piece lengths achieved (92% greater than 1 km).

The strand R&D presently underway includes measurements of the effect of tensile strain on the critical current of the 54/61 strand, being carried out by NIST in Boulder, Colorado. Results are expected this coming summer. Studies of the 108/127 strand are focused on mapping the effect of different heat treatments on J_c and stability.

During the development of the heat treatment for the 54/61, tests were conducted only at 4.2 K. The heat treatment chosen, 72 h/200 °C + 48 h/400 °C + 48 h/640 °C, yielded strand that was stable at low fields (~ 3 T) up to currents at least twice the current in the magnet. Recent magnets at 1.9 K have not reached quench currents higher than those reached at 4.2 K, and with greater quench-to-quench variation in current (e.g., Fig. 2). This has been observed in several magnets. It appears highly likely that the magnets are limited by conductor instability, rather than construction. It is thought that the magnet performance is related to results of strand tests at 1.9 K and 4.2 K (Fig. 3). In this test, the strand stability is greater than 1000 A at low field at both temperatures, but has a lower stability threshold at medium fields (~ 6 T) at the lower temperature. This issue is under study at the strand level.

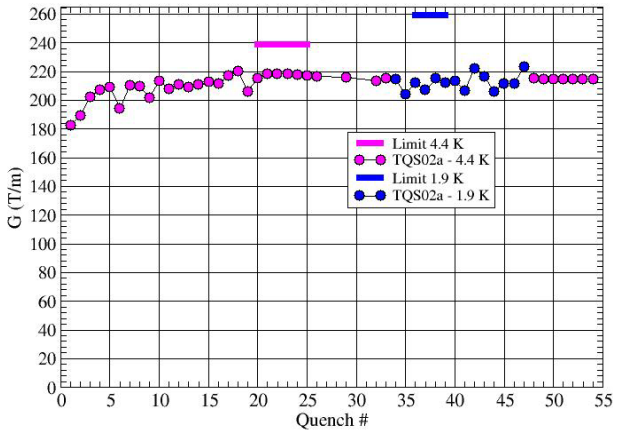

Figure 2. Quench test results for the 1m-long, 90 m-aperture quadrupole TQS02.

In order to better understand this issue, LARP will test 1 m sections of cable during the coming months in the FRESCA facility at CERN, where tests can be carried out at both 4.2 K and 1.9 K. (Cable testing was not undertaken earlier due to budget limitations.) Cable tests are also planned for the National High Magnetic Field lab in Florida. At this facility, testing is at 4.2 K and the load on the cables can be varied at cryogenic temperatures.

*Work supported by the U.S. Department of Energy, Office of High Energy Physics
#wanderer@bnl.gov

This allows for efficient measurements of cable critical current versus transverse compressive stress.

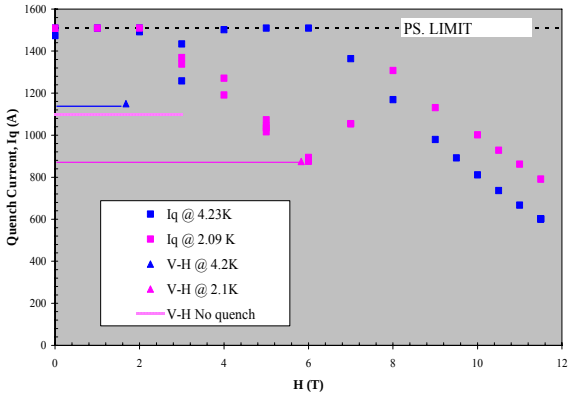

Figure 3. Quench test results for 0.7 mm Nb_3Sn strand at 4.2 K and 2.09 K. The V-H data were taken with a constant magnet current and a ramped field.

DC magnetic field measurements of the quadrupoles have shown behavior of the transfer function G/I (Fig. 4) and the duodecapole (Fig. 5), the first allowed harmonic in agreement with calculation. Interestingly, the duodecapole during the "front porch" (the period of time when the current is held constant while the LHC is filled with protons) is constant (Fig. 6). This is qualitatively different than the behavior of this harmonic in NbTi magnets. The reason is not yet understood.

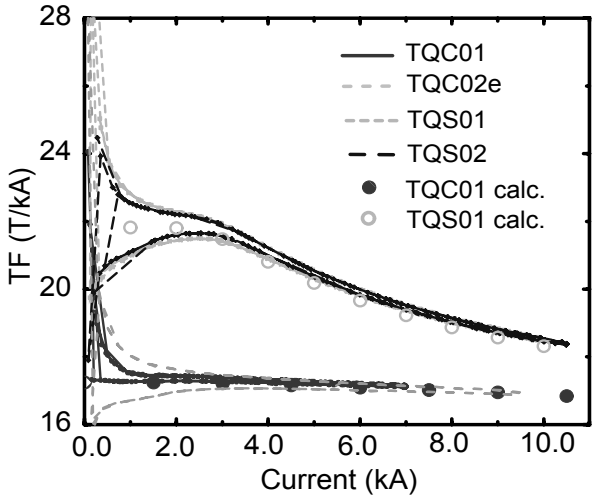

Figure 4. Measured and calculated values of the transfer function of two quadrupoles. Differences in the saturation are due to differences between the collar (TQC) and shell (TQS) support structures.

The dynamic effects are quite significant (Fig. 7). At a ramp rate which roughly corresponds to the LHC ramp rate, 10 A/s, change in the transfer function due to ramping varies 1% between magnets. This effect is likely due to eddy currents which flow between the strands in the cable. The strands are sintered together during reaction which effectively makes the cross-over resistance very low. The eddy currents can be greatly reduced by making cable made with a 25 μm stainless steel strip ("core") between the top and bottom layers. NbTi cables have been made in this fashion. Time and budget permitting, this method of reducing eddy currents will be introduced to LARP magnets also.

RACETRACK MAGNETS

To provide an early test for possible length effects in coils, a pair of 3.6 m long racetrack coils was assembled using a "shell" support structure (LRS01). The support structure is relatively simple to build because the only significant Lorentz forces are perpendicular to the plane of the coils (Fig. 8). The forces are transmitted via keys (which control the preload) through the iron yoke to the aluminum shell. The initial quench test of the magnet (LRS01) yielded good results (Fig. 9).

During one of the ramps to quench, there was a sudden loss of axial strain in the shell (Fig. 10). The axial strain in the shell was built up during cooldown and was due to the difference between the thermal contraction of the shell (integral $\delta l/l \sim 4 \times 10^{-3}$ from room temperature to 4.5 K) and that of the yoke (integral $\delta l/l \sim 2 \times 10^{-3}$).

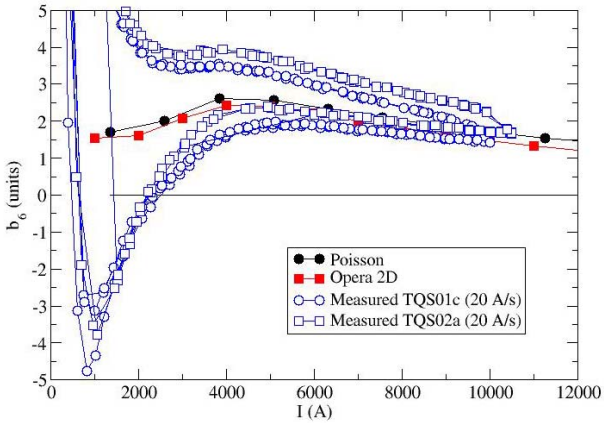

Figure 5. Measured and calculated values of the first allowed harmonic for collared and shell quadrupoles. The calculation does not include the effects of the magnetization currents.

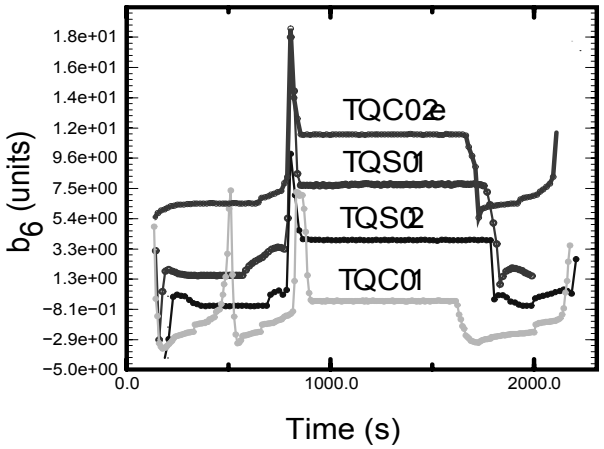

Figure 6. Measured values of the first allowed harmonic for two collar and two shell quadrupoles, versus time, for a simulated LHC injection cycle.

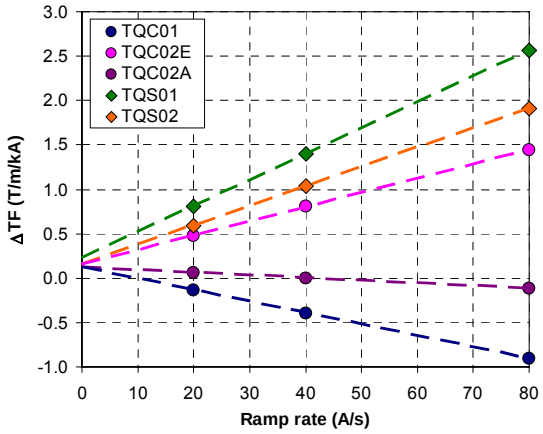

Figure 7. Measurement of the eddy current effect on the transfer function at a gradient of 45 T/m.

This loss of axial strain in the shell did not affect the quench performance of the magnet. However, it was decided to reduce this stick-slip effect by segmenting the shell into four lengths of ~1 m [1]. The coils were reassembled into the segmented shell support structure and tested (LRS02). The change of axial strain was reduced by a factor of ~ 4, as expected (Fig. 11). The quench performance of the magnet improved, to ~ 96% of the estimated limit of the conductor (Fig. 9). The peak field on the conductor at the maximum quench current was ~ 11.5 T [2].

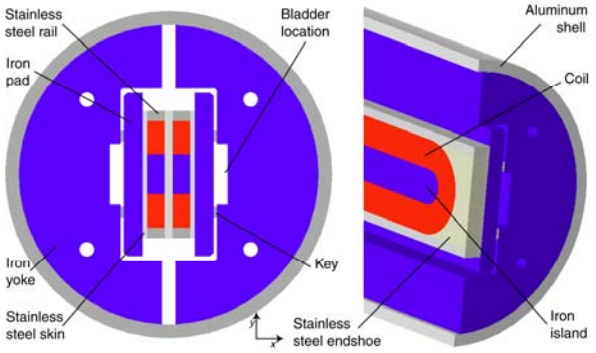

Figure 8. Cross section and angle views of the 3.6 m long racetrack magnet, LRS.

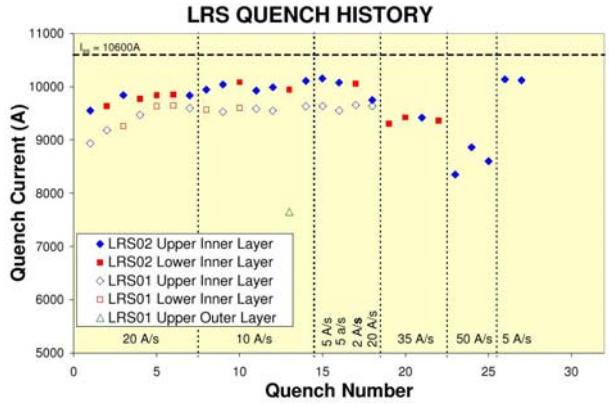

Figure 9. Quench history of LRS01 (open symbols) and LRS02 (solid symbols).

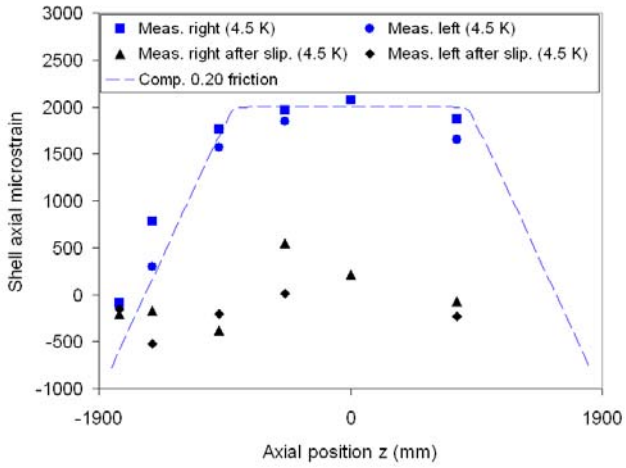

Figure 10. Shell axial strain versus length for LRS01 at 4.5 K, before and after the loss of strain.

The good performance of LRS02 allowed the quench current to be measured as a function of ramp rate between 5 A/s and 35 A/s (Fig. 12). Although there is no well-established calculation for extrapolating to a ramp rate of zero, a linear or near-linear extrapolation yields a conductor quench limit that is consistent with the extracted strand data for the magnet. This suggested that the thermal margin expected for this conductor is available in the magnet.

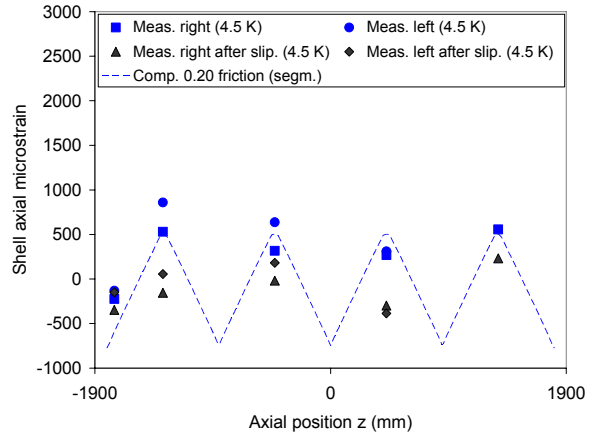

Figure 11. Shell axial strain versus length for LRS02 at 4.5 K, before and after the loss of strain.

TECHNOLOGY QUADRUPOLES

The Technology Quadrupole (TQ) program for 1 m-long, 90 mm-aperture magnets is developing coil manufacturing methods and two different coil support structures, collar (TQC) and shell (TQS). The discussion in this note is limited to a brief comparison of the two support structures. Detailed presentations of the TQ program were made in other contributions to this workshop [3, 4].

Collar support structures (Fig. 13) are well known through their use in NbTi accelerator magnets. The coils are supported azimuthally by stainless steel collars and, for these magnets, also by the welding of the stainless

steel skin around the iron yoke. Preload is controlled via shims at the midplanes of the coils and by shims between the collars and yoke. A significant portion of the azimuthal preload is created during assembly. The axial preload is modest – sufficient to keep the coil in contact with the end shoe under all conditions [4].

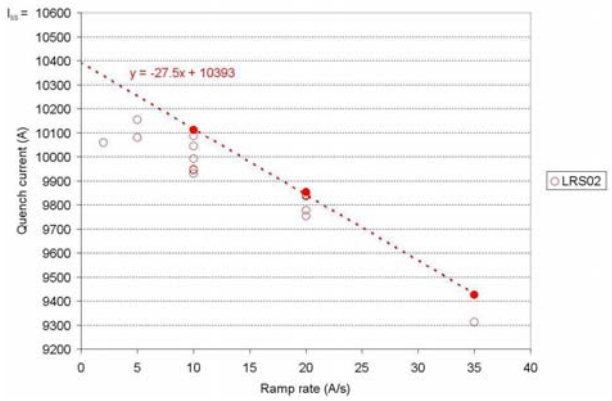

Figure 12. Quench currents in LRS02. The fit is to the highest currents at each ramp rate (solid symbols).

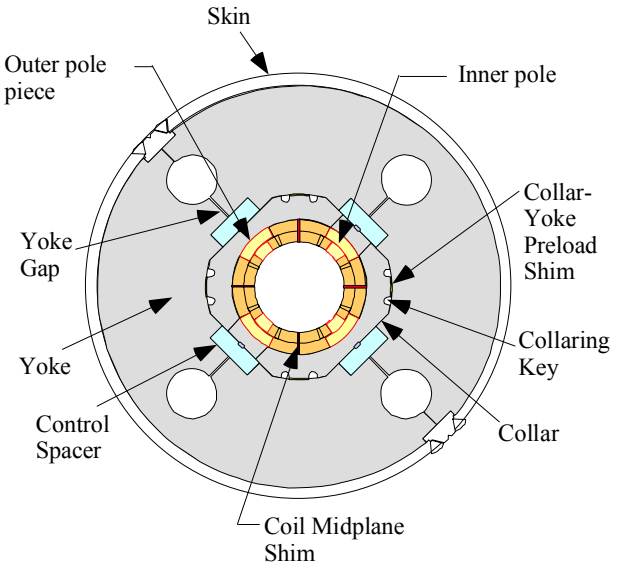

Figure 13. Cross section of collar support structure (TQC).

Shell support structures (Fig. 14) make use of "bladder and key" technology to establish the room temperature preload [1]. The coils are assembled with a small azimuthal preload using iron pads. Separately, the yoke is assembled inside a thick aluminum shell. The coil and pad assembly is then installed into the yoke and shell. Stainless steel bladders, placed between the two assemblies, are inflated to obtain the desired azimuthal preload. Keys are installed to lock in the preload and the bladders removed. The largest part of the azimuthal preload is created by the aluminum shell during cooldown. The preload during assembly is modest. The axial preload is high, to limit the motion of the coil ends during excitation. It is implemented by full-length aluminum rods (Fig. 15).

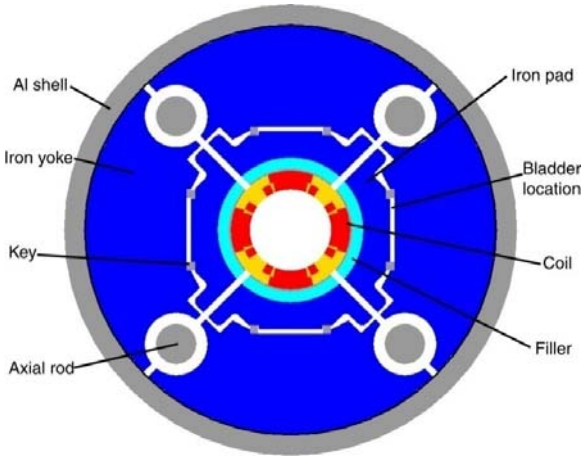

Figure 14. Cross section of shell support structure (TQS).

Figure 15. Photo of a completed TQS quadrupole. The four thick rods provide the strong axial support.

Magnets made in the TQ program routinely reach, and sometimes exceed, 200 T/m [3, 4]. The test results also give baseline values for field quality, quench propagation, and quench protection. Looking ahead, the TQ support structures will be used to test needed developments in, e.g., the conductor and cable, in 1 m magnets before being implemented in 3.6 m magnets.

LONG QUADRUPOLES

The success of the long racetrack magnets indicates that there is no fundamental problem in extending the quadrupole length to 3.6 m. Work is underway to build and test 3.6 m-long, 90 mm-aperture quadrupoles in both collar (LQC) and shell (LQS) support structures. The goal is to reach a gradient of 200 T/m by the end of December, 2009 [5]. The collar support structure will be the same as the TQC, except longer. The shell support structure has evolved somewhat (Fig. 16), and now includes the use of pieces called "masters" that will facilitate assembly with the segmented yoke and shell [1].

A key feature of the LQ R&D plan is to use the same set of coils in both support structures. This minimizes the time and resources needed to test both structures, increasing the paths to the Dec. 2009 goal. The most efficient way to do this is to test the coils in the shell support structure first, because it is faster to remove the coils from a shell structure (using the bladders) than from a collar structure (which requires the skin to be cut off). In order to make coils faster, facilities for reacting and impregnating coils are being built at both BNL and Fermilab. All winding and curing will be at Fermilab.

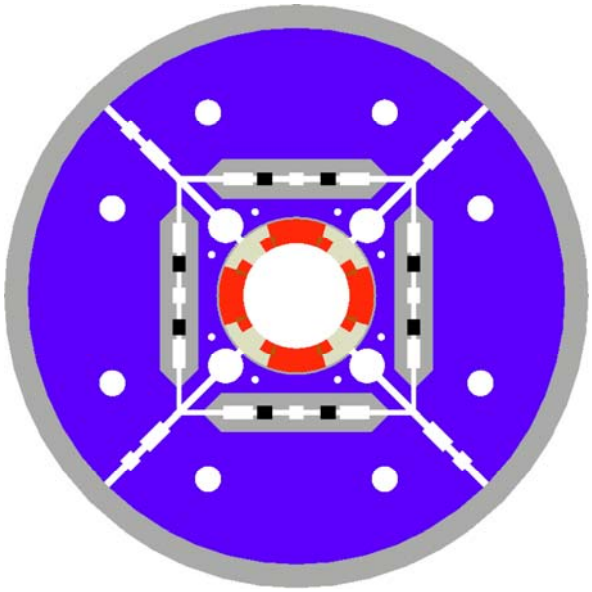

Figure 16. Shell support structure for long quadrupoles. One each side, the masters (grey) are spaced by two keys (black). The keys determine the preload.

The fixtures used for curing, reaction, and impregnation LQ coils process one coil at a time. The same fixtures used to make TQ coils processed two coils at once. The change was made when left-right asymmetries were discovered in the TQ coils. Processing one coil at a time is expected to reduce the asymmetries. At the time of WAMSDO, practice coils from copper and Nb_3Sn had been wound and cured. Initial debugging of the reaction fixture (adding a flat plate to remove a bow that occurred during reaction of the first Nb3Sn coil, as shown in Fig. 17) has taken place.

The quench protection system is designed to keep the coil temperature below 380 K and the MIITS below 7.5, calculated for a 60 mΩ dump resistor and with the adiabatic approximation. In the calculation, a quench detection time of 5 ms and a heater delay time of 12 ms have been used (values based on TQ experience). To achieve this, the coils will be outfitted with quench protection heaters on both inner and outer layers. Because of the flux jumps (which decrease in amplitude as the current increases), it will be necessary to begin the ramp with a quench detection threshold of several volts. At high current, the threshold will be about ¼ volt.

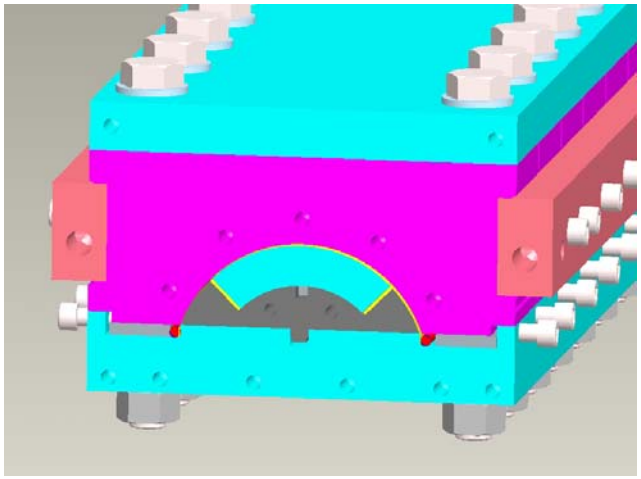

Figure 17. View of the tooling that will be used to react and impregnate 3.6 m quadrupole coils.

LARGE APERTURE QUADRUPOLES

Design of a large aperture (~110 mm – 130 mm) 1 m-long quadrupole, HQ, is currently underway [6]. The aperture of this two-layer magnet will be close to that of the NbTi quad planned for the LHC Phase 1 Upgrade [7, 8]. It is felt that comparison of the design and performance of this magnet with that of the NbTi quad will permit easier evaluation of the features of Nb_3Sn important for its use in an accelerator.

The follow-on to HQ is a 3.6 m-long version, QA. The quadrupoles to be built for the Phase 2 Upgrade are called QB.

SUMMARY

The LARP Magnet R&D program has yielded 1 m-long, 90 mm-aperture quadrupoles that reliably reach 200 T/m. It has also produced a racetrack magnet with a shell support structure that reached 96% of the conductor limit. Practice coil for a 3.6 m-long quadrupole have been made, in line with the schedule which calls for a 3.6 m quadrupole to reach 200 T/m by the end of 2009. Design of a large aperture quadrupole is well underway.

ACKNOWLEDGEMENTS

This work has been accomplished by the close collaboration of the magnet R&D groups at Fermilab, Lawrence Berkeley Lab, and Brookhaven Lab under the LARP program. My colleagues and I appreciate the support of the Office of High Energy Physics in the U.S. Department of Energy.

For help in preparing this paper I would like to thank my colleagues G. Ambrosio, M. Anerella, E. Barzi, R. Bossert, S. Caspi, D. Dietderich, P. Ferracin, H. Felice, A. Ghosh, F. Nobrega, G. Sabbi, J. Schmalzle, and A. Zlobin. I would also like to thank S. Peggs for advice and encouragement in this work.

REFERENCES

[1] P. Ferracin, "Shell-based Support Structures for Nb_3Sn Accelerator Quadrupole Magnets," WAMSDO 2008 – Workshop on Accelerator Magnet, Superconductor, Design, and Optimization, CERN, Geneva, Switzerland, May 19-23, 2008

[2] P. Wanderer et al., "Test Results of LARP 3.6 m Nb_3Sn Racetrack Coils Supported by Full-Length and Segmented Shell Structures," LARP note 2008-01-01, February 13, 2008 (unpublished).

[3] S. Caspi, "Test Results of Nb_3Sn Quadrupole Magnets Using a Shell-based Support Structure," WAMSDO, op. cit.

[4] A. Zlobin, "Nb_3Sn Accelerator Magnet and Superconductor R&D at Fermilab," WAMSDO, op. cit.

[5] G. Ambrosio, "LQ Overview," LARP 10th Collaboration Meeting, April 23-25, 2008, Port Jefferson, NY (unpublished).

[6] H. Felice, "Nb_3Sn Quadrupole Designs for the LHC Upgrade," WAMSDO, op. cit.

[7] R. Ostojic, "A New IR for the LHC (Phase I Upgrade)," WAMSDO, op. cit.

[8] P. Fessia, "Magnets for the Phase I LHC Upgrade," WAMSDO, op. cit.

SHELL-BASED SUPPORT STRUCTURES FOR Nb_3Sn ACCELERATOR QUADRUPOLE MAGNETS*

P. Ferracin#, LBNL, Berkeley, CA 94720, U.S.A.

Abstract

Shell-based support structures are being fabricated and tested as part of the development of large-aperture Nb_3Sn superconducting quadrupoles for future upgrades of the LHC Interaction Regions. These structures utilize water pressurized bladders for room-temperature pre-load control, and rely on a pre-tensioned aluminum shell to deliver a substantial part of the coil pre-stress during cool-down. The coil final pre-load is therefore monotonically approached from below, without overstressing the strain-sensitive conductor. This method has been adopted by the US LARP collaboration to test subscale racetrack coils (SQ series), 1 m long cos-theta coils (TQS series), and 4 m long magnets (LRS and LQS series). We present recent progress in the development of shell-based support structures, with a description of the principles of operations and the future plans.

INTRODUCTION

As part of the LHC Accelerator Research Program (LARP [1]), three US national laboratories (BNL, FNAL, and LBNL) are currently engaged in the development of Nb_3Sn superconducting magnets for a future upgrade of the LHC Interaction Regions (IR). In order to contain the superconducting coils during magnet excitation and minimize conductor motion induced by electro-magnetic forces, LBNL has developed shell-based support structures for quadrupole magnets. The main components and features of these structures are the following:

- An external aluminum segmented shell (solid tube).
- A 4-piece iron yoke with gaps open during all magnet operations.
- Assembly performed through two sub-assemblies.
- Pre-loading obtained with water pressurized bladders.
- Maximum coil stress reached after cool-down.
- Axial coil support provided by end-plate and axial rods.

These support structures have been originally adopted by the LBNL Superconducting Magnet Program to cope with the needs of high field Nb_3Sn magnets, which, because of large e.m. forces acting on a brittle superconducting material, require a precise control of the coil pre-load [2-3]. In this paper with give an overview of how these structures have been applied to quadrupole magnets, we describe their main principles of operation and finally we present how, through LARP, accelerator quality features are in the process of being included in the design.

*Work supported by the U.S. D0E (No. DE-AC02-05CH11231)
#pferracin@lbl.gov

OVERVIEW OF LARP SHELL-BASED STRUCTURES

Four different structures have been adopted for the following LARP quadrupole magnets (Fig. 1).

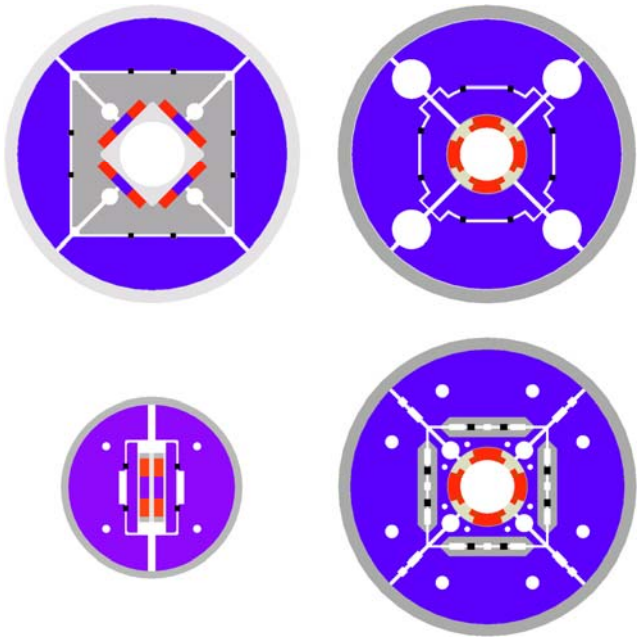

Figure 1: Cross-sections of LARP magnets with shell-based support structures (in scale): SQ (top left), TQ (top right), LR (bottom left), and LQ (bottom right).

SQ (Subscale Quadrupole)

The subscale quadrupole magnet SQ [4-7] was the first magnet where the shell-base structure concept was applied to a quadrupole configuration. The cross-section is shown in Fig. 1 (top left). The 300 mm long magnet features four racetrack coils and an aperture of 110 mm. The coils and the structure were fabricated and assembled at LBNL and a total of 5 tests (first test in 2005) were performed at LBNL and FNAL. The design includes alignment features for the structure components and the coils. The maximum conductor peak field of 11.8 T (98% of the expected magnet limits), corresponding to a gradient of 89 T/m, was reached during the SQ02b test at 1.9 K.

TQ (Technology Quadrupole)

The technology quadrupole magnet TQ [8-13] was the first magnet where the shell-base structure concept was applied to a cosθ-type quadrupole magnet. The cross-section is shown in Fig. 1 (top right). The 1 m long magnet features four cosθ coils and an aperture of 90 mm.

The coils were fabricated at FNAL and LBNL, and assembly and loading were carried out at LBNL and CERN. A total of 5 tests (first test in 2006) were performed at LBNL, FNAL, and CERN. The design does not include alignment features for the structure components and the coils. The maximum conductor peak field of 11.2 T (90% of the expected magnet limits), corresponding to a gradient of 220 T/m, was reached during the TQS02a test at 4.5 K.

LR (Long Racetrack)

The long racetrack magnet LR [14-17] was the first magnet where the shell-base structure concept was applied to long racetrack coils. The cross-section is shown in Fig. 1 (bottom left). The 3.6 mm long magnet features two racetrack coils in common coil configuration and no bore. The coils were fabricated at BNL, while LBNL was responsible for the fabrication of the structure, as well as the assembly and loading of the magnet. A total of 2 tests (first test in 2007) were performed at BNL. The design does not include alignment features for the structure components and the coils. The maximum conductor peak field of 11.5 T (96% of the expected magnet limits) was reached during the LRS02 test at 4.5 K.

LQ (Long Quadrupole)

The long quadrupole magnet LQ [18-19] is going to be the first magnet where the shell-base structure concept will be applied to a long cosθ-type quadrupole magnet. The cross-section is shown in Fig. 1 (bottom right). The 3.5 m long magnet features four cosθ coils and an aperture of 90 mm. The coils are fabricated at FNAL and BNL while LBNL is responsible for the fabrication of the structure, as well as the assembly and loading of the magnet. The first test is expected in 2009. The design includes alignment features only for the structure components. The maximum expected conductor peak field at 1.9 K is 12.3 T, corresponding to a gradient of 240 T/m.

PRINCIPLES OF OPERATION

Coil azimuthal and radial support

The shell-based support structure comprises several components: pads surrounding the coils, iron yokes, and an aluminum outer shell. As a first step in the assembly, the four pads are bolted around the coils. The coil-pad sub-assembly is then inserted into a structure composed by the four-piece iron yoke and the aluminum shell. A 5 mm gap between pads and yokes provided room for inserting four pressurized bladders.

The pre-loading operation is depicted in Fig. 2 using deformed shapes computed by a 2 D finite element model with displacements enhanced by a factor 20. The contact pressure between coil and pole during assembly, cool-down, and excitation is plotted in Fig. 3 assuming different bladder pressures. Both figures refer to the LQ case. The bladders generate the primary force needed to spread the yoke apart, apply tension to the shell and pre-compress the coil-pads subassembly (Fig 2, top left). Once the structure is locked by interference keys, the bladders are deflated and removed (Fig 2, top right). During cool-down, the shell generates further pre-load on the coils, due to the different thermal contractions of aluminum and iron (Fig 2, bottom left).

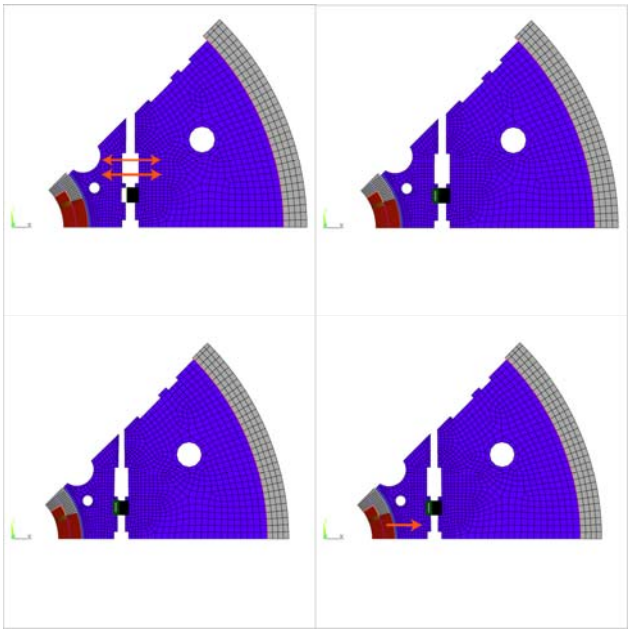

Figure 2: Principles of operation (deformed shape of a 2D finite element model with displacements enhanced by a factor 20): insertion-pressurization of bladders (top left), insertion of interference key and deflation-removal of bladders (top right), cool-down (bottom left), and excitation (bottom right).

The e.m forces push the coil against the structure (Fig 2, bottom right), at the same time unloading the pole: the bladder pressure is chosen in order to guarantee full contact between coil and pole when the magnet is energized (Fig. 3)

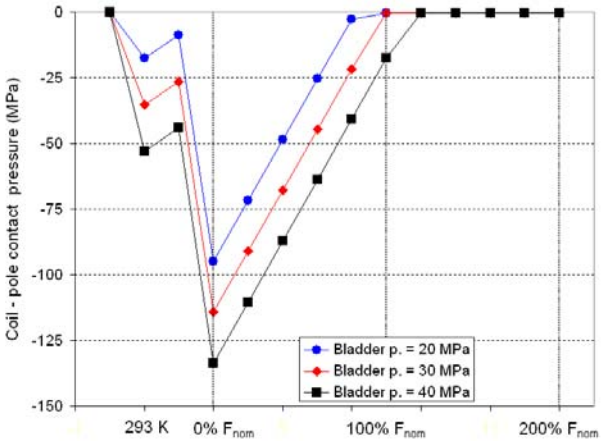

Figure 3: Contact pressure between coil and pole (MPa) during assembly, cool-down, and excitation (as a function of the fraction of nominal electro-magnetic force). Data

are plotted assuming three different bladder pressures.

Coil axial support

In order to reduce the conductor motion in the end region resulting from axial e.m forces, a longitudinal support system is included in the design (Fig. 4 left). Four aluminum rods are inserted in the four holes of the pads, and bolted to two stainless steel end plates. The rods are pre-tensioned with an axial piston at room temperature (Fig. 4 right) and, similarly to the outer shell, they significantly increased their stress during cool-down.

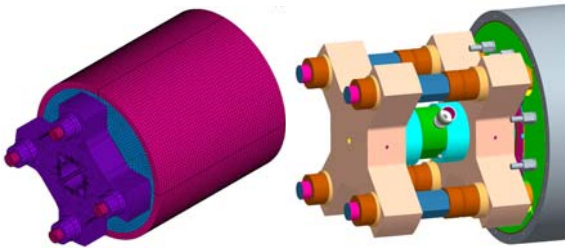

Figure 4: Coil axial support: end-plate (left) and pre-load system composed by an additional plate and a piston (right).

NEXT STEP: HQ

Following the experience gained with the SQ, TQ, and LQ programs, LARP is now designing HQ, whose goals are to explore the performance limits in terms of peak fields (≥ 15 T), forces and stresses, and to include in the design accelerator quality features as alignment and LHe containment. A preliminary cross-section of HQ is shown in Fig. 5. The structure components are aligned through round pins between shell and yokes and keys between pads and yokes. The coil is surrounded by aluminum bolted collars which align the coil poles to the pads. An external stainless steel tube is currently considered as a possible LHe containment.

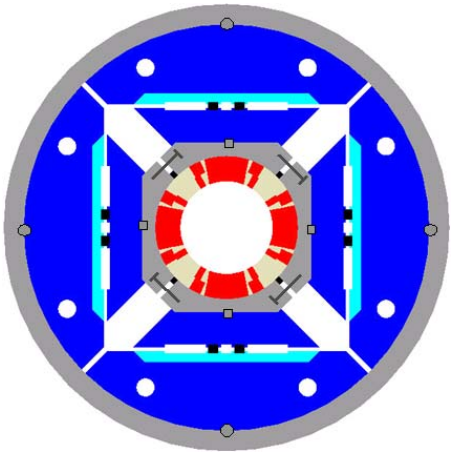

Figure 5: Cross-section of HQ.

REFERENCES

[1] S.A. Gourlay, et al., “Magnet R&D for the US LHC Accelerator Research Program”, IEEE Trans. Appl. Superconduct. 16 (2005) 324.

[2] A. R. Hafalia, et al., “An approach for faster high field magnet technology development”, IEEE Trans. Appl. Superconduct. 13 (2003) 1258.

[3] A. R. Hafalia, et al., “A new support structure for high field magnets” IEEE Trans. Appl. Superconduct. 12 (2002) 47.

[4] P. Ferracin, et al., “Development of a large aperture Nb_3Sn racetrack quadrupole magnet”, IEEE Trans. Appl. Supercond. 15 (2005) 1132.

[5] P. Ferracin, et al., “Assembly and test of SQ01b, a Nb_3Sn quadrupole magnet for the LHC Accelerator Research Program”, IEEE Trans. Appl. Supercond. 16 (2006) 382.

[6] P. Ferracin, et al., “Assembly and Tests of SQ02, a Nb_3Sn Racetrack Quadrupole Magnet for LARP”, IEEE Trans. Appl. Supercond. 17 (2007) 1019.

[7] P. Ferracin, et al., “Effect of Axial Loading on Quench Performance in Nb_3Sn Magnets”, IEEE Trans. Appl. Supercond. 18 (2008) 285.

[8] G. Sabbi et al., “Nb_3Sn quadrupole magnets for the LHC IR”, IEEE Trans. Appl. Superconduct. 13 (2003) 1262.

[9] S. Caspi, et al., “Mechanical design of a second generation LHC IR quadrupole”, IEEE Trans. Appl. Supercond. 14 (2004) 235.

[10] A. R. Hafalia et al., “Structure for an LHC 90 mm Nb_3Sn quadrupole magnet”, IEEE Trans. Appl. Supercond. 15 (2005) 1444.

[11] S. Caspi et al., “Design and analysis of TQS01, a 90 mm Nb_3Sn model quadrupole for the LHC luminosity upgrade based on a key and bladder assembly”, IEEE Trans. Appl. Supercond. 16 (2006) 358.

[12] S. Caspi, et al., “Fabrication and Test of TQS01—A 90 mm Nb_3Sn Quadrupole Magnet for LARP”, IEEE Trans. Appl. Supercond. 17 (2007) 1122.

[13] S. Caspi, et al., “Test and Analysis of Technology Quadrupole Shell (TQS) Magnet Models for LARP”, IEEE Trans. Appl. Supercond. 18 (2008) 179.

[14] P. Ferracin, et al., “Assembly and Test of a Support Structure for 3.6 m Long Nb_3Sn Racetrack Coils”, IEEE Trans. Appl. Supercond. 18 (2008) 167.

[15] P. Wanderer, et al., “LARP Long Nb_3Sn Racetrack Coil Program”, IEEE Trans. Appl. Supercond. 17 (2007) 1140.

[16] P. Ferracin, et al., “Design and Fabrication of a Supporting Structure for 3.6 m Long Nb_3Sn Racetrack Coils”, IEEE Trans. Appl. Supercond. 17 (2007) 1023.

[17] P. Wanderer, et al., “Construction and Test of 3.6 m Nb_3Sn Racetrack Coils for LARP”, IEEE Trans. Appl. Supercond. 18 (2008) 171.

[18] G. Ambrosio, et al., “Design of Nb_3Sn Coils for LARP Long Magnets”, IEEE Trans. Appl. Supercond. 17 (2007) 1035.

[19] G. Ambrosio, et al., “LARP Long Nb_3Sn Quadrupole Design”, IEEE Trans. Appl. Supercond. 18 (2008) 268.

TEST RESULTS OF NB3SN QUADRUPOLE MAGNETS USING A SHELL-BASED SUPPORT STRUCTURE

S. Caspi, LBNL, Berkeley, CA 94720, U.S.A.

Abstract

In support of the development of a 90 mm aperture Nb_3Sn superconducting quadrupole for the US LHC Accelerator Research Program (LARP), test results of five quadrupole magnets are compared. All five assemblies used key and bladder technology to compress and support the coils within an iron yoke and an aluminium shell. The first three models (TQS01a, b, c) used Nb_3Sn MJR conductor and segmented bronze poles. The last two models (TQS02a, b) used Nb_3Sn RRP conductor, and segmented titanium alloy (TiAl6V4) poles, with no axial gaps during reaction. This presentation summarizes the magnets performance during assembly, cool-down and excitation and compares measurements with design expectations.

MAGNET DESIGN

Conceptual design and parameters

The magnet technology development effort of the U.S.-LHC Accelerator Research Program (LARP) is a partnership between magnet physicists and engineers from BNL, FNAL and LBNL [1]. The program's long term goal is to demonstrate that Nb_3Sn magnets are a viable choice for an LHC IR upgrade [2], by the year 2009. A successful test requires a gradient above 200 T/m, in a 3.6 m long magnet, having a 90 mm bore. Within the past three years a Technology Quadrupole (TQ, see Fig. 1) program investigated 1 m long cos-theta coils in two different structures: 1) TQC - a collar based structure and 2) TQS a shell based structure that utilizes bladder & key technology [5] to pre-stress the coils inside an iron yoke and tensioned aluminium shell (see Fig. 2). Test results of the TQS tests are presented here.

Fig. 1: A ready-for-testing TQS magnet shows the outer aluminum shell, its strain diagnostics, and the yoke. The four large axial rods axially compress the coil-ends, via a thick stainless-steel end-plate.

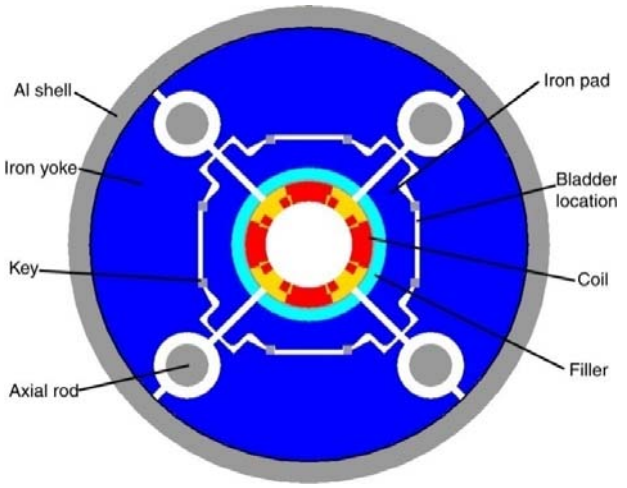

Fig. 2: TQS magnet cross-section showing coils, fillers, pads, keys, yokes, shell and axial supporting rods.

The shell-based structure uses bladders and keys for precise magnet assembly pre-stress control, with negligible stress "overshoot". Interference keys are inserted to retain the 300 K pre-stress and allow bladder removal. A tensioned aluminum shell compresses internal iron and coil components, and applies a substantial fraction of the operational pre-stress during cool-down, during which the final coil pre-stress is monotonically approached from below, without overstressing the fragile conductor [2-6]. Plotted in Figure 3 is some of the reasoning why high field magnets need to move from collared structures to shell based structures.

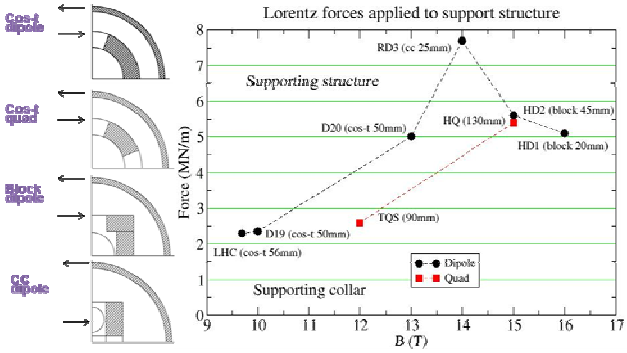

Fig. 3: Lorentz forces as applied to different structure.

TQS01 and TQS02 test results

The three TQS01 tests (a, b, c) used coils with segmented bronze islands and MJR conductor. Except TQS01a, which used virgin coils, tests b and c combined virgin and previously tested coils, see Table I. Small adjustments to pre-stress and friction coefficients were

made with minimal impact on the magnet performance. During all three tests quench-origins clustered around the first pole-turn near the gaps in the segmented pole-islands. These gaps (combined thickness of ~2 mm) were introduced to prevent excessive strain on the conductor during reaction, and maintained during impregnation. Based on TQS01 quench-origins and additional ANSYS analysis, the bronze islands were replaced with titanium alloy (Ti6Al4V) islands for TQS02. This eliminated the need for any gaps during reaction and axially compressed the pole-island while cold (the conductor is therefore under axial tension).

TQS02 coils showed no pole-segment gaps after the reaction, and the coil ends remained attached to the end spacers and shoes. This resulted in the "best looking" coils yet produced in the TQ-program. The coil conductor was RRP with an SC current density of 2740 A/mm^2 at 12 T, 4.2 K (extracted strand, with no self field correction), a measured RRR of ~200, and a Cu to non-Cu ratio of 0.87.

Table I. TQS magnet tests

Magnet	Cond.	Coils	Island	T (K)	Test date
TQS01a	MJR	**5,6,7,8**	Bronze	4.4	Apr. 2006 LBNL
TQS01b	MJR	**14**,**15**,7,8	Bronze	4.4	Nov. 2006 LBNL
TQS01c	MJR	5,15,7,8	Bronze	4.4, 1.9	Mar. 2007 FNAL
TQS02a	RRP	**20,21,22,23**	Ti	4.4, 1.9	Jun. 2007 FNAL
TQS02b	RRP	22,23,**28,29**	Ti	4.4, 1.9	Mar. 2008 CERN
TQS02c	RRP	22,23,28,20	Ti	4.4, 1.9	Jun. 2008 CERN

TEST RESULTS

Training

The training curves of 5 tests are shown in Fig. 4 and 5. At 4.4 K the TQS01a reached its plateau value in less than a dozen quenches with a plateau current of 10625 A or 193 T/m and a maximum gradient of 199 T/m at 3.23 K. TQS02a trained slower, but achieved a plateau of 12000A or 215 T/m at 4.4 K, a onetime maximum of 12270 A or 219 T/m at 4.4 K, (90% short sample limit without self field correction). At 1.9 K, TQS01c gained ~1000 A (as expected), but after many quenches. However, TQS02a was erratic, with no net increase after 14 attempts. Its onetime maximum current and gradient were 12460 A and 222 T/m at 2.17 K. This anomalous 1.9 K training remains unexplained. Conductor limits are given in Table II. Plots with the measured stresses in the coil and in the structure are given in Fig. 6-8.

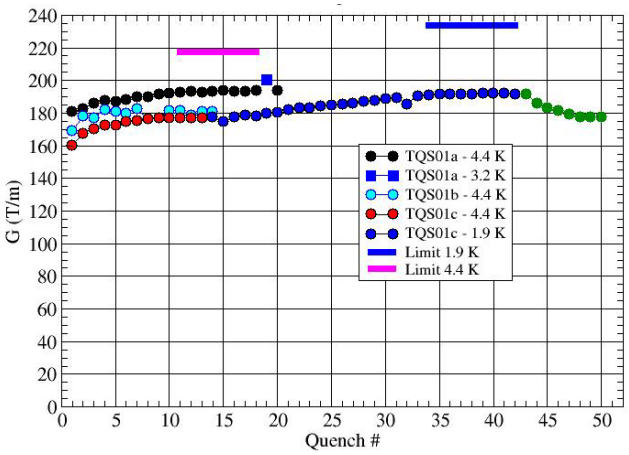

Fig. 4: Training curves of three TQS01 tests.

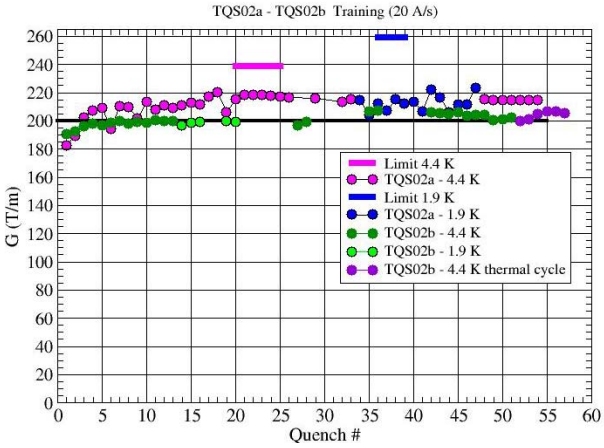

Fig. 5: Training curves of two TQS02 tests.

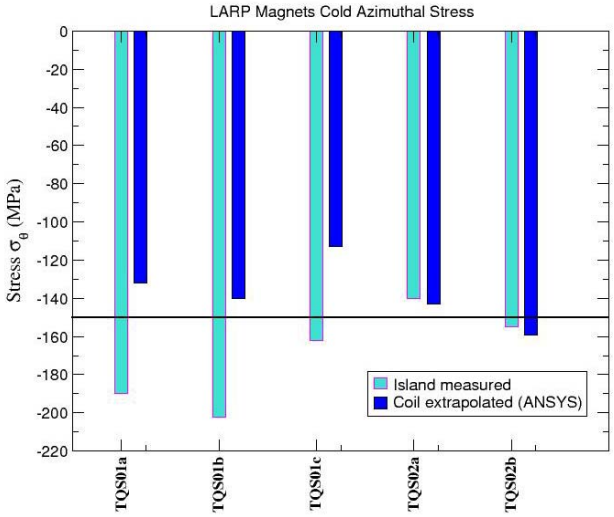

Fig. 6: Measured azimuthal stress in the island and in the corresponding coil next to it.

Table II. TQS conductor limits.

Magnet	TQS01	TQS02
Conductor	MJR	RRP
Iss 4.4 K	12100	13600
Gss 4.4 K	216	239
Iss 1.9 K	13200	14800
Gss 1.9 K	234	259

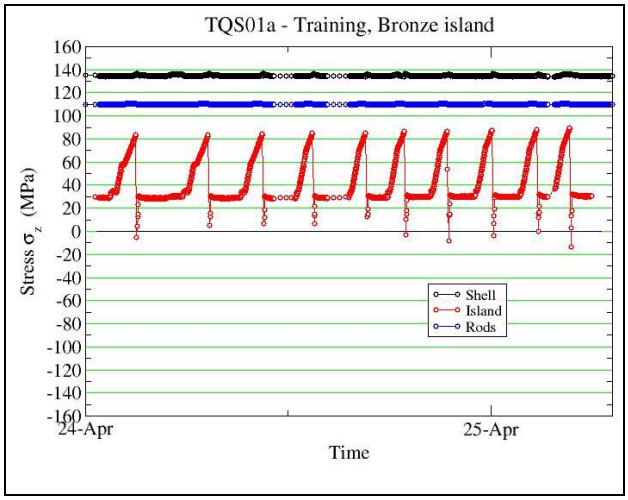

Fig. 7 Measured stress in TQS01a islands shell and rods (bronze islands).

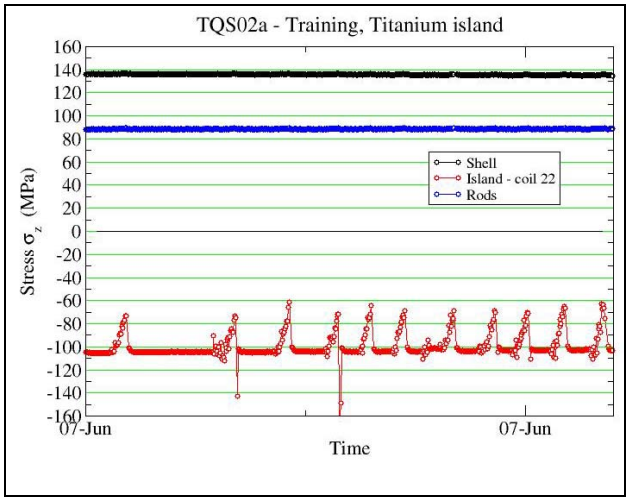

Fig. 8 Measured stress in TQS02a islands shell and rods (titanium islands).

CONCLUSIONS

The shell based magnets were tested using keys and bladder assembly. Measurements of strain in coils and structure followed expectations analyzed with the program ANSYS. So far we had 6 assemblies and 5 tests. The TQS magnets met the 200 T/m goal:

- Maximum gradients at 4.4 K: 180-222 T/m; plateau reached after 4-20 quenches with 80-90% of short-sample.
- Maximum gradients at 1.9-3.2 K: 192-225 T/m; plateau reached after 20 quenches with 77-84% of short-sample.
- In TQS02, bronze islands were replaced by titanium islands
- Quench location: TQS01 quenches were in the inner layer straight section (near island gaps), whereas TQS02a was dominated by outer layer quenches.
- A technology transfer of the bladder and key assembly structure to CERN has been successfully carried out for TQS02b,c.

Issues regarding the slow or no training at 1.9 K as well as the cause for outer layer quenches will require further studies.

ACKNOWEDGEMENT

We thank the LBNL technical staff for their work and dedication. Special thanks go to the FNAL and CERN test teams for their professional work. This work was supported by the Director, Office of Energy Research, Office of High Energy and Nuclear Physics, High Energy Physics Division, U. S. Department of Energy, under Contract No. DE-AC02-05CH11231.

REFERENCES

[1] S.A. Gourlay, *et al.*, "Magnet R&D for the IS LHC Accelerator Research Program", *IEEE Trans. Appl. Supercond.*, vol. 16, no. 2, June 2006, pp. 324-327.

[2] G. Sabbi *et al.*, "Nb3Sn quadrupole magnets for the LHC IR", *IEEE Trans. Appl. Supercond.*, Vol. 13, no. 2, June 2003, pp. 1262-1265.

[3] P. Ferracin, *et al.*, "Assembly and Test of a Support Structure for 3.6 m Long Nb_3Sn Racetrack Coils", paper 3E02 this conference.

[4] S. Caspi, *et al.*, "The use of pressurized bladders for stress control of superconducting magnets", *IEEE Trans. Appl. Supercond.*, Vol. 11, no. 1, March 2001, pp. 2272-2275.

[5] A. R. Hafalia, *et al.*, "A new support structure for high field magnet", *IEEE Trans. Appl. Supercond.*, Vol. 12, no. 1, March 2002, pp. 47-50.

[6] S. Caspi, *et al.*, "Design and analysis of TQS01, a 90 mm Nb_3Sn model quadrupole for the LHC luminosity upgrade based on a key and bladder assembly", *IEEE Trans. Appl. Supercond.*, vol. 16, no. 2, June 2006, pp. 358-361.

NB_3SN QUADRUPOLES DESIGNS FOR THE LHC UPGRADES

H. Felice, LBNL, Berkeley, CA 94720, USA

Abstract

In preparation for the LHC luminosity upgrades, high field and large aperture Nb_3Sn quadrupoles are being studied. This development has to incorporate all the relevant features for an accelerator magnet like alignment and cooling channels.

The LARP HQ model is a high field and large bore quadrupole that will meet these requirements. The 2-layer coils are surrounded by a structure based on key and bladder technology with supporting iron yoke and aluminum shell. This structure is aimed at pre-stress control, alignment and field quality. We present here the magnetic and mechanical design of HQ, along with recent progress on the development of the first 1-meter model.

INTRODUCTION

The main objective of LARP is to demonstrate the feasibility of the Nb_3Sn technology for the LHC upgrades. The increase of the baseline luminosity requires IR quadrupoles with high performing gradients. Although NbTi solutions are considered, Nb_3Sn remains the best candidate to achieve the performance required for the LHC Upgrade Phase 2. In this context, LARP has developed several series of Nb_3Sn magnets:

- The SQ series (Subscale Quadrupole) provided a gradient of 90 T/m in 110 mm aperture using subscale Nb_3Sn racetrack coils and included alignment [1,2].

- The TQ series (Technologic Quadrupole) consists of 1-meter long, 90 mm aperture cosine theta quadrupole magnets with a peak field of the order of 12 T and a measured gradient between 200 and 220 T/m [3,4].

- The LR magnet (Long Racetrack in a common coil arrangement) relied on two 3.6 m Nb_3Sn racetrack coils assembled in a shell-based structure to demonstrate the scalability of Nb_3Sn racetracks [5].

- The LQ series (Long Quadrupole) is a scale up of the TQ series aiming at demonstrating the scalability of Nb_3Sn cosine theta quadrupole [6].

In order to meet the requirements for Phase 2, the next series of magnet will have to reach 14-15 T at 1.9 K in a large aperture (above 110 mm) with alignment features (to provide field quality), cooling channels and LHe containment. The objective of the HQ series (High gradient, high field Quadrupole) is to address these requirements [7].

This leads to technical challenges: in terms of coil design and mechanical structure design. The magnetic efficiency will have to be combined with mechanical efficiency. The mechanical structure will have to withstand large Lorentz forces while remaining compact enough to fit within the LHC tunnel. The cable design is also a very important step for the design: to reach high field and to manage mechanical stress in the coil, the use of a 15 mm wide cable is necessary. The windability and the cabling degradation have to be watched closely. HQ aperture is not yet determined but apertures ranging between 114 and 134 mm have been considered. We summarize here the results for a 114 mm aperture.

This work was supported by the Director, Office of Energy Research, Office of High Energy and Nuclear Physics, High Energy Physics Division, U.S. Department of Energy, under contract No. DE-AC02-05CH11231.

H.Felice is with Lawrence Berkeley National Laboratory, Berkeley, CA 94720 USA (e-mail: HFelice@lbl.gov).

MAGNETIC DESIGN

Conductor

The strand is 0.8 mm in diameter with a copper/non copper ratio of 0.87. The cable is made of 35 strands. The keystone of the cable is of the order of 0.75. Some cable optimization is in progress in order to reduce current degradation due to cabling. The cable dimensions used to design the magnetic cross-section are summarized in Table 1:

Table 1: Conductor parameters

Dimensions	Units	Values
Width	mm	15
Mid thickness	mm	1.405
Insulation	mm	0.11

Magnetic Cross-section

For the same aperture, several magnetic cross-sections have been studied and compared in terms of:

- gradient
- peak field
- field quality
- pole angle in order to facilitate the windability
- maximum mechanical stress in the coil for a given mechanical structure.

This study brought to light the importance of combining the magnetic design with the mechanical design. Two different 134 mm aperture cross-sections are presented in Figure 1. The mechanical stresses induced by the Lorentz forces are compared for a gradient of 200 T/m. In both cases, the mechanical structure is infinitely rigid and the coil layers can slide one with respect to the other.

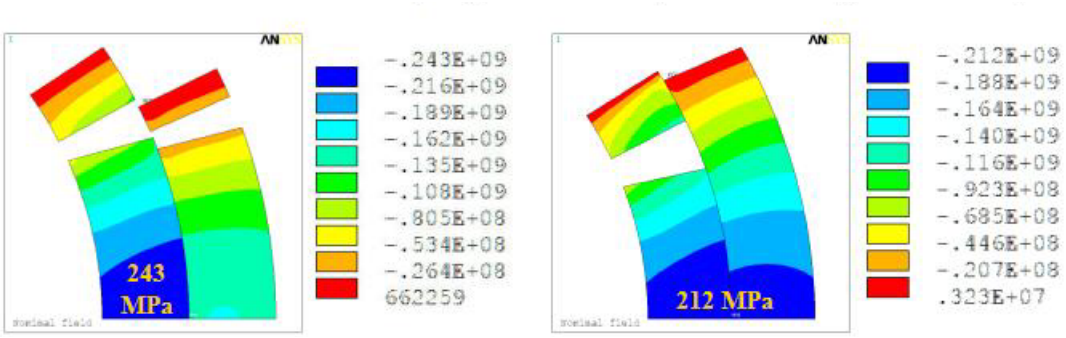

Figure 1: Azimuthal stress distribution due to Lorentz forces at 200 T/m in an infinitely stiff structure with sliding between layers for two 134 mm aperture cross-sections. Left: $F_\theta L_1$ = -3.58 MN/m $F_\theta L_2$ = -2.46 MN/m – Right: $F_\theta L_1$ = -2.7 MN/m $F_\theta L_2$ = -3.4 MN/m

In the first case (Fig. 1 left), the azimuthal force is much higher in the inner layer L_1 inducing high compressive stress on the mid-plane. In the second case (Fig. 1 right), the outer layer L_2 exhibits a greater Lorentz force than the inner layer L_1 leading to a more homogeneous stress distribution in the coil. We clearly see here that the mechanical stresses induced in the coil depend strongly on the azimuthal Lorentz forces distribution between layer 1 and layer 2.

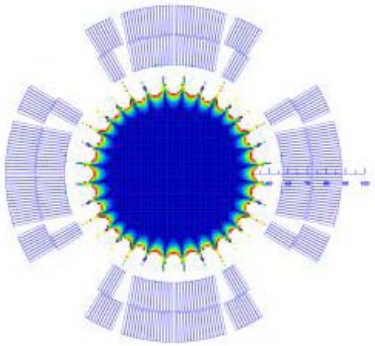

Figure 2: HQ 114 mm aperture cross-section designed by Vadim Kashinkhin, FNAL

Based on these considerations, a magnetic cross-section has been designed (Fig. 2) using the conductor described in Table 1.

The magnet short sample limit parameters at the operating operation T_{op} = 1.9 K are presented in Table 2. The critical current density taken into account in the computation is 3000 A/mm^2 at 12 T and 4.2 K.

Table 2: Magnet parameters at T_{op} = 1.9 K

Dimensions	Units	Values
G_{SS}	T/m	234
B_{SS}	T	15.39
I_{SS}	kA	19.18
$F_\theta L_1/L_2$ at I_{SS}	MN/m	2.5 / 2.99
Stored energy	MJ/m	1.31

The iron yoke is located at 10 mm from the coil. For the magnetic computation, the outer radius is equal to 260 mm.

MECHANICAL DESIGN

The mechanical structure relies on an aluminum shell surrounding an iron yoke and four support pads.
The coils are wound around a Titanium pole. For a 114 mm aperture, the aluminum shell is 25 mm thick and the overall diameter of the magnet is 550 mm. The axial preload is provided by axial rods, which are pre-tensioned at room temperature and shrink during cool-down. The main objectives of this structure are to provide mechanical support up to the short-sample limit of the magnet and to implement alignment. The different components of the mechanical structure are shown in Figure 3. At 200 T/m, the ANYS 2D simulation shows a maximum azimuthal stress in the coil of the order of –135 MPa. At the short sample limit, that is to say for a gradient of 234 T/m, this maximum stress is equal to –177 MPa.

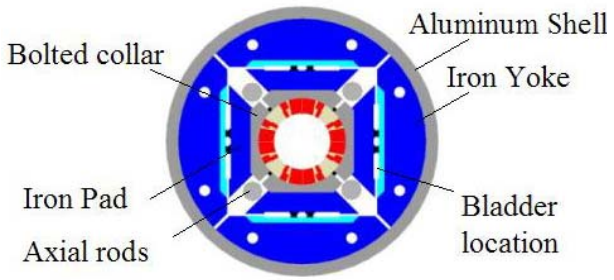

Figure 3: HQ mechanical structure

The optimization of this mechanical structure is in progress in order to incorporate all the accelerator quality features required for a LHC upgrade (cooling channel, alignment, LHe containement).

NEXT STEPS

In parallel to the mechanical analysis, the tooling is being designed. Magnetic 3D computations have also started in order to optimize the ends design and the iron shape.

REFERENCES

[1] P. Ferracin et al., "Development of a large aperture Nb_3Sn Racetrack Quadrupole Magnet," IEEE Trans. Appl. Supercond., Vol. 15, Issue 2, June 2005.

[2] P. Ferracin et al., "Assembly and Tests of SQ02, a Nb_3Sn Racetrack Quadrupole Magnet for LARP," IEEE Trans. Appl. Supercond., Vol. 17, Issue 2, June 2007.

[3] S. Caspi et al., "Fabrication and Test of TQS01 – A 90 mm Nb_3Sn Quadrupole Magnet for LARP," IEEE Trans. Appl. Supercond., Vol. 17, Issue 2, June 2007.

[4] S. Caspi et al., "Test and Analysis of Technology Quadrupole Shell (TQS) Magnet Models for LARP," IEEE Trans. Appl. Supercond., Vol. 18, No 2, June 2008.

[5] P. Wanderer et al., "Construction and Test of 3.6 m Nb_3Sn Racetrack Coils for LARP," IEEE Trans. Appl. Supercond., Vol. 18, No 2, June 2008.

[6] G. Ambrosio et al., "LARP Long Nb_3Sn Quadrupole Design," IEEE Trans. Appl. Supercond., Vol. 18, No 2, June 2008.

[7] H. Felice et al., "Magnetic and Mechanical Analysis of the HQ Model Quadrupole Designs for LARP," IEEE Trans. Appl. Supercond., Vol. 18, No 2, June 2008

15 T AND BEYOND – DIPOLES AND QUADRUPOLES*

G. Sabbi, LBNL, Berkeley, CA

Abstract

Starting with the invention of the cyclotron by Lawrence, accelerator-based experiments have been the primary source of new discoveries in particle physics. In order to progress toward higher energy and luminosity, higher field magnets are required. R&D programs are underway to take advantage of new developments in superconducting materials, achieve better efficiency and simplify magnet fabrication while preserving accelerator-class field quality. A review of recent progress on high field dipole and quadrupole magnets is presented.

INTRODUCTION

The Large Hadron Collider (LHC) will soon replace Fermilab's Tevatron as the world's most powerful accelerator. LHC will collide proton beams with 14 TeV center-of-mass energy and 10^{34} $cm^{-2}s^{-1}$ luminosity. The maximum dipole field is 8.3 T, obtained using Niobium-Titanium (NbTi) conductor at 1.9 K. After several years of LHC operation, performance upgrades will be required to maintain its potential for new discoveries. Current plans involve a series of luminosity upgrades followed by an energy upgrade aiming at doubling the center of mass energy [1]. Both the luminosity and energy upgrades require very high field magnets, operating well beyond the fundamental limits of NbTi.

Superconductors suitable for high field applications are brittle and strain sensitive, requiring new design concepts and fabrication methods to complement or replace the ones established for NbTi. Niobium-Tin (Nb_3Sn) is currently the most advanced material for practical applications [2]. It carries current densities similar to NbTi at more than twice the field, and is available in long lengths with uniform properties. Nb_3Al offers lower strain sensitivity with respect to Nb_3Sn, but requires further improvements in the manufacturing process. The low-temperature properties of HTS materials such as Bi-2212 are far superior to both Nb_3Sn and Nb_3Al. However, many fundamental technology issues need to be addressed before practical magnet designs can be developed and implemented in prototypes.

Because of their brittleness, high field superconductors cannot be drawn to thin filaments like NbTi, but have to be formed in the final geometry by high-temperature heat treatment. In the fully reacted state, the filaments are extremely sensitive to strain. Therefore, attempting to wind reacted cable in coils may result in unacceptable critical current degradation at the ends. A first approach (wind-and-react) is to wind coils using un-reacted cable, when components are still ductile, and perform the heat treatment after coil winding. This technique requires the use of special insulation and coil structural components that can withstand the high reaction temperatures. A second approach (react-and-wind) is to modify the coil design to avoid sharp bending, allowing the use of pre-reacted cable.

During the last 15 years, LBNL has been developing accelerator magnet technology towards progressively higher fields, using Nb_3Sn conductor in different coil configurations. Since each configuration has specific advantages and drawbacks, the available design options should be evaluated in the context of specific applications as part of an optimization process involving both the magnet and the accelerator. This paper presents prototype test results and design studies of dipoles and quadrupole magnets aiming at coil peak fields above 15 Tesla.

HIGH FIELD DIPOLES

Coil layouts

Shell-type ($\cos\theta$) coils using keystone Rutherford cable have been adopted in most superconducting accelerator magnets due to their self-supporting Roman-arch structure and optimal use of superconductor in the design range of interest. Wind-and-react technology allows extending this approach to Nb_3Sn. In the mid-90s, the University of Twente dipole MSUT and the Berkeley dipole D20 were built using a costθ layout, reaching fields of 11T and 13T, respectively [3]-[4]. However, several considerations have prompted designers to explore alternative schemes based on block-type coil geometry with flat cables.

The arc dipoles are a major cost driver for next-generation colliders. Large stored energy, magnetic forces and conductor requirements tend to limit the bore size to smaller values than in previous machines. As the field increases and the aperture decreases, the advantages of shell-type coils are progressively diminished. Wide cables are desired in high field magnets to limit the number of layers and magnet inductance. At the same time, keystone angles are limited by degradation at the narrow edge. Under these conditions, $\cos\theta$ coils need to allocate a larger fraction of the coil volume to wedges, decreasing the magnetic efficiency. Winding issues also become critical due to tight bending radii at the ends. Azimuthal force accumulation results in high stress levels at the mid-plane.

Conversely, block-type coil geometries offer several potential advantages: high packing factors with no wedges; use of flat cables with minimal degradation; simplification of end part design and coil winding procedures; good alignment of the conductor to the field

*Work supported by the US Department of Energy

lines, allowing efficient grading; physical separation between high-field and high-stress points, leading to reduced sensitivity to stress degradation. These attractive features need to be weighted against the loss of high-field magnetic aperture to provide internal coil support against pre-load, and generation of large horizontal forces. Also, deviations from the simplicity of planar racetrack coils are necessary to address issues of conductor efficiency and field quality. The design, fabrication and test of prototypes is therefore required to evaluate the properties of block-coil dipoles under realistic conditions, and demonstrate performance and cost suitable for future accelerator applications.

The HD Prototype Series

The "HD" magnet series was conceived as a vehicle for developing Nb_3Sn technology at the maximum attainable fields using single-bore block-coils [5]. The first magnet in this series, HD1, was based on a flat racetrack coil configuration and had a 10 mm bore. These features were consistent with the HD1 goals: exploring the Nb_3Sn conductor performance limits at the maximum fields and under high stress.

Providing adequate coil support in high-field magnets based on brittle superconductors requires new mechanical designs that can generate large forces while minimizing stress on the conductor at all stages of magnet fabrication and operation. A special support structure was developed at LBNL for high field dipoles and applied to HD1 [6]-[7]. This concept is based on the use of water-pressurized bladders to compress the coil pack while tensioning a thick aluminum shell. When the shell reaches the required tension, interference keys are inserted and the bladders deflated and removed. During cool-down, the stress in the shell almost doubles due to differential thermal contraction relative to the iron yoke. This allows limiting the peak coil stress during assembly, and reducing the shell thickness taking advantage of its increased strength at lower temperature. The pre-load is controlled in both the horizontal and vertical direction. To restrain the coil against axial forces, pre-tensioned aluminum rods are used to compress thick stainless steel plates against the coil ends [8].

Fig. 1: HD1 Dipole

HD1 was tested in 2003 and achieved a maximum bore field of 16 T under coil stresses approaching 180 MPa [9]. This result demonstrated that Nb_3Sn block-coils have the potential to achieve very high fields. However, in order to further develop this concept for future high-field accelerators, larger aperture and improved field quality are needed. The first technical challenge to be confronted is a loss of magnetic aperture to provide structural support against the pre-load forces in the magnet bore. In addition, conductor placement in the vicinity of the magnetic mid-plane is desirable for magnetic efficiency and field quality, but leads to deviations from a flat geometry in the coil ends, where the conductors have to clear the magnet bore. The second prototype in the series (HD2) addresses these issues aiming at a central dipole field above 15 T, a clear bore diameter above 36 mm, and nominal field harmonics within a fraction of one unit. The cross-section combines two double-layer coil modules in a block configuration. A stainless steel tube, inserted between the winding poles, provides the bore support. The coil ends are still of the racetrack type, but a ramp is included to avoid obstructing the beam path [10].

The HD2 mechanical structure, similar to the one used for HD1, is composed of horizontal and vertical load pads, bridges, yoke and aluminum shell. Interference keys located between pads and yokes tension the shell and compress the coil-pack in both the vertical and the horizontal direction. Hydraulic bladders are used to provide clearance for inserting the keys. Horizontal and vertical pushers transfer the load from the pads to the coils. Four aluminum rods provide axial pre-stress, to minimize displacements in the coil end regions [11].

Each coil is a double-layer wound around an aluminum-bronze pole, with a minimum winding radius of 12.5 mm. A 0.8 mm wire diameter is chosen due to practical considerations relating to strand availability. However, this design concept would be easily scalable to larger diameter wires, resulting in a better aspect ratio for the cable, lower cost of fabrication and lower inductance. The coil aperture is approximately square, 45 mm on each side. A mid-plane spacer separates the coils. The winding poles have a round cutout on the side facing the magnetic mid-plane. This cutout is used to assemble the coil modules around a stainless steel tube, providing a 36 mm diameter clear bore.

TABLE I
CONDUCTOR PARAMETERS FOR HD2 AND HD1

Parameter	Unit	HD2	HD1
Strand diameter	mm	0.8	0.8
Design Ic (16 T, 4.2K)	A	322	322
Cu/Sc ratio		0.94	0.94
No. strands		51	36
Cable height	mm	22.0	15.75
Cable thickness	mm	1.36	1.36
Insulation thickness (h/v)	μm	93/130	93/130
No. turns/quadrant		54	69

TABLE II
DESIGN PARAMETERS FOR HD2 AND HD1

Parameter	Unit	HD2	HD1
Bore size	mm	36	8
Short sample current*	kA	15.2	11.4
Central dipole field	T	15.1	16.7
Coil peak field	T	16.1	16.1
Copper current density	kA/mm^2	1.3	1.3
Inductance	mH/m	7.7	10.2
Stored energy	MJ/m	0.89	0.66
Fx (quadrant)	MN/m	5.9	4.75
Fy (quadrant)	MN/m	-2.7	-1.55
Ave. Lorentz stress (x)	MPa	140	150

The HD2 coil peak field at short sample is about 16 T, similar to HD1. The higher bore field in HD1 due in part to the smaller aperture and in part to the contribution of the iron pole to the field. A non-magnetic (Titanium) pole is used in HD2, to avoid generating a saturation effect. The conductor volume and Lorentz forces show relatively modest increases from HD1 to HD2. The inductance is lower in HD2, due to the use of a wider cable and fewer turns. As it was previously noted, the HD2 coil cross-section is suitable for a further increase of the wire (and cable) size. The resulting reduction of the inductance would be beneficial for protection of long magnets in a large accelerator

At high field, all HD2 design harmonics are below 0.1 units at 10 mm radius (R_{ref}). Despite the absence of inter-turn spacers in this coil, it is possible to optimize the geometric harmonics to low values by tuning the thickness of the mid-plane spacer, the number of turns in each layer, and the relative position of the two conductor blocks. In this design, the geometric harmonics b_3 and b_5 are very small and would be likely dominated by magnetization effects, iron saturation and random errors. The yoke was optimized for saturation effects. And a thin magnetic insert in the bore compensates for persistent current effects.

Three HD2 test were performed to date, achieving a maximum dipole field of 13.8 T, and a coil peak field of 14.5 T. Details of the test results are provided in another paper presented at this workshop [12].

LARGE APERTURE QUADRUPOLES

A staged upgrade of the LHC and its injectors is under study to achieve a luminosity of 10^{35} cm^{-2}s^{-1}, a 10-fold increase with respect to the baseline design. Replacing the first-generation NbTi IR quadrupoles with higher performance magnets is one of the required steps in this direction. Although improved designs based on NbTi will be used as an intermediate solution (Phase 1 upgrade), Nb_3Sn conductor is required to meet the ultimate performance goals for operating field and temperature margin. The new IR magnets need to provide increased focusing power and at the same time be able to operate under radiation loads corresponding to the 10^{35} cm^{-2} s^{-1} luminosity target.

Minimizing the superconductor volume is not a critical design consideration for the IR quadrupoles, since their number is limited. However, efficient field generation is essential in order to achieve high gradients. Several design studies have shown that in the parameter range of interest, cos2θ coils provide optimal magnetic efficiency.

Starting in 2004, the LHC Accelerator Research Program (LARP) has been coordinating the US effort to develop prototype magnets for the luminosity upgrade [13]. Following a series of "Technology Quadrupoles" (TQ) with 90 mm aperture and 220-250 T/m gradient, larger aperture and higher field designs were developed, aiming at coil fields above 15 T. These studies allowed to investigate the main technical issues (magnetic, mechanical, quench etc) and to explore the aperture design space in the range of 90-140 mm. Coil stresses above 180 MPa are expected and conductor degradation due to high stress represents a major factor potentially limiting the magnet performance. Comparison of different layouts shows differences in the accumulated Lorentz

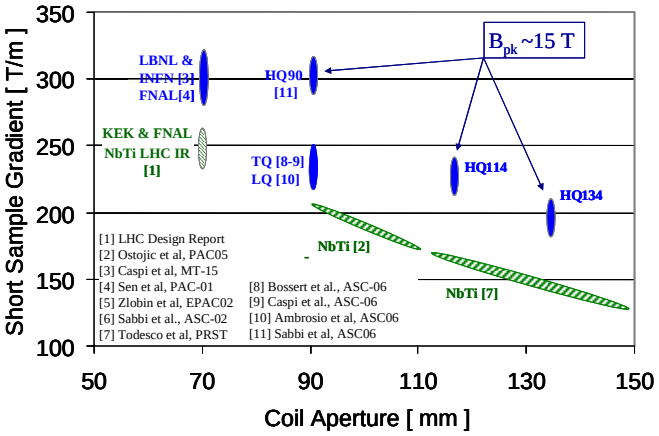

Fig. 2: Quadrupole designs for the LHQ IR.

forces that may be exploited to minimize the peak coil stress. Therefore, stress considerations need to be taken into account already when selecting the coil cross-section. In order to include the effect of deflections and friction among layers, the stress patterns for each candidate cross-section were evaluated using a 2D mechanical analysis. As for the high field dipoles, the mechanical structure is based on a thick Aluminum shell over iron yoke, assembled using water-pressurized bladders and interference keys [14].

The IR quadrupoles need to provide high field quality, in particular during collision. Therefore, precise coil fabrication and structure alignment are required. In addition, field errors due to persistent current effects are a concern. Nb_3Sn wires exhibit large magnetization due to high critical current density and large filament size. Compensation of persistent current effects by saturation of carefully designed iron inserts is being actively explored as an intermediate solution. Ultimately, wires with larger number of sub-elements are being developed to decrease the effective filament size [15]-[16].

The upgrade quadrupole design will be developed through a series of 1 meter models (HQ) and then implemented in a series of 4 meter models (QA). The magnets will initially use the parameters and accelerator quality specifications of the "Phase 1" NbTi quads to facilitate their evaluation for use in the LHC. Goal of both HQ and QA is to demonstrate large performance margins with respect to the NbTi quads, on the timescale of the Phase-1 upgrade. The full set of features needed for an accelerator magnet will be gradually incorporated into successive HQ magnets and used in QA.

In the last months, considerable progress was made toward the start of HQ model fabrication. Prototype cables were evaluated from both the mechanical and electrical standpoint. Several cross-sections were optimized, and detailed analyses of the coil stresses were carried out for different variants of the supporting structure geometry. End parts were fabricated and used for winding experiments. After a final iteration of the coil and tooling design, component procurements will start, followed by winding of the first practice coil. Test of the first HQ model is expected in November 2009.

HTS COILS

Our studies indicate that the ultimate magnetic field in a practical dipole configuration using Nb_3Sn technology is limited to 17-18 T by the material's maximum $\mu_0 H_{c2}$ of about 29 T. In order to develop dipoles approaching 20 T and higher, a material with a higher H_{c2} is required. The most promising candidate for this purpose is $Bi_2Ca_2CuSr_2O_{8+x}$ (Bi-2212), which is available in round wires and has been made in sufficient lengths for the fabrication of coils based on Rutherford-type cables.

Since both Nb_3Sn and Bi-2212 are brittle and require a wind-and-react approach to coil fabrication, the magnet

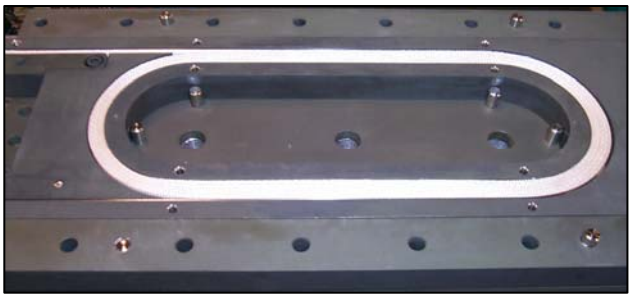

Fig. 3: Bi-2212 sub-scale coil fabrication.

design methods developed for Nb_3Sn provide a starting point for work on Bi-2212. However, constructing a magnet using Bi-2212 is significantly more complicated than using Nb_3Sn. The new technological challenges are related to cabling of the wires, higher strain sensitivity, high formation reaction temperature in an oxygen-rich environment, and chemical compatibility of the insulation and construction materials during the reaction heat treatment.

The implementation of HTS for high-field magnets requires a development program that addresses the novel characteristics of the superconductor and its implementation in real magnets. Issues that are readily apparent include: (a) developing and selecting insulation, tooling, fabrication procedures and structural materials suitable for a wind and react approach; (b) detailed analysis of the stress/strain state of the magnet throughout fabrication and operation; (c) design of support structures for their control; (d) protection of the magnet during a quench [17].

Despite these challenges, several factors are contributing to an efficient program start. Previous development of Bi-2212 cables at LBNL, in close collaboration with wire manufacturers, has resulted in sufficient experience to design a cable suitable for sub-scale coils. The available structures and tooling from the Nb_3Sn program can be adapted to the HTS coils with relatively small modifications. A modified tooling for sub-scale coil winding and reaction was designed, and several coils were fabricated and tested. The thermal characteristics of these mechanical coils will be suitable for optimization of the reaction schedule. Nevertheless, it is recognized that Nb_3Sn technology, particularly related to fabrication processes and magnet protection, is not directly applicable to HTS-based magnets.

Taking into consideration the high cost of Bi-2212, and its relatively low current carrying capability at fields below 15 T, a hybrid Nb_3Sn-Bi2212 coil represent an optimal approach in terms of efficiency and cost. The Bi-2212 insert is wound from a high current Rutherford-type cable, resulting in high packing factor, high magnetic efficiency and low inductance. Specific R&D issues that need to be addressed are: protecting the Bi2212 insert from excessive stress during pre-load and excitation; current matching and high-field splicing between sub-coils (for a series-connected hybrid) or independent

powering of the sub-coils.

SUMMARY

Intensive magnet R&D efforts are needed to meet the requirements of future colliders at the energy frontier. In recent years, new design approaches and technology developments have resulted in cost-effective designs that include accelerator quality features. Record dipole fields have been achieved, and further progress is enabled by improvements in high field superconducting materials. The LHC luminosity and energy upgrades provide the opportunity to apply the results obtained in proof-of-principle models to full-size production magnets suitable for operation in the challenging accelerator environment.

REFERENCES

[1] F. Ruggiero (editor) et al., "LHC Luminosity and Energy Upgrade: a feasibility study", LHC Project Report 626, December 2002.

[2] S. Hong, et al., "Latest Improvement of Current Carrying Capability of Nb_3Sn", Presented at the 19th International Conference on Magnet Technology, Genoa, Italy, September 2004.

[3] A. den Ouden et al., "Application of Nb_3Sn superconductors in accelerator magnets", IEEE Trans. Appl. Supercond. Vol. 7, 1997.

[4] A. McInturff et al., "Test Results for a High Field (13 T) Nb_3Sn Dipole", PAC-97, Vancouver, May 1997.

[5] S. Gourlay and G. Sabbi, "Future Expectations, Limits and Operational Issues for High Field Superconducting Accelerator Dipole Magnets", Proceedings of EPAC 2002, Paris, France.

[6] S. Caspi, et al., "The use of pressurized bladders for stress control of superconducting magnets", IEEE Trans. Appl. Superconduct., vol. 11, no. 1, pp. 2272-2275, March 2001.

[7] R. Hafalia, et al., "HD1: Design and Fabrication of a 16 Tesla Nb3Sn Dipole Magnet", IEEE Trans. Appl. Supercond. vol. 14, June 2004.

[8] P. Ferracin, et al., "Mechanical analysis of the Nb3Sn dipole magnet HD1", IEEE Trans. Appl. Superconduct., Vol. 15, no. 2, pp. 1119-1122, June 2005.

[9] A. F. Lietzke, et al., "Test Results for HD1, a 16 T Nb_3Sn Dipole Magnet", *IEEE Trans. Appl. Supercond.* vol. 14, June 2004.

[10] G. Sabbi, et al., "Design of HD2: a 15 T Nb_3Sn dipole with a 35 mm bore", IEEE Trans. Appl. Superconduct., Vol. 15, no. 2, pp. 1128-1131, June 2005.

[11] P. Ferracin, S. Caspi, D. W. Cheng, D. R. Dietderich, A. R. Hafalia, C. R. Hannaford, H. Higley, A. F. Lietzke, J. Lizarazo, A. D. McInturff, and G. Sabbi, "Development of the 15 T Nb3Sn Dipole HD2", IEEE Trans. Appl. Supercond., vol. 18, no. 2, June 2008, pp. 277-280.

[12] P. Ferracin, "Test Results of HD2", these proceedings

[13] S.A. Gourlay, et al., "Magnet R&D for the US LHC Accelerator Research Program", IEEE Trans. on Appl. Superconduct., vol. 16, no. 2, June 2006, pp. 324-327.

[14] H. Felice, et al., "Magnetic and Mechanical Analysis of the HQ Model Quadrupole Designs for LARP", IEEE Trans. Appl. Supercond., vol. 18, no. 2, June 2008, pp. 281-284.

[15] S. Caspi, "Reduction of Magnetization Harmonics in Superconducting Magnets", LBNL report SC-MAG-691, October 1999.

[16] V. Kashikhin, A. Zlobin, "Correction of the Persistent Current Effect in Nb3Sn Dipole Magnet", IEEE Trans. Appl. Supercond. 11(1), 2001.

[17] 12. A. Godeke, D. Cheng, D. R. Dietderich, P. Ferracin, S. O. Prestemon, G. Sabbi, and R. M. Scanlan, Limits of NbTi and Nb3Sn, and Development of W&R Bi–2212 High Field Accelerator Magnets, IEEE Trans. on Appl. Supercond. 17, no. 2, 1149, (2007).

THE HIGH FIELD MAGNET PROGRAM IN EUROPE

Gijs de Rijk, CERN, Geneva, Switzerland.

Abstract

With the LHC, magnets of 10 T peak flux density Nb-Ti technology were developed and this technology reached full maturity. The next step in flux density level, with a peak in the range of 15 T, will be needed for the LHC Phase II upgrade. For this upgrade the temperature margin and radiation resistance of the Nb-Ti coil technology is not sufficient. Beginning 2008 CERN started a program to develop high field magnets for LHC upgrades and other future programs. For this mostly Nb_3Sn conductors will be employed, but also HTS conductors will be considered. In this paper an overview will be presented of the projects for which this HFM technology will be needed. The program will be presented in terms of R&D chapters and work packages. The need and opportunities for collaborations with other institutes will be discussed.

MOTIVATION

The physics potential of hadron colliders is determined by the maximum beam energy and the luminosity. The maximum energy of circular hadron accelerators is in its turn determined by the flux density in the main bending magnets and the circumference of the machine, whereas the maximum machine circumference is limited by economic and organizational parameters. On the other hand, the luminosity is fixed by a set of parameters where the gradient of the quadrupoles in the low-β insertions and their aperture play an important role. Thus any technology step which allows to increase the flux density in accelerator magnets also enables the construction of more powerful machines with a larger physics potential.

In this respect the technology of Nb-Ti superconducting magnets with an operational flux density around 4 T was inaugurated by the ISR low-β upgrade (1983) and it opened the way for building the Tevatron at FNAL in the early eighties. HERA at DESY and RHIC at BNL soon followed with magnets based on a similar technology. A major R&D program permitted CERN to stretch the technology to its limit and thus to double the operational flux density range of Nb-Ti accelerator magnets to 8 T, enabling the construction of the LHC, which will see its first beams in summer 2008.

To prepare for future luminosity upgrades of the LHC or for the construction of higher energy machines new high field magnet technology based on other conductors than Nb-Ti will have to be developed.

LHC LUMINOSITY UPGRADE

The luminosity limit of the LHC is estimated to be $L = 10^{34}$ cm^{-2}s^{-1}. The β* value in the two high luminosity interaction points is limited to 0.55 m mostly due to the available aperture in the positions of the highest β values in the insertion. The coil inner diameter of the quadrupoles at this position is 70 mm. It should be noted that the cold bore and the beam screen reduce the available beam aperture even further to 60 mm. In order to squeeze the beam down to smaller β* values, the aperture in the quadrupoles has to be significantly increased. A program, called SLHC Phase I upgrade, has been started at CERN to double the peak luminosity by using a β* value of 0.25 m and a larger beam current and should be implemented by 2013. Magnet modelling has started for quadrupoles, which will have a 120 mm inner coil diameter, an operational gradient of about 120 T/m and will be made with Nb-Ti technology [1]. On a longer timescale (>2017) more powerful magnets with a gradient of around 180 T/m and with an aperture of up to 150 mm will be needed to reach luminosities of $\geq 10^{35}$ cm^{-2}s^{-1} [2][3][4]. Such magnets are beyond what can be done with Nb-Ti conductors and will have to be made with Nb_3Sn conductors, as the peak flux density on the coils will exceed 10 T. These magnets will have to face large radiation doses coming from the debris of the interactions in the experiments from which the most damaging is the neutron flux of up to a few times 10^{17} cm^{-2}year^{-1} on an unprotected coil. The interaction debris will also impose a large heat load on the coil, which can locally go over 50 mW/cm^3, necessitating a very good heat removal from the coil and a large temperature margin of the superconductor.

Low-β insertion upgrade scenarios also comprise options with an early separation dipole placed in the experimental straight section [5]. This 1.5 m long magnet should have a flux density of 5 T in a 300 mm aperture. Due to its forward position, radiation and heat load (~75 W in total) will be very important on this magnet. A large, multi Kelvin, temperature margin will be needed, for which Nb_3Sn conductors might be required.

LHC luminosity upgrades will also include improvements to the collimation [6]. One candidate upgrade is to add an off-momentum particle collimator in the dispersion suppressors around the two high luminosity insertions. To position this collimator, a space of 5 m has to be created in the dispersion suppressor. For this a standard 15 m long 8 T two-in-one dipole should be replaced with a 10 m long 12 T two-in-one dipole. This type of magnet has to be made with Nb_3Sn conductor due to the flux density level. In a separate upgrade proposal the dog-leg in the cleaning insertions could be increased in order to improve the cleaning efficiency. For this 5 T dipoles would be needed. These magnets required Nb_3Sn conductors for their large temperature margin as they are subjected to the particle showers from the collimators.

For similar reasons the very forwardly positioned corrector magnets will also have to be made with high temperature margin Nb_3Sn conductors.

For the operation of the LHC with Pb ions a beam profile monitor is foreseen based on the detection of the synchrotron light emitted by the beam in an undulator. For this a small period (< 150 mm) with a flux density around 5 T in a 60 mm gap is needed. Due to the high peak flux density on the coil, this magnet will have to be made with Nb_3Sn conductor.

LHC ENERGY UPGRADE

On a timescale of 20 years it would be possible to consider an LHC successor machine with 2 - 3 times the LHC energy (DLHC). Such a machine would need magnets of the 20 T range. For flux densities above 15 T in accelerator magnets a hybrid HTS-Nb_3Sn coil system should be considered. Knowing the very long lead-time of 10 - 20 years for the development of new magnet technology, this development should start now if the HEP community wants to consider such a machine in the 2020-ies.

NEUTRINO AND MUON FACTORY

The neutrino community is presently considering a neutrino factory [7]. Two types of factories are being discussed, the first type is based on beams of radioactive isotopes (beta-beam) [8] and the second type is based on beams of decaying muons. The generation of the muon beams for the latter option is very much similar to what would be needed for a muon collider and hence these two programs present a common approach and operate from one collaboration. For both types of beam, unstable particles are stored in a storage machine where the decays in the long straight sections give rise to collimated neutrino beams. The other decay products, an ion and an electron or positron for the beta beam and an electron or positron for the muon machines, impose a very large radiation load on the magnets of the accelerators. These debris particles are swept out of the beam mostly in the horizontal plane thus impinging on the coil. For this application the development of open mid plane magnets with a flux density range of 4 T - 8 T is needed. Also here, Nb_3Sn conductors are required for their large temperature margin as they are subjected to the particle showers from the collimators.

HIGH FIELD MAGNET PROGRAM

Now that the construction of the LHC is complete, CERN has started a High Field Magnet R&D program, which is defined for the next 6 years. The main aim of the program is to develop the technologies necessary for high field accelerator magnets and to build demonstrators to show the feasibility of these magnets. In this respect CERN is joining into the efforts, which are already ongoing in the US since a few years within the LARP collaboration [9] and core programs at BNL, FNAL and LBNL, on the development of large aperture high gradient quadrupoles for LHC upgrades and very high field dipoles. It has to be kept in mind that to date there exists no “accelerator grade” Nb_3Sn magnet. The presently existing Nb_3Sn magnets are either short models, racetrack magnets without apertures and none of them has yet the required field quality or stability suitable for an accelerator like the LHC. A comprehensive effort in all institutes in a collaborative spirit is needed to make the next step and produce ‘installable” Nb_3Sn magnets.

CERN HFM program

The HFM program is divided up in 4 chapters: Conductor, Enabling technologies, Model Magnet and Prototype magnet. In these chapters a total of 49 work packages are defined. The program comprises collaborations with other laboratories and universities and the HFM work-package of the FP7-EuCARD proposal is anchored in this program.

A description of the chapters can be found below:.

1. Conductor.

The core of HFM development is the conductor. The critical current density (J_c) is a key parameter of the conductor to be developed. Nb_3Sn conductor displays a degradation of J_c with the imposed mechanical strain. The aim of the development is to get Nb_3Sn strand commercially available in large lengths with the following parameters: J_c (non-Cu part) ≥ 3 kA/mm^2 at 12 T and 150 MPa imposed stress. This conductor has to be stabilized at low flux density against instabilities. The strand has to be worked into a Rutherford type cable where the loss of J_c due to the cabling deformations should be below 5%. Furthermore the inter-strand resistance has to be controlled. The activities in the conductor chapter will run over the full 6 years.

2. Enabling technologies.

In order to prepare for the first construction of model magnets several outstanding technology issues have to be resolved.

A coil geometry concept has to be found for dipoles and quadrupoles such as to provide high flux density (e.g. $B > 12$ T in a dipole) with a good field quality ($\Delta B/B \sim 10^{-4}$) while keeping the maximum stress in the coil limited to manageable levels ($\sigma \leq 150$ MPa).

In order to evacuate the heat generated by the radiation impinging on the coil, a solution has to be found to circulate liquid helium in the coil. For this, either porous epoxy based impregnation or porous ceramic insulators have to be developed. The radiation resistance of the superconductor and the insulation materials have to be certified. The thermal behaviour of the coil will be modelled and verified with a thermal properties measurement program. The mechanical behaviour of the various candidate coil and magnet structures will be tested on samples and small mechanical models. Quench behaviour and quench protection schemes will be modelled. The coil and magnet concepts will be first checked in sub-scale models. In this chapter also the first steps will be made towards HTS insert magnets for dipoles. The undulator-wiggler development is also situated here. Most of these activities will be done in the first 3-4 years of the 6 year program.

3. Model Magnet

Three types of model magnets should be constructed to try out the concepts proposed in the technology chapter.
A 13 T dipole model of 1.5 m length and with a 100 mm aperture is to be constructed in the years 2009-2012. In the latter 3 years of the program a quadupole model with a 150 mm aperture and a gradient of 180 T/m will be constructed. During the last 2 years, models for the various corrector magnet types will also be constructed.

4. Prototype magnet

A last step in the 6 year development program is the construction of a 4 m long prototype magnet. The type (dipole or quadrupole) is still to be determined and is to be coordinated with the work by the LARP collaboration in the US.

EuCARD proposal

In the first quarter of 2008 a consortium of 40 institutes and universities has submitted the EuCARD proposal on a EU FP7 infrastructures call. Work Package 8 of this proposal concerns the high field magnets for the upgrades of European accelerator infrastructures. This proposal is closely intertwined with the CERN HFM program. It comprises 6 R&D tasks from which 5 have their CERN component in the CERN HFM program. The 6 tasks are: Support studies, High field model, Very high field dipole insert, High T_c superconducting link, Superconducting wiggler for ANKA, Short period helical superconducting undulator. Only the task on the superconducting high T_c link is based in a different activity at CERN. For this proposal the result of the selection will be known this summer. The EuCARD proposal is a very good occasion to link the activities and programs of all the laboratories involved in HFM development together and to give them a good starting point for further collaboration.
The large aperture dipole model of this program will, apart from being a test bed for Nb_3Sn accelerator magnets, later on serve to upgrade the CERN cable test facility FRESCA from an operational flux density of 10 T to 12 T. The same magnet can then also be used to provide the background field for the HTS dipole insert magnet, which is to be a very first step to hybrid HTS-Nb_3Sn accelerator magnets in the 20 T range.

Present activities

During the first half of 2008 the activities which have already been started:

- Construction of a sub-scale race-track models in a collaboration between CEA, LBNL, STFC-RAL and CERN.
- Detailed re-testing in the CERN test station of a TQS model quadrupole, made by the LARP collaboration in the US. This re-test is done in an LBNL - CERN collaboration.
- Pre-design studies of the dipole model

At present the main work is on consolidating the program and to form a larger collaboration on high field magnet development for accelerator applications.

REFERENCES

[1] L. Evans, “SLHC Accelerator and Injector Upgrades”, SLHC kick-off event, CERN, 8-9 April 2008, CERN, http://info-slhc-pp.web.cern.ch/info-SLHC-PP/ .

[2] J-P. Koutchouk, R. Assmann, E. Métral, E. Todesco, F. Zimmermann, R de Maria, G Sterbini, “A Concept for the LHC Luminosity Upgrade Based on Strong Beta* Reduction combined with a Minimized Geometric Luminosity Loss Factor”, PAC’07, Albuquerque, NM, USA, June 2007, http://www.JACoW.org .

[3] F. Zimmermann, “LHC Upgrade Scenarios”, PAC’07, Albuquerque, USA, June 2007, http://www.JACoW.org.

[4] E. Todesco and J-P. Koutchouk, “Scaling laws for Beta* in the LHC interaction regions”, 3rd CARE-HHH-APD Workshop, IFIC, Valencia, Spain, 16 - 20 Oct 2006, CERN-2007-02, CARE–Conf–07–004–HHH, pp.61-70.

[5] G.Sterbini, D. Tommasini, “A feasibility study of superconducting dipole for the early separation scheme for LHC”, to be published at EPAC08, WEPD025

[6] R. Assmann, “Intensity limitations: collimation in PS2, SPS, LHC”, presentation at 3rd CARE-HHH-APD Workshop, IFIC, Valencia, Spain, 16 - 20 Oct 2006.

[7] A. Baldini et al, “Beams for European Neutrino Experiments (BENE) Midterm scientific report”, CARE–20006-009-BENE, CERN–2006–005, ECFA/06/242, 22 May 2006

[8] A. Chancé, J. Payet, “The beta-beam decay ring design”, EPAC’06, Edinburgh, Scotland, 2006, http://www.JACoW.org.

[9] The LARP collaboration, http://www.agsrhichome.bnl.gov/LARP/

Nb_3Sn QUADRIPOLE DEVELOPMENT AT CEA/SACLAY

J.M. Rifflet, M. Durante, M. Segreti, CEA, IRFU, SACM, F-91191 Gif-sur-Yvette, France.

Abstract

CEA/Saclay is fabricating a Nb_3Sn quadrupole magnet. This magnet is aimed at learning the technology needed for using Nb_3Sn in accelerator magnets and its design is based on that of LHC main quadrupole. Particularities induced by the use of Nb_3Sn material in the fabrication process will be described and the current status of the development will be given.

INTRODUCTION

At the beginning of the eighties, a 90-mm-inner-bore Nb_3Sn dipole magnet reaching a 5.3 T central magnetic field was built at CEA/Saclay [1].

During the following years, the activity at CEA/Saclay in the field of accelerator magnets was mainly devoted to machines under construction: HERA (DESY, Hamburg), SSC (Dallas, USA) and LHC (CERN, Geneva). All these projects were based on Nb-Ti superconductor.

In the second half of the nineties, this R&D was reactivated and the construction of a Nb_3Sn quadrupole magnet was launched. This R&D activity suffered of an important lack of resources, mainly due to the priority given to the LHC project. Nevertheless, the construction of this quadrupole magnet is now nearly finished

Nb_3Sn QUADRUPOLE MAGNET

The main goal of this project is not to build a very performing magnet but to learn the technology of Nb_3Sn magnets. It was then decided to rely on the LHC main quadrupole [2] design in order to minimise the amount of new components and tooling, and to try to use process which could be transferred to industry. The model relies on the same coil geometry as the LHC arc quadrupole magnets, but without iron yoke. The nominal field gradient is 211 T/m at 11,870 A and 4.2 K, leading to a maximum field on conductors of 8.3 T. The model length is about 1 m.

COILS

The coils are wound from Nb_3Sn Rutherford-type cable insulated with S2 glass, heat-treated and impregnated with epoxy resin. This cable was developed in collaboration with Alstom/MSA [3] Due to the high sensitivity of Nb_3Sn to deformation after the heat-treatment, the so-called "wind, react and impregnate" method is used.

All coil components have to resist to the severe reaction heat treatment at 660° during 10 days. In particular, the end spacers are machined out of CuAl9. Their sharp edge can then destroy locally the fragile glass cloth insulation.

In total, 6 coils were wound. Two of them exhibited short circuits between turns after resin impregnation. After accurate localisation, the coils were repaired and one of them was used in the magnet assembly. Even if the repair was made with as much care as possible, we are not sure that the superconducting properties have not been degraded because Nb_3Sn is very sensitive to deformation. The answer to this question will be raised only during the cold tests.

MAGNET AND COLD MASS ASSEMBLY

The assembly of the Nb_3Sn coils is very similar to that of classical NbTi coils. Great care must however be taken during coils handling and when electrical joint between Nb_3Sn and NbTi cables used for coils interconnect are realized.

STATUS

The four selected coils are assembled and collared and the instrumentation wires are in place. The inertia tube surrounding the collared coil is mounted and being closed to form the cold mass, which will be installed in the horizontal Saclay's test facility during the next weeks. The cold test should start in summer 2008.

More detailed description of magnet construction and warm test will be presented at ASC 2008 conference in Chicago, USA.

CONCLUSION

The Saclay's Nb_3Sn quadrupole magnet fabrication will be finished in a few weeks. This fabrication has turned to be long and difficult and there is still a lot of work to perform in order to get a safe and reliable process.

The magnet cold test should start during summer. It will confirm that the construction was satisfactory and that the repairs on one coils have not degraded the superconducting behaviour of the Nb_3Sn.

Further development is planed for the coming years: CEA/Saclay will participate to the study and realization of a challenging 13 T dipole magnet in the framework of EUCard project submitted to European community [4].

REFERENCES

[1] J. Perot, "Construction and test of a synchrotron dipole model using Nb_3Sn cable", IEEE Trans. on magnetics, vol. MAG-19, N° 3, May 1983.

[2] M. Peyrot, et al., "Construction of the new prototype of main quadrupole cold mass for the arc short straight sections of LHC", IEEE Trans. Appl. Supercond., Vol. No 1, pp 170-173, 2000.

[3] M. Durante, et al. "Development of a Nb_3S_n multifilamentary wire for accelerator magnet applications", Physica C: Superconductivity, vol. 354, pp. 449-453, May 2001.

[4] G. de Rijk, "High field program in Europe", these proceedings, Wamsdo 2008, May 2008.

NB_3AL HIGH FIELD ACCELERATOR MAGNET R&D

K. Sasaki*, T. Nakamoto, K. Tsuchiya, A. Terashima, A. Yamamoto, KEK, Tsukuba, Japan
L. Rossi, A. Verweij, L.R. Oberli, CERN, Geneva, Switzerland
A. Kikuchi, T. Takeuchi, NIMS, Tsukuba, Japan
G.L. Sabbi, S. Caspi, P. Ferracin, H. Felice, R. Hannaford, R. Hafalia, LBNL, Berkeley, USA
R. Yamada, E. Barzi, A. Zlobin, FNAL, Batavia, USA

Abstract

KEK has been developing the Nb_3Al strand and cable for a high field accelerator magnet in collaboration with NIMS for many years. And also the development of subscale magnet has been started practically since last year. KEK has studied on the effect of number of filaments and matrix ratio on non-Cu Jc for last two years and also developed continuous Cu electro-plating apparatus. NIMS has fabricated the trial Rutherford cable with 27 strands successfully in collaboration with Fermi lab. And also double-layer common coil has been fabricated and tested successfully. The magnetic and mechanical design of 15 T subscale magnet has been started practically since last year, and the preparation of drawings and tools is ongoing in parallel.

INTRODUCTION

Developments of high field magnets for the LHC luminosity upgrade have been continued for many years, and Nb_3Sn conductor is the first candidate for the high field magnet because of the high current density, availability and cost. On the other hand, it is a brittle material and required careful management in terms of the design and fabrication of high field magnets. Based on the CERN-KEK collaboration for the development of high field magnets, KEK has been developing Nb_3Al conductor in collaboration with National Institute of Material Science, NIMS. That material has a better strain tolerance compared to Nb_3Sn, therefore, it could be an interesting candidate for a high field accelerator magnet, which requires a high pre-stress in order to endure a strong Lorentz force. In parallel with the conductor development, KEK has started the development program of a 15 T magnet using Nb_3Al conductor practically since last year.

This paper summarizes the present status of the development of the conductor and the design study of the 15 T subscale magnet.

STRAND AND CABLE R&D

The Nb_3Al strand is processed by a Rapid Heating Quenching, RHQ, process [1]. The unique feature of this process is the first heat treatment to convert multifilamentaly Nb/Al precursor wires into a Nb/Al supersaturated bcc solid solution. In this heat treatment, the precursors are rapidly heated up to about $2000\ ^\circ\mathrm{C}$ by ohmic heating, and then subsequently quenched in a Ga bath at about $50\ ^\circ\mathrm{C}$. This RHQ technique enables us to fabricate 1 km-class strands, however, it is difficult to attach a copper stabilizer onto the strand. The copper stabilizer has to be attached after the RHQ operation, otherwise, the Cu would melt and react with the Nb/Al composites during ohmic heating more than $1900\ ^\circ\mathrm{C}$.

The development items of Nb_3Al strand and cable are as follows; 1) improvement of non-Cu J_c, 2) development of the Cu stabilizing technique, 3) improvement of low field instabilities and 4) Cabling Rutherford cable. KEK and NIMS are developing these items to some extent in parallel.

KEK Activities

The major development items at KEK are to increase the non-copper Jc, to figure out a good stabilization method, and also to improve a low field instability. As for the first item, KEK has tried to improve the non-Cu Jc by optimizing the fabrication process, i.e., structure of cross section, heat treatment condition and ratio of area reduction after Cu stabilization. Especially, the effects of the matrix ratio and number of filaments have been studied mainly for last two years. Several wires with different Nb-matrix ratios and filament numbers were fabricated; (Matrix ratio : Filament number) = (0.6:294), (0.69 : 294) and (0.79 : 546). The previous development [2] revealed that the non-Cu Jc is increased by decreasing the Nb-matrix ratio from 1 to 0.8, however, in the strands described above, the non-Cu Jc wasn't improved as expected. In addition, there were many breakings of strand during drawing in the strand with a large number of filaments. It is found from these results that the better structures are that the matrix ratio and filament number are 0.8 and 222, respectively.

Regarding the Cu stabilization method, a special copper electroplating technique to deposit a thick Cu layer on the surface of the wire was developed. In this technique, a compound on the surface of the wire is removed by a physical and chemical methods first, and then the Ni layer in 0.5 μm thickness is deposited by Ni strike plating method in order to obtain good mechanical, electrical and thermal bonding strength between the Nb-matrix and Cu. After that, a thick Cu stabilizer is deposited by electroplating, and finally, a heat treatment to stabilize the bonding. A

* ken-ichi.sasaki@kek.jp

prototype, which can continuously treat a long strand with the process above, is developed. The strand in 50 m length could be fabricated successfully with the Cu thickness of 170 μ and the process speed of 1.5 m/h. Further improvement in order to increase the process speed is in progress.

KEK has also studied the improvement of low field instabilities, and fabricated the trial strand with a tantalum matrix. The measurement of non-Cu Jc and magnetization is ongoing.

NIMS Activities

The major development items at NIMS are to develop the Cu stabilizing technique, to improve low field instabilities and to make a Rutherford cable.

NIMS has developed new Cu stabilization technique using a ion-plating method [3], which is different from KEK technique. In this technique, the bare strand is pre-coated with Cu buffer layer in 1 μm thickness by using a continuous Cu ion-plating apparatus, and then thick Cu layer is deposited onto the Cu buffer layer by high speed electroplating apparatus. The ion-plating apparatus developed by NIMS successfully achieved the process speed of 4 m/min with the strand length of more than 1 km. The electroplating apparatus has developed by Hikifune corporation in Japan. The processing speed of this apparatus increases with time, and successfully reached to 7 m/h at the moment. Further improvements are in progress for both plating apparatuses.

As for the cable development, in 2006, 27 strand Rutherford cable was fabricated successfully in collaboration with Fermi lab, and some tests were performed [4]. The extracted strand shows no degradation of critical current due to the cabling. NIMS also measured cable critical currents with respect to the external field up to 11 T using FRESCA facility at CERN, and the quench currents above 9T reached to only about 85 % of the short sample limit in spite of no degradation in the extracted strand. Although the reason for this degradation in the cable is still not clear, it seems to be caused by a thermal insulation in the present sample holder.

After the successful cabling, NIMS and Fermi lab fabricated and tested a subscale common coil magnet [5]. The peak field could be reached to 9.3 T at 21.8 kA and 3.95 K, corresponding to nearly load line limit.

In order to improve low field instability, NIMS has fabricated the strand with the Ta matrix in 2007 [6]. In this strand, the low field instability at 4.2 K was apparently improved by using a Ta barrier for the interfilament matrix of precursor. Following this success, another strand with the Ta matrix has been fabricated and tested. This strand has almost the same structure but a Cu ratio is decreased from 1.0 to 0.6, aiming for the increase of the critical current. The study for this strand is ongoing.

MAGNET

Design

Basic Concept Following the successful fabrication of the subscale common coil magnet in Fermi lab described in the section , KEK has started the high field magnet development with Nb_3Al practically since 2007, in parallel with the strand and cable development. The first goal of the development is to fabricate 15 T subscale magnet for demonstrating feasibility of high field magnet with Nb_3Al.

The design of the Nb_3Al subscale magnet is based on three following concepts. The first one is to adopt a shell structure, which is developed by LBNL because of the features of easy assembly and disassembly. The second concept is to adopt a common coil configuration in order to maximize the peak field in the coil. Compared with a block dipole configuration, the support structure for this configuration could be simplified because the profile of the Lorentz force is simpler than that of a block dipole configuration. The third concept is to make use of existing Nb_3Sn coils as back up coils. This hybrid coil configuration enables us to save the conductor length of Nb_3Al. These Nb_3Sn coils are supposed to be SC-15 and 16 which were fabricated at LBNL [7], in practice.

2D Magnetic Design First, the basic parameters in terms of magnetic design were optimized using OPERA 2D, the number of strands in the cable, the yoke diameter, the numbers of layers and turns of Nb_3Al coils. Fig. 1 illustrates the result of the magnetic design. This design consists of three Nb_3Al coils with 2 layers and 15 turns and two Nb_3Sn coils of LBNL. The Nb_3Al coil placed at the center of the magnet is a two-layer common coil, and other two Nb_3Al coils are usual double-pancake coils. In this magnetic design, the yoke is 20 cm away from the coils for installing coil support structures. This model assumes the rectangular cable with the 27 strands, and the width and the thickness are 14.2 mm and 1.78 mm, respectively. The critical current of the strand is expected to be 400 A at 15 T, 4.2 K, which is based on the results of F3 strand [6]. The peak field is expected to be 14.3 T at 12.3 kA and 4.2 K.

2D Mechanical Design Based on the 2D magnetic design parameters, 2D mechanical model was designed using ANSYS. Fig. 2 shows the ANSYS quadrant model around the coil packages for the stress distribution analysis. This design concept is based on the SD-01 magnet which was developed by CEA Saclay [8]. In order to uniform the stress distribution in the coils after the excitation up to the peak current, the configuration of G10 spacers between coils is modified in such a way that the only coil part is covered with the spacer in the central common coil as shown in Fig. 2.

In the shell structure, most of the pre-stress required to react the Lorentz force is provided by the thermal contraction of the Al shell, which is much higher than other materials in the magnet. The pre-load by the thermal contraction

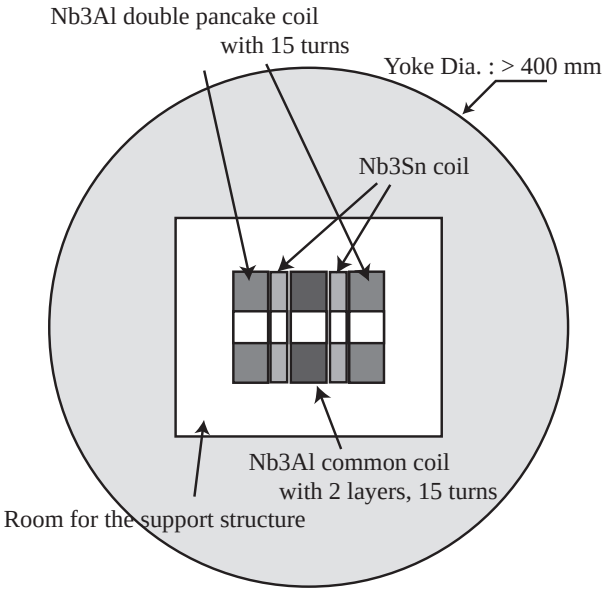

Figure 1: Magnetic design parameters of 15 T subscale magnet with Nb_3Al.

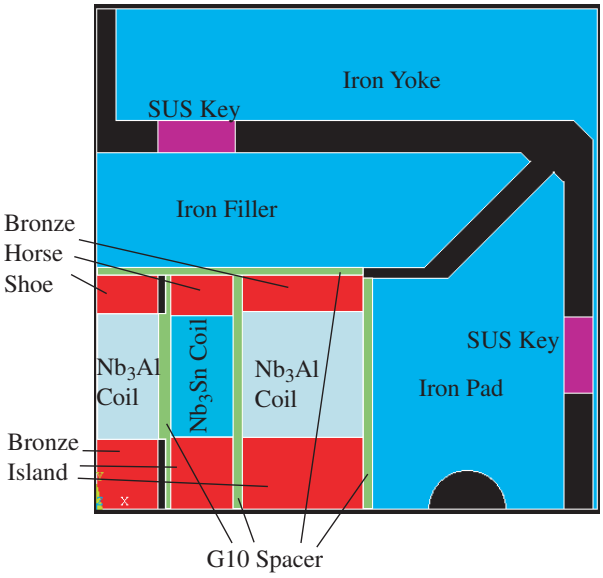

Figure 2: The quadrant ANSYS model of mechanical design.

mainly depends on the thickness and the diameter of the shell. Fig. 3 shows the relationship between the shell thickness, the yoke diameter and the pre-stress at room temperature, which is required to balance the Lorentz force with the pre-stress in the coil after cooling down to 4.2 K. Concerning the magnetic design results and the constraint of the test facility in KEK, we chose the shell thickness of 42 mm and the yoke diameter of 480 mm.

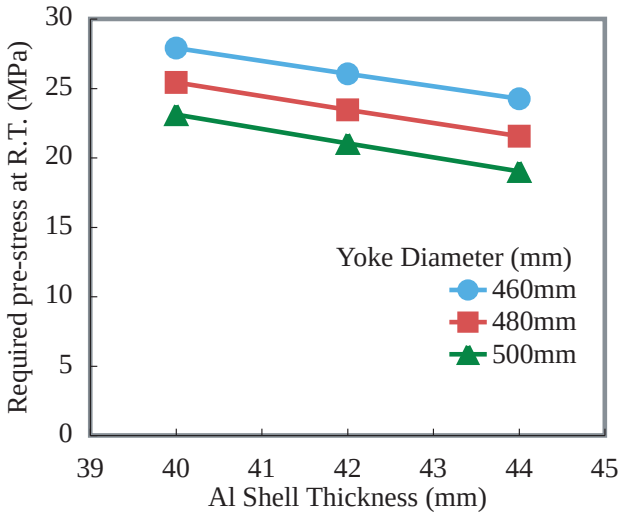

Figure 3: Relationship between the shell thickness, the yoke diameter and the pre-stress at room temperature.

Bladder Test

A bladder is an essential component in the pre-loading process at room temperature [9]. The four bladders were fabricated in Japan, and the destructive tests are performed using the test tools of LBNL. Two of four bladders could not be set in the test tools, because the blocks to feed a water into the bladder were welded in slightly wrong direction. The new fabrication process adjusting the welding tolerance would be performed next time. Other two bladders could be put in the test tools and pressurized with water. The first bladder had a spot leak at one corner just after reaching the pressure of 10000 psi. The bladder expanded up to 2.1 mm from 0.3 mm in thickness at that point. The second bladder could be pressurized up to 10000 psi with 2.1 mm in thickness. And, during the second pressurization in which the bladder was allowed to expand more than 3 mm in thickness, the bladder bursted at the welded edge near the block at 7200 psi and 3.1 mm in thickness, as shown in Fig. 4. This burst was typical and similar to one happened in many bladders which were fabricated and used at LBNL. These results indicate that the bladders made in Japan could be used for the practical magnet fabrication, although the thickness after pressurization should be controlled properly below 1 to 2 mm.

SUMMARY

High field superconducting magnets with Nb_3Al conductor is being developed in KEK for the LHC luminosity upgrade. The development of the conductor is performed in collaboration with NIMS and FNAL. In order to improve the non-Cu Jc, KEK has been optimizing the structure of the strand and the fabrication process for the high field magnet, and the matrix ratio and the number of filaments could be almost optimized from the test results of several

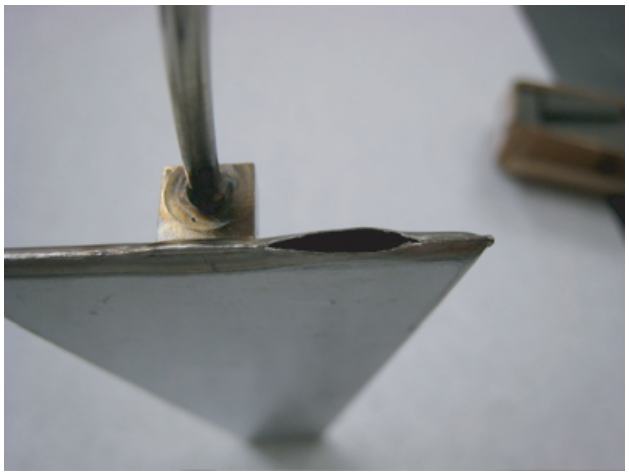

Figure 4: Bursting edge of the bladder.

strands with different structures.

The continuous Cu stabilizing techniques were developed successfully by both KEK and NIMS with their own method. As for the low field instability, it is found that Ta barrier between filaments could prevent from flux jumps below 4 T at 4.2 K. The trial fabrications of Rutherford and rectangular cables were carried out, and the test results of the strand extracted from the first cable show almost no degradation due to the cabling.

The subscale common coil magnet using this cable was fabricated and tested successfully in FNAL. The peak field could reached to 9.3 T at 21.8 kA and 3.95 K. The development of 15 T small magnet with Nb_3Al has been started practically since last year, and the 2D magnetic and mechanical design have been almost finished. As a part of preparations of fabrication tools, the prototypes of the bladder were fabricated in Japan and successfully tested in LBNL.

Aiming to complete the fabrication of 15 T subscale magnet in 2010, the preparation of the magnet parts is now underway. New two 1 km - class Nb_3Al strands are fabricating, and the cabling of these strands will be performed in this Autumn. The detail design and the fabrication of the coil parts are also ongoing, and the winding of the first coil will be started hopefully at the end of 2008.

REFERENCES

[1] Y. Iijima, M. Kosuge, T. Takeuchi and K. Inoue, "Nb_3Al Multifilamentary Wires Continuously Fabricated by Rapid-Quenching", *Adv. Cryo. Eng.*, Vol. 40 A (1994), 899 - 915.

[2] K. Tsuchiya, C. Mitsuda, A. Terashima, T. Takeuchi, et al., "Nb_3 Wire Development for Future Accelerator Magnets", *IEEE Trans. on Appl. Superconductivity*, Vol. 16, No. 2 (2006), 1204 - 1207.

[3] A. Kikuchi, K. Tagawa, M. Kobayashi, Y. Iijima, et al., "Fabrication of Cu Stabilizer into Long-length RHQT-processed Nb_3Al Round Wire", *IEEE Trans. on Appl. Superconductivity*, Vol. 16 (2006), 1224 - 1227.

[4] R. Yamada, A. Kikuchi, G. Ambrosio, N. Andreev, et al., "Feasibility Study of Nb_3Al Rutherford Cable for High Field Accelerator Magnet Application", *IEEE Trans. on Appl. Superconductivity*, Vol. 17(2007), 1461 - 1464.

[5] R. Yamada, A. Kikuchi, M. Tartaglia, G. Ambrosio, et al., "Quench Tests of Nb_3Al Small Racetrack Magnets", presented at MT 20.

[6] A. Kikuchi, R. Yamada, E. Barzi, M. Lamm, T. Takeuchi, et al., "Cu Stabilized Nb_3Al Strands for the High Field Accelerator Magnet", presented at MT 20.

[7] P. Ferracin, et. al., "Assembly and Test of SQ01b, a Nb_3Sn Quadrupole Magnet for the LHC Accelerator Research Program", *IEEE Trans. on Appl. Superconductivity*, Vol. 16, No. 2 (2006), 382 - 385.

[8] H. Felice, S. Caspi, D.R. Dietderich, P. Ferracin, S.A. Gourlay, et al., "Design and Test of a Nb_3Sn Subscale Dipole Magnet for Training Studies", *IEEE Trans. on Appl. Superconductivity*, Vol. 17, No. 2 (2007), 1144 - 1147.

[9] A. R. Hafalia et al.,"A new support structure for high field magnet", *IEEE Trans. on Appl. Superconductivity*, Vol. 12, No. 1 (2002), 47 - 50.

THE Bi-2212 CONDUCTOR AND MAGNET PROGRAM AT THE NATIONAL HIGH MAGNETIC FIELD LABORATORY

D. Larbalestier, E. Hellstrom, J. Jiang, F. Kametani, M. LoSchiavo, D. Myers, J. Schwartz, T. Shen and U. Trociewitz, National High Magnetic Field Laboratory, Tallahassee, FL 32310 U.S.A.

Abstract

The NHMFL has had a long running program to develop $Bi_2Sr_2CaCu_2O_x$ (Bi2212) for high field magnets. The recent development of round wire Bi2212 (RW2212) has strengthened the effort to develop solenoid magnets with fields substantially greater than can be achieved with Nb_3Sn. The present paper briefly summarizes some of the results obtained at the NHMFL in the past 12 months. It summarizes the talk given by David Larbalestier at WAMSDO on May 24, 2008. Much of the work is ongoing and will be reported in the normal peer reviewed literature in late 2008.

INTRODUCTION

This paper briefly summarizes the principal goals and recent achievements of the program at the National High Magnetic Field Laboratory which is aimed at utilizing $Bi_2Sr_2CaCu_2O_x$ (Bi2212) superconductors for constructing very high field solenoids. The principal driver for NSF support of this program at the NHMFL is that the lab presently spends ~$6 million per year on electricity to enable world-wide users to access the suite of world record DC magnets at the NHMFL in Tallahassee. These 20 MW Florida Bitter magnets generate 35 T in a 32 mm warm bore, 31 T in a 50 mm bore and 20 T in a 200 mm bore. The highest DC field of 45 T is generated by the hybrid (11.5T superconducting outsert and 34 T 32 mm bore 25 MW insert). Unfortunately the price of electricity is rising significantly year by year as the recent strongly increasing cost of oil reminds us. At present costs, each hour of magnet use costs about $1000. Together these facts make all-superconducting magnets that could break the barrier of 22 T, to which Nb_3Sn is limited, very attractive. Two recent test magnets show that >30T, all-superconducting magnet systems are foreseeable. In 2003 Weijers *et al.*[1] constructed a Bi2212 tape magnet which achieved 25T in the 20T background of the 20 cm large bore resistive magnet (LBRM). In 2007 a 10-pancake coil of YBCO coated conductor made by Hazelton *et al.*[2] of SuperPower was tested to 26.8T in the 19 T background of the LBRM at the NHMFL. The National Academy Panel COHMAG[3] also recommended construction of a 30T class HTS NMR magnet. These various considerations have incited a multi-group effort on HTS technology at the NHMFL. In this paper I briefly review recent work on round wire (RW) Bi-2212 since this is of greatest interest to the high energy physics community because it enables Rutherford cables[4].

This work was supported by NSF Division of Materials Research through DMR-0654118, the U.S. Department of Energy and the State of Florida.

*larbalestier@asc.magnet.fsu.edu

MAGNET GOALS

The immediate goal of the present NHMFL RW2212 program is to design and construct a 30 mm cold bore solenoid made in 4 sections using the wind-and-react (W&R) process which will yield 7 T when tested in the 20 T LBRM[5]. An overview of the design is shown in Fig. 1. To achieve this goal, which is an essential proof of principle for our program, we must be capable of reacting coils without leakage of the BSCCO core to any significant extent, be able to uniformly react thick multi-layer windings without concern for inhomogeneities of temperature, oxygen partial pressure or other significant process variable, and then energize the magnet without damage due to electromagnetic stress or to normal zone propagation. To our knowledge there is no demonstration of all these points in a magnet of the size and scale envisaged here, though some significant progress towards these goals was reported by Marken *et al.*[6] using RW2212 small coils that generated self fields up to ~2.3T.

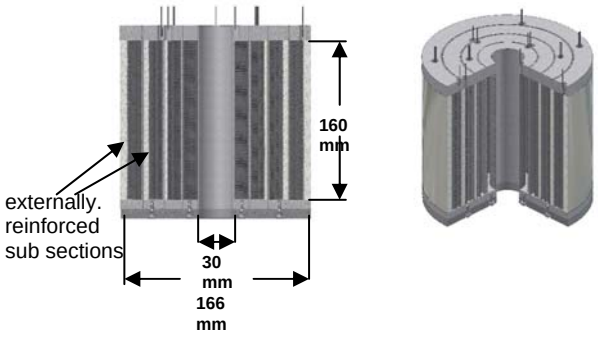

Figure 1: The NHMFL 7T insert solenoid design.

The conductor that is the heart of the coil is shown in Fig. 2. It is a double-stacked 85 x 7 design in which filaments are well separated before reaction but bridge extensively after reaction. As noted by Miao *et al.*[7] J_c falls off slowly from an engineering J_E (J_c referred to the whole wire cross-section, about 25% of which is Bi2212) of ~600 A/mm^2 at 5T, 4.2K to ~360 A/mm^2 at 30T. Such J_E values are high enough to make our coil feasible and probably not so high as either to cause self damage by Lorentz forces or under quench conditions. What is holding us back at present is the propensity of small coils containing 20-50 m of 1 mm diameter wire to leak Bi2212 in a small number of unpredictable places. We consider such leakage not acceptable for a robust coil technology.

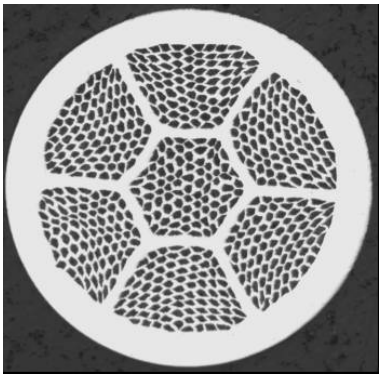

Figure 2: The OST Bi-2212 round wire conductor at a size of 1 mm diameter. The outer Ag web is alloyed with Mg while the remaining Ag is pure.

In fact of the 12 small coils that we made in 2007, 11 exhibited leakage. Most leakage was intermittent of the sort shown in Fig. 3, sometimes with greater and sometimes with lesser frequency. On occasions the leakage produced a rupture defect which was quite clear in the cross-section of the wire[8], where evident reactions with the mullite wire insulation were also seen[9]. As noted earlier by Wesolowski *et al.* [10] the presence of many materials in proximity to RW2212 leads to wicking of the 2212 core through the silver sheath. We occasionally find that leakage occurs at obviously damaged sections of the wire, but this is not invariably true. Research to understand this leakage better is ongoing[8].

A second challenge to be faced is that the behavior of the test coils was highly variable, the coils achieving I_c values varying from 60 to 281A in a background of 5T at 4.2K[5]. What is noteworthy about these I_c values is that they correspond to J_E values ranging from ~75 to 350 A/mm^2, well below the champion values of 600 A/mm^2 quoted above. While part of the discrepancy is to be associated with the higher electric field of Miao's report (5μV/cm) and part with their wire being at a smaller and more favorable size (0.8 mm), a common feature of long versus short samples is that significant J_c is easily lost for reasons that remain unclear.

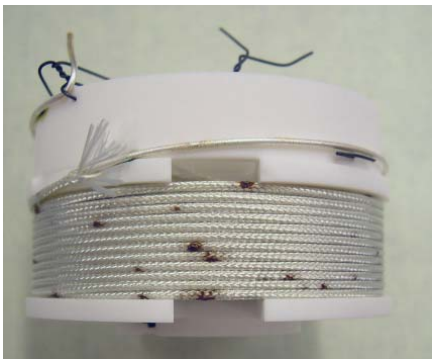

Figure 3: Intermittent leakage on the surface of the mullite-braid-insulated wire after reaction of test coil 3.

One set of experiments carried out in recent months to try to understand whether the J_c variation seen in our standard reactions can be attributed to variations of vortex pinning or of connectivity or of some unknown mixture of the two is shown in Fig. 4. An extensive series of variable temperature magnetization curves[9] have been performed, two of which are shown in Fig. 4, where the highest J_c smaller diameter wire (0.8 mm) is contrasted with a typical 1 mm dia. sample cut from a deconstructed test coil. What is true of these two is true of all. Even though J_c is varying by more than a factor of 4, the irreversibility field defined by the linear extrapolation of the Kramer pinning function remains constant for standard reactions. It thus appears that J_c is independent of vortex pinning and controlled by connectivity.

A reconsideration of the reaction conditions for wires is also underway[11] following extensive consideration of the reaction studies of Rikel *et al.*[12] These studies are indeed showing that there is much to improve in the processing of wires to higher J_c, as will be forthcoming soon.

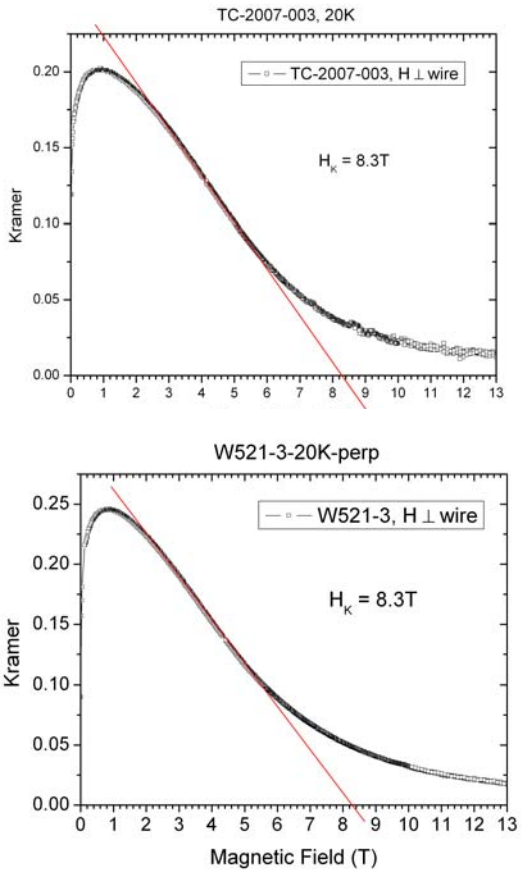

Figure 4: Hysteretic magnetization, reduced to Kramer function units, of two samples of RW2212 with very different J_c values. Both have almost identical Kramer fields equivalent to H_{irr} of 8.3T at 20K, even though test coil 3 sample (1 mm dia.) had $J_E(5T, 4.2K)$ = 270 A/mm^2, while the optimum-sized (0.8 mm dia.) wire W521 had J_E = 700 A/mm^2. J_c appears to be controlled by connectivity rather than vortex pinning changes.

These recent experiments to test the capabilities of RW2212 are soon likely to be expanded by a more

extensive collaboration between groups at BNL, FNAL, LANL, LBNL, NHMFL, NIST and Texas A&M, with interest and expertise in Bi-2212. We hope that the essential tests of this very attractive conductor technology will be greatly advanced by this joint effort.

ACKOWLEDGEMENTS

We are grateful to Dr Seung Hong and his colleagues at Oxford Superconducting Technology for their long term collaborations and to Mark Rikel for many stimulating discussions about the processing of Bi2212. Dr Denis Markiewicz of the NHMFL is also thanked for many helpful discussions.

REFERENCES

[1] H. W. Weijers, U. P. Trociewitz, K. Marken, M. Meinesz, H. Miao, and J. Schwartz, Supercond. Sci. Technol., **17**, 636–644, 2004.

[2] D. Hazelton, V. Selvamanickam, D. Markiewicz, D. Larbalestier private communication.

[3] COHMAG, Committee on Opportunities in High Magnetic Field Science, "Opportunities in High Field Science," National Academies Press, Washington, D.C., (2005).

[4] A. Godeke, D. Cheng, D. R. Dietderich, C. D. English, H. Felice, C. R. Hannaford, S. O. Prestemon, G. Sabbi, R. M. Scanlan, Y. Hikichi, J. Nishioka, and T. Hasegawa, *IEEE Trans. Appl. Supercond.*, 18 (2008) 516-519.

[5] U. Trociewitz *et al.* private communication and to appear.

[6] K. R. Marken, Jr., H. P. Miao, M. Meinesz, B. Czabaj, and S. Hong, IEEE Trans. Appl. Supercond., **16**, 992–995, 2006.

[7] H. Miao, K.R. Marken, M. Meinesz, B. Czabaj, S. Hong, M.O. Rikel, and J. Bock, Adv. in Cryo. Eng. **52**, 673-682 (2006).

[8]. M. LoSchiavo *et al.* private communication and to appear.

[9] J. Jiang *et al.* private communication and to appear.

[10] D. E.Wesolowski, M. O. Rikel, J. Jiang, S. Arsac, and E. E. Hellstrom, Supercond. Sci. Technol., **18**, 934–943, 2005.

[11] T. Shen *et al.* private communication and to appear.

[12] M O Rikel, S Arsac, E Soileux, J Ehrenberg, J Bock, K Marken, H Miao, C-E Bruzek, S Pavard, A Matsumoto, E Hellstrom, and L Motowidlo, Journal of Physics: Conference Series **43** (2006) 51–54.

STATUS OF THE SUPERCONDUCTING MAGNET SYSTEM FOR THE J-PARC NEUTRINO BEAM LINE

T. Nakamoto#, KEK, Tsukuba, Japan

Abstract

Superconducting combined function magnets will be utilized for the 50 GeV, 750 kW proton beam line for the J-PARC neutrino experiment. The magnet is designed to provide a dipole field of 2.6 T combined with a quadrupole field of 19 T/m in a coil aperture of 173.4 mm at a nominal current of 7345 A. Construction of the magnet system is underway.

INTRODUCTION

A second generation of long-baseline neutrino oscillation experiments has been proposed as one of the main projects at the J-PARC [1], [2] and the construction of the facility is in progress. Superconducting combined function magnets, SCFMs, will be utilized for the 50 GeV, 750 kW proton beam line for the neutrino experiment. The magnet is designed to provide a dipole field of 2.6 T combined with a quadrupole field of 19 T/m in a coil aperture of 173.4 mm at a nominal current of 7345 A. A series of 28 magnets in the beam line will be operated DC in supercritical helium cooling below 5 K. Since the main accelerator will be operated at 30 GeV in the beginning, the SCFM was designed for proton beam energies of 30 to 50 GeV. A cross sectional view of the SCFM is shown in Fig. 1 and the main design parameters are listed in Table 1.

STATUS OF CONSTRUCTION OF THE MAGNET SYTEM

The detail of the magnet system development was reported in the previous reports [3]-[8]. This report focuses on the status of the construction of the magnet system.

Main SCFMs

The SCFM has a unique design feature of the left-right asymmetry of the coil cross section: current distributions for superimposed dipole- and quadrupole- fields are combined in a single layer coil. Another design feature is the adoption of glass-fiber reinforced phenolic plastic spacers for electrical insulation to reduce the labor and inspection costs. Beam optics calculations confirmed that the design magnetic field of the SCFM within a tolerance of 10^{-3} at a reference radius of 50 mm was sufficiently acceptable. The coil is mechanically supported by a keyed yoke made of fine-blanked iron laminations. The iron yoke also functions as a magnetic flux return.

The contract to build 32 production magnets and 16 cryostats was given to Mitsubishi Electric. Fabrication of the magnets was completed by June 2008 and the excitation tests for all magnets in liquid helium at 4.2 K in the vertical cryostat were carried out at KEK. All magnets were successfully excited up to 7700 A corresponding 105 % nominal current at a ramp rate of 20 A/s without a spontaneous training quench. Magnetic field measurements were performed with a 500 mm-long rotating printed circuit board. It was confirmed that the field qualities for all magnets were good enough to fulfill the specifications.

Two-in-One Structure Cryostats

Figure 2 shows top and side views of the cryostat with support structure of the magnets. Design of the cryostat was based on the LHC arc dipole magnet [8]. Dimensions of cryostat are 0.94 m in outer diameter, 10 m in length and it weighs 22 tons. It consists of two vacuum vessels and one connecting part in-between, forming one united

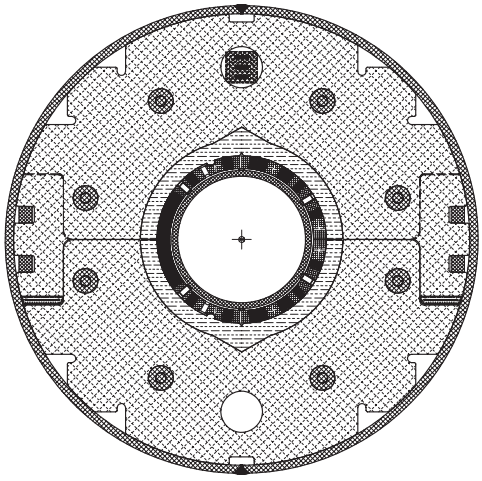

Figure 1: Cross sectional view of the superconducting combined function magnet, SCFM, for the 50 GeV proton beam line for the J-PARC neutrino experiment.

Table 1: Main Design Parameters for the SCFM

Physical & Magnetic Length	3630 & 3300 mm
Coil In. & Out. Diameter	173.4 & 204.0 mm
Yoke In. & Out. Diameter	244 & 550 mm
Shell Outer Diameter	570 mm
Dipole & Quad. Field	2.59 T & 18.7 T/m
Coil Peak Field	4.7 T
Load Line Ratio	72 %
Operational Current	7345 A
Inductance & Stored Energy	14.3 mH & 386 kJ

#tatsushi.nakamoto@kek.jp

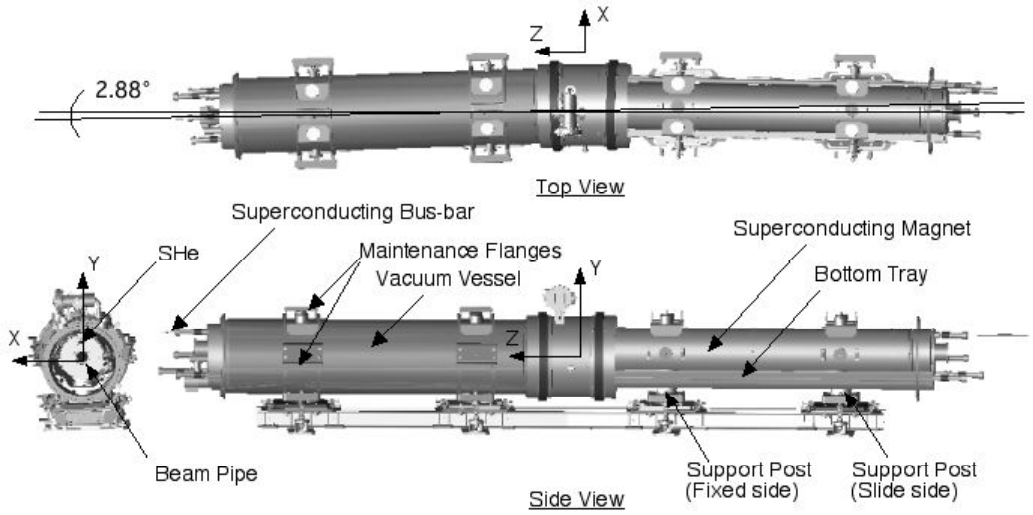

Figure 2: Top and side views of "Two in One structure" cryostat. Right half of the views show inside of the vacuum vessel and radiation shield to describe support structure in the vessel.

cryostat. The cryostat has mechanical bending angle of 2.88 degree at the center to accommodate the beam bending. Two GFRP support posts from the vessel, as shown in Figure 2, support each magnet. The post at the end has slide mechanism to cope with thermal shrinkage of the magnet along the longitudinal direction (z-axis) of the cryostat. They are designed so that the magnetic center sits on the designed location when the magnets are cooled down to 4.5 K, taking into account thermal shrinkage.

Cooling down test of the prototype cryostat was carried out and the cryostat was successfully cooled down to 4.5 K. In this test, cryostat performances such as mass flow rate of supercritical helium, heat loads and magnet displacement due to cooling down were experimentally evaluated [8].

So far, 14 out of 16 production cryostats have been built. Lowering the cryostat down to the neutrino beam line tunnel was started in February 2008 and 10 cryostats have been already installed by June.

Interconnect Cryostats

The superconducting neutrino beam line has 13 interconnect regions between main cryostats and we decided to develop 3 types of "interconnect cryostats": 5 proton beam monitors, 3 superconducting corrector magnets, 4 quench relief valve units for main magnets (and 1 vacancy). This concept leads to standardization of the main cryostat.

The superconducting corrector magnets for the beam steering were built by BNL and supplied to KEK as a US in-kind contribution to the J-PARC neutrino experiment. The magnet with a copper bobbin consists of a 2-layer normal dipole over a 2-layer skew dipole, and the coils can be independently energized to generate the field integral of 0.1 Tm at 50 A. The coils are wound by using "direct winding technology" with a serpentine coil

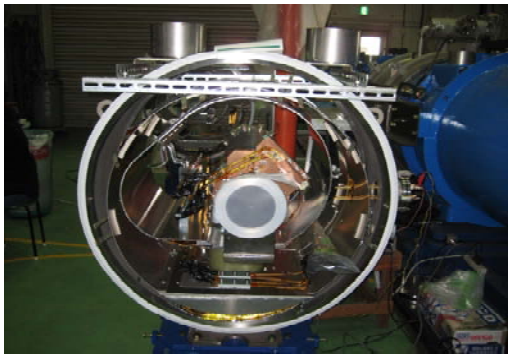

Figure 3: Interconnect cryostat containing a superconducting corrector magnet for beam steering.

Figure 4: Installed superconducting magnet system in the J-PARC neutrino beam line.

pattern. The corrector magnet will be operated under the conduction cooling: thanks to a huge cooling power of the supercritical helium line, the corrector magnet can be operated at the temperature below 6 K.

Fabrication of 13 interconnect cryostats was completed and 9 of them have been installed in the neutrino beam line. Interconnect work such as pipe welding, soldering of superconducting bus lines for the main magnets and beam tube connection is underway.

SUMMARY AND SCHEDULE

Following success of the R&D program for the superconducting magnet system for the J-PARC neutrino beam line, the production magnets and cryostats have been fabricated by Mitsubishi Electric since 2005. All magnets showed good excitation performance and good field qualities fulfilled the specification. Magnet installation in the beam line tunnel was started at February of 2008 and will last until the autumn. The hardware commissioning will be carried out from December of 2008. The neutrino experiment is anticipated at April of 2009.

REFERENCES

[1] Y. Itow et. al., "The JHF-Kamioka neutrino project," *hep-ex/0106019*.

[2] M. Furusaka et. al., "The joint project for high-intensity proton accelerators," *KEK Report 99-1; JAERI-Tech 99-056; JHF-99-3*, 1999.

[3] T. Ogitsu et al., "Superconducting combined function magnet system for J-PARC neutrino experiment", *IEEE Trans. Appl. Superconduct*, Vol. 15, No. 2, 1175-1180, 2005.

[4] T. Nakamoto et. al., "Design of superconducting combined function magnets at the 50 GeV proton beam line for the J-PARC neutrino experiment," *IEEE Trans. Appl. Superconduct*., vol. 14, no. 2, pp. 616-619, 2004.

[5] T. Nakamoto et al., "Development of superconducting combined function magnets for the proton transport line for the J-PARC neutrino experiment", *Proceedings of 2005 Particle Accelerator Conference, Knoxville, Tennessee*, 495-499, 2005.
http://accelconf.web.cern.ch/AccelConf/p05/PAPERS/TOAA006.PDF

[6] K. Sasaki et. al., "Test results of superconducting combined function magnets for the J-PARC neutrino beam line", *IEEE Trans. Appl. Superconduct*., vol. 17, no. 2, pp. 1083-1086, 2007.

[7] K. Sasaki et. al., "Magnetic field measurement system in superconducting combined function magnets for the J-PARC neutrino beam line" , *IEEE Trans. Appl. Superconduct*., vol. 18, no. 2, pp. 142-145, 2008.

[8] N. Kimura et. al., "Development of full-scale prototype cryostat of superconducting magnet system for J-PARC neutrino experiment" , *Proceedings of International Cryogenic Engineering Conference 21*, pp. 117-120, 2007.

DESIGN CONSIDERATIONS OF TRANSMISSION LINE SUPERCONDUCTORS FOR FAST-CYCLING ACCELERATOR MAGNETS*

H. Piekarz**, FNAL, Batavia, Il 60510, U.S.A.

Abstract

Novel design options of HTS and LTS superconductor lines for fast-cycling accelerator magnets are presented. The cryogenic power losses in using these conductors in transmission line application to energize the accelerator magnet string are discussed. A test arrangement to measure power loss of the proposed superconductor lines operating up to 2 T/s ramp rate and 0.5 Hz repetition cycle is described.

MOTIVATION

There are a number of large scale fast-cycling proton synchrotrons considered for a possible construction in a near future, e.g. PS2 at CERN [1] and DSFMR [2] at Fermilab. The use of the superconducting magnets rather than the conventional ones allows to significantly reduce magnetic core sizes and consequently to save valuable space in the accelerator tunnel. This is especially true for the DSFMR with its two accelerator rings to be fit in the existing Tevatron tunnel. Powering the magnet string with a transmission-line conductor allows further minimization of the space required for the magnets, and in addition the magnet interconnections are also much simplified providing convenient space for the corrector magnets. Although there have been already considerable efforts [3] aimed at designing fast-cycling superconducting magnets new approaches are needed to reduce the dynamic power losses to a level that is acceptable for a large synchrotron. With this in mind we are considering a novel arrangement of both the HTS single-filament tape strands and the LTS wire strands to construct the superconducting power lines for the fast-cycling magnets.

HTS AND LTS SUPERCONDUCTOR LINE DESIGN CONSIDERATIONS

A brief description of the HTS and the LTS conductor conceptual design is given in [4]. These conductors can be arranged as the power lines which are wrapped around the magnetic core in a conventional magnetic design, or used as the straight-through power lines in a transmission-line mode of energizing the magnet. The size of the individual line has been chosen to minimize the space required for the line within a magnetic core, and also to facilitate bending of the line at rather small radius as it may be required for the magnet interconnections. A conceptual design of both the HTS and the LTS conductor lines is shown in Fig. 1.

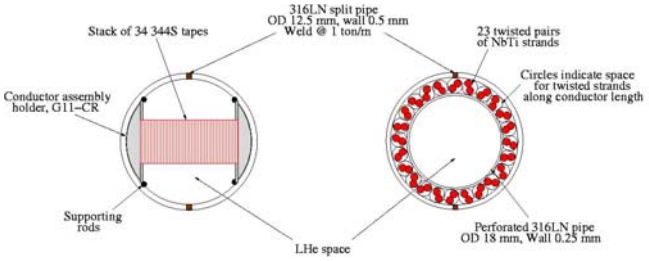

Figure 1: Conceptual designs of HTS (left) and LTS conductors (right).

Both these lines were designed to carry about the same transport current of ~ 20 kA. The HTS line consists of 34 the 344S YBCO tapes of the American Superconductor Inc., while the LTS line consists of 46 NbTi strands of the SSC outer dipole type. The major difference between the two approaches is the allowable temperature margin (~20 K for the HTS and ~2 K for the LTS) for the operating temperature of 4.5 K. We will evaluate below supercritical helium flow pressure drop and the allowable heat transfer from the flowing helium to conductor strands in these lines as a function of the LHe flow rate (which is equivalent to the Reynold's Number).

The cryogenic parameters of proposed CICC (Cable-In-Conduit-Conductor) HTS and LTS conductor lines are listed in Table 1. We assume use of supercritical helium of average temperature 4.75 K and 0.26 MPa pressure, with only minimal rise of temperature (e.g. < 0.2 K) and minimal pressure drop (e.g. < 0.05 MPa) allowed while the liquid is passing through conductor line. This allows keep the basic physical parameters (density, specific heat, viscosity) of the flowing liquid He within rather a narrow range which helps make predictions of a friction factor more reliable.

The pressure drop ΔP in a pipe is directly proportional to the frction factor F_f as indicated in formula (1) from [5]:

$$\Delta P/L = 0.5\, F_f\, [P_{\text{cooled}}\ (dm/dt)^2\ ] / [\rho\ (A_{\text{flow}})^3] \qquad (1)$$

where L is the pipe length, P_{cooled} is the cooled perimeter, dm/dt is the flow rate, ρ is the LHe density and A_{flow} is the helium flow cross-section area. For a turbulent flow in a smooth pipe the friction factor, F_f, is calculated using an empirical formula (2):

$$F_f = 0.3164\ Re^{-0.25} \qquad (2)$$

* This work has been authored by Fermi Research Alliance, ILC under DOE Contract DE-AC02-07CHI1359

** On behalf of Fast-Cycling Superconducting Magnet Group at FNAL: J. Blowers, D. Harding, S. Hays, Y. Huang, A. Klebaner, T. Peterson, H. Piekarz, V. Shiltsev, J. Theilacker and D. Wolff

where Reynolds Number $Re=4[(dm/dt)/(kP_{cooled})]$ and k is the viscosity of the fluid.

Table 1: Cryogenic parameters of proposed conductors

CICC geometry	HTS	LTS
Pipe outer diameter [mm]	12.5	12.5
Pipe inner diameter [mm]	11.5	11.5
Number of strands	35	46
Single strand area [mm^2]	0.90	0.43
Total strand area [mm^2]	31.5	19.8
Void fraction	0.70	0.81
LHe flow area [mm^2]	73	84
Pipe perimeter [mm]	36	64
Total strand perimeter [mm]	263	120
Cooled perimeter [mm]	300	184
Hydraulic diameter [mm]	0.97	1.83

For a non-smooth pipe a "roughness" parameter ε/D [6], with ε being a size of a continuing disturbance and D the diameter of the pipe, is used to modify the friction factor projected with formula (2). Based on the graphs given in [6] we scale the F_f parameter for Reynolds Numbers of (2600 – 26000), corresponding to the LHe (4.7 K @ 0.26 MPa) flow rates of (0.5 – 5) g/s in the proposed LTS and HTS conductor lines. The result is shown in Figure 2. We observe that the friction factor is higher at the lower flow rates, and it increases further (not shown in the figure) in the laminar flow region which is below the Re ~ 2600. A more detailed dependence of the friction factor on the roughness parameter, ε/D, is shown in figure 3 for the Reynolds Numbers of 4000, 10000 and 20000.

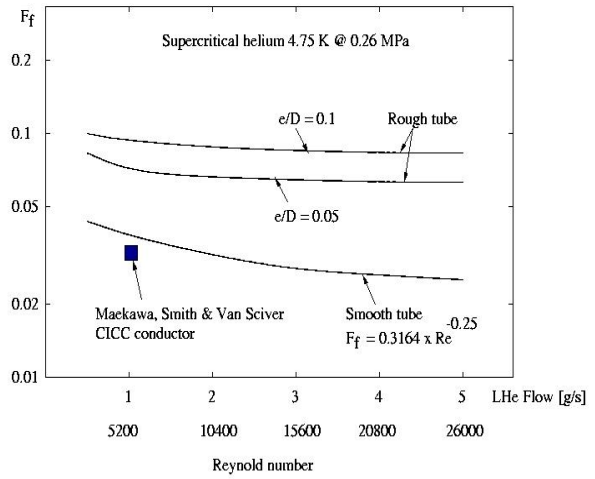

Figure 2: Friction factor in rough tubes of ε/D = 0.05 and 0.1 as compared to that of a smooth tube.

It is interesting to note that in the experiment [5] with a large number of strands in the CICC conductor the friction factor was found consistent with a smooth tube. This may suggest that if the strands have smooth surface their presence in the cable-in-conduit pipe does not necessarily increase friction factor for the helium flow. Consequently for the HTS conductor with 344S tapes of a very smooth surface we assumed the friction factor F_f ~ 0.035, or consistent with a smooth tube. For the LTS conductor with the twisted pairs of the NbTi strands, however, we assumed that the wire diameter constitutes "roughness", and so the friction factor F_f would be ~ 0.1 in this case.

With the friction factors determined in this way we can estimate pressure drop for the liquid helium flow in both LTS and HTS conductors using the formula (1). The results for the supercritical helium (4.7 K @ 0.26 MPa) are shown in Figure 4. One can see that the pressure drop increases strongly with increase of the helium flow rate, and the pressure drop is higher for the HTS conductor.

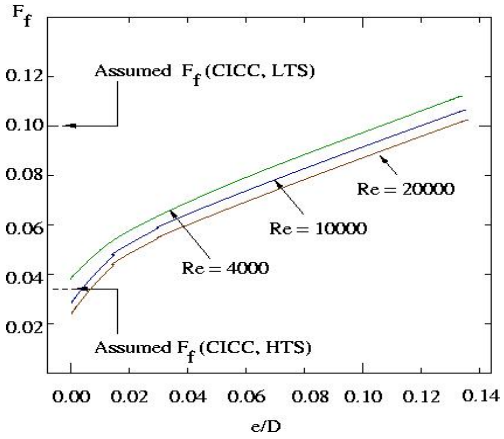

Figure 3: Friction factor as a function of roughness for the Reynolds Numbers of 4000, 10000 and 20000

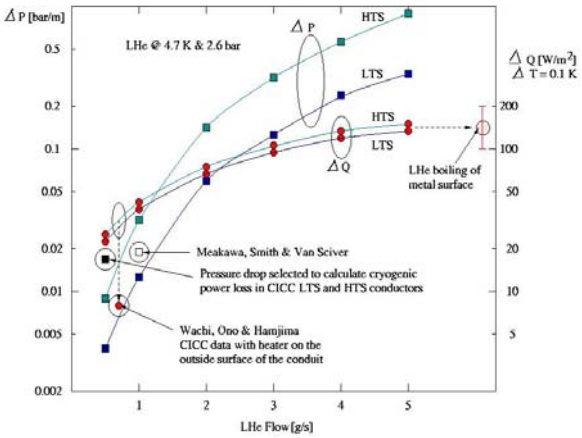

Figure 4: Pressure drop in LTS and HTS conductors and ideal heat transfer.

The available heat transfer from the flowing liquid helium to the conductor strands inside the CICC tube is a second most important factor in the conductor design. The ideal steady-state turbulent flow heat transfer Q in a smooth pipe is given in [7] as:

$$Q = 0.0259\,(k/D_h)\,Re^{0.80}\,Pr^{0.4}\,(T_c / T_{He})^{-0.716} \qquad (3)$$

where D_h is hydraulic diameter, Pr is the Prandtl Number and T_c and T_{He} are the temperatures of the conductor and the flowing helium, respectively. We also find that the Nusselt Numbers are large for our design of both LTS and HTS conductor lines suggesting that the convection will be a dominant process for the heat transfer.

Using the formula (3) we project ideal heat transfer for the proposed LTS and HTS conductors operating with supercritical helium of average 4.7 K temperature and 0.26 MPa pressure. We observe that the heat transfer increases by about a factor of 5 from 0.5 g/s to 5 g/s flow rate strongly indicating that higher flow rates in CICC conductors are beneficial for the heat transfer. But it is also interesting to note that the expected heat transfer saturates at flows of about 5 g/s to that of the LHe boiling off the metal surface.

The only available data [7] for the heat transfer in a CICC conductor suggests that the efficiency of the heat transfer is only at about 25%. In addition to that there is also a "delay in response" meaning that there is a time delay for the heat to be passed from the flowing liquid helium through the surface of the conductor to its interior. This time delay is very difficult to estimate as it depends strongly on the physical properties of both the contact surface and the conductor internal structure. The time delay, however, is very detrimental in a quench situation. For this reason superconductors should operate with wide temperature margins so the heat absorption can take place with as high efficiency as possible in the case of a quench.

As shown in figure 4, the effects of the helium flow rate on availability of the heat transfer, and on the pressure loss in the CICC conductors are contradicting each other. In an ideal case one would like to use the lowest possible liquid helium flow rate (but above the laminar state) to minimize the required power of the cryogenic plant. So, the efficiency of the heat transfer from the flowing liquid helium to the conductor strands is of greatest concern. Consequently, our CICC conductors were designed to optimize as much as possible the heat transfer. Both the HTS and the LTS conductors are designed with large void fractions (70%-80%), and with at least 50% of a direct contact area of strands to the helium coolant. In addition, the heat transfer through a convection process which is dominant one in our conductor line designs is viewed as the most efficient one.

CRYOGENIC COOLING IN A MAGNET ENERGIZED BY A TRANSMISSION LINE CONDUCTOR

The arrangement of the conductor winding in a magnet plays a very significant role in the determination of the required cooling power per magnet length. In principle there are two options for the arrangement of conductor winding: (1) multiple turn, and (2) single turn. A multiple turn option is a standard one used in most accelerator magnet constructions. A single turn option is rather a novel approach for a large scale application and it was first proposed for the VLHC [8]. The two options of the conductor windings are shown in Fig. 5. In a single turn winding the liquid helium coolant can be supplied and returned in the path of the individual magnet length (or the selected magnet string). In a multiple turn winding the path of the liquid helium coolant is equal to that of the total length of the conductor winding. Consequently, the pressure drop of the liquid helium coolant in a magnet of N-turns conductor is at least N times larger than in a magnet of the same length but a single turn conductor. Naturally the drawback of a magnet with a single turn conductor is that the required current is N times higher. In the same time, however, the magnet inductance is N^2 times lower. The low inductance of single turn conductor magnet minimizes the stored energy which helps for the quench protection but it increases the difficulty of the current regulation of a magnet string. The power supply design will need to manage both high current and small Ldi/dt voltage in fast-ramping and fast-cycling operations.

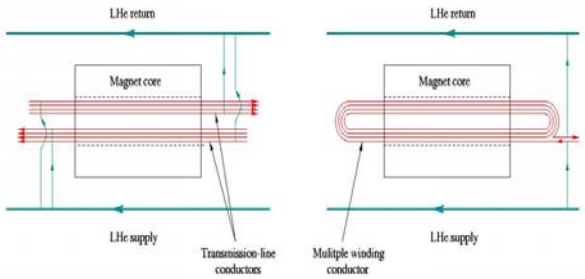

Figure 5: Single and multiple winding magnet options

Accelerator magnet string of single turn conductors is powered by a transmission-line conductor with a single power supply. The liquid helium supply and return lines run parallel to the magnet string with inlets and exits for the individual magnets (or magnet string subsets) as required by the allowed pressure drop and temperature rise. Such arrangement is efficient for minimization of the required cryogenic power and it allows simplify magnet interconnections as illustrated in Figure 6. The single turn HTS or LTS conductor lines can be easily bent in the horizontal plane to create space for the corrector magnets set. This is also a convenient area for splicing conductors and to provide inlet and outlet for liquid helium coolant.

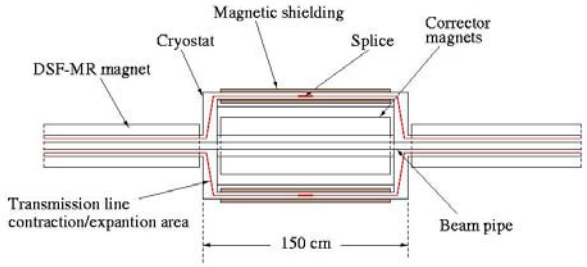

Figure 6: Top view of possible connection of 2 magnets in a transmission-line conductor arrangement with a step out around the corrector magnets

For the DSFMR accelerator the assumed length of a single magnet is 5 m which makes the single conductor length of minimum of 6 m. We use this conductor length to tentatively estimate the required cryogenic cooling power for the DSFMR accelerator based on the HTS and LTS conductor line designs described above. Assuming the initial liquid helium of 4.4 K and 2.6 bar we use the projections from Figure 4 to calculate the pressure drop for a 5 m long magnet powered with 8 parallel conductor lines each of 6 m length, in a transmission-line mode of operations as indicated in Figure 5. In order to project the ideal heat transfer we assume two values of the allowed temperature rise: (1) 0.03 K per meter or 0.2 K per 6 meters and (2) 0.1 K per meter or 0.6 K per 6 meters; with the first one assumed to be characteristic of the power loss in the HTS conductor [6] and the second one of the LTS one [5]. With 0.5 g/s flow rate we assume pressure drop to be 0.1 bar (figure 4) in both HTS and LTS lines. The initial helium coolant enthalpy is 1.09 e^4 J/kg, and the enthalpy after LHe flow through the 6 m long powered conductors is then 1.19 e^4 J/kg for the HTS case, and 1.50 e^4 J/kg for the LTS one. This leads to 0.49 W per 6 m and 2.05 W per 6 m of the used cryogenic power in the HTS and the LTS case, respectively. As there are 8 conductor lines per magnet the projected total used cooling power is about 3.9 W (HTS) and 16.4 W (LTS) for the magnets of 5 m length. This result produces the overall required DSFMR cryogenic power of ~8 kW (HTS) and ~ 34 kW (LTS). The 34 kW power projected with the LTS conductor much exceeds the currently available cryogenic power of 24 kW for the Tevatron operations.

TEST ARRANGEMENT OF THE CONDUCTORS FOR THE FAST CYCLING MAGNET

The projections of the capability of cryogenic power for the fast cycling magnets powered with transmission line conductors presented above indicate that although there is a promising venue (especially with the HTS conductor) a strong R&D effort is required to actually measure this capability as a function of both dynamic and static power losses before embarking on a serious accelerator design. With this in mind we have begun constructing a test setup for the fast cycling superconducting magnets at Fermilab. The test is located in E4R enclosure that is equipped with a cryoplant producing 5 g/s flow of supercritical helium (no power loss). The test arrangement is show in figure 7. The 1.3 m long test conductor lines will be placed inside the CDA magnet gap. The test conductor is connected to the power supply through a water cooled copper conductor loop. The test conductor is connected to that loop through a pair of conventional leads. The test conductor is cooled with a supercritical helium flow while the leads are cooled independently with two-phase liquid helium supplied from 500 l dewars. The temperature at the inlet and outlet of the test conductor will be measured together with the helium flow rate from the cryoplant.

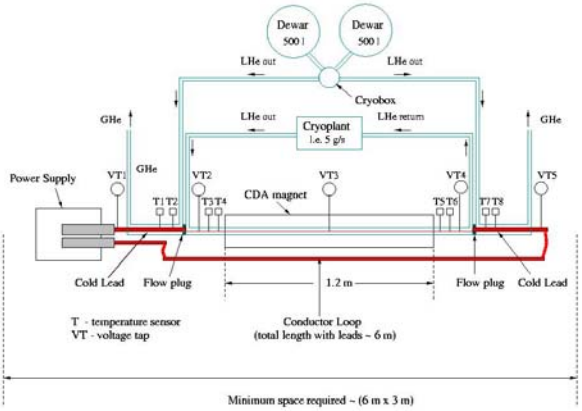

Figure 7: Schematic view of the conductor test arrangement

The CDA magnet shown in Fig. 8 allows to generate dipole field up to 0.7 T with repetition rate exceeding 50 Hz, if required. The *dB/dt* power loss will be measured with power supply off. The DSFMR magnet B-filed is 2 T and a repetition rate of 0.5 Hz, so operating the CDA magnet at 0.7 T with repetition rates up to 5 Hz will allow exceed even multiple times the DSFMR magnet design parameters. The CDA magnet has a very large gap (82.5 mm height x 305 mm width) facilitating installation of the test conductors, and their removal from the magnet for e.g. the *di/dt* induced power loss measurements. For these measurements the power supply will be powered to currents of up 10 kA. In spite of the large gap the B-field quality is rather good as indicated in Fig. 9 below.

Figure 8: CDA dipole for the HTS and LTS conductor tests

A schematic view of the HTS conductor assembly is shown in figure 1, and the connection of the conductor to the leads is shown in figure 10. This connection is arranged in a way that it will be possible to rotate the conductor relative to the dipole field lines in the CDA magnet gap. This will allow investigate the HTS power losses as a function of the angle between the wide side of the tape and *B*-field orientation.

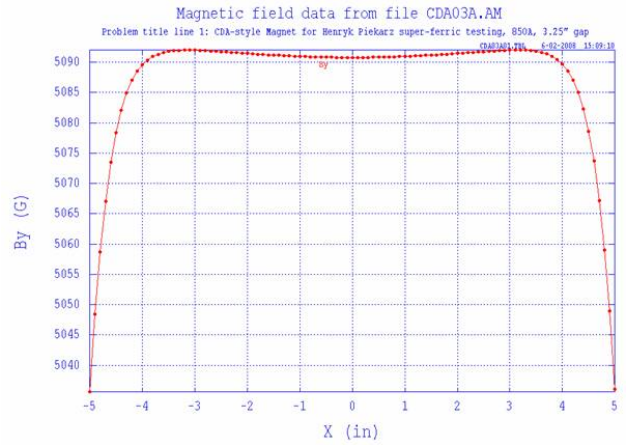

Figure 9: CDA magnet B-field profile at 0.5 T

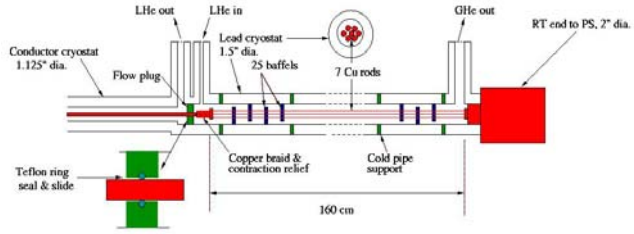

Figure 10: A schematic view of current leads connection to the test conductor and the power supply

The engineering design in progress of the HTS conductor and the lead to conductor connection is shown in Figs. 11, 12. The engineering design of the LTS conductor, as conceptually shown in Figure 1, will follow.

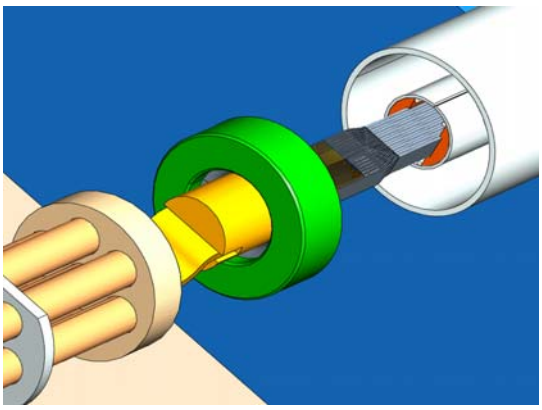

Figure 11: A 3-D view of power lead end and its connection to superconductor line.

The power leads are scaled down from the VLHC-LF magnet design. Each lead is made of seven, 1/4" diameter, 160 cm length low resistance copper rods. The overall size of the lead assembly is designed to allow its passing through the CDA magnet gap facilitating change of the test conductors. The warm end of the lead is a 2" diameter copper rod that is only clamped to the power supply end thus allowing for the conductor assembly rotation inside the CDA magnet gap.

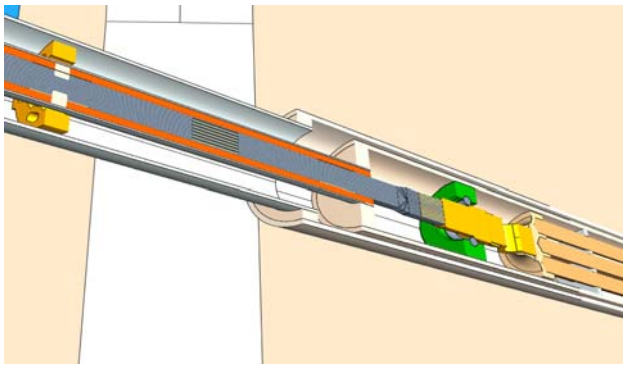

Figure 12: A horizontally sliced 3-D view of HTS conductor. Showing form left: cold pipe support (yellow), baffle (beige), HTS strands (grey), flow plug (green) and copper braid connection to copper rods of the lead (gold).

REFERENCES

[1] L. Bottura, "Fast cycled superconducting magnets for PS2", WAMSDO-08, CERN, May 19-23, 2008

[2] H. Piekarz, S. Hays, Y. Huang and V. Shiltsev, Design Considerations of Fast-Cycling Synchrotrons Based on Superconducting Transmission Line Magnet", EPAC-2008, and FERMILAB-CONF-08-176 APC

[3] G. Moritz, "Superconducting Magnets for the Intern. Accelerator Facility for Beams of Ions & Antiprotons at GSI", Applied Superconductivity Conf. Houston, TX August 4-9, 2002

[4] H. Piekarz, S. Hays, Y. Huang, V. Kashikhin, G. de Rijk, L. Rossi, "Design Considerations for Fast-Cycling Superconducting Magnets of 2 T B-field Generated by a Transmission Line Conductor of up to 100 kA Current", MT-20, 2007

[5] Meakawa, M.R. Smith, S.W. Sciver., "Pressure Drop Measurements of Prototype NET-CEA CICC Cond.", IEEE Trans. Apl. Superc., vol 5, no 2, 1995

[6] Moody Diagram using the Darcy-Weibash equation, http://en.wikipidia.org

[7] Y. Wachi, M. Ono, T. Hamajima, "Heat Transfer Characteristics of the Supercritical Helium in CICC Conductors", IEEE Trans. Apl. Superc. Vol 5, 1995

[8] G. Ambrosio et al, "Design Study for a Staged Very Large Hadron Collider" , Fermilab-TM-2149, 2001

FULL SIZE MODEL MANUFACTURING AND ADVANCED DESIGN STATUS OF THE SIS100 MAIN MAGNETS *

E. Fischer†, P. Schnizer, GSI, Darmstadt, Germany
A. Akishin, H. Khodzhibagiyan, A. Kovalenko, JINR, Dubna, Russia
R. Kurnyshov, Elektroplant, Protvino, Russia
P. Shcherbakov, IHEP, Protvino, Russia
G. Sikler, W. Walter, BNG, Würzburg, Germany

Abstract

Following an intensive R&D period on short model magnets, GSI launched the production of three full size dipoles and a quadrupole magnet for SIS 100 in 2007 within the framework of the FAIR project. The first straight dipole manufactured at BNG Würzburg was already shipped to GSI and is prepared for testing. The other magnets to be manufactured applying different technological solutions will be completed until the second half of 2008 by JINR Dubna (a straight dipole and a quadrupole) and by BINP Novosibirsk (a curved dipole). We give a brief description of the main construction details and the technological solutions chosen. We will show the critical parameters to be studied on these magnets and their influence on the final design. We will exemplify that on the dipole, whose design was changed recently to provide even more intensive cycles.

INTRODUCTION

The aim of the FAIR project [1] is to provide high intensity primary and secondary beams of ions and antiprotons for experiments in nuclear, atomic and plasma physics. This requires an upgrade of the existing GSI accelerator facility and the construction of a new accelerator complex. It consists of 2 synchrotrons in one tunnel, SIS100 (100 Tm rigidity), SIS300 (300 Tm rigidity), and several storage rings. SIS100 is the most intensively used accelerator considered as "work horse" of the facility. It will accelerate ions and protons at a high repetition rate at about 1 Hz and either sends them to the targets for Radioactive Ion Beam or Antiproton Beam production or to the SIS300 for further acceleration to higher energies. The Collector Ring / Recycled Experimental Storage Ring complex will cool the secondary beams and accumulate the antiprotons. High Energy Storage Ring and New Experimental Storage Ring are the experimental storage rings for antiprotons and ions, respectively. This paper focuses on the fast ramped superconducting dipoles and quadrupoles of the SIS100 synchrotron. The Nuclotron ring of the JINR Dubna[2] was the starting point for our magnet design. In a first R&D step the main operation criteria (AC loss, magnetic field quality and mechanical stability of the coil) had been improved and were experimental tested on mockups and short model magnets [4]. These results have to be scaled to the larger aperture and increased length of the SIS100 main magnets, which is required to realize the challenging beam characteristics. We present a short overview of the different achievements, made during the R&D on the Nuclotron model magnets, the manufacturing status of the actual full size models, estimate their expected operation limits, discuss two design alternatives with enhanced operation performance next to finite element calculations of the cryogenic loads of the first full size magnet already delivered.

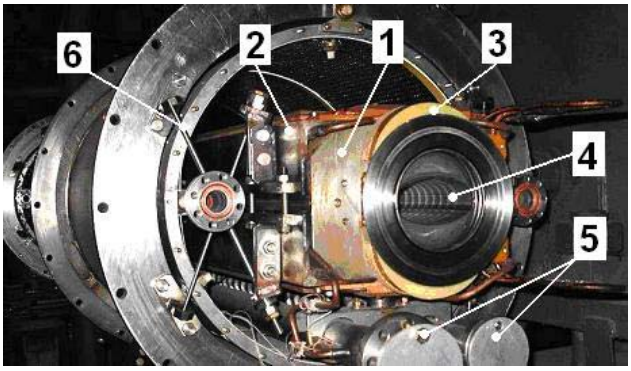

Figure 1: View of the Nuclotron dipole inside cryostat: 1- yoke end plate, 2 brackets, 3 coil end loop, 4 beam pipe, 5 helium headers, 6 suspension

NUCLOTRON MODEL MAGNETS FOR AC LOSS REDUCTION

Dipole

At the original Nuclotron magnets (see figure 1and 2) large AC losses occur during continuously cycling due to eddy currents induced in the cable, in the iron yoke, in the structural elements, (see figure 1 and 2), with 70 % from the cold yoke and 30% from the coil. Further heat is created by the eddy currents in the beam pipe. The yoke losses consist of hysteresis and eddy current losses in the iron and the structural support elements of the magnet. To reduce

* This work is supported by the EU FP6 Design Study (contract 515873 - DIRAC secondary beams) and by the BMBF.
† e.fischer@gsi.de

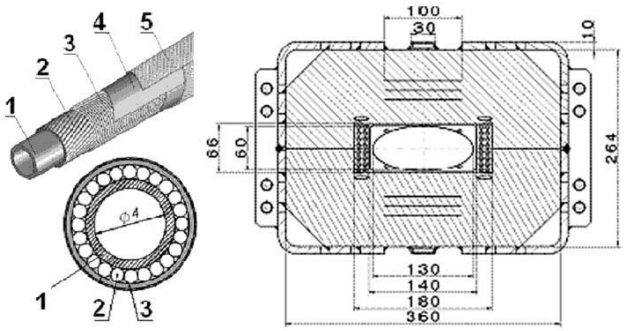

Figure 2: Nuclotron type cable: 1- cooling tube, 2 - Superconducting wire (multifilament NbTi/Cu), 3 - Nichrome wire, 4 - Kapton tape, 5 adhesive Kapton tape. Right: simplified 2D layout of the SIS100 straight dipole with the 2 8 turn two layer coil and the forced flow cooled beam pipe. The six horizontal slits are introduced to suppress the eddy current effects caused by the longitudinal field component near the yokes ends.

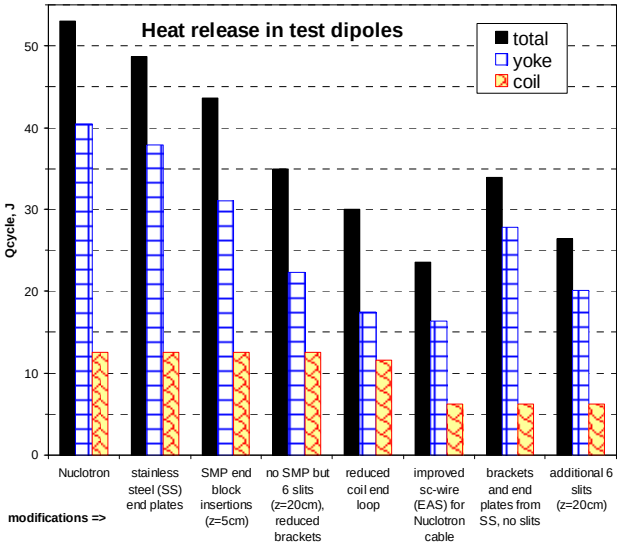

Figure 3: AC losses measured for the different magnet models

.

the load on the cryogenic supply system and thus the operational costs of SIS 100 many single steps were required to obtain a loss reduction[4]. First common sense analysis indicated that the parts made of solid steel (brackets holding the lamination together and the end plates) are the biggest contributors (see figure 3). So the end plates were replaced with stainless steel (SS) ones. Not having reached the set goal the end field was analysed, showing that the component dBz/dz generates losses in the yoke. Following the original idea of the lamination sintered metallic blocks were inserted (SMP) the next step used sheets with slits forming barriers to these currents. The coil ends were modified to fit the beam pipe as closely as possible to reduce the field spreading into the yoke. Cable R&D was carried out

Table 1: Calculated and Measured Dipole Losses

	P_{eddy} [W]	P_{hyst} [W]	[W]	measured [W]
Nuclotron	28.4	16.7	45.1	42 $\pm$2
SS	13.1	9.8	22.9	20

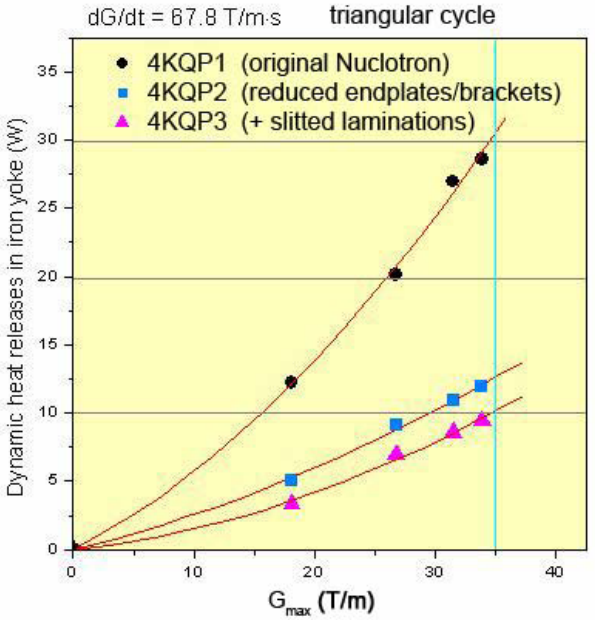

Figure 4: The measured yoke AC loss in a triangular cycle for the different quad- rupoles versus the field gradient at maximum ramp rate

to reduce the losses in the coil; the improved wire ("EAS" wire [5]) with a filament size of 4.1 m was used to fabricate a Nuclotron type cable which reduced the losses even further. In parallel intensive computational studies were conducted. As a result, these losses can be fully calculated by commercial computer programs of today matching the measured values within the measurement precision (see Table 1 [6, 7, 8, 9]).

Quadrupole

Similar improvements were made on the quadrupoles, using the results already obtained in the dipole R&D (see figure 3 [10, 11]). One can see that the maximum loss depends on the maximum gradient. Smaller end plates and slits in the yoke lamination sheets reduced the losses to a third with respect to the Nuclotron magnet.

FULL SIZE MODEL MAGNETS

In the beginning of 2006 the FAIR parameters were actualised within the Baseline Technical Report (FBTR)[12]. According to this status the SIS100 lattice concept had defined the requirements for the straight dipoles and

Table 2: Full Size Modell Magnets

Parameter	Dipole		Quadrupole	
	straight	curved		elongated
maximum field	2.11 T	1.9 T	32 T/m	27 T/m
Magnetic length	2.756 m	3.062 m	1.1 m	1.3 m
Bending angle	3 deg	3 deg	-	-
Curvature radius	47.368 m	52.632 m	-	-
Usable aperture (h·v) mm^2	130·60	115·60	135·65	135·65
Number of magnets	108	108	168	168

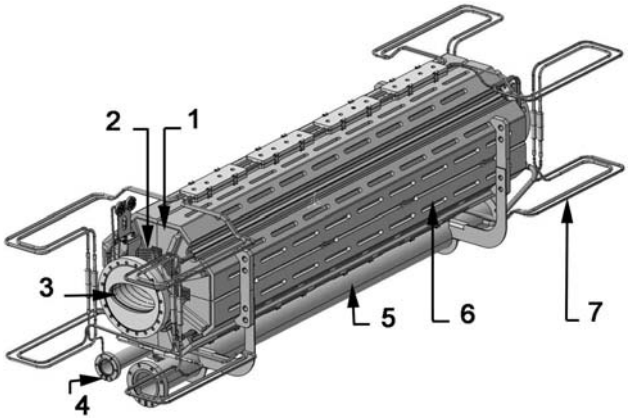

Figure 5: 3D quadrupole model: 1 - end-plate, 2 - coil, 3 - beam pipe, 4 and 5 supply and return helium headers, 6 - brackets fixing the yoke, 7 - bus bars.

quadrupoles as given in Table 2. The following intensive discussion between lattice and magnet designers had shown that an alternative concept using curved dipoles and longer quadrupoles is possible and promising [13]. Table 2 shows the significant reduction of the equivalent horizontal aperture size in the curved dipole due to the eliminated sagitta. The maximum field parameters are substantially reduced too. That offers a more relaxed situation to optimise the field quality. Both these aspects make it possible to reduce the cross section of the laminated yoke as well as the operation current in the coil. This lowers the maximum energy stored in the magnet and also the parasitic AC loss due to eddy currents and hysteresis effect. Besides the cost arguments mentioned above, the minimisation of the total heat loss budget of the dipole is especially important because it limits the possible operation intensity of the synchrotron. The R&D results mentioned above were scaled to the full size magnets in accordance with the SIS100 parameters and had to be verified experimentally. It is also necessary to investigate the technological problems of the intended series production in collaborating with GSI institutes or industry and to gain experience for the magnet tests in the new GSI test facility as well as the methodology of field analysis [14, 15].

Following the decision of the GSI management detailed specifications for the dipole and the quadrupole versions were been worked out. Three collaboration contracts were signed until the end of 2006. The contractors agreed to build two straight dipoles (at JINR Dubna and BNG Wuerzburg), one curved dipole (BINP Novosibirsk) and the elongated Quadrupole (JINR). The tight time scale of the manufacturing processes has been requiring intensive communication and consequent interaction between all the participants. The final design work to prepare the production drawings, the tooling and the technological tests are already completed. The two layer design of the dipole coil is obvious in figure 2. Figure 5 presents the 3D design of the quadrupole chosen for the first full size model. The detailed parameters of this 6 turn per pole option are given

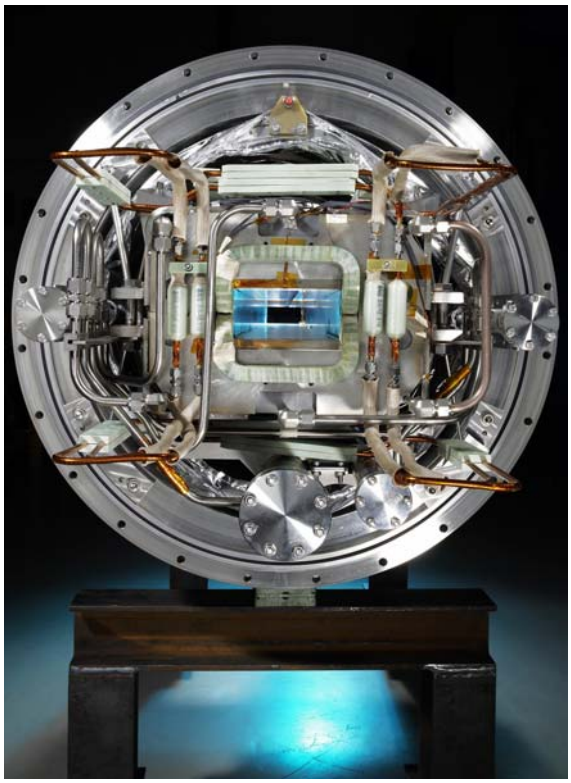

Figure 6: The straight dipole produced by BNG.

in [16]. The required length of the superconducting cable is already produced, i.e. available for all coil winding and the bus bars. The first magnet has already arrived at GSI (see figure 6) and is awaiting its test. The other magnets are expected to follow swiftly during this year [17].

OPERATION CYCLES AND COOLING LIMITS

The practical test of the cooling conditions on the full size models is an important research goal defining the main

Table 3: Operation cycles and expected losses

Cycle	$B_{max}\,[T]$	$t_f\,[s]$	cycle period $[s]$	$Q_d\,[J/cycle]$	$P_d\,[W]$	$Q_q\,[J/cycle]$	$P_q\,[W]$
1	1.2	0.1	1.4	35.2	25.2	13.1	9.4
2a	1.2	0.1	1.4	35.2	25.2	13.1	9.4
2b	0.5	0.1	1.0	8.8	8.8	3.3	3.3
2c	2.0	0.1	1.8	89	48.9	24.4	18.9
3a	1.2	1.3	2.6	35.2	13.5	13.1	5.0
3b	0.5	1.0	1.9	8.8	4.6	3.3	1.8
3c	2.0	1.7	3.4	89	26.2	34.4	10.1
4	2.0	0.1	5.0	89	17.8	34.4	6.9
5	2.0	0.1	5.0	89	17.8	34.4	6.9

operation parameters of the SIS100. The models are based on the hollow Nuclotron cable. Their cooling limits have to be adjusted with the heat loads of the various operation cycles and with the hydraulic resistance of the coil to guaranty a stable two-phase helium flow and a sufficient temperature margin for the superconductor.

Estimation of the Cooling Limits for the Straight dipole

The actual proposed SIS 100 cycles [18] are given for the straight dipole version in Table 3. The injection requires a field of 0.24 T over 0.8 seconds. Then the magnets are ramped up with 4 T/s to the maximum field B_{max}, followed by a flat top time of t_f. The expected dynamic loss per cycle and the average loss power values Q_d, P_d are extrapolated from measurements on short model dipoles. More then 80% of the total AC loss at 4.5 K comes from the iron yoke due to the large cross section. Q_q and P_q are the respective parameters for the quadrupole. Hydraulic calculations had shown that the most intensive cycle 2c should be close to the upper cooling limit [19]. In addition also the low loss limit should be considered in more detail to provide a stable forced flow cooling for all requested operation cycles. These strategic questions will be soon clarified testing the first full size magnet.

Operation test on an equivalent Dipole System

A full length equivalent dipole system was tested to estimate the limits for the cycles. This model dipole consisted of a serial combination of the standard Nuclotron dipole and an optimised short model magnet, both individually tested before. The sum of the AC loss of both 1.4 m long models was close to the total loss expected for the 2.8 m straight dipole. The cooling scheme of the tests is given in figure 7. The coils of the magnets were connected in series with respect to the helium flow and the supply current. For these measurements the cryostat and the power supply system were redesigned at the JINR magnet test facility.

In these measurements the mass flow rate was adjusted for $x_6 \approx 1$, i.e. the mass vapour content at T6 was always close to the critical line of the two-phase helium region.

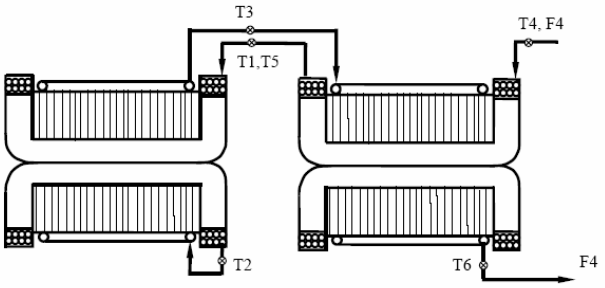

Figure 7: Cooling schema of the equivalent dipole model: T1, T2,...T6 - temperature measurement points, F4 - measured helium flow. The two-phase helium flow enters the laminated yoke after cooling the two short coils all connected in series.

The loss data are in adequate agreement with the values obtained for the individual magnets [20] and confirm our estimations of the cooling limits for the full length dipole. The quench current of the system reached 7916 without preliminary training. The genuine cycle 2c could not be realized, the pause between the ramping had to be increased at least to a cycle period of 2.2s (cycle 2c'). The results are summarised in figure 8. The measured helium pressure drop ΔP dependence on the corresponding time averaged heat loss Q_a in the model dipole is plotted for the cycles given in Table II. A two parameter fit for $\Delta P = c_0 \cdot Q_a^n$ defines $n = 1.733$ and c_0. The parameter $n = 1.75$ is the well know mass flow rate exponent describing the pressure rise due to friction, so $c_0 = 0.00153$ is the only adjusted coefficient. The results for cycle 2c' had shown, that under the given cooling conditions and ramp rates the upper limit for stable cycle operation is defined by $Q_{aL+} = 35\,W$. Using this characteristic value and introducing the maximum pressure drop ΔP_0 we obtain $\Delta P = \Delta P0(Q_a/Q_{aL+})^{1.75}$ with $\Delta P_0 = 0.77$ bar, the microscopic description of these parameters is given in detail in [21]. For the stable cycle 2b (ΔP = 0.15 bar) and the unstable cycle 3b (ΔP =0.10 bar) the loss values could not been measured and was calculated using the fit line. The experimentally obtained stability limit was closer to cycle 3b so we can estimate it as

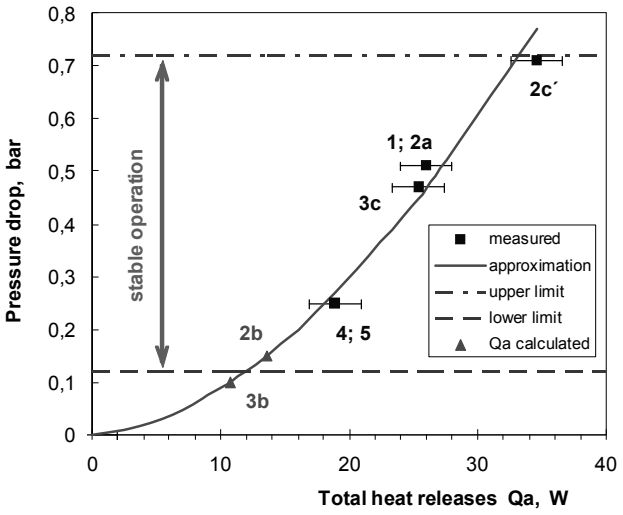

Figure 8: Cryogenic stability range of the 2.8 m long equivalent model dipole. The cycle names are plotted near their data points.

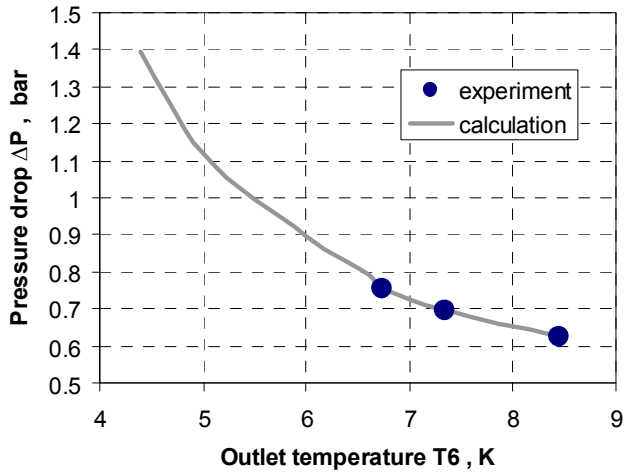

Figure 9: The pressure drop dependence on the yoke outlet temperature at the equivalent model dipole tested and calculated for a stable triangular cycle with the total heat load of 50.5 W.

$P_{min} = 0.12$ bar or $Q_{aL-} = 12W \approx 1/3 Q_{aL+}$.

More intensive cycles require to increase Q_{L+}. This can be achieved by changing the yoke outlet temperature T6 into the vapour area, but assuring $x_2 < 1$ at the outlet of the coil. The method is demonstrated in figure 9 showing the results obtained for the composite dipole, tested this way in a stable triangular cycle with a heat load of 50.5 W, i.e. 50QL+ . In this operation mode the pressure drop spread is reduced by a factor of two (the higher values are calculated). For a cooling scenario with T6=4.4 K (x6=1) we have P = 1.39 bar, i.e. an impossible mode, but the high load cycle was demonstrated with P=0.627 bar choosing T6=8.45K. The same ideas could be applied to extend the SIS100 magnets operation to higher intensities, i.e. for continuous triangular cycles, not shrinking the main cycle limits defined in figure 8. This means, that the magnet design should be optimised for cycle 2c, the more intensive cycles can be provided as shown in this section. Based on a final decision for the main magnet parameters and for the complete required cycle spectra, the magnet design and the cooling modes should be analysed carefully. The optimal operation scenario will be chosen to provide an energy efficient operation of the SIS100.

FINAL DESIGN FOR EXTENDED PERFORMANCE

The performance analysis for the straight model has to be compared with the parameters of the curved dipole. In addition a single layer magnet design was considered given that it provides a much higher cooling power due to the reduced hydraulic resistivity of the coil [20, 22, 23, 24].

Magnetic field of a single layer dipole

A magnet design with the minimal required magnet aperture allows also to reduce the required yoke size and was thus favoured in the beginning. A magnet design was made [25] and the field deterioration analysed. For that circular multipoles of the type

$$\mathbf{B}(\mathbf{z}) = B_0 \sum_{n=1}^{\infty} \mathbf{c_n} \left(\frac{\mathbf{z}}{R_{Ref}} \right)^{n-1} \qquad (1)$$

were used, with the Cartesian coordinates $\mathbf{z} = x + iy$, the magnetic field $\mathbf{B} = B_y + iB_x$ the reference radius R_{Ref} and the relative circular multipoles $\mathbf{c_n}$. These multipoles were obtained by calculated elliptic multipoles and then recalculating them to the circular multipoles using analytical transformations[15, 26], which produces multipoles representing the field within the whole aperture with good accuracy. The relative sextupole b_3 and dekapole b_5 are presented in Fig 10. One can clearly see that the sextupole of the "minimal design" is much bigger at even medium fields than for the double layer version. Thus the free aperture between the coils was increased from 130 to 140 mm (option "CSLD"). One can see that this option provides a sextupole comparable to the curved double layer dipole. The dekapole is even smaller than the one of the curved double layer dipole.

Cooling

Along with the curved single layer dipole a two layer dipole alterantive (C2LD-a) was considered to ensure stable operation modes up to the triangular cycle. The CSLD version is based on our previous R&D on high current Nuclotron type cables experimentally tested in short model dipoles equipped with 8 turn single layer coils [27, 28]. The results had to be adjusted to the parameters and requirements of SIS100 [23]. Besides the CSLD design some other versions and a 10 turn coil were considered too, but

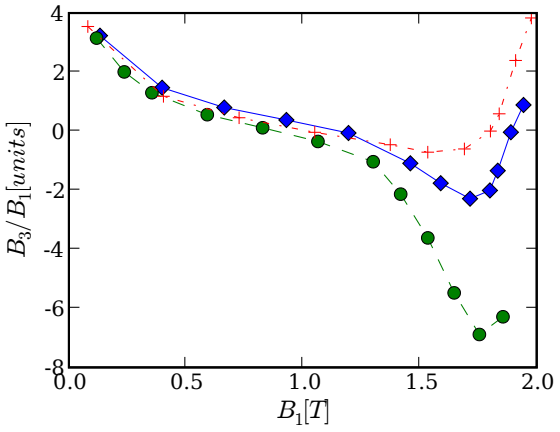

(a) sextupole

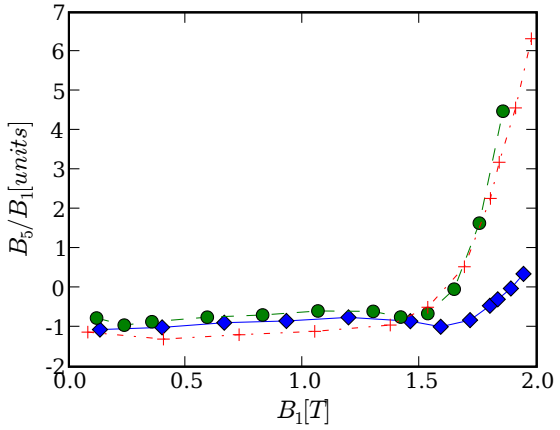

(b) dekapole

Figure 10: The relative strength of the sextupole and octupole (in units) versus the dipole field strength (in Tesla). One unit equals 100 ppm. The blue solid line represents the data for the CSLD, the green dashed line for the design with the minimal aperture and the red dashed dotted line for the curved double layer design.

Table 4: SIS 100 Dipole Options

Parameter Version	straight	curved	C2LD-a	CSLD
Maximum field, T	2.11	1.9	1.9	1.9
Magnetic length, Tm	2.756	3.062	3.062	3.062
Turns per coil	16	16	16	8
Usable aperture, mm2	130 · 60	115 · 60	115 · 60	140 · 60
Cables				
Number of strands	31	31	38	23
Outer diameter, mm	7.36	7.36	7.5	8.25
Cooling tube inner diameter, mm	4	4	4.7	4.7
Length of the cable in the coil, m	110	110	110	57
Bus bars length, m	37	39	39	39
Operating current	7163	6500	6500	13000
Critical current @ 2.1 T, 4.7 K	11900	11900	11900	19840
Wires				
Strand diameter, mm	0.5	0.5	0,46	0.8
Filament diameter, μm	2.5 - 4	2.5 - 4	2.5 - 4	3.5 - 4
Filament twist pitch, mm	45	4-5	4-5	5-8
loss and hydraulic				
Static heat flow, W	7	7	7	7
Heat load to bus bars, W	0.5	0.5	0.5	0.5
cycle 2c				
AC losses, W	36.3	35.4	35.4	35.7
Pressure drop, bar	1.10	1.15	0.604	0.389
T_{max} of He in the coil (for $x_6 \approx 1$) , K	4.94	4.95	4.78	4.64
triangular cycle [dB/dt = 4 T/s, tcycle = 2Bmax / (dB/dt)]				
AC losses, W	75.1	74.0	74.0	74.6
Pressure drop, bar	1.14	1.20	0.657	0.486
T_{max} of He in the coil, K	5.08	5.10	4.86	4.72
with T_6 at	$8K$	$8K$	$8K$	$7K$

detailed field calculations, loss estimations and stability analyses had shown that the CSLD option is clearly the most appropriate alternative [25]. The main design and estimated operation parameters of the actual manufactured full size models and the two alternative options are summarised in Table 4.

For the hydraulic calculations as in [21] the following effects were considered: 1.) Dynamic heat load to the inner layer: 75% of the coil AC loss. 2.) Dynamic heat load to the outer layer: 25% of the total coil AC loss, and 25% of the yoke AC loss. 3.) Dynamic heat load to yoke cooling channel: 75% of the yoke AC loss. The heat load generated by the vacuum chamber, touching the coil, is not even considered here. The lower part of Table 4 shows, that:

1. The actual manufactured full size dipoles (straight and curved) should operate at their physical limit to provide the most intensive triangular cycle and will not be stable.

2. This problem was identified and thus the CSLD was chosen as design for the SIS 100 main dipole [29] as it can provide the requested triangular cycles as well as a safety cooling margin for additional, not yet identified, heat loads.

THERMAL ANALYSIS USING ANSYS

A real accelerator magnet uses different materials for different parts. The field in the iron and in the aperture is influenced by the 3D geometry of the yoke and the beam pipe structure as well as by the steel B H curves which are

nonlinear and anisotropic, as the yoke is laminated. During an intensive R&D the Nuclotron dipole and quadrupole model magnets were modelled with all their details in ANSYS and it was shown that the AC losses can be calculated agreeing well with the measurements [9]. Based on this knowledge analogous calculations of eddy current and hysteresis losses were conducted for the actual design of the full length SIS100 dipole as built by BNG. Using the results of the electromagnetic field calculations, the analysis is extended to investigate the thermal effects in the main construction elements of the magnet and to estimate the temperature margins of the superconductor and of the cryo-pump functionality of the beam pipe [30].

The superconducting dipole

The straight dipole manufactured by BNG features a yoke, made of laminated electrical steel (1 mm thick), and brackets and end plates of stainless steel. The two layers of its coil are embedded in a G11 matrix. The vacuum chamber structure consists of an elliptical beam pipe (inner aperture: 130 mm 60 mm, 0.3m thick stainless steel), cooling tubes and the mechanical stabilising transversal ribs (1 mm thickness, 20 mm transposition pitch). The thermal contact between vacuum chamber, coil and yoke is provided by electrically insulating G11 plates. The specific problems of finite element simulations for the real geometry of fast ramping superferric magnets, consisting of various ferromagnetic and non magnetic steels with a sophisticated 3D geometry, have been solved with ANSYS using edge elements. To construct an appropriate electromagnetic-thermal 3D model for the new SIS100 full size dipoles and for a correct FE analysis, the design details and material properties of the vacuum chamber are very important, as well as its connection to the coil and the yoke. The middle of the magnet is basically uniform in z, except for the rib structure of the vacuum pipe. Thus a magnet model with a length equal to the period of the rib structure was formed to reduce the number of elements. This requires choosing correct boundary conditions, in particular enforcing eddy current traces always perpendicular to the cross section of our model. The 3D magnetic and the thermal models of magnet centre, equal to one period of the vacuum chamber with ribs, are shown in figures 11 and 12.

The triangular cycle, continuously ramping with 4T/s between the injection field $B_{min}0.24\,T$ and $B_{max} = 2.1T$, is actually the most demanding operation mode for the SIS 100 dipoles [24]. For the analysis the approximation $B_{min} = 0T$ was used as well as a fixed current ramp $|dI/dt| = const$ with a cycle repetition rate of 1Hz. The thermal calculations are done using the time averaged power of the AC loss. The inaccuracy of the so calculated results was estimated to be less then the uncertainties caused by the variation of the material data, i.e., $dB(I)/dt$ is especially sensitive to the material properties B(H) and the real packing factor of the yoke. Following the method given here, the exact calculation will be straight forward

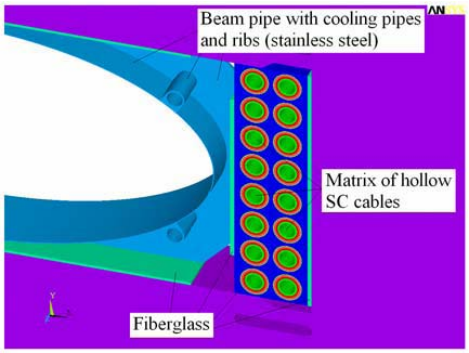

Figure 11: Layout of the main parts of the SIS100 dipole FE model.

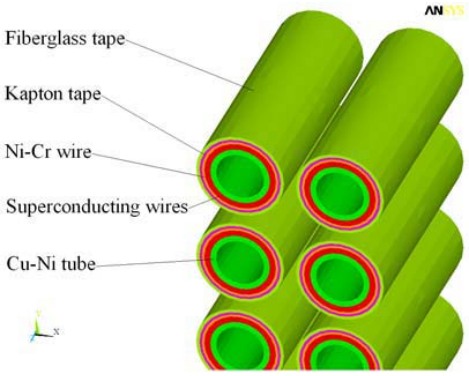

Figure 12: Layout of the turns of the SC coil of the SIS100 dipole magnet.

for all required cycles and all different magnet sizes.

AC Loss Results

The heat sources for the thermal calculations are the magnetic hysteresis and the eddy current loss in the structures of the yoke, the SC coil and the vacuum chamber. The hysteresis loss per cycle is not frequency dependent and can be determined in the static magnetic mode. The eddy current loss was calculated as a transient process. The specific data and methods given in [31, 32] were used for calculating the hysteresis loss in the laminated yoke and in the superconducting multifilamentary wires. The applied electrical resistivities of the conductive materials at 4.2 K are provided in Table 5. The AC loss was integrated over all elements to obtain the contribution of each design unit of the magnet. The main loss sources are summarised in Table 6. The coil loss data are strongly dependent on the SC wire design. The upper extremes of the loss values for

Table 5: Resistivity of materials at 4.2 K $10^{-7}\Omega m$

Electrical steel	Stainless steel	Copper	CuNi	NiCr
3.2	5	0.017	1.4	12

Table 6: Loss per cycle in the different parts of the magnet

	Yoke assembly		Vacuum chamber		SC coil	
	Yoke Hysteresis	Yoke Eddy Currents	Elliptical tube	Cooling pipes	Hysteresis in filaments	Eddy in matrix
AC loss, [J/m]	9.63	0.34	5.18	4.83	2.03-4.1	3.13-6.3
Total	10.05		10.1		5.18-10.4	

the SC coil are given for the wires already tested with a filament diameter of 6 m, the lower values are estimated for wires with 2.5 m filaments. The total values include also the eddy losses in the brackets (0.076 W/m) and the yoke cooling pipe (0.0067 W/m). The loss in the ribs of the vacuum chamber (0.097 W/m) is also negligible as well as the value obtained for the CuNi tubes of the cable (0.021 W/m). To estimate the total thermal loss of the dipole, to be cooled at 4 K, one also has to consider the end field effects ($\approx$ 5 W/dipole) and the static heat load.

Impact on temperature

All thermal contacts between the different electrical conducting or insulating materials of the dipole construction, including the fine structure of the SC cable had been modelled thoroughly. The temperature boundary conditions are chosen to be T = 4.5 K at all inner surfaces of the cooling tubes; the heat flow from surfaces in contact with vacuum was approximated to be zero. The temperature dependence is considered for the thermal properties of all materials (thermal conductivity and specific heat capacity). Some characteristic values of the thermal conductivity and the specific heat capacity at 4.2 K are given in Table 7. The thermal analysis can be carried out in transient or steady state mode, but most of the analysis was performed in steady state mode due to the stable cycle repetition frequency of 1 Hz. The transient calculations, using the time-averaged loss power density, had shown that the steady state is achieved after approximately 60 cycles. The time averaged AC power loss density function was applied to the thermal model and the steady state thermal problem was solved. To check the cryo-pump functionality of the beam pipe, the 3D distributions of the temperature was analysed for different versions of the vacuum chamber construction: (I) for the complete chamber assembly, (II) with the ribs, but without cooling pipes, and (III) the beam pipe with cooling tubes but without ribs (see figure 13) as well as the transversal temperature profiles of the beam pipe in the plane of the rib starting from the small half axis to the large half axis. The maximum temperatures are 11.5 K 13 K and 24.1 K for version I, II and III respectively. The corresponding values between the ribs are 15.3 K, 17.3 K and 24.1 K. This small difference of the data for version I and II suggests, that the thermal contact of the vacuum chamber to the coil and the yoke cools the beam pipe more efficiently than the given cooling tube arrangement. This result is also important for the heat flow balance between the iron yoke and the coil. That finally defines the operation temperatures of the superconducting cable and its temperature margin. The temperature distribution in the superconducting wires, modelled by a cylindrical layer in the hollow superconducting cable, is presented in figure 14 for the two different versions I and III. The CuNi tubes are not shown. It has been obtained from these calculations, that the temperature gradient between the SC wires layer, contacting the outer surface of the CuNi tube, and the inner site of this tube, contacting the flowing helium at 4.5 K, is in the order of 0.01-0.03 K. Taking into account the additional temperature drop between the CuNi cooling tube and the two-phase helium flow as well as the complicated fine structure of the contact surface of the 31 superconducting wires the experimental values should be slightly higher. A maximum temperature difference of 0.2 K was measured in special experiments on Nuclotron dipoles[33]. This shows that the temperature margin of the SC wire is defined by the temperature profile of the two phase helium flow depending on the operation modes.

CONCLUSION

- The main R&D goals for the SIS100 magnets have been reached and were used to specify the design of the first full length model magnets for industrial production.
- The first full size dipole is ready for testing at GSI, a second dipole, a quadrupole and a curved dipole will be ready in third quarter of 2008.
- The comprehensive test of these models will give us important information required to optimise the final design and to specify the pre-series magnets.
- The redesign toward an optimised curved dipole with a single layer coil can fulfil the recently updated operation requirements of the FAIR SIS100 accelerator.
- The ramping fields introduce eddy currents in the current vacuum chamber assembly, which create a significant additional heat load on the superconductor.

ACKNOWLEDGMENT

The authors thank all those who contributed to this work, especially all people from the participating laboratories; in particular from GSI, IHEP, JINR, BNG, BINP and FZK.

Table 7: Thermal conductivity λ and specific heat C of materials at 4.2 K

	Electrical steel	Stainless steel	Copper	CuNi	G11	Kapton
λ W/(mK)	0.8	0.21	630	1.30	0.08	0.012
C, J/(kgK)	0.4	2.1	0.1	0.11	1.55	0.8

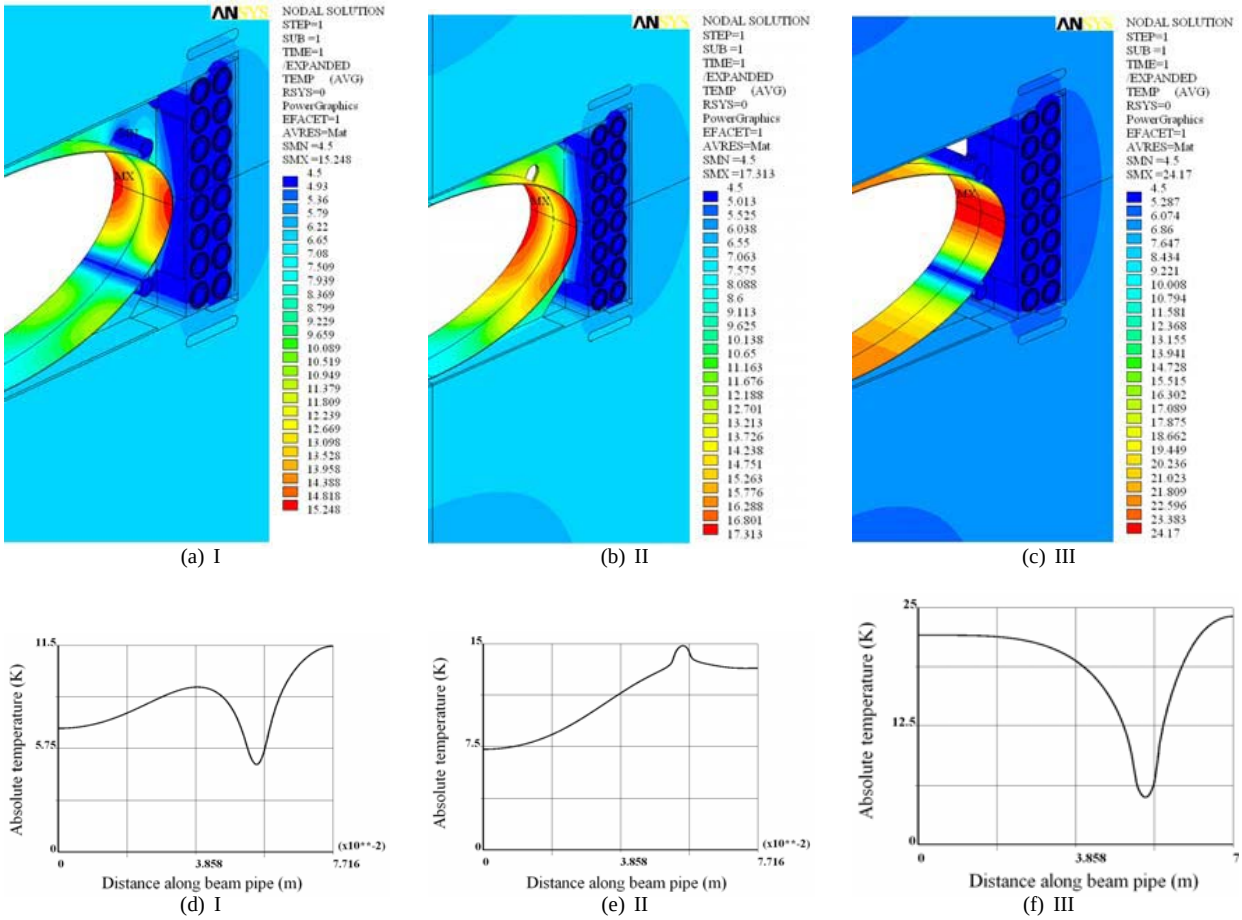

(a) I (b) II (c) III

(d) I (e) II (f) III

Figure 13: Temperature field on the vacuum chamber

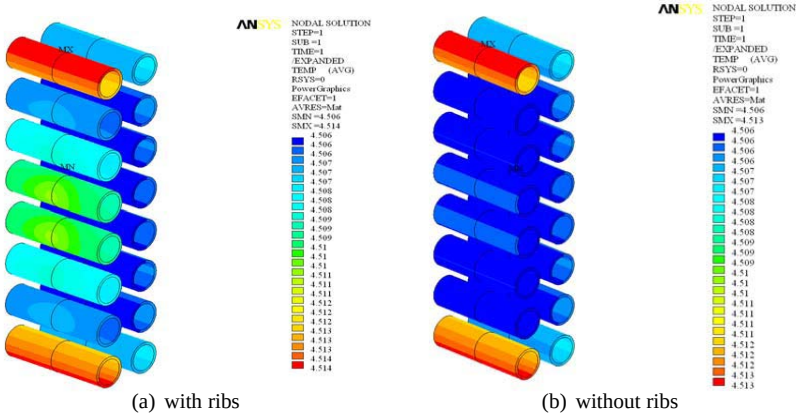

(a) with ribs (b) without ribs

Figure 14: Temperature field in the SC wires of the coil turns.The CuNi tubes, on which the wires are placed, are not shown.

REFERENCES

[1] An International Accelerator Facility for Beams of Ions and Antiprotons. Conceptual Design Report, (2001), http://www.gsi.de/Future/

[2] H.G. Khodzhibagiyan, A.A. Smirnov "The concept of a superconducting magnet system for the Nuclotron", Proc. of the Twelfth Int. Cryogen. Eng. Conf., ICIC12, Southampton, 1988, pp.841-844.

[3] G. Moritz et al., "Towards fast pulsed superconducting synchrotron magnets," in Proc. PAC'2001, Chicago, June 2001, pp. 211-214.

[4] Alexander Kovalenko et.al., "New Results on Minimizing AC Power Losses in a Fast Cycling 2T Superferric Dipole with a Cold Yoke", IEEE Trans. Appl. Supercond., vol. 16, N2, 2006, pp.338-341

[5] "European advanced superconductor," http://www.advancedsupercon.com.

[6] P. Shcherbakov. et .al "3D field computations for the mai prototype magnets of the SIS 100 accelerator of the FAIR Project", Proceedings of EPAC 2006, Edinburgh, June 2006

[7] E. Fischer. et .al "Analysis of the superferric quadrupol magnet design for the SIS 100 accelerator of the FAIR project", Proceedings of EPAC 2006, Edinburgh, June 2006

[8] P. Shcherbakov. et .al "3D Magnetic field and eddy cur rent loss calculations for iron dominated accelerator mag nets using ANSYS compared with results of non commer cial codes", Proceedings of EPAC 2006, Edinburgh, Jun 2006

[9] E. Fischer, R. Kurnyshov and P. Shcherbakov, "Finite element calculations on detailed 3D models for the superferric main magnets of the FAIR SIS100 synchrotron" Cryogenics, (47) 2007, pp 583-594

[10] "Report on research and development contract No 6 between GSI and JINR Dubna", March 2006

[11] EU FP6 'DIRAC secondary Beams', 1st Annual Report, Annex 3: Design report on structural analysis (Deliverable 53 of task 22)

[12] FAIR Baseline Technical Report, GSI, Darmstadt Germany, 2006

[13] E. Fischer, H. Khodzhibagiyan, A. Kovalenko "SIS100: Magnet Design options to minimize the Energy losses, Investment and Operation Costs", MT-INT-EF-2006-002, GSI, 08, 2006

[14] A. Stafiniak et al "Commissioning of the Prototype Test Facility for Rapidly-Cycling Superconducting Magnets for FAIR", IEEE Trans. Appl. Supercon, vol. 18 (2), 2008, pp1625-1628

[15] P. Schnizer, B. Schnizer, P. Akishin, E. Fischer " Magnetic field analysis for superferric accelerator magnets using elliptic multipoles and its advantages", IEEE Trans. Appl. Supercon, vol. 18 (2), 2008, pp1648-1651

[16] E. Fischer, A. Alfeev, A. Kalimov , H. Khodzhibagiyan, A. Kovalenko, G. Kuznetsov, G. Moritz, C. Muehle, and V. Seleznev "Status of the Design of a Full Length Superferric Dipole and Quadrupole Magnets for the FAIR SIS 100 Synchrotron", IEEE Trans. Appl. Supercond., vol. 17, N2, 2007, pp.1078-1082.

[17] A.Kovalenko et. al "Full Size Magnets for Heavy Ion Superconducting Synchrotron SIS100 at GSI: Status of Manufacturingand Test at JINR", 11^{th} European Particle Accelerator Conference, June, 2008, Genova

[18] P. Schuett, "Operation modes of the new accelerator complex for ions and antiprotons", Report on EMAC II, GSI, Darmstadt, October 2003.

[19] E. Fischer, H. Khodzhibagiyan, A. Kovalenko "SIS 100 dipole cooling limits ", MT-INT-EF-2007-002, GSI, 20.05.2007

[20] E. Fischer "FAIR: SIS 100 Synchrotron R&D Status Main Magnets and Full Length Models", miniTAC sc Magnets and Cryogenics, May 24/25 2007, Egelsbach

[21] H. Khodzhibagiyan, A. Kovalenko, and E. Fischer "Some aspects of cable design for fast cycling superconducting synchrotron magnets", IEEE Trans. Appl. Supercond., vol. 14, N2, 2004, pp.1031-1034.

[22] E.Fischer et al., "Minimization of AC Power Losses in Fast Cycling Window Frame 2T Superferric Magnets with the Yoke at T=4.5K", presented at ASC 2004; Internal GSI Note, MT-INT-EF-2004-09

[23] E. Fischer, H. Khodzhibagiyan "SIS 100 dipole alternatives", MT-INT- EF-2007-003, GSI, 15.06.2007

[24] E. Fischer, H. Khodzhibagiyan and A. Kovalenko, IEEE Trans. Appl. Supercon., June, (18) 2008, p 260-263

[25] P. Akishin, E. Fischer, P. Schnizer "A single layer dipole for SIS 100" Gesellschaft für Schwerionenforschung mbH, Tech. Rep., July 2007.

[26] P. Schnizer, B. Schnizer, P. Akishin, E. Fischer "Theoretical Field Analysis for Superferric Accelerator Magnets Using Plane Elliptic or Toroidal Multipoles and its Advantages", 11^{th} European Particle Accelerator Conference, June, 2008, Genova

[27] Khodzhibagiyan, H. E. Fischer, A. Kovalenko, G. Moritz, L. Potanina, A. Shikov, G. Vedernikov "Design and test of a hollow superconducting cable based on keystoned NbTi composite wire", IEEE Trans. Appl. Supercond. (2005) 15 2 1529-1532

[28] H. Khodzhibagiyan, N. Agapov, A. Kovalenko, A. Smirnov, A. Starikov "Development of fast-cycling superconducting magnets at JINR", CRYOPrague 06, Prague, July 2006.

[29] An International Accelerator Facility for Beams of Ions and Antiprotons. Technical Design Report, Synchrotron SIS 100, to be published

[30] E. Fischer, R. Kurnyshov, and P. Shcherbakov, "Analysis of coupled electromagnetic-thermal effects in superconducting accelerator magnets", J. Phys.: Conf. Ser. 97 (2008) 012261 (6pp)

[31] P. Shcherbakov et al. 2004 Magnetic properties of silicon electrical steels and its applications in fast cycling SC magnets at low temperatures, (RUPAC-2004, Dubna) pp 298-300

[32] Superconducting Material Database, article 5. Thermal, Electrical and Mechanical Properties of Materials at Cryogenic Temperatures N 11 FDR 42 01-07-05 R 0.1

[33] H. Khodzhibagiyan et al. "Design of new hollow superconducting NbTi cables for fast cycling synchrotron magnets", IEEE Trans.Appl.Supercond. 2003, 13, N2, pp.3370-3373.

CRITICAL ASPECTS IN THE DEVELOPMENT OF A CURVED FAST RAMPED SUPERCONDUCTING DIPOLE FOR FAIR SIS300 SYNCHROTRON

P. Fabbricatore, S. Farinon, R. Musenich, INFN Genova , Via Dodecaneso 33, I-16146 Genova, I
F. Alessandria, G. Bellomo, M. Sorbi and G. Volpini, INFN- LASA, Via Fratelli Cervi Milano I
U. Gambardella, INFN Laboratori di Frascati, Via E. Fermi Frascati, I
J. Kaugerts, G. Moritz , H. Müller, FAIR Magnet Technology Group – GSI Darmstadt, D
R. Marabotto, ASG Superconductors, Corso Perrone Genova, I

.

Abstract

The FAIR facility, under development at GSI, includes a large synchrotron for heavy ions acceleration: the SIS300, so called for having a magnetic rigidity of 300 Tm. The dipoles of this synchrotron shall be pulsed at the rate of 1 T/s up to 4.5 T maximum field in a bore of 100 mm. The magnets have a magnetic length ranging from 3.94m to 7.89 m with a cos-theta configuration. The coils with have the particular characteristic to be curved (the sagitta is 114 mm for the long dipoles). Design activities, coupled with conductor R&D and model coil construction, are under way for developing a curved fast-cycled superconducting dipole, suitable for operations of the SIS300. The main goal is the construction, before the end of 2009, of a prototype magnet, including cold mass, fully integrated into a horizontal cryostat. An important intermediate milestone is the industrial feasibility assessment of the winding technology developed for a curve cos-theta dipole, through the construction of cured curved magnet poles, actually under way. The paper covers the critical aspects of this development, with particular emphasis on the constructive problems.

INTRODUCTION

This paper deals with R&D activities in progress at Italian Institute for Nuclear Physics aimed at developing the high field rapidly-cycling super-conducting dipoles needed for SIS300 [1]. In order to have the maximum possible acceptance at a minimum field volume, a curved design with a radius of 66.67 m was proposed for the bending dipoles by FAIR team. The present lattice design includes 48 long dipoles with magnetic length 7.89 m and 12 short dipoles with magnetic length 3.94 m. The coils have two main features: they is curved with a sagitta of 114 mm for long dipoles), and they are fast ramped. Both these characteristics demanded for a challenging R&D, aimed at the development of the required low loss conductor, a robust design with respect fatigue issues and a suitable winding technology. The Italian National Institute of Nuclear Physics (INFN) proposed to perform this R&D in a larger framework aimed to construct a model magnet. A project, called DISCORAP ("Dipoli SuperCOnduttori RApidamente Pulsati"), started in 2006 according a specific INFN-FAIR Memorandum of Understanding signed by both institutions in December 2006. The aim is to have a complete cold mass prototype of the short dipole ready in the summer of 2009. After a preliminary test of the cold mass in a vertical cryostat, it will be integrated in a horizontal cryostat for a test campaign at GSI.

BASIC DESIGN CONCEPTS

Table 1 shows the main characteristics of the model coil. The basic assumption for the design was that the coil should be wound curved, because in this way one can avoid the problem of spring back effects during all manufacturing stages and coil operation.

At an initial stage the choice of a curved winding led the design to a layout based on a single layer coil mechanically supported only by the collars. This basic choice was due to the envisaged manufacturing difficulties related to the mechanical coupling between two curved layers or between a curved collared coil and a curved yoke. Nevertheless later on we realized that the iron yoke must have a role in limiting the mechanical deformations of the collared coil. If not, we could have fatigue failures in some locations of the collar.

Table 1: Characteristics of the model coil

Nominal Field (T) :	4.5
Ramp rate (T/s)	1
Radius of magnet curvature (m)	66,67
Magnetic Length (m)	3.784
Bending angle (deg)	3 1/3
Coil aperture (mm)	100
Max operating temperature (K)	4.7

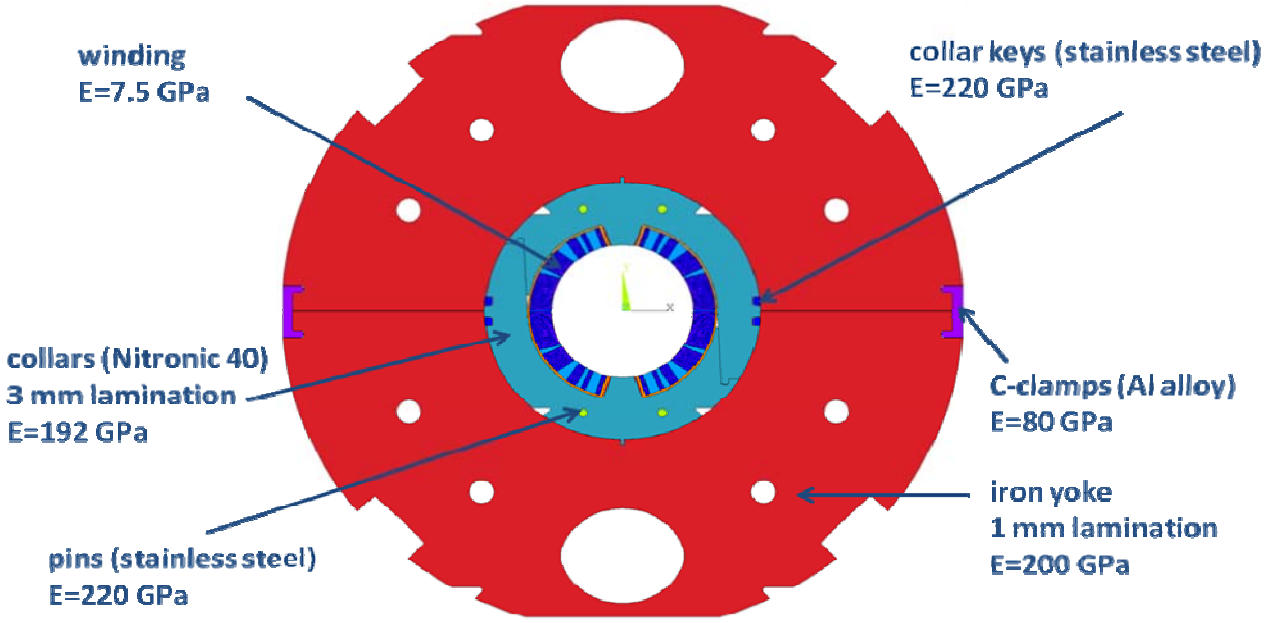

Figure 1: Cross section of the cold mass with some details of mechanical properties

On this basis a 5 block lay-out was chosen. The mechanical strength is provided by a 30 mm thick collar in high strength austenitic steel (Nitronic 40). The winding is pre-stressed up to 70 MPa at room temperature. The iron lamination is mechanically coupled to the collared coil in a way to give no further pre-stress but to limit the deformation during magnetic energization.

Fig. 1 shows the cross section of the cold mass, while the main parameters of conductor and winding are summarised in Table 2 and Table 3. Fig. 2 shows how the cold mass could appear once completed while Fig. 3 shows a detail of the coil end.

The conductor under development [2,3] is based on a cored Rutherford cable with 36 strands (similar to the LHC outer layer), whose main characteristics are shown in Table II. This conductor is characterized by having several components sized for low ac losses. In particular the cable is cored using a thin (25 μm) stainless steel foil (AISI 316L) for increasing the inter-strand electrical resistance, so minimizing the coupling currents.

Table 2: Characteristics of the conductor

Strand characteristics :	
Filament diameter (μm)	2.5 to 3.5
Strand Diameter (mm)	0.825
Twist Pitch (mm)	5
Cable characteristics :	
Number of strands	36
Width (mm)	15.1
Thickness: Thin/Thick edges (mm)	1.362/ 1.598
Core material/thickness (μm)	AISI 316 L/ 25
Critical Current @5T , 4.22K	>18540 A

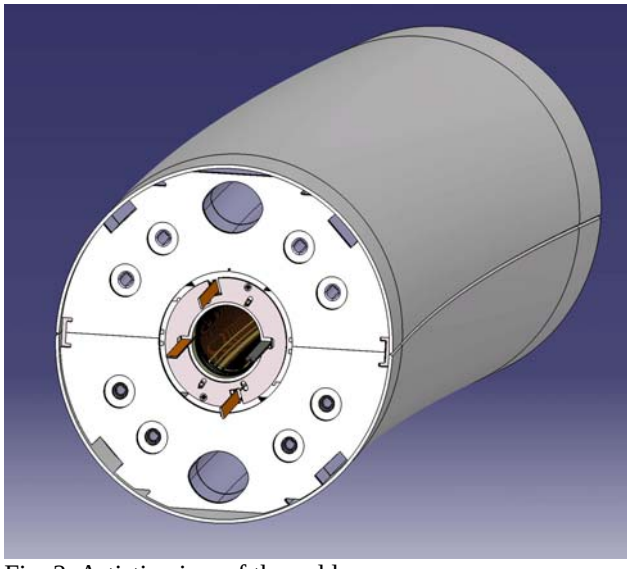

Fig. 2: Artistic view of the cold mass

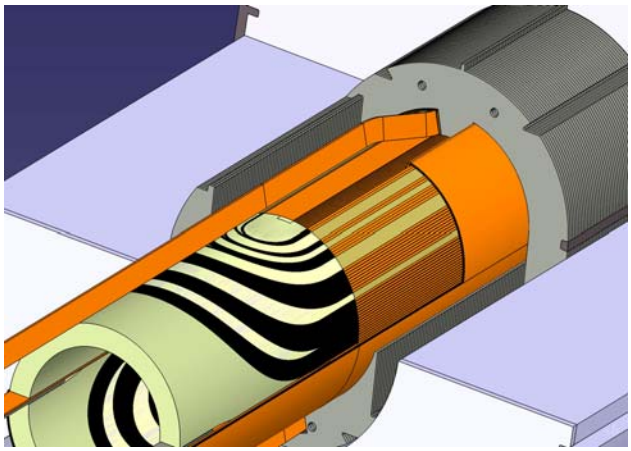

Fig. 3 A detail of the coil end

Table 3: Characteristics of the Winding

Block number	5
Turn number/quadrant	34 (17+9+4+2+2)
Operating current (A)	8920
Yoke inner radius (mm)	96.85
Yoke outer radius (mm)	240.00
Peak field on conductor (with self field) (T)	4.90
B_{peak} / B_o	1.09
Working point on load line	69%
Current sharing temperature (K)	5.69

WINDING TECHNOLOGY

The need to have a SS core inside the cable makes the conductor stiffer than a standard Rutherford cable, causing much more difficult winding operations. For this reason we considered crucial to develop the winding techniques of a cored cable for a curved coil at an industrial level.

This activity is presently under way at ASG Superconductors in Genova, Italy, under an INFN contract. The winding tests are done using both the LHC dipole outer layer cable and a trial winding conductor made of 36 wires, used in the LHC dipole outer layers, cabled around a SS core (See fig.4). A special winding machine has been developed for winding a Rutherford cable on a curved mandrel. An important milestone has been recently achieved, with the successfully completion of the winding test aimed at assessing the developed winding technology. Fig. 5 shows the winding operation of a curved coil and Fig. 6 a detail of the coil end.

The next step of the R&D is the construction of two cured poles with a trial conductor by July 2008. Soon afterwards. The construction activities of the model magnet will start. Our plan is to have the cold mass finished by the summer 2009

Fig.4. The “dummy” conductor used for the winding tests.

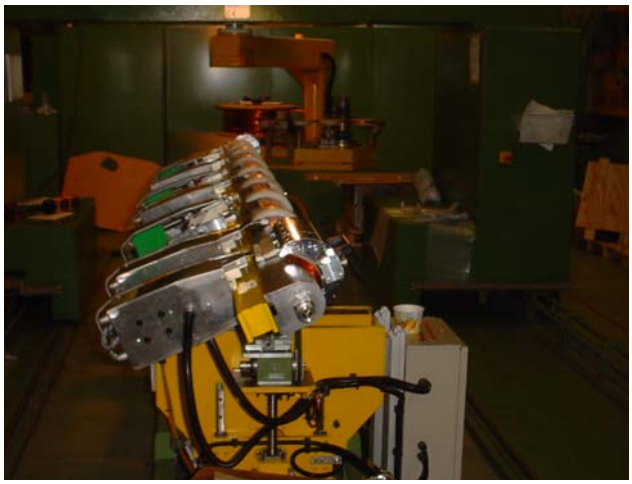

Figure 5: Winding operations with dummy cable

Figure 6: Detail of the coil end (the one with electrical exits)

REFERENCES

[1] P.Fabbricatore, F. Alessandria, G. Bellomo, S. Farinon, U. Gambardella , J.Kaugerts, R.Marabotto, R.Musenich, G.Moritz, M. Sorbi, and G. Volpini “Development of a Curved Fast Ramped Dipole for FAIR SIS300”IEEE Trans. On Appl. Superc. 18 No 2, 232-235, 2008

[2] P. Fabbricatore P, Farinon S, Gambardella U, and G.Volpini, “Rapid cycling superconducting magnets” *NUCLEAR PHYSICS B*-154: 157-162, 2006

[3] G. Volpini, F. Alessandria, G. Bellomo, P. Fabbricatore, S. Farinon, U. Gambardella, M. Sorbi, “Low-loss NbTi Rutherford Cable for Application to the Development of SIS-300 Dipoles,” contributed paper to Magnet Technology MT-20.

ELECTROMAGNETIC DESIGN OF THE PROTOTYPE DIPOLE FOR THE FAIR SIS300*

M. Sorbi#, F. Alessandria, G. Bellomo,and G. Volpini, INFN Milano, LASA Lab., Italy
P. Fabbricatore, S. Farinon, R. Musenich, INFN Genova, Italy
U. Gambardella, INFN LNF, Italy.

Abstract

Design activities, conductor R&D and model coil construction are under way for developing a curved fast cycled superconducting dipole for the SIS300 synchrotron at FAIR. The main target is the construction within 2009 of a half-length prototype magnet (cold mass fully integrated in a horizontal cryostat). This magnet is designed for a maximum central field of 4.5 T in a bore of 100 mm, with a ramp rate of 1 T/s. The magnetic length of the prototype is 3.8 m with a curvature radius of 66.67 m (27 mm of sagitta).

This paper describes the magnetic design of the dipole. Emphasis is given also to the study of the losses due to the eddy currents in collar and yoke. The study has been performed with finite element codes, and it allowed to optimize the configuration in order to minimize both the peak field on the conductor and the total losses.

INTRODUCTION

The FAIR facility at GSI (Darmstadt, Germany) in the second phase of its program, will rely on the 300 Tm synchrotron SIS300. The dipoles of this synchrotron have a maximum field of 4.5 T, in a 100 mm bore, and are fast ramped at 1 T/s. The 7.8 m long dipole has a curvature radius of 66.67 m. In a R&D collaboration between GSI and INFN, the INFN sections of Milano (LASA), of Genova and the Frascati Laboratory have agreed to design, build and commission a prototype dipole, of half length (3.9 m). The main goal of the prototype is to demonstrate the feasibility of a curved superconducting dipole, working in pulsed condition, with good field quality and reasonable heat losses in the cold mass. The 2-D design of the magnet is described in [1], where the main losses in the conductors are also reported. This paper is devoted to summarize the coil end design and to the calculation of the losses in the zone of the coil ends.

COIL END DESIGN

The coil ends have been designed in order to minimize the integral value of sextupole and decapole in the final regions of the magnet, to control the value of magnetic field in conductor, and to obtain a mechanical configuration for the conductor shape feasible during the winding process.

The design has been performed initially with Roxie [2], with the “constant perimeter” option. The Fig. 1 shows a view of the coil end, whereas the Fig. 2 shows a cross section of the coil end with the behaviour of sextupole and decapole.

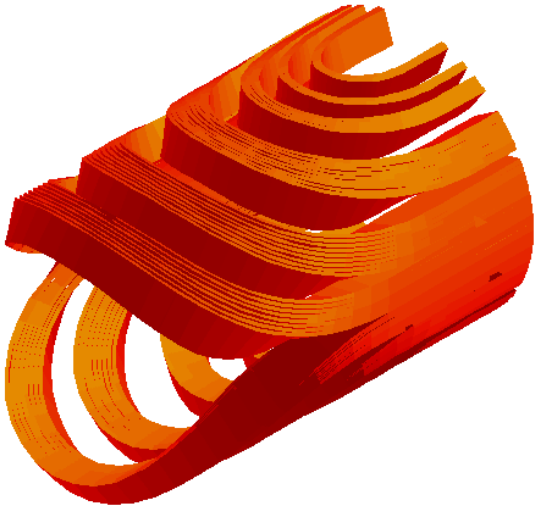

Figure 1: View of the coil end.

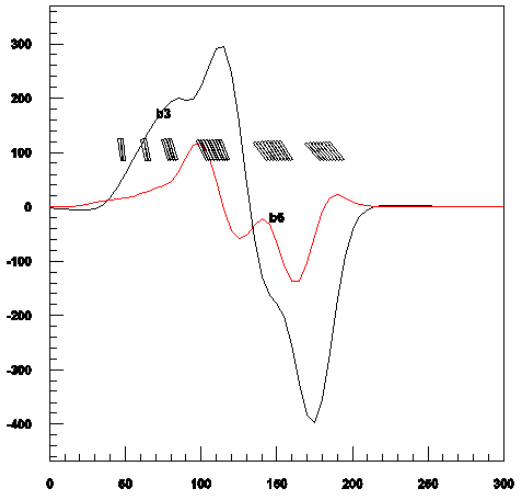

Figure 2: Cross section of coil ends, with the sextupole and decapole behaviour.

The integral value of sextupole and decapole, without the contribution of the iron yoke is given by:

$$b_3^{\,coil-end} = \frac{1}{B_0}\frac{1}{\Delta z}\int_0^{\Delta z} B_3 dz = 0.63 \text{ units}$$

$$b_5^{\,coil-end} = \frac{1}{B_0}\frac{1}{\Delta z}\int_0^{\Delta z} B_5 dz = 0.04 \text{ units}$$

*Work supported by INFN and partially by GSI
#massimo.sorbi@mi.infn.it

with:

$$B_0 = 4.5\,\mathrm{T}\,, \quad \Delta z = 300\,\mathrm{mm}$$

In order to decrease the conductor peak field, the iron yoke in the coil end region is substituted by stainless steel. In this way the peak field is 4.59 T, i.e. 0.37 T less respect to a configuration with "long yoke". The peak field in the coil ends results also lower than the peak field in the 2-D section of the magnet (4.90 T).

LOSSES

A large source of losses in the coil ends is due to eddy currents in the lamination. Eddy currents are present also in the straight part of the magnet: in this section, the 2-D magnetic field B has only components parallel to the lamination. Consequently the eddy currents have components mainly parallel to the lamination and have simple symmetries along the thickness. From a simplified analysis, the volumetric losses can be calculated easily from the variation of the magnetic field $\dot{B}$ parallel to the lamination:

$$p_{B//}(x,y) = \frac{1}{12\rho}\dot{B}_{//}(x,y)^2 \Delta s^2 \qquad (1)$$

where ρ is the electrical resistivity and Δs is the lamination thickness.

The variation of the magnetic field $\dot{B}$ is proportional to the magnetic field and can be evaluated from a magnetostatic analysis.

In the coil end regions, beside this kind of losses, there are additional losses due to the eddy currents generated by the field component perpendicular to the lamination plane. If the magnetic field varies smoothly in the perpendicular direction of the lamination, the currents can be assumed constant in the thickness Δs of the lamination. The values of these currents have been calculated with the F.E. code ELEKTRA, transient analysis, assuming for the laminations a continuum anisotropic material, with zero electrical conductivity in the direction normal to the lamination. In the yoke lamination, the perpendicular component of the field is strongly dependent by the actual reluctivity of iron, which is reduced by the stacking factor. As consequence, the iron yoke has been considered as a magnetic non-linear material, with an anisotropic behaviour for the reluctivity and electrical conductivity.

It is easy to demonstrate that the total loss is given by the sum of the loss due to the perpendicular component of the field (calculated with ELEKTRA) and the one due to the parallel component of the field (calculated by means of (1) with a magnetostatic analysis).

RESULTS

In Fig. 3 we show 1/8 of the model: in yellow the collar, in green the iron yoke, in violet lamination in stainless steel which substitute the iron in coil end regions, and in blue the cylindrical vessel for the helium.

In Fig. 4 we show the losses (colour) and eddy currents (arrows). A large fraction of the currents flows from the lamination through the cylindrical helium vessel, which is an homogenous material. Consequently, during the assembly of the magnet, a particular care has to be put to electrically insulate the cylindrical vessel from the lamination, especially in the coil end region.

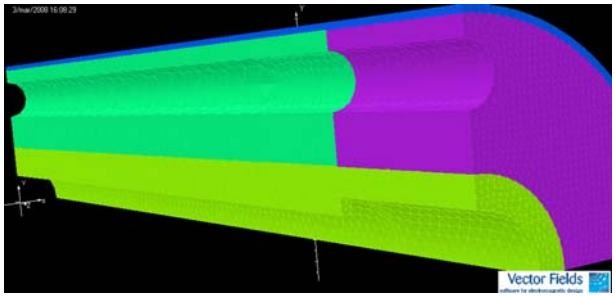

Figure 3: 1/8 of the model.

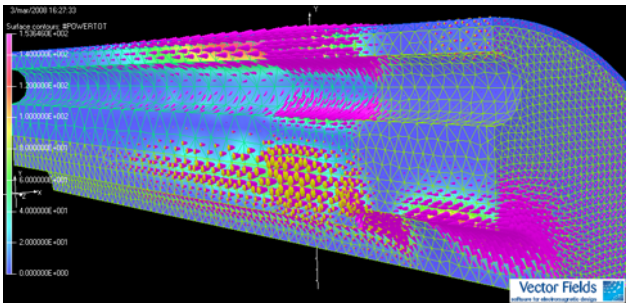

Figure 4: Losses (colours) and eddy currents (arrows) in the laminations.

Other large sources of eddy currents are present in the pins and keys that are used to mechanically connect the laminations of collars and yoke. The Fig. 5 is a view of the yoke pins and key, with the eddy currents calculated by ELEKTRA 3D.

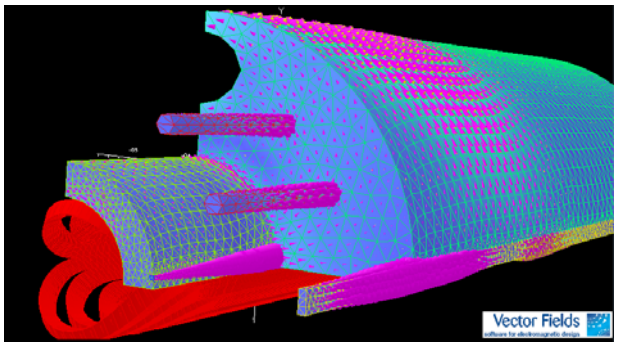

Figure 5: View of pins and keys, with the eddy currents (arrows).

CONCLUSIONS

The design of the coil ends for the SIS300 prototype dipole is almost completed. A method to estimate the losses in collar and yoke lamination has been found. A preliminary analysis shows that during the ramp-up of the magnet, the total losses in the magnet cold mass are about 9 W/m.

REFERENCES

[1] M. Sorbi, F. Alessandria, G. Bellomo, S. Farinon, U. Gambardella, P. Fabbricatore, and G. Volpini, "Field Quality and Losses for the 4.5 T Superconducting Pulsed Dipole of SIS300," IEEE Trans. on Applied Superconductivity, Vol. 18 N.2 June 2008, p.138-141

[2] S. Russenschuck "Electromagnetic Design and Mathematical Optimization Methods in Magnet Technology," eBook, January 2006, http://russ.home.cern.ch/russ, ISBN: 92-9083-242-8

COMPUTATIONAL CHALLENGES IN PRESENT AND FUTURE PROJECTS (FROM A ROXIE DEVELOPER'S PERSPECTIVE)

B. Auchmann*, N. Schwerg, S. Russenschuck, CERN, Geneva, Switzerland.

Abstract

The CERN field computation program ROXIE has evolved into a comprehensive design and simulation environment for superconducting and resistive magnets. We give an overview of the latest improvements in the software, in particular in the field of quench simulation. A discussion of the challenges and limitations of today's approaches to numerical field calculation is followed by our views on the future development of the discipline.

EVOLUTION OF ROXIE

ROXIE** was started in 1992 as a tool for the optimization of coil cross-sections in cosine-theta type magnets. The code consisted of an optimization loop, a set of geometry macros, a Biot-Savart solver, and a routine for the harmonic analysis of aperture fields [1]. At the time, the design effort for LHC magnets was at full swing. Numerous features were added at the request of magnet designers. It became apparent that ROXIE was filling a niche: commercial software cannot provide the specific models and post-processing options that are required in the design of accelerator magnets. All the superconducting magnets of the LHC apart from D1 and D2 have been designed with ROXIE; two examples are shown in Fig. 1.

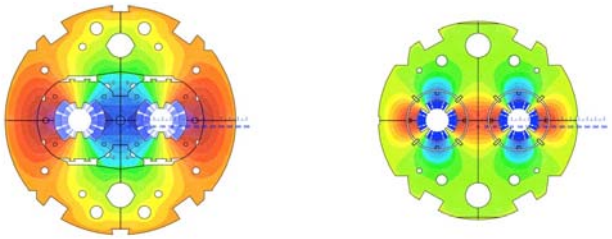

Figure 1: Main Bending- (left) and Main Quadrupole- (right) magnet cross-sections, as designed with ROXIE.

Important extensions to the initial features include:

- ROXIE supports two solvers for the numerical calculation of fields in the nonlinear iron yoke: The finite-element method (FEM) using a reduced vector-potential formulation, that was implemented in collaboration with the university of Graz, Austria [2]; and the coupling of FEM with the boundary-element method, using scalar- and vector-potential formulations, implemented in collaboration with the university of Stuttgart and the Robert Bosch GmbH, Germany [3].
- Models for transient effects in superconducting cables were implemented. We can consider the effect of persistent currents, inter-filament coupling currents, and inter-strand coupling currents on field quality and in terms of thermal losses during a ramp cycle. Special care is taken to solve the interdependence of coil-fields, iron-yoke magnetization, and cable eddy-currents in an efficient, accurate, and numerically stable way [4].
- The latest addition to the ROXIE framework is the simulation of quenches in superconducting magnets. This feature builds upon the transient field-calculation modules in ROXIE, and adds thermal modelling and electric-network simulation.

In the following sections we will give details on the computational challenges in the simulation of quenches, discuss the bottle-necks in 3-dimensional field computation as well as possible remedies, and mention some of the challenges in the field of multi-physics simulations for accelerator magnets.

COMPUTATIONAL CHALLENGES IN QUENCH SIMULATION

A quench is the resistive transition of a superconductor that occurs if the current density, the magnetic field in the cable, or the cable temperature exceeds a critical value. From this description it is evident that quench simulation requires a multi-physics approach.

Modelling Challenges

Fig. 2. displays the different models that interact in the ROXIE quench simulation module [5]. The models are characterized by:

- Coupling: Coupling occurs in two ways: a) the state of one model is the source in another model, e.g., the electric network drives the current in the coil cross-section, the field of which drives the BEM-FEM problem, the result of which drives the transient models, the losses of which drive the thermal computation. b) the state of one model influences the nonlinear material parameters in another model, e.g., field and temperature influence the magnetic permeability, electric resistivity, heat capacity, and many more.
- Nonlinearity: The material properties in the various models exhibit very nonlinear behaviour. Moreover, material values may jump at the transition points between different quantum-mechanical regimes.

* bernhard.auchmann@cern.ch

** Acronym for Routine for the Optimization of X-sections, Inverse problems, and Endspacer design.

- Time scale: Most mathematical models are given in the form of first-order systems of differential equations. The time-constants of the individual systems can be on different scales. Moreover, during one simulation the nonlinear materials can make the time constants vary by orders of magnitude.
- Computational cost: There is a large difference in computational cost between the solution of an electrical-network equation, and that of a BEM-FEM coupled system.
- Achievable accuracy: The achievable accuracy is determined by a) the sophistication of the model, and b) the accuracy of the input data, mostly material parameters. Many parameters are notoriously difficult to determine, e.g., cross-over and adjacent resistances in Rutherford-type cable, and heat-conductivities.
- Required accuracy: The most important output of quench calculation being hot-spot temperature, current-decay curve (for comparison with measurement), and internal voltages, the exact solution of the electromagnetic field problem is only of secondary importance.

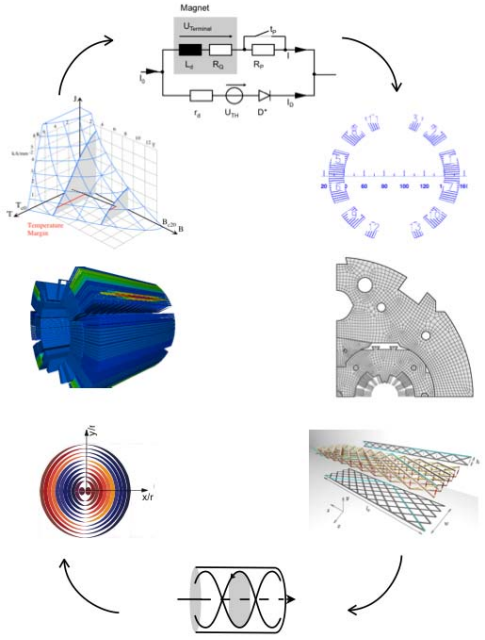

Figure 2: Different models interacting in a quench simulation. Clockwise starting at 1h00: a) geometrical model of the coil, analytical field calculation, b) BEM-FEM model of the nonlinear iron yoke, c) network model of inter-strand coupling currents, d) magnetization model of inter-filament coupling currents, e) magnetization model of persistent currents, f) thermal network model of heat conduction and quench heaters, g) fit of the critical surface of the superconductor, h) electrical network of powering and protection measures.

We identify two big challenges in the simulation of quenches in superconducting accelerator magnets. The first challenge is the accurate, computationally efficient, and numerically stable solution of the above-characterized dynamic models. To this end, adaptive time stepping, iteration schemes, and event-control loops (for the detection of resistive transitions) need to be implemented. Nonetheless quench simulations may take up to several days to be carried out on standard 2.5 GHz desktop computers.

The second challenge is found to be the procurement of all necessary input data for a simulation. The user must supply data for the characterization of quench-heater systems, protection circuits and –electronics, electrical and thermal properties of compound cable materials and insulators, geometrical and magnetic data of the magnets, and many more components. The data must be available at different cryogenic temperatures, and for a range of fields and pressures.

The quench module in ROXIE was written by Nikolai Schwerg in the course of his PhD thesis.

Modelling Results

The above-mentioned dynamical models are implemented in the ROXIE framework. Given the large number of empirical parameters in the models, it must be noted a large part of the simulation work consists in the determination of parameters such that the simulation matches the measurement. It is important to realise that only when

- all relevant phenomena have been taken into account,
- all material parameters have been chosen realistically and within the given range of uncertainty,
- the simulation result match the measured data,

we are able to reproduce the internal states of a quenching magnet, i.e., observe quantities that evade measurement (hot spot temperature, internal voltages).

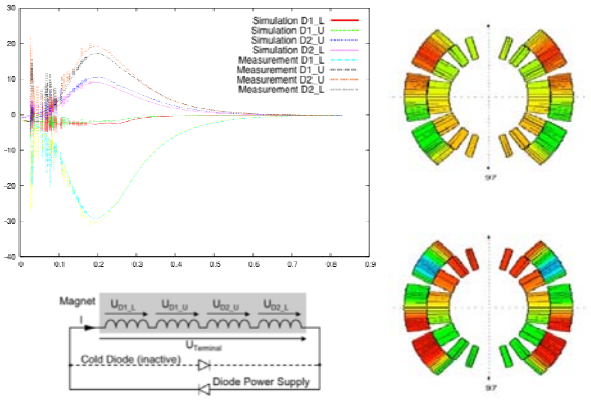

Figure 3: Left: Measured and simulated voltages on the four coils of a LHC main bending magnet on the test bench during a quench. Below: Electric circuit representing the four coils, short-circuited by the power-supply's diode. Right: Electric potentials of conductors in the cross-section at two points in time during a quench.

Fig. 3 shows voltages on the four coils of an LHC main bending on a test bench. We observe spikes in the first third of the measured voltage curves. Interestingly, the spikes are reproduced by simulation [6]. They are explained by the fact that the voltage over all four coils is fixed to the voltage on the diode (compare Fig. 3 bottom). Whenever a conductor quenches, an additional resistive-voltage term emerges in the circuit, which needs to be counter-balanced by a redistribution of inductive voltages in all four coils. We therefore find that the spikes disappear once the whole magnet is quenched.

COMPUTATIONAL CHALLENGES IN 3-D SIMULATIONS

The available RAM on today's workstations limits the accurate 3-D simulation of accelerator magnets. We give two examples and discuss current developments in the computational-electromagnetism community.

3-D Static Simulation

At the request of the CERN AB department, a 3-D electromagnetic model of the PS (proton synchrotron) resistive main magnet should be created. The task was carried out in ANSYS [7], using first-order edge elements and a reduced vector-potential formulation. The PS main magnet is a conventional combined-function magnet, consisting of 10 blocks of C-shaped yokes and a number of different coils for powering and correction. The goal of the exercise was to predict the exact integrated field quality of the magnet for any combination of input currents.

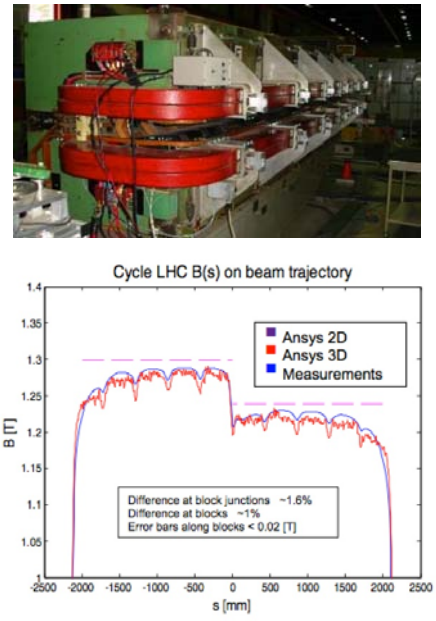

Figure 4: Top: Photo of a PS combined-function magnet. Bottom: Comparison of measured and simulated main field on the beam orbit, [8].

A geometrical model of the yokes and the coils was created with ANSYS workbench and the mesh-density was progressively increased, with a strong bias on the beam tube. By the time the simulation exhausted the ANSYS server's memory, the results were still far from convergence, compare Fig. 4. No reliable field quality could be extracted from the simulated fields.

3-D Transient Simulation

Another example for the limitation of today's field computation algorithms is given by the simulation of eddy currents in the end parts of accelerator magnets. The fast-ramping SIS100 magnets at GSI, Germany, have been the subject of several simulation campaigns on this topic, e.g. [9] [10]. We refer to [11] for the data on convergence and computation time that is presented in Table 1.

The bottom line is that, although a highly-advanced parallelized 2nd order finite-element solver was used, the results only just converge when the memory limit is reached at 4,600,000 degrees of freedom. For field quality simulations in the aperture of the magnet, this accuracy would still not be sufficient.

Table 1: Integrated eddy-current losses over one cycle with simulation times and numbers of degrees of freedom on a 4-processor shared memory workstation.

# Degrees of Freedom	Time [h]	Losses/Cycle [J]
22,000	0.09	54.96
82,000	0.75	45.84
526,000	6.00	30.16
1,537,000	18.75	25.51
3,100,000	40.00	23.98
4,600,000	54.00	23.37

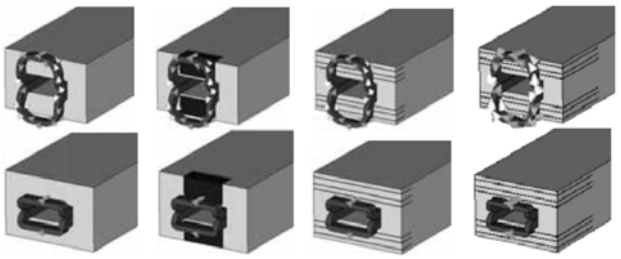

Figure 5: Eight considered magnet-end configurations of the SIS100 magnet, [11]. Picture courtesy of H. de Gersem, S. Koch and T. Weiland.

Numerical Techniques for Future Field Computation Tools

Possible solutions to the above-mentioned memory limitation are given below:

- The coupling method of boundary elements and finite elements (BEM-FEM) needs only to mesh the nonlinear and/or conductive material, i.e., air regions need not be meshed. The number of degrees of freedom is reduced dramatically. The accuracy in the air domain and thus in the magnet aperture is

increased by the use of the boundary element method. The coils are modelled as sets of line-currents in the BEM domain. The drawback of the method is that the boundary-element matrices are fully populated, i.e., they consume large amounts of memory. A remedy this problem lies in compression techniques of the BEM matrices, than can reduce memory consumption to as little as 4% of the initial storage [12].

- The coupling of finite elements and spectral elements is a promising candidate for the simulation of very long magnets. Spectral elements are well suited to represent field distributions that vary only very little over long stretches of a domain. Those end-regions that see important field changes could be modelled with finite elements.
- Whichever method is chosen, distributed computing will be the way to solve memory and runtime limitations in the future. Yet, efficient parallelization of field computation programs is difficult and is mastered today only by a small number of research institutes. It is commonly believed that the commercialization of such tools will take another few years.

COMPUTATIONAL CHALLENGES IN MULTI-PHYSICS SIMULATIONS

Eventually we want to mention the challenges related to complex multi-physics phenomena and their simulation:

- Thermal-electromagnetic coupling: In quench-simulations, an accurate model of the cooling by helium is required. Yet the properties of super-fluid, super-critical, boiling, and fluid helium and the phase transitions are difficult to cast into a reasonably complex model.
- Beam losses: the energy-deposit of beam losses in the superconducting coil depends strongly on the electromagnetic field distribution in the coils. In turn, the beam losses can be taken into account in quench simulations. An interface to, e.g., the FLUKA software [13] is a desirable feature for the ROXIE program.
- Mechanics-electromagnetic coupling: Lorentz forces are a crucial input for the mechanical simulation of a magnet [14]. Yet, the internal stress distribution also affects the material properties in the electromagnetic simulation. In a comprehensive simulation, both ways of interaction needs to be taken into account. To this end, a tight interface between, e.g., ANSYS and ROXIE needs to be established.

CONCLUSIONS

Future accelerator projects will require the simulation of fast-ramping superconducting magnets, as well as high-field magnets and magnets with new materials (other than Nb-Ti). The computational challenges lie in the integration of various dynamic models, the user-friendly input of a multitude of empirical parameters, the simulation of the protection measures in case of a quench, and the accurate 3-D simulation of static and transient problems. Some of these challenge are within reach, others will not be met until several years of research and development. The high degree of specialization in the field of superconducting accelerator magnets requires the creation of specialized, well-integrated models. This can be best done in an integrated development and simulation environment such as the ROXIE program at CERN.

REFERENCES

[1] S. Russenschuck. “Electromagnetic Design and Mathematical Optimization Methods in Magnet Technology.” eBook at http://cern.ch/russ, 3rd edition, February 2006.

[2] O. Biro, K. Preis, and C. Paul. “The use of a reduced vector potential Ar formulation for the calculation of iron induced field errors.” Proceedings of the first international ROXIE user’s meeting and workshop, CERN, Geneva, March 1998.

[3] S. Kurz and S. Russenschuck. “Numerical simulation of superconducting accelerator magnets.” IEEE Transactions on Magnetics, 12(1):1442–1447, March 2002.

[4] B. Auchmann, R. de Maria, and S. Russenschuck. “Calculation of field quality in fast-ramping superconducting magnets.” IEEE Transactions on Applied Superconductivity, accepted for publication, 2007.

[5] N. Schwerg, B. Auchmann, and S. Russenschuck. “Quench simulation in an integrated design environment for superconducting magnets.” IEEE Transactions on Magnetics, submitted for publication, 2007.

[6] N. Schwerg, B. Auchmann, and S. Russenschuck. “Validation of a coupled thermal-electomagnetic quench model for accelerator magnets.” IEEE Transactions on Applied Superconductivity, accepted for publication, 2007.

[7] ANSYS, Inc., http://www.ansys.com

[8] M. Juchno, S. Gilardoni, private communication, 2008.

[9] E. Fischer, R. Kurnyshov, G. Moritz, and P. Shcherbakov, “3-D transient process calculations for fast-cycling superferric accelerator magnets.” IEEE Transactions on Applied Superconductivity, 16(2): 407–410, June 2006.

[10] S. Koch, H. D. Gersem, T. Weiland, E. Fischer, and G. Moritz. “Transient 3D finite element simulations of the SIS100 magnet considering anisotropic, nonlinear material models for the ferromagnetic yoke.” IEEE Transactions on Applied Superconductivity, accepted for publication, 2008.

[11] H. D. Gersem, S. Koch, and T. Weiland. “Magnetodynamic formulation resolving eddy-current effects in the yoke and the superconductive

cable of the FAIR dipole magnets." Proceedings of ICAP 2006, Chamonix, France.

[12] M. Bebendorf. "Approximation of boundary element matrices." Numerische Mathematik, 4:565-589, 2000.

[13] A. Fasso, A. Ferrari, J. Ranft, and P.R. Sala. "FLUKA: a multi-particle transport code", CERN-2005-10 (2005), INFN/TC_05/11, SLAC-R-773

[14] S. Caspi and P. Ferracin. "Toward integrated design and modeling of high field accelerator magnets." IEEE Transactions on Applied Superconductivity, 16(2):1298–1303, June 2006.

SEMI-ANALYTICAL APPROACHES TO MAGNET DESIGN

F. Borgnolutti, P. Fessia, F. Regis, L. Rossi, E. Todesco, CERN, Geneva, Switzerland

Abstract

We summarize the equations that have been derived in the past three years to evaluate the short sample field, stresses and forces, and the magnetic energy in superconducting quadrupoles and dipoles. We present the equations, which are based on simplified sector coils and on empirical corrective factors. The agreement with realistic coil lay-outs and the validity limits of this approach are discussed.

INTRODUCTION

During the conceptual phase of design of an accelerator or of part of it, it can be useful to have equations providing the expected level of field, coil width, stress and stored energy in an accelerator magnet using a given technology. In this paper we summarize the results of several works that have been carried out along this direction in the past years [1-5]. With respect to previous works [6,7] we focus ourselves on a sector coil rather than on a cosθ or cos2θ lay-out.

These equations are usually precise within 10% in a rather wide validity range, and can be used for a fast exploration of different solutions without the need of going for the complete magnet design. A relevant spin-off of these equations is also that they provide a benchmark for judging the efficiency of a coil design.

In the first section we present the usual linear fit for the Nb-Ti critical surface, and a novel hyperbolic fit for the Nb_3Sn that, contrary to the Summer law, allows to derive explicit equations for the short sample quantities. In the second section we derive the short sample field, gradient and current for dipoles and quadrupoles. We then give an estimate of the stress, and finally of the magnetic energy.

CRITICAL SURFACES

Nb-Ti critical surface is usually described by the Fitz-Webb [8] fit

$$j_{sc,c}(B) = C(T,\varepsilon)B^{\alpha-1}\left(1-\frac{B}{B^*_{c2}(T)}\right)^{\beta}. \qquad (1)$$

A linear fit

$$j_{sc,c}(B) = c(b-B), \qquad (2)$$

corresponding to a pinning force parabolic in B, is accurate within a few percent in most of the range which is currently used in superconducting magnets (5 T to 9 T at 4.2 K, 6 T to 12 T at 1.9 K, see Fig. 1). Typical values of the fitting constants are b=10 T at 4.2 K, 13 T at 1.9 K, and c=6×10^8 A/(Tm^2). The linear fit has the advantage of providing explicit solutions to the short sample field and current, which are given by the intersection of the loadline with the critical surface.

Nb_3Sn critical surface is usually described by the Kramer [9] fit

$$j_{sc,c}(B) = \frac{C(T,\varepsilon)}{\sqrt{B}}\left(1-\frac{B}{B^*_{c2}(T,\varepsilon)}\right)^2, \qquad (3)$$

which corresponds to the Fietz-Webb fit with α=0.5 and β=2. An hyperbolic fit

$$j_{sc,c}(B) = c\left(\frac{b}{B}-1\right) \qquad (4)$$

works well (within a few percent) in the interesting region for superconducting accelerator magnets, namely in the range of 8-17 T. see Fig. 1. Typical values of the fitting constants for a high current density conductor carrying 3000 A/mm^2 at 4.2 K and 12 T are b=21 T at 4.2 K, 23 T at 1.9 K, and c=4×10^9 A/m^2. The hyperbolic fit corresponds to a linear pinning force

$$j_{sc,c}(B)B = c(b-B). \qquad (5)$$

Also in this case, the hyperbolic fit has the advantage of providing explicit solutions to the short sample values for current and fields.

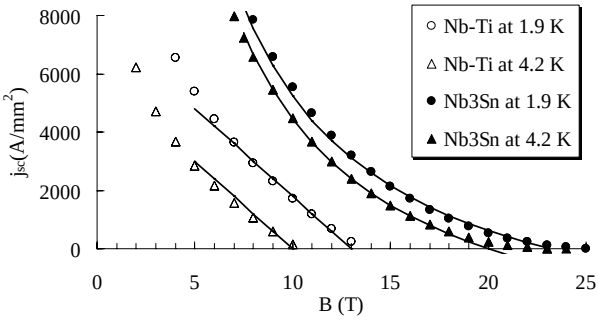

Fig. 1 Critical surface of Nb-Ti and Nb_3Sn according to Fitz-Webb and Kramer fit (markers) and linear and hyperbolic fits (solid lines).

In the following we will use sector coil models, where the coil is made up of insulated cables; therefore we have to rely on the usual definition of engineering current density

$$j_c(B) = \kappa c(b-B) \qquad (6)$$

$$j_c(B) = \kappa c\left(\frac{b}{B}-1\right), \qquad (7)$$

where the filling factor κ takes into account of the dilution of the superconductor present in the insulated coil. This is mainly given by the Cu/non-Cu ratio, plus the voids in the cable, and the contribution of the insulation. The factor κ ranges in between 0.25 to 0.35 in most of the cables used in accelerator magnets.

COIL LAY-OUTS AND EQUIVALENT WIDTH

Throughout the paper, all the equations will be derived for a lay-out based on a simple sector coil, in most cases of 60° angular width for a dipole (30° for a quadrupole). Indeed, the coil lay-outs feature several sectors and possibly several layers, with wedges to optimize field quality (see Fig. 2, left). In order to be able to apply our results to a generic coil made up of blocks and layers, we convert the total surface of the coil A to an equivalent width according to the equation

$$w_{eq} \equiv \left(\sqrt{1 + \frac{3A}{2\pi r^2}} - 1 \right) r , \tag{8}$$

where r is the aperture radius. The equivalent coil width is the width of the coil assuming that all the cables would fill a 60° sector of radial width w_{eq} (30° for a quadrupole), see Fig. 2. All lengths are given in meters.

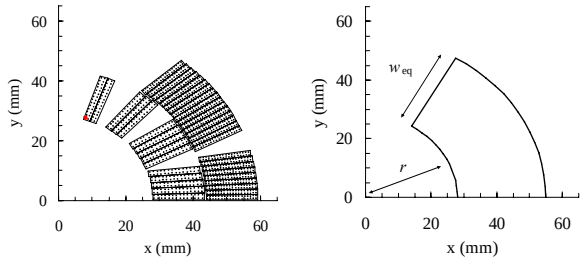

Fig. 2 Coil cross-section of the LHC dipole (one quarter, left side) and equivalent coil with the same area and inner radius (one quarter, right side).

SHORT SAMPLE FIELD AND GRADIENT

Dipoles

According to the approach developed in [1], the short sample field in T for a Nb-Ti dipole is given by

$$B_{ss} \sim j_{ss} \gamma_0 w_{eq} \sim \frac{\kappa c b \gamma_0 w_{eq}}{1 + \kappa c \gamma_0 (w_{eq} + ar)} , \tag{9}$$

where the constants values are γ_0=6.63×10^{-7} Tm/A and a=0.04. The short sample current in A/m^2 is given by

$$j_{ss} \sim \frac{\kappa c b}{1 + \kappa c \gamma_0 (w_{eq} + ar)} . \tag{10}$$

Please remember that all quantities are given in the international system, and in particular current densities in A/m^2 and lengths in m. In the Nb_3Sn case one has

$$B_{ss} \sim j_{ss} \gamma_0 w_{eq} \sim \frac{\kappa c \gamma_0 w_{eq}}{2} \left(\sqrt{\frac{4b}{\kappa c \gamma_0 (w_{eq} + ar)} + 1} - 1 \right) \tag{11}$$

$$j_{ss} \sim \frac{\kappa c}{2} \left(\sqrt{\frac{4b}{\kappa c \gamma_0 (w_{eq} + ar)} + 1} - 1 \right) , \tag{12}$$

where the values of the constant γ_0 and a are the same as for Eq. (9), whereas b and c are the parameters of the Nb_3Sn hyperbolic fit (4).

The above equations rely on an empirical fit of the ratio λ between peak field and central field

$$\lambda = 1 + a \frac{w}{r} , \tag{13}$$

which has been derived for a sector coil. The fitting value a=0.04 implies that for a coil width equal to the aperture radius, the field in the coil is 4% larger than the central field. This estimate is valid for w_{eq}/r>0.15. For very thin coils or very large apertures, giving rise to a relevant difference between peak field in the coil and central field, the estimate is not applicable.

The above estimates are valid for the coil without grading and without iron. Iron has the main effect of allowing to get the same field with a lower current density; this effect can be estimated according to the standard formulas [1]. Moreover, iron has some impact on the short sample field. This effect becomes small (a few percent) for w_{eq}/r>0.5. Graded coil mainly allow to reach the same field with less coil. They also allow a larger short sample; for accelerator magnets a gain of up to 5% has been obtained [1].

Quadrupoles

According to the approach developed in [2], the short sample gradient for a Nb-Ti quadrupole is given by

$$G_{ss} \sim j_{ss} \gamma_0 \ln\left(1 + \frac{w_{eq}}{r}\right) \sim \sim \frac{\kappa c b \gamma_0 \ln\left(1 + \frac{w_{eq}}{r}\right)}{1 + \kappa c r \left(a_{-1} \frac{r}{w_{eq}} + 1 + a_1 \frac{w_{eq}}{r} \right) \gamma_0 \ln\left(1 + \frac{w_{eq}}{r}\right)} \tag{14}$$

where the constants values are γ_0=6.63×10^{-7} Tm/A as for the dipoles, and a_{-1}=0.04 and a_1=0.11. The short sample current in (A/m^2) is given by

$$j_{ss} \sim \frac{\kappa c b}{1 + \kappa c r \left(a_{-1} \frac{r}{w_{eq}} + 1 + a_1 \frac{w_{eq}}{r} \right) \gamma_0 \ln\left(1 + \frac{w_{eq}}{r}\right)} \tag{15}$$

In the Nb_3Sn case one has

$$G_{ss} \sim j_{ss} \gamma_0 \ln\left(1 + \frac{w_{eq}}{r}\right) \sim \sim \frac{\kappa c}{2} \gamma_0 \ln\left(1 + \frac{w_{eq}}{r}\right) \left(\sqrt{\frac{4b}{\left(a_{-1} \frac{r}{w_{eq}} + 1 + a_1 \frac{w_{eq}}{r} \right) \gamma_0 \ln\left(1 + \frac{w_{eq}}{r}\right) r \kappa c} + 1} - 1 \right) \tag{16}$$

$$j_{ss} \sim \frac{\kappa c}{2} \left(\sqrt{\frac{4b}{\left(a_{-1} \frac{r}{w_{eq}} + 1 + a_1 \frac{w_{eq}}{r} \right) \gamma_0 \ln\left(1 + \frac{w_{eq}}{r}\right) r \kappa c} + 1} - 1 \right) \tag{17}$$

where the values of the constant γ_0 and a_1, a_{-1} are the same as for Eq. (14), and b and c are the parameters of the Nb_3Sn hyperbolic fit (4).
The above equations rely on an empirical fit of the ratio λ between peak field and gradient times aperture

$$\lambda = a_{-1}\frac{r}{w} + 1 + a_1\frac{w}{r}, \qquad (18)$$

which has been derived for a sector coil. The fitting value a_1=0.11 and a_{-1}=0.04 implies that for a coil width equal to the aperture radius, the field in the coil is 15% larger than the central field. As in the dipole case, the estimate is valid for w_{eq}/r>0.15. For very large coils w_{eq}/r>1 the sector coil estimate can be pessimist, i.e. one can find other lay-outs where λ does not diverge (see [2] for more details).
The above equations neglect both iron and grading. Analysis of several lay-outs has shown that graded coils can give short sample gradient up to 10% larger than what given in (14) and (16). For the iron influence, one can apply the same considerations made for the dipoles.

FORCES AND STRESSES

Dipoles

According to the approach developed in [3], the stress in the midplane for a dipole made up of a sector coil is estimated by

$$\sigma_\varphi \sim \frac{\sqrt{3}}{6\pi} j^2 \mu_0 \mathrm{Max}_{\rho\in[r,r+w_{eq}]}\left[\frac{3\rho^2(r+w_{eq}) - r^3 - 2\rho^3}{\rho}\right] \qquad (19)$$

where the variable ρ spans over the coil midplane, i.e. from r to $r+w_{eq}$. The expression accounts for the usual part dependent on the square of the current, plus a geometric part which is the argument of the Max function. To get the stress in short sample conditions one has to substitute the expressions (10) for Nb-Ti and (12) for Nb_3Sn. The equation is derived by keeping the first order terms of the expression for a 60° sector coil. In general, coil lay-outs with a relevant difference between the angular width of the first and the second layer feature a larger stress. The equation is derived for a coil without iron and without grading.

Quadrupoles

A similar method has been developed in [4], thus leading to the estimate of the forces in the midplane of a quadrupole

$$\sigma_\varphi \sim \frac{\sqrt{3}}{16\pi} j^2 \mu_0 \mathrm{Max}_{\rho\in[r,r+w_{eq}]}\frac{1}{\rho^2}\left[\rho^4 - r^4 + 4\rho^4 \ln\left(\frac{r+w_{eq}}{\rho}\right)\right] \qquad (20)$$

Also in this case, the variable ρ spans over the coil midplane, i.e. from r to $r+w_{eq}$, and the expression accounts for a part dependent on the square of the current and a geometric part. To get the stress in short sample conditions one has to substitute the expressions (15) for Nb-Ti and (17) for Nb_3Sn. The same considerations given for the dipoles apply to the quadrupole case.

MAGNETIC ENERGY

Quadrupoles

According to [5], the magnetic energy in a quadrupole of aperture radius r and equivalent coil width w, with a current density j is given by

$$U \sim \frac{3\mu_0 j^2}{16} r^4 \left(\left[\left(1+\frac{w_{eq}}{r}\right)^4 - 1\right] - 4\ln\left(1+\frac{w_{eq}}{r}\right)\right) \qquad (21)$$

This expression is independent of the conductor type, which only affects j. The current density at short sample can be computed using the estimates (15) or (17). The equation is derived for an ironless case with no grading. It is based on a Fourier analysis of the current density, keeping the first harmonics, i.e. the $\cos 2\theta$ component. For graded coils one can apply the corrective term

$$\Delta U_{grad} = d\left[\left(1+\frac{A_g}{A}(g-1)\right)^2 - 1\right]U \qquad (22)$$

where g is the grading, i.e. the ratio between the current densities in the two layers, A_g is the area of the graded coil, A the total area of the coil, and d=1.16 is a fitting constant. In presence of unsaturated iron, the energy is enhanced by the following factor

$$\Delta U_{iron} = \left(\frac{r}{r_i}\right)^4 \frac{(1+t)^2\left[(1+t)^4 - 1\right]\ln(1+t)}{\frac{1}{2}\left[(1+t)^4 - 1\right] - 2\ln(1+t)}U \qquad (23)$$

where $t=w_{eq}/r$, and r_i is the iron radius. The equation (21) with the two corrective factors (22) and (23) allow estimating the magnetic energy (and the inductance) with a precision of the order of 10% (calculations done on a set of lay-outs found in the literature, see [7]).

SUMMARY OF PARAMETERS AND CONSTANTS

The set of equations given in the previous sections include constants and parameters. We give a summary of the notations to ease the reader in their implementation.

Magnet parameters: aperture radius r, in meters.

Coil parameters:

- Area A: surface of the coil in m^2.
- Equivalent width w_{eq}, in meters, defined according to Eq. (8) as the width of the coil which has the same area A of a 60° (30° for quadrupoles) sector.
- Graded area A_g: surface of the graded coil in m^2 (only for magnetic energy).
- Iron radius r_i in meters (only for magnetic energy equations).

Cable parameters:

- Filling ratio κ. It is the fraction of non-Cu present in the area of the insulated coil.

- Grading *g*: ratio between current density in the outer and in the inner layer (only for magnetic energy equations).

Superconductor parameters:

- *c*: is related to the slope of the critical surface, $c=6\times10^8$ A/(Tm^2) for the Nb-Ti and $c=4\times10^9$ A/m^2 for the Nb_3Sn. Please note that units are different for the two materials.
- *b*: extrapolation of the critical field, in T, according to the fit, *b*=10 or 13 T at 4.2 or 1.9 K for Nb-Ti, *b*=21 or 23 T at 4.2 or 1.9 K for Nb_3Sn

Constants:

- $\gamma_0=6.63\times10^{-7}$ Tm/A is a constant related to the field given by a sector coil through an integration of Biot-Savart equations
- a, a_{-1}, a_1 are constants used for the empirical fitting of the ratio peak field/central field (or gradient times aperture for quadrupoles). For dipoles a=0.04, for quadrupoles a_1=0.11 and a_{-1}=0.04.
- *d*=1.16 is a constant derived in the empirical fitting to take into account for the effect of grading in magnetic energy (only for magnetic energy equations).
- $\mu_0=4\ \pi\ 10^{-7}$ is the permeability constant.

CONCLUSION

In this paper we summarized equations giving an estimate of the short sample current, field and gradient, midplane stress and magnetic energy in superconducting dipoles and quadrupoles. The equations are based on sector coils and make use of a semi-analytical approach. Empirical fittings are used in some case as well as corrective factors to include grading and iron. The validity limits are outlined.

These equations can be used both for a fast exploration of the parameter space in the phase of a conceptual design, or for benchmarking realistic coil lay-outs based on Rutherford cables.

REFERENCES

[1] L. Rossi, E. Todesco, Phys. Rev. STAB 10 (2007) 112401.
[2] L. Rossi, E. Todesco, Phys. Rev. STAB 9 (2006) 102401.
[3] P. Fessia, F. Regis, E. Todesco, IEEE Trans. Appl. Supercond. 19 (2009) in press.
[4] P. Fessia, F. Regis, E. Todesco, IEEE Trans. Appl. Supercond. 17 (2007) 1269.
[5] F. Borgnolutti, A. Mailfert, E. Todesco, IEEE Trans. Appl. Supercond. (2007) in press.
[6] S. Caspi, P. Ferracin, Particle Accelerator Conference (2005) 107.
[7] S. Caspi, P. Ferracin, S. Gourlay, IEEE Trans. Appl. Supercond. 16 (2006) 354.
[8] W. A. Fietz, W. W. Webb, Phys. Rev. 178 (1969) 657.
[9] E. J. Kramer, J. Appl. Phys. 44 (1973) 1360.

MAGNETIC MEASUREMENT SYSTEMS FOR FUTURE HIGH PERFORMANCE MAGNETS

M. Buzio, R. Beltron, L. Bottura, D. Cote, G. Deferne, O. Dunkel, L. Gaborit,
J. Garcia Perez, D. Giloteaux, L. Walckiers, CERN, Geneva, Switzerland
P. Arpaia, G. Golluccio, V. Inglese, G. Montenero, G. Spiezia, Università del Sannio, Italy

Abstract

This paper describes CERN's current capabilities and plans concerning the measurement of accelerator magnets, focusing on the challenge represented by upcoming projects featuring high-field, high-ramp rate dipoles and quadrupoles. After a brief overview of the existing instrument park we discuss the main future requirements, the issues they raise and the solutions we propose. In particular we describe three ongoing projects based on high-performance digital integrators (FDI), a related C++ software framework (FFMM) and a fast harmonic measurement system (FAME). Finally, we solicit timely input from the magnet community concerning key design parameters and we summarize our conclusions.

INTRODUCTION

As of 2007, magnetic measurement services at CERN are centralized in two work units: one (PH-DT-M1 [1]) is concerned with experimental magnets, while the other (AT-MEI-MM [2]), to which the authors belong, is responsible of all accelerator magnets, i.e., either permanent, resistive or superconducting, excluding only very fast-pulsed kickers (their dynamics fall partially in the RF domain and have traditionally been dealt with by specialists).

Our service has accumulated equipment and know-how from many projects and groups over the whole of CERN's lifetime. As most instruments were originally optimized for a specific application or magnet family, adaptations to new demands are often necessary even if not always practical. While the variety leads to a high maintenance cost, as well as some duplication of functionality and a few inconsistencies among hardware and software platforms, on the whole our park has been proven capable to fulfil very satisfactorily all past and current needs.

Today, at the start of the LHC exploitation phase, we are able to test magnetically all repaired or replacement magnets for any of the accelerators in operation, with the same or better accuracy than the original measurements. In order to improve the performance of the LHC magnetic model (the "FiDeL" project [3]) we are already started work aimed at extending our instruments' capabilities. To cope with the forthcoming high-field, high-performance magnets, however, we must continue in this direction to rebuild the hardware and software foundations of our systems.

CURRENT CAPABILITIES AND LIMITATIONS

Our current capabilities, in terms of what can be measured as a function of the type of magnet, are summarized in Table 1. For each of our instruments, grouped by sensor principle, we list first the typical physical parameters of the compatible magnets (aperture, maximum length, field, ramp rate and temperature), then the quantities that can be measured (field strength, harmonics, axis and direction) and finally the space and time resolution. Bibliographical references are also given where available.

Measurement accuracies are not reported in the table because the end results depend on a variety of additional factors such as field strength, frequency of calibration, accessibility of the volume to be tested, environmental and test conditions. In general, we find that the relative uncertainty of field strength measurements is of the order of a few 10^{-4} for dipoles and about 10^{-3} for quadrupoles; the relative uncertainty of harmonics is about 10^{-5}; the absolute precision of magnetic axis measurements is around 0.1~0.2 mm [11][12]. The main limitations to the accuracy are found to be the bit resolution of the converters, the precision of machined parts and positioning tools, as well as thermal, mechanical and electrical perturbations during calibration and test.

As it can be seen, most devices are designed for (quasi) steady-state conditions, the main limitation being output bandwidth. This is generally due to the combination of different factors such as the mechanical speed of moving parts (e.g. rotating coil, translating stretched wire), the throughput of electronic components (such as the VFC-based digital integrators currently in operation, discussed further on) and the response time of old digital interfaces like RS-232 or VME-MXI. In case of time-varying field, fluxmeter-based instruments (i.e. search coils and stretched wires) are further limited by the total surface area of the coil, which determines the output voltage $V= -\partial\Phi/\partial t$. Standard integrators and voltmeters accept normally inputs up to ±10 V; even if voltage dividers can be implemented, the accuracy of the end result will suffer. A harder constraint comes from the insulation of the coil wire, which is usually very thin and cannot withstand more than a few ~100 V.

Another major limitation is represented by the size of the magnet aperture, most instruments being adapted for typical diameters between 10 and 70 mm. While today we

Table 1: Current magnetic measurement capabilities of the AT-MEI Group. A measurand marked as "±" denotes a potential capability yet to be fully validated developed. "W" and "C" denote respectively room-temperature and cryogenic conditions. Where the field bound limit is marked as *n.a.*, it means that the actual limitation comes from the total magnetic flux rather than the field strength. Note that scanning probes are not limited (within reason) by magnet length, and that certain kinds of fluxmeters such as Stretched Wire systems cannot detect only integral fields.

			magnet parameters						measurand			performance	
									axis		field dir.	resolution	
	System	T	Field [T]	dB/dt [T/s]	L_{MAX} [m]	Gap/Φ [mm]	∫BdL ∫GdL	b_n a_n	magn	mech		time [s]	length [mm]
harmonic coil	15m shaft ("TRU") [4]	W/C	0.01 - 10	0.007	15	40	✓	✓				10	1150
	Shafts for vertical cryostats [5]	W	0.05 - 10	0.007	3	50-70	✓	✓	✓			10	1000
	Industry dipole moles DIMM [6]	W	0.01 - 0.05	*steady-state*	*any (scan)*	50	✓	✓			✓	*steady-state*	200-750
	Industry quad moles QIMM [6]	W	0.01 - 0.05	*steady-state*	*any (scan)*	45-70	✓	✓			✓	*steady-state*	750
	AC mole [7]	W/C	10^{-5}	*steady-state*	*any (scan)*	40-50		±	✓	✓	±	*steady-state*	100-200
	Linac 2 bench	W	0.001-1	*steady-state*	0.2	20-30	✓	✓	✓		✓	*steady-state*	*integral*
fixed coil	Fluxmeter + digital integrator	W	*n.a.*	$f(N_{TURNS}A_{COIL})$	2	> 20	✓	±				10^{-2}	*integral*
	Fluxmeter + digital integrator SPS	W	*n.a.*	2	8	> 20						10^{-2}	*integral*
	Fluxmeter + fast ADC	W	*n.a.*	$f(N_{TURNS}A_{COIL})$	2	> 20						10^{-5}	*integral*
	PS ("Huron") bench	W	*n.a.*	1	1.5	> 20	✓		✓		✓	10^{-2}	30-1000
	Linac 2 bench	W	*n.a.*	300	0.2	20-30	✓	✓	✓		✓	*n.a.*	*integral*
S.W.	Single Stretched Wire [8]	W/C	0.01 - 10	*steady-state*	20	> 10	✓	±	✓		✓	*steady-state*	*integral*
	Double Stretched Wire	W/C	*n.a.*	$f(L_{MAGNET})$	20	> 10	✓					*steady-state*	*integral*
Hall	3-axis Hall probe scanner	W	30	*steady-state*	1.5	> 30	✓	✓				*steady-state*	2
	B3-B5 Hall probe ring [9]	C	10	0.007	*any (scan)*	40		✓				10^{-3}	2
	Polarity checker [10]	W	0.1	*steady-state*	*any (scan)*	50	±					*steady-state*	2

cannot measure at all magnets substantially smaller than that, in case of larger aperture one can always use a smaller coil and extrapolate field harmonics according to the standard power series law; however, errors increase exponentially with harmonic order and this method is unusable when the outer coil diameter is smaller than, typically, $^2/_3$ or the region of interest.

Many other tradeoffs are unavoidable when choosing the best instrument for a given magnet. Longitudinal scanning probes ("moles") are practical and versatile, but cannot be easily moved transversally and take a long time to integrate the field of long magnets. Hall probes provide a fast response, but give only point-like measurements with poor long-term stability. Motors and inclinometers installed in instruments conceived for room-temperature tests of superconducting magnets, where the field is of the order of a few millitesla, are usually not compatible with high fields. In practice, a combination of multiple tests with different instruments and techniques is often necessary to completely characterize a magnet.

Manufacturing capabilities

The measurement of the field of accelerator magnets requires specifically designed instrumentation that, with the exception of point-like NMR and Hall sensor teslameters, cannot be generally found in the commerce. CERN is equipped from the beginning with the tools and the expertise needed to manufacture the specialized components needed, primarily search coils, and to design and assemble complete systems.

Our group today has state-of-the-art facilities for winding a wide range of coils, either toroidal or rectangular, straight or curved, from a few mm to about 2 m long, which may include up to a few thousand turns making use of mono- or multi-filamentary wires (these, in particular, guarantee a very uniform cross-section geometry and a higher accuracy of the results). Different ceramic or composite supports and different kinds of glue can be used according to the conditions of utilisation [13].

The coils are normally sorted for optimal bucking, pre-assembled in arrays or sandwiches and then mounted in the finished instrument. Sophisticated skills in micro-welding and micro-connectors have been developed to ensure reliable operations. At multiple stages of this process mechanical, electrical and magnetic tests are carried out to assess the quality of the product and to obtain harmonic calibration coefficients.

For what concerns the manufacturing of acquisition electronics, our group has a strong expertise in the fields of designing and testing computer-controlled analogue and digital cards compatible with various industry standards. For all but the simplest cases, the actual assembly of the components is carried out by CERN's centralized service or subcontracted (the same philosophy applies to high precision mechanical work).

REQUIREMENTS AND ISSUES

We shall now briefly outline the upcoming requirements in terms of magnet parameters and measurement objectives. We consider the LHC, along

with the four nearest CERN upgrade projects, that is: Linac 4 (construction already started), LHC IR Upgrade Phase I and II and the superferric proposal for PS2. The orders of magnitude of the relative field and geometric parameters are given in Table 2.

Not surprisingly, one can observe a trend towards extreme apertures (consider also a machine like the future CLIC or ILC, with apertures down to few millimetres), higher fields and ramp rates and as a consequence higher eddy current forces, which scale as B·dB/dt and might have consequences for both magnets and probes.

First of all, the move towards high fields will raise the problem of finding adequate measurement references to calibrate the sensors and characterize materials and devices; consider, for example, that the common Metrolab NMR Teslameter PT2025 is limited at 14 T. Moreover, different machines pose specific challenges:

- LHC: history-dependent dynamic superconductor effects such as the decay and snapback of the sextupole, which affects directly the chromaticity, might if uncontrolled destroy the beam. To model and control adequately these effects it is desirable to increase the bandwidth of harmonic measurements from about 0.03 to 3 Hz, and to improve their accuracy from about 0.4 to 0.05 units [14].
- Linac4: this machine includes quadrupoles with an aperture as narrow as 20 mm, both resistive (ramped up in as little as 500 μs) and permanent. The challenge here is represented by the limited size of the coil and the high bandwidth necessary for the integration. In addition, it might become necessary to measure the magnetic axis of all individual permanent quadrupoles after installation in a drift tube module (20~30 magnets over a total length of about 1.5 m).
- LHC IR Upgrades: field integral, harmonics and magnetic axis will have to be measured inside apertures up to about three times larger than installed magnets.
- PS2: in this case, similar to that of all other fast-cycled magnets, a high-resolution measurement of eddy current transients will be paramount to understand and control the dynamics of the field. It is also possible that real-time measurements on a reference magnet in parallel with the machine ("B-train") shall be needed, as is the case today in the PS and in other machines, to stabilize quickly the field at the end of ramp-up.

Main problems

Measurements are certainly facilitated by higher field, higher ramp rates and larger apertures, which allow for bigger probes and result in stronger signals. However, there are also difficulties. Considering in particular harmonic coil systems, in order to maintain a reasonable dynamic range the coil surface cannot be reduced too much; thus, we must modulate either the rotation speed (better accuracy) and/or the amplifier gain (more practical). This problem is exacerbated by the need to increase the rotation speed when high bandwidth is desired (e.g. during ramps or snapback transients). In any case, for all the applications considered the existing integrators are inadequate in terms of both bandwidth and signal resolution.

Table 2 – Order-of-magnitude parameters for some of the future high-performance magnets, compared to a main LHC dipole. The dΦ/dt is referred to the whole aperture, while BdB/dt is calculated where the field peaks.

	L [m]	$\varnothing_{ap}$ [mm]	B [T]	dB/dt [T/s]	dΦ/dt [V]	BdB/dt [T/s]
LHC	14	40-70	9	0.007	0.007	0.06
Linac 4	0.3	20-70	1	700	4.200	700
Phase I	10	110-130	10	0.007	0.009	0.07
Phase II	10	130-150	15	0.007	0.011	0.11
PS2 (SF)	3	70	1.8	2	0.420	3.60

As for the aperture sizes, the figures for Linac4 magnets are quite close to the smallest quadrupole-compensated coils that can be built using current technology. At the other extreme, large coils are undoubtedly easier to build and provide plenty of room to insert, for example, optical targets; however, existing ceramic- or fibreglass-based designs cannot be scaled up for reasons of weight and cost, so new technical solutions must be sought. Finally, let us remark that coils larger than ~100 mm cannot be calibrated in the reference magnets available at CERN and some alternative must be found.

CURRENT AND FUTURE PROJECTS

The issues discussed above are long known and, since about three years, our group has already taken some initiatives to tackle the main problems, especially in view of the demands expected from the LHC. We started from the basic infrastructure of our measurement systems by launching some R&D on new acquisition electronics (integrators) and related software. These activities are well advanced and are already deployed, in prototype form, as the base for a fast magnetic measurement system for main LHC dipoles and quadrupoles. All three projects are described more in detail in the sections below.

Considering future accelerators, the project making fastest progress concerns the measurement of permanent and resistive quadrupoles for Linac4. The existing Linac2 bench is being modified to accommodate new mechanics, harmonic coils (see Fig. 1) and motorization to enable accurate measurements of assembled drift tubes and fast-pulsed magnets in stepwise rotating mode. Integration with the new acquisition electronics and software is under way and we expect to be ready to start measurements upon arrival of the first series magnets in 2009.

Figure 1: Prototype quadrupole-compensated harmonic coil for Linac4 permanent magnets.

As for the next machines, here follows a list of the activities planned:

- LHC IR Upgrades: the main R&D effort will be directed towards large diameter harmonic coils for which suitable materials, geometries and calibration procedures have yet to be identified. As it emerged clearly during recent tests of LARP/CERN Nb_3Sn models, the most urgent need concerns short coil shafts for vertical cryostats in CERN's Bloc4 test station. By 2010, we shall also need long coil shafts, adapted to work at room-temperature inside an anticryostat, to measure series cryoassemblies in SM18 test station. The possible need for adapted short scanning probes, providing the opportunity to carry out local magnetic axis measurements, should also be assessed. It must be stressed that the lead times for some mechanical components (e.g. coil supports, anticryostat tubes) can be quite long and it is very important to know the cold bore geometry in due time for prototyping. In addition, other parameters such as the cable twist pitch length and the position of magnets in a cryoassembly are fundamental to fix the geometry of a coil shaft (coil length and gap between coils must be a multiple of the twist pitch in order to obtain an accurate field integral by canceling out the effect of periodical oscillations).
- Fast-cycled, high-field magnets: the preparation for this class of magnets requires, as a start, testing the compatibility of material and components such as motors, inclinometers and encoders. Moreover, recent eddy current measurements of quadrupoles and octupoles for the PS, with peak dB/dt up to about 60 T/s, have shown that our instrumentation is not completely adequate to detect subtle and rapid transients (below, say, a few 10^{-4} of relative amplitude and ~0.1 ms). More work is needed in this area to ensure better electromagnetic compatibility, finer control of power supplies and elimination of transmission line artifacts.
- "SuperMole": our park currently includes more than 40 scanning probes of 8 different types, based either on search coils or Hall plates, each one optimized for a particular application. To get ready for the next generations of magnets, avoiding at the same time onerous maintenance and training with ever reducing staff, we must streamline this assortment and combine the different functionalities as much as possible. The outline of a modular design is gradually emerging, making use of the techniques that have been proved more accurate and reliable on the field. These include: tangential coil arrays, able to operate in harmonic or stationary (AC) mode; tracking via centrally placed retro-reflectors; high-field compatible piezoelectric motors; additional Hall plates for the measurement of local fields and the disambiguation of polarities.
- Unified magnetic measurement station: to date, our activities for magnet testing and equipment manufacturing and calibration are carried out in six different laboratories scattered all around CERN sites (bldg. 30, 230, 373 (ISR tunnel – I8), 867, 892 (Bloc4), 2173 (SM18)). This situation, which leads to a waste of time and duplication of equipment, will become unsustainable in a few years considering the expected reduction in staff numbers. A proposal concerning a unified laboratory for all room-temperature activities, ideally situated in proximity of the cryogenic test stations for maximum efficiency, is currently being prepared.
- Coil manufacturing and calibration: while the technology to obtain conventional harmonic coils is firmly established, new needs are emerging. In this area we plan to initiate developments along different lines, including: streamlining and automation of existing procedures; investigation of new coil support materials and techniques, such as multi-layer printed circuit coils; improvement of the accuracy of the calibration, e.g. by testing bucked arrays in known multipole magnets; extension of metrology and calibration procedures to new classes of coils, such as large ones or strongly curved ones.

FAST DIGITAL INTEGRATORS

The workhorse of our existing harmonic coil systems is a VME Precision Digital Integrator (PDI) board, having the general function of deriving magnetic flux increments from an induced voltage signal [15]. Several hundred units have been in operation during the two last decades at CERN where, among the rest, they have been instrumental to measure all ~10000 of LHC magnets. However, the current architecture is starting to show its age. The PDI is based on a Voltage-to-Frequency converter working typically at 50 kHz/V, which actually represent a hard limit to the resolution in case of weak signal or short integration times. An additional bottleneck

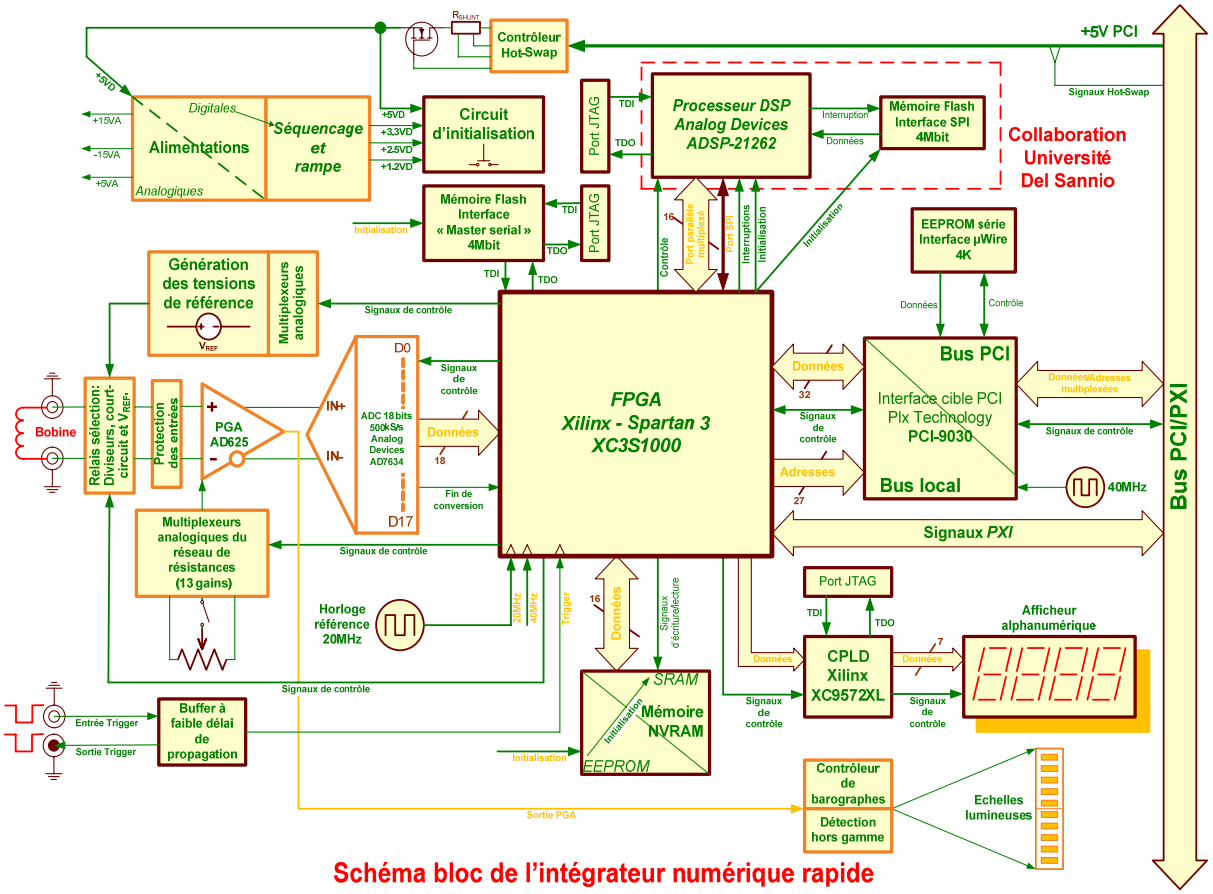

Figure 2: Schematic layout of the PXI Fast Digital Integrator board

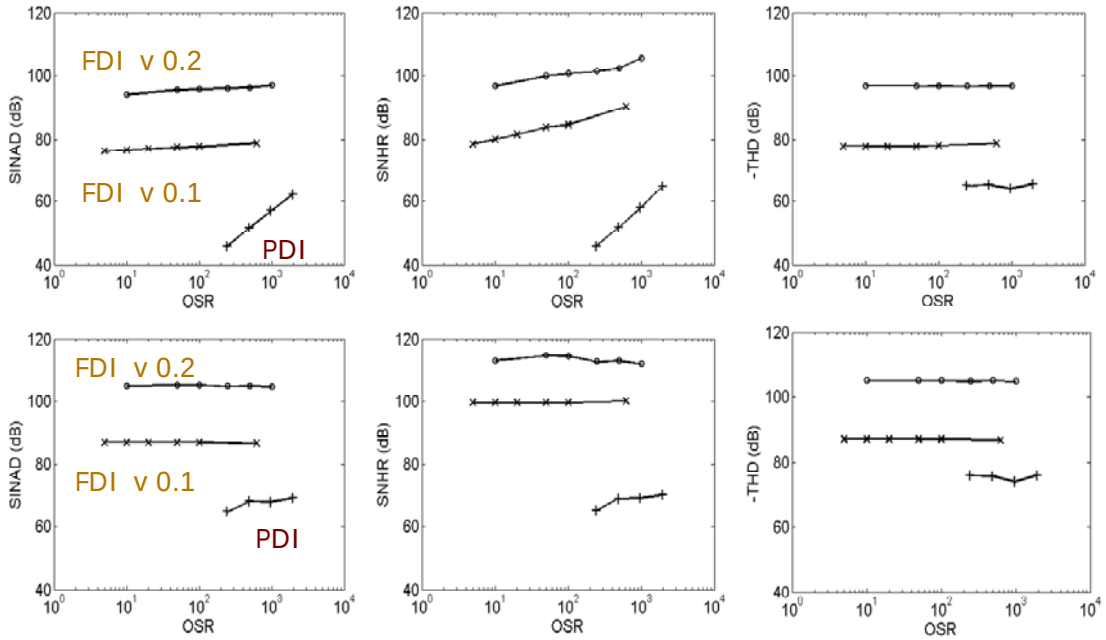

Figure 3: Three different Signal-to-Noise performance metrics to compare the new Fast Digital Integrators against the Precision Digital Integrators as a function of the oversampling ratio. The top row of plots represents the performance as a simple digitizer, while the bottom row as an integrator.

is represented by the VME/MXI interface to the host workstation, which is already strained near its maximum doing standard measurements of LHC cryodipoles with 24 rotating coils in parallel.

For these reasons a new project was started in 2004 to design a new Fast Digital Integrator (FDI) making full use of contemporary electronics and able to cope with future demands in terms of bandwidth and accuracy [16]. The board (whose layout is shown in Fig. 2) is based on the industry-standard PXI architecture and includes an analogue front-end, a fast-switchable, programmable divider/amplifier, a 18-bit, 500 kHz ADC and a DSP carrying out the numerical integration. A reference voltage source with a precision resistor network provides the facility of automatic self-calibration, while an FPGA binds logically the components and drives the external interface. The flexibility of this design is enhanced by the possibility to upgrade the DSP with new integration, filtering, FFT or any other signal processing algorithms. The firmware has been developed in close collaboration with the Università del Sannio, Italy and is tightly integrated with the FFMM C++ framework (see next section).

The performance advantage of the FDI w.r.t. the old PDIs is apparent in Fig. 3, which shows the results of different standard Signal-to-Noise (S/N) tests as a function of the oversampling ratio (i.e. the ratio between ADC sampling rate and integrator trigger rate). As it can be seen the S/N is improved from about 70 dB to more than 110 dB (equivalent to a resolution of 0.5 nVs), which importantly remains constant even at very low oversampling ratios. As a digitizer, as expected, the S/N of the FDI is slightly lower at around 100 dB, however it remains competitive with commercial acquisition boards. The bandwidth of a single card can reach up to 250 kS/s, vs. about 1 kS/s for the PDI, thus enabling an entirely new range of applications (it should be noted that in the current version the bandwidth is limited by the bus interface and therefore is shared between all cards in the same chassis).

To date, a prototype run of a few dozen units is being manufactured and a few FDIs are already employed at CERN for magnetic measurements. The whole project is the object of a Technology Transfer agreement between CERN and Metrolab, Geneva, which will eventually result in the industrial commercialization of the board, including CERN-developed industry-standard LabView drivers. The practical advantage for our group lies obviously in the availability of low-cost hardware and dedicated support. Pending the results from the current testing and validation campaign, a number of hardware, firmware and driver software improvements are already planned:

- DMA-based bus interface to increase aggregated throughput by up to two orders of magnitude.
- Nanosecond-accuracy synchronization of the time-base of the integrators in the same chassis.
- Software-controlled internal generation of triggers, also necessary for the card to function more flexibly in pure ADC mode.
- Generation of reference voltages for self-calibration via a programmable 18-bit DAC, providing more accuracy, flexibility and the additional possibility for the card to work as a signal generator.
- Different compression algorithms to reduce bus traffic and output file size (e.g. adaptive sampling rate modulation for arbitrary signals and FFT-based filtering for harmonic measurements).
- Development of a stand-alone unit with USB connectivity.

FLEXIBLE FRAMEWORK FOR MAGNETIC MEASUREMENTS

Throughout the long LHC design and construction phase most of the software infrastructure at the heart of our instrumentation has been based on a vast collection of LabView modules, developed upon our specification by CERN's Control Systems Group (AB/CO) and utilised in a number of specialised versions of the Magnetic Measurement Program [17]. As such, this complex software solution is not compatible with our new integrator's architecture, and no resources are available to adapt it readily. As a consequence, new software is being developed to control the integrators and solve the general problem of carrying out the measurement, analyse and store the results.

Since we are now in a phase of prototyping new instruments, it is very important to shorten the cycle going from the specification of new functionality to its implementation, testing and debugging. An object-oriented C++ class framework called FFMM (Flexible Framework for Magnetic Measurements) has been chosen as the most efficient solution, and the development has been internalized as of 2005 via a fruitful collaboration accord with the Università del Sannio, Italy [18].

The framework includes at present several dozen classes to drive, besides the integrators, a variety of instruments such as sensors, motors, encoders and power supplies, and the library is foreseen to expand to cover almost the totality of our equipment. At the core of the project is the capability to specify the test logic via a simplified script, containing the necessary magnet and test parameters alongside the sequence of operations to be performed. In perspective, the framework will decouple the definition of the measurement algorithm and all technical parameters, which are in the domain of the test engineer, from the complexities of the underlying C++ machinery. In this way, even non-software specialists shall be able to make full use of the system.

To date, a stable prototype version of the framework is already being used to measure LHC cryodipoles, as described in the next section. A long list of essential improvements is planned for the next three years covered by the collaboration accord. Among these:

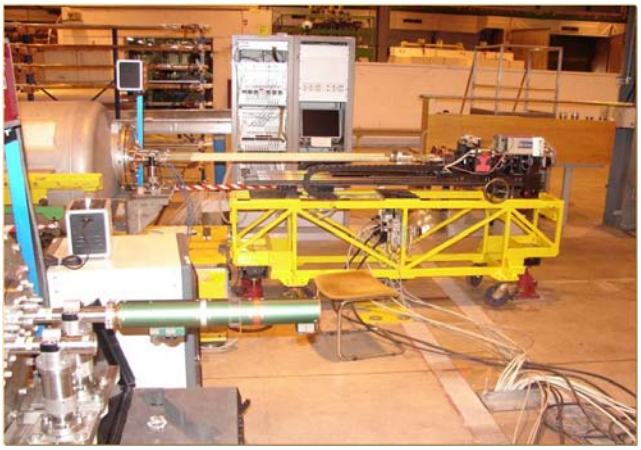

Figure 4: A visual comparison between the Twin Rotating Units, which can be seen in the background while driving two coil shafts inserted in a LHC cryodipoles, and the new Mobile Rotating Unit (in the foreground), directly attached to the anticryostat.

- Close integration with the development of the FDI cards, including specifically in the drivers efficient simultaneous management of large numbers of cards acquiring at full speed.
- Implementation of additional features in the framework, such as data logging, fault detection, debugging facilities and automatic scheduling and synchronization of events and algorithms. The underlying theme is to increase the level of abstraction of the test script w.r.t. C++ programming aspects.
- In the longer term, development of user-friendly graphical interfaces for script programmers and end users.

On a parallel path, the framework is also gradually encompassing different data analysis and post-processing tasks. Most data reduction algorithms are in fact closely related to the procedure followed and to the test conditions, which are inherently known to the acquisition software. From this reason, programming both within the same context can lead to improved consistency and efficiency. Taking also into account that the existing web-based facilities used for the analysis of LHC data are being phased out, we plan the following developments:

- On-line calculation of test results (field strengths, harmonics, statistical indicators etc.) to provide real-time feedback to the test operator and facilitate system diagnostics.
- Off-line data reduction tasks such as the automatic calculation of field harmonics, various types of integrals or feature extraction. Of particular importance (and sophistication) is the detection of invalid or unrealistic measurements and the subsequent recalculation of final results taking into account missing data points.
- Network connection with online repositories (typically CERN-standard Oracle databases) to obtain input test data, such as magnet parameters or harmonic coil geometry data, and to store raw or processed test results.

FAST MEASUREMENT SYSTEM

As recalled above, the exploitation of LHC is likely to require integral measurement of field strength and harmonics in main dipoles and quadrupoles with a higher bandwidth and precision than those obtained during series tests. With this aim in mind, the development of a FAst MEasurement system (FAME) has been launched in 2006 and today the first prototype unit is operation to measure LHC cryodipoles SM18 [19].

The system, which is depicted in Fig. 4, is based on the following components:

- A modified version of the long ceramic coil shafts with 12 dipole-compensated coil sectors (1/6 of the turns of a standard system), better mass balancing and sturdier connectors.
- A novel Mobile Rotating Unit (MRU), including 54-channel slip rings for continuous unidirectional rotation up to 8 Hz. This attaches directly to the anticryostat and replaces the previous bulky Twin Rotating Units [3].
- A patch panel at the output allows one to make arbitrary series connection of the available coils, thus permitting changes in the compensation schemes or combination of several coils in a single "supersector", which can be used to measure the integral saving on the number of integrators.
- A rack of FDI integrators, necessary to cope with the increased bandwidth
- A host PC running the FFMM software to control the hardware and perform the acquisition.

It must be noted that the convenience of the MRU comes at the price of fixing rigidly the longitudinal position of the coils, which usually should be symmetrical w.r.t. magnet end fields; moving the coils at a new position requires the insertion of apposite spacers.

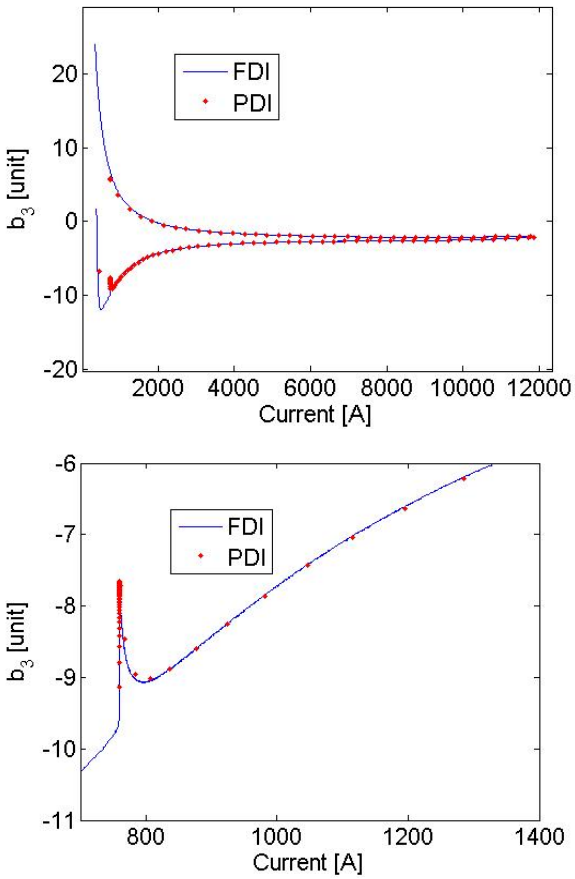

Figure 5: Two consecutive hysteresis curves of the normal sextupole in MBA 2551 taken with old and new integrators at the center of the dipole. The expanded view of the decay and snapback phase (bottom graph) gives an indication of the improvement of the precision that can be attained.

At present, the existing prototype system is being metrologically characterized and the results obtained on spare LHC main dipoles are being compared to those issued from the old acquisition system. As an example, in Fig. 5 we can consider the hysteresis curve of the sextupole component measured at the centre of a dipole, obtained during two consecutive LHC cycles with the two systems. The improvement in the precision of the measurement is striking.

Our plans for the further development of the FAME system cover the following points:

- Finalization of the design of the MRUs and of the spacers (needed for longitudinal centering on the corrector magnets installed in different cryoassemblies).
- Production of one more system for dipole and one for quadrupole cryoassemblies, in prevision of further tests for LHC in the framework of FiDeL activities (tracking tests, investigation of new machine cycles, characterization of poorly-known magnet types).
- Further development of control and analysis software, including more robust and user-friendly operation, as well as improved data reduction algorithms (e.g. more accurate harmonic analysis when the field is changing, if necessary with high-speed progressive update during coil rotation).
- Adaptation of the MRUs to other test benches, namely vertical cryostats for short models and upcoming large diameter coil system.

CONCLUSIONS

CERN historical experience shows that targeting measurement systems at individual magnet classes, as it was possible when adequate resources were available, produces optimized results but may lead to subsequent waste and difficulties. Today, we are in a position to compact and rationalize the existing instrument park and, at the same time, plan to meet future requirements. By pursuing the lines of development discussed above, we believe that it shall be possible to get equipped to respond efficiently to all these challenges.

To reach this goal, we would like to call attention to the importance of receiving in due time certain key bits of information, taking into account the delays associated with the subcontracting of critical components (primarily high precision mechanics, but, recently, also some electronic parts due to the global industry changeover to lead-free technologies).

In particular:

- The size of the magnet bore, if outside the popular 40-70 mm range, is the most urgent parameter to be known (long lead times for harmonic coil shafts and anticryostats).
- The cable twist pitch and the longitudinal position of magnets are also very important in the case of long coil shafts for cryoassemblies.
- Other parameters driving instrument design include the ranges of *B* and *dB/dt*, length and radius of curvature of the magnet, shape and size of the good field region, nature and position of optical or mechanical references.
- Realistic accuracy requirements from beam optics are also welcome.

To conclude, let us recall our need for appropriate high-performance magnets to be used to qualify materials and components, calibrate coils and cross-check instruments. Such magnets, perhaps, could be included in the planning for the construction of models and prototypes for future machines.

REFERENCES

[1] http://ph-dep-dt.web.cern.ch/ph-dep-dt
[2] http://at-dep-mei.web.cern.ch/at-dep-mei
[3] M. Di Castro, D. Sernelius, L. Bottura, L. Deniau, N. Sammut, S. Sanfilippo, W. Venturini Delsolaro, “Parametric field modelling for the LHC main magnets in operating conditions”, PAC 2007,

Albuquerque, NM, 25-29 June 2007, p. 1586-1588 (2007)

[4] J. Billan, L. Bottura, M. Buzio, G. D'Angelo, G. Deferne, O. Dunkel, P. Legrand, A. Rijllart, A. Siemko, P. Sievers, S. Schloss, L. Walckiers, "Twin rotating coils for cold magnetic measurements of 15 m long LHCdipoles", IEEE Trans. Appl. Supercond., Vol. 10, Mar. 2000, pp. 1422-1426

[5] J. Billan, C.R. Gregory, P. Legrand, L. Oberli, A.P. Verweij, L. Walckiers, "Test of 1 m long model magnets for LHC", IEEE Transactions on Magnetics, Vol. 28, Jan. 1992, pp. 362-365

[6] J.G. Perez, J.Billan, M. Buzio; P. Galbraith, D. Giloteaux, V. Remondino, "Performance of the Room Temperature Systems for Magnetic Field Measurements of the LHC Superconducting Magnets", IEEE Transactions on Applied Superconductivity, Volume 16, Issue 2, June 2006 Page(s): 269 – 272

[7] M. Buzio, P. Galbraith, J. Garcia Perez , E. Laface, S. Pauletta, "A Device to Measure Magnetic and Mechanical Axis of Superconducting Magnets for the Large Hadron Collider at CERN", Proceedings of the IEEE Instrumentation and Measurement Technology Conference, Sorrento, Italy, 2006.

[8] J. Di Marco *et al.*, "Field alignment of quadrupole magnets for the LHC interaction regions", IEEE Trans. Appl. Supercond, vol. 10, Jan. 2000, pp.127-130

[9] N.J. Sammut, E. Benedico-Mora, L. Bottura, P. Galbraith, D. Giloteaux, G. Greco, M. Haverkamp, M. Marchesotti, A. Masi, J. Micallef, T. Pieloni, N. Smirnov, A. Tikhov, "A Hall Plate Based Instrument to Measure the Snapback in the Large Hadron Collider Superconducting Dipole Magnets", Proceedings of the IEEE Instrumentation and Measurement Technology Conference IMTC 2006, 24-27 Apr 2006, pp. 61-66.

[10] M. Buzio, L. Bottura, G. Brun, G. Fievez, P. Galbraith, J. Garcia Perez, R. Lopez, A. Masi, S. Russenschuck, N. Smirnov, A. Tikhov, L. Walckiers, "Checking the Polarity of Superconducting Multipole LHC Magnets", IEEE Transactions on Applied Superconductivity, June 2006, Volume: 16, Issue: 2, pp. 1391- 1394

[11] L. Walckiers, L. Bottura, M. Buzio, P. Schnizer, N. Smirnov, "Sensitivity and accuracy of the systems for the magnetic measurements of the LHC magnets at CERN", Proceedings of EPAC 2000, Vienna, 26-30 June 2000, pp 2184-2187 (2000)

[12] L. Bottura, M. Buzio, S. Pauletta, N. Smirnov, "Measurement of magnetic axis in accelerator magnets: critical comparison of methods and instruments", Proceedings of the IEEE Instrumentation and Measurement Technology Conference IMTC 2006, pp. 765-770 (2006)

[13] O. Dunkel *et al.*, "Magnetic Calibration System for Rotating-Coil-Based Measurement Instrumentation at CERN", Proceedings of the International Workshop on Magnetic Measurments IMMW 15, Fermilab, Batavia, IL, 21-24 Aug. 2007

[14] L. Bottura, "RMS status report", LTC meeting, 23 June 2004

[15] http://www.metrolab.com/index.php?id=24#par104

[16] P. Arpaia, L. Bottura, P. Cimmino, D. Giloteaux, A. Masi, J. Garcia Perez, G. Spiezia, L. Walckiers, "A Fast Digital Integrator for Magnetic Field Measurements at Cern", Proceedings of the IEEE Instrumentation and Measurement Technology Conference IMTC 2006, 24-27 April 2006, pp. 67-71

[17] H. Reymond, "Experience with configurable acquisition software", Proceedings of the 14th International Magnetic Measurement Workshop, CERN, Geneva, 26-29 Sept. 2005

[18] P. Arpaia, M. L. Bernardi, L. Bottura, M. Buzio, L. Deniau, G. Di Lucca, V. Inglese, J. Garcia Perez, G. Spiezia, L. Walckiers,, "Kernel Design of a Flexible Software Framework for Magnetic Measurements at CERN", IEEE Instrumentation and Measurement Technology Conference Proceedings IMTC 2008, 12-15 May 2008, pp. 607-611

[19] L. Bottura, N. Brooks, M. Buzio, D. Cote, O. Dunkel, P. Galbraith, D. Giloteaux, J. García Perez, A. Masi, "Fast Magnetic Measurement Equipment", 15th International Magnetic Measurement Workshop, Fermilab, Batavia, IL, August 21-24, 2007

COLD TESTING OF RAPIDLY-CYCLING MODEL MAGNETS FOR SIS 100 AND SIS 300 – METHODS AND RESULTS*

A. Stafiniak#, C. Schroeder, E. Floch, P. Schnizer, H. Mueller, E. Fischer, G. Moritz, F. Marzouki, F. Walter, M. Kauschke, J. Kaugerts, GSI ,64291 Darmstadt, Germany

Abstract

The two synchrotrons SIS 100 and SIS 300 of the FAIR project are equipped with rapidly-cycling superconducting magnets. For quality assurance of SC magnet the Prototype Test Facility at GSI was commissioned. It allows measuring all relevant parameters of the rapidly-cycling magnets: hydraulic resistance, cryogenic losses (V-I and cryogenic method), quench behaviour and field quality.

A SIS 300 (GSI001) model dipole of the cos(θ)– type, cooled with supercritical helium, constructed at BNL, a SIS 100 superferric model dipole (4KDP6a), cooled with 2-phase helium, constructed at JINR (Dubna), were tested.

INTRODUCTION

Within an international collaboration it is planned on the GSI site to construct a new accelerator complex FAIR, which will provide high intensity primary and secondary beams of ions and antiprotons for different experiments. It will consist of 2 synchrotrons in one tunnel, SIS100 (100 Tm rigidity) and SIS300 (300 Tm rigidity), and several storage rings. The SIS100 will accelerate ions and protons at a high repetition rate and either send them to the targets for Radioactive Ion Beam (RIB) or Antiproton Beam production or to the SIS300 for further acceleration to higher energies. The Collector Ring (CR)/ Recycled Experimental Storage Ring (RESR) complex will cool the secondary beams and accumulate the antiprotons. High Energy Storage Ring (HESR) and New Experimental Storage Ring (NESR) are the experimental storage rings for antiprotons and ions, respectively [1]. Fig. 1 gives an overview of the facility.

GSI PROTOTYPE TEST FACILITY

The first planning of Prototype Test Facility (PTF) takes place in 2001. Since 2006 the test facility is in operation. The first model of SC magnet was installed and tested in September 2006. The Mandate of the PTF is:

- Test FAIR Model, Prototype and Preseries of SC magnets
- Develop Test Procedures for Factory Acceptance Tests (FAT) and Site Acceptance Tests (SAT)
- Develop Acceptance Criteria for FAT and SAT
- Develop Diagnostic Methods
- Investigate "non conforming" magnets

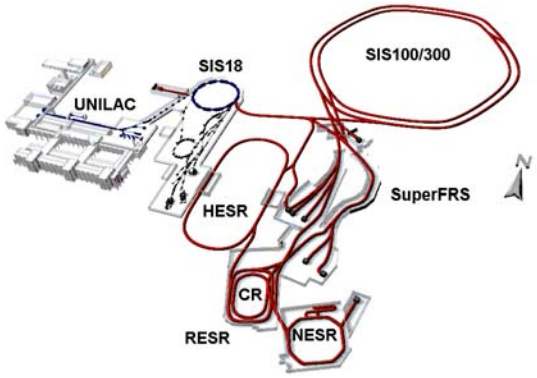

Figure 1: Overview of FAIR facility.

General Layout of Prototype Test Facility

Fig. 2. shows a schematic sketch of PTF. The PTF is equipped with a cryo-pant Linde TCF50. It has a cooling capacity of about 350W at 4.5K. The distribution box, allows using one of 3 different cooling schemes:

- bath cooling
- 2 phase flow cooling up to 5g/s
- supercritical cooling up to 200g/s

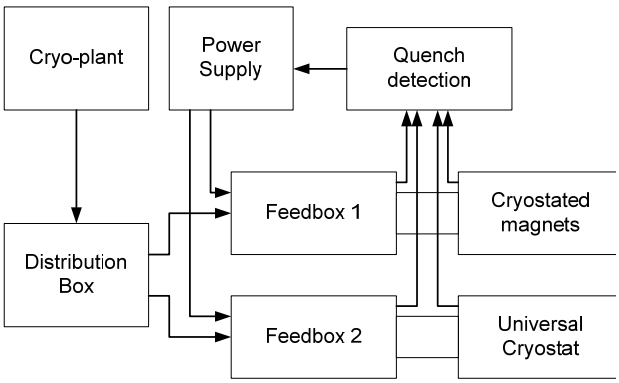

Figure 2: General layout of Prototype Test Facility.

One can vary the magnet inlet temperature down to 3.9K and the inlet pressure from 1.3bar to 5 bar. The power supply has a maximum current of 11kA (100V). The Feedboxes supply the magnets with helium and electrical current. Standard current leads (optimized for 6.5kA working up to 11kA) are made from cooper and are cooled by helium vapour.

*Work supported by EU FP6 - Design Study (contract 515873 – DIRACsecondary-Beams)
#a.stafiniak@gsi.de

The Feedboxes contains the "standard instrumentation" for:

- mass flow (warm and cold)
- temperatures
- pressures

These measured properties are used to calculate the cryogenic heat loss of a magnet.

Feedbox 1 is foreseen to test magnets with its own cryostat. At Feedbox 2 we have a universal cyostat, which allows testing only the cold mass of a magnet or other devices [2].

Quench Detection and Magnet Protection

Although most single magnets (except SIS300 dipole and quadrupole) are self-protecting, a protection system allows minimizing the recovery time (necessary for cool down) after a quench occurred due to the possibility of energy extraction. The voltage taps are isolated wires soldered to the magnet cable. Voltage differences between two symmetric coil parts of the magnet are measured. In addition an unbalanced current through a centre tap is measured. The scheme of functionality is shown in Fig.3. The main components are the separated voltage detection, the security matrix for safety actions and a data acquisition system for storage. The security matrix triggers the following safety actions:

- switch off the power converter which will switch a dump resistor into the coil circuit for energy extraction
- open the active quench valve in the feedbox
- activate the quench heaters for magnets (if applicable)

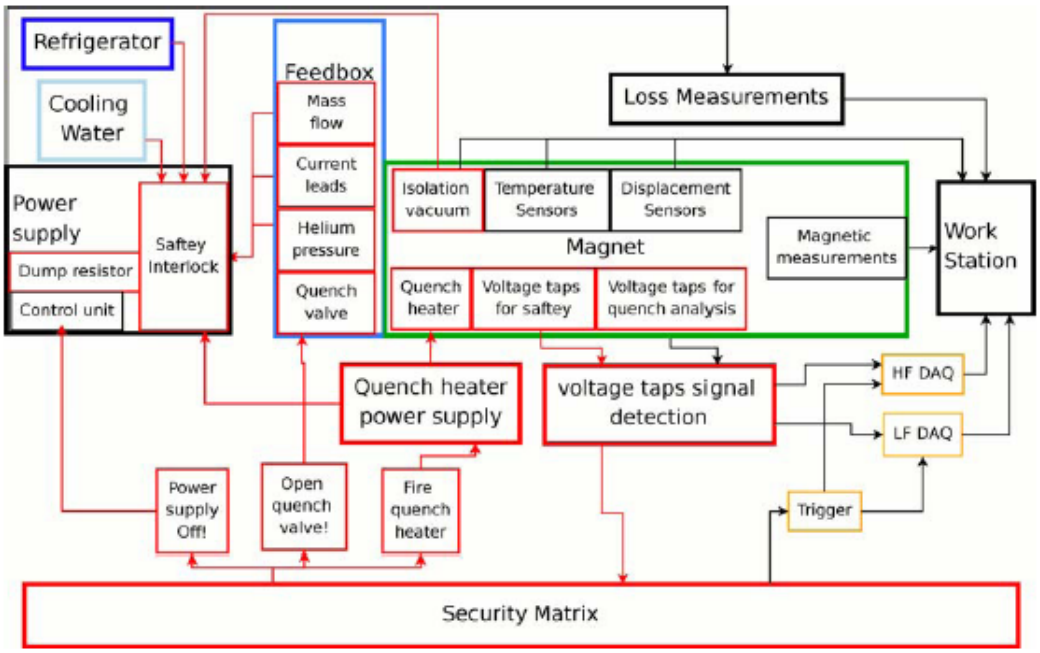

Figure 3: Scheme of the functionality of the test facility for superconducting magnets The blue parts show cooling sources. Security related devices and communication channels are given in red. Arrows show the flow of various signals. On the left the cryogenic supply, cooling water and electrical power supply are shown. The power supply provides a safety interlock, a dump resistor and its control unit. The isolation vacuum of the cryostat is monitored. The magnet is equipped with temperature sensors and displacement sensors. Voltage taps allow supervising the voltage drop on the magnet coils. Dedicated electronics treat the signal of these taps and generates triggers in case a quench has occurred (security matrix)

MEASUREMENT PRINCIPLES AND METHODS

Cryogenic losses – calorimetric method for supercritical cooling magnets (SIS300-type)

By measuring the inlet and outlet temperatures and pressures one can calculate the enthalpy difference.

The mass flow in this setup is measured directly by Coriolis sensors. Two sensors are measuring the mass flow of the current lead cooling and the mass flow at the exit of the shield at warm. One Coriolis sensor (two are shown for two different metering ranges) is measuring the total inlet mass flow at cold. Based on this measurement one can calculate the mass flow through the magnet. By knowing the magnet mass flow one can calculate the heat loss with:

$$Q_{magnet} = \dot{m}_{He} \cdot \left[h_{out}\left(T_{out}, P_{out}\right) - h_{in}\left(T_{in}, P_{in}\right) \right]$$

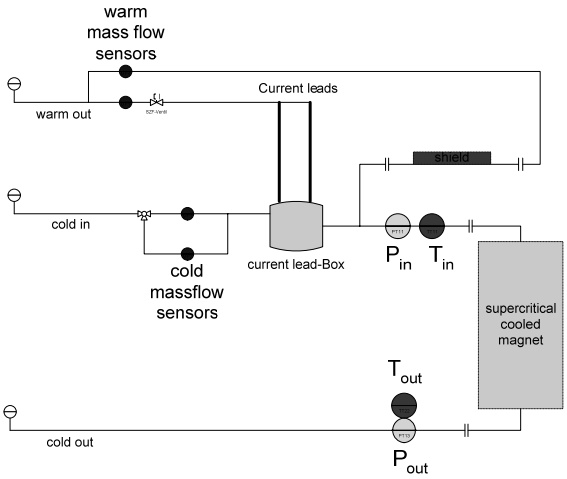

Figure 4: Cryogenic measurement of supercritical cooled magnets.

Cryogenic losses – calorimetric method for 2 phase flow cooled magnets (SIS100-type)

In this setup it's possible to measure separately the heat introduced into the coil and into the yoke. For that one varies the mass flow in order to find the mass flow at which one gets exactly 100% gas (X=1) at the coil outlet. For the coil inlet it always a pure liquid (X=0). Assuming that the total pressure drop only occurs in the coil the heat introduced is calculated by:

$$Q_{coil} = \dot{m}_{He} \cdot \left(h_{vapor}\left(x = 1, P_{out}\right) - h_{liquid}\left(x = 0, P_{in}\right) \right)$$

$$Q_{yoke} = \dot{m}_{He} \cdot \left(h_{out}\left(T_{out}, P_{out}\right) - h_{CY}\left(T_{CY}, P_{out}\right) \right)$$

The mass flow is measured by an additional overheating of the gas in the outlet line. Measuring the heater power and the temperatures before and after the heater the mass flow is given by:

$$\dot{m}_{He} = \frac{Q_{superheating}}{h_{heater\_out}\left(T_{heater\_out}, P_{out}\right) - h_{heater\_in}\left(T_{heater\_in}, P_{out}\right)}$$

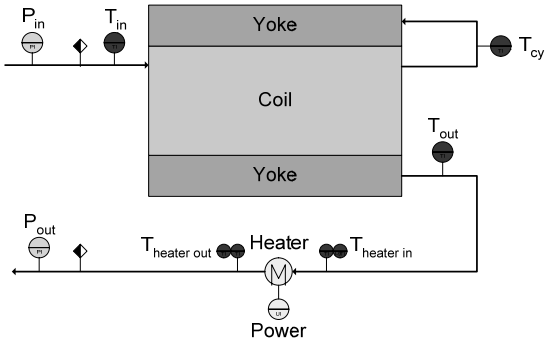

Figure 5: Cryogenic measurement of 2 phase flow cooled magnets.

Cryogenic losses – V-I method

The schematic setup of the V-I method is shown in Fig. 6. The DVM's are high accuracy digital multimeters HP 3458 A.

The current (Current DVM) is measured as indicated by the output voltage of a Zero-Flux Current Transformer (DCCT). The voltage (Voltage DVM) is measured across the magnet. The output trigger signal from Current DVM is used to trigger the Voltage DVM. The integration time of the DVMs is 20ms and the processing time (delay) between the measurements is 50µs. The power loss is calculated as the sum of the products of current and voltage over the current cycle.

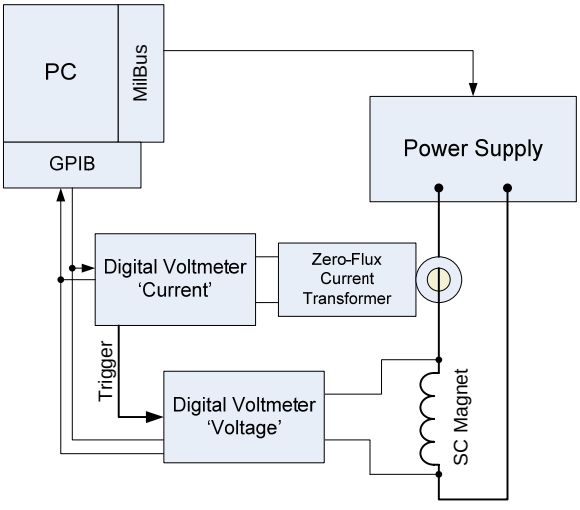

Figure 6: Set-up for losses measurement - V-I method.

The energy loss is calculated by:

$$E = \sum_{i=1}^{N} V_i \cdot I_i \cdot \Delta t_i$$

The power loss is calculated by:

$$P = \frac{1}{\sum_{i=1}^{N} \Delta t_i} E$$

with : Δti = 20.05ms , N – corresponds to 1 current cycle.

This method has several limitations. The most important are: voltage offset, measurement accuracy, measurement resolution and DVM triggering [3].

Cold Magnetic Measurements

Cold magnetic measurements are performed with the magnet at operating (cryogenic) temperatures while the measuring equipment is working at room temperature. Anti-cryostats are inserted in the magnets, wherein the measurement equipment is placed. A non-metallic anti-cryostat was fabricated to avoid additional eddy current losses in fast-ramped magnets, which can significantly distort the magnetic field quality and thus its measurement [4, 5, 6].

A "Mole" based approach was selected for measuring the superconducting magnets. A mole is a rotating coil probe based magnetometer, where the main auxiliary components (the motor, the inclinometer and the angular encoder) form an entity able to operate in high magnetic field [6].

TESTS RESULTS OF SUPERCONDUCTING MAGNETS

GSI001

GSI001 has the same coil cross section than RHIC magnets with 32 turns and 4 blocks. A phenolic spacer is placed between the coil and the iron yoke of the RHIC magnets whereas for GSI001 the coil is hold by stainless steel collars. For loss reduction a stainless steel core was inserted into the RHIC cable and the wire twist pitch was reduced. The Parameters of the GSI001 dipole are given in Table 1; a cross section of the magnet is shown in Fig. 7. The training curve of GSI001 is presented in [2].

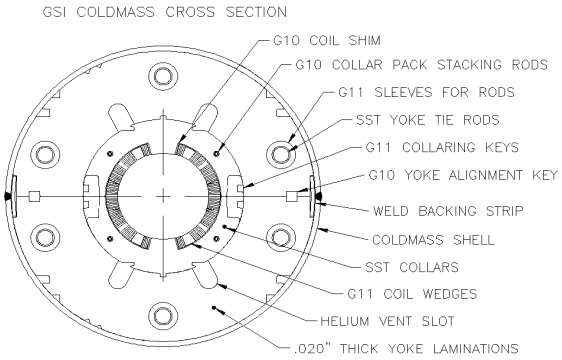

Figure 7: Cross section of GSI001 dipole

Table 1: Characteristics of the GSI001 dipole

GSI 001 characteristics	
magnet length (m)	1
I (A)	6000
Bcentral (T)	3.5
coil bore diameter (mm)	80
number of blocks	4
number of turns per pole	32
between coil and iron yoke	stainless steel collar
measured inductance (mH)	2.8
rl293K (mΩ/m)	2.551
R_2_poles_293K (Ohm)	0.394
cable length = R_2_poles_293K/ rl293K (m)	154.51
Bmax on cable / Bcentral (computed by BNL)	1.22
number of strands	30
core	2 stainless strips of 25 μm thickness each
strand diameter (mm)	0.641
α	2.21
twist pitch (mm)	4
filament diameter (μm)	6
RRR	187
R_a (μΩ)	64
R_c (mΩ)	62.5
ρ_{et} (Ωm)	1.24×10^{-10} + 0.9×10^{-10} B(T)

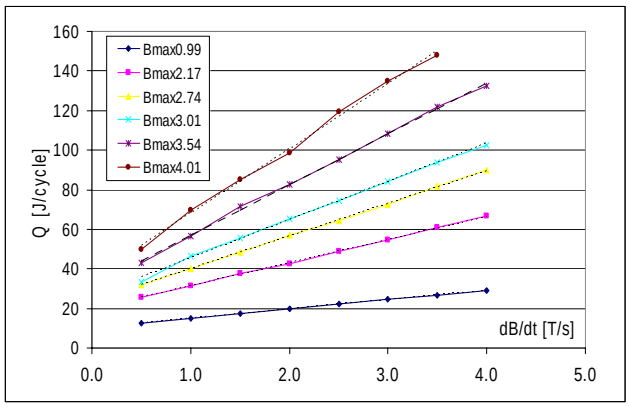

Figure 8: AC losses of GSI001 V-I method (with beam pipe), measured at GSI.

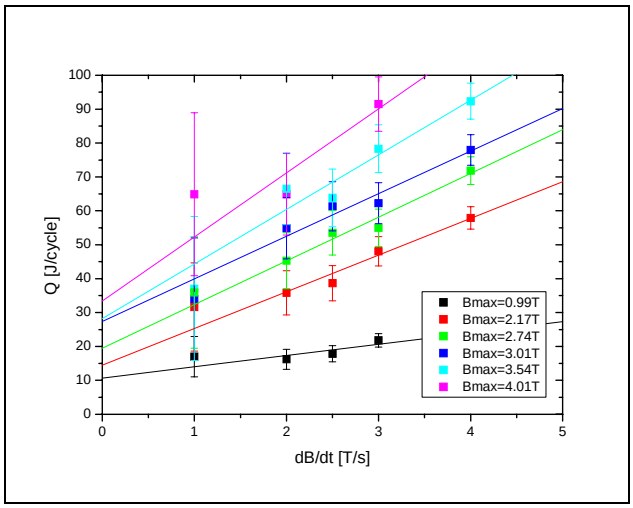

Figure 9: AC losses of GSI001 calorimetric method (with beam pipe taken at GSI).

Loss measurements have been performed electrically by BNL [7, 8] and GSI and calorimetrically by GSI alone. The results of the measurements at GSI are shown in Fig. 8 and Fig. 9 for the electrical and calorimetric methods, respectively. The results of the measurements can be split in a hysteresis part, originating from the iron hysteresis and the persistent currents in the superconductor, and an eddy current part, originating from interstrand and interfilament coupling currents in the superconductor, as well as eddy currents created in the beam tube. The contribution of the eddy currents and the hysteresis are presented in Fig. 10 and Fig 11. Calculations of the losses were performed assuming that the heat load depends linearly on the ramp rate [9]. A good agreement was found between theory and all the measurements for the hysteresis part. Concerning the eddy currents the theoretical calculations agree well with the calorimetric measurements. For the electrical measurements an enhancement of the losses can be found for magnetic fields higher than 2T. As magnetic flux leaks out from the yoke for field levels above this level, this can be explained by the presence of a thermal shield made of Cu in the cryostat used at GSI, as eddy currents are then induced into it.

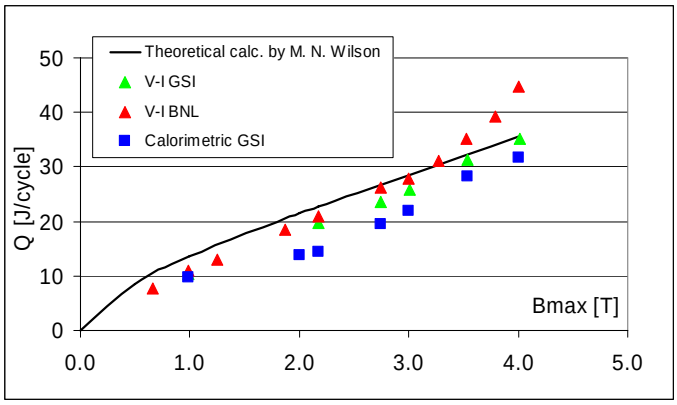

Figure 10: Hysteresis losses of GSI001 (with beam pipe)

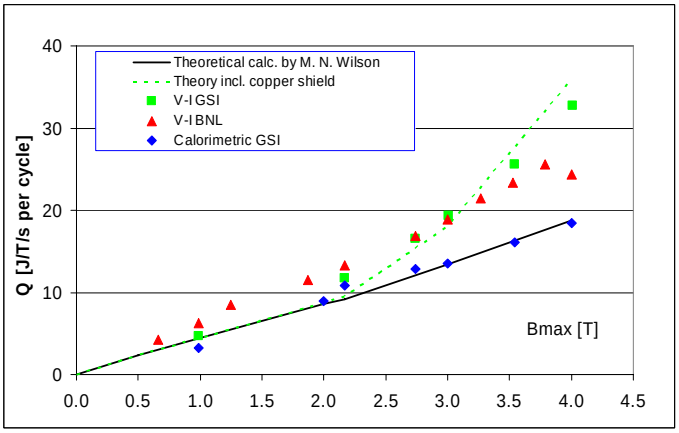

Figure 11: Eddy current losses of GSI001 (with beam pipe).

V-I loss measurements were also performed for the upper and lower half coil itself. The eddy current part of these measurements is shown in Fig. 12 together with fitting lines using the adjacent interstrand resistance Ra as a free parameter. The results seem to indicate a top-bottom asymmetry of the magnet, but this still needs further investigation.

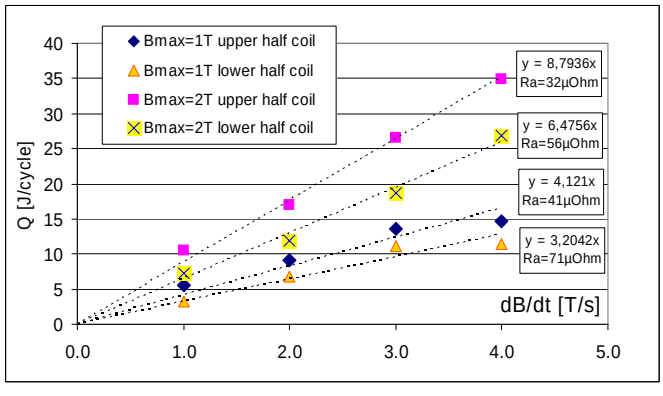

Figure 12: Top-down asymmetry of GSI 001 coil.

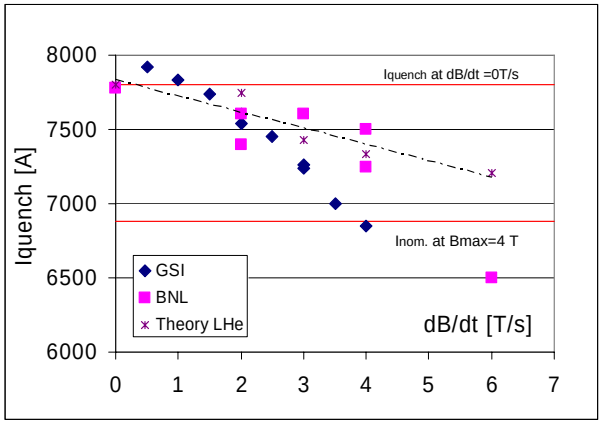

Figure 13: GSI 001 Ramp Rate Limitation. The upper red line gives the value of the DC quench current the lower red line represents the nominal operating current of the magnet.

Fig. 13 shows the measured quench current I_q as a function of the ramp rate dB/dt. The measurements at GSI were carried out in supercritical helium whereas BNL used a helium bath. As expected the cooling is more effective in the case of liquid helium. The observed curves show that the ramp rate limitation is due to AC-heating of the conductor [8, 9]

4KDP6a

The first SIS100 dipole prototype (called 4KDP6a), was tested at GSI. This magnet was manufactured in Dubna and is an upgraded version of Nuclotron magnets.

Fig. 14 presents the cable used in 4KDP6a. It is made of a CuNi tube in which the He flows and around which 31 strands (0.5 mm in diameter) are wound. One NiCr wire is used to fix the strands around the tube. The insulation is made of polyimide and impregnated fibre glass. The strand average copper ratio is 1.24 with and a RRR of 196.

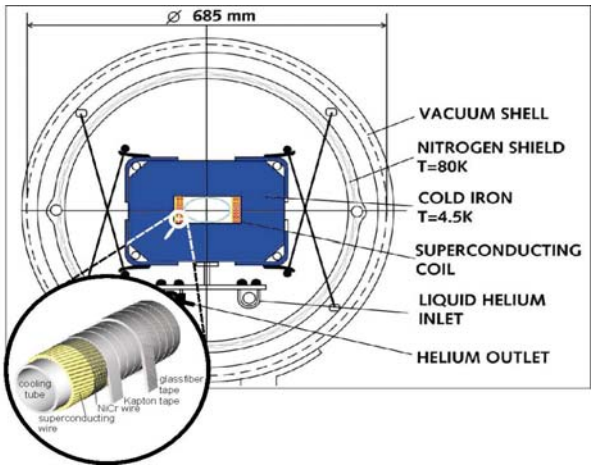

Figure 14: Cross section of 4KDP6a dipole.

Figure 15: 4KDP6a dipole (connection side).

Table 1: Characteristics of 4KDP6a dipole

4KDP6a characteristics	
iron+end plates length (m)	1.37
I (A)	5936
Bgap (T)	2
Bmax (T)	2.11
yoke gap size (mm*mm)	h=146* v=56.4
number of turns per pole	8
coil length (m)	1.475
measured inductance (mH)	1
number of strands	31
strand diameter (mm)	0.5
α	1.24
filament diameter (μm)	6
RRR	196
Tcs - 4.7 K (K)	1.53

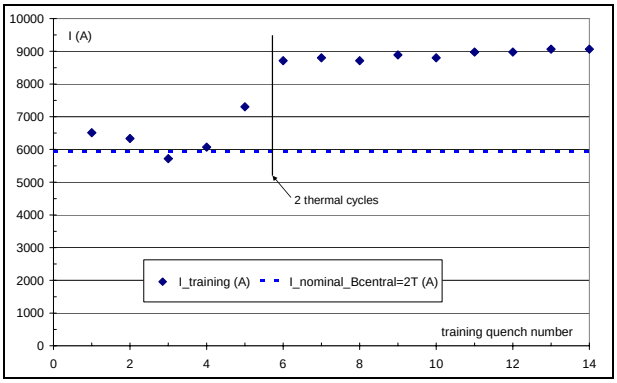

Figure 16: Training of 4KDP6a dipole (2 thermal cycles).

Fig. 16 presents the magnet training that was done in 2 steps separated by a thermal cycle. A more detailed analysis will be presented at ASC 2008 [10]

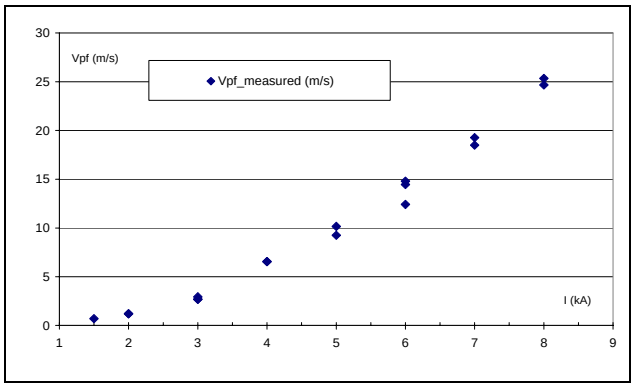

Figure 17: Quench propagation velocity in the 4KDP6a bus bars.

Because the coil is wrapped with impregnated fibre glass, it is very difficult to insert a spot heater inside the coil to investigate its quench behaviour. The quench study was therefore performed on the bus bars placed on top of the iron core.

Fig. 17 shows that the propagation velocities, measured between 1.5 and 8 kA, range from 0.7 to 25.3 m/s.

All the computations and analysis of the quench measurements performed on this magnet will be presented at ASC2008 [11].

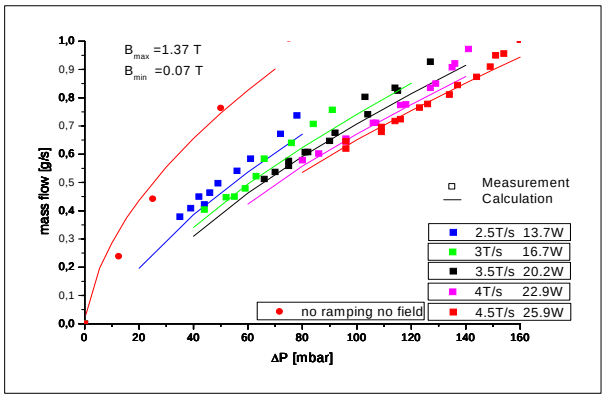

Figure 18: 4KDP6a – mass flow vs. pressure drop (2-phase flow).

Save operation of 2 phase cooled magnets requires a thorough understanding of the hydraulic behaviour and its limits. Previous studies are reported in [12] and showed that a curved single layer dipole can provide the cooling power required with the required safety margin.

As different ramp rates created different eddy current and hysteresis losses, the pressure drop of the model 4kDP6a was studied for different ramp rates and different mass flow rates and compared to calculations (see Fig. 18). The accordance allows predicting also the expected pressure drop of longer magnets as well as the mass flow rates; limited by the measurement precision as well as the required extrapolation.

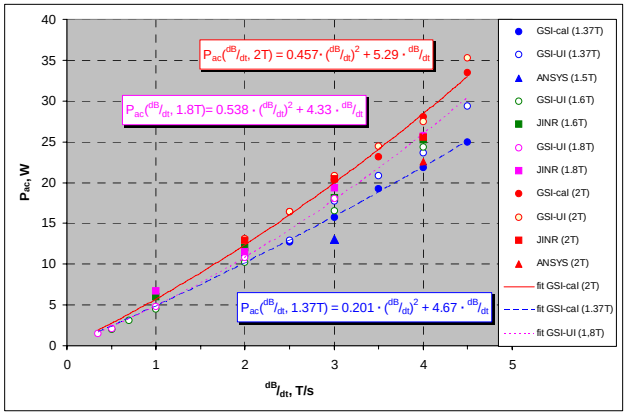

Figure 19: 4KDP6a – Calculated and measured AC Losses @ 4 K. for different ramp rates and different maximum field.

The heating power created by the eddy currents and the hysteresis was calculated using ANSYS [12, 13] and measured at JINR and at GSI (see Fig 19). One can see that the two measurement campaigns agree well and that the calculations correctly predict the magnets behaviour. Further one can clearly see that the dissipated power depends nonlinearly on the ramp rate (red curve).

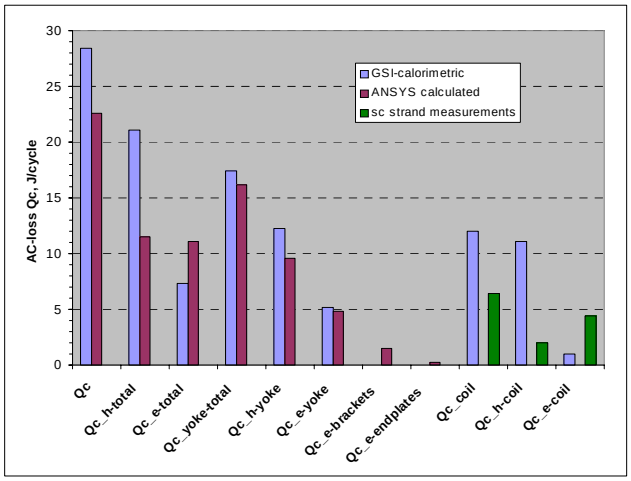

Figure 20: The heat created by the yoke and the coil. Comparison of the calorimetric measurement to the calculated data and a separate strands measurement.
Qc – total heat, Qc_h-total – total hysteresis loss,
Qy_e-total – total eddy current loss,
Qc_h-yoke – hysteresis loss in the yoke,
Qc_e-yoke – eddy current loss in the yoke,
Qc_e-brackets – eddy current loss in the brackets of magnets,
Qc_e-endplates – eddy current loss in the end-plates of magnets,
Qc_coil – the total loss in the coil,
Qc_h-coil – the hysteresis loss in the coil,
Qc_e-coil – the eddy current loss in the coil.

The calorimetric method allows separating the source of the heat impact (see Fig. 20). Further the eddy current contribution was separated by the hysteresis contribution assuming that the hysteresis contribution can be obtained extrapolating the fit curves of Fig 19 to a ramp rate of 0.

If one subtracts the strand measurements of the coil from the total heat impact measured, the measurement agrees well with the calculations. This is appropriate as the heat impact created in the coil were neglected in the model.

One can see that the larger part of the heat is created in the yoke and that the hysteresis effects are greater than the eddy current effects. The agreement is a bit worse for the subparts of the magnet. On the other hand the yoke and the coil are in thermal contact and the cooling of the yoke by the coil was not asserted separately. Thus the difference between calculation and measurement can be attributed to this unavoidable shortcoming of the experiment. All details of the magnet as well as the parameters of the materials used have to be taken into account to get numerical results matching the measurements [13].

REFERENCES

[1] FAIR – Technical Design Reports 2008

[2] A. Stafiniak, E. Floch, P. Hahne, G. Hess, M. Kauschke, F. Klos, F. Marzouki, G. Moritz, H. Mueller, M. Rebscher, P. Schnizer, C. Schroeder, G. Walter, F. Walter, H. Welker, “Commissioning of the Prototype Test Facility for Rapidly-Cycling Superconducting Magnets for FAIR”, ASC2007, August 27-31, 2007, Philadelphia, PA, USA, IEEE Trans. Appl. Superconductivity, June 2008 Volume 18, No 2, pages 1625-1628.

[3] A. Stafiniak, D. Kosobudzki, “Metrological analysis of AC losses measurement utilizing V-I method”. accepted for ASC2008.

[4] P. Schnizer et al. "Magnetic Field Characteristics of a SIS 100 Full Size Dipole", Presented at 12th European Particle Accelerator Conference, Genova 2008

[5] P. Schnizer et. al. "Superferric rapidly cycling magnets: Optimized Field Design and measurement", this publication

[6] P. Schnizer et. al. "A mole for measuring pulsed superconducting Magnets", IEEE Trans. Appl. Supercon. 18, 2008, pp 1648-1651

[7] M. N. Wilson et al, “Measured and Calculated Losses in Model Dipole for GSI´s Heavy Ion Synchrotron”, IEEE Trans. Appl. Supercon, 14,2, 2004 pp. 306-309.

[8] G. Moritz et al, “Recent Test Results of the Fast-Pulsed 4 T Cosθ Dipole GSI 001”, Proceedings of the Particle Accelerator Conference, 2005, pp.683-685

[9] M. N. Wilson et al, “Cored Rutherford Cables for the GSI Fast Ramping Synchrotron”, IEEE Trans. Appl. Supercon., 13,2, 2003, pp.1704-1709

[10] A. Stafiniak, C. Schroeder, E. Floch, F. Marzouki, F. Walter, “The GSI cryogenic test facility - measurement equipment and first experience gained on superconducting prototype magnets of the FAIR project”. Accepted for ASC2008.

[11] E.Floch, A. Stafiniak, F. Marzouki, F. Walter, C. Schroeder, H. Mueller, H. Leibrock, E. Fischer, G. Moritz, “Quench study of first SIS100 dipole prototype”. Accepted for ASC2008.

[12] E. Fischer, H. G. Khodzhibagiyan, A. D. Kovalenko, Full Size Model Magnets for the FAIR SIS 100 Synchrotron" IEEE Trans. on Appl. Supercon., 18, 2008 pp. 260-263

[13] E.Fischer, R. Kurnishov, and P. Shcherbakov, "Finite element calculations on detailed 3D models for the superferric main magnets of the FAIR SIS100 synchrotron", Cryogenics, 47, 583--594, 2007.

SUPERFERRIC RAPIDLY CYCLING MAGNETS OPTIMIZED FIELD DESIGN AND MEASUREMENT *

P. Schnizer†, E. Fischer, H.R. Kieswetter, T. Knapp, T. Mack GSI, Darmstadt, Germany
B. Schnizer, TUG, Graz, Austria
P. Akishin, JINR, Dubna, Russia
R. Kurnyshov, Elektroplant, Moscow, Russia
P. Shcherbakov, IHEP, Protvino, Russia
G. Sikler, W. Walter, BNG, Würzburg, Germany

Abstract

FAIR will feature two superconducting fast ramped synchrotrons. The dipole magnets for one of them, SIS 100, have been designed and full size magnets were built. The properties of the magnetic field were analysed using OPERA (for DC operation) and ANSYS for dynamic calculations. Elliptic multipoles fulfilling the Laplace Equation in plane elliptic coordinates describe the field within the whole aperture consistently within a single expansion. Further circular multipoles, valid within the ellipse, can be calculated analytically from the elliptic multipoles. The advantage of this data representation is illustrated on the FEM calculation performed for SIS 100 dipoles and quadrupoles currently foreseen for the machine.

INTRODUCTION

The Facility of Proton and Iron Research (FAIR) will construct a set of accelerators and storage rings at GSI. The SIS 100 synchrotron, the core component uses superferric magnets, operated at 4 T/s and 1.9 T maximum field. The coil of these magnets use the Nuclotron type cable, where superconducting wires are wrapped around a NiCr tube cooled by a forced two phase Helium flow. The whole concept of the SIS 100 follows the JINR/Nuclotron design, but used the opportunity of the second generation machine to improve various parameters. These include: the loss per magnet, improved field quality and thorough investigation using commercial Finite Element Codes [1]. The first SIS 100 full size dipole was produced last year and is ready for testing (see Fig. 1).

Conventional magnets found in accelerators provide typically a rectangular aperture and for accelerators of small circumference (up to a radius of a few tens of meter) these are also of curved shape. These magnets were typically measured using search coil probes. As these SIS 100 synchrotron magnets are housed in a interconnected cryostat, introducing additional magnetic elements requires to warm up the machine, cut the connections, and reweld them afterwards as well as a cooling them down again. Therefore the field properties have to be fully understood right from the beginning and a sufficently accurate and concise field description is required.

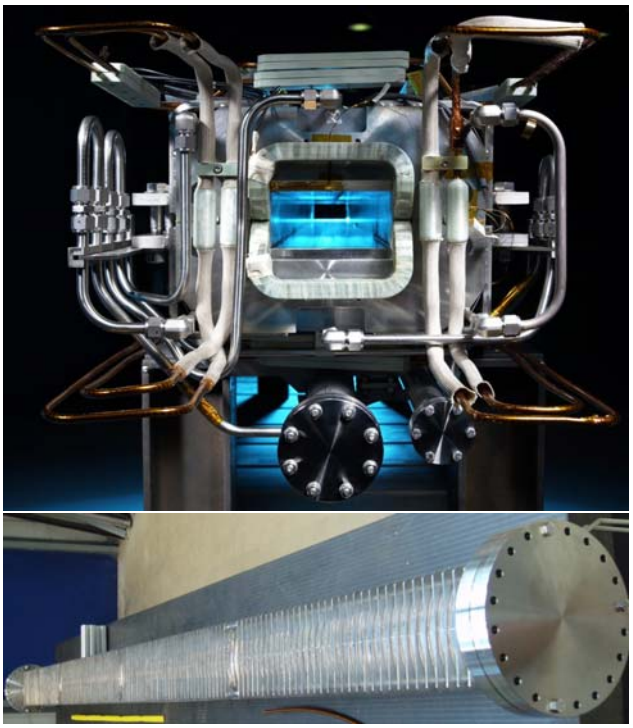

Figure 1: The first SIS 100 full size dipole (top) and the vacuum chamber (bottom).

A common type of such a description is an expansion in plane circular multipoles [2]. We generalized the concept by introducing plane elliptic multipoles [3, 4] as particular solutions of the potential equation in elliptical coordinates. The complete set of basis function needed for an expansion of an arbitrary solution is only a true subset of all these solutions. The advantage is that the reference curve is an ellipse accomodated to the rectangular transverse gap cross section, which covers a larger area than that of a possible reference circle. This expansion prooved to be superior to the circular expansion. A method to extract the elliptic expansion coefficients from experimental data acquired by rotating coils has been proposed and tested numerically[4].

As the SIS 100 dipoles are curved we started to investigate this question by another generalization defining plane

* This work is supported by the EU FP6 Design Study (contract 515873 - DIRAC secondary beams)
† p.schnizer@gsi.de

toroidal multipoles. These are again particular solutions of the potential equation in local toroidal coordinates. With the separation method analytical solutions in these coordinates can be calculated approximately using only power series expansions in the inverse aspect ratio (= the fraction minor/larger radius), cf. eq.(11). This method is well-known in the microwave theory for curved waveguides [5]. The multipole solutions so obtained show very clearly the effects of the curvature and their magnitude, which is of the order of the inverse aspect ratio.

THEORY

The SIS 100 magnets provide an elliptic aperture and the dipoles are curved to follow the beam sagitta. For a thorough understanding of the measurement a solution of $\Delta\Phi = 0$ is required.

Circular Multipoles

The two field components B_x, B_y of a plane irrotational source-free static magnetic field are combined to a complex field $\mathbf{B} := B_y + iB_x$ depending on the complex variable $\mathbf{z} := r\, e^{i\theta}$; they are expanded in circular multipoles

$$\mathbf{B} = \sum_{m=0}^{M} \mathbf{C}_m\, (r/R_{Ref})^m\, e^{im\theta} \quad (1)$$

$$\mathbf{C}_m = \frac{1}{2\pi}\int_{-\pi}^{\pi} \mathbf{B}(\mathbf{z} = R_{Ref}\, e^{-im\theta})\, e^{-im\theta} d\theta, \quad (2)$$

with M the number of multipoles used. The expansion coefficients may be computed from field values given along the reference circle $r = R_{Ref}$ as indicated in eq.(2). The US notation is used within this paper (0 ... dipole, 1 ... quadrupole, ...) as the following calculations are then more straight forward. The coefficients $\mathbf{C}_m$ can be recalculated using

$$b_n + ia_n = \mathbf{c_n} = \mathbf{C_m}/\mathbf{C_{main}} \quad (3)$$

with C_{main} the main harmonic of the magnet. The b_n's and a_n's are dimensionless constants.

Elliptic Multipoles

A reference ellipse with semi-axes $a > b$ accomodated to a rechtangular gap covers a larger domain than a reference circle of radius R_{Ref}. The excentricity e specifies the corresponding elliptic coordinates η, ψ, [6, 4, 3]

$$x = e\cosh\eta\cos\psi, \quad 0 \le \eta \le \eta_0 < \infty; \quad (4)$$

$$y = e\sinh\eta\sin\psi, \quad -\pi \le \psi \le \pi. \quad (5)$$

$\eta_0 = \tanh^{-1}(b/a)$ gives the reference ellipse. A plane irrotational source-free field is expanded w.r.t. the complete system of elliptic multipoles as

$$\mathbf{B} = \sum_{n=0}^{M} \mathbf{E}_n\, \cosh[n(\eta + i\psi)]/\cosh(n\eta_0),$$

$$\mathbf{E}_n = \frac{1}{\pi}\int_{-\pi}^{\pi} \mathbf{B}(\mathbf{z} = e\cosh(\eta_0 + i\psi))\, \cos(n\psi)\, d\psi. \quad (6)$$

The expansion coefficients $\mathbf{E}_n$ may be computed from field values given along the reference ellipse (6).

The two sets of expansion coefficients belonging to the same $\mathbf{B}$ may be converted to each other using

$$\mathbf{E}_n/\cosh(n\eta_0) = \sum_{m=0}^{M} \mathbf{C}_m\, \beta^m\, d_{mn}, \quad (7)$$

$$2\,\mathbf{C}_m\, \beta^m = \sum_{n=0}^{M} \mathbf{E}_n/\cosh(n\eta_0)\, c_{nm} \quad (8)$$

with $\beta := e/(2R_{Ref})$. The transformation matrices $D = (d_{mn})$ and $C = (c_{nm}) = D^{-1}$ are given by

$$d_{mn} = [1 + (-1)^{m+k}] \begin{pmatrix} m \\ (m-k)/2 \end{pmatrix}. \quad (9)$$

The elements of C may be found by symbolic or numeric inversion of D; closed expressions have been given elsewhere [3]; in [7] they are computed by recurrences. In this paper the coefficients b_n and a_n are given in units i.e. $1\,unit = 100\,ppm$ at a R_{Ref} of $40\,mm$. We chose this free parameter such that the relative allowed harmonics b_n can then be represented as convenient numbers in the order of 1 to 10. Using (6) the field can be interpolated with sufficient accuracy within an ellipse with half axes a, b.

Toroidal Multipoles

In a curved magnet a torus segment ($|\varphi| \le \varphi_0$) is introduced as a reference volume. Dimensionless local toroidal coordinates are defined by

$$X + iY = R_C\, h\, e^{i\varphi},\ Z = R_{Ref}\sin\vartheta,\ h = 1 + \epsilon\rho\cos\vartheta. \quad (10)$$

R_{Ref} (R_C) are the minor (major) radii of the torus.

$$\epsilon := R_{Ref}/R_C \quad (11)$$

is the inverse aspect ratio, on which the curvature effects depends. As $\epsilon << 1$ working with power series in ϵ is a useful approximation scheme. The centre of the fundamental Cartesian system (X, Y, Z) coincides with that of the torus, Z is normal to the equatorial plane. The quasi-radius $R_{Ref} \cdot \rho$, $0 \le \rho \le 1$, is the normal distance of the field point from the centre circle; the poloidal angle $-\pi \le \vartheta \le \pi$, is around the centre circle; the toroidal angle $-\pi \le \varphi \le \pi$ agrees with the common azimuth, cf. [8], [5]. Only toroidally uniform fields are considered; their field components B_ρ, B_θ are confined to the planes φ = const. and are independent of φ.

The potential equation independent of φ is solved by an approximate R-separation. Thus the approximate multipole solution for the potential is (m = integer)

$$\Phi_m = \rho^{|m|}\, e^{im\vartheta} - \frac{\epsilon}{4}\,\rho^{|m|+1}\big(e^{i(m+1)\vartheta} + e^{i(m-1)\vartheta}\big) + O(\epsilon^2). \quad (12)$$

So the curvature adds just the two adjacent multipoles; the magnitude of these admixture is not larger than $\epsilon/2$. Expressions for the corresponding magnetic fields have been derived as well as their orthogonality relations. This permits us to give the field expansion w.r.t. the basis fields and to calculate the expansion coefficients for a field given along the reference circle. A report will be published.

Tests

The formulae described above were used to analyse all the magnet data calculated for the SIS 100 main magnet designs. The field quality was calculated for the **C**urved **S**ingle **L**ayer **D**ipole with **8** turns [4, 9, 10, 11], the dipole design chosen for the main dipole for the SIS 100 machine of FAIR. The field quality of this magnet is calculated by

$$\mathbf{\Delta B(z)} = (\mathbf{B(z)} - \mathbf{B(0)}/\,\mathbf{B(0)} \cdot\ 10^4\,. \qquad (13)$$

They are now applied to fields to demonstrate that all these steps are necessary to interpolate the field within the ellipse with a precision of better than the maximum tolerable field deviation of 600 ppm or 6 units (1 unit corresponds to 100 ppm). The original distribution is given in Fig. 2(a) at a current of $873kA$ yielding a field of $\approx\ 0.13T$. The field was taken along the ellipse and the elliptic multipoles were calculated as defined in (6). Using the first 20 coefficients the field was interpolated within the aperture (see Fig. 2(b)). The naked eye can not see any difference to the original data (Fig. 2(a)). The original field was subtracted from the interpolated one. One can see from Fig. 2(c) that this difference is well below half a unit and thus sufficiently precise. Normally circular multipoles are used. So we calculated them using a Fourier Transform of the data along a circle. Again the interpolation data was calculated (see Fig. 2(g)) and the difference to the original data (see Fig. 2(d)) using the first 15 coefficients. One can see that the interpolation works well within the circle but outside the circle soon the errors get unacceptably large. The difference outside of the circle is even larger if more coefficients are used. At last the circular multipoles were calculated from the elliptic ones as described in (9) (see Fig. 2(e) for the interpolation and Fig. 2(f)) for the difference). One can see that contrary to the circular interpolation, this interpolation works even outside the circle and within the whole ellipse.

PRODUCTION REVIEW

The magnetic field quality is defined by the yokes geometry (in the centre) and by the yokes end shape and the coils' position (in the ends). Thus all magnets (108 dipoles) must match each other and the temporal evolution of their field on each cycle. This will be guarantied by a very reliable mechanical fixture of the superconducting cable, especially in the head parts of the coil.

A cable machine was dedicated to produce the Nuclotron-type cable, which was optimised to guarantee and maintain constant cable parameters. This cable is wound to half coils of $4 \cdot 2$ windings in two layers and is supported by a precisely machined surrounding mechanical fixture made of glass-fibre reinforced plastic (GRP). The poles are finally shaped in a combined heat pressure treatment with an accuracy of the outside dimensions $< 0.05mm$ (also in the coil ends) and thus the superconducting wires positions is predominantly defined by the manufacturing tolerances of the GRP structural elements ($< 0.1mm$).

The soft-magnetic iron yoke of this dipole is made of two half shells which are bolted together. This allows to insert and remove the beam pipe and the coils. The yoke laminations are of "electrical sheet metal" with a thickness of 1 mm. They were laser-cut and stacked to sub-packs of approximately 150 mm length. The laminations were covered with adhesive which is activated and hardening when heated. The sub-packs are glued together in a furnace under pressure to form a solid compound for further assembly. Each of these packs show a packing factor of 99.5 %. (Smaller packing factors can be reached controlling the pressure during the backing process). The sub-packs are set up in a string along with the two specially shaped end-packs and a compensating pack to reach the required magnet length. On the outside corners of the yoke cooling tubes and angular sheets of stainless steel are placed. The stainless steel- angels form an outside frame for the yoke. They are TIG-welded at various positions to each sub-pack along the whole length of the yoke. The heat introduced during the welding process can distort the shape, thus the welding pattern was optimised to keep the distortion small and the evenness of the relevant yoke surfaces within the tolerance of 0.3 mm (over the whole length of 2.8m).

EXPECTED FIELD QUALITY

Static

Many different models were built and investigated in 2 and 3 dimensions to obtain a magnetic field design providing a field quality according to the specifications. The design to prefer was chosen based on the circular multipoles calculated from the elliptic ones. A side to that the influence of the packing factor was studied for the dipole as foreseen for SIS 100 (see Fig. 3, gap height was 66 mm for this study). One can see that the influence of the packing factor on the field quality is rather small up to a field of $\approx 2.1\,T$ (roughly half a unit for b_3 and 0.1 unit for b_5) and less than 0.1 units at injection.

Dynamic

As the SIS 100 machine is designed to run with an frequency of roughly 1 Hz, the dipole magnets must be ramped from the injection field of $\approx\ 0.23\,T$ to $\approx\ 1.9\,T$ in the order of half a second. The ramping field generates eddy currents in different parts of the magnet [1] and also in the vacuum chamber [12]. The same model as in [12] was used again to calculate the magnetic field using AN-

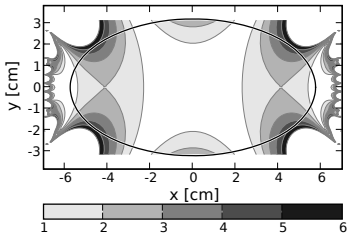

(a) Deviation of original data from a pure dipole field

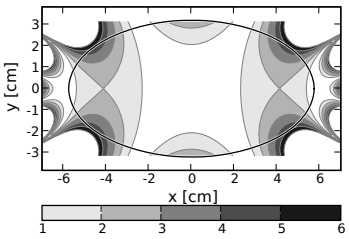

(b) Deviation of field computed by elliptic expansion from dipole field

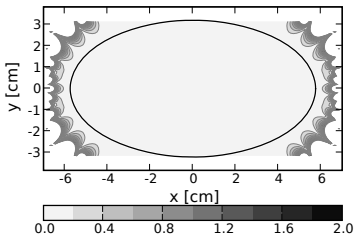

(c) Difference between original field data and those computed by elliptic expansion

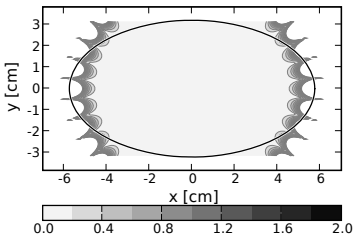

(d) Difference between original field data and those computed by circular expansion

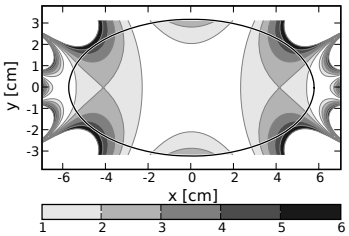

(e) Deviation of field computed by circular expansion with circular coefficients converted from elliptic coefficients, eq.(9)

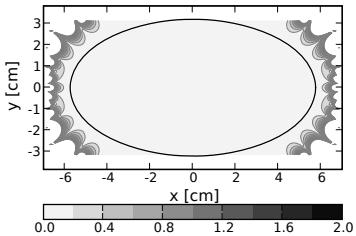

(f) Deviation of original field data from data computed as described at left

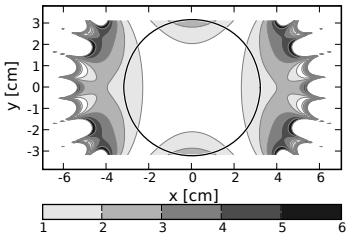

(g) Deviation of field computed by circular expansion from dipole field

Figure 2: Test of the interpolation for the CSLD8b at a current of $873\,kA$ and a field of $\approx 0.13\,T$. The field B_y in the aperture is plotted. The gray indicates the absolute value of the deviation (in units). The original data are given on top. The upper row shows the data as reconstructed using the interpolation and the lower columns shows the absolute value of the difference between the reconstructed and the original data.

SYS (see Fig. 4) in the "2D" section of the magnet. The model was evaluated for static operation without the vacuum chamber, for static operation with the vacuum chamber and for the dynamic operation with the vacuum chamber (see Fig. 5 to Fig. 8). One can see that the field does not change in the longitudinal position, but that at injection the eddy currents create a distortion at least twice larger than the field the magnet provides (see also Fig. 9). At intermediate field levels (see Fig. 6) the relative contribution of the eddy currents is comparable to the static ones. Above 1.8 Tesla the iron starts to saturate. Thus the field quality is dominated by saturation levels above this value. The elliptic multipoles and the circular ones derived from the elliptic ones [3, 13] were calculated and the field was reconstructed using them. Fig. 9 demonstrates that the interpolation represents the original field with sufficient accuracy. The multipoles along the load line on the ramp up are given in Fig. 10.

One can see that the vacuum chamber adds the largest distortion at the injection field level, as the effect only depends on $\mathrm{d}B/\mathrm{d}t$ and thus is constant for constant ramp rate, whereas the other artefacts contributions increase with increasing field level.

MEASUREMENT

Rotating Coils in Elliptic apertures

Search coils are normally used to measure dipoles with rectangular apertures. These, however, are useful instruments when they can be moved on perfectly machined surfaces (e.g. pole shoes). Rotating coils have been proposed as a work horse for measuring the synchrotrons at GSI, as

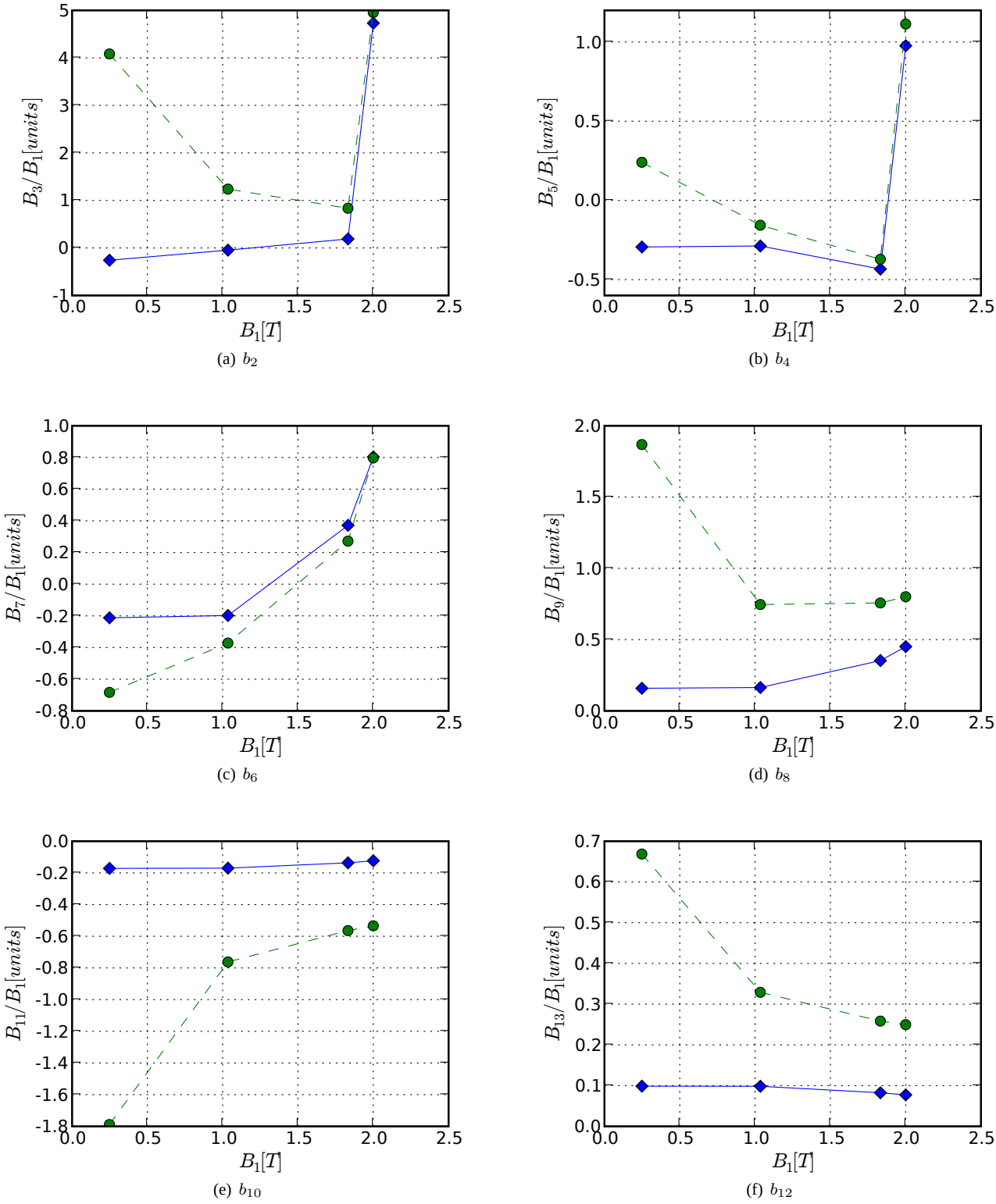

(a) b_2 (b) b_4 (c) b_6 (d) b_8 (e) b_{10} (f) b_{12}

Figure 10: The field quality for the BNG magnet. The solid blue line represents the **static** field **without** vacuum chamber, the green dashed line represents the **dynamic** field **with** vacuum chamber at a ramp rate of $\approx 4\,T/s$. One can see that at injection the field is considerably distorted due to eddy current effects.

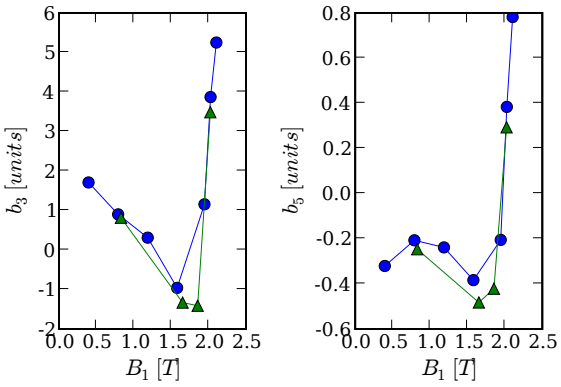

Figure 3: Relative 2D harmonics of the static field quality versus the main field for different packing factors (circles 98 %, tripods 100 %). The difference between the lines is not large compared to a maximum tolerable field error of 6 units.

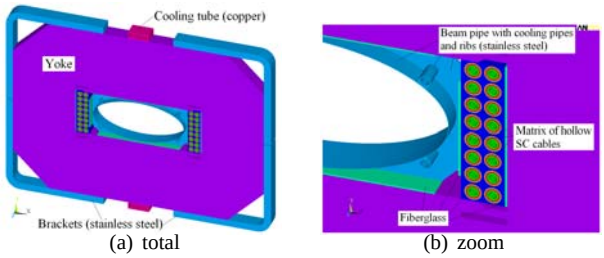

(a) total (b) zoom

Figure 4: The model of the middle section of the dipole magnet and the vacuum chamber. The vacuum chamber is supported by ribs and equiped with separate cooling tubes.

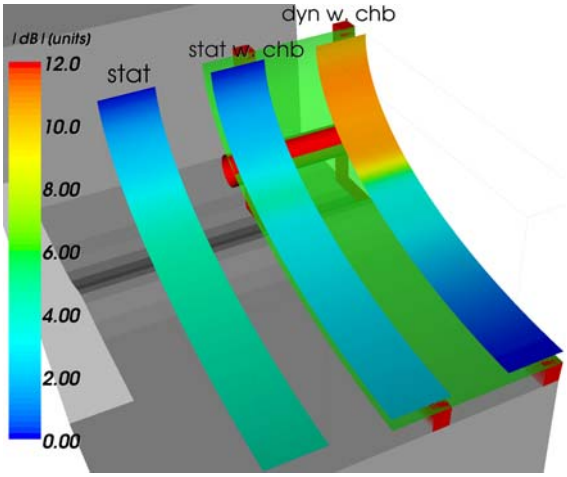

Figure 5: The field deviation in units (1 unit = 100 ppm) at injection is plotted along the ellipse. left → the static field without vacuum chamber, middle → static field with the vacuum chamber, right → the dynamic field with the vacuum chamber. The quater yoke is indicated in gray, the vacuum chamber in green and in red the supporting ribs and cooling tube. The eddy currents create the main distortion.

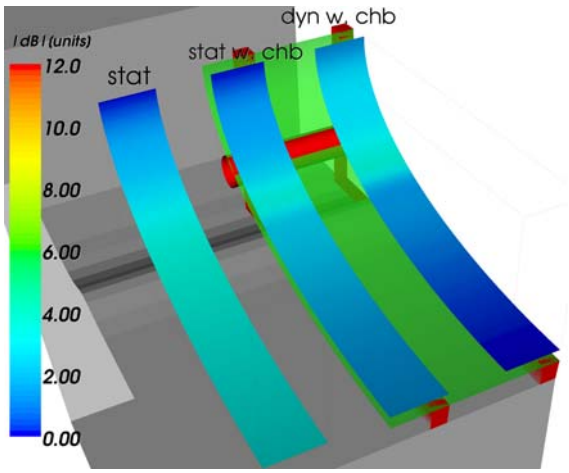

Figure 6: The field quality at a current of roughly $1.04T$ at a time of $250\,ms$. The maximum deviation is about 5 units for all, but the dynamic one has a higher variation (i.e. additional multipoles)

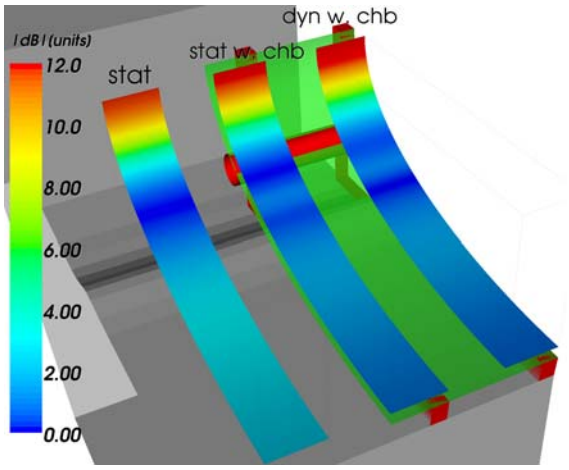

Figure 7: The field quality at a current of roughly $1.832T$ at a time of $450\,ms$. One can see that the saturation is the main reason for the field detioriation, but the eddy currents generate higher order multipoles and it is a factor 3 (dynamic case) to 10 (static case) higher than at injection.

they provide the field within their rotation radius. This does not cover the whole aperture, and thus they must be placed laterally at different positions. The measurements can then be used to calculate the field on the ellipse using appropriate weights for the different measurements [4]. The circular multipoles are then calculated as described by (9).

Ramping field

Rotating coils are typically operated at rotation speeds of roughly one revolution per second measuring the flux at different angular position (≈ 100 positions). This approach is not appropriate for SIS 100, as the machine cycle time is also in the order of one second. Therefore the "step by step" method is used. Here the coil probe is placed at some

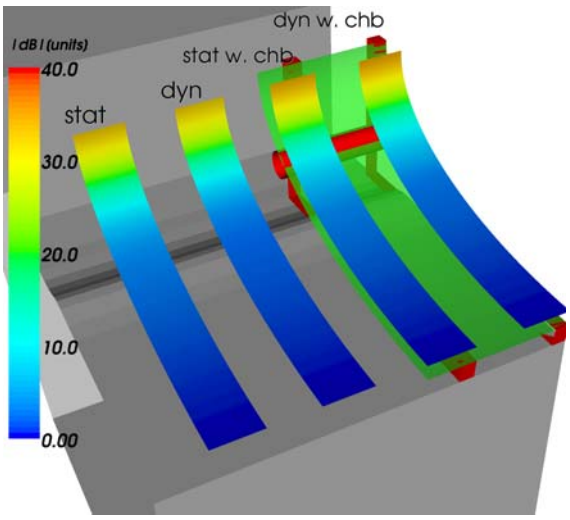

Figure 8: The field quality at a current of roughly $2.00T$ at a time of $500\,ms$. The field quality in mainly determined by the saturation of the iron. The effect of the vaccuum chamber and the effect of the eddy currents does not contribute significantly.

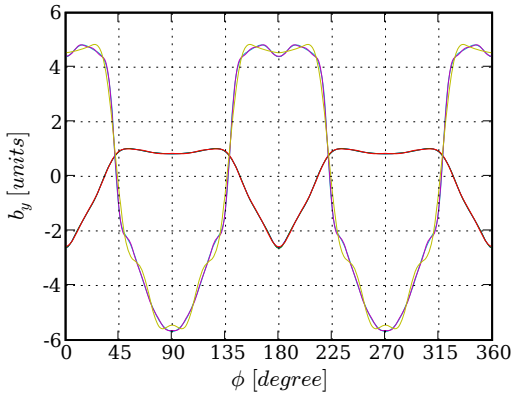

Figure 9: The field B_y at injection versus the angle ϕ around the ellipse. The static field (variation $\approx$ 2 units) versus the dynamic field (variation $\approx$ 10 units). The data calculated with ANSYS are plotted next to the interpolation using the elliptic multipoles and the circular multipoles derived from the elliptic ones.

start angle θ_0. The magnet is then pulsed once and the field is measured. Then the coil is advanced by some angle $\delta\theta = 2\pi/m$. The magnet is pulsed again and the field measured. This is performed until the start angle is reached again. Now the data of the different pulses are resorted for each point in time, and then the multipoles are calculated [14].

Using a "compensating coil probe array", which suppresses the voltage induced by the main harmonic by a factor of 100 – 1000, one can not only reduces the required electronics accuracy but also reduces the artifacts created by angular positioning errors on higher order harmonics. This approach was tested on the magnet "GSI 001" using a simple test setup and comparing the results to the measurements obtained by A. Jain at BNL [15].

CONCLUSION

The first SIS 100 full size dipole has been delivered and is made ready for testing at GSI. Elliptic multipole expansions for a plane irrotational, source-free, static magnetic field were demonstrated in a domain bounded by an ellipse as reference curve similar as for circular multipoles within a circle. In both cases the expansion coefficients of the complex field can be computed from the field given along the reference curve. The ellipse covers a larger area in the gap and thus the convergence properties are better for the elliptic expansion. The calculated static and dynamic field quality were presented. The 2D static field quality is mainly determined by the imperfections of the magnets geometry whereas the dynamic field quality is considerably affected by the eddy currents in the vacuum chamber. This magnet will be tested this summer, measured magnetically and the results presented here will be checked with the measurement data. A second full size dipole is under construction at JINR / Dubna and will be tested there soon and afterwards retested at GSI [16].

REFERENCES

[1] E. Fischer, R. Kurnishov, and Shcherbakov P., "Finite element calculations on detailed 3D models for the superferric main magnets of the FAIR SIS100 synchrotron", *Cryogenics*, 47:583–594, 2007.

[2] A. K. Jain, "Basic theory of magnets". CERN 98-05, European Organization for Nuclear Research, Geneva 1998. pp.1 - 26.

[3] P. Schnizer, B. Schnizer, P. Akishin, E. Fischer, "Field representations for elliptic apertures" February 8th, 2007. GSI Internal Communication. Revised January 16th, 2008.

[4] P. Schnizer, B. Schnizer, P. Akishin, E. Fischer, "Magnetic field analysis for supperferric accelerator magnets using elliptic multipoles and its advantages". 20-th Magnet Technology Conference, August 27-30, 2007, Philadelphia, Pa., USA IEEE Trans. on Applied Superconductivity, Volume 18 , 2008

[5] L. Lewin, D.C. Chang, E.F. Kuester, Electromagnetic Waves and Curved Structures. IEE Electromagnetic wave series 2, 1977.

[6] P. Moon, D. E. Spencer, Field theory handbook: Including coordinate systems, differential equations and their solutions. Springer, 1988. pp. 112 - 115, Fig.4.04.

[7] F. R. Peña and G. Franchetti, Elliptic and circular representation of the magnetic field for SIS 100. GSI Acc-Note-2008.

[8] W.D. D'haeseleer, W.N.G. Hitchon, J.D. Callen, J.L. Shohet, Flux coordinates and magnetic field structure. Springer, 1990.

[9] E. Fischer, H. G. Khodzhibagiyan, "SIS 100 dipole alternatives" Technical Report, GSI, 2007

[10] E. Fischer, H. G. Khodzhibagiyan, A. D. Kovalenko, "Full Size Model Magnets for the FAIR SIS 100 Synchrotron" 20-th Magnet Technology Conference, August 27-30, 2007, Philadelphia, Pa., USA IEEE Trans. on Applied Superconductivity, Volume 18, 2008

[11] P. Akishin, E. Fischer, P. Schnizer, "A single layer dipole for SIS 100", Technical Report, GSI, July 2007

[12] E. Fischer, R. Kurnyshov, and P. Shcherbakov, "Analysis of coupled electromagnetic-thermal effects in superconducting accelerator magnets", In *8^{th} European Conference On Applied Superconductivity, 16 - 20 September 2007, Brussels, Belgium*, volume 97. IOP Journal of Physics: Conference Series, 2008.

[13] P. Schnizer, B. Schnizer, P. Akishin, and E. Fischer, "Theoretical Field Analysis for Superferric Accelerator Magnets Using Elliptic Multipoles and its Advantages" Presented at 12^{th} European Particle Accelerator Conference, Genova, 2008

[14] P. Schnizer et. al "A mole for measuring pulsed superconducting magnets" 20-th Magnet Technology Conference, August 27-30, 2007, Philadelphia, Pa., USA IEEE Trans. on Applied Superconductivity, Volume 18, 2008

[15] A. Jain, G. Ganetis, W. Louie, A. Marone, R. Thomas, and P. Wanderer, "Field quality measurements at high ramp rates in a prototype dipole for the FAIR project," 20-th Magnet Technology Conference, August 27-30, 2007, Philadelphia, Pa., USA IEEE Trans. on Applied Superconductivity, Volume 18, 2008

[16] A. D. Kovalenko et. al, "Full size model magnets for heavy ion superconducting synchrotron SIS100 at GSI: status of manufacturing and test at JINR", Presented at 12^{th} European Particle Accelerator Conference, Genova, 2008